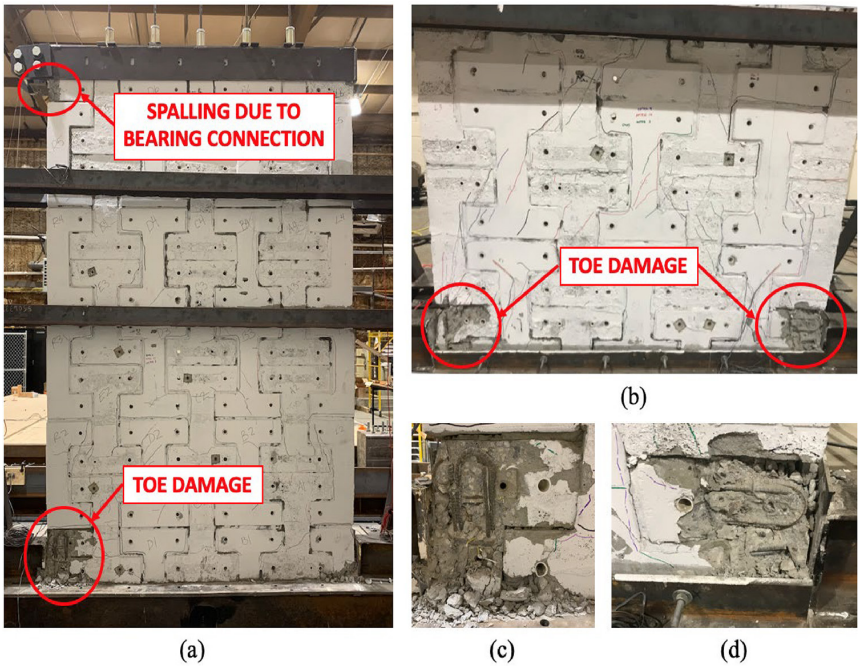
V. 121, NO. 5
SEPTEMBER 2024

ACI STRUCTURAL JOURNAL

A JOURNAL OF THE AMERICAN CONCRETE INSTITUTE



American Concrete Institute

CONTENTS

Editorial Board
Michael Kreger, Editor-in-Chief
University of Alabama
Catherine French
University of Minnesota
Mary Beth Hueste
Texas A&M University
David Sanders
Iowa State University
Gustavo Parra-Montesinos
University of Wisconsin–Madison

Board of Direction

President
Michael J. Paul

Vice Presidents
Maria Juenger
Scott M. Anderson

Directors
Corina-Maria Aldea
Oscar R. Antommattei
Peter Barlow
Arturo Gaytan Covarrubias
James H. Hanson
Carol Hayek
Werner K. Hellmer
Robert C. Lewis
Enrique Pasquel
Anton K. Schindler
Matthew R. Sherman
Lawrence L. Sutter

Past President Board Members
Cary S. Kopczynski
Charles K. Nmai
Antonio Nanni

Executive Vice President
Frederick H. Grubbe

Staff
Publisher
John C. Glumb

Managing Director, Engineering and Professional Development
Michael L. Tholen

Engineers
Will J. Gold
Matthew R. Senecal
Michael L. Tholen
Gregory M. Zeisler

Managing Editor
Lauren E. Mentz

Associate Editor
Kimberly K. Olesky

Editors
Erin N. Azzopardi
Lauren C. Brown
Kaitlyn J. Dobberteen
Tiesha Elam
Angela R. Noelker
Kelli R. Slayden

ACI STRUCTURAL JOURNAL

SEPTEMBER 2024, V. 121, NO. 5

A JOURNAL OF THE AMERICAN CONCRETE INSTITUTE
AN INTERNATIONAL TECHNICAL SOCIETY

3 **Steel-/Carbon Fiber-Reinforced Polymer-Prestressed Concrete Girders in Simulated Hydrocarbon Fire**, by Jun Wang and Yail J. Kim

19 **Strength and Serviceability of Shear-Critical Post-Tensioned Girders**, by Sangyoung Han, Jarrod Zaborac, Jongkwon Choi, Anca C. Ferche, and Oguzhan Bayrak

37 **Cyclic Test of Precast Reinforced Concrete Tessellated Shear Wall**, by G. F. Crocker, B. E. Ross, M. C. Kleiss, P. Okumus, and N. E. Khorasani

51 **Theoretical Model for Calculating Shear Strength of Fiber-Reinforced Polymer-Reinforced Concrete Beams**, by Jahanzaib and Shamim A. Sheikh

65 **Assessment of Use of Steel Bars with Unintended High Strength in Tied Columns**, by Muhammad Masood Rafi and Muhammad Saad Khan

77 **Experimental Study on Scale Effect of Eccentrically Compressed Reinforced Concrete Columns Strengthened with Carbon Fiber-Reinforced Polymer**, by Jianhui Si, Yuan Zhou, Zhaobao Zeng, Kai Li, Jiannan Hu, Zewei Liu, and Xinchao Ding

89 **Study on Seismic Damage Model of Fly Ash Foamed Concrete Wall**, by Yunhong Hao, Hongze Wang, Yupeng Zhao, Chakelehan, and Yong Shi

99 **Failure Analysis of Reinforcing Semi-Grouted Sleeve Node Connection**, by Jingshuang Zhang, Ruihan Qin, Fei Lv, Yonghua Shu, and Yanqing Wu

109 **Prestressing Analysis of Large Three-Dimensional Systems and Prestress Management**, by Hiroshi Nishio, Yosuke Yagi, and Yasuaki Ishikawa

123 **Dowel Bar Contribution to Bond Deterioration under Cyclic Loading**, by Edom A. Zewdie, Chikako Fujiyama, and Koichi Maekawa

133 **Effect of Mechanical Splice to Seismic Performance of Precast Column-Foundation Connection**, by Wei Zhang and Deuckhang Lee

147 **Uniaxial Compressive Behavior of Fiber-Reinforced Rubberized Recycled Concrete Column**, by Md. Shahjalal, Kamrul Islam, Mohammad Tiznobaik, M. Shahria Alam, and Raquib Ahsan

161 **Tensile Behavior of Small Screw Anchors under Cyclic Crack Openings**, by Chandani Chandra Neupane, Jessey Lee, Tilak Pokharel, Hing-Ho Tsang, and Emad Gad

Contents continued on next page

ACI Structural Journal
© 2024 American Concrete Institute. All rights reserved.

This material may not be reproduced or copied, in whole or in part, in any form or by any means, including making copies by any photo process, or by electronic or mechanical device, printed, written, graphic, or oral, or recording for sound or visual reproduction for use in any knowledge or retrieval system or device, without the written consent of ACI. This material may not be used by data mining, robots, screen scraping, or similar data gathering and extraction tools such as artificial intelligence ("AI") for purposes of developing or training a machine learning or AI model, conducting computer analysis or creating derivatives of this material, without the written consent of ACI.

American Concrete Institute®, ACI®, Always Advancing®, *ACI Structural Journal®*, and *ACI Materials Journal®* are registered trademarks of American Concrete Institute.

The *ACI Structural Journal* (ISSN 0889-3241) is published bimonthly by the American Concrete Institute. Publication office: 38800 Country Club Drive, Farmington Hills, MI 48331. Periodicals postage paid at Farmington, MI, and at additional mailing offices. Subscription rates: $199 per year, payable in advance. POSTMASTER: Send address changes to: *ACI Structural Journal*, 38800 Country Club Drive, Farmington Hills, MI 48331.

Canadian GST: R 1226213149.

Direct correspondence to 38800 Country Club Drive, Farmington Hills, MI 48331. Telephone: +1.248.848.3700. Facsimile (FAX): +1.248.848.3701. **Website: http://www.concrete.org.**

PRINTED WITH SOY INK®

CONTENTS

175 **Numerical Modeling of Squat Reinforced Concrete Shear Walls with High-Strength Materials**, by Robert D. Devine, Steven M. Barbachyn, Yahya C. Kurama, and Ashley P. Thrall

189 **Thermomechanical Hysteresis of Reinforced Concrete Beams Retrofitted with Carbon Fiber-Reinforced Polymer and Ultra-High-Performance Concrete**, by Yail J. Kim and Ibrahim Bumadian

203 **Effectiveness of Carbon Fiber-Reinforced Polymer Sheets for Torsional Strengthening of Reinforced Concrete Beams**, by Yail J. Kim and Abdulaziz Alqurashi

MEETINGS

SEPTEMBER 2024

4-6—7th International Conference on Smart Monitoring, Assessment and Rehabilitation of Civil Structures (SMAR 2024), Salerno, Italy, www.smar2024.org

4-6—4th RILEM International Conference on Concrete and Digital Fabrication (Digital Concrete 2024), Munich, Germany, https://digital-concrete.com/frontend/index.php

11-13—4th International Conference on Concrete Sustainability (*fib* ICCS2024), Guimarães, Portugal, https://fibiccs.org

12-13—2nd Cal Poly Pomona Civil Engineering Conference, Pomona, CA, www.cpp.edu/engineering/ce/events/articles/second-conference.shtml

15-18—BEFIB 2024 – XI International Symposium on Fiber Reinforced Concrete, Dresden, Germany, www.befib2024.org

18-21—ENLACE GDL 2024 – Encuentro Latinoamericano de Capítulos Estudiantiles ACI 2024, Zapopan, Mexico, https://linktr.ee/enlace_gdl

19—ACTS Future Concrete Construction Conference 2024 – Concrete Durability and Structural Integrity, Beirut, Lebanon, https://acts-int.com/conferences/Concrete-Durability-and-Structural-Integrity

22-25—14th Central European Congress on Concrete Engineering (CCC 2024), Mikulov, Czech Republic, www.cbsbeton.eu/en/seminars

ACI CONCRETE CONVENTION: FUTURE DATES

2024—November 3-6, Philadelphia Marriott Downtown, Philadelphia, PA
2025—March 30-April 3, Sheraton Centre Toronto Hotel, Toronto, ON, Canada
2025—Oct. 26-29, Hilton Baltimore & Marriott Baltimore Inner Harbor, Baltimore, MD

For additional information, contact:
Event Services, ACI
38800 Country Club Drive
Farmington Hills, MI 48331
Telephone: +1.248.848.3795
email: conventions@concrete.org

ON COVER: 121-S66, p. 42, Fig. 5—Photographs of damage in: (a) north side of specimen; (b) lower half of south side of specimen; (c) toe tile on north side of specimen; and (d) toe tile on south side of specimen.

Permission is granted by the American Concrete Institute for libraries and other users registered with the Copyright Clearance Center (CCC) to photocopy any article contained herein for a fee of $3.00 per copy of the article. Payments should be sent directly to the Copyright Clearance Center, 21 Congress Street, Salem, MA 01970. ISSN 0889-3241/98 $3.00. Copying done for other than personal or internal reference use without the express written permission of the American Concrete Institute is prohibited. Requests for special permission or bulk copying should be addressed to the Managing Editor, *ACI Structural Journal*, American Concrete Institute.

The Institute is not responsible for statements or opinions expressed in its publications. Institute publications are not able to, nor intend to, supplant individual training, responsibility, or judgment of the user, or the supplier, of the information presented.

Papers appearing in the *ACI Structural Journal* are reviewed according to the Institute's Publication Policy by individual experts in the subject area of the papers.

Contributions to *ACI Structural Journal*

The *ACI Structural Journal* is an open forum on concrete technology and papers related to this field are always welcome. All material submitted for possible publication must meet the requirements of the "American Concrete Institute Publication Policy" and "Author Guidelines and Submission Procedures." Prospective authors should request a copy of the Policy and Guidelines from ACI or visit ACI's website at **www.concrete.org** prior to submitting contributions.

Papers reporting research must include a statement indicating the significance of the research.

The Institute reserves the right to return, without review, contributions not meeting the requirements of the Publication Policy.

All materials conforming to the Policy requirements will be reviewed for editorial quality and technical content, and every effort will be made to put all acceptable papers into the information channel. However, potentially good papers may be returned to authors when it is not possible to publish them in a reasonable time.

Discussion

All technical material appearing in the *ACI Structural Journal* may be discussed. If the discussion is received within four months of the paper's print publication, it will appear in the issue dated ten months from this journal's date. Discussion material received after specified dates will be considered individually for publication or private response. ACI Standards published in ACI Journals for public comment have discussion due dates printed with the Standard. Discussion should be complete and ready for publication, including finished, reproducible illustrations. Discussion must be confined to the scope of the paper and meet the ACI Publication Policy.

Follow the style of the current issue. Discussions should not exceed 1800-word equivalents (illustrations and tables count as 300 words each). References should be complete. Do not repeat references cited in original paper; cite them by original number. Numbering of additional references, figures, tables, and equations should follow sequentially from the original manuscript throughout the discussion. The discusser must indicate the month, year, volume number, issue number, authors' names, and manuscript number of the original manuscript. Closures responding to a single discussion should not exceed 1800-word equivalents in length, and to multiple discussions, approximately one half of the combined lengths of all discussions. Closures are published together with the discussions.

Discuss the paper, not some new or outside work on the same subject. Use references wherever possible instead of repeating available information.

Discussion offered for publication should offer some benefit to the general reader. Discussion which does not meet this requirement will be returned or referred to the author for private reply.

Send manuscripts to:
http://mc.manuscriptcentral.com/aci
Send discussions to:
Journals.Manuscripts@concrete.org

ACI STRUCTURAL JOURNAL TECHNICAL PAPER

Title No. 121-S64

Steel-/Carbon Fiber-Reinforced Polymer-Prestressed Concrete Girders in Simulated Hydrocarbon Fire

by Jun Wang and Yail J. Kim

This paper presents the implications of a hydrocarbon fire on the behavior of bridge girders prestressed with either steel strands or carbon fiber-reinforced polymer (CFRP) tendons. Stemming from a recent bridge fire that occurred in Lakewood, CO, numerical investigations are conducted employing a computational method called agent-based modeling to understand the intricate responses of these girders under thermomechanical loading. As the convection and radiation of surroundings are transformed to conductional thermal energy, the temperature of girder concrete rises, and the internal temperature differentials dwindle over time. Thermally induced damage in the prestressing elements is a function of distance from the surface heat. When loaded without thermal distress, the moment-carrying mechanism of the steel- and CFRP-prestressed girders is analogous; however, with the presence of heat, the development of lever arms and tensile strains of the girders demonstrates palpable differences. The maximum usable strains of the steel and CFRP vary with the degree of thermal exposure, thereby dominating the load-carrying capacity of the girders. From a design perspective, no evidence is noted to distinguish the performance of the steel- and CFRP-prestressed girders under service loadings, and contrary to commonplace notion, their fire ratings are found to be comparable because of sequential heat transfer.

Keywords: bridge; carbon fiber-reinforced polymer (CFRP); fire; modeling; prestressed concrete; thermal loading.

INTRODUCTION

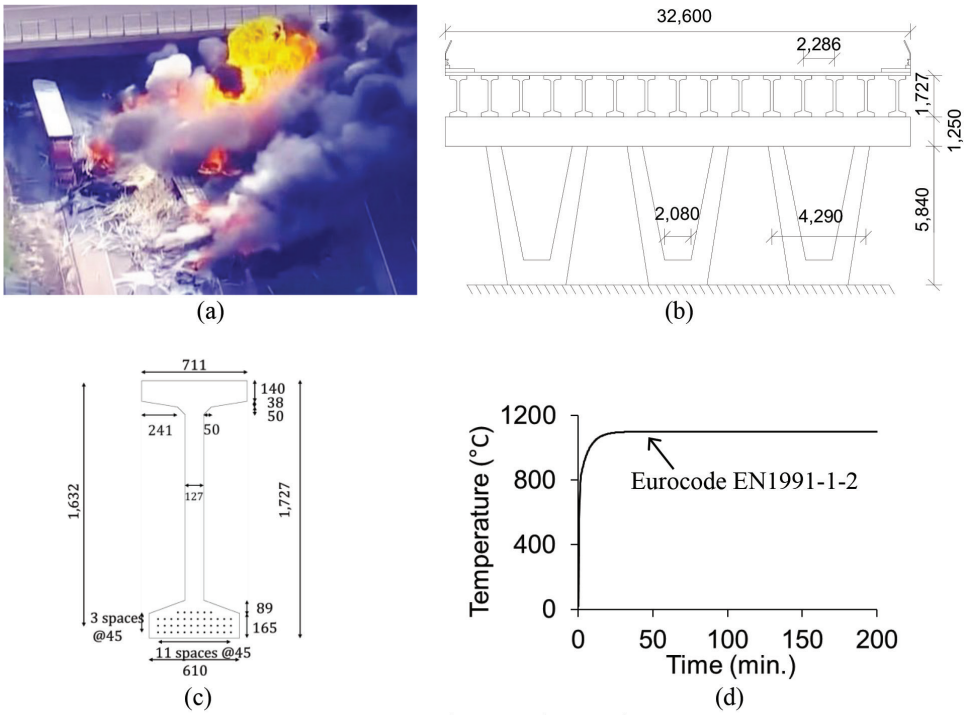
Fire, albeit sporadic, is a critical problem for constructed bridges. Statistics publicized that from 1999 to 2009, an average of 2049 bridge fires took place every year in the United States.[1] The ensuing economic consequences are remarkable, as evidenced by a recent bridge fire in Atlanta, GA, that caused a direct cost of $16.6 million and substantial disruptions to over 220,000 daily commuters.[2] Compared with the case of buildings, fire suppression is difficult in highway bridges because flammable petrochemicals are the primary source of ignition, water-discharging systems are absent on site, and members are not insulated. Despite the devastating nature of structural fires, these are not explicitly considered in the design of bridge elements: the "Extreme Events" specified in the American Association of State Highway and Transportation Officials (AASHTO) Load and Resistance Factor Design (LRFD) Bridge Design Specifications (BDS) incorporate earthquakes, ice loads, vehicle and vessel collisions, and floods.[3] A survey showed that 3.2% of bridge failures in the nation were attributed to fire, greater than the failure rates of 1.8% and 2.1% associated with wind and seismic loadings, respectively.[4] The most widely referenced fire model in the structural engineering community is ASTM E119-20,[5] which generates elevated temperatures to assess the response of building materials and constituents in a controlled environment. For this reason, its applicability to highway bridges is questionable, and hydrocarbon fire is deemed a more realistic approach for representing high temperatures induced by a combustible liquid in an open space.[6] Technically speaking, the ASTM E119 and hydrocarbon fires differ in several contexts, such as heat intensity, ventilation, growth and decay, spatial uniformity, and development rate.[7] Further information on bridge fires is available in review articles.[8,9]

Carbon fiber-reinforced polymer (CFRP) tendons emerged as a promising alternative to conventional steel strands for prestressed concrete structures in the 1990s.[10] These nonmetallic materials furnish high strength, light density, noncorrosiveness, adjustable geometry, and favorable constructability.[11] In spite of these benefits, the functionality of CFRP-prestressed concrete girders degrades when subjected to a fire. The reason is that the mechanical and thermal properties of a polymeric resin binding unidirectional carbon fibers alter due to a transition of internal chains from glassy to noncrystalline states with temperature.[12] Specifically, the mobility of chain segments prompts large deformations and thus weakens the degree of crosslinking in the entangled molecules.[13] From a structural safety perspective, when elevated temperatures apply, the polymeric attribute of CFRP leads to the loss of stiffness and strength, which brings about premature rupture of the tendon.[14] Multilayered tendons will experience sequential failure, depending upon the degree of heat transfer, and subsequent consequences are of great concern. Whereas a few early studies examined the behavior of CFRP tendons and CFRP-prestressed concrete members under fire loadings,[15,16] technical findings are limited owing to the simplified nature of laboratory testing (for instance, a small number of single-layered tendons). As a prerequisite for developing design provisions with regard to CFRP-prestressed concrete bridge girders at high temperatures, their detailed thermal responses need to be elucidated, with an emphasis on heat transfer and mechanical characteristics.

In this paper, computational simulations are conducted to understand the full-range behavior of steel- and CFRP-prestressed concrete girders under a hydrocarbon fire. A

ACI Structural Journal, V. 121, No. 5, September 2024.

MS No. S-2022-259.R1, doi: 10.14359/51740846, received March 17, 2024, and reviewed under Institute publication policies. Copyright © 2024, American Concrete Institute. All rights reserved, including the making of copies unless permission is obtained from the copyright proprietors. Pertinent discussion including author's closure, if any, will be published ten months from this journal's date if the discussion is received within four months of the paper's print publication.



[1 mm = 0.0394 in.; °F = (°C × 1.8) + 32]

Fig. 1—Description of Lakewood Bridge in Colorado: (a) fuel-induced fire (photo courtesy of 9News.com); (b) dimensions (units in mm); (c) girder dimensions (units in mm); and (d) hydrocarbon fire.

benchmark bridge is taken from the 2019 truck crash accident in Lakewood, CO. The modeling work renders insights into the in-fire performance of those girders, rather than residual behavior, and is extended to address practical gaps in the discipline of prestressed concrete by suggesting design guidelines.

RESEARCH SIGNIFICANCE

Prescriptive design methods are exclusively employed for prestressed concrete girders.[3] As such, regardless of tendon type, specific requirements cannot be stipulated at elevated temperatures, which are crucial to warrant user safety. The National Fire Protection Association (NFPA) 502 Standard[17] is the only source handling bridge fires; however, implementable information is not contained.[18] Notwithstanding extensive endeavors, the behavior of CFRP-prestressed concrete girders under fire is not well documented nor fully understood. Their relative performance against traditional steel-prestressed concrete girders, as a substitute load-bearing member, is also unknown. Contemplating that load levels are a principal factor controlling fire ratings (the duration for which a member can maintain its structural integrity),[5,19] the ramifications of synergistic distress incorporating thermal and mechanical components are of particular interest. The pragmatic importance of the current numerical study lies in the technical knowledge established on the basis of an actual truck crash event appertaining to the thermomechanical couplings of a highway bridge exposed to a hydrocarbon fire.

MOTIVATION

Descriptions of a steel-prestressed concrete bridge that has suffered from a fire are delineated with a digest of the accident. The structural configurations and constituent properties of the bridge are also covered. A hypothetical case with CFRP tendons is taken into account for comparative investigations.

Lakewood Bridge

Catastrophic multiple collisions detonated 28 vehicles and three semi-trailers in the vicinity of a bridge on Interstate 70 on April 25, 2019, as pictured in Fig. 1(a). The two-span bridge, 78 m (256.5 ft) long and 32.6 m (107 ft) wide, was supported by 15 bulb-tee prestressed concrete girders on a six-column pier system (Fig. 1(b)). Local news reported that a semi-trailer fully loaded with lumber had malfunctioning brakes and smashed against other cars, which resulted in a series of pileups. The ignited gasoline burst into flames and burned the lumber; afterward, the crumpled vehicles exploded. Because of the massive destruction with intense heat alongside toxic gas, four people died and more than a dozen were injured. The Colorado Department of Transportation (CDOT) announced that the bridge was damaged in the pavement and railing portions; nonetheless, it was diagnosed as structurally sound. This dreadful disaster offered motivation to explore the consequences of a fuel-driven fire on the behavior of bridge members. Furthermore, the fact that material types are a salient factor dominating the extent of impairment in highway bridges at elevated temperatures[20] justifies the need to examine the contrasting responses of steel- and CFRP-prestressed concrete girders under such a detrimental circumstance.

Prestressed concrete girders

Figure 1(c) shows the schematic dimensions of the Colorado G68 girder that was part of the foregoing bridge system. According to the as-built documents received from CDOT, the 28-day compressive strength of the concrete was f_c' = 42.3 MPa (6135 psi), while the strength at transfer was f_{ci}' = 39.2 MPa (5685 psi). The elastic modulus of the concrete was estimated as $E_c = 4700(f_c')^{0.5}$ MPa $(1820(f_c')^{0.5}$ ksi).[3] A total of 42 steel strands (nominal cross-sectional area = 98.7 mm^2 [0.153 in.^{2}], each) were used for each girder, and their ultimate strength and elastic modulus were f_{psu} = 1860 MPa (270 ksi) and E_{ps} = 195 GPa (28,500 ksi), respectively. For a numerical parametric study, another G68 girder was designed with 42 CFRP tendons, which had nearly the same flexural capacity as the steel strands. The tendon (nominal cross-sectional area = 127 mm^2 [0.196 in.^{2}] with a diameter of 13 mm [0.5 in.], each) possessed an ultimate strength of f_{pfu} = 1724 MPa (250 ksi) and a tensile modulus of E_{pf} = 124 GPa (18,000 ksi) at a rupture strain of ε_{pfu} = 1.5%.[21] A glass-transition temperature of T_g = 100°C (212°F) was taken with a thermal decomposition temperature of T_d = 400°C (752°F).[22-25] The eccentricities of the resultant steel strands and CFRP tendons were e_p = 766 mm (30.2 in.), and the self-weight moment of the girder was M_{sw} = 1844 kN·m (1360 ft·kip). In light of the regional climate, an average relative humidity of H = 70% was set. Regarding relaxation, prestress losses (Δf_R) were assumed to be 16.6 MPa (2.4 ksi) for the low-relaxation steel strands and 2% of the initial stress for the CFRP tendons.[3,26] It is noted that all these properties are designated as baseline properties to avoid confusion when thermal effects are associated. To simulate the repercussions effectuated by the combustible gasoline, a hydrocarbon fire model (Fig. 1(d)) was adopted from EN 1991-1-2:2002.[27]

COMPUTATIONAL MODELING

This section describes predictive methodologies, including heat-transfer theory, constitutive equations, and structural mechanics. Figure 2 illustrates a flowchart of the proposed modeling approach, which is explained as follows.

Framework

An advanced modeling paradigm often used in computational sociology, agent-based modeling, was the primary simulation platform for the present study. It is a branch of mathematical complexity, as in the case of cellular automata and game theory.[28,29] Entities without external control interact and comprise a dynamic system to comprehend the response of a macroscopic network. In accordance with predefined rules, this novel approach deals with interactions among constituent agents. Both temporal and spatial domains are iteratively solved to gain essential information. The asynchronism and heterogeneity of agent-based modeling, which autonomously treats discrete agents and their surroundings, are representative benefits relative to classical numerical analysis entailing differential equations; for example, a single decentralized agent that adaptively responds to intricately intertwined situations can impact the behavior of the whole system. Supplementary contents regarding

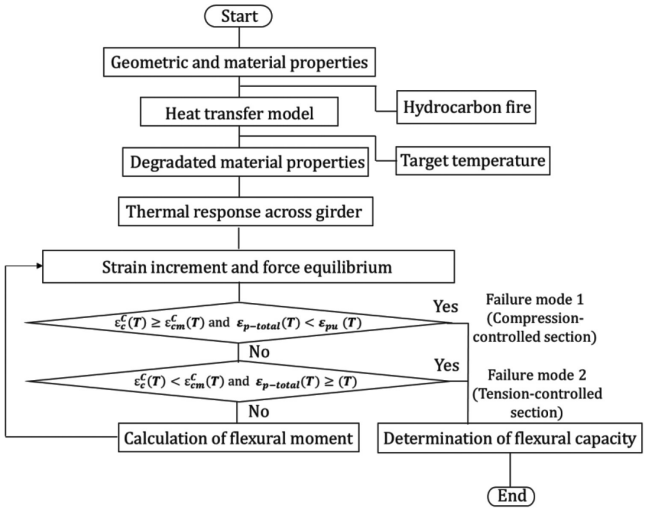


Fig. 2—Flowchart of modeling approach.

the principle and application of agent-based modeling can be found elsewhere.[30] Employing agent-based modeling software called NetLogo,[31] the aforementioned prestressed concrete girder was modeled, as shown in Fig. 3(a), where decentralized agents (6.35 x 6.35 mm [0.25 x 0.25 in.] in size, each) were allocated in a Euclidean space and evolved over time to transit a state from one to another under thermal loading applied to the girder surface (Fig. 3(b)).

Numerical heat flow

The transfer of thermal energy is modeled by Fourier's law, which may be discretized into an approximate form for numerical analysis[32]

$$T_{i,j}^{t+1} = k\left(T_{i-1,j}^{t} + T_{i+1,j}^{t} + T_{i,j-1}^{t} + T_{i,j+1}^{t}\right) + (1 - 4k)T_{i,j}^{t} \quad (1)$$

where $T_{i,j}^{t}$ is the temperature at location (i, j) in the Cartesian space at time t (Fig. 3(a)); and k is the thermal constant ($k = \lambda\Delta t/(\rho C_p \Delta x^2)$, in which λ is the thermal conductivity; ρ is the density; C_p is the specific heat; and x is the location. For stable computation, the upper limit of k was set at 0.25.[32] The variation in temperature under a hydrocarbon fire can be attained from[27]

$$T = 1080(1 - 0.325e^{-0.167t} - 0.675e^{-2.5t}) + T_0 \quad (2)$$

where t is the time in minutes; and T_0 is the reference temperature (T_0 = 20°C [68°F]). Considering heat convection and thermal radiation on a concrete surface subjected to the fire, the total heat-transfer rate (q) may be expressed as[33,34]

$$q = q_{conv} + q_{rad} = \alpha_c(T_{applied} - T_{surface}) + \varepsilon_{em}\psi((T_{applied} + 273)^4 - (T_{surface} + 273)^4) \quad (3)$$

where q_{conv} and q_{rad} are the transfer rates for the convection and radiation processes, respectively; $T_{applied}$ is the applied temperature in Celsius (Eq. (2)); $T_{surface}$ is the surface temperature at time t; α_c is the convection coefficient (α_c = 50 W/(m^2·K))[27]; ε_{em} is the emissivity (ε_{em} = 0.9 for concrete[35]);

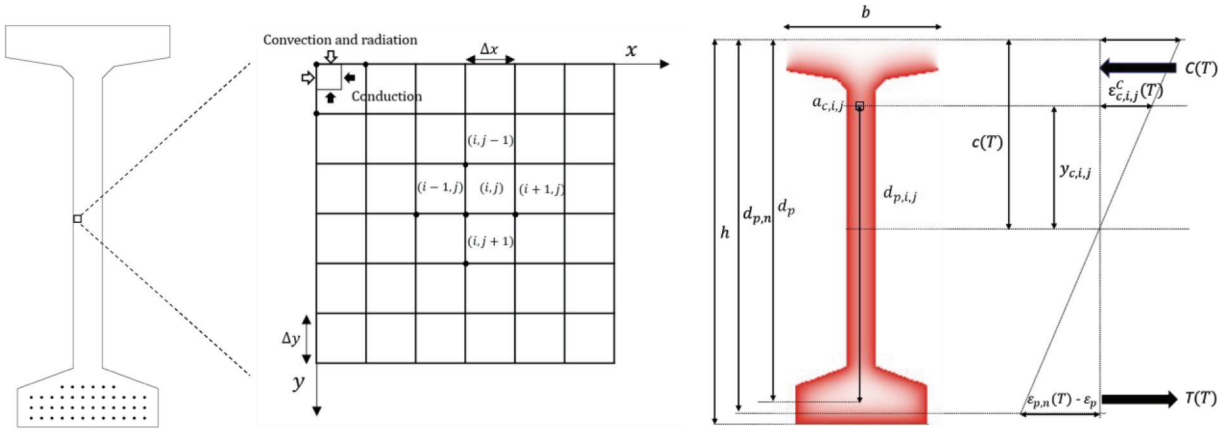


Fig. 3—Agent-based modeling: (a) space discretization; and (b) description of equivalent sectional analysis.

and ψ is the Stefan-Boltzmann constant (ψ = 5.67 × 10^{-8} W/(m^2·K^4)). An increment in temperature between two adjacent time steps is equated with the heat transferred to the concrete surface[36]

$$\rho C_p \Delta x^2 \frac{T_{i,j}^{t+1} - T_{i,j}^t}{4\Delta t} = \lambda\left(\frac{T_{i,j+1}^t + T_{i+1,j}^t - 2T_{i,j}^t}{2} + q\Delta x\right) \quad (4)$$

The continuum bridge girder was represented by a discrete form with Δt = 1.2 seconds and Δx = 6.35 mm (0.25 in.). Because reinforcing elements negligibly affect heat transfer in a concrete structure,[37] the thermal properties of the steel strands and CFRP tendons were not taken into consideration.

Constitutive modeling

Concrete—The temperature-dependent compressive strength of concrete ($f_c'(T)$) may be predicted by[38]

$$f_c'(T) = \frac{f_c'}{1 + \frac{T}{T_1} + \left(\frac{T}{T_2}\right)^2 + \left(\frac{T}{T_8}\right)^8 + \left(\frac{T}{T_{64}}\right)^{64}} \quad (5)$$

where f_c' is the baseline compressive strength at 28 days; and T_1, T_2, T_8, and T_{64} are the empirical constants (T_1 = 15,000, T_2 = 800, T_8 = 579, and T_{64} = 100,000). The maximum usable strain of the concrete in compression ($\varepsilon_{cm}^C(T)$) can be obtained from[39]

$$\varepsilon_{cm}^C(T) = \varepsilon_{cu} \text{ for } 20°C\ (68°F) \le T < 200°C\ (392°F) \quad (6a)$$

$$\varepsilon_{cm}^C(T) = 0.00001156T + 0.000686 \le 0.0082 \text{ for } 200°C\ (392°F) \le T \quad (6b)$$

where ε_{cu} is the baseline crushing strain of the concrete (ε_{cu} = 0.003). The stress-strain relationship of the concrete is given for compression (Eq. (7)) and tension (Eq. (8)) at temperature T[40-42]

$$\sigma_{c,i,j}^C(T) = f_{c,i,j}'(T)\left[1 - \left(\frac{\varepsilon_{cm}^C(T) - \varepsilon_{c,i,j}^C(T)}{\varepsilon_{cm}^C(T)}\right)^2\right] \quad (7)$$

$$\sigma_{c,i,j}^C(T) = E_c(T)\varepsilon_{c,i,j}^T(T) \text{ for } \varepsilon_{c,i,j}^T(T) \le \frac{f_r(T)}{E_c(T)} \quad (8a)$$

$$\sigma_{c,i,j}^T(T) = \frac{f_r(T)}{1 + \sqrt{200\varepsilon_{c,i,j}^T(T)}} \text{ for } \frac{f_r(T)}{E_c(T)} < \varepsilon_{c,i,j}^T(T) \le \frac{15f_r(T)}{E_c(T)} \quad (8b)$$

$$\sigma_{c,i,j}^T(T) = 0 \text{ for } \frac{15f_r(T)}{E_c(T)} < \varepsilon_{c,i,j}^T(T) \quad (8c)$$

where $\sigma_{c,i,j}^C(T)$ and $\sigma_{c,i,j}^T(T)$ are the compressive and tensile stresses of the concrete at location (i, j), respectively; $\varepsilon_{c,i,j}^C(T)$and $\varepsilon_{c,i,j}^T(T)$ are the compressive and tensile strains of the concrete, respectively; and $E_c(T)$ and $f_r(T)$ are the moduli of elasticity and rupture, respectively, in MPa[43]

$$E_c(T) = (1 - 0.0015T)E_c \text{ for } 20°C\ (68°F) \le T \le 200°C\ (392°F) \quad (9a)$$

$$E_c(T) = (0.87 - 0.00084T)E_c \text{ for } 200°C\ (392°F) < T \le 700°C\ (1292°F) \quad (9b)$$

$$E_c(T) = 0.28E_c \text{ for } 700°C\ (1292°F) < T \quad (9c)$$

$$f_r = 0.6\lambda_c\sqrt{f_c'}\frac{f_c'(T)}{f_c'} \quad (10)$$

where E_c is the baseline elastic modulus of the concrete; and λ_c is the concrete density factor (λ_c = 1.0 for ordinary concrete). Table 1 summarizes the thermal properties of the concrete,[44] which are necessary for heat-transfer simulations.

Steel strands—The stress-strain curve of the prestressing strands at elevated temperatures is defined by[44]

$$\sigma_{ps,n}(T) = E_{ps,n}(T)\varepsilon_{ps,n}(T) \text{ for } \varepsilon_{ps,n}(T) < \frac{f_{pp,n}(T)}{E_{ps,n}(T)} \quad (11a)$$

Table 1—Thermal properties of concrete

Property	Temperature	Value*
Thermal conductivity l, W/(m·K)	20°C (68°F) ≤ T ≤ 1200°C (2192°F)	$\lambda = (1.36 - 0.136)(T/100) + 0.0057(T/100)^2$
Specific heat C_p, J/(kg·K)	20°C (68°F) ≤ T < 100°C (212°F)	900
	100°C (212°F) ≤ T < 200°C (392°F)	$900 + (T - 100)$
	200°C (392°F) ≤ T < 400°C (752°F)	$1000 + (T - 200)/2$
	400°C (752°F) ≤ T ≤ 1200°C (2192°F)	1100
Density r, kg/m^3	20°C (68°F) ≤ T < 115°C (239°F)	ρ_{20}
	115°C (239°F) ≤ T < 200°C (392°F)	$\rho_{20}(1 - 0.02(T - 115)/85)$
	200°C (392°F) ≤ T < 400°C (752°F)	$\rho_{20}(0.98 - 0.03(T - 200)/200)$
	400°C (752°F) ≤ T ≤ 1200°C (2192°F)	$\rho_{20}(0.95 - 0.07(T - 400)/800)$

*Temperature in Celsius (°C × 9/5 + 32 = °F).

Note: ρ_{20} is reference density of 2300 kg/m^3 (143 lb/ft^3) at 20°C (68°F); 1 kg/m^3 = 0.062 lb/ft^3; 1kg = 2.2 lb.

$$\sigma_{ps,n}(T) = f_{pp,n}(T) - c_n + \left(\frac{b_n}{a_n}\right)\left[a_n^2 - (0.02 - \varepsilon_{ps,n}(T))^2\right]^{0.5} \quad \text{for } \frac{f_{pp,n}(T)}{E_{ps,n}(T)} \le \varepsilon_{ps,n}(T) < 0.02 \tag{11b}$$

$$\sigma_{ps,n}(T) = f_{py,n}(T) \text{ for } 0.02 \le \varepsilon_{ps,n}(T) < \varepsilon_{pt,n}(T) \tag{11c}$$

$$\sigma_{ps,n}(T) = f_{py,n}(T)\left[1 - \frac{\varepsilon_{ps,n}(T) - \varepsilon_{pt,n}(T)}{\varepsilon_{pu,n}(T) - \varepsilon_{pt,n}(T)}\right] \quad \text{for } \varepsilon_{pt,n}(T) \le \varepsilon_{ps,n}(T) < \varepsilon_{pus,n}(T) \tag{11d}$$

$$\sigma_{ps,n}(T) = 0 \text{ for } \varepsilon_{ps,n}(T) = \varepsilon_{pus,n}(T) \tag{11e}$$

$$a_n^2 = \frac{0.02 - \dfrac{f_{pp,n}(T)}{E_{ps,n}(T)}}{0.02 - \dfrac{f_{pp,n}(T)}{E_{ps,n}(T)} + c_n/E_{ps,n}(T)} \tag{12a}$$

$$b_n^2 = c_n\left[0.02 - \frac{f_{pp,n}(T)}{E_{ps,n}(T)}\right]E_{ps,n}(T) + c_n^2 \tag{12b}$$

$$c_n = \frac{\left[f_{py,n}(T) - f_{pp,n}(T)\right]^2}{\left[0.02 - \dfrac{f_{pp,n}(T)}{E_{ps,n}(T)}\right]E_{ps,n}(T) - 2\left[f_{py,n}(T) - f_{pp,n}(T)\right]} \tag{12c}$$

where $\sigma_{ps,n}(T)$ and $\varepsilon_{ps,n}(T)$ are the stress and strain of the individual steel strands at temperature T, respectively; and $f_{pp,n}(T)$, $f_{py,n}(T)$, $E_{ps.n}(T)$, $\varepsilon_{pt,n}(T)$, and $\varepsilon_{pus,n}(T)$ are the temperature-dependent parameters listed in Table 2,[44,45] including the baseline elastic modulus and ultimate strength of the steel strands (E_{ps} and f_{pus}, respectively).

CFRP tendons—The stress-strain graph of the CFRP tendons is generated using

$$\sigma_{pf,n}(T) = E_{pf,n}(T)\varepsilon_{pf,n}(T) \text{ for } \varepsilon_{pf,n}(T) \le \varepsilon_{pfu,n}(T) \tag{13a}$$

$$\sigma_{pf,n}(T) = 0 \text{ for } \varepsilon_{pfu,n}(T) < \varepsilon_{pf,n}(T) \tag{13b}$$

where $\sigma_{pf,n}(T)$ and $\varepsilon_{pf,n}(T)$ are the stress and strain of CFRP at temperature T, respectively; and $E_{pf,n}(T)$ and $\varepsilon_{pfu}(T)$ are the elastic modulus (Eq. (14))[23] and the ultimate strain of CFRP (Eq. (15)), respectively

$$E_{pf,n}(T) = E_{pf} \quad \text{for } 0°C\ (32°F) \le T < 100°C\ (212°F) \tag{14a}$$

$$E_{pf,n}(T) = E_{pf}(1.175 - 0.00175T) \quad \text{for } 100°C\ (212°F) \le T < 300°C\ (572°F) \tag{14b}$$

$$E_{pf,n}(T) = E_{pf}(1.625 - 0.00325T) \quad \text{for } 300°C\ (572°F) \le T < 400°C\ (752°F) \tag{14c}$$

$$\varepsilon_{pfu}(T) = \frac{f_{pfu,n}(T)}{E_{pf,n}(T)} \tag{15}$$

The ultimate strength of the tendons ($f_{pfu}(T)$) is the stress at the rupture of CFRP[23]

$$f_{pfu,n}(T) = f_{pfu} \quad \text{for } 20°C\ (68°F) \le T < 100°C\ (212°F) \tag{16a}$$

$$f_{pfu,n}(T) = f_{pfu}(1.267 - 0.00267T) \quad \text{for } 100°C\ (212°F) \le T \le 400°C\ (752°F) \tag{16b}$$

Flexural resistance

In compliance with force equilibrium and strain compatibility, the force and moment components of the girder section are determined

$$C_n(T) = T_n(T) \tag{17}$$

Table 2—Temperature-dependent parameters for steel strands

Steel temperature, °C	$f_{pp,n}(T)/(\beta f_{pus})$	$f_{py,n}(T)/(\beta f_{pus})$	$E_{ps,n}(T)/E_{ps}$	$\varepsilon_{pt,n}(T)$	$\varepsilon_{pus,n}(T)$
20	1.00	1.00	1.00	0.050	0.100
100	0.68	0.99	0.98	0.050	0.100
200	0.51	0.87	0.95	0.050	0.100
300	0.32	0.72	0.88	0.055	0.105
400	0.13	0.46	0.81	0.060	0.110
500	0.07	0.22	0.54	0.065	0.115
600	0.05	0.10	0.41	0.070	0.120
700	0.03	0.08	0.10	0.075	0.125
800	0.02	0.05	0.07	0.080	0.130
900	0.01	0.03	0.03	0.085	0.135
1000	0.00	0.00	0.00	0.090	0.140
1100	0.00	0.00	0.00	0.095	0.145
1200	0.00	0.00	0.00	0.100	0.150

Note: f_{pus} = 1860 MPa (270 ksi); E_{ps} = 195 GPa (28,500 ksi); β = 0.9 for medium-ductility steel strands; °F = (°C × 9/5) + 32.

$$C_n(T) = \left(\sum_{j=1}^{j=n_c}\sum_{i=1}^{i=n_c}\sigma_{c,i,j}^{C}(T)\right)A_a \tag{18}$$

$$T_n(T) = \left(\sum_{p=1}^{p=n_p}\sigma_p(T)\right)A_p \tag{19}$$

$$M_n(T) = \left(\sum_{j=1}^{j=n_c}\sum_{i=1}^{i=n_c}\sigma_{c,i,j}^{C}(T)d_{p,i,j}(T)\right)A_a \tag{20}$$

where $C_n(T)$ and $T_n(T)$ are the resultant compression and tension forces at temperature T, respectively; n_c is the number of agents in the concrete section; $\sigma_p(T)$ is the stress of either steel strands ($\sigma_{ps}(T)$) or CFRP tendons ($\sigma_{pf}(T)$); n_p and A_p are the number and cross-sectional area of the prestressing elements, respectively; $M_n(T)$ is the flexural resistance of the girder; and $d_{p,i,j}(T)$ is the distance from the centroid of each agent to the individual prestressing elements. For the calculation of the concrete stress in compression ($\sigma_{c,i,j}^{C}(T)$) along with Eq. (7)

$$\varepsilon_{c,i,j}^{C}(T) = \frac{\varepsilon_{p,n}(T)}{\left(d_{p,n} - c(T)\right)}y_{c,i,j} \tag{21}$$

where $d_{p,n}$ is the effective depth of the prestressing elements; $c(T)$ is the neutral axis depth of the girder; $y_{c,i,j}$ is the distance from the neutral axis to the center of the individual agents in the girder section; and $\varepsilon_{p,n}(T)$ is the strain of the respective prestressing elements from the decompression state: $\varepsilon_{p,n}(T) = \varepsilon_{p\text{-}total,n}(T) - \varepsilon_p$, in which $\varepsilon_{p\text{-}total,n}(T)$ is the total strain of the elements at the flexural failure of the girder; and ε_p comprises the effective and decompression strains (ε_{pe} and ε_d, respectively)

$$\varepsilon_p = \varepsilon_{pe} + \varepsilon_d \tag{22}$$

$$\varepsilon_{pe} = \frac{f_{pe}}{E_p} \tag{23}$$

$$\varepsilon_d = \frac{f_{pe}A_p}{A_gE_c} + \frac{f_{pe}A_pe_p^2}{I_gE_c} \tag{24}$$

$$f_{pe} = f_{pi} - \Delta f_{pL} \tag{25}$$

where f_{pe} is the effective prestress; E_p, A_p, and e_p are the elastic modulus, cross-sectional area, and eccentricity of either steel strands (E_{ps}, A_{ps}, and e_{ps}) or CFRP tendons (E_{pf}, A_{pf}, and e_{pf}), respectively; and A_g is the cross-sectional area of the girder section. The initial prestress (f_{pi} in Eq. (26)) is a fraction of the ultimate strength (k_p = 0.75 and 0.65 were approximated for the steel strands and CFRP tendons, respectively[3,11]), and the prestress loss (Δf_{pL}) is the sum of the elastic shortening (Δf_{pES} in Eq. (27))[3] and the long-term reduction (Δf_{pLT} in Eq. (28))[3]

$$f_{pi} = k_p f_{pu} \tag{26}$$

$$\Delta f_{pES} = \frac{A_p f_{pi}\left(I_g + e_p^2A_g\right) - M_{sw}e_pA_g}{A_p\left(I_g + e_p^2A_g\right) + \frac{A_gI_gE_{ci}}{E_p}} \tag{27}$$

$$\Delta f_{pLT} = 10\frac{f_{pi}A_p}{A_g}\gamma_h\gamma_{cc} + 12\gamma_h\gamma_{cc} + \Delta f_R \tag{28}$$

where I_g is the moment of inertia of the girder; M_{sw} is the self-weight moment; E_{ci} is the elastic modulus of the concrete at transfer ($E_{ci} = 4{,}700(f_{ci}')^{0.5}$ MPa [$1820(f_{ci}')^{0.5}$ ksi]); γ_h and γ_{cc} are the correction factors for relative humidity ($\gamma_h = 1.7 - 0.01H$) and concrete strength at the time of prestress transfer ($\gamma_{cc} = 5/(1 + f_{ci}')$, where f_{ci}' is the initial stress in ksi[3]); and Δf_R is the relaxation loss. The insignificant loss of prestress due to the relaxation before casting the concrete was ignored.[46]

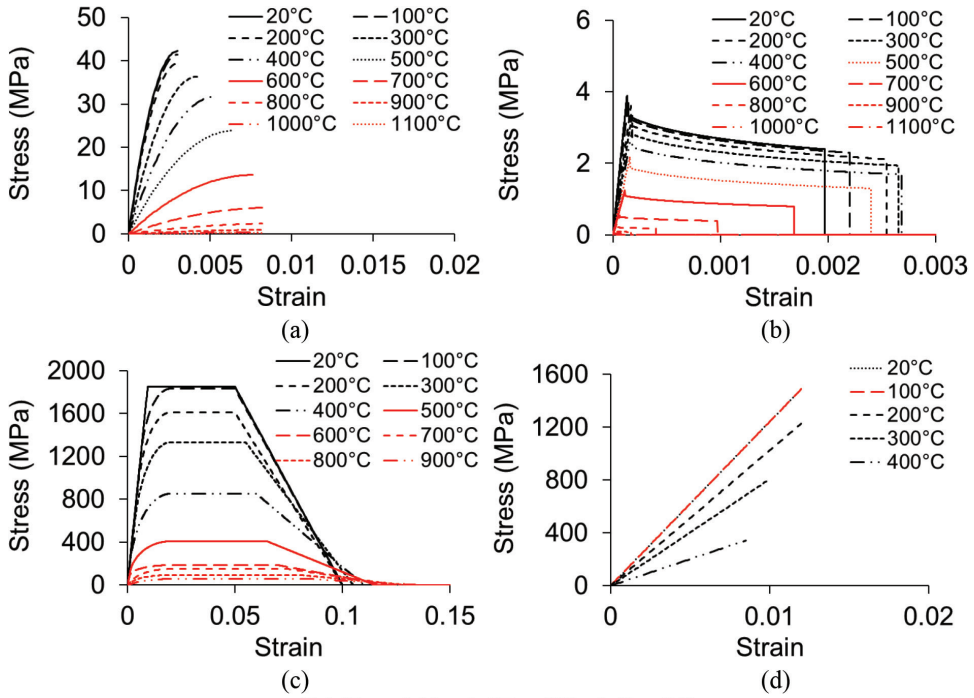


Fig. 4—Temperature-dependent stress-strain curves: (a) concrete in compression; (b) concrete in tension; (c) steel strands in tension; and (d) CFRP tendons in tension.

Implementation

To evaluate the implications of thermomechanical loading, the girder behavior was simulated with and without elevated temperatures. The strain of the prestressing elements was incremented, equivalent to the development of a flexural moment, until the girders failed by either Mode 1 (compression-controlled) or Mode 2 (tension-controlled). Concrete crushing was engaged with Mode 1; on the other hand, the maximum usable strain of the steel strands and the rupture strain of the CFRP tendons were the governing factors in Mode 2 (for the assessment of full-range behavior, complete failure of the prestressing elements was regarded as a prime criterion). Because the occurrence of a fire changed the elastic modulus and strain-dependent stress of the steel and CFRP (Fig. 4), tensile forces decreased beyond a certain exposure time, and hence, corresponding concrete strains and the neutral axis depth of the section were adjusted to achieve equilibrium during simulations (to be described).

Validation

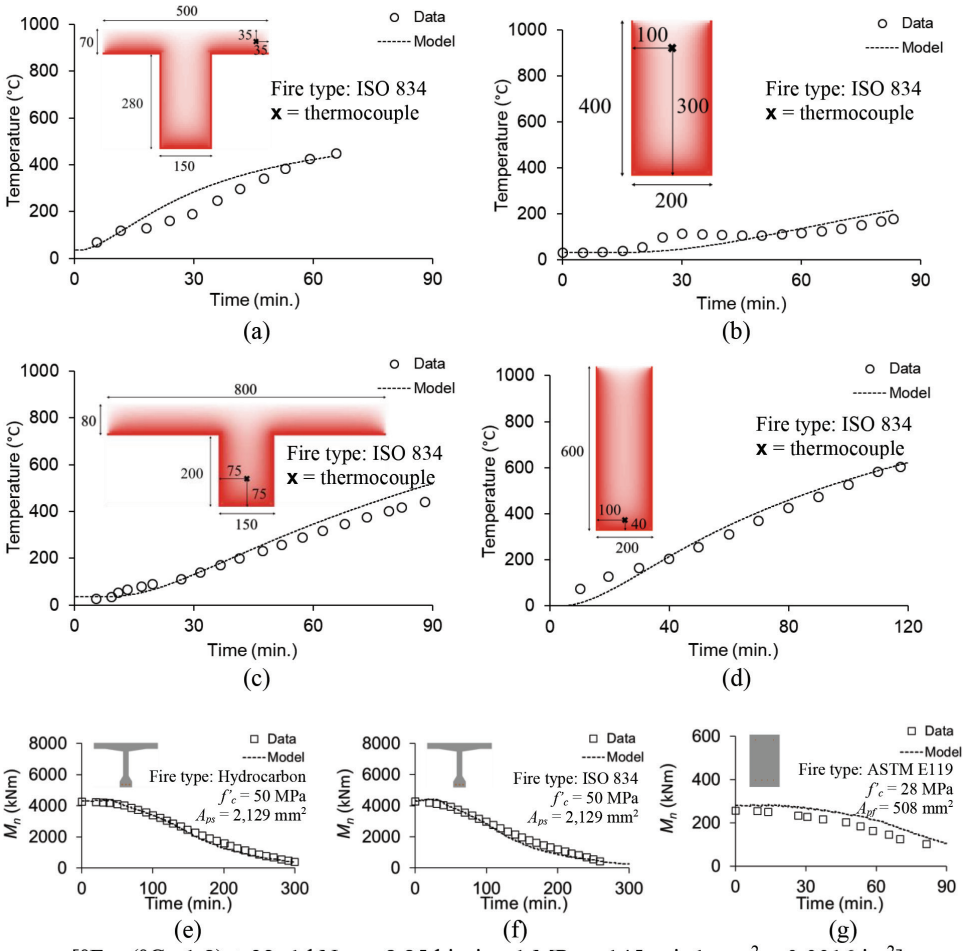
A two-phase validation process was conducted to examine the adequacy of the proposed approaches: 1) heat transfer; and 2) load-carrying capacity under various fire protocols. Figures 5(a) to (d) exhibit the rising temperatures of assorted structural sections exposed to the ISO 834-10:2014 standard fire,[47] taken from the literature.[48-51] Although local fluctuations were not plotted at the locations where thermocouple wires were affixed, the model agreed with the measured thermal responses. The unfactored moment capacities (M_n) of bulb-tee and rectangular beam sections[52,53] were compared with predicted values in Fig. 5(e) to (g). Irrespective of the fire types (hydrocarbon fire, ISO 834, and ASTM E119) and prestressing elements (steel strands and CFRP tendons), the capacity variation of the formulated analytical methods matched the variation excerpted from the references.

RESULTS

The established modeling approach is employed to determine the thermomechanical characteristics of steel- and CFRP-prestressed concrete girders exposed to a hydrocarbon fire. Both element- and structure-level examinations are expounded within a simulation period of 200 minutes.

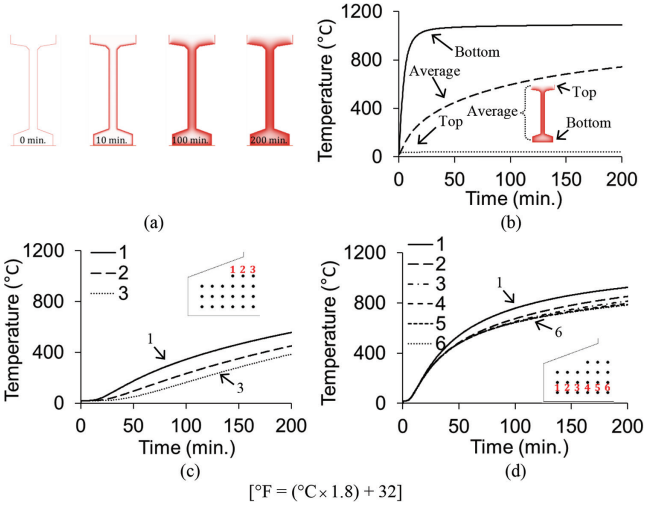
Thermal conduction

The propagation of heat inside the girder is depicted in Fig. 6(a). Conforming to conduction theory,[54] the constituent molecules near the fire held more kinetic energy and jostled neighboring ones (that is, the collision of contacting atoms through vibrations) to convey the applied heat until thermal equilibrium was achieved. The temperature gradient (dT/dx) across the girder boundary thus tended to decrease with the flow of heat; namely, the distinction between the reddish and white regions of the girder lessened. Figure 6(b) provides the growth of the girder temperature versus exposure time. Contrary to the lower flange's precipitously ascending pattern within the first 20 minutes, the temperature of the upper flange was maintained below 40°C (104°F) for the 200-minute duration of the fire. The stabilized temperature of the lower flange after 50 minutes implies that a steady state was accomplished between the flange concrete and the surroundings. The average of the girder temperatures taken from all concrete agents revealed a gradual increase, which may be usable for the grillage model of bridge structures.[9] The position of the prestressing elements was an important factor for temperature differentials (Fig. 6(c) and (d)). Scilicet, a physical distance from the source of thermal



[°F = (°C × 1.8) + 32; 1 kNm = 8.85 kip-in.; 1 MPa = 145 psi; 1 mm² = 0.0016 in.²]

Fig. 5—Validation of multidirectional heat-transfer modeling approaches (dimensional units in mm): (a) heat transfer for tee beam[51]; (b) heat transfer for rectangular beam[49]; (c) heat transfer for tee beam[50]; (d) heat transfer for rectangular beam[48]; (e) flexural capacity of tee beam prestressed with steel strands[53]; (f) flexural capacity of tee beam prestressed with steel strands[53]; and (g) flexural capacity of rectangular beam with CFRP tendons.[52]



[°F = (°C × 1.8) + 32]

Fig. 6—Temperature development at various locations: (a) simulated heat transfer; (b) girder concrete; (c) prestressing elements in Layer 1; and (d) prestressing elements in Layer 4.

energy governed the escalation rate with time (Fig. 6(c)); nonetheless, the effect of multidirectional heat transfer dwindled as the elements were away from the side of the lower flange (No. 3 to 6 in Fig. 6(d)). These observations substantiate the need for monitoring temperature rises in all places to accurately predict the thermomechanical behavior of the girders, which cannot be handled by conventional sectional analysis relying on simplified resultant forces. It is worthwhile to declare that, from a microscale standpoint, a mismatch between the coefficients of thermal expansion in the concrete and CFRP may cause microcracks,[55] precipitating local bond failure; however, such material-level investigations would require complex methodologies and thus were outside the scope of the present structure-scale study.

Material properties

The dependence of the concrete, steel, and CFRP properties on elevated temperatures is shown in Fig. 7 and 8. When the hydrocarbon fire initiated, the concrete at the very bottom of the steel-prestressed girder quickly lost the compressive strength (Fig. 7(a)); in contrast, the strength of the top concrete was marginally influenced by the thermal loading, with a maximum change of 0.4%. The average drop of the concrete strength was 73.7% from an exposure period of 0 to 200 minutes when the surface temperature of the girder rose from 20 to 1089°C (68 to 1992°F). As far

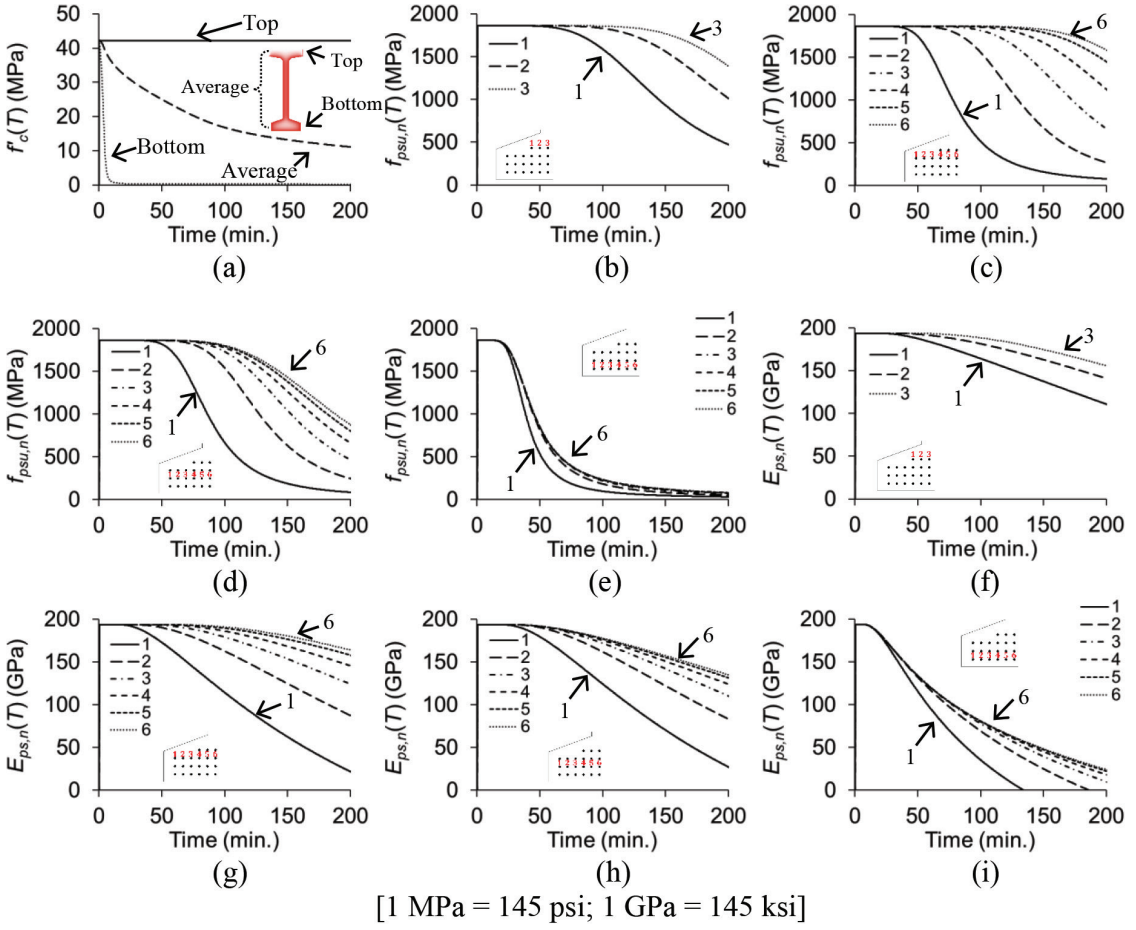


Fig. 7—Effects of temperature on material properties of steel-prestressed concrete girder: (a) compressive strength of concrete; (b) ultimate strength of steel in Layer 1; (c) ultimate strength of steel in Layer 2; (d) ultimate strength of steel in Layer 3; (e) ultimate strength of steel in Layer 4; (f) elastic modulus of steel in Layer 1; (g) elastic modulus of steel in Layer 2; (h) elastic modulus of steel in Layer 3; and (i) elastic modulus of steel in Layer 4.

as the ultimate strength of the steel strands is concerned (Fig. 7(b)), the strength of the interior strands (No. 2) lay between those of the exterior and innermost strands (No. 1 and 3, respectively), and such a tendency was preserved in all strand layers (Fig. 7(c) to (e)). Unlike the wide breadth of the responses between No. 1 and 6 strands in Layers 2 and 3 (Fig. 7(c) and (d), respectively), the strength of the strands in Layer 4 plummeted with minimal dissimilarities (Fig. 7(e)) owing to their close proximity to the source of heat that facilitated the transport of thermal energy. As is the case for the ultimate strength of the strands, the modulus of elasticity dropped (Fig. 7(f) to (i)), which was particularly critical at a temperature of 400°C (752°F) and higher (Fig. 4(c)). The thermal response of the concrete in the CFRP-prestressed girder (Fig. 8(a)) was equal to that in the steel-prestressed girder, whereas the declined strength of the CFRP tendons and their degradation rates were discernable until the thermal decomposition temperature of 400°C (752°F) was reached (Fig. 8(b) to (e)). This fact is attributable to the changes in molecular structures in the polymeric resin (the crosslinking of the entangled chains loosens as the conformation of the polymer shifts from crystalline to liquid[13]) and the progressive failure of the interface between the fibers and resin matrix.[56] Akin to the unstable elastic moduli of the steel strands in Fig. 7, the moduli of CFRP plunged with exposure time, and the response magnitude was reliant upon the location of the tendons (Fig. 8(f) to (i)).

Flexural resistance

Mechanism of carrying external moment—In line with the fact that the resistance of a flexural member (M_n) is calculated by the product of the tensile force (T) and lever arm (jd), the evolution of steel and CFRP strains (ε_{ps} and ε_{pf}, respectively) and correlated lever arms is visible in Fig. 9(a) to (d). For illustration purposes, two exposure periods were selected under Failure Mode 1 (compression-controlled) at 0 and 50 minutes, representing the mechanical and thermo-mechanical loadings, respectively. In the absence of thermal exposure at 0 minutes, the growth of the lever arms between the steel and CFRP girders was virtually indistinguishable (Fig. 9(e)): a linear propensity was apparent up to a lever arm of 1360 mm (53.5 in.), beyond which the moment-development rate quickened because the bending moment sensitively responded to a small increment in the forces with the maximized lever arm in the upper and lower flanges. However, as shown in Fig. 9(f), a divergence between those girders commenced at 50 minutes with a considerable drop in the moment that pertained to a lever arm exceeding jd = 1500 mm (59 in.), aligning with a transition of the failure mode (to be discussed).

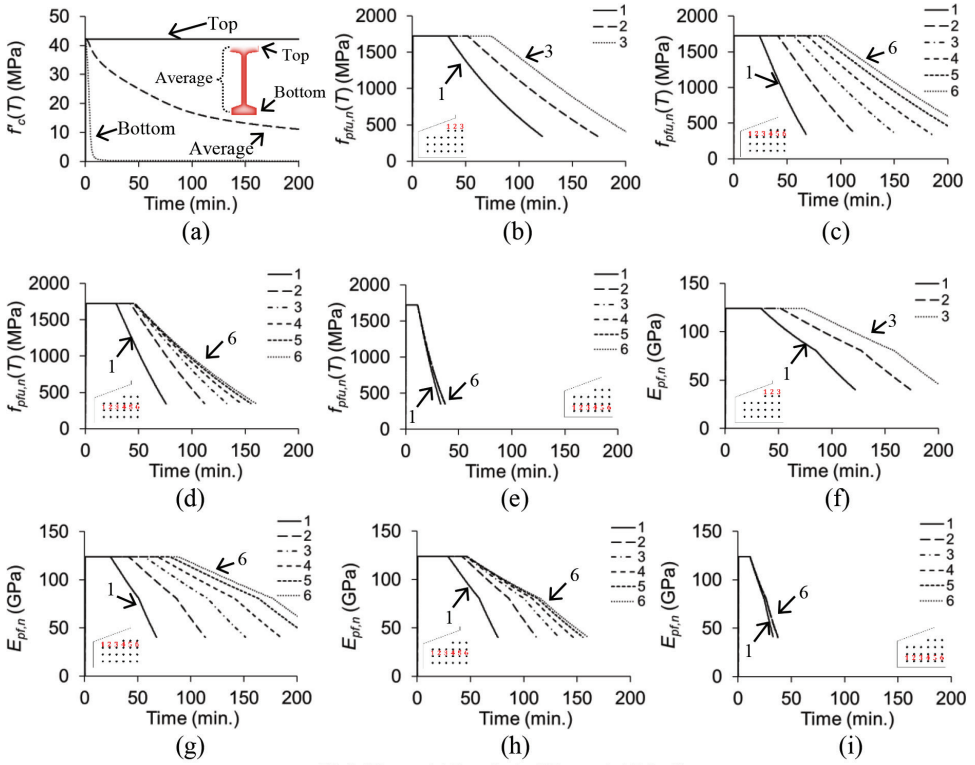


Fig. 8—Effects of temperature on material properties of CFRP-prestressed concrete girder: (a) compressive strength of concrete; (b) ultimate strength of CFRP in Layer 1; (c) ultimate strength of CFRP in Layer 2; (d) ultimate strength of CFRP in Layer 3; (e) ultimate strength of CFRP in Layer 4; (f) elastic modulus of CFRP in Layer 1; (g) elastic modulus of CFRP in Layer 2; (h) elastic modulus of CFRP in Layer 3; and (i) elastic modulus of CFRP in Layer 4.

Moment development—Figure 10 displays the interdependence of the moment development with the concrete and steel strains to clarify the susceptibility of the compressive and tensile components of the girders against elevated temperatures. When the girder was loaded in flexure without heat (Fig. 10(a)), the tensile strain of the concrete in the cambered state proceeded toward the compression side, and the girder failed by crushing ($\varepsilon_{c,i,j} = \varepsilon_{cu}$). In like manner, the strains of the pretensioned steel strands went up with negligible differences between the layers (Fig. 10(b)). As the girder was subjected to a surface temperature of 1081°C (1977°F), the ability to develop the flexural resistance degenerated, and the slope of the moment-strain relationship appreciably decreased (Fig. 10(c)). In addition, the influence of strand locations (Fig. 10(d)) was not as significant as the amount of heat transferred to the layers (Fig. 7(b) to (i)). At the surface temperature of 1089°C (1992°F), tantamount to an exposure period of 200 minutes, retracted concrete strains were observed (Fig. 10(e)) to retain force equilibrium with the degraded steel strands (Fig. 10(f)).

A comparison of the moment developments between the steel- and CFRP-prestressed concrete girders is made in Fig. 11, contingent upon the exposure time. For the leftmost strands in Fig. 11(a), the developed moment was essentially identical up to 6000 kN·m (4425 kip·ft), after which bifurcations were noticed with the so-called work softening caused by the transferred heat through the flange concrete. When the exposure period was longer than 50 minutes at a surface temperature of 1069°C (1956°F), the softening became evident, and the moment-strain curves were extended substantially (Fig. 11(b)). The moment development with the CFRP tendons was similar to that with the steel strands within the first 40 minutes of fire exposure (Fig. 11(c)); by contrast, obvious alterations were found over 50 minutes (Fig. 11(d)) on account of the drastically deteriorated tensile strength of the tendons (Fig. 4(d)). The abated strength and modulus of CFRP, elaborated in Fig. 8, were the source of the heightened sensitivity to the heat, which provoked a large reduction in the girder moment (Fig. 11(d)).

Moment capacity

Figure 12(a) plots the increased usable strain of the steel strands with temperature, arising from the extended softening behavior of the strands in the post-peak regime (Fig. 12(a), inset) for which the dislocation of polycrystalline configurations in the steel's microstructure is responsible.[57] As opposed to the steel strands, the rupture strain of the CFRP tendons diminished with an increase in temperature (Fig. 12(b)). Considering that the thermal decomposition of CFRP was taken as an executable demarcation, the operational temperature zone of CFRP was restricted up to 400°C (752°F) for the computation of moment capacity (M_n). Figures 12(c) and (d) demonstrate the fire endurance of the girders, signifying their declining load-carrying capacities. For clarity of instruction, surface temperatures ($T_{surface}$) were indicated at 0 and 200 minutes. As the thermomechanical loadings were associated, the capacities of the steel-prestressed girder plummeted (Fig. 12(c)): the decreased stress

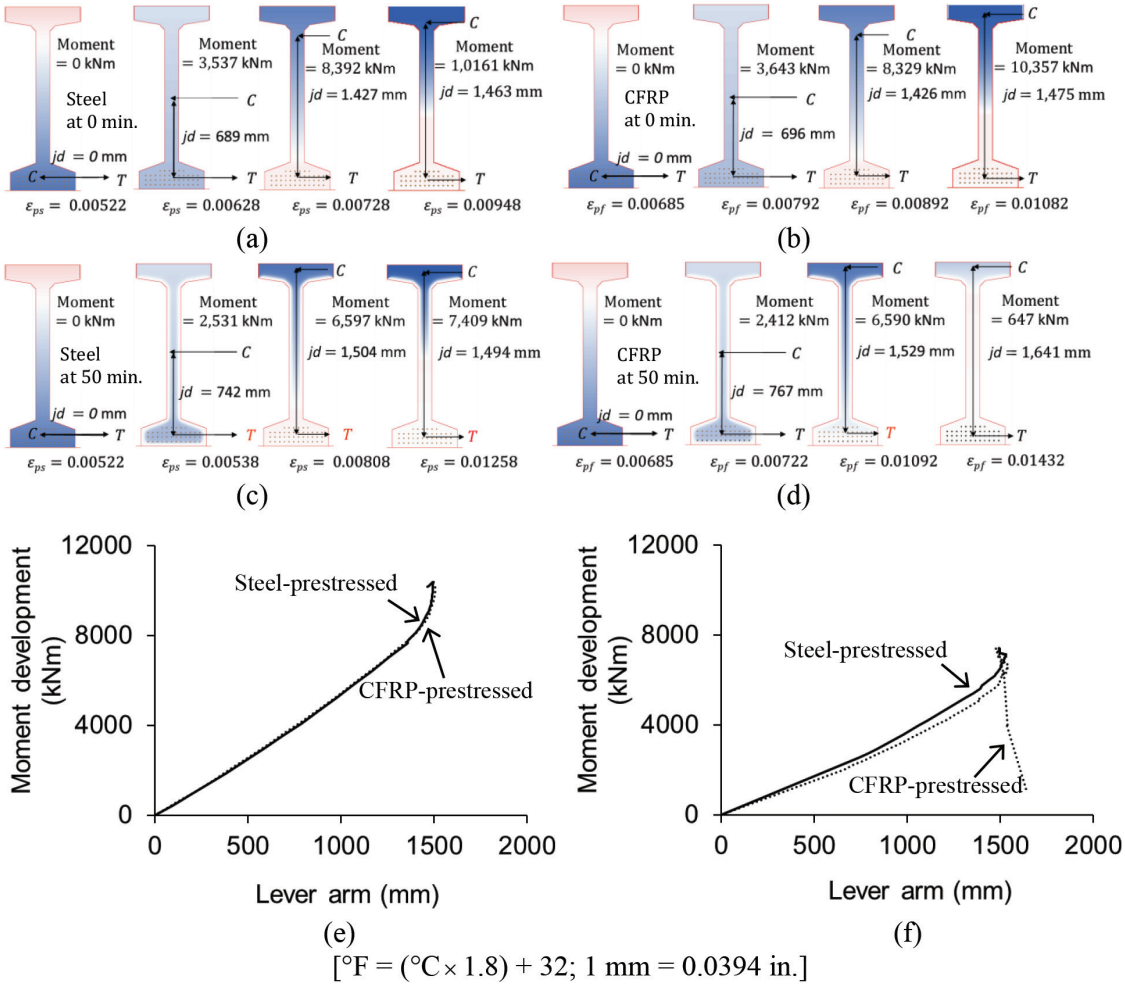


Fig. 9—Variation in lever arm between resultant forces in compression and tension under flexural loading: (a) steel-prestressed girder at 0 minutes ($T_{surface}$ = 20°C [68°F]); (b) CFRP-prestressed girder at 0 minutes ($T_{surface}$ = 20°C [68°F]); (c) steel-prestressed girder at 50 minutes ($T_{surface}$ = 1069°C [1956°F]); (d) CFRP-prestressed girder at 50 minutes ($T_{surface}$ = 1069°C [1956°F]); (e) moment development at 0 minutes ($T_{surface}$ = 20°C [68°F]); and (f) moment development at 50 minutes ($T_{surface}$ = 1069°C [1956°F]).

of the steel strands with the increased temperature (Fig. 4(c)) lowered the tensile forces and, thereby, the flexural resistance of the girder descended. Likewise, the CFRP-prestressed concrete girder suffered from the high temperatures (Fig. 12(d)). Because the temperature of the inner tendons was less than the thermal decomposition temperature, a complete collapse of the girder was not observed with a moment capacity of 765 kN·m (564 kip·ft) at 200 minutes. The exposure time for a transition from the compression- (Mode 1) to tension-controlled (Mode 2) sections with the steel strands (Fig. 12(c)) was 224.5% longer than its CFRP counterpart (Fig. 12(d)), epitomizing the functional vulnerability of the composite tendons in fire.

PERFORMANCE-BASED DESIGN

Upon completion of the numerical investigations, the performance of steel- and CFRP-prestressed concrete girders is evaluated against a predetermined protocol that addresses the limitations of prescriptive guidelines. By means of a state-of-the-art design philosophy, fire ratings are particularized, and the validity of the girders is discovered.

Performance criteria

Table 3 enumerates the criteria of performance-based design for concrete members subjected to fire.[58] The four performance levels (P-I to P-IV) are classified as per the remaining capacity of the members, denoting the extent of thermal damage. The implementation of these criteria is graphed in Fig. 13(a) and (b), where the ordinate refers to the normalized capacities of the steel- and CFRP-prestressed girders, respectively. For a full-range appraisal, both failure modes were involved (Modes 1 and 2 are in solid and dotted lines, respectively). The transition of failure from Mode 1 to Mode 2 took place within the "life safety" level (P-III), implying that concrete crushing was dominant when these girders failed under service loadings (P-I is "full design loads" and P-II is "ordinary service loads"). This is reaffirmed in Fig. 13(c), contrasting the flexural capacities of the girders to the full-service loading ($1.0M_{DL} + 1.0M_{LL}$, where M_{DL} and M_{LL} are the dead and live load moments, respectively). The design load of ASCE/SEI 7-22[59] under fire ($1.2M_{DL} + 0.5M_{LL}$) approached the P-III level (limited service loads), which was reasonable to manifest the effect of restricted vehicular loadings. In terms of the performance

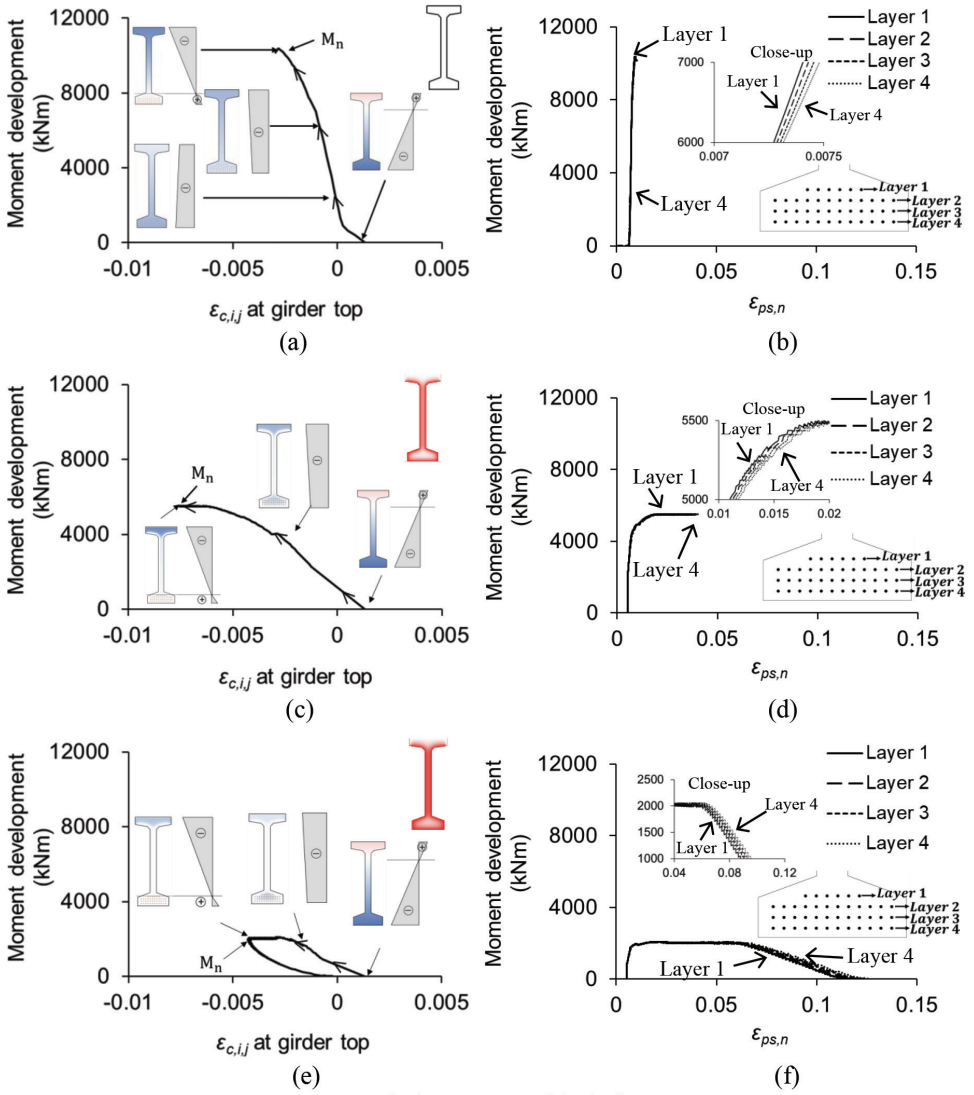


Fig. 10—Moment development of steel-prestressed concrete girder: (a) with concrete strain at girder top under mechanical loading ($T_{surface}$ = 20°C [68°F]); (b) with steel strain under mechanical loading ($T_{surface}$ = 20°C [68°F]); (c) with concrete strain at girder top under thermomechanical loading ($T_{surface}$ = 1081°C [1977°F]); (d) with steel strain under thermomechanical loading ($T_{surface}$ = 1081°C [1977°F]); (e) with concrete strain at girder top under thermomechanical loading ($T_{surface}$ = 1089°C [1992°F]); and (f) with steel strain under thermomechanical loading ($T_{surface}$ = 1089°C [1992°F]).

levels, the steel- and CFRP-prestressed girders were almost the same (Fig. 13(c)), justifying the use of the nonconventional prestressing element for highway bridges exposed to a potential fire.

Fire rating

The fire ratings of the girders at specific performance levels are charted in Fig. 13(d). The durations of P-I and P-II were less than 0.3 hours and 0.7 hours, respectively, without regard to the type of the prestressing element. On the contrary, the rating of the steel-prestressed girder became longer for the P-III and P-IV levels than the CFRP-prestressed girder by 26.2% and 26.5%, respectively. The inset of Fig. 13(d) brings to light the relative performance of those girders. In opposition to the archetypal misconception that CFRP materials are unsuitable for concrete structures under a fire hazard, the predicted fire endurance of the CFRP-prestressed girder was not notably lower than that of the steel-prestressed girder, including a fire rating of 1.66 hours at the "near collapse" level (P-IV). While previous research corroborates that highway bridges undergo structurally critical states accompanied by an imminent collapse within 1 to 3 hours from the ignition of a fire,[2,60,61] full-scale testing is recommended to verify this numerical hypothesis.

SUMMARY AND CONCLUSIONS

This paper discussed the behavior of bridge girders prestressed with steel strands and carbon fiber-reinforced polymer (CFRP) tendons under a hydrocarbon fire. Based on an actual bridge fire in Lakewood, CO, numerical simulations were carried out to account for the complex load-bearing mechanisms and failure characteristics of these girders. Agent-based modeling, a novel computational platform, processed heat transfer and predicted the progression of strains and stresses in the structural components at elevated temperatures. Design aspects were emphasized to appraise

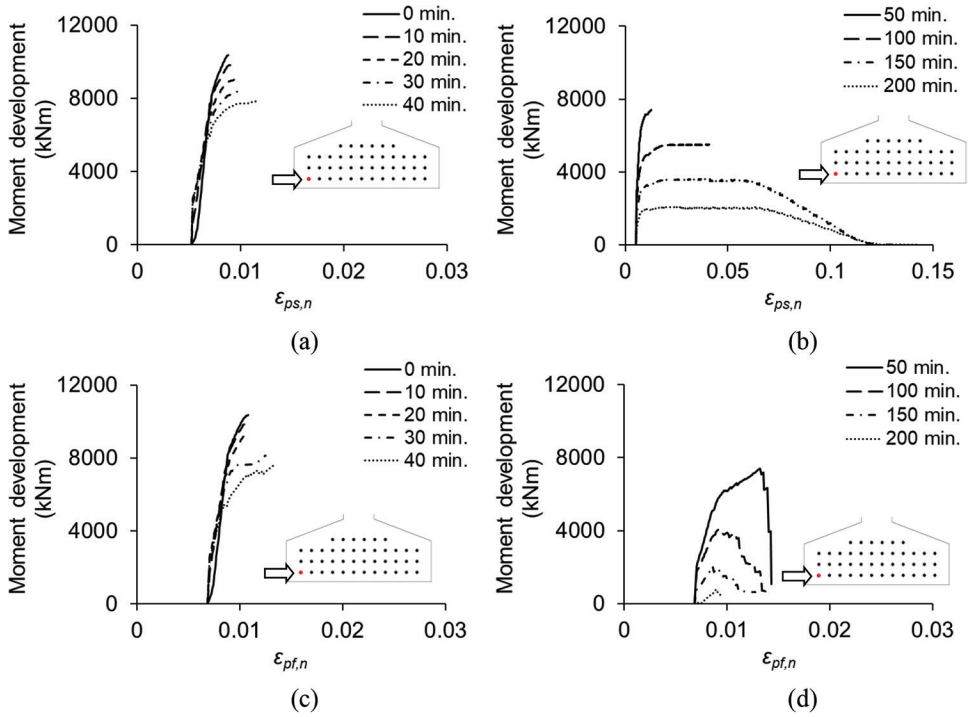


Fig. 11—Comparison of moment development between steel and CFRP in Layer 4: (a) steel strands from 0 to 40 minutes ($T_{surface}$ = 20 to 1063°C [68 to 1945°F]); (b) steel strands from 50 to 200 minutes ($T_{surface}$ = 1069 to 1089°C [1956 to 1992°F]); (c) CFRP tendons from 0 to 40 minutes ($T_{surface}$ = 20 to 1063°C [68 to 1945°F]); and (d) CFRP tendons from 50 to 200 minutes ($T_{surface}$ = 1069 to 1089°C [1956 to 1992°F]).

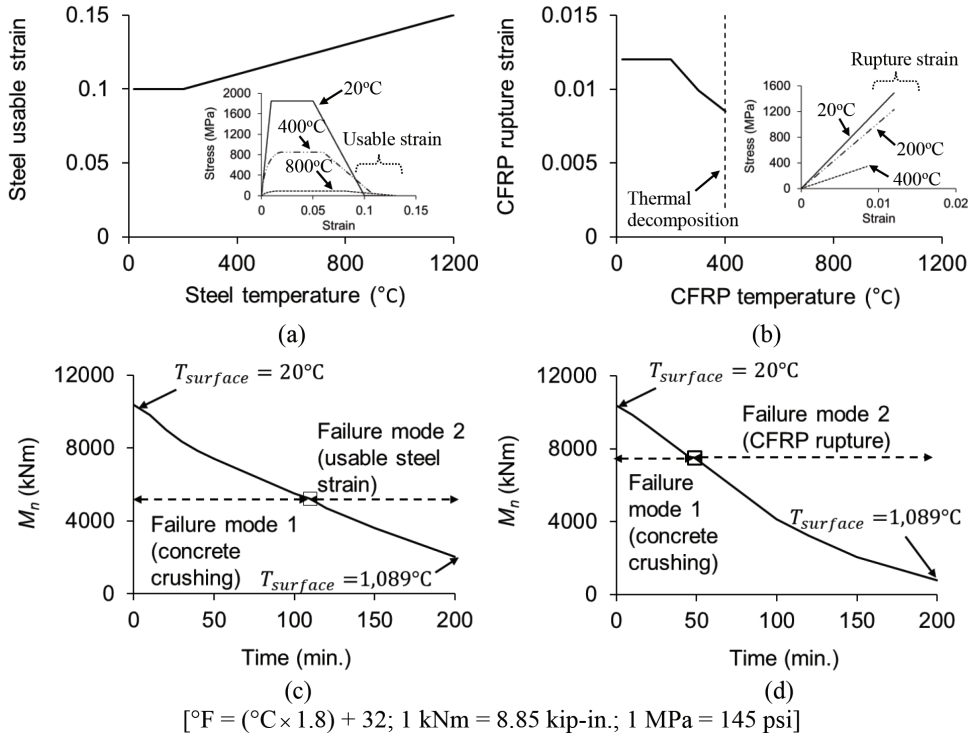


Fig. 12—Degraded flexural capacity due to thermal loading: (a) usable strain of steel; (b) rupture strain of CFRP; (c) steel-prestressed girder; and (d) CFRP-prestressed girder.

the adverse outcomes of the thermomechanical distress from a practical point of view. To improve predictions, future research may address the limitations of the current modeling work, such as temperature-dependent concrete spalling, the probabilistic nature of material and geometric properties, risk analysis, and experimental evaluations. The following are concluded:

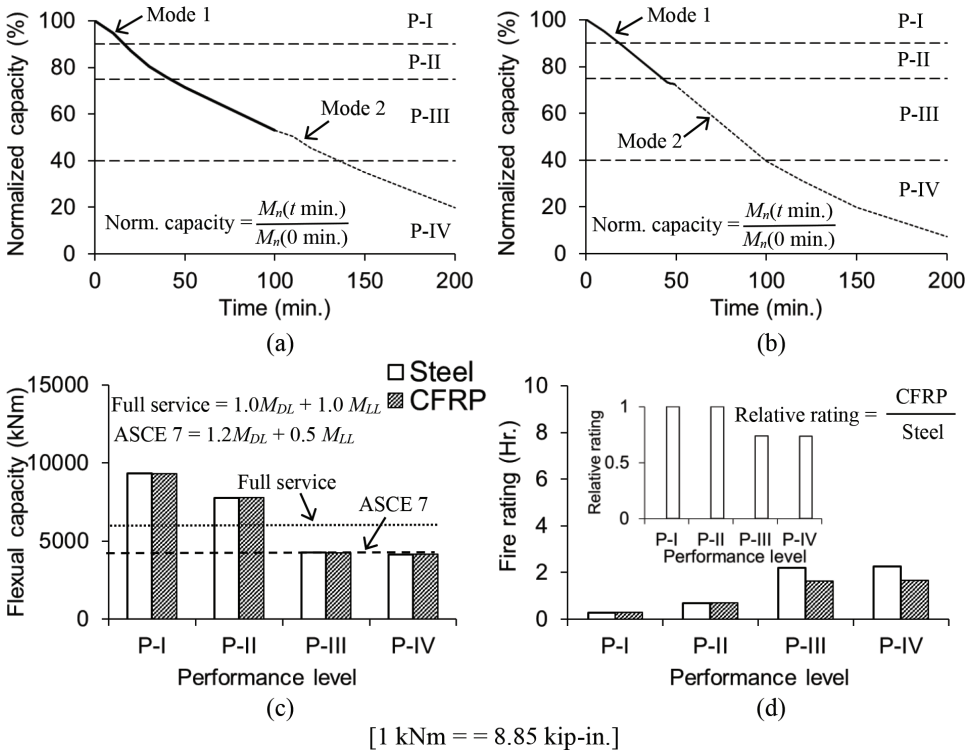


Fig. 13—Performance-based design: (a) steel-prestressed girder; (b) CFRP-prestressed girder; (c) assessment of performance levels; and (d) fire rating.

Table 3—Performance criteria

Performance level	Description	Condition of live load	Remaining capacity
P-I	Fully operational	Full design loads	90 to 100%
P-II	Operational	Ordinary service loads	75 to 89%
P-III	Life safety	Limited service loads	41 to 74%
P-IV	Near collapse	No occupancy	<40%

- Temperature differentials inside the girder exposed to the multidirectional heat transfer decreased over time and, after 50 minutes, the surface concrete reached thermal equilibrium with the surroundings. The distance of the prestressing elements from the applied heat was a crucial factor in ascertaining the degree of temperature-induced damage. The mechanical properties of the steel and CFRP declined with temperature, and both experienced noticeable changes before and after 400°C (752°F), at which point the thermal decomposition of the composite occurred.
- Under the flexural loading without thermal stress, the moment-carrying mechanism of the steel- and CFRP-prestressed girders was alike in terms of the lever arm, camber growth, and tensile strain developments. When thermal loading was involved, their responses bifurcated after an exposure period of 50 minutes (surface temperature = 1069°C [1956°F]), and the work-softening behavior through the flange concrete became prominent with extended steel strains.
- The usable post-peak strain of the steel strands increased by 50% at high temperatures, while the rupture strain of the CFRP tendons declined by 29% until the thermal decomposition temperature of 400°C (752°F) was reached. The trend of thermally degraded moment capacities was not controlled by the type of the prestressing element; however, the compression-controlled failure (Mode 1) of the steel-prestressed girder was maintained 224.5% longer than that of the CFRP-prestressed girder.
- In conformity with the performance-based design concept (P-I to P-IV), the steel- and CFRP-prestressed girders revealed comparable performance levels. Concrete crushing was the primary failure of the girders under service loadings (the P-I [full design loads] and P-II [ordinary service loads] levels). The ASCE/SEI 7-22 design load was paired with the P-III (limited service loads) level.
- The fire ratings of the girders belonging to P-I and P-II were 0.3 hours and 0.7 hours, respectively. The steel-prestressed girder outperformed the CFRP-prestressed one by approximately 26% in P-III and P-IV apiece. Overall, the fire endurance of the CFRP-prestressed girder was analogous to that of the steel-prestressed girder.

AUTHOR BIOS

Jun Wang *is an Assistant Professor in the Department of Civil, Environmental and Construction Engineering at the University of Hawai'i at Mānoa, Honolulu, HI. She received her BS from Northeast Forestry University, Harbin, Heilongjiang, China, and her MS and PhD from the University of Colorado Denver, Denver, CO. Her research interests include multi-object interactions, concrete structures, and advanced computer simulations.*

Yail J. Kim, *FACI, is President of the Bridge Engineering Institute, An International Technical Society, and a Professor in the Department of Civil Engineering at the University of Colorado Denver. He is past Chair of ACI Committee 345, Bridge Construction and Preservation, and ACI Subcommittee 440-I, FRP-Prestressed Concrete, and is a member of ACI Committees 342, Evaluation of Concrete Bridges and Bridge Elements; 377, Performance-Based Structural Integrity & Resilience of Concrete Structures; and 440, Fiber-Reinforced Polymer Reinforcement; and Joint ACI-ASCE Committee 343, Concrete Bridge Design. He received the Chester Paul Siess Award for Excellence in Structural Research in 2019. His research interests include advanced composite materials for rehabilitation; structural informatics; complex systems; and science-based structural engineering, including statistical, interfacial, and quantum physics.*

ACKNOWLEDGMENTS

The authors would like to acknowledge support from the U.S. Department of Transportation through the Mountain-Plains Consortium. Technical contents presented in this paper are based on the opinions of the writers and do not necessarily represent those of others.

REFERENCES

1. Wright, W.; Lattimer, B.; Woodworth, M.; Nahid, M.; and Sotelino, E., "Highway Bridge Fire Hazard Assessment," NCHRP 12-85, Virginia Polytechnic Institute and State University, Blacksburg, VA, 2013, 492 pp.

2. Park, J.; Cho, Y. K.; and Shim, J., "Resilient Fire Prevention and Management Strategies for Structures and Materials Stored under Urban Bridges," *Construction Research Congress 2018: Safety and Disaster Management*, New Orleans, LA, 2018, pp. 584-593.

3. AASHTO, "AASHTO LRFD Bridge Design Specifications," ninth edition, American Association of State Highway and Transportation Officials, Washington, DC, 2020.

4. Lee, G. C.; Mohan, S. B.; Huang, C.; and Fard, B. N., "A Study of U.S. Bridge Failures (1980-2012)," Technical Report MCEER-13-0008, Multidisciplinary Center for Earthquake Engineering Research, State University of New York at Buffalo, Buffalo, NY, 2013, 148 pp.

5. ASTM E119-20, "Standard Test Methods for Fire Tests of Building Construction and Materials," ASTM International, West Conshohocken, PA, 2020, 36 pp.

6. Wu, X.-Q.; Huang, T.; Au, F. T. K.; and Li, J., "Posttensioned Concrete Bridge Beams Exposed to Hydrocarbon Fire," *Journal of Structural Engineering*, ASCE, V. 146, No. 10, Oct. 2020, p. 04020210. doi: 10.1061/(ASCE)ST.1943-541X.0002791

7. Beneberu, E., and Yazdani, N., "Performance of CFRP-Strengthened Concrete Bridge Girders under Combined Live Load and Hydrocarbon Fire," *Journal of Bridge Engineering*, ASCE, V. 23, No. 7, July 2018, p. 04018042. doi: 10.1061/(ASCE)BE.1943-5592.0001244

8. Garlock, M.; Paya-Zaforteza, I.; Kodur, V.; and Gu, L., "Fire Hazard in Bridges: Review, Assessment and Repair Strategies," *Engineering Structures*, V. 35, Feb. 2012, pp. 89-98. doi: 10.1016/j.engstruct.2011.11.002

9. Hu, J.; Carvel, R.; and Usmani, A., "Bridge Fires in the 21st Century: A Literature Review," *Fire Safety Journal*, V. 126, Dec. 2021, Article No. 103487. doi: 10.1016/j.firesaf.2021.103487

10. Dolan, C. W., "FRP Prestressing in the U.S.A," *Concrete International*, V. 21, No. 10, Oct. 1999, pp. 21-24.

11. ACI Committee 440, "Prestressing Concrete Structures with FRP Tendons (ACI 440.4R-04) (Reapproved 2011)," American Concrete Institute, Farmington Hills, MI, 2004, 35 pp.

12. Wang, G.-B.; Na, J.-X.; and Chen, X., "Characterization and Rapid Prediction of the Effect of Hygrothermal Ageing on the Interlaminar Shear Strength of CFRP at a High Temperature," *Journal of Materials Science*, V. 57, No. 26, July 2022, pp. 12653-12671. doi: 10.1007/s10853-022-07428-w

13. Hu, W., *Polymer Physics: A Molecular Approach*, Springer-Verlag Wien, Vienna, Austria, 2013, 248 pp.

14. Grace, N. F.; Mohamed, M. E.; Chynoweth, M.; Kose, N.; and Bebawy, M., "Effect of Elevated Temperatures on the Mechanical Properties and Relaxation of CFRP Strands," *Journal of Composites for Construction*, ASCE, V. 25, No. 3, June 2021, p. 04021019. doi: 10.1061/(ASCE)CC.1943-5614.0001127

15. Maluk, C.; Terrasi, G. P.; Bisby, L.; Stutz, A.; and Hugi, E., "Fire Resistance Tests on Thin CFRP Prestressed Concrete Slabs," *Construction and Building Materials*, V. 101, Part 1, Dec. 2015, pp. 558-571. doi: 10.1016/j.conbuildmat.2015.10.031

16. Jeyashree, T. M.; Kannan Rajkumar, P. R.; and Satyanarayanan, K. S., "Developments and Research on Fire Response Behaviour of Prestressed Concrete Members – A Review," *Journal of Building Engineering*, V. 57, Oct. 2022, Article No. 104797. doi: 10.1016/j.jobe.2022.104797

17. NFPA 502, "Standard for Road Tunnels, Bridges, and Other Limited Access Highways," National Fire Protection Association, Quincy, MA, 2020.

18. Hou, W.; Zhang, G.; and He, S., "Fire Resistance Tests on Prestressed Concrete Box Girder with Intumescent Fire-Retardant Coatings," *Fire Technology*, V. 58, No. 1, Jan. 2022, pp. 107-131. doi: 10.1007/s10694-021-01145-7

19. Kumar, P., and Kodur, V. K. R., "Response of Prestressed Concrete Beams under Combined Effects of Fire and Structural Loading," *Engineering Structures*, V. 246, Nov. 2021, Article No. 113025. doi: 10.1016/j.engstruct.2021.113025

20. Liu, X.; Yu, C.; Quan, W.; and Chen, L., "Inspection, Materials Testing and Field Testing of a Prestressed Concrete Box Bridge after Fire Exposure," *Fire Safety Journal*, V. 108, Sept. 2019, Article No. 102852. doi: 10.1016/j.firesaf.2019.102852

21. Hughes Brothers, "Carbon Fiber Reinforced Polymer (CFRP) Rebar," Hughes Brothers, Inc., Seward, NE, 2017.

22. Plecnik, J. M.; Bresler, B.; Cunningham, J. D.; and Iding, R., "Temperature Effects on Epoxy Adhesives," *Journal of the Structural Division*, ASCE, V. 106, No. 1, Jan. 1980, pp. 99-113. doi: 10.1061/JSDEAG.0005362

23. Saafi, M., "Effect of Fire on FRP Reinforced Concrete Members," *Composite Structures*, V. 58, No. 1, Oct. 2002, pp. 11-20. doi: 10.1016/S0263-8223(02)00045-4

24. Chen, H.; Wang, F. S.; Ma, X. T.; and Yue, Z. F., "The Coupling Mechanism and Damage Prediction of Carbon Fiber/Epoxy Composites Exposed to Lightning Current," *Composite Structures*, V. 203, Nov. 2018, pp. 436-445. doi: 10.1016/j.compstruct.2018.07.017

25. Najafabadi, E. P.; Oskouei, A. V.; Khaneghahi, M. H.; Shoaei, P.; and Ozbakkaloglu, T., "The Tensile Performance of FRP Bars Embedded in Concrete under Elevated Temperatures," *Construction and Building Materials*, V. 211, June 2019, pp. 1138-1152. doi: 10.1016/j.conbuildmat.2019.03.239

26. Kim, Y. J., and Micnhimer, D., "Stochasticity on Long-Term Behavior of Steel-/Carbon Fiber-Reinforced Polymer Prestressed Girders," *ACI Structural Journal*, V. 118, No. 2, Mar. 2021, pp. 33-47.

27. EN 1991-1-2:2002, "Eurocode 1: Actions on Structures – Part 1-2: General Actions – Actions on Structures Exposed to Fire," European Committee for Standardization, Brussels, Belgium, 2002, 61 pp.

28. Li, T. M., *Cellular Automata*, Nova Science Publishers, Hauppauge, NY, 2011, 295 pp.

29. Tadelis, S., *Game Theory: An Introduction*, Princeton University Press, Princeton, NJ, 2013, 416 pp.

30. Manzo, G., *Agent-based Models and Causal Inference*, John Wiley & Sons, Inc., Hoboken, NJ, 2022, 176 pp.

31. Wilensky, U., and Rand, W., *An Introduction to Agent-Based Modeling: Modeling Natural, Social, and Engineered Complex Systems with NetLogo*, The MIT Press, Cambridge, MA, 2015, 504 pp.

32. Taler, J., and Duda, P., *Solving Direct and Inverse Heat Conduction Problems*, Springer-Verlag Berlin Heidelberg, Berlin, Germany, 2006, 889 pp.

33. Bergman, T. L.; Lavine, A. S.; Incropera, F. P.; and DeWitt, D. P., *Introduction to Heat Transfer*, sixth edition, John Wiley & Sons, Inc., Hoboken, NJ, 2011, 960 pp.

34. Biondini, F., and Nero, A., "Cellular Finite Beam Element for Nonlinear Analysis of Concrete Structures under Fire," *Journal of Structural Engineering*, ASCE, V. 137, No. 5, May 2011, pp. 543-558. doi: 10.1061/(ASCE)ST.1943-541X.0000307

35. Branco, F. A., and Mendes, P. A., "Thermal Actions for Concrete Bridge Design," *Journal of Structural Engineering*, ASCE, V. 119, No. 8, Aug. 1993, pp. 2313-2331. doi: 10.1061/(ASCE)0733-9445(1993)119:8(2313)

36. Xiong, M.-X.; Wang, Y.; and Liew, J. Y. R., "Evaluation on Thermal Behavior of Concrete-Filled Steel Tubular Columns Based on Modified Finite Difference Method," *Advances in Structural Engineering*, V. 19, No. 5, May 2016, pp. 746-761. doi: 10.1177/1369433215622864

37. Hajiloo, H.; Green, M. F.; Noël, M.; Bénichou, N.; and Sultan, M., "Fire Tests on Full-Scale FRP Reinforced Concrete Slabs," *Composite Structures*, V. 179, Nov. 2017, pp. 705-719. doi: 10.1016/j.compstruct.2017.07.060

38. Hertz, K. D., "Concrete Strength for Fire Safety Design," *Magazine of Concrete Research*, V. 57, No. 8, Oct. 2005, pp. 445-453. doi: 10.1680/macr.2005.57.8.445

39. Khennane, A., and Baker, G., "Uniaxial Model for Concrete under Variable Temperature and Stress," *Journal of Engineering Mechanics*, ASCE, V. 119, No. 8, Aug. 1993, pp. 1507-1525. doi: 10.1061/(ASCE)0733-9399(1993)119:8(1507)

40. Lie, T. T., and Lin, T. D., "Fire Performance of Reinforced Concrete Columns," *Fire Safety: Science and Engineering*, ASTM STP 882, T. Harmathy, ed., ASTM International, West Conshohocken, PA, 1985, pp. 176-205.

41. Vecchio, F. J., and Collins, M. P., "The Modified Compression-Field Theory for Reinforced Concrete Elements Subject to Shear," *ACI Journal Proceedings*, V. 83, No. 2, Mar.-Apr. 1986, pp. 219-231.

42. Cai, J.; Burgess, I.; and Plank, R., "A Generalised Steel/Reinforced Concrete Beam-Column Element Model for Fire Conditions," *Engineering Structures*, V. 25, No. 6, May 2003, pp. 817-833. doi: 10.1016/S0141-0296(03)00019-1

43. Xiao, J., and König, G., "Study on Concrete at High Temperature in China—An Overview," *Fire Safety Journal*, V. 39, No. 1, Feb. 2004, pp. 89-103. doi: 10.1016/S0379-7112(03)00093-6

44. EN 1992-1-2:2004, "Eurocode 2: Design of Concrete Structures – Part 1-2: General Rules – Structural Fire Design," European Committee for Standardization, Brussels, Belgium, 2004, 99 pp.

45. Gilbert, R. I.; Mickleborough, N. C.; and Ranzi, G., *Design of Prestressed Concrete to Eurocode 2*, second edition, CRC Press, Boca Raton, FL, 2017, 699 pp.

46. Nawy, E. G., *Prestressed Concrete: A Fundamental Approach*, Prentice Hall, Hoboken, NJ, 2010, 949 pp.

47. ISO 834-10:2014, "Fire Resistance Tests — Elements of Building Construction — Part 10: Specific Requirements to Determine the Contribution of Applied Fire Protection Materials to Structural Steel Elements," International Organization for Standardization, Geneva, Switzerland, 2014, 61 pp.

48. Dotreppe, J.-C., and Franssen, J.-M., "The Use of Numerical Models for the Fire Analysis of Reinforced Concrete and Composite Structures," *Engineering Analysis*, V. 2, No. 2, June 1985, pp. 67-74. doi: 10.1016/0264-682X(85)90056-5

49. Wu, H. J.; Lie, T. T.; and Hu, J. Y., "Fire Resistance of Beam-Slab Specimens – Experimental Studies," Internal Report No. 641, National Research Council of Canada, Institute for Research in Construction, Ottawa, ON, Canada, 1993, 47 pp.

50. Xu, Q.; Chen, L.; Han, C.; Harries, K. A.; and Xu, Z., "Experimental Research on Fire-Damaged RC Continuous T-Beams Subsequently Strengthened with CFRP Sheets," *Engineering Structures*, V. 183, Mar. 2019, pp. 135-149. doi: 10.1016/j.engstruct.2019.01.025

51. Yu, Y.; Hang, Z.; Zhao, W.; and Zhao, X., "Fire-Resistance Mechanism and Residual Bearing Capacity of Prestressed Concrete Beams after Fire Exposure," *Journal of Structural Engineering*, ASCE, V. 147, No. 8, Aug. 2021, p. 04021109. doi: 10.1061/(ASCE)ST.1943-541X.0003070

52. Yu, B., and Kodur, V. K. R., "Factors Governing the Fire Response of Concrete Beams Reinforced with FRP Rebars," *Composite Structures*, V. 100, June 2013, pp. 257-269. doi: 10.1016/j.compstruct.2012.12.028

53. Zhang, G.; Kodur, V.; Hou, W.; and He, S., "Evaluating Fire Resistance of Prestressed Concrete Bridge Girders," *Structural Engineering and Mechanics*, V. 62, No. 6, June 2017, pp. 663-674.

54. Chabay, R. W., and Sherwood, B. A., *Matter & Interactions*, third edition, John Wiley & Sons, Inc., Hoboken, NJ, 2011, 1099 pp.

55. Toumpanaki, E.; Lees, J. M.; and Terrasi, G. P., "Analytical Predictive Model for the Long-Term Bond Performance of CFRP Tendons in Concrete," *Composite Structures*, V. 250, Oct. 2020, Article No. 112614. doi: 10.1016/j.compstruct.2020.112614

56. Yatim, N. M.; Shamsudin, Z.; Shaaban, A.; Sani, N. A.; Jumaidin, R.; and Shariff, E. A., "Thermal Analysis of Carbon Fibre Reinforced Polymer Decomposition," *Materials Research Express*, V. 7, No. 1, Jan. 2020, Article No. 015615. doi: 10.1088/2053-1591/ab688f

57. Khalaf, J., and Huang, Z., "Analysis of the Bond Behaviour between Prestressed Strands and Concrete in Fire," *Construction and Building Materials*, V. 128, Dec. 2016, pp. 12-23. doi: 10.1016/j.conbuildmat.2016.10.016

58. Kim, Y. J., and Wang, J., "Thermal Performance of Concrete Slabs Reinforced with Glass Fiber-Reinforced Polymer Bars," *ACI Structural Journal*, V. 119, No. 6, Nov. 2022, pp. 67-82.

59. ASCE/SEI 7-22, "Minimum Design Loads and Associated Criteria for Buildings and Other Structures," American Society of Civil Engineers, Reston, VA, 2022, 1072 pp.

60. Bajwa, C. S.; Easton, E. P.; Adkins, H.; Cuta, J.; Klymshyn, N.; and Suffield, S., "The MacArthur Maze Fire and Roadway Collapse: A 'Worst Case Scenario' for Spent Nuclear Fuel Transportation?" *Proceedings of the ASME 2012 Pressure Vessels and Piping Conference (PVP2012)*, Toronto, ON, Canada, July 2012, pp. 261-269.

61. de Melo, M.; Wheatley, R.; Gibbin, N.; Gonzalez-Quesada, M.; and Harwood, K., "Assessment and Repair of a Fire-Damaged Pre-stressed Concrete Bridge," *Structural Engineering International*, V. 24, No. 3, 2014, pp. 408-413. doi: 10.2749/101686614X13844300210272

ACI STRUCTURAL JOURNAL TECHNICAL PAPER

Title No. 121-S65

Strength and Serviceability of Shear-Critical Post-Tensioned Girders

by Sangyoung Han, Jarrod Zaborac, Jongkwon Choi, Anca C. Ferche, and Oguzhan Bayrak

The results of an experimental program conducted to evaluate the performance of shear-critical post-tensioned I-girders with grouted and ungrouted ducts are presented. The experimental program involved the design, construction, and testing to failure of six full-scale specimens with different duct layouts (straight, parabolic, or hybrid) and using both grouted or ungrouted ducts. All tests resulted in similar failure modes, such as localized web crushing in the vicinity of the duct, regardless of the duct condition or layout. Furthermore, the normalized shear stresses at ultimate were similar for the grouted and ungrouted specimens. The current shear design provisions in the AASHTO LRFD Bridge Design Specifications (AASHTO LRFD) were reviewed, and updated shear-strength reduction factors to account for the presence of the duct in the web and its condition (that is, grouted or ungrouted) were proposed. The data generated from these tests served as the foundation for updated shear-strength reduction factors proposed for implementation in AASHTO LRFD.

Keywords: AASHTO LRFD; flexible filler; post-tensioned concrete member; post-tensioning; prestressed I-girder; shear; spliced precast girder.

INTRODUCTION

Spliced post-tensioned girder technology emerged as a powerful construction application in the United States in the 1970s.[1,2] This construction process has several advantages, including faster construction and the ability to achieve bridge spans of approximately 300 ft (91 m), surpassing the limitations of traditional approaches limited to 170 ft (52 m) due to transportation constraints such as weight and length restrictions.[3] When spliced girders with multistrand post-tensioning systems (that is, post-tensioning tendons) are used, the post-tensioning ducts are injected with a cement-based mixture as the primary choice for corrosion protection, referred to as grouted duct hereafter.[2]

Multistrand post-tensioning systems have traditionally employed cementitious grout to fill the duct to protect the tendons against corrosion and, for bonded post-tensioning, to facilitate the transfer of force between the tendon and the surrounding concrete. The quality of the grout is vital to the tendon performance and durability—any compromise results in significant and accelerated deterioration. Although recently, grout quality has improved significantly, inspection and long-term quality assurance of tendons embedded in grout continue to be challenging, and corrosion issues have been reported.[3] More importantly, the bond between the tendon and the grout makes it significantly difficult to replace potentially damaged tendons. This led to the interest in post-tensioned concrete girders that use flexible fillers in lieu of cementitious grout to fill the post-tensioning ducts, referred to as ungrouted duct hereafter. Hamilton et al.[4] evaluated the constructability of ungrouted duct systems using non-cementitious flexible filler materials, such as petroleum wax, grease, and gel, and successfully demonstrated viable options for the replacement of the grout mixture. The use of flexible fillers can overcome the innate problem of grout quality and ease prospective tendon replacement procedures. To this end, a non-cementitious material to fill the post-tensioning duct has been adopted by the Florida Department of Transportation.[3]

Design applications for spliced girders have been embodied in various code provisions, such as the AASHTO general procedure,[5] AASHTO segmental procedure,[6] PCI Bridge Design Manual,[7] Eurocode 2[8], and *fib* Model Code.[9] Invariably, for the calculation of the shear capacity, the aforementioned provisions apply a web-width reduction factor (k), intended to account for the effect of the post-tensioning duct on the shear strength. As summarized in Table 1, the design provisions adopt different values for the web-width reduction factor. The most recent edition of the AASHTO general procedure for shear design (hereafter referred to as AASHTO LRFD), includes a web-width reduction factor, in addition to the novel inclusion of a shear-strength reduction factor (λ_{duct}). To assess the adequacy of the AASHTO LRFD reduction factors (k and λ_{duct}), Moore et al.[10] conducted tests on large-scale post-tensioned members with grouted ducts only. As a result, the AASHTO LRFD provisions were verified against an incomplete database of specimens and could result in potentially inadequately designed

Table 1—Web-width reduction factors for codes considered

Code provision	Ungrouted steel duct	Grouted steel duct	Ungrouted plastic duct	Grouted plastic duct
AASHTO general procedure[5]	1.0	0.0	1.0	0.0
AASHTO segmental procedure[6]	1.0	0.5	1.0	0.5
PCI Bridge Design Manual[7]	0.5	0.25	0.5	0.25
Eurocode 2[8]	1.2	0.5	1.2	1.2
fib Model Code[9]	1.2	0.5	1.2	0.8

ACI Structural Journal, V. 121, No. 5, September 2024.
MS No. S-2022-398.R4, doi: 10.14359/51740847, received March 27, 2024, and reviewed under Institute publication policies. Copyright © 2024, American Concrete Institute. All rights reserved, including the making of copies unless permission is obtained from the copyright proprietors. Pertinent discussion including author's closure, if any, will be published ten months from this journal's date if the discussion is received within four months of the paper's print publication.

post-tensioned girders with the ungrouted ducts. Thus, large-scale testing was necessary to investigate the response of ungrouted post-tensioned specimens.

The work presented herein was conducted to advance the knowledge of the response of shear-critical post-tensioned girders with ungrouted ducts and address the lack of large-scale experimental data on the response of this type of structural member. A thorough experimental program was designed to compare the structural performance of girders with different post-tensioning profiles and either grouted or ungrouted ducts. The experimental program focused on two main variables: 1) three different duct layouts (that is, straight, parabolic, and hybrid); and 2) grouted and ungrouted ducts for each layout. As the contribution of flexible fillers to the shear behavior is negligible, it was assumed that the shear performance of post-tensioning girders with flexible fillers would be similar to those with empty ungrouted ducts.[11] Despite its extensive scope, the testing program did not aim to incorporate every conceivable design variable. Instead, it prioritized the most influential ones to significantly enhance the knowledge and comprehension of the behavior of shear-critical post-tensioned girders with grouted and ungrouted ducts.

The experimental program comprised three key components: 1) fabrication of six test specimens in a precast plant, ensuring consistent fabrication practices with those employed for precast bridge elements; 2) conducting 12 full-scale laboratory tests on the girders to study the shear behavior; and 3) analyzing the structural response data. As a result of this research, modifications were suggested to enhance the calculation of shear resistance in the AASHTO LRFD general procedure of post-tensioned members. These advancements contribute to a better understanding of the shear response in post-tensioned concrete members and pave the way for improved design practices.

RESEARCH SIGNIFICANCE

The research significance of this study lies in the growing interest in unbonded multistrand post-tensioning systems using flexible fillers, which address the durability concerns introduced by cementitious grout. Understanding the large-scale behavior of such members, especially in terms of shear performance, is crucial. The primary goal of this research was to enhance the understanding of the response exhibited by shear-critical post-tensioned girders with ungrouted ducts concerning both strength and serviceability. Through an extensive experimental program, direct comparisons were made between the behavior of I-girders with grouted and ungrouted ducts. The findings from testing of large-scale specimens offered valuable insight into the behavior and governing failure mechanisms. This research's meticulous analysis of large-scale test data shed light on the underlying shear-resisting mechanisms of post-tensioned concrete members. Consequently, the research led to proposed modifications for the calculation of shear resistance in the AASHTO LRFD general procedure for shear design. These modifications aim to improve the design practices for post-tensioned concrete girders.

BACKGROUND: AASHTO LRFD GENERAL SHEAR DESIGN PROVISIONS

The AASHTO LRFD general procedure for sectional shear design is based on the Modified Compression Field Theory (MCFT).[12] A series of simplifying assumptions were made to recast the MCFT into design equations, including: the longitudinal strain is assumed to be distributed linearly over the depth of the member, the orientation of the compressive stress field is unchanged over the depth, and it is assumed the stirrups yield before concrete crushing occurs. These simplifications facilitate the application of the MCFT to practical design scenarios, allowing for the calculation of shear capacity in reinforced and prestressed concrete members in accordance with AASHTO LRFD guidelines.

Nominal shear resistance in AASHTO LRFD

The nominal shear resistance in AASHTO LRFD[5] is calculated as the lesser of the following two equations

$$V_{n1} = V_c + V_s + V_p \tag{1}$$

$$V_{n2} = 0.25 f_c' b_v d_v + V_p \tag{2}$$

Equation (1), referred to as V_{n1} hereafter, represents the shear resistance provided by the concrete component (V_c), the transverse reinforcement (V_s), and the component of the prestressing force in the direction of the shear force (V_p), which is taken as positive if it is resisting the applied shear. Equation (2), referred to as V_{n2} hereafter, is an upper limit on the nominal shear resistance intended to ensure that the concrete in the web will not crush prior to the yield of the transverse reinforcement.

The shear resistance contribution of the concrete, V_c, represents the ability of cracked concrete to carry shear stresses through aggregate interlock action, and it is evaluated as

$$V_c = 0.0316\beta\sqrt{f_c'}\, b_v d_v \text{ (Imperial units)} \tag{3}$$

The shear resistance provided by the transverse reinforcement, V_s, is calculated as

$$V_s = \frac{A_v f_y d_v (\cot\theta + \cot\alpha)\sin\alpha}{s}\lambda_{duct} \tag{4}$$

One of the assumptions of the shear design provisions in AASHTO LRFD is that the stirrups shall yield before the concrete fails in compression through web crushing. A study by Bentz et al.[13] derived an ultimate shear stress limit of $0.25f_c'$ and validated the normalized shear stress to prevent concrete crushing prior to stirrup yielding. This led to the development of Eq. (2) as an upper limit imposed on the nominal shear resistance.

Effective web-width factor, b_v

The reduction in shear resistance due to the presence of ungrouted ducts is taken into account by reducing the web width, as per Article 5.7.2.8 in AASHTO LRFD. The effective web width, b_v, is calculated as

$$b_v = b_w - k\phi_{duct} \quad (5)$$

For post-tensioned members with ungrouted ducts, the web width is reduced by the diameter of the duct; therefore, k has a value equal to 1.0. No web-width reduction is applied for grouted ducts; as such, k has a value equal to 0.0. Originally, the coefficient k was evaluated based on results obtained from small-scale panel tests, designed to be representative of the diagonal compressive strut formed by shear loading within a beam.[14,15] The coefficient k was assigned values based on the duct material (corrugated metal or plastic), as well as the duct conditions (grouted or ungrouted). The current values for k in AASHTO LRFD were derived from large-scale post-tensioned I-girder specimens conducted by Moore et al.[10] that solely considered grouted duct conditions.

Shear-strength reduction factor, λ_{duct}

AASHTO LRFD accounts for the reduction in shear resistance due to the presence of grouted ducts through the shear-strength reduction factor, λ_{duct}, introduced in the calculation of the transverse reinforcement contribution, V_s. The shear-strength reduction factor, λ_{duct}, was derived based on the reduction in the strength of the concrete compressive diagonal strut due to the presence of a post-tensioning duct. The reason behind this approach is rooted in the fact that the transverse reinforcement contribution to the nominal shear strength is limited by the ability of the truss mechanism to resist the shear force demand through both the tensile capacity of the transverse reinforcement and the compressive capacity of the concrete in the web.[10,16]

The discontinuity in the concrete compressive stress field, introduced by the presence of the duct, disrupts the internal force transfer in the assumed truss mechanism between the transverse reinforcement and the concrete compression struts. The detrimental effect of the presence of the duct was expressed through the introduction of λ_{duct} in the calculation of the force developed in the concrete compression strut, V_{web}, as per Eq. (6)

$$V_{web} = \lambda_{duct} f_2 \cos\theta d_v b_w \quad (6)$$

From equilibrium, the vertical component of the concrete compressive strut is equal to the force developed in the tie, representing the transverse reinforcement, as shown in Eq. (7)

$$(\lambda_{duct} \cdot f_2 \cos\theta d_v b_w)\sin\theta = \frac{A_v f_y d_v \cot\theta}{s} \cdot \lambda_{duct} \quad (7)$$

Thus, the nominal shear resistance, V_{n1}, can be expressed as per Eq. (8), which is similar to the AASHTO LRFD[5] shear-strength equation when the direction of transverse reinforcement is vertical ($\alpha = 90$ degrees).

$$V_{n1} = V_c + V_s + V_p$$

$$= 0.0316\beta\sqrt{f_c'} b_v d_v + \frac{A_v f_y d_v \cot\theta}{s}\lambda_{duct} + V_p \quad (8)$$

The factor, λ_{duct}, is calculated as a function of the duct diameter correction factor, δ, duct diameter, ϕ_{duct}, and gross web width, b_w, as shown in Eq. (9)

$$\lambda_{duct} = 1 - \delta \cdot \left(\frac{\phi_{duct}}{b_w}\right)^2 \quad (9)$$

The value of δ accounts for whether the duct is grouted or ungrouted. Moore et al.[10] validated the value of δ equal to 2.0 for grouted ducts based on the results of their large-scale test. For ungrouted ducts, the value of δ was taken as 0.0, as no data were available.

EXPERIMENTAL INVESTIGATION

Design of test specimens

In this experimental program, the test specimens were designed using representative construction practices of the Texas Department of Transportation (TxDOT). The specimens were 600 in. (1524 cm) long, 62 in. (158 cm) tall I-girders with an 8 in. (20 cm) thick deck on top. The web width and the duct diameter were selected as 9 and 4 in. (23 and 10 cm), respectively. This section is commonly referred to as the Tx62-Girder. To accommodate post-tensioning anchorages at the end regions of the Tx62-Girder, a typical enlarged end block was employed from the reference design of the Washington State Department of Transportation (WSDOT).[17]

For the precast test specimens, 0.6 in. (1.5 cm) low-relaxation strands were used for the pretensioning. A total of 58 pretensioning strands were provided. Each test specimen contained one or two post-tensioning multistrand systems comprised of nineteen 0.6 in. (1.5 cm) low-relaxation pretensioning strands. Anchorage assemblies and corrugated high-density polyethylene (HDPE) ducts for post-tensioning by VSL International were used as the multistrand post-tensioning system. The overall dimensions of these girders are shown in Fig. 1, and more detailed geometry information is found in Appendix A.*

The girder specimens were designed with three different post-tensioning duct profiles: one straight duct, one parabolic duct, and a combination of one parabolic and one straight duct, as shown in Fig. 2. More specifically, the first set of specimens, referred to as Tx62-0SG (grouted duct) and Tx62-0SU (ungrouted duct), were fabricated with a straight duct positioned at the midheight of the composite girder. The second set of test specimens, referred to as Tx62-P0G (grouted duct) and Tx62-P0U (ungrouted duct), were fabricated with a parabolic duct to investigate the effect of tendon curvature on sectional stress flow. The last set of fabricated specimens, referred to as Tx62-PSG (grouted duct) and Tx62-PSU (ungrouted duct), had a parabolic duct at the same location as the second set and one additional straight duct at the intersection between the web and bottom flange. The locations of couplers, shown in Fig. 2, were selected to avoid any undesired influence that the larger-diameter

*The Appendix is available at **www.concrete.org/publications** in PDF format, appended to the online version of the published paper. It is also available in hard copy from ACI headquarters for a fee equal to the cost of reproduction plus handling at the time of the request.

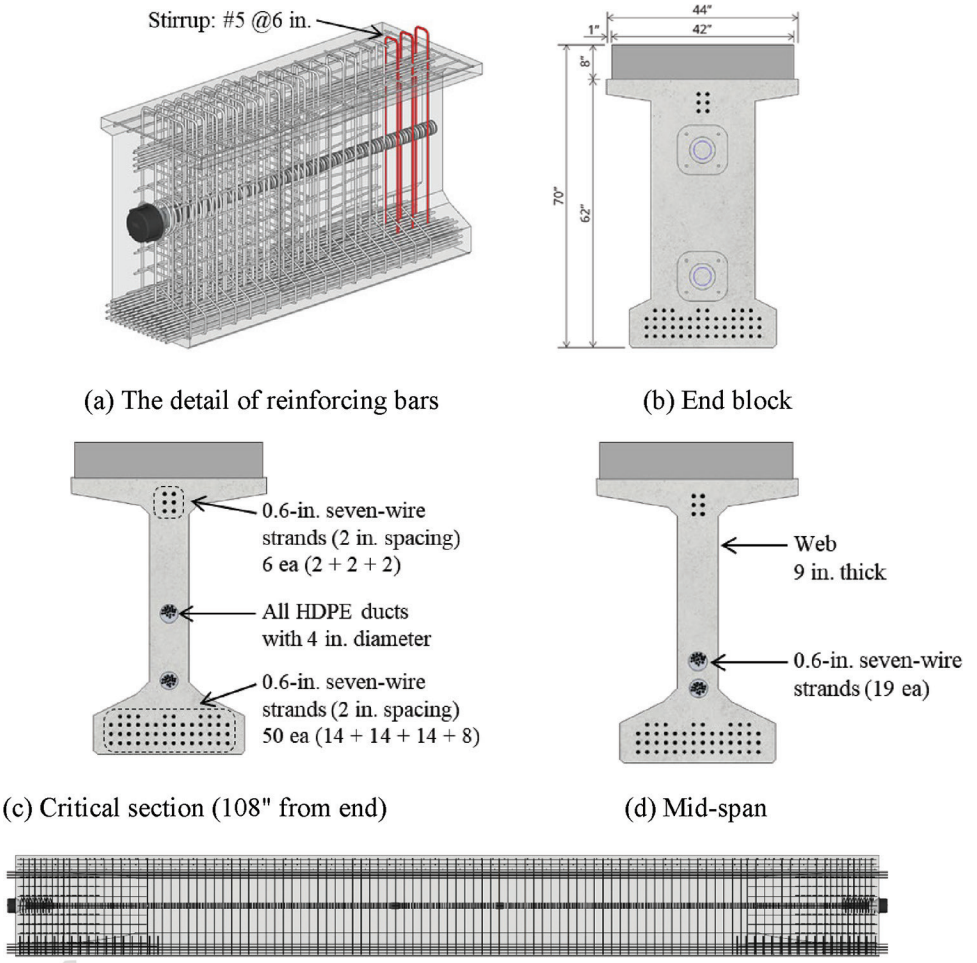


Fig. 1—Details of reinforcing bars and cross sections of test specimens of Tx62-PSG and Tx62-PSU. (Note: 1 in. = 25.4 mm.)

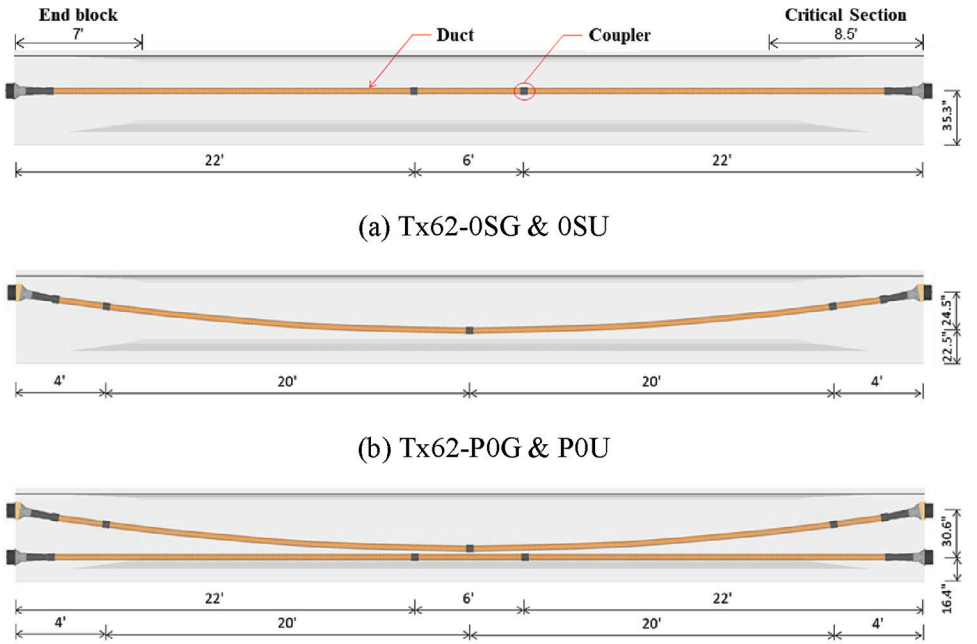
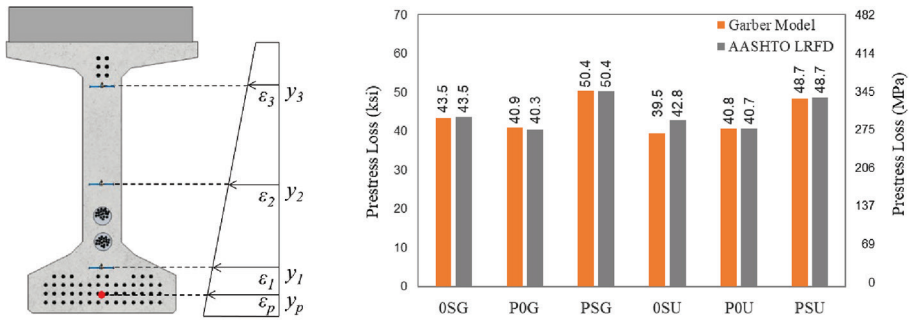


Fig. 2—Duct layout with location of couplers. (Note: 1 in. = 25.4 mm; 1 ft = 304.8 mm.)



(a) Garber Model by internal distribution (b) Determined prestress loss

Fig. 3—Prestress loss of test specimen to determine shear strength.

duct coupler could have on the shear performance within the test region.

Test specimen fabrication

The specimens were fabricated at a local precast plant, Valley Prestress Products, Inc. (VPP) in Eagle Lake, TX, thereby ensuring fabrication practices are consistent with those used for precast bridge elements. The process of pretensioning was conducted up to the design prestress level of 202 ksi (1393 MPa) according to the limiting stress of $0.75f_{pu}$.[5] The actual observed prestress was 206 ksi (1420 MPa), within the acceptable tolerance of ±5%.[18] Finally, the work process of the individual strand prestressing release was conducted for all test specimens, after checking that the cylinder compressive strength of 10.1 ksi (69.6 MPa), f_{ci}', was greater than the design strength of 7.5 ksi (52 MPa).[18] After the fabrication of precast girders from the local plant, the test specimens were transferred to the Ferguson Structural Engineering Laboratory (FSEL) at The University of Texas at Austin, where a specialized post-tensioning operating company, Structural Technologies in Dallas, TX, performed the post-tensioning and grouting. Similar to the pretensioning, the stress level of post-tensioning was conducted up to the design prestress level of 202 ksi (1393 MPa). To better predict the structural behavior of post-tensioned members, it is imperative to quantify the time-dependent prestress loss in the tendon. Garber et al.[19] developed a novel method for prestress loss estimation using the internal strain distribution. This method, using data from embedded strain gauges, calculates the prestress loss at events such as prestress transfer, post-tensioning, and deck casting. Figure 3 illustrates the prestress loss at different stages before testing, comparing the Garber model[19] with AASHTO LRFD. The research report by Han et al.[20] provides further details on the fabrication process of the specimens, including the pretensioning, post-tensioning, precast, and cast-in-place concrete casting.

Material properties

A self-consolidating concrete (SCC) mixture was used to cast the specimens, consistent with standard practice for the construction of Tx-girders. All girders were cast with the same concrete mixture supplied by the VPP batch plants. The concrete mixture design used is provided in Table 2. Standard cylindrical concrete samples accompanying each test specimen (a total number of 120 samples for six girders) were cast for compression tests at prestressing release, 28 days after casting, post-tensioning, and structural testing. Figure 4(a) shows the compression test results[21] at 28 days and on the structural test day. In addition, tensile tests were performed on the nonprestressed reinforcing bars and the 0.6 in. (1.5 cm) seven-wire strands (low-relaxation). Note that the design of transverse reinforcement in the general section consisted of No. 5 double-stirrup deformed reinforcing bar (0.625 in. [15.875 mm]) with the uniform spacing of 6 in. (152 mm) along the length of girder (reinforcement ratio of 1.15%). Figure 4(b) shows the average yield strength of three samples that satisfied the ASTM standards for reinforcing bars[22] (67 ksi [462 MPa] for No. 5 and 72 ksi [496 MPa] for No. 4) and 0.6 in. (1.5 cm) seven-wire strands[23] (274 ksi [1889 MPa] for pretensioning and 262.5 ksi [1810 MPa] for post-tensioning), respectively. The measured material properties were used to calculate the nominal shear resistance using AASHTO LRFD.

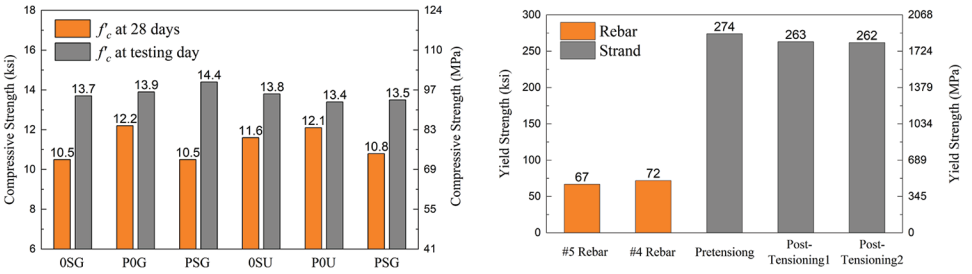
Table 2—Concrete mixture design

Material	Detail	Amount	Units
Cementitious material	Type III cement	600 (356)	lb/yd³ (kg/m³)
	Class F fly ash	150 (89)	
Fine aggregate	Sand (fineness modulus = 2.88)	1266 (751)	
Coarse aggregate	Natural gravel (3/4 in. nominal maximum)	1733 (1028)	
Water	Water	235 (139)	
	w/cm	0.34	
Admixtures	High-range water-reducing admixture	7.0 (456)	oz./100 lb cementitious materials (mL/100 kg)
	Water reducer/retarder	1.0 (65)	
	Corrosion inhibiter	51.0 (3325)	
	Viscosity modifier	3.5 (228)	

Note: *w/cm* is water-cementitious materials ratio.

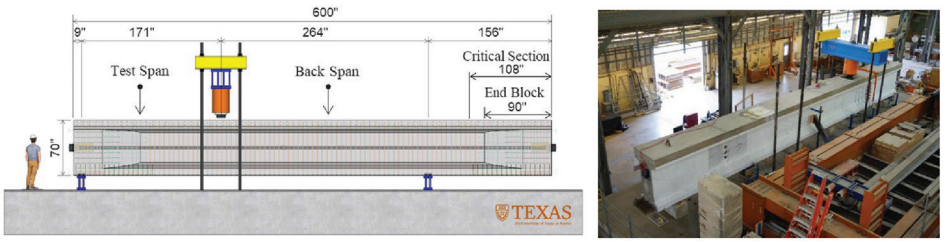
Structural test configuration and protocol

In this experimental program, six test specimens were fabricated, and 12 shear tests were conducted. The failure load was estimated using the AASHTO LRFD[5] shear provision to be less than 1800 kip (8000 kN). A 20% reserve

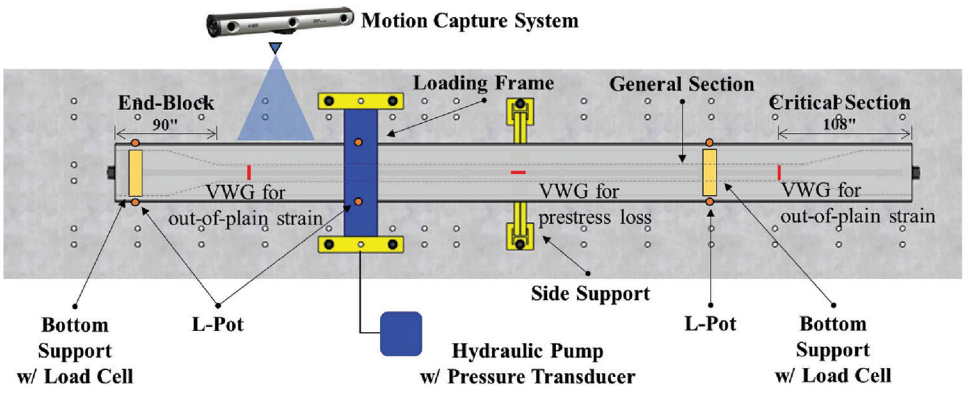


(a) Compressive test results of concrete (b) Yield strength of reinforcing bars

Fig. 4—Results of material tests. (Note: 1 ksi = 6.9 MPa.)



(a) Elevation for the shear structural test (b) Structural setup with test specimen



(c) Plan for the instrumentation setup along with the test specimen

Fig. 5—Design and rendering of shear structural test schematic. (Note: 1 in. = 25.4 mm.)

capacity was provided to the test setup to account for potential overstrength. Thus, the test frame was designed for 2000 kip (8900 kN). The strength of the loading frame was verified by its calculated resistance using an American Institute of Steel Construction (AISC) provision in terms of sectional flexural capacity, sectional shear capacity, and welding strength.[24] Figure 5 shows the structural setup and monitoring area designed for this study. Two tests were conducted on each of the six specimens. The load was applied monotonically until shear failure occurred. The load was applied in 50 kip (222 kN) increments until the first diagonal shear crack detection. After crack detection, the loading was applied in 75 kip (333 kN) increments. The loading was paused to measure and map cracks up until the critical shear crack developed. The loading was then increased until the test specimen experienced failure. After failure, the applied load was removed, and a final cracking survey was performed.

AASHTO LRFD takes the location of the critical shear section for the girder, determined as the effective shear depth (d_v) from the edge of the bearing pad (65 in. [165 cm]); however, this is located within the end block (the general beam section starts 90 in. [229 cm] from the end). A more practical approach to determining the critical section relates to the failure cracks, based on a visual inspection of Moore et al.'s test results,[10] because the geometric condition of test specimens is precisely replicated. The most vulnerable area for shear force was reported to be approximately 18 in. (46 cm) from the termination of the end block, defined as the critical section for this experimental study. This determined critical section of the test specimen serves as the critical location for the calculation of shear force and the various instrumentation applied to the specimens. In conclusion, the experimentally determined critical section from Moore et al.[10] is reasonably close to the location of the governed failure crack in this study.

EXPERIMENTAL RESULTS AND DISCUSSION

Failure mechanism

All girders behaved and failed in a similar manner. First, hairline cracks were observed at the duct location,

which further developed along the length of the girder as the applied load increased. At approximately 80% of the ultimate load, a dominant shear crack developed from the center of the web to the top and bottom flanges in the test span. Note that this study conducted the stiffness analysis and determined the specimen's change point from linear to nonlinear behavior (details are provided in Appendix B). This change point coincided with the onset of a fully developed diagonal shear crack, consistently occurring at load levels of approximately 80% of the ultimate load. Finally, the test specimens failed due to concrete compression failure in the vicinity of the post-tensioning duct, a result otherwise known as web crushing.

Cracking development and ultimate failure mode were consistent in the grouted and ungrouted post-tensioning ducts. Figure 6 illustrates the three different cracking modes related to load and deflection. In addition, Fig. 7 shows load-deflection plots and failure crack patterns for all 12 tests. Given that a direct comparison of the ultimate shear capacity across specimens may be compromised in the absence of normalization, the subsequent discussion will focus on elucidating the ultimate behavior within the context of the "Ultimate level" section. With respect to the diagonal cracking propagation, each specimen containing the same profile of post-tensioning duct experienced a similar cracking pattern, with an average crack spacing recorded between 6.5 and 7.0 in. (16.5 and 17.8 cm)—a finding closely paralleling the 6.4 in. (16.3 cm) computed by Collins and Mitchell.[2] Moreover, the inclination of the diagonal cracks ranged from 26 to 30 degrees, aligning closely with approximately 29 degrees as determined by the AASHTO LRFD.[5]

After testing, the specimens were cut with a wire saw at the critical section as an additional visual inspection to further analyze the cross-sectional behavior and identify potential particularities specific to specimens containing grouted or ungrouted ducts. Figure 8 shows the visual inspection for the developed cracking patterns, such as diagonal shear crack, localized web crushing, and splitting cracks. More importantly, the internal cracking survey revealed the splitting cracks that developed around the duct. This splitting cracking behavior was the result of the splitting stresses in the vicinity of the duct; the embedded vibrating-wire gauges (VWGs) quantified this behavior.

Web behavior in out-of-plane direction

The presence of post-tensioning ducts in the web region of a Tx62 girder introduces a sectional discontinuity that influences the stress distribution around the duct and affects the shear behavior and capacity of the girder. Figure 9 depicts the early studies that addressed the phenomenon and shows a deviation in the compressive stress flow in the vicinity of a post-tensioning duct.[25] The through-thickness tensile stresses develop where the compressive stresses start to deviate toward the grouted duct area because the grout was assumed to be typically stiffer than the surrounding concrete. However, in a section with an empty duct, the compressive stresses flow around the empty duct and through-thickness tensile stresses develop in the immediate vicinity of the duct. In both cases, through-thickness tensile stresses are induced by the deviation in compressive stresses, which resulted in a reduction in the shear capacity of the member.[14,16]

The previous study on the panel-based analogy did not include an investigation of the actual structural boundary conditions.[14,15] Moore et al.[10] pointed out that the contrasting results between the panel-based tests and the large-scale tests were primarily due to different governing failure mechanisms. Specifically, all panel-based tests conducted by Wald et al.[15] reported splitting failure in the out-of-plane direction, which resulted from the compressive-controlled boundary condition. This test setup is unlikely to accurately simulate the shear mechanism that develops in structural members, such as an I-girder, and leads to a governed splitting failure, similar to concrete tests assessing splitting tensile strength.[26] Therefore, caution should be exercised when extrapolating findings from panel-based tests to understand the shear performance of complex structural members such as I-girders. Large-scale tests on actual structural elements are essential for obtaining accurate and reliable data on their shear behavior.

In this study, a series of VWGs were strategically placed in the vicinity of ducts to measure out-of-plane strains during the structural test. Depending on the duct profile, either four or six VWGs were embedded. Table 3 presents the measured tensile strain at each location during the test. Notably, in the region around the duct area, the VWG recorded increasing tensile strains in the out-of-plane direction. To evaluate tensile strain levels in the out-of-plane direction, three stages were selected: 1) prior to the development of the first hairline shear crack; 2) at the point of initiating nonlinearity in the

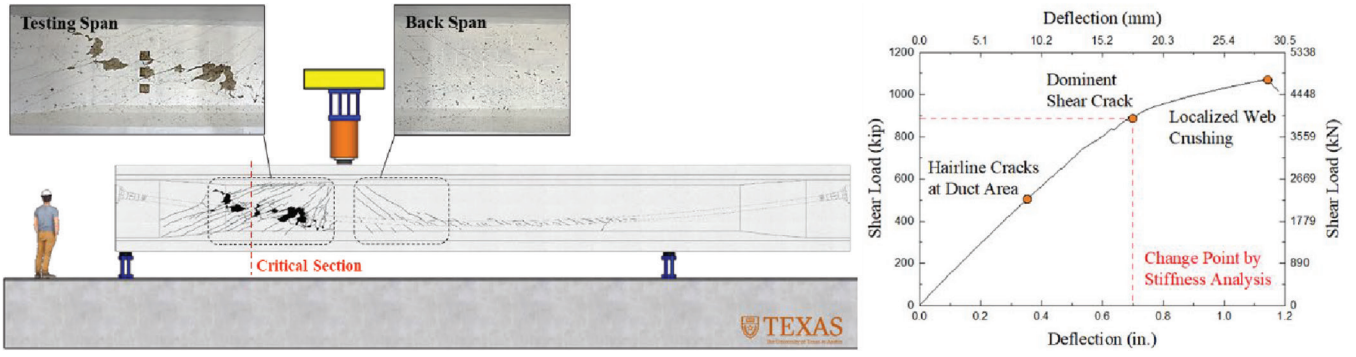
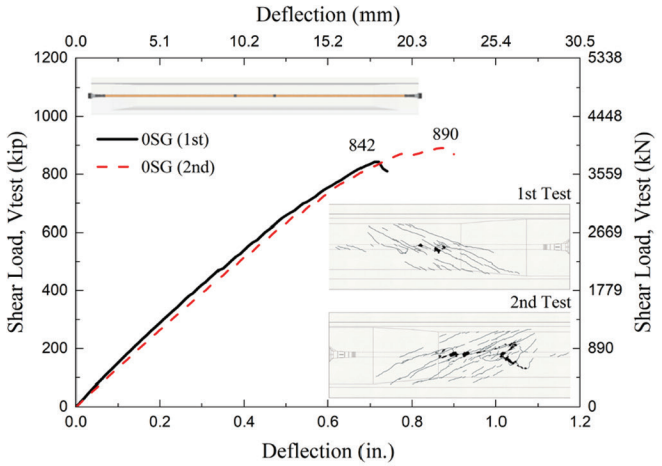
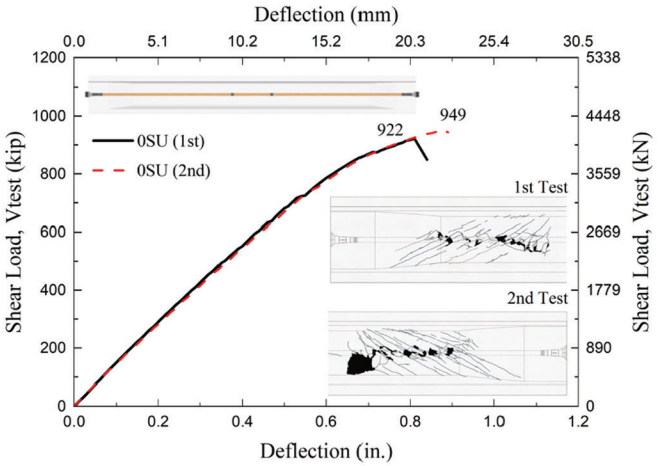


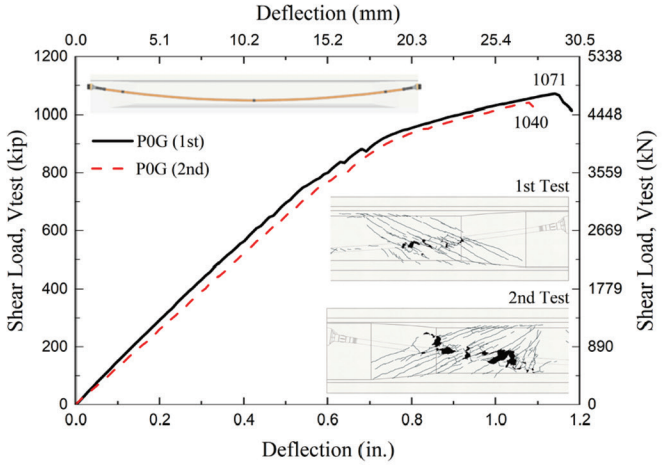
Fig. 6—Structural setup and three distinct cracking modes related to loading and deflection.



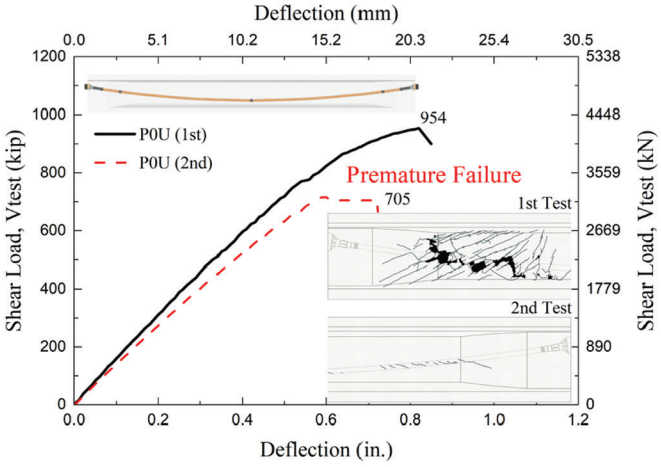
(a) Tx62-0SG



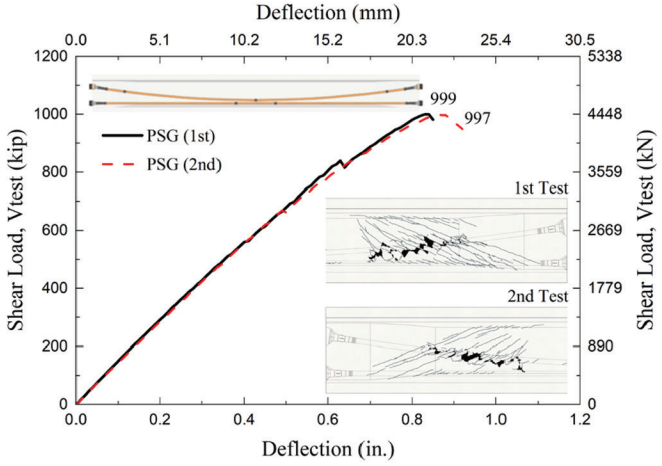
(b) Tx62-0SU



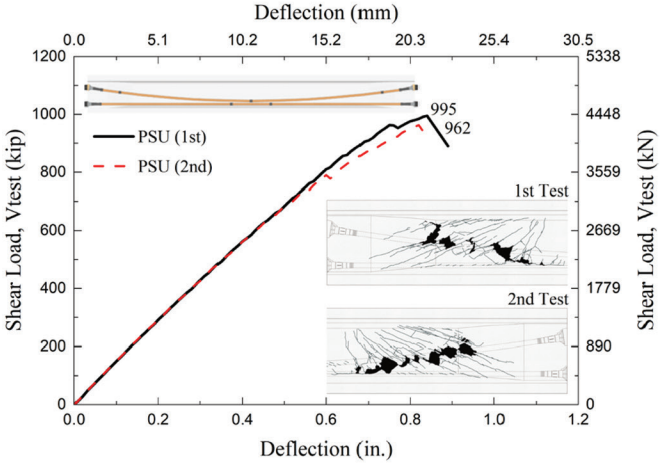
(c) Tx62-P0G



(d)Tx62-P0U



(e) Tx62-PSG



(f) Tx62-PSU

Fig. 7—Shear load-deflection plots of all test specimens with surface cracks.

behavior; and 3) at the level of ultimate load. Following the initiation of nonlinearity, a noticeable escalation in tensile strains was observed, although the intensity of these tensile strains exhibited a certain degree of variation. Of particular significance, two locations near the duct at the middle of the web height (referred to as Mid 1 and Mid 2) exhibited substantial expansion in the out-of-plane direction regardless of duct condition. This observation contradicts the findings of the study on the panel-based analogy,[14,15] as shown in Fig. 9.[25] The discrepancy suggests that the shear behavior and failure mechanism in these structural members, particularly

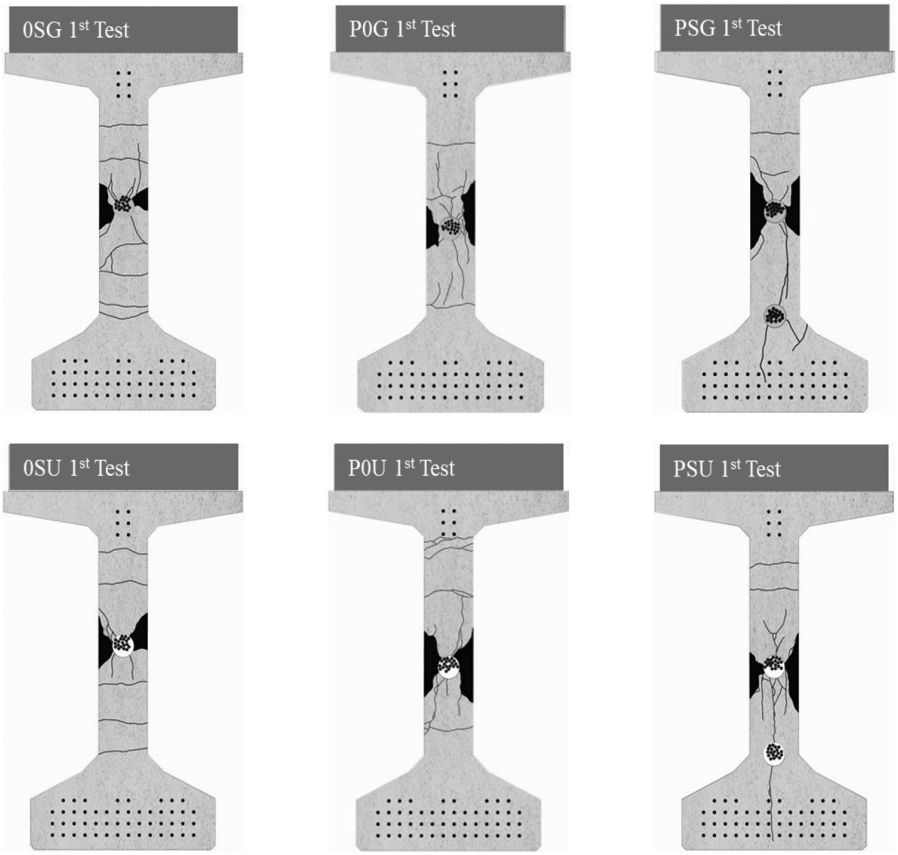


Fig. 8—Internal cracking survey at critical section.

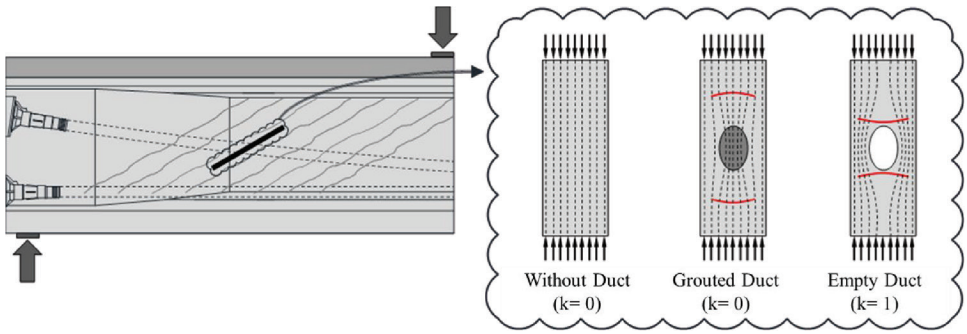


Fig. 9—Internal compressive stress flow in web of post-tensioned girder and concrete panel analogy of specimens without duct, grouted duct, and empty duct.[25]

in the vicinity of ducts, differ significantly from what the panel-based analogy previously indicated.

Web behavior in in-plane direction

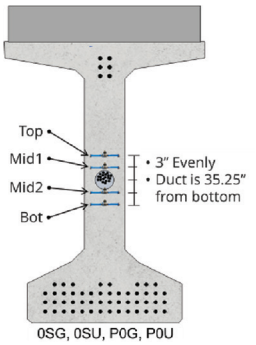
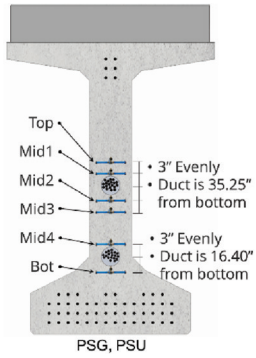
In addition to measuring physical displacements, this study monitored the strains during the structural test using a motion-capture system. This motion-capture system tracks the position of infrared light-emitting diodes referred to as markers. These data were post-processed and used to investigate the web area's strain distribution, which aided in identifying the controlled failure mechanism over the course of the structural test. For this study, the markers were installed to form a 6 in. (152 mm) grid within the test region. The recorded displacements of the markers were used to estimate the average strain of each 6 x 6 in. (152 x 152 mm) quadrilateral element. Note that data were only collected for four specimens—Tx62-0SG, 0SU, P0G, and PSU—due to an unexpected instrumentation malfunction for specimens Tx62-P0U and PSG. Thus, this paper will discuss the available motion-capture data from Tx-0SG, 0SU, P0G, and PSU only.

In post-processing, the data collected from the markers was subdivided from the quadrilateral elements defined by four markers into two triangles, each defined by three markers. The shape functions from constant strain triangle elements estimate the strain based on the nodal displacements. Finally, an area-weighted average of the two triangles determines the average strain in the quadrilateral region.

Service-level cracking

The serviceability of structural components and their structural performance at the service level of loading are

Table 3—Web expansion at critical section determined by VWGs

Measurement location	ID	Shear load, kip (kN)	Top, με	Mid 1, με	Mid 2, με	Mid 3, με	Mid 4, με	Bottom, με
 0SG, 0SU, P0G, P0U	0SG	600 (2669)†	6	43	38	—	—	–11
		722 (3212)‡	16	200	223	—	—	–8
		842 (3746)§	18	450	459	—	—	4
	P0G	600 (2669)†	–1	25	42	—	—	–21
		888 (3950)‡	1223	1781	1489	—	—	347
		1071 (4764)§	OR*	OR*	OR*	—	—	OR*
	PSG	600 (2669)†	5	42	41	–18	–25	–33
		751 (3340)‡	16	799	862	–12	–27	–13
		998 (4437)§	OR*	OR*	OR*	1682	127	4
 PSG, PSU	0SU	600 (2669)†	10	197	48	—	—	–12
		739 (3289)‡	26	758	353	—	—	–10
		918 (4083)§	849	OR*	OR*	—	—	1646
	P0U	600 (2669)†	2	35	91	—	—	–22
		823 (3662)‡	45	1025	OR*	—	—	341
		955 (4247)§	1066	OR*	OR*	—	—	2061
	PSU	600 (2669)†	–3	43	63	–25	–29	–43
		843 (3751)‡	23	622	424	–21	–5	–23
		995 (4424)§	OR*	OR*	OR*	OR*	55	–18

*OR (out-of-range) indicates that tensile strain in out-of-plane direction exceeded gauge's measurement range.

†Specimen statement subjected to in-plane shear loading before shear crack.

‡Specimen statement subjected to in-plane shear loading starting nonlinear.

§Specimen statement subjected to in-plane shear loading ultimate failure.

considered in the aspects of cracking, deformation, and concrete stresses according to AASHTO LRFD.[5] The current version of ACI 318[27] removed the crack-width-based limitation to define the serviceability. However, ACI 224R-01[28] and the *fib* Model Code[9] continue to use the crack width as a metric for serviceability. Based on the notion of determining the serviceability using the crack width criteria, an early study by Birrcher et al.[29] provided an experimental-based methodology to determine the serviceability performance of elements subjected to in-plane shear loading. The Birrcher model adopts the ratio of the shear-resistance factor (ϕ) to the load factor (η), which is approximately equal to the ratio of the service-level load to the nominal capacity. The ratio of service-level load to nominal capacity is determined as

$$\phi \cdot \text{Nominal Capacity} = \eta \cdot \text{Service-Level Load} \quad (10)$$

where ϕ is the shear-resistance factor of 0.75; and η is the load factor defined as a function of the load case and the distribution of the loads.

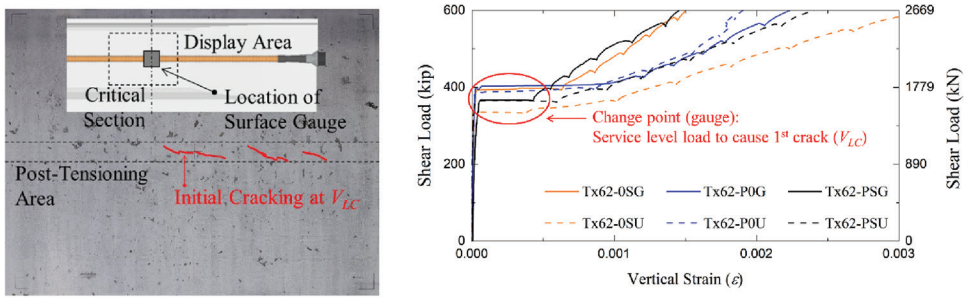
This study uses the suggested η factor equal to 1.4 based on the assumptions of: 1) Strength I—basic load combination relating to the normal vehicular use of the bridge without wind—in AASHTO LRFD[5] governs design, 1.25 dead load (DL) + 1.75 live load (LL); and 2) 75% of the service load is DL and 25% of the service load is LL.

Using Eq. (10), Birrcher et al.[29] reported the proposed model to compute the ratio of service-level load to experimental capacity can be calculated as

$$\frac{V_n}{V_{test}} \cdot \frac{\phi}{\eta} = \frac{1}{1.3} \cdot \frac{0.9}{1.4} = 0.5 \quad (11)$$

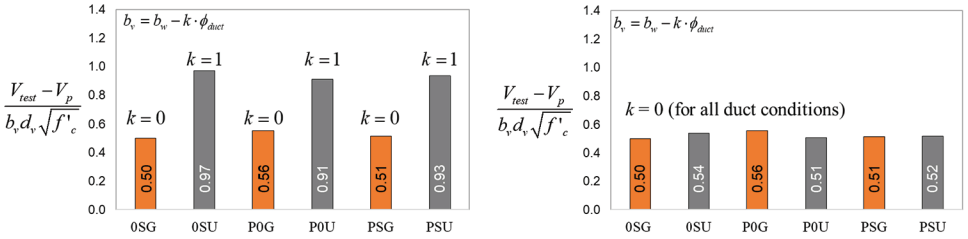
where V_n is the nominal shear resistance; and V_{test} is the shear strength from the test. In this study, the ratio of the nominal shear resistance to ultimate strength equals 1.3. The computed ratio of approximately 0.5, which is related to the relationship between the experimental ultimate shear capacity and the nominal capacity of a section, is the service-level load as a function of V_{test} for this study.

This study reviews Birrcher et al.'s approach to determine the serviceability of post-tensioned concrete members. The service load is compared with the measured shear load that caused the first cracking (referred to as V_{LC}) to evaluate the serviceability of the specimens. All post-tensioned test specimens, regardless of duct conditions, experienced initial hairline cracks in the duct area, as shown in Fig. 10(a), which occurred at a shear-force level of V_{LC}. To refine the



(a) Initial cracking at V_{LC} (b) Vertical strain development

Fig. 10—Analysis of service-level loading.



(a) Using the varying k based on AASHTO (b) Using the gross web width ($k = 0$)

Fig. 11—Normalized ultimate shear stress.

Table 4—Service-level cracking for grouted and ungrouted specimens

Specimen ID		V_{LC}, kip (kN)	V_{test}, kip (kN)	V_{LC}/V_{test}	Normalized shear stress*
Grouted specimens	Tx62-0SG	403 (1793)	855 (3803)	0.47	0.18
	Tx62-P0G	418 (1859)	1082 (4813)	0.39	0.19
	Tx62-PSG	383 (1704)	1011 (4497)	0.38	0.16
Ungrouted specimens	Tx62-0SU	352 (1566)	961 (4275)	0.37	0.15
	Tx62-P0U	411 (1828)	966 (4297)	0.43	0.18
	Tx62-PSU	381 (1695)	1005 (4470)	0.38	0.17

*Normalized shear stress calculated as $(V_{LC} - V_p)/(b_w d_v \sqrt{f_c'})$, unitless.

serviceability analysis, this study monitored the occurrence of cracking within the test span using the strain development of the surface gauge. Figure 10(b) shows the vertical strain development containing the change point of distinctly elevated strain. This change point of shear load level (V_{LC}) was validated by the visual inspection for the occurrence of initial hairline cracks.

Table 4 presents the analysis of serviceability in terms of the shear force for the service-level crack (V_{LC}) based on the change point by using the surface gauge, the ratio of V_{LC} to V_{test}, and normalized shear stress. The ratio of V_{LC} to V_{test} roughly mirrors the reference level of 0.5, as suggested by the Birrcher model. Nevertheless, it presents challenges when comparing the serviceability of test specimens between grouted and ungrouted ducts due to the variations in the concrete strengths. To address this issue, the normalization of shear stress at the level of service load was implemented using Eq. (12).

$$v_{LC} = \frac{V_{LC} - V_p}{b_w d_v \sqrt{f_c'}} \quad (12)$$

The normalized shear stress (v_{LC}) of both grouted and ungrouted specimens indicated similar stress levels ranging from 0.15 to 0.19 to trigger the onset of the diagonal shear cracks in the post-tensioning duct area. In other words, no difference in serviceability performance was observed regardless of the duct condition. These results align with the theoretical service-load levels by the Birrcher model.

Ultimate level

The failure loads obtained from each pair of tests were within 5% of each other. For clarity, the average failure load from each pair of tests is used for the comparison with AASHTO LRFD shear resistance. Figure 7 reports the ultimate shear loads for each specimen; however, the comparison analysis of the ultimate shear capacity for each specimen could be obscured without normalization. As such, the ultimate shear stress was normalized by using Eq. (13).

$$v_{normal} = \frac{V_{test} - V_p}{b_v d_v \sqrt{f_c'}} \quad (13)$$

The coefficient of effective web width (k) plays a pivotal role in estimating the shear capacity of the post-tensioned concrete member. For example, the current edition of AASHTO LRFD[5] establishes different values for k based on the filler condition of the duct due to the different internal stress flows, as shown in Fig. 9. Accordingly, Fig. 11(a) shows the normalized shear stress calculated using the effective web width (b_v), which applies the appropriate values of k to the specimens containing grouted and ungrouted ducts, respectively. It clearly indicates that, using the current AASHTO LRFD procedure, higher shear stress levels are calculated for the specimens with ungrouted ducts than for the grouted ones. Further, Fig. 11(b) shows the normalized shear stress calculated using the gross web width ($k = 0$) regardless of the duct condition. Remarkably, all test specimens are calculated to develop a similar level of normalized shear stress.

The survey of the cracking in the web revealed well-distributed, fan-shaped shear cracks for all test specimens. This indicates that the entire web engages in the shear force-resistance mechanism (for example, $k = 0$). As the cracked concrete component carries shear through the aggregate interlock at the crack interfaces, similar patterns of diagonal cracking could expect a similar shear resistance from the effect of aggregate interlock on the cracks.[30] Consequently, similar web-width correction factors should be considered for both grouted and ungrouted ducts. To further understand the shear mechanism of post-tensioned concrete members and to determine appropriate values for k, the web behavior is further analyzed in the following section.

Experimental versus AASHTO LRFD shear resistance

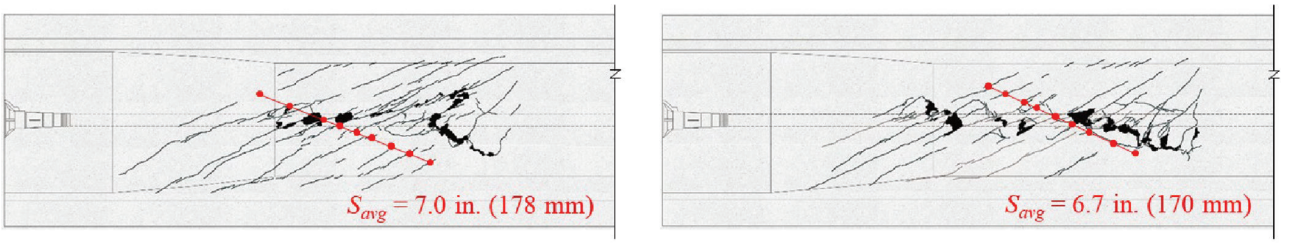
The experimental shear resistance, V_{test}, was calculated at the critical section based on the measured ultimate load from each test. Specimen properties, such as prestress loss, material, and geometry conditions, were used to calculate the nominal shear resistance, V_n, using the current AASHTO LRFD.[5] Table 5 presents the comparison between the experimental shear resistance, V_{test}, and the calculated resistance using the AASHTO LRFD shear design, V_n. Moreover, information on reduction factors, such as the web-width reduction factor, k, duct diameter correction factor, δ, and shear-strength reduction factor, λ_{duct}, are provided to evaluate the current version of shear strength design according to the AASHTO LRFD provisions. Because the primary purpose of this procedure is to evaluate the nominal shear capacity of test girders, the load and resistance factors were taken as 1.0. The experimental capacities of the specimens with grouted ducts were, on average, 30% larger than the calculated capacities. This level of conservatism is generally regarded as adequate for shear-critical specimens based on the shear test database research.[31] On the contrary, the calculated capacities for the specimens with ungrouted ducts produced capacity estimates with a smaller safety margin, averaging approximately 10%. Therefore, the shear-strength reduction factors associated with ungrouted ducts need to be revised to ensure consistent levels of conservatism compared to the grouted case. This revision is crucial to maintain a balanced and reliable design approach for post-tensioned concrete members.

DEVELOPMENT OF DESIGN RECOMMENDATIONS

This section presents the development of shear design recommendations for the post-tensioned girders that incorporate the effects of grouted and ungrouted ducts on the shear-resistance mechanism. The proposed changes to the shear design of post-tensioned members are founded on the experimental observations made in this study and are further supplemented by relevant data available from tests conducted by Moore et al.[10] For detailed information about

Table 5—Test results summary with ratio of test results to nominal shear resistance

Specimen ID	k	δ	λ_{duct}	V_n	V_{test}	V_{test}/V_n
	Web-width reduction	Duct diameter correction	Shear-strength reduction	Nominal shear resistance, kip (kN)	Shear strength, kip (kN)	Ratio
Tx62-0SG	0	2	0.605	694 (3087)	879 (3910)	1.27
Tx62-P0G	0	2	0.605	766 (3407)	1066 (4742)	1.39
Tx62-PSG	0	2	0.605	809 (3599)	1009 (4488)	1.25
Tx62-0SU	1	0	1.000	816 (3629)	948 (4217)	1.16
Tx62-P0U	1	0	1.000	891 (3963)	966 (4297)	1.08
Tx62-PSU	1	0	1.000	919 (4087)	990 (4404)	1.08



(a) Tx62-0SG (b) Tx62-0SU

Fig. 12—Crack propagation and average crack spacing at ultimate load level.

the test specimen configurations and specifics, please refer to Appendix C.

Proposed modification for calculation of $V_{n1} = V_c + V_s + V_p$

Effective web-width factor, b_v—Figure 12 depicts the surveyed crack patterns for the specimens with straight grouted and ungrouted ducts. Well-distributed, fan-shaped diagonal cracks developed, which had similar average crack spacings regardless of the duct condition. Similar cracking patterns were observed for all test specimens. Also, the average crack spacing observed ranged from 6.5 to 7.0 in. (16.5 to 17.8 cm)—findings that align closely with the estimations provided by Collins and Mitchell,[2] which predict an average crack spacing of 6.4 in. (16.3 cm) for all specimens, as calculated using Eq. (14).

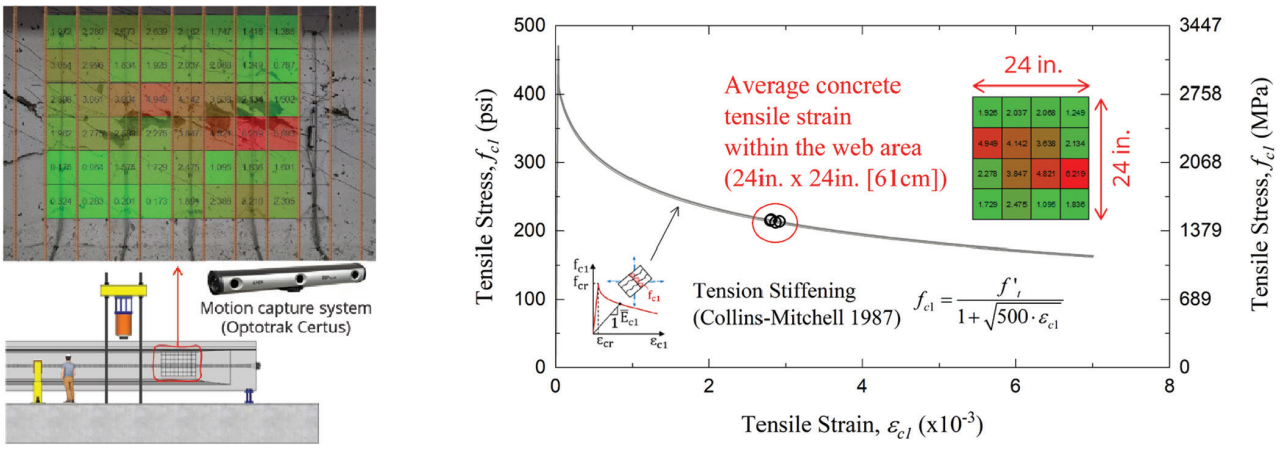
$$s_m = 2\left(c + \frac{s_2}{10}\right) + k_1 k_2 \frac{d_b}{\rho_{ef}} \quad (14)$$

This indicated that the entire web engaged in the shear force-resisting mechanism and provided insight into the calculation of the concrete contribution to the nominal shear resistance.

Moreover, the strains were monitored during the structural test using the aforementioned motion-capture system, shown in Fig. 13(a). The average strains from the selected quadrilateral web region, sized 24 x 24 in. (610 x 610 mm), were used to calculate the residual tensile stresses in the cracked concrete component using the Collins-Mitchell 1987 model.[32] Figure 13(b) shows the post-cracking tensile stresses calculated for specimens of Tx62-0SG, 0SU, P0G, and PSU, indicating similar performance. This leads to the conclusion that the disparities are negligible in terms of the value of the average tensile strains and the concrete tensile stresses between specimens with grouted and ungrouted ducts. Therefore, the effective web-width correction factor, k, in AASHTO LRFD[5] should be updated to the value of zero for both grouted and ungrouted conditions, to reflect the engagement of the gross web width (b_w), based on the results and numerical analysis.

In summary, the following conclusions can be made based on the development of cracks and the state of post-cracking concrete tensile stress:

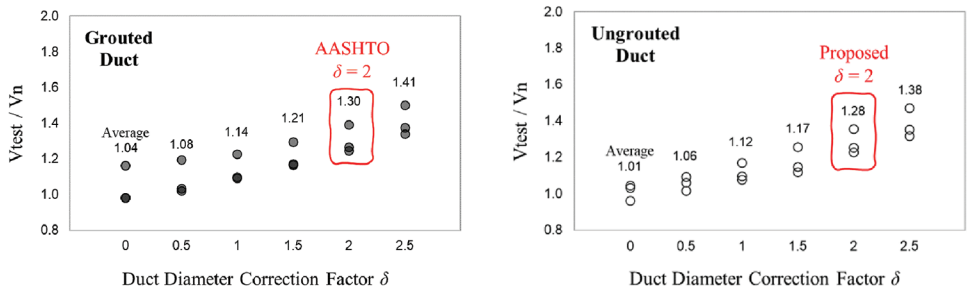
- The entire web engages the shear-transfer mechanism, as indicated by the occurrence of well-distributed, fan-shaped diagonal shear cracks for specimens with either grouted or ungrouted ducts.
- No significant difference was observed between the specimens with grouted and ungrouted ducts with respect to the post-cracking tensile stresses of the concrete component.
- As such, the gross web width, b_w, should be used in the calculation of the concrete contribution to the shear strength capacity.



(a) Vision system monitoring test span

(b) State of tensile stress

Fig. 13—State of residual tensile stress using motion-capture system. (Note: 1 in. = 25.4 mm.)



(a) Specimens with grouted tendon

(b) Specimens with ungrouted tendon

Fig. 14—Determination of duct diameter correction factor, δ.

Duct diameter correction factor, δ—Figure 14 shows the variation of the experimental-to-calculated ratios as a function of the duct diameter correction factor, δ, in the grouted and ungrouted tendons, respectively. For δ taken as 2.0, the same level of conservatism is achieved for specimens with ungrouted ducts as for those with grouted ducts. Based on the changes proposed for the effective web-width correction factor (k), the proposed value of 2.0 for the duct diameter correction factor (δ) ensures similar structural conservativeness in both grouted and ungrouted tendons. Note that this study's proper conservative level (approximately 30%) is in agreement with the data-driven shear test database research.[31]

Proposed modification for calculation of $V_{n2} = 0.25f_c'b_vd_v$

The nominal shear resistance (V_{n2}) limits the shear stress level to $0.25f_c'$ to avoid compressive failure of the concrete, as suggested by Bentz et al.[13] All test specimens experienced localized web-crushing failure in the vicinity of the post-tensioning duct at the ultimate load level, regardless of whether ducts were grouted or ungrouted, as illustrated in Fig. 15. The current edition of AASHTO LRFD uses different values for k for bonded tendons as the gross web width (k = 0) and unbonded tendons as the effective web width (k = 1). This approach is not in agreement with the test results, which indicate similar failure mechanisms.

Specifically, the value of k is 0.0 for bonded tendons, as stiff grout is assumed to resist the intruding compressive stress. On the other hand, k is 1.0 for unbonded tendons because the empty duct is expected to redirect the internal stress flow, potentially decreasing the resistance of compressive force, as shown in Fig. 16(a). Nevertheless, this assumed internal stress flow is only validated in the condition of elasticity and linear behavior, which implies no growth of macrocracks in the concrete component.

This study surveyed the cracking at the critical section by cutting the tested specimen, as conceptually illustrated in Fig. 16(b). Three cracking patterns were identified: 1) the horizontal crack, which is the inclined shear crack; 2) localized web crushing; and 3) internal cracks around the duct due to the splitting force. When the internal cracks form around the duct, they decrease the bond strength between the duct and adjacent concrete. At the ultimate load level, accounting for the plasticity in the post-tensioned girder, this debonded condition redirects the internal compressive stress flow toward the outside of the cross section, similar to unbonded tendons. This plasticity mechanism approach is rational because the nominal shear resistance should be determined at the moment of ultimate load level.

The motion-capture system data at the ultimate load level were used to calculate the principal strains (ε_1 and ε_2) in two quadratic regions: the web (24 x 24 in. [610 x 610 mm]) and the duct (6 x 6 in. [152 x 152 mm]) at the critical section. The Vecchio-Collins compression-softening model[33] was used to calculate the compressive stress of web and duct regions, respectively, as shown in Fig. 17(a). This state of compressive stress and strain indicates that the duct region typically crushes locally before the rest of the web region, which is located in the plateau of compression softening. Moreover,

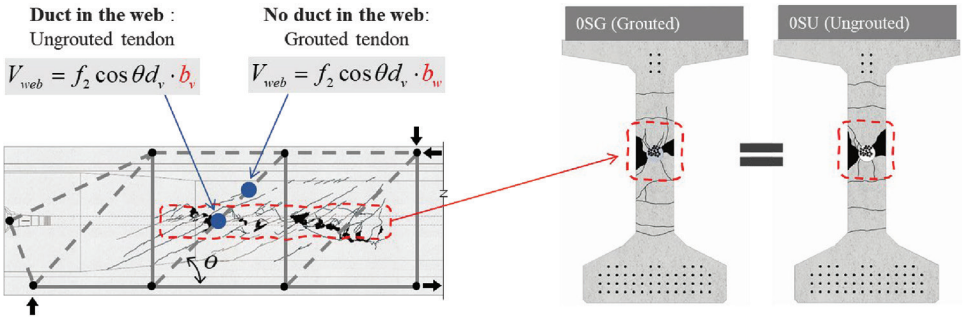


Fig. 15—Ultimate failure mode of localized web crushing in specimens with grouted or ungrouted ducts.

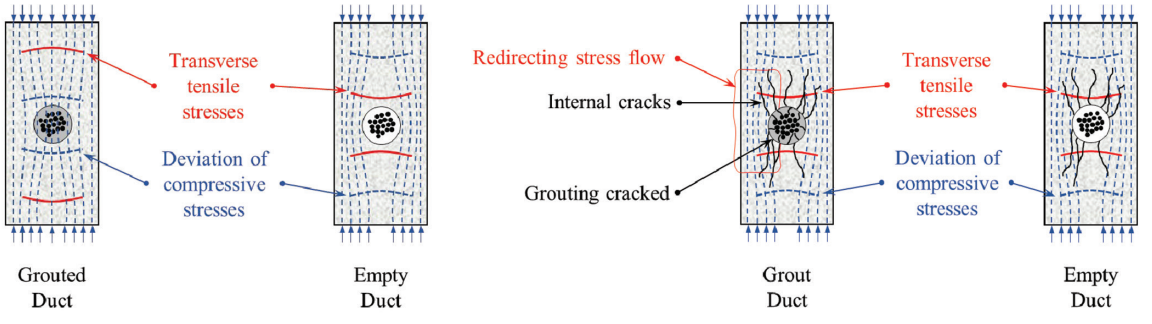
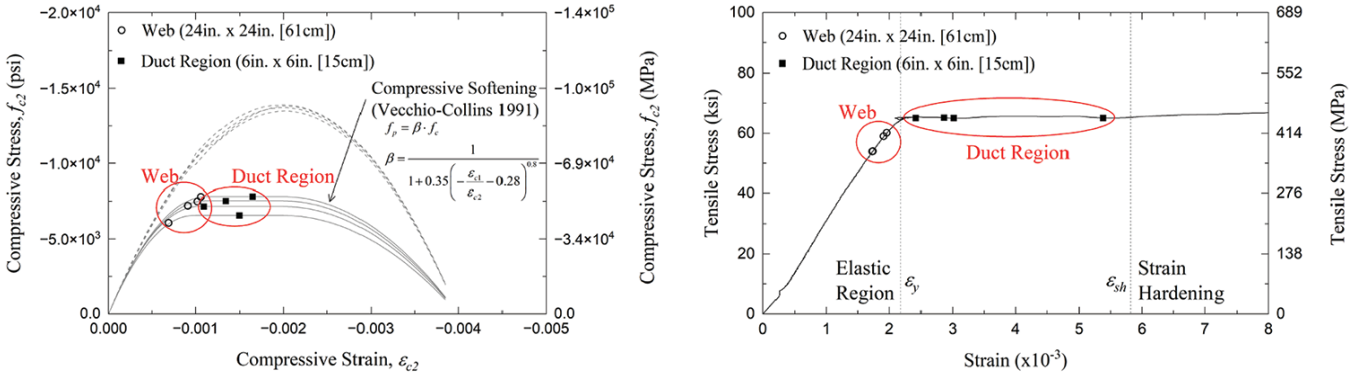


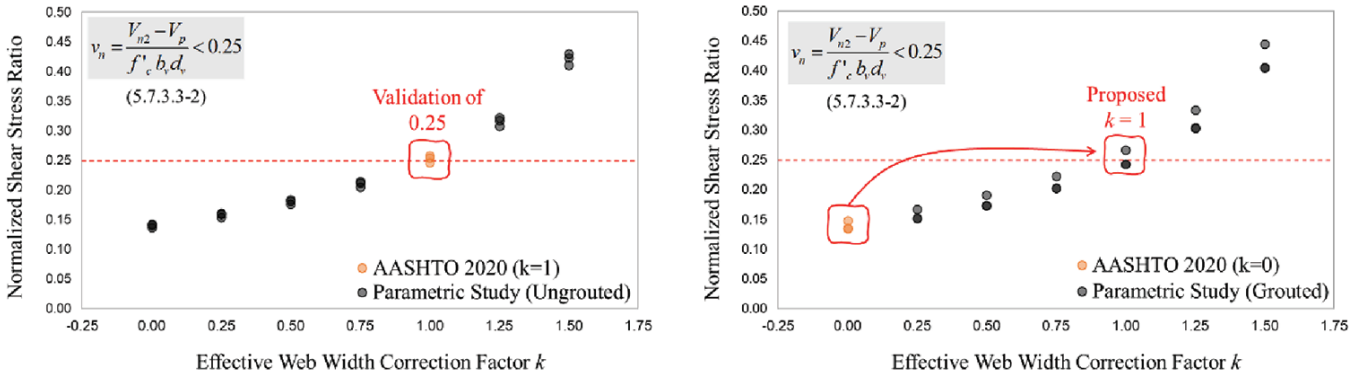
Fig. 16—Conceptual theory of internal stress flow for bonded and unbonded tendons.



(a) Concrete component

(b) Transverse reinforcement component

Fig. 17—State of stress condition in each component. (Note: 1 in. = 25.4 mm.)



(a) Specimens with ungrouted duct

(b) Specimens containing grouted duct

Fig. 18—Normalized shear stress level using structural test with respect to effective web-width correction factor, k.

this analysis predicted similar failure modes regardless of the tendon conditions, which aligns with the test results.

In the same manner, the strength contribution of the transverse reinforcement can be determined, as shown in Fig. 17(b). Using the average vertical strain (ε_y), the transverse reinforcement at the duct region is highly expected to yield (that is, yield strain of 0.0022) based on the stress and strain curve from the material test of the reinforcing bar. The stress levels of the concrete and transverse reinforcement components show the failure mode was initiated by yielding of the transverse reinforcement and localized web crushing. This numerical analysis reflects the failure modes from the test results, as shown in Fig. 15. It is important to note that Bentz et al.[13] assumed small concrete compression strains (that is, within the linear-elastic region) in their original derivation that led to Eq. (2). However, Fig. 17 shows that the estimated strains in the girder webs are in the nonlinear region. The condition of the duct for V_{n2} will be discussed in the following section, as this research proposes the effective web-width correction factor (k).

To determine the proper value of the effective web-width correction factor, k, the normalized shear stress using Eq. (15) was computed with respect to k. Because V_{n2} was related to the concrete compressive strength, the normalization should apply the compressive strength of concrete, f_c' in Eq. (15).

$$v_{normal} = \frac{V_{n2} - V_p}{f_c' b_v d_v} \quad (15)$$

Figure 18 shows the results of a parametric study performed. The shear stress level for specimens with ungrouted ducts has a value equal to $0.25f_c'$ when $k = 1.0$, corresponding to the current AASHTO LRFD value for k. Based on the internal stress profile shown in Fig. 16, a value of 1.0 for k is reasonable for an ungrouted duct, reflecting the localized web crushing in the test specimen.

On the other hand, the shear stress levels calculated for the specimens with grouted tendons using the current edition of AASHTO LRFD ($k = 0$) are below the value of $0.25f_c'$ (approximately 0.15 normalized shear stress ratio). These results disagree with the failure mode observed during the test: web crushing at the onset of transverse reinforcement yielding. To address this issue, this study proposes using a value of 1.0 for k, leading to calculated normalized shear stress levels in the range of $0.25f_c'$, as per Fig. 18(b). This recommendation also aligns with the internal stress flow, as shown in Fig. 16, considering plasticity in the concrete girder containing the post-tensioning duct.

The following conclusions can be drawn:

- The level of concrete compressive stress determined using the Vecchio-Collins compression-softening model[33] justifies the experimentally observed web crushing for specimens with either grouted or ungrouted ducts.

Table 6—Proposed modification for shear design of girders with post-tensioned ducts

	AASHTO LRFD[5]		Proposed modification	
Nominal shear resistance V_n*	$V_{n1} = V_c + V_s + V_p$	$V_{n2} = 0.25f_c'b_vd_v$	$V_{n1} = V_c + V_s + V_p$	$V_{n2} = 0.25f_c'b_vd_v$
Effective web-width correction factor, $b_v = b_w - k \cdot \phi_{duct}$	$k = 0$ (grouted) $k = 1$ (ungrouted)	$k = 0$ (grouted) $k = 1$ (ungrouted)	$k = 0$ (grouted) $\underline{\boldsymbol{k = 0}}$† (ungrouted)	$\underline{\boldsymbol{k = 1}}$† (grouted) $k = 1$ (ungrouted)
Duct diameter correction factor, $\lambda_{duct} = 1 - \delta \cdot \left(\frac{\phi_{duct}}{b_w}\right)^2$	$\delta = 2$ (grouted) $\delta = 0$ (ungrouted)	Not applicable	$\delta = 2$ (grouted) $\underline{\delta = 2}$† (ungrouted)	Not applicable

*V_n is determined by lesser of V_{n1} and V_{n2}.

†Proposed coefficient based on results of this study in bold with underline.

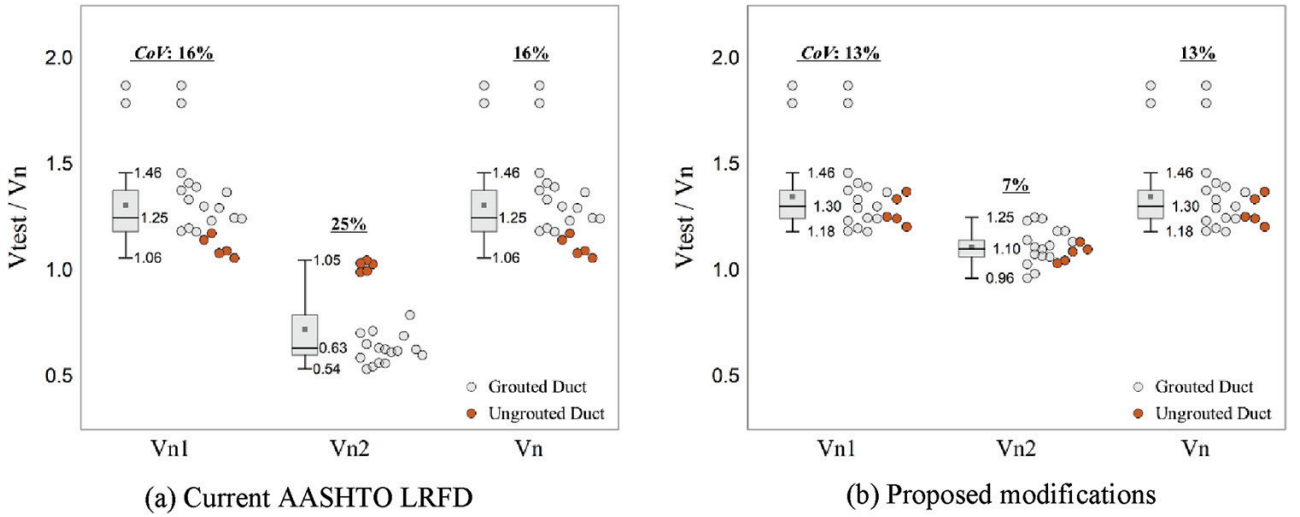


Fig. 19—Calculation of nominal shear resistance.

- The tested specimens containing ungrouted ducts experienced the localized web crushing at the normalized shear stress level of $0.25f_c'$.
- When k equals 1.0, as proposed, the shear stress level at the failure of specimens with grouted ducts becomes similar to that of specimens with ungrouted ducts. This aligns well with the failure mode of localized web crushing.

Evaluation of proposed modifications

Table 6 presents a summary of the proposed modifications to the current edition of AASHTO LRFD.[5] The proposed modifications have a similar approach to the shear design of post-tensioned systems with grouted and ungrouted ducts. They include: 1) the shear-strength reduction factor, λ_{duct}, should be used in the calculation of the transverse reinforcement contribution, V_s, to the nominal shear resistance; 2) the gross web width, b_w, should be used in the calculation of the concrete contribution, V_c, to the nominal shear resistance, V_{n1}; and 3) the upper limit on the nominal shear resistance ($V_{n2} = 0.25f_c'b_vd_v$) should be calculated using the effective web width, b_v, reduced to account for the presence of the duct.

Figure 19 shows the comparison between the shear-strength predictions obtained using the current AASHTO LRFD shear design equations and the proposed modifications, in terms of experimental-to-calculated ratios. The proposed changes were derived from the findings and in-depth analyses of the results of the experimental program undertaken from this study, as well as additional relevant test data reported in the literature.[10]

The results of both $V_{n1} = V_c + V_s + V_p$ and $V_{n2} = 0.25f_c'b_vd_v$ are shown, and the lesser value, V_n, is given in the third column. The coefficient of variance (CoV) decreases for the predictions obtained employing the proposed modifications while maintaining a level of structural conservativeness similar to the current AASHTO LRFD equations. In addition, the results obtained for $V_{n2} = 0.25f_c'b_vd_v$ employing the proposed modifications are in significantly better agreement with the experimental results, with a ratio of $V_{test}/V_n = 1.10$, compared to the current AASHTO LRFD equation, which stands at $V_{test}/V_n = 0.63$. For all specimens, the calculated values for V_{n1} were lower than the values obtained for V_{n2}; as such, the nominal shear resistances, V_n, have the values of V_{n1}. In essence, the introduced modifications manifest a significant enhancement in the reliability of shear design equations applicable to post-tensioned concrete elements, as evidenced by the reduction in CoV from 16% to 13% for V_{n1} and from 25% to 7% for V_{n2}.

SUMMARY AND CONCLUSIONS

A comprehensive experimental program was undertaken to investigate the shear behavior of post-tensioned concrete members with post-tensioning ducts, selecting the grouting conditions and duct layout as test variables. The experimental program involved the construction and testing of

six Tx62 I-girder specimens. The structural tests resulted in similar failure modes, initiated by localized web crushing, regardless of the duct condition and tendon profile. The extensive instrumentation that monitored the experimental behavior of the specimens provided valuable insight into the underlying mechanisms that governed the response. These tests serve as a foundation for the proposed changes to the shear resistance calculation in AASHTO LRFD.

Summary of experimental results and discussion

- This study found that all test specimens experienced a similar failure mechanism regardless of the tendon condition (bonded or unbonded) and profile (straight, parabolic, or hybrid).
- Around the duct area, the vibrating-wire gauges (VWGs) measured increasing tensile strains in the out-of-plane direction for both grouted and ungrouted duct conditions.
- In the analysis of service-level cracking, the normalized shear stress of both grouted and ungrouted conditions indicated similar stress levels to trigger the onset of the diagonal shear cracks in the post-tensioning duct area.
- All test specimens developed similar levels of normalized shear stress at the ultimate load level.

Summary of development of design recommendations

- The entire web engaged the shear-transfer mechanism based on the occurrence of well-distributed, fan-shaped diagonal shear cracks for specimens with either grouted or ungrouted tendons.
- No significant difference was found between the grouted and ungrouted tendons with respect to the aggregate interlock force based on the numerical analysis using the Collins-Mitchell 1987 model.[32]
- As such, the gross web width, b_w, should be used in the calculation of the concrete component, V_c, to the shear strength capacity.
- The level of concrete compressive stress determined using the Vecchio-Collins compression-softening model[33] justifies the experimentally observed web crushing for specimens with either grouted or ungrouted tendons.
- The specimens containing ungrouted tendons experienced localized web crushing at the normalized shear stress level of $0.25f_c'$.
- When k equals 1.0, as proposed, the calculated shear stress level at failure of specimens with grouted tendons is similar to that of specimens with ungrouted tendons. This aligns well with the failure mode of localized web crushing.

Proposed changes to AASHTO LRFD

The current AASHTO LRFD provisions for the shear design of post-tensioned concrete members account for a reduction in the shear capacity due to the detrimental effect caused by the presence of ducts in the web region, varying based on the condition of the ducts. The current shear design procedure was not found to align with the observed failure mechanism of the post-tensioned concrete members. This led to the following proposed modifications:

- The entire web engages the shear-transfer mechanism, regardless of whether the specimen's tendons are grouted or ungrouted. As such, the gross web width (b_w) should be used in the calculation of the concrete component to the shear strength capacity for V_{n1}, Eq. (5.7.3.3-1) in AASHTO LRFD.[5]
- The normalized shear stress level of specimens containing grouted tendons is similar to that of specimens with ungrouted tendons when the value of k is 1.0, as proposed. This is in agreement with the observed failure mode, localized web crushing. Thus, when calculating V_{n2}, Eq. (5.7.3.3-2) in AASHTO LRFD, the effective web width (b_v) should be reduced by the diameter of the duct.[5]
- Based on the changes proposed for the effective web-width correction factor (k), the proposed value of 2.0 for the duct diameter correction factor (δ) ensures similar structural conservativeness for both grouted and ungrouted tendons.

AUTHOR BIOS

Sangyoung Han *is an Assistant Professor in the Department of ICT Integrated Ocean Smart City Engineering at Dong-A University, Busan, South Korea. He received his PhD from The University of Texas at Austin, Austin, TX. His research interests include the concrete mixture characteristics and analysis of reinforced and prestressed concrete structures.*

Jarrod Zaborac *is a Graduate Engineer in the Diagnostics Group at Walter P Moore in Austin, TX. He received his PhD from The University of Texas at Austin in 2021.*

ACI member **Jongkwon Choi** *is an Assistant Professor in the Department of Civil and Environmental Engineering at Hongik University, Seoul, South Korea. He received his BS and MS from Seoul National University, Seoul, South Korea, and his PhD from The University of Texas at Austin. His research interests include the mechanical behavior, experiments, and analysis of reinforced concrete and prestressed concrete structures, and structural assessment of aging concrete structures.*

Anca C. Ferche *is an Assistant Professor in the Department of Civil, Architectural and Environmental Engineering at The University of Texas at Austin. She received her PhD from the University of Toronto, Toronto, ON, Canada. She is a member of Joint ACI-ASCE Committee 447, Finite Element Analysis of Reinforced Concrete Structures. Her research interests include performance assessment and analysis of reinforced concrete structures, concrete deterioration mechanisms, and sustainability of concrete structures.*

Oguzhan Bayrak, *FACI, is a University Distinguished Professor in the Department of Civil, Architectural and Environmental Engineering, where he serves as the Director of the Concrete Bridge Engineering Institute and holds the Cockrell Family Chair in Engineering No. 20, at The University of Texas at Austin. He is a member of ACI Committees S803, Faculty Network Coordinating Committee, and 341, Performance-Based Seismic Design of Concrete Bridges, and Joint ACI-ASCE Committees 441, Reinforced Concrete Columns, and 445, Shear and Torsion.*

ACKNOWLEDGMENTS

The authors are grateful to the Texas Department of Transportation (TxDOT) for providing funds to conduct this research study (Report No. FHWA/TX-22/5-6652-01-1, Grant No. 5-6652-01). The contributions of the Project Monitoring Committee—J. Steele (Project Manager), C. Gutierrez, G. Turco, J. Tucker, J. Roche, L. Flournoy, and M. Hyzak—are deeply appreciated. Many thanks are due to Valley Prestress Products, Inc., in Eagle Lake, TX, for fabricating the girders that were used for the experimental program. Special thanks are also offered to the numerous students and staff members at Ferguson Structural Engineering Laboratory for ensuring the successful completion of the research study.

NOTATION

A_{cef} = area of effective embedment zone of concrete where reinforcing bars can influence crack width
A_s = area of steel considered to be effectively bonded to concrete
A_v = area of transverse reinforcement within distance s
b_v = effective web width
b_w = gross web width
c = clear concrete cover
d_b = bar diameter
d_v = effective shear depth
f_c' = compressive strength of concrete for use in design, and β indicates ability of diagonally cracked concrete to transmit tension and shear
f_y = specified minimum yield strength of reinforcement
f_2 = average principal (diagonal) compressive stress
k = effective web-width correction factor
k_1 = coefficient that characterizes bond properties of bars ($k_1 = 0.4$ for deformed bars and $k_1 = 0.8$ for plain bars)
k_2 = coefficient to account for strain gradient, $k_2 = 0.25(\varepsilon_1 + \varepsilon_2)/2\varepsilon_1$ (ε_1 and ε_2 are largest and smallest tensile strains in effective embedment zone, respectively)
s = spacing of transverse reinforcement
s_2 = maximum spacing between longitudinal reinforcing bar but shall not be taken greater than $15d_b$
V_n = nominal shear resistance
V_{n1} = nominal shear resistance given in Eq. (5.7.3.3-1)
V_{n2} = nominal shear resistance given in Eq. (5.7.3.3-2)
V_p = vertical component of prestressing force
V_{test} = maximum shear force carried by test specimen
α = angle of inclination of transverse reinforcement to longitudinal axis
β = factor indicating ability of diagonally cracked concrete to transmit tension and shear
δ = duct diameter correction factor
ε_x = average longitudinal strain acting on member
ε_y = average vertical strain acting on member
ε_1 = average principal tensile strain of concrete acting perpendicular to principal diagonal tensile stress
ε_2 = average principal compressive strain of concrete in direction of principal diagonal compressive stress
ϕ = shear-resistance factor
ϕ_{duct} = duct diameter
λ_{duct} = accounts for reduction in shear strength due to presence of post-tensioning duct in thin web
θ = angle of inclination of diagonal compressive stresses
ρ_{ef} = A_s/A_{cdf}

REFERENCES

1. Castrodale, R. W., and White, C. D., "Extending Span Ranges of Precast Prestressed Concrete Girders," NCHRP Report 517, Transportation Research Board, Washington, DC, 2004, 603 pp.

2. Collins, M. P., and Mitchell, D., *Prestressed Concrete Structures*, Prentice Hall, Englewood Cliffs, NJ, 1991, 766 pp.

3. FDOT, "New Directions for Florida Post-Tensioned Bridges," Florida Department of Transportation, Tallahassee, FL, 2004, 95 pp.

4. Hamilton, H. R.; Rice, J. A.; Abdullah, A. B. M.; Bhatia, R.; Brenkus, N.; and Skelton, D., "Replaceable Unbonded Tendons for Post-Tensioned Bridges," Florida Department of Transportation, Tallahassee, FL, 2017, 669 pp.

5. AASHTO, "AASHTO LRFD Bridge Design Specifications," ninth edition, American Association of State Highway and Transportation Officials, Washington, DC, 2020, 1914 pp.

6. AASHTO, "Guide Specifications for Design and Construction of Segmental Concrete Bridges," second edition, American Association of State Highway and Transportation Officials, Washington, DC, 1999, 96 pp.

7. PCI, "PCI Bridge Design Manual (MNL-133-14)," third edition, Precast/Prestressed Concrete Institute, Chicago, IL, 2014, 1620 pp.

8. EN 1992-1-1:2004, "Eurocode 2: Design of Concrete Structures - Part 1-1: General Rules and Rules for Buildings," European Committee for Standardization, Brussels, Belgium, 2004, 225 pp.

9. *fib*, "*fib* Model Code for Concrete Structures 2010," International Federation for Structural Concrete, Lausanne, Switzerland, 2013, 434 pp.

10. Moore, A.; Williams, C.; Al-Tarafany, D.; Felan, J.; Massey, J.; Nguyen, T.; Schmidt, K.; Wald, D.; Bayrak, O.; Jirsa, J.; and Ghannoum, W., "Shear Behavior of Spliced Post-Tensioned Girders," Report No. FHWA/TX-14/0-6652-1, Center for Transportation Research, The University of Texas at Austin, Austin, TX, 2015, 220 pp.

11. Skelton, D., and Hamilton, H. R., "Shear Behavior of Webs Post-Tensioned with Tendons Containing Flexible Fillers," Florida Department of Transportation, Tallahassee, FL, 2021, 198 pp.

12. Vecchio, F. J., and Collins, M. P., "The Modified Compression-Field Theory for Reinforced Concrete Elements Subjected to Shear," *ACI Journal Proceedings*, V. 83, No. 2, Mar.-Apr. 1986, pp. 219-231.

13. Bentz, E. C.; Vecchio, F. J.; and Collins, M. P., "Simplified Modified Compression Field Theory for Calculating Shear Strength of Reinforced Concrete Elements," *ACI Structural Journal*, V. 103, No. 4, July-Aug. 2006, pp. 614-624.

14. Muttoni, A.; Burdet, O. L.; and Hars, E., "Effect of Duct Type on the Shear Strength of Thin Webs," *ACI Structural Journal*, V. 103, No. 5, Sept.-Oct. 2006, pp. 729-735.

15. Wald, D. M.; Moore, A.; Bayrak, O.; and Jirsa, J. O., "Compressive Behavior of Concrete Panels Containing Steel and Plastic Ducts," *ACI Structural Journal*, V. 114, No. 5, Sept.-Oct. 2017, pp. 1167-1176. doi: 10.14359/51689721

16. Kuchma, D., "Effect of Ducts on Shear Strength of Prestressed and Non-Prestressed Members [Interview] (15 June 2013)," The University of Texas at Austin, Austin, TX, 2013.

17. WSDOT, "Bridge Design Manual LRFD," Washington State Department of Transportation, Olympia, WA, 2023, 1050 pp.

18. TxDOT, "Bridge Design Manual - LRFD," Texas Department of Transportation, Austin, TX, 2021, 95 pp.

19. Garber, D.; Gallardo, J.; Deschenes, D.; Dunkman, D.; and Bayrak, O., "Effect of New Prestress Loss Estimates on Pretensioned Concrete Bridge Girder Design," Report No. FHWA/TX-12/0-6374-2, Center for Transportation Research, The University of Texas at Austin, Austin, TX, 2013, 300 pp.

20. Han, S.; Zaborac, J.; Webb, Z. D.; Choi, J.; Ferche, A. C.; and Bayrak, O., "Shear Behavior of Spliced Post-Tensioned Girders with Ungrouted Tendons," Report No. FHWA/TX-22/5-6652-01-1, Center for Transportation Research, The University of Texas at Austin, Austin, TX, 2022, 181 pp.

21. ASTM C39/C39M-14, "Standard Test Method for Compressive Strength of Cylindrical Concrete Specimens," ASTM International, West Conshohocken, PA, 2014, 7 pp.

22. ASTM A615/A615M-20, "Standard Specification for Deformed and Plain Carbon-Steel Bars for Concrete Reinforcement," ASTM International, West Conshohocken, PA, 2020, 8 pp.

23. ASTM A416/A416M-18, "Standard Specification for Low-Relaxation, Seven-Wire Steel Strand for Prestressed Concrete," ASTM International, West Conshohocken, PA, 2018, 5 pp.

24. AISC, "Steel Construction Manual," 15th edition, American Institute of Steel Construction, Chicago, IL, 2017, 2324 pp.

25. Moore, A. M.; Williams, C. S.; Massey, J. B.; Bayrak, O.; Ghannoum, W. M.; and Jirsa, J. O., "Shear Behavior of Post-Tensioned Girders," *ACI Structural Journal*, V. 114, No. 6, Nov.-Dec. 2017, pp. 1615-1625. doi: 10.14359/51700835

26. ASTM C496-96, "Standard Test Method for Splitting Tensile Strength of Cylindrical Concrete Specimens," ASTM International, West Conshohocken, PA, 1996, 4 pp.

27. ACI Committee 318, "Building Code Requirements for Structural Concrete (ACI 318-19) and Commentary (ACI 318R-19) (Reapproved 2022)," American Concrete Institute, Farmington Hills, MI, 2019, 624 pp.

28. ACI Committee 224, "Control of Cracking in Concrete Structures (ACI 224R-01) (Reapproved 2008)," American Concrete Institute, Farmington Hills, MI, 2001, 46 pp.

29. Birrcher, D.; Tuchscherer, R.; Huizinga, M.; Bayrak, O.; Wood, S.; and Jirsa, J., "Strength and Serviceability Design of Reinforced Concrete Deep Beams," Report No. FHWA/TX-09/0-5253-1, Center for Transportation Research, The University of Texas at Austin, Austin, TX, 2009, 400 pp.

30. Wight, J. K., *Reinforced Concrete: Mechanics and Design*, seventh edition, Prentice Hall, Hoboken, NJ, 2015, 1164 pp.

31. Reineck, K.-H.; Bentz, E.; Fitik, B.; Kuchma, D. A.; and Bayrak, O., "ACI-DAfStb Databases for Shear Tests on Slender Reinforced Concrete Beams with Stirrups," *ACI Structural Journal*, V. 111, No. 5, Sept.-Oct. 2014, pp. 1147-1156. doi: 10.14359/51686819

32. Collins, M. P., and Mitchell, D., "Prestressed Concrete Basics," Canadian Prestressed Concrete Institute, Ottawa, ON, Canada, 1987, 614 pp.

33. Vecchio, F. J., and Collins, M. P., "Compression Response of Cracked Reinforced Concrete," *Journal of Structural Engineering*, ASCE, V. 119, No. 12, 1993, pp. 3590-3610. doi: 10.1061/(ASCE)0733-9445(1993)119:12(3590)

ACI STRUCTURAL JOURNAL TECHNICAL PAPER

Title No. 121-S66

Cyclic Test of Precast Reinforced Concrete Tessellated Shear Wall

by G. F. Crocker, B. E. Ross, M. C. Kleiss, P. Okumus, and N. E. Khorasani

This paper describes the experimental testing of a reinforced concrete tessellated shear wall. The wall specimen was tested as part of a National Science Foundation-funded research project designed to demonstrate the concept of tessellated structural-architectural (TeSA) systems. TeSA systems are constructed of topologically interlocking tiles arranged in tessellations, or repeating geometric patterns. As such, these systems are designed with easy repair and reuse in mind. The specimen discussed in this paper is a TeSA shear wall constructed from individually precast I-shaped tiles. This paper presents the results of reverse cyclic loading of the specimen, including load-displacement behavior, crack propagation, and energy dissipation. A simplified analytical model for predicting the wall's flexural capacity is also discussed.

Keywords: flexural capacity; low-damage; modular; reverse cyclic loading; seismic; self-centering; topologically interlocking; unbonded post-tensioning.

INTRODUCTION

Tessellated structural-architectural (TeSA) systems use repeating geometric patterns known as tessellations in structural applications. One such application is a structural shear wall comprised of topologically interlocking precast reinforced concrete tiles. Such a wall combines the architectural appeal of tessellation geometry with the unique capabilities of tessellated structures. One capability of a TeSA shear wall is that of localized failure; due to the discrete tiles, there is greater resistance to crack propagation in TeSA walls compared to monolithic shear walls. Instead, the damage is isolated to individual tiles, allowing for repair or replacement after an extreme event (Ross et al. 2020).

This paper examines the performance of a reinforced concrete TeSA shear wall under reverse cyclic lateral loading. The wall's experimental strength, energy dissipation, and damage behavior are discussed. A simplified flexural strength model, based on the work from Perez et al. (2007), is presented for TeSA shear walls and compared to the test. The work was completed as a part of the first author's doctoral studies (Crocker 2022). Additional details not included in the current paper can be found in the reference dissertation.

RESEARCH SIGNIFICANCE

The TeSA concept is a nascent one; this paper discusses the first test of a reinforced concrete tessellated structure. Previous testing has been performed on small-scale interlocking tessellations; however, laboratory testing of a tessellated structure on a large scale had not yet been performed prior to this experiment.

BACKGROUND

Tessellations are defined mathematically as patterns of repeating convex shapes with no gaps or overlap (Fig. 1, left). However, in an architectural context, it is common to loosen this definition. In this paper, a tessellation is a repeating pattern of similar tiles. For the most part, architectural applications of tessellations have been strictly aesthetic in nature. For example, the Mulberry House in New York has a precast tessellated façade (Fig. 1, right).

Some tessellations are also part of the structure; a common example is a brick wall. While this is an example of a simple tessellation whose elements do not interlock with each other, it fits the criteria of a load-bearing structural element comprised of discrete repeating "tiles."

The current paper investigates topologically interlocking tessellations. Unlike a brick wall, these tessellations have no load-bearing binder or mechanical connection between the elements. Instead, they transfer force strictly through interlocking geometry and tile-to-tile bearing. An early example of topologically interlocking tiles is the Abeille Vault, designed in 1699 by French Architect Joseph Abeille. Abeille proposed a two-dimensional floor system comprised of geometrically identical tiles, each rotated 90 degrees with respect to one another. In practice, these tiles were able to support out-of-plane loading (Fleury 2009). A more recent example is that of a topologically interlocking system of road pavers called G-blocks (Glickman 1984). G-blocks are three-dimensionally interlocking tetrahedrons that were used to spread applied loads to the subsurface. Both the Abeille Vault and G-block systems required edge restraint (much like an arch requiring buttressing) to ensure the tiles remained in place.

The mechanical behavior of topologically interlocking tessellations has been investigated on a small scale, starting with Dyskin et al. (2001). Studies have been performed to explore the behavior of small (0.48 in. [12.25 mm] edge size) topologically interlocking cubes arranged in a plane (Estrin et al. 2004; Molotnikov et al. 2007; Schaare et al. 2008). Researchers observed that damage was isolated to certain elements of the tessellation, as cracks were unable to propagate as they would in a monolithic system. This behavior of topologically interlocking systems makes them attractive for

ACI Structural Journal, V. 121, No. 5, September 2024.

MS No. S-2022-401.R2, doi: 10.14359/51740848, received February 26, 2024, and reviewed under Institute publication policies. Copyright © 2024, American Concrete Institute. All rights reserved, including the making of copies unless permission is obtained from the copyright proprietors. Pertinent discussion including author's closure, if any, will be published ten months from this journal's date if the discussion is received within four months of the paper's print publication.



Fig. 1—Example of simple periodic tessellation (left) (Widewalls 2016); and example of architectural tessellation as used in the Mulberry House (right) (Manning 2009).

concrete structural elements. Studies have evolved to investigate the behavior of less regular interlocking tile shapes, such as osteomorphic blocks first proposed by Dyskin et al. (Dyskin et al. 2003; Akpanya et al. 2023).

An analytical study of the behavior of TeSA walls was conducted in parallel to the experimental testing presented in the current paper. Syed et al. (2021) examined the behavior of precast TeSA walls under lateral loading using finite element analysis in comparison to the behavior of monolithic shear walls. This study concluded that the arrangement of boundary tiles has little effect on the flexural strength of a TeSA wall, while changing the reinforcement ratio has a significant impact.

In some ways, interlocking concrete masonry systems are closely related to TeSA wall structures. Interlocking concrete masonry units (CMUs) are often dry-stacked and resist applied force only through self-weight and topologically interlocking shear keys (Hines 1995). However, interlocking masonry differs from the TeSA shear wall system in a critical way; the TeSA system is designed with rapid repair in mind. Interlocking CMUs may not offer this advantage, as the number of masonry units is very high and shear keys prevent removal after construction. Similar challenges are presented by other proposed civil engineering applications, such as the osteomorphic bricks studied by Yong (2011) and Javan et al. (2020).

In-plane load tests of precast rocking walls with unbonded post-tensioning have been performed and compared to both simplified models and numerical models with considerable success (Perez et al. 2007; Aaleti and Sritharan 2009; Basereh et al. 2020). Much of the research concerning rocking walls also focuses on the concept of rapid repair, similar to TeSA walls. For example, several studies have investigated the use of replaceable plates for reinforced concrete rocking wall repair with some success (Li et al. 2020; Fan et al. 2023).

Previous researchers have addressed the mechanics of tessellated structures, interlocking wall systems, and concrete shear walls with unbonded reinforcement. However, an investigation of the in-plane testing of a large-scale reinforced concrete tessellated shear wall has not been performed prior to the current study. In fact, this is the first study to test a reinforced concrete tessellated structure of any kind.

EXPERIMENTAL METHODS

Specimen design and construction

The TeSA shear wall specimen was 114.75 in. (2.92 m) tall, and 73 in. (1.85 m) wide. The wall's thickness was 5.5 in. (13.97 cm). A detailed description of the fabrication process was previously reported in a conference paper (Crocker 2021). Essential details are also provided here. The test specimen was constructed of 39 geometrically interlocking tiles prepared by a precast concrete fabricator using a master form that could be reused and adjusted to fabricate the individual tile shapes. All tiles were reinforced with reinforcing bars with a diameter of 0.375 in. (9.525 mm, Fig. 2). Specified and tested material properties are listed in Table 1.

The primary tile shape is referred to as an "I-shaped tile." Various inserts could be used with the master form to create the other tile shapes: corner tiles ("L-shaped"), horizontal boundary tiles ("T-shaped"), and vertical boundary tiles ("C-shaped"). For practical purposes of getting the wall built and tested, tiles were designed to be the smallest size possible while achieving confinement of concrete with two-plane reinforcement and appropriate cover (Fig. 2).

Each tile was cast with a 1.25 in. (32 mm) diameter polyvinyl chloride (PVC) pipe running through it longitudinally. These pipes were used to house vertical unbonded post-tensioned (PT) strands, having a diameter of 0.6 in. (15 mm). The strands provided precompression and flexural strength to the wall. Non-prestressed reinforcement within the tiles carried local tensile forces. Unbonded post-tensioning was specifically chosen to provide self-centering and because it could be removed as part of future wall repair.

A low-strength grout was placed between the tiles. The grout space had an average thickness of 0.375 in. (0.95 cm). Grout was not intended to contribute any tensile or shear strength, but rather to maintain consistent spacing and provide a means of transferring compressive stresses between tiles.

Once all tiles were grouted in place, a steel transfer beam/cap was placed on top of the wall, and the PT strands were installed and tensioned to approximately 22 kip (98 kN),

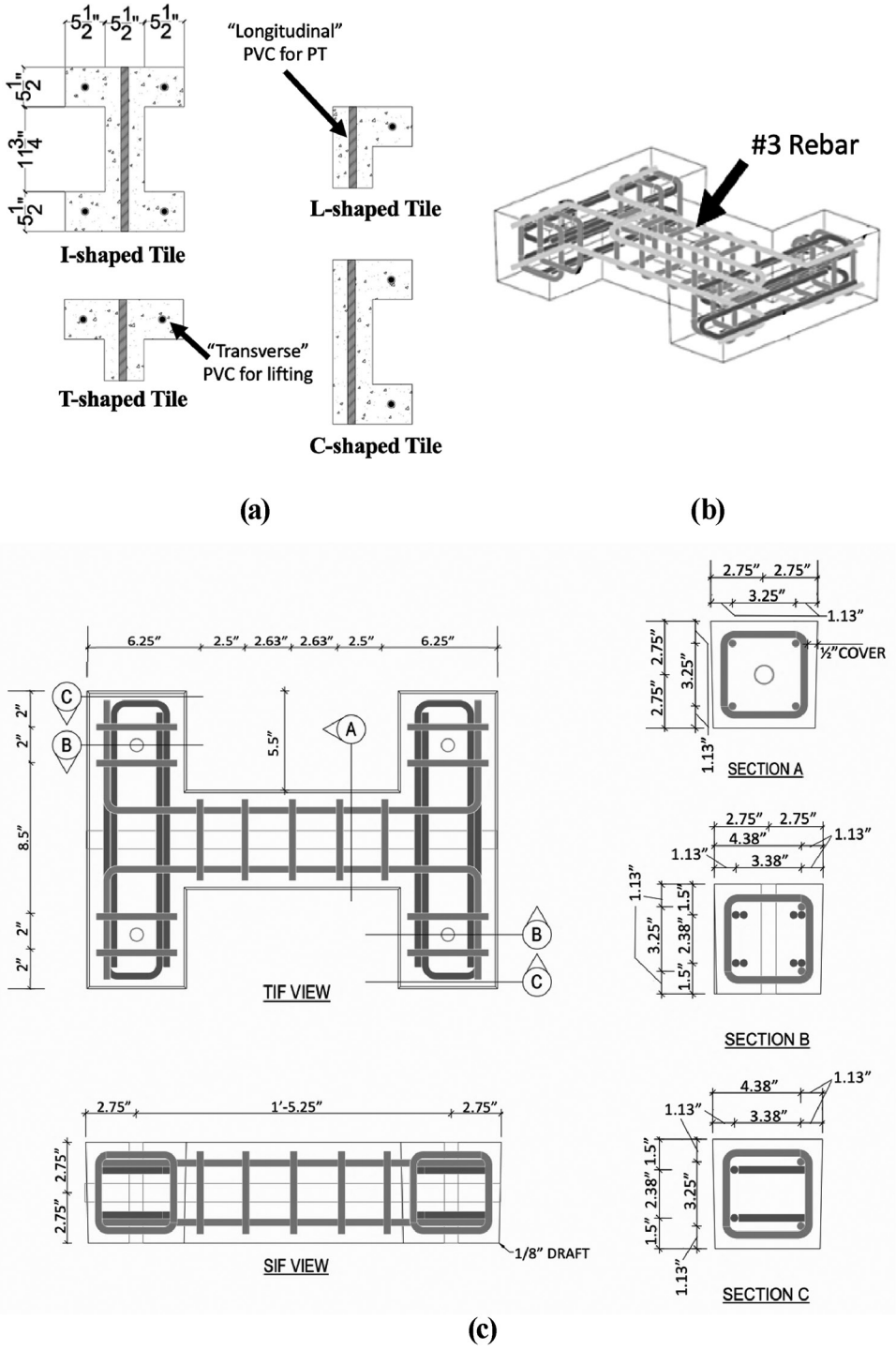


Fig. 2—(a) Overall tile dimensions; (b) isometric view of tile reinforcement; and (c) tile reinforcement details.

resulting in an axial stress in the wall equivalent to approximately 6% of the concrete specified compressive strength.

Test setup

Figure 3 shows the test setup. A steel test frame was fabricated, which included a base to transfer forces from the wall to the test floor, as well as lateral bracing members. The unbonded strands were anchored to the base. Horizontal shear reactions at the base of the wall were provided through bearing by steel blocks welded to the base. Six steel bolts with a diameter of 0.625 in. (16 mm) were used to attach the lower row of tiles to the base and provide a nominal degree of shear and uplift capacity. A hydraulic actuator in displacement-control was used to apply the lateral load. Lateral displacement was recorded at various locations by linear potentiometers. The load was measured by the hydraulic actuator's internal load cell.

Additional load cells were installed on the outermost two strands to aid in initial stressing, as well as record their internal forces throughout testing. The lateral slip and uplift of the test frame, while small, was also monitored using linear potentiometers. This data was used to adjust the gross lateral displacement to correct for the effects of base rocking and slip. Rocking of the wall relative to the steel base was

Table 1—Specified and tested material properties

Material	Specified minimum strength	Tested strength	Tested modulus of elasticity
Precast concrete tiles	f_c' = 6000 psi (41.4 MPa)	6840 psi (47.2 MPa) compression	3090 ksi (21.3 GPa)
No. 3 reinforcing bar	f_y = 60 ksi (414 MPa)	73 ksi (503 MPa) tension	27,700 ksi (191 GPa)
0.6 in. (15 mm) diameter steel strands	f_{pu} = 270 ksi (1860 MPa)	289 ksi (ultimate) (1990 MPa) 258 ksi (at 1% strain) (1780 MPa)	28,700 ksi (198 MPa)

monitored using linear potentiometers at the bottom corners of the specimen.

The specimen was tested under cyclical lateral loading that was based on the protocol in ACI ITG-5.1-07 (2008). This document provides a test methodology and acceptance criteria for the reverse cyclic loading of unbonded PT precast walls that do not meet the requirements of Chapter 21 in ACI 318-02.

The test protocol involved displacement "sets" that increased the drift ratio as testing progressed. Three reversed cycles were performed in each set. According to ACI ITG-5.1-07, the first of these sets must be performed with an applied load of no more than 60% of the nominal load capacity of the wall. An initial finite element analysis estimated the maximum load capacity of 110 kip (490 kN); therefore, a load of 66 kip (290 kN) was used to calculate the maximum drift angle and corresponding displacement for the cycle set. Details of the finite element modeling can be found in Syed et al. (2021). According to the model, a load of 66 kip (290 kN) corresponds to a drift ratio of approximately 0.3%; any drift less than this limit is an acceptable starting point, so the first set of load cycles was set to a drift of 0.05%. ACI ITG-5.1-07 specifies that up to 60% of the wall's nominal capacity, the drift ratio for the subsequent load cycle set can be determined by multiplying the previous drift ratio by 2.5. Thereafter, the drift ratio can be determined by multiplying the preceding ratio by 1.25 to 1.5. The testing should continue until either the specimen fails, or the drift ratio exceeds

$$0.90 \le 0.8[h_w/l_w] + 0.5 \le 3.0 \quad (1)$$

where h_w represents the height of the specimen; and l_w represents the length of the wall. For the TeSA specimen, the limiting drift ratio from Eq. (1) was 1.73%.

Although ACI ITG-5.1-07 does not require testing beyond the calculated 1.73%, the TeSA wall specimen did not exhibit significant loss of strength at this level of drift. Therefore, the loading was continued beyond 1.73% to a maximum average drift of 2.24%. Due to small amounts of slip in the connections between the actuator and wall, the resulting wall displacements when "pushing" (positive displacement) and "pulling" (negative displacement) the specimen differed. The difference is most noticeable during the first cycle set.

Table 2—Displacement rate for each cycle set

Cycle sets	Displacement rate
1 to 2	0.005 in./s (0.013 cm/s)
3 to 7	0.01 in./s (0.025 cm/s)
8	0.02 in./s (0.051 cm/s)
9 to 10	0.03 in./s (0.076 cm/s)
11	0.04 in./s (0.102 cm/s)

Thereafter, the actuator displacements were adjusted to account for slip, and the displacements were more proportional in later sets. Figure 4 shows the displacement protocol for the 11 cycle sets that were performed.

For the first and second cycle sets, a displacement rate of 0.005 in. (0.13 mm) per second was selected. As the drift was increased throughout the cycle sets, it was deemed appropriate to increase the rate of displacement as well. Table 2 lists the displacement rate for each cycle set.

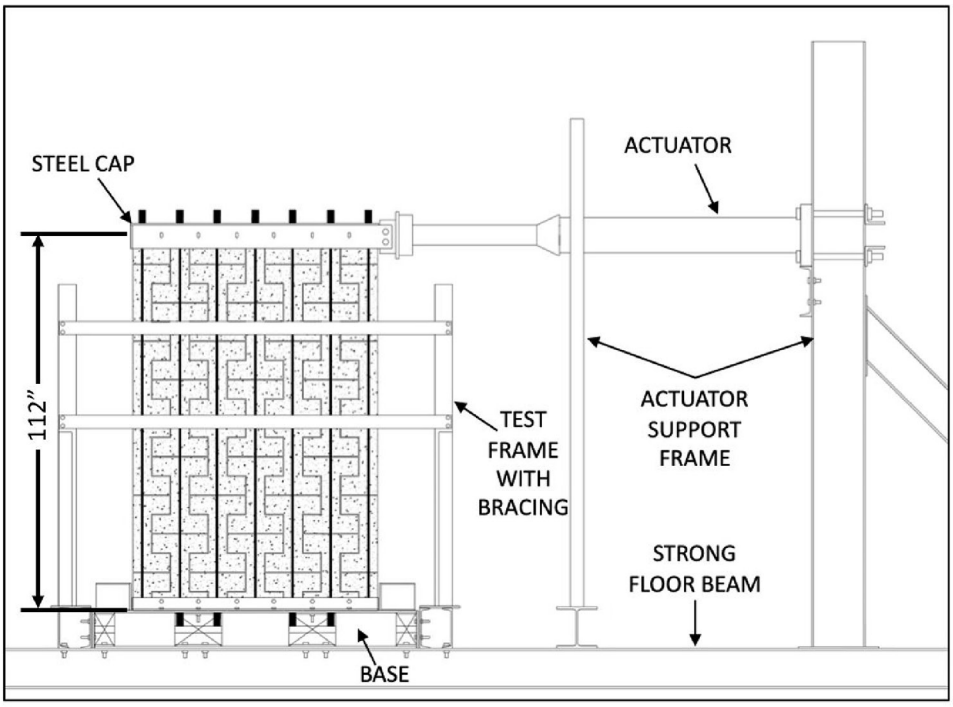
In addition to the data collected by electrical instrumentation, crack propagation was also monitored using a crack gauge card and digital photography. ImageJ software (Rasband 1997) was used to measure crack widths from the digital images, using a procedure similar to that described by Murphy (2021). Crack width measurements focused on cracks within the tiles but not within the grout.

RESULTS AND DISCUSSION

Visible damage

The most severe damage in the specimen occurred in the L-shaped "toe" pieces at the bottom corners of the wall, with particularly severe spalling damage observed on the south side of the wall (Fig. 5). The toe pieces had horizontal and vertical bearing on the frame, due to the shear and moment in the wall, respectively. The bolts connecting the lower tiles to the base also contributed to wall damage, depending on their location. The wall uplift was sufficient to engage the outermost bolts, leading to cracking in the L-shaped concrete tiles adjacent to the bolts and the eventual yielding of the bolts during the final cycle set. The uplift of the wall was not sufficient to fully engage bolts toward the interior of the wall, and the tiles surrounding these bolts exhibited significantly less damage than the toe tiles. Some spalling was also observed in the upper corner boundary tiles and is attributed to bearing of the steel transfer cap (Fig. 5).

Visible damage was initially observed after the eighth cycle set, during which an average of 1.22% drift was reached. Initial damage was primarily cracking of grout between tiles; however, a few small cracks were also observed in tiles at this stage of the test. The progression of damage in the concrete tiles from the last four cycle sets (from approximately 1.22 to 2.24% drift) can be seen in Fig. 6. As shown in the figure, the number of cracks increased as the drift value increased. Cracking and spalling were present on both sides of the wall, but were more pronounced on the south side. As discussed earlier, the spalling occurred at the toes and at one of the corner tiles at the top of the wall. The observed damage highlights a key advantage of TeSA; cracking in a



(a)



(b)

Fig. 3—(a) Drawing of test setup design; and (b) physical test setup in laboratory.

given tile typically did not propagate into the adjacent tile. Cracks tended to start and stop at the tile edges.

To characterize the damage, a scale was created based on recommendations found in FEMA 306 (1999), FEMA P-58/BD-3.8.8 (2009), and FEMA P-58/BD-3.8.9 (2011). All of these documents present recommendations for damage criteria for reinforced concrete walls with aspect ratios similar to the test specimen. The damage observed in the TeSA wall did not fit squarely into any of the categories suggested by these documents, so the suggested criteria for walls which fail most similarly to the specimen were reviewed and used to define damage states for the TeSA wall. Crack widths of 0.02 and 0.12 in. (0.5 and 3 mm) are commonly used thresholds and were therefore selected to help develop the criteria in the current paper. The damage criteria and the recommended repair methods for each category can be found in Table 3. The categorization in the table was applied to the discrete tiles rather than the entire

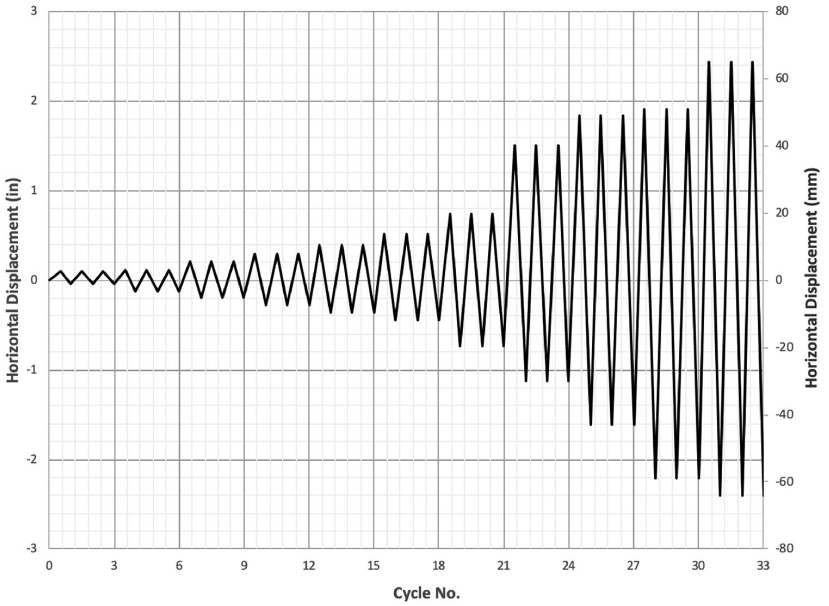


Fig. 4—Test protocol based on ACI ITG-5.1-07, showing experimental peak displacements for push and pull directions of each cycle set.

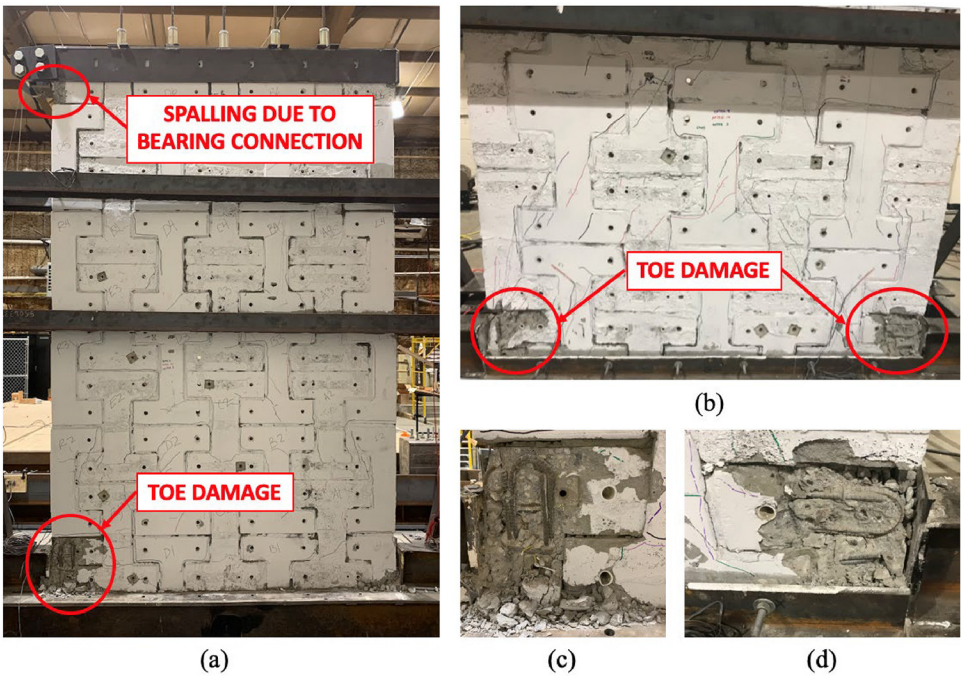


Fig. 5—Photographs of damage in: (a) north side of specimen; (b) lower half of south side of specimen; (c) toe tile on north side of specimen; and (d) toe tile on south side of specimen.

specimen. Therefore, various tiles in different damage states can all exist in the wall simultaneously.

Each tile was assigned to a damage category based on its largest crack or the presence of spalling. Damage was assessed after each displacement set after unloading the specimen. The progression of damage in terms of the damage criteria can be found in Fig. 7. A darker shade in the figure indicates a worse damage state, as defined by Table 3. As discussed previously, the most severe damage is concentrated in the toe regions of the wall, and in a corner tile at the bearing of the steel cap. The damage states of the tiles are generally but not strictly symmetric, with higher levels of displacement in the later cycles corresponding to higher levels of damage.

Load-displacement response

Testing was halted after a welded connection in the supporting base failed in tension during the second cycle of the 11th cycle set (Fig. 8). Concrete spalling in the lower corner tiles had occurred by this point and significant loss of wall capacity was imminent. The maximum drift angle specified by the ACI protocol had been exceeded when testing was stopped. Based on the observed trends in the response and the damage state of the wall, it is probable that additional

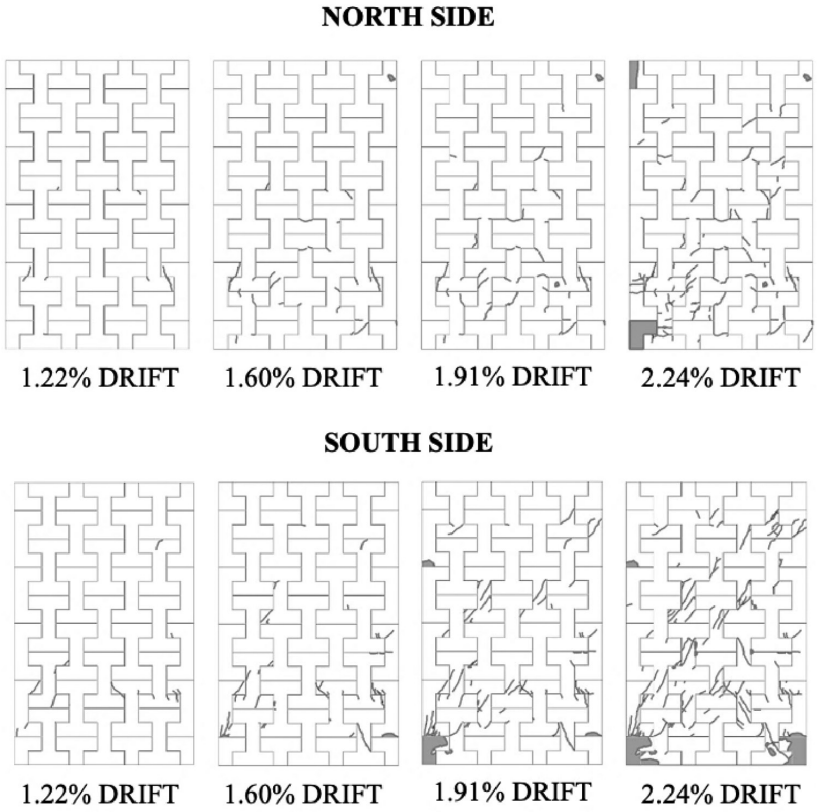


Fig. 6—Progression of damage after eighth, ninth, 10th, and 11th loading cycle sets for north and south sides of wall, respectively. Black lines represent cracks, and gray area represents spalling.

Table 3—Summary of damage states and relevant repair methods, color-coded by severity

Damage state	Crack size	Repair method
No damage	—	None
Slight	<0.02 in. (<0.5 mm)	None
Moderate	≥0.02 and <0.12 in. (≥0.5 and <3 mm)	None
Significant	≥0.12 in. (≥3 mm), some minor spalling	Epoxy injection and carbon fiber wrap, as needed
Severe	Major spalling (>2 in. [51 mm] from corner)	Replace tile

cycles would have resulted in a reduced load capacity but increasing displacement.

The specimen's lateral load-displacement hysteretic response is shown in Fig. 9. The basic shape of the hysteresis loop is as expected, with maximum lateral loads of 81.3 kip (362 kN) occurring in the 10th set of loading cycles in the push direction and 84.9 kip (378 kN) in the 11th set of cycles in the pull direction. A basic static analysis was performed to determine the theoretical lateral load (approximately 52 kip [231 kN]) required to cause uplift to occur, as indicated by a dashed line in Fig. 9. Some residual displacement was observed, particularly in the last three cycle sets. This indicates that the specimen experienced a loss in self-centering ability at approximately 1.60% drift, which was approaching the maximum drift specified by the ACI protocol (1.73%). Stiffening was observed at approximately 1.2% drift, particularly in cycle sets 9 to 11 (approximately 1.60 to 2.24% drift); this behavior is attributed to the bolts connecting the wall to the steel base being engaged. Due to tolerances in the hole and bolt sizes, the bolts were not engaged at lower drift levels. The subsequent softening during the final cycle set may be attributed to these bolts yielding.

The backbone curve is also shown in Fig. 9, indicating effectively symmetric behavior in the push and pull directions, as well as similar lateral load capacities and maximum drift angles. The only major discrepancy between the push and pull directions was the peak load in the pull direction of cycle set 11. This is the point in the bottom-left of the figure where the backbone curve shows a strength gain. One possible explanation for this behavior is strain-hardening of the bolts that connected the wall to the steel base. After the test, the bolts were removed and observed to have experienced significant plastic deformation. Due to this, the peak load supported by the specimen will be considered as 81.3 kip (362 kN) during the later discussion of a simplified model for predicting flexural capacity.

Energy dissipation

The relative energy dissipation ratio was calculated based on the procedure provided by ACI ITG-5.1-07. This ratio is found by dividing the area of the last cycle in the hysteresis loop by the area of a parallelogram inscribed by the peak load of the final cycle set and the hypothetical drift ratio found by unloading the final cycle at the initial stiffness exhibited by the specimen (Fig. 10). The resulting relative

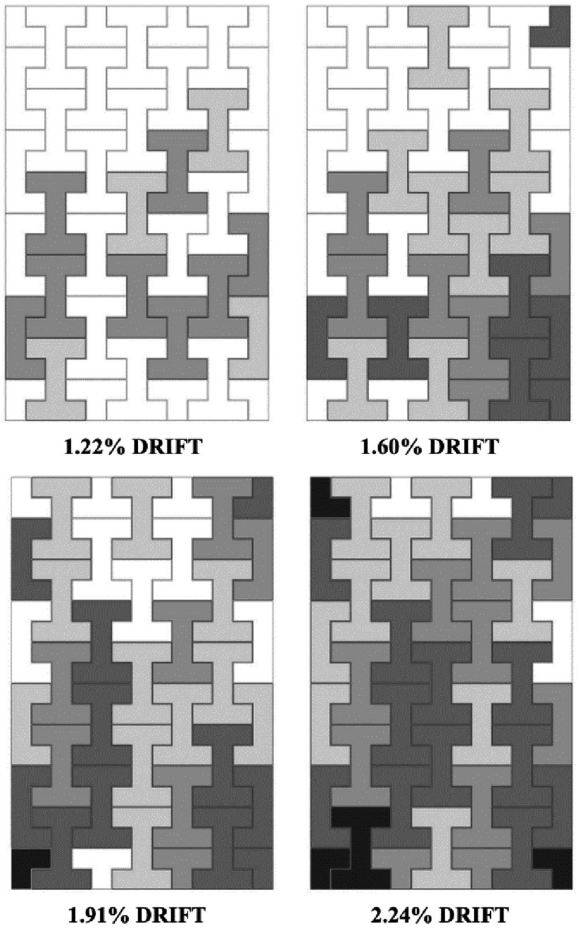


Fig. 7—Damage states after cycle sets 8, 9, 10, and 11 by tile as seen from south side of wall. Darker gray indicates more-severe damage state, as indicated by Table 3.

energy dissipation ratio calculated for the final cycle for this specimen was 0.174. According to the ACI protocol, the minimum acceptable ratio for relative energy dissipation during the final set of the final cycle of testing is 0.125, as lower ratios may result in excessive deformations following an earthquake due to low-cycle fatigue effects; therefore, the TeSA specimen exhibited an acceptable level of energy dissipation according to ACI ITG-5.1-07.

Post-tensioning strand stress

Recall that based on material testing results from a strand sample, the empirical ultimate stress of the 0.6 in. (15 mm) diameter PT strands was 289 ksi (1990 MPa) and the empirical yield stress was 258 ksi (1780 MPa). The two outermost strands were monitored throughout testing using load cells (Fig. 11). The peak stresses observed in the outermost west and east strands during any load cycle were 224 and 227 ksi (1540 and 1570 MPa), respectively. It was therefore determined that the outermost strands were approaching yield stress, but not yet yielding during the final cycle set (average 2.24% drift). To approximate the experimental stress in the other five strands, the strand strain was assumed to vary linearly along the length of the wall. This assumption will be discussed further in the simplified flexural model section. Based on this assumption, it was therefore considered unlikely that any strands yielded during testing.

It is evident from Fig. 11 that significant PT losses occurred between cycle sets. Figure 12 illustrates the PT losses incurred throughout testing. The first significant loss of PT stress occurred after cycle set 5, which corresponds to the first visible signs of damage in the wall. The second significant loss occurred after cycle set 8, which corresponds the maximum drift angle defined by ACI-ITG-5.1-07. The PT loss in the outermost west strand was particularly notable. It was qualitatively observed throughout testing that damage to the wall was not symmetric, which is likely the reason that PT losses in the east and west strands were not symmetric.

Secant stiffness

The loss of stiffness in the specimen over the course of testing was quantified by determining the secant stiffness, a ratio of peak applied load to peak displacement, for each cycle set (K_i). This secant stiffness for each cycle set was then normalized to K_1, the secant stiffness determined from the first load cycle set. Results are shown in Fig. 13. As expected, a general downward trend in the stiffness of the specimen can be observed during each cycle set. As the drift ratio increased, the loss of stiffness decreased between each cycle set, particularly after cycle set 8, during which approximately 1.22% drift was reached. This was likely due to the formation of cracks in the grout between tiles, which became visible after the eighth cycle set. Once these cracks formed, the tiles were able to shift locally for the remainder of the cycle sets. This localized behavior made the entire system more flexible, and the secant stiffness began to plateau.

SIMPLIFIED FLEXURAL CAPACITY MODEL

An iterative simplified approach was used to predict the flexural capacity of the reinforced concrete TeSA shear wall. The term "simplified" is used to describe the model to differentiate from the finite element model proposed by Syed et al. (2021). The simplified model was guided by Perez et al.'s (2007) approach for analyzing reinforced concrete walls with unbonded post-tensioning. Their approach considered a trilinear idealization of wall behavior, which included: 1) a linear range up to the effective linear limit of the wall; 2) a linear stage from the wall's effective linear limit to yielding of the PT steel; and 3) a linear plateau from the yielding of the PT steel to crushing of the confined concrete. The simplified model presented here is based on stages 1 and 2 of the Perez model. Recall that the testing on the specimen discussed throughout this chapter was halted very near the empirical yield stress of the PT strands. Therefore, post-yielding behavior is not considered.

Additionally, Perez et al.'s model is only used to calculate the shear forces associated with stages 1 and 2 in this paper. While a method is proposed to calculate theoretical drifts by Perez et al., it does not accurately capture the flexibility of the TeSA wall due to the rotation of individual tiles, which creates a more flexible system than a traditional shear wall (this phenomenon will be discussed in more detail later). As a result, theoretical drifts calculated from an analytical model intended to be used with monolithic walls such as the Perez et al. model are significantly lower than the actual drifts observed in the experiment.

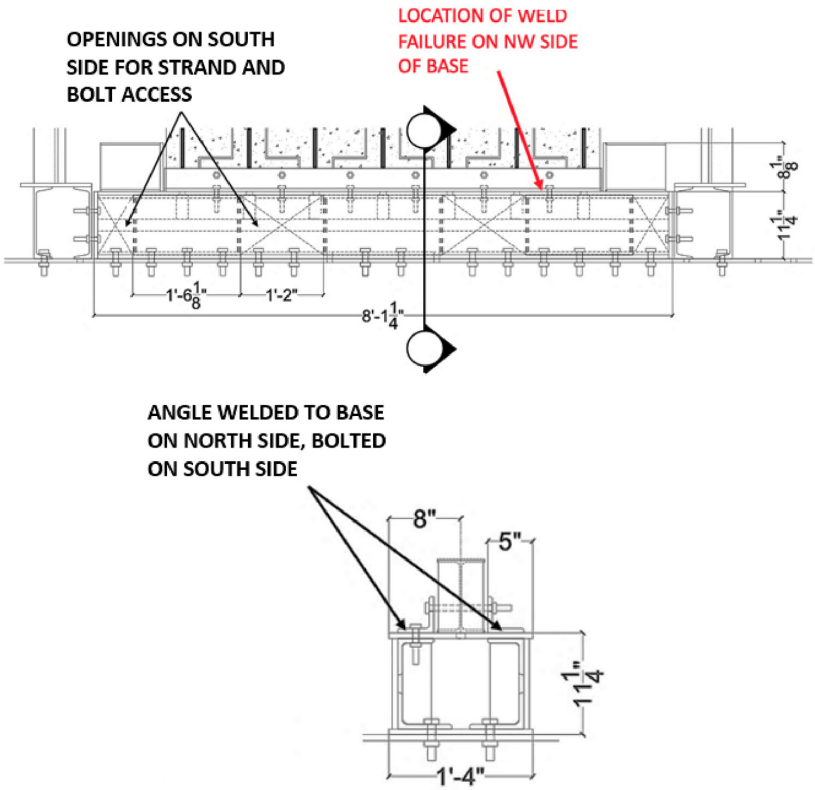


Fig. 8—Design of test base with cross section. Location of failure which occurred in cycle set 11 is indicated.

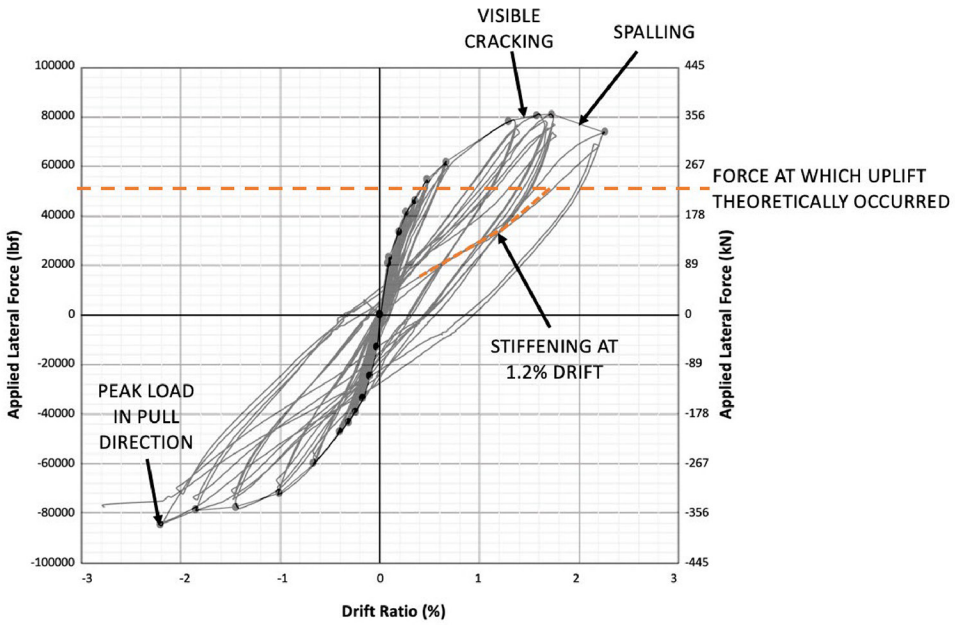


Fig. 9—Load-displacement response, including backbone curve.

The model assumes that all of the tensile capacity of the wall is provided by the PT strands, and all of the compressive strength is provided by the confined concrete in the compression zone. Consistent with detailing of the TeSA specimen, it is assumed that no bond exists between the PT strands and concrete. Any contribution to the wall's capacity by the mild reinforcement is neglected; it is assumed that flexural failure will occur at the base of the wall, and no mild reinforcement is continuous through the foundation. Despite the observation of bolt engagement in the last three cycle sets during testing, the contribution by the bolts connecting the lowest level of tiles to the base were neglected to ensure a more conservative estimate. The contact length of the wall with the base is calculated as the depth of the compression zone, while the rest of the wall is assumed to experience linear rocking (Fig. 14). It is also assumed that the wall is under-reinforced, and therefore yielding of the outermost strand will occur before the concrete at the toes crushes. Only the confined concrete is considered; cover is assumed to have spalled off. This model differs slightly from the

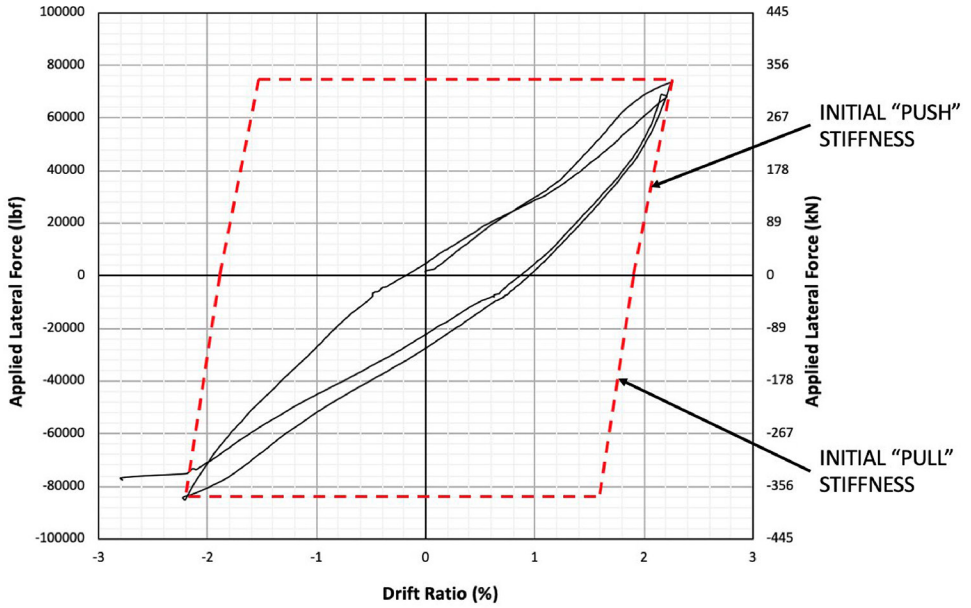


Fig. 10—Shapes used to calculate relative energy dissipation ratio for 11th cycle set; ratio is calculated as area inside hysteretic loop divided by area inside combined parallelograms shown with dashed lines.

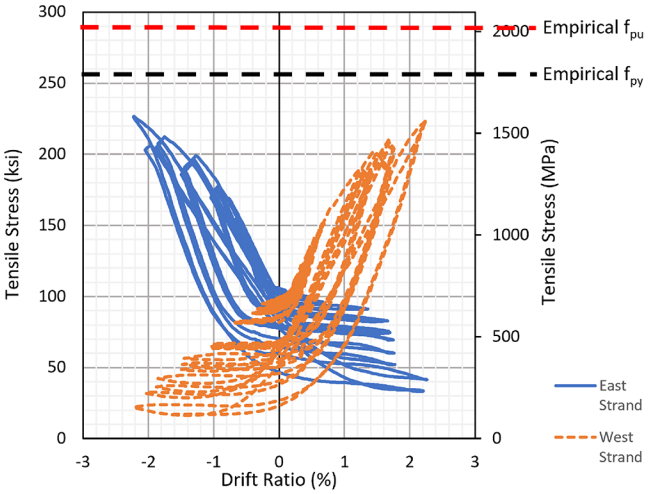


Fig. 11—Stress in outermost PT strands during testing.

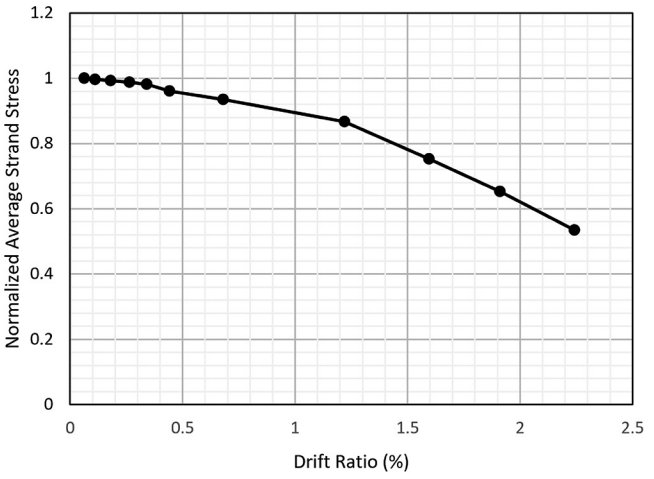


Fig. 12—Change in PT strand stress by cycle. Stress values represent average stress in outermost strands measured at beginning of each cycle set.

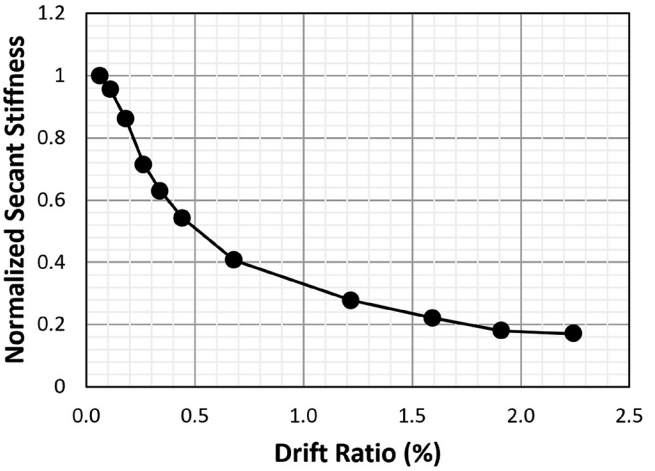


Fig. 13—Normalized secant stiffness of specimen as drift ratio increased.

Perez et al. model due to the larger number of PT strands used. Additionally, the unconfined concrete material properties are used for simplicity, as well as to ensure a more conservative approach.

The base shear force V_{ell} associated with the wall's theoretical effective linear limit (stage 1) using the simplified flexural approach is calculated as follows:

1. Calculate the resultant compressive force at the base of the wall

$$C = \sum T_{i,i} \tag{2}$$

where $T_{i,i}$ is the precompression tensile force in PT strand i at the start of testing.

2. Calculate the depth of the equivalent compression stress block

$$a = \frac{C}{0.85 f_c' t_w} \tag{3}$$

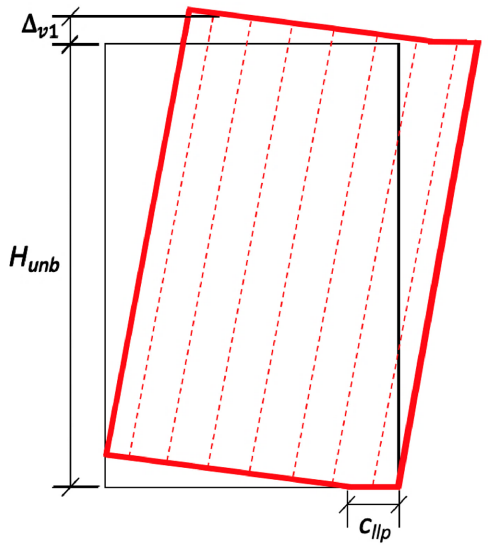


Fig. 14—Assumed behavior of wall for simplified flexural model.

where f_c' is the concrete compressive strength from material tests; and t_w is the thickness of the wall. The thickness is measured from the center of the layers of confining reinforcement.

3. Calculate the base shear at the effective linear limit

$$V_{ell} = \min\begin{cases} V_{ell,1} = \dfrac{\sum T_{i,i} d_i - C\left(\frac{a}{2}\right)}{h_{eff}} \\ V_{ell,2} = 2.5 V_{dec} \end{cases} \quad (4)$$

where d_i is the distance from the edge of the confined concrete to strand i; h_{eff} is the effective height of the wall, calculated as the moment arm between the line of action along which the load is applied and the line of action along which the base shear resistance is provided; and V_{dec} is the base shear when the precompression of the PT strands is overcome at one edge of the wall by the overturning moment from the applied lateral load (calculated using statics).

According to Perez et al., $V_{ell,1}$ accounts for softening due to nonlinear material properties, while $V_{ell,2}$ accounts for gap opening along the base of the wall. In this case, V_{ell} was found to be equal to $V_{ell,1}$, which was calculated as 49 kip (218 kN). Recall that V_{dec}, or the theoretical load required to cause uplift, was calculated as 52 kip (230 kN; refer to Fig. 9). Therefore, this model indicates that the specimen should begin to exhibit softening around the same time uplift at the base is first observed. However, nonlinear data can be clearly observed in the experimental data at approximately 40 kip (178 kN) of applied lateral force. Therefore, this model provides a somewhat unconservative estimate of the effective linear limit for this TeSA specimen. The premature softening can be attributed to the grout between tiles beginning to crush and allow some movement of individual tiles.

The procedure for determining the base shear force V_{llp} associated with first yield of the outermost PT strands (stage 2) using the simplified flexural approach includes the following:

1. Calculate an initial "guess" for the contact length between the wall and base (that is, depth of neutral axis)

$$c = \frac{T}{0.85\beta f_c' t_w} \quad (5)$$

where T is the sum of the tensile forces in the PT strands at yield strength; and β is calculated based on f_c' using Table 22.2.2.4.3 in ACI 318-19 (ACI Committee 318 2019). For the initial guess, it is assumed that all PT strands yield.

2. Find the uplift at the outermost strand, strand 1, assuming that it yields

$$\Delta_{v1} = \frac{(f_{py} - f_{p1i})}{E_p} H_{unb} \quad (6)$$

where f_{py} is the yield stress of the PT strand (obtained from material testing); f_{p1i} is the effective stress in the strand at the beginning of testing; E_p is the elastic modulus of the PT steel; and H_{unb} is the unbonded height of the PT steel. The model assumes that wall capacity is controlled by yielding of the outermost strand and that strands exhibit a perfectly elastic response up to yielding.

3. Find strain in each strand using material properties of steel and the uplift found in step 2. The strain in strand i can be found using the following equation

$$\varepsilon_{pi} = \begin{cases} \dfrac{\Delta_{v1}}{H_{unb}} \cdot \dfrac{l_i}{l_1} + \dfrac{f_{p1i}}{E_p}, & l_i > 0 \\ \dfrac{f_{p1i}}{E_p}, & l_i \le 0 \end{cases} \quad (7)$$

where l_i is the distance from the end of the contact length (that is, the wall neutral axis) to the center of strand i.

4. Find tension force in each strand

$$T_i = \varepsilon_{pi} \cdot E_p \cdot A_{pi} \quad (8)$$

where A_{pi} is the area of PT strand i.

5. Find the new iterated contact length, c_{new}, of the wall to the base

$$c_{new} = \frac{\Sigma T_i}{0.85\beta f_c' t_w} \quad (9)$$

Repeat steps 3 through 5 until the contact length converges. The final contact length will be referred to as c_{llp}. For the test wall, the contact length after the third iteration converged to within 0.5% of the third iteration. The ratio of contact length to the total length of the confined concrete was 0.192, which is within reason based on typical values for rocking and hybrid-rocking walls.

6. Calculate the moment contribution from each strand

$$M_{ni} = T_i\left(d_i - \frac{a'}{2}\right) \quad (10)$$

where a' represents the iterated length of the confined concrete stress block. This distance is simply βc_{llp}.

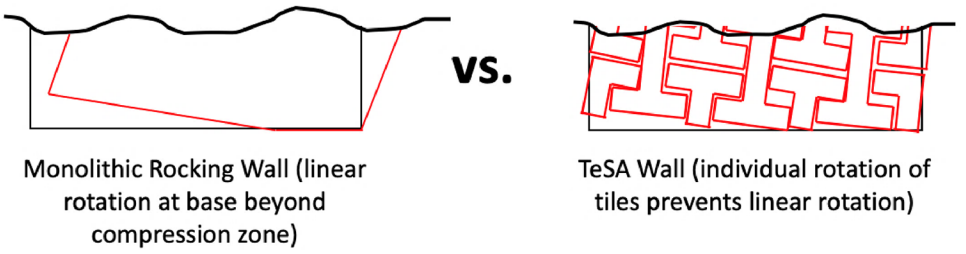


Fig. 15—Assumption of linear rocking may result in unconservative capacity estimates because local tile movements are not considered.

7. Calculate the total moment capacity of the specimen and corresponding base shear capacity

$$V_{llp} = \frac{\Sigma M_{ni}}{h_{eff}} \quad (11)$$

Applying this approach to the test specimen resulted in an expected flexural failure at a base shear of approximately 91.4 kip (407 kN). This calculated capacity is 12.4% higher than the test capacity of the wall (81.3 kip [362 kN]).

A few notes of caution should be discussed. The theoretical formulation included multiple conservative assumptions to simplify the analysis. The bolts connecting the lowest level of tiles were neglected, and the unconfined concrete strength was used to determine the depth of the concrete bearing. Even with these conservative assumptions, the calculated theoretical capacity was 12.4% higher than the experiment. Considering the bolts and confined concrete properties would have increased the discrepancy and made the theoretical capacity more unconservative.

Lack of conservatism in the model is partially attributed to the assumption of linear rocking at the base of the wall. In the experiment, it is likely that rotation of tiles occurred after grout between the tiles was damaged (Fig. 15). Indeed, opening and closing of cracks at the tile interfaces was observed as the load changed from push to pull. Local rotation of tiles affected contact with the base, thereby reducing the internal moment arm of the tension reinforcement.

Another probable explanation for the unconservative estimate of the model was the specimen's violation of one of the model's assumptions. While it is critical that the wall should be under-reinforced and fail in flexure for the model to accurately to predict its capacity, the specimen experienced crushing due to localized compression forces at its toe rather than flexural strain at the extreme fibers. This concern was validated by the load data collected for the outermost strands, which indicated that these strands were approaching but had not yet reached the yield stress determined by material tests. Additionally, strain data collected during testing indicated that strain at the extreme fibers of the specimen had not yet reached crushing strain for reinforced concrete. Another assumption of the model is that no PT losses occur over the course of testing. This assumption was also violated, as can be seen in Fig. 12. Based on these conditions and the higher-than-experimental theoretical capacity, the simplified model as presented here is only recommended for calculating upper bound flexural capacity of TeSA walls.

CONCLUSIONS

In this experiment, a novel tessellated structural-architectural shear wall was tested. Overall, the tessellated structural-architectural (TeSA) specimen exhibited desirable structural behavior for a shear wall of its material and geometric properties:

- The specimen supported a peak lateral load of 84.9 kip (378 kN).
- The average peak drift ratio achieved by the specimen in the final cycle set was approximately 2.24%, which corresponds to 2.42 in. (6.15 cm) of lateral displacement.
- The relative energy dissipation ratio for the final cycle of loading for this specimen was 0.174. This relative energy dissipation ratio is greater than the ACI-specified minimum value for this ratio (0.125), indicating that this specimen demonstrated a desirable seismic response.
- A simplified approach for determining the flexural capacity of reinforced concrete TeSA walls based on Perez et al. (2007) was compared to the test results. The model was unconservative, but calculated the experimental capacity to within 13%. The model is only recommended for estimating the upper-bound capacity of TeSA walls, as it considers the wall as a rigid monolithic system and does not consider the local rotation of individual tiles.

Forthcoming publications will discuss the repair and retesting of the TeSA shear wall specimen. Additionally, shear testing has been completed on a TeSA beam specimen constructed from the same precast tiles used to construct the TeSA wall specimen discussed in the current paper. The results from the shear testing were used to develop a simplified shear model for TeSA precast structures, which will be discussed in a forthcoming publication.

AUTHOR BIOS

ACI member **Grace F. Crocker** *is a Lecturer of General Engineering at Clemson University, Clemson, SC, where she received her BS, MS, and PhD in civil engineering in 2018, 2019, and 2022, respectively. Her research interests include resilient structural-architectural systems, as well as interdisciplinary education for undergraduate structural engineering and architecture students.*

ACI member **Brandon E. Ross** *is the Cottingham Associate Professor in the Glenn Department of Civil Engineering at Clemson University. He received his BS in architectural engineering and MS in civil engineering from the University of Wyoming, Laramie, WY, in 2001 and 2002, respectively, and his PhD in civil engineering from the University of Florida, Gainesville, FL, in 2012. He is a member of Joint ACI-PCI Committee 319, Precast Structural Concrete Code, and Joint ACI-ASCE Committee 423, Prestressed Concrete. His research interests include adaptable building design and low-cost housing systems for developing communities.*

Michael Carlos Kleiss *is an Associate Professor of Architecture at Clemson University. He received his bachelor's in architecture from Universidad de los Andes, Merida, Venezuela, in 1993; his master of architecture degree from the Pratt Institute, Brooklyn, NY, in 1999; and his PhD in architecture from the Massachusetts Institute of Technology, Cambridge, MA, in 2006. His research interests include the use of computers to aid designers throughout the architectural design process, as well as morphology, biomorphic and bio-mimetic design, parametric design, shape grammars, and origami.*

ACI member **Pinar Okumus** *is an Associate Professor in the Department of Civil, Structural and Environmental Engineering at the University at Buffalo, Buffalo, NY. She received her BS in civil engineering from Middle East Technical University, Ankara, Turkey, in 2006, and her MS and PhD in civil engineering from the University of Wisconsin–Madison, Madison, WI, in 2008 and 2012, respectively. She is a member of ACI Committees 123, Research and Current Developments, and 342, Evaluation of Concrete Bridges and Bridge Elements. Her research interests include infrastructure resiliency and longevity as applied to reinforced and prestressed concrete structures.*

ACI member **Negar Elhami Khorasani** *is an Assistant Professor in the Department of Civil, Structural and Environmental Engineering at the University at Buffalo. She received her BASc and MASc in civil engineering from the University of Toronto, Toronto, ON, Canada, in 2008 and 2010, respectively, and her PhD in civil engineering from Princeton University, Princeton, NJ, in 2015. Her research interests include performance-based design, resilient communities, and risk assessment.*

ACKNOWLEDGMENTS

This research project is being funded through the United States National Science Foundation. The project title is "Collaborative Research: Tessellated Structural-Architectural Systems for Rapid Construction, Repair, and Disassembly" and is conducted under award numbers 1762899 and 1762133. Any opinions, findings, and conclusions or recommendations expressed in this material are those of the authors and do not necessarily reflect the views of the National Science Foundation.

This research was supported by S. Black, S. Dodd, M. Baker, C. Eubanks, and I. Stewart.

Specimen was fabricated by Tindall Corporation. Test frame was fabricated by Clemson Machining and Technical Services. Materials for the project were donated by Tindall Corporation, Prestress of the Carolinas, General Technologies, Inc., JVI, and Dayton Superior.

NOTATION

A_{pi} = area of PT strand i
a = depth of equivalent compression stress block
a' = βc_{llp} (iterated length of confined concrete stress block)
C = resultant compressive force at base of wall
c = initial assumption for contact length between wall and base
c_{llp} = final converged contact length of wall to base
c_{new} = iterated contact length of wall to base
d_i = distance from edge of confined concrete to strand i
E_p = elastic modulus of PT steel
f_c' = compressive strength of concrete
f_{pu} = ultimate strength of PT strand
f_{py} = yield stress of PT strand
f_{p1i} = effective stress in strand at beginning of testing
f_y = yield stress of reinforcing bar
H_{unb} = unbonded height of PT steel
h_{eff} = effective height of wall, calculated as moment arm between line of action along which load is applied and line of action along which base shear resistance is provided
h_w = height of wall
K_i = secant stiffness of wall after cycle set i
l_i = distance from end of contact length to center of strand i
l_w = length of wall
M_{ni} = moment contribution from strand i
T = sum of tensile forces in PT strands at yield strength
T_i = tension force in each strand
$T_{i,i}$ = precompression tensile force in PT strand i at start of testing
t_w = thickness of wall
V_{dec} = base shear when precompression of PT strands is overcome at one edge of wall by overturning moment from applied lateral load
V_{ell} = base shear at effective linear limit
$V_{ell,1}$ = possible base shear at effective linear limit, which accounts for softening due to nonlinear material properties
$V_{ell,2}$ = possible base shear at effective linear limit which accounts for softening due to gap openings
V_{llp} = base shear capacity at first yield of PT
β = calculated based on f_c' using Table 22.2.2.4.3 in ACI 318-19 (2019)
Δ_{y1} = uplift at outermost strand at yield
ε_{pi} = strain in strand i

REFERENCES

Aaleti, S., and Sritharan, S., 2009, "A Simplified Analysis Method for Characterizing Unbonded Post-Tensioned Precast Wall Systems," *Engineering Structures*, V. 31, No. 12, pp. 2966-2975. doi: 10.1016/j.engstruct.2009.07.024

ACI Committee 318, 2019, "Building Code Requirements for Structural Concrete (ACI 318-19) and Commentary (ACI 318R-19) (Reapproved 2022)," American Concrete Institute, Farmington Hills, MI, 625 pp.

ACI ITG-5.1-07, 2008, "Acceptance Criteria for Special Unbonded Post-Tensioned Precast Structural Walls Based on Validation Testing and Commentary," American Concrete Institute, Farmington Hills, MI, 19 pp.

Akpanya, R.; Goertzen, T.; Wiesenhuetter, S.; Niemeyer, A. C.; and Noennig, J. R., 2023, "Topological Interlocking, Truchet Tiles and Self-Assemblies: A Construction-Kit for Civil Engineering Design," *Proceedings of Bridges 2023: Mathematics, Art, Music, Architecture, Culture*, Halifax, NS, Canada, pp. 61-68.

Basereh, S.; Okumus, P.; and Aaleti, S., 2020, "Reinforced-Concrete Shear Walls Retrofitted Using Weakening and Self-Centering: Numerical Modeling," *Journal of Structural Engineering*, ASCE, V. 146, No. 7, p. 04020122. doi: 10.1061/(ASCE)ST.1943-541X.0002669

Crocker, G. F., 2021, "Design, Fabrication and Assembly of a Tessellated Precast Concrete Shear Wall," 2021 PCI National Convention, New Orleans, LA.

Crocker, G. F., 2022, "Tessellated Structural-Architectural Systems: Experimental Testing and Interdisciplinary Student Projects," PhD dissertation, Clemson University, Clemson, SC, https://tigerprints.clemson.edu/all_dissertations/3149. (last accessed July 12, 2024)

Dyskin, A. V.; Estrin, Y.; Kanel-Belov, A. J.; and Pasternak, E., 2001, "A New Concept in Design of Materials and Structures: Assemblies of Interlocked Tetrahedron-Shaped Elements," *Scripta Materialia*, V. 44, No. 12, pp. 2689-2694. doi: 10.1016/S1359-6462(01)00968-X

Dyskin, A. V.; Estrin, Y.; Pasternak, E.; Khor, H. C.; and Kanel-Belov, A. J., 2003, "Fracture Resistant Structures Based on Topological Interlocking with Non-Planar Contacts," *Advanced Engineering Materials*, V. 5, No. 3, pp. 116-119. doi: 10.1002/adem.200390016

Estrin, Y.; Dyskin, A. V.; Pasternak, E.; Schaare, S.; Stanchits, S.; and Kanel-Belov, A. J., 2004, "Negative Stiffness of a Layer with Topologically Interlocked Elements," *Scripta Materialia*, V. 50, No. 2, pp. 291-294. doi: 10.1016/j.scriptamat.2003.09.053

Fan, Z.; Huang, W.; Miao, X.; Hu, G.; and Liu, K., 2023, "A Self-Centering Hybrid Braced Precast Wall with Replaceable U-Shaped Flexural Plates: Experimental and Theoretical Analysis," *Journal of Building Engineering*, V. 70, p. 106424. doi: 10.1016/j.jobe.2023.106424

FEMA 306, 1999, "Evaluation of Earthquake Damaged Concrete and Masonry Wall Buildings: Basic Procedures Manual," Federal Emergency Management Agency, Washington, DC, 270 pp.

FEMA P-58/BD-3.8.8, 2009, "Damage States and Fragility Curves for Low Aspect Ratio Reinforced Concrete Walls," Federal Emergency Management Agency, Washington, DC.

FEMA P-58/BD-3.8.9, 2011, "Fragility Functions for Slender Reinforced Concrete Walls," Federal Emergency Management Agency, Washington, DC.

Fleury, F., 2009, "Evaluation of the Perpendicular Flat Vault Inventor's Intuitions through Large Scale Instrumented Testing," *Proceedings of the Third International Congress on Construction History*, Brandenburg University of Technology, Cottbus, Germany, pp. 611-618.

Glickman, M., 1984, "The G-Block System of Vertically Interlocking Paving," *Second International Conference on Concrete Block Paving*, Delft, the Netherlands, pp. 345-348.

Hines, T., 1995, "Using Dry-Stacked Concrete Masonry for Affordable Construction," *Aberdeen's Magazine of Masonry Construction*, V. 8, No. 2, pp. 76-80.

Javan, A. R.; Seifi, H.; Lin, X.; and Xie, Y. M., 2020, "Mechanical Behaviour of Composite Structures Made of Topologically Interlocking Concrete Bricks with Soft Interfaces," *Materials & Design*, V. 186, p. 108347. doi: 10.1016/j.matdes.2019.108347

Li, X.; Wu, G.; Kurama, Y. C.; and Cui, H., 2020, "Experimental Comparisons of Repairable Precast Concrete Shear Walls with a Monolithic

Cast-in-Place Wall," *Engineering Structures*, V. 216, p. 110671. doi: 10.1016/j.engstruct.2020.110671

Manning, L., 2009, "290 Mulberry St (Image Modified from the Original)," https://flic.kr/p/6UTqAN. (last accessed July 12, 2024)

Molotnikov, A.; Estrin, Y.; Dyskin, A. V.; Pasternak, E.; and Kanel-Belov, A. J., 2007, "Percolation Mechanism of Failure of a Planar Assembly of Interlocked Osteomorphic Elements," *Engineering Fracture Mechanics*, V. 74, No. 8, pp. 1222-1232. doi: 10.1016/j.engfracmech.2006.07.012

Murphy, A. J., 2021, "Comparison of Flexural Cracking in Reinforced Concrete Beams with Different Rebar Coatings," master's thesis, Clemson University, Clemson, SC, https://tigerprints.clemson.edu/all_theses/3535. (last accessed July 12, 2024)

Perez, F. J.; Sause, R.; and Pessiki, S., 2007, "Analytical and Experimental Lateral Load Behavior of Unbonded Posttensioned Precast Concrete Walls," *Journal of Structural Engineering*, ASCE, V. 133, No. 11, pp. 1531-1540. doi: 10.1061/(ASCE)0733-9445(2007)133:11(1531)

Rasband, W., 1997, "ImageJ (Computer Software)," NIH, Bethesda, MD.

Ross, B. E.; Yang, C.; Kleiss, M. C.; Okumus, P.; and Elhami Khorasani, N., 2020, "Tessellated Structural-Architectural Systems: Concept for Efficient Construction, Repair, and Disassembly," *Journal of Architectural Engineering*, ASCE, V. 26, No. 3, p. 04020020. doi: 10.1061/(ASCE)AE.1943-5568.0000418

Schaare, S.; Dyskin, A. V.; Estrin, Y.; Arndt, S.; Pasternak, E.; and Kanel-Belov, A., 2008, "Point Loading of Assemblies of Interlocked Cube-Shaped Elements," *International Journal of Engineering Science*, V. 46, No. 12, pp. 1228-1238. doi: 10.1016/j.ijengsci.2008.06.012

Syed, M.; Moeini, M.; Okumus, P.; Elhami-Khorasani, N.; Ross, B. E.; and Kleiss, M. C. B., 2021, "Analytical Study of Tessellated Structural-Architectural Reinforced Concrete Shear Walls," *Engineering Structures*, V. 244, p. 112768. doi: 10.1016/j.engstruct.2021.112768

Widewalls, 2016, "Tessellation Patterns - From Mathematics to Art," https://www.widewalls.ch/magazine/tessellation-mathematics-method-art. (last accessed July 12, 2024)

Yong, H. T. D., 2011, "Utilisation of Topologically-Interlocking Osteomorphic Blocks for Multi-Purpose Civil Construction," doctoral thesis, The University of Western Australia, Perth, WA, Australia.

ACI STRUCTURAL JOURNAL TECHNICAL PAPER

23-03567

Theoretical Model for Calculating Shear Strength of Fiber-Reinforced Polymer-Reinforced Concrete Beams

by Jahanzaib and Shamim A. Sheikh

This paper investigates the shear behavior of concrete beams longitudinally reinforced with fiber-reinforced polymer (FRP) bars. Beams with and without glass fiber-reinforced polymer (GFRP) stirrups are analyzed in the paper. Results of 93 large-scale FRP-reinforced concrete beam specimens were shortlisted, and the experimentally determined shear strengths were predicted using the available design algorithms in the literature. Modified Compression Field Theory, which can successfully predict the shear strength of steel-reinforced concrete members, was revisited in this study to incorporate the low-modulus and high-strength behavior of FRP bars. The proposed model gives an average predicted-to-experimental strength ratio of 0.96 with a coefficient of variation (COV) of 13% for beams without any transverse reinforcement and an average strength ratio of 1.00 with a COV of 16% for beams reinforced with GFRP stirrups.

Keywords: concrete contribution; fiber-reinforced polymer (FRP) members; FRP stirrups; Modified Compression Field Theory (MCFT); shear strength.

INTRODUCTION

Even though the behavior of fiber-reinforced polymer (FRP)-reinforced concrete (RC) members in shear has been studied for more than three decades, no holistic theoretical model has been proposed to successfully capture the different mechanical behavior of FRP bars. Several empirical models are available in the literature, and these models include different modification parameters, which were developed based on the available experimental test results. Bywalski et al. (2020) compiled 20 different algorithms for determining the concrete shear strength of RC elements longitudinally reinforced with FRP bars. These elements contained no transverse reinforcement. The ratio of predicted to experimental shear strengths using those algorithms was found to vary from 0.46 to 1.12 with a significant coefficient of variation (COV).

This high variability can be attributed to the complex mechanism by which the shear stresses are resisted in RC beams, especially FRP-RC beams. FRP-reinforced members experience higher strains in the longitudinal bars, and the bond behavior of different types of FRP bars (sand-coated, helically wrapped, or ribbed) is different. Most current models are empirically developed and are based on the analogy of perfect bond and longitudinal bars generally stiffer than the FRP bars. Therefore, it is necessary to develop a model that takes into account different variables associated with the responses of FRP-reinforced members.

A database of approximately 93 large-scale FRP-RC beam specimens was generated in this paper. The accuracy of four design algorithms—ACI 440.1R-15 (ACI Committee 440 2015), CSA S806 (2012), CSA S6 (2019), and Bentz et al. (2010)—was evaluated against this database. Equations provided in ACI 440.1R-15 and CSA S806-12 are based on the experimental work. The shear provisions in CSA S6:19 were developed using the Modified Compression Field Theory (MCFT) (Vecchio and Collins 1986) and are similar to the ones for steel-reinforced members in CSA A23.3 (2019). This is the main reason why shear provisions by CSA S6:19 underestimate the shear strength of FRP-RC members (Johnson 2014). Hoult et al. (2008) and Bentz et al. (2010) revised the steel-based shear provisions, which were developed using the MCFT, for FRP-reinforced members. The accuracy of those provisions is also checked in this paper against the assembled database, and further modifications are suggested to make the model more accurate.

RESEARCH SIGNIFICANCE

The research reported in this paper addresses the effects of higher FRP strains on crack spacing and aggregate size modification factors on the shear behavior of concrete beams. Additionally, the effects of different surface conditions of FRP bars have also been considered in the current model to determine shear crack spacing. The proposed model based on the MCFT has resulted in a significant improvement in predicting the shear strength of FRP-RC members compared to the currently available shear provisions developed using the MCFT.

CURRENT SHEAR PROVISIONS

Available provisions evaluated in the current study for the shear design of glass FRP (GFRP)-RC beams are summarized in Table 1. The equations to predict the shear contribution from concrete are developed based on either theoretical or empirical approaches. Shear forces in a beam without any transverse reinforcement are resisted through a combination of different mechanisms, including: 1) resistance from uncracked concrete in the compression zone; 2) shear carried along cracks through aggregate interlock; and 3) dowel action in the longitudinal reinforcement.

ACI 440.1R-15 considers uncracked concrete in compression as the primary source of shear resistance and ignores the contribution of aggregate interlock. The omission of shear

ACI Structural Journal, V. 121, No. 5, September 2024.
MS No. S-2023-035.R2, doi: 10.14359/51740851, received March 21, 2024, and reviewed under Institute publication policies. Copyright © 2024, American Concrete Institute. All rights reserved, including the making of copies unless permission is obtained from the copyright proprietors. Pertinent discussion including author's closure, if any, will be published ten months from this journal's date if the discussion is received within four months of the paper's print publication.

Table 1—Provisions to predict shear capacity of GFRP-RC members

Description	Equations
ACI 440.1R-15 code provisions	
Shear strength by concrete	$V_c = \frac{2}{5}\sqrt{f_c'}\, b_w k d$ $k = \sqrt{(2\rho_f n_f + (\rho_f n_f)^2} - \rho_f n_f$ $\rho_f = A_f/bd$ $n_f = E_f/E_c$
Shear strength by FRP stirrups	$V_s = \frac{A_{fv} f_{fv} d}{s}$
Limit on FRP stirrup strain	$f_{fv} = 0.004E_f \le f_{fb}$ $f_{fb} = \left(0.05\frac{r_b}{d_b} + 0.3\right) f_{fu} \le f_{fu}$
CSA S806-12 code provisions	
Shear strength by concrete	$V_c = 0.05\lambda k_m k_r k_a k_s (f_c')^{1/3} b_w d_v$ $k_m = \sqrt{\left(\frac{V_f d}{M_f}\right)} \le 1.0$ $k_a = \frac{2.5Vd}{M}$; $1.0 \le k_a \le 2.5$ $k_r = 1 + (E_f\rho_f)^{1/3}$ $k_s = \frac{750}{450 + d} \le 1.0$ for members with $d > 300$ mm
Shear strength by FRP stirrups	$V_s = \frac{0.4A_{fv} f_{fv} d_v}{s}\cot(\theta)$ $\theta = 30° + 7000\epsilon_x \le 60°$ $\epsilon_x = \frac{\left(\frac{M_f}{d_v}\right) + V_f}{2E_f A_f}$
Limit on FRP stirrup strain	$f_v = 0.005E_f$
CSA S6:19 Code provisions	
Shear strength by concrete	$V_c = 2.5 f_{cr} \beta b_w d_v$ $\beta = \left(\frac{0.4}{1 + 1500\epsilon_x}\right)\left(\frac{1300}{1000 + s_{xe}}\right)$ $\epsilon_x = \frac{\left(\frac{M_f}{d_v}\right) + V_f}{2E_f A_f} \le 0.003$
Shear strength by FRP stirrups	$V_s = \frac{A_{fv} f_{fv} d_v}{s}\cot(\theta)$ $\theta = (29°+7000\epsilon_x)\left(0.88 + \frac{s_{xe}}{2500}\right)$
Limit on FRP stirrup strain	f_{fv} = lesser of $0.004E_f$ or $\frac{\left(0.05\frac{r_b}{d_b} + 0.3\right) f_{fu}}{1.5}$
Bentz et al. (2010) shear provisions	
Shear strength by concrete	$V_c = \beta\sqrt{f_c'}\, b_w d_v$ $\beta = \left(\frac{0.30}{0.5 + (1000\epsilon_x + 0.15)^{0.7}}\right)\left(\frac{1300}{1000 + s_{xe}}\right)$ $\epsilon_x = \frac{\left(\frac{M_f}{d_v}\right) + V_f}{2E_f A_f}$ and $s_{xe} = \frac{31.5d}{16 + a_g}$
Shear strength by FRP stirrups	$V_s = \frac{A_{fv} f_{fv} d_v}{s}\cot(\theta)$ $\theta = (29°+7000\epsilon_x)\left(0.88 + \frac{s_{xe}}{2500}\right)$
Limit on FRP stirrup strain	f_{fv} = less of f_{fu} or $\frac{\left(0.05\frac{r_b}{d_b} + 0.3\right) f_{fu}}{1.5}$

carried along the cracks through aggregate interlock results in conservative estimates. Moreover, FRP bars result in higher strains due to a low modulus of elasticity, which may result in wider cracks and lower shear strength. This effect, known as the strain effect, is accounted for in the ACI procedure with the help of an additional factor, k, in the equation, as shown in Table 1.

CSA S806-12 code provisions for the concrete contribution to shear resistance are based on the work by Razaqpur and Isgor (2006). A variety of independent modification factors are employed in the equation to account for the strain and size effect in shear. The factor k_m accounts for the moment-to-shear ratio, k_r for the reinforcement ratio, and k_s for the size effect, and an additional factor, k_a, accounts for the positive influence of arching action in deep members with a shear span-depth ratio of less than 2.5.

The CSA S6:19 equations were developed based on the MCFT, which considers both longitudinal strain and size effects. Aggregate interlock capacity is determined with an estimate of the crack width. As the cracks grow wider, the aggregate interlock resistance decreases and consequently reduces the shear capacity. Hence, any factors that increase the crack widths are expected to decrease the shear capacity. The equation to estimate the shear contribution from concrete in the code is developed on the simple estimate of crack width using Eq. (1)

$$w = \varepsilon \times s \tag{1}$$

where w is the crack width; ε is the average strain perpendicular to the crack; and s is the crack spacing perpendicular to the crack. Crack spacing can be taken as directly proportional to the effective depth of the beam, and this is how the size effect is considered. Higher strains, especially in the case of FRP reinforcement, would result in wider cracks and, hence, lower shear strength.

It is important to note that the accuracy of predictions from these equations mainly depends on the β-factor, which is the function of middepth strain and crack spacing. CSA S6:19 defines this parameter in the same manner as recommended in CSA A23.3:19 for steel-reinforced members. The current equation to determine the β parameter in CSA S6:19 is listed in Eq. (2)

$$\beta = \left(\frac{0.4}{1 + 1500\epsilon_x}\right)\left(\frac{1300}{1000 + s_{xe}}\right) \tag{2}$$

Because CSA S6:19 shear provisions for FRP-RC members are directly taken from CSA A23.3:19 without any changes for FRP reinforcement, the CSA S6:19 provisions tend to underestimate the shear capacity of FRP-RC members.

To predict the shear strength of members with a lower elastic modulus and hence higher longitudinal strains at shear failure, as can occur with FRP reinforcement, Bentz et al. (2010) used the nonlinear expression (Eq. (3)) derived by Hoult et al. (2008) for the determination of the β-factor, as given in Eq (3). This equation was found to be more accurate than Eq. (2)

$$\beta = \left(\frac{0.30}{0.5 + (1000\epsilon_x + 0.15)^{0.7}}\right)\left(\frac{1300}{1000 + s_{xe}}\right) \tag{3}$$

Table 2—Geometric and material properties of beams

Paper	No.	Name	b_w, mm	h, mm	d, mm	L, mm	s, mm	a, mm	A_L, mm^2	A_R, mm^2	f_c', MPa	ρ_L, %	ρ_T, %	$f_{fu}(E)$, MPa (GPa)	$f_{fv}(E)$, MPa(GPa)	f_{fb}, MPa
C1	C2	C3	C4	C5	C5	C6	C7	C8	C9	C10	C11	C12	C13	C14	C15	C16
Gross et al. (2003)*	1	FRP-1-26-NS	229	286	226	2286	—	915	568	—	36.3	1.11	—	690 (40.3)	—	—
	2	FRP-2-26-NS	178	286	226	2286	—	915	568	—	36.3	1.42	—	690 (40.3)	—	—
	3	FRP-3-26-NS	229	286	226	2286	—	915	858	—	36.3	1.66	—	690 (40.3)	—	—
	4	FRP-4-26-NS	276	286	226	2286	—	915	1142	—	36.3	1.81	—	690 (40.3)	—	—
	5	FRP-5-26-NS	254	286	224	2286	—	915	1161	—	36.3	2.05	—	690 (40.3)	—	—
	6	FRP-6-26-NS	229	286	224	2286	—	915	1161	—	36.3	2.27	—	690 (40.3)	—	—
	7	FRP-1-26-HS	203	286	226	2286	—	915	568	—	46.1	1.25	—	690 (40.3)	—	—
	8	FRP-2-26-HS	152	286	226	2286	—	915	568	—	46.1	1.66	—	690 (40.3)	—	—
	9	FRP-3-26-HS	165	286	224	2286	—	915	774	—	46.1	2.10	—	690 (40.3)	—	—
	10	FRP-4-26-HS	203	286	224	2286	—	915	1161	—	46.1	2.56	—	690 (40.3)	—	—
Ashour (2006)	1	Beam 1	150	200	167	2000	—	667	113	—	34	0.45	—	650 (38)	—	—
	2	Beam 3	150	250	212	2000	—	667	226	—	34	0.71	—	705 (32)	—	—
	3	Beam 5	150	300	263	2000	—	667	339	—	34	0.86	—	705 (32)	—	—
	4	Beam 7	150	200	167	2000	—	667	339	—	59	1.39	—	705 (32)	—	—
	5	Beam 9	150	250	212	2000	—	667	339	—	59	1.06	—	705 (32)	—	—
	6	Beam 11	150	300	263	2000	—	667	452	—	59	1.15	—	705 (32)	—	—
El-Sayed et al. (2006a)	1	CN-1	250	400	326	3250	—	1000	710	—	50	0.87	—	1536 (128)	—	—
	2	GN-1	250	400	326	3250	—	1000	710	—	50	0.87	—	608 (39)	—	—
	3	CN-2	250	400	326	3250	—	1000	1010	—	44.6	1.24	—	986 (134)	—	—
	4	GN-2	250	400	326	3250	—	1000	995	—	44.6	1.22	—	754 (42)	—	—
	5	CN-3	250	400	326	3250	—	1000	1400	—	43.6	1.72	—	986 (134)	—	—
	6	GN-3	250	400	326	3250	—	1000	1395	—	43.6	1.71	—	754 (42)	—	—
El-Sayed et al. (2006b)	1	CN-1.7	250	400	326	3250	—	1000	1400	—	43.6	1.72	—	986 (134)	—	—
	2	GN-1.7	250	400	326	3250	—	1000	1395	—	43.6	1.71	—	754 (42)	—	—
	3	CH-1.7	250	400	326	3250	—	1000	1395	—	63	1.71	—	769 (135)	—	—
	4	GH-1.7	250	400	326	3250	—	1000	1395	—	63	1.71	—	754 (42)	—	—
	5	CH-2.2	250	400	326	3250	—	1000	1795	—	63	2.20	—	769 (135)	—	—
	6	GN-2.2	250	400	326	3250	—	1000	1795	—	63	2.20	—	754 (42)	—	—
Bentz et al. (2010)	1	L05-0	450	1000	937	8000	—	3050	2152	—	46	0.51	—	397 (37)	—	—
	2	M05-0	450	500	438	4000	—	1525	1076	—	35	0.55	—	397 (37)	—	—
	3	S05-0	450	250	194	2000	—	762	580	—	35	0.66	—	474 (37)	—	—
	4	L05-1	450	1000	937	8000	400	3050	2152	169	46	0.51	0.10	397 (37)	760 (40.8)	441
	5	L05-2	450	1000	937	8000	200	3050	2152	169	49	0.51	0.20	397 (37)	760 (40.8)	441
	6	L20-0	450	1000	857	8000	—	3050	8608	—	36	2.23	—	397 (37)	—	—
	7	M20-0	450	500	405	4000	—	1525	4304	—	35	2.36	—	397 (37)	—	—
	8	S20-0	450	250	188	2000	—	762	2151	—	35	2.54	—	397 (37)	—	—
	9	L20-1	450	1000	857	8000	400	3050	8608	169	36	2.23	0.10	397 (37)	760 (40.8)	760
	10	M20-1	450	500	405	4000	400	1525	4304	169	35	2.36	0.10	397 (37)	760 (40.8)	441
	11	L20-2	450	1000	857	8000	200	3050	8608	169	42	2.23	0.20	397 (37)	760 (40.8)	760

DATABASE OF FRP-RC BEAM SPECIMENS

To evaluate the accuracy and reliability of the aforementioned design procedures, 93 beam tests from 10 different studies were investigated in this study. Detailed information about the geometrical and material properties of these shortlisted specimens is presented in Table 2. Likewise, the main test results from these specimens are listed in Table 3. It should be noted that in conducting the comprehensive investigation of the shear behavior of these 93 specimens, various aspects of the specimens were evaluated, which is

Table 2 (cont.)—Geometric and material properties of beams

Johnson and Sheikh (2016)	1	JSC32-NT	400	650	575	3640	—	1680	2400	—	32	1	—	1265 (61.2)	1003 (57.5)	531
	2	JSV40-NT	400	650	575	3640	—	1680	2364	—	40	1	—	1264 (71.2)	655 (41.5)	507
	3	JSC32-22B	400	650	575	3640	250	1680	2400	224	32	1	0.22	1265 (61.2)	1003 (57.5)	531
	4	JSC32-40B	400	650	575	3640	150	1680	2400	224	32	1	0.40	1265 (61.2)	1003 (57.5)	531
	5	JSC32-50B	400	650	575	3640	112	1680	2400	224	32	1	0.50	1265 (61.2)	1003 (57.5)	531
	6	JSV40-22B	400	650	575	3640	250	1680	2364	254	40	1	0.22	1264 (71.2)	655 (41.5)	507
	7	JSV40-40B	400	650	575	3640	150	1680	2364	254	40	1	0.40	1264 (71.2)	655 (41.5)	507
	8	JSV40-50B	400	650	575	3640	112	1680	2364	254	40	1	0.50	1264 (71.2)	655 (41.5)	507
Khodaie (2018)	1	S6-0.12-2A	229	178	146	2434	—	457	201	—	32.1	0.6	—	849 (43.2)	—	—
	2	S6-0.12-3A	229	178	146	2434	—	457	201	—	32.1	0.6	—	849 (43.2)	—	—
	3	S3-0.12-1A	114	330	292	3348	—	914	201	—	32.1	0.6	—	849 (43.2)	—	—
	4	S3-0.12-2A	114	330	292	3348	—	914	201	—	32.1	0.6	—	849 (43.2)	—	—
	5	S1-0.12-1A	457	978	883	9143	—	2743	2412	—	29.5	0.6	—	476 (41.0)	—	—
	6	S1-0.12-2B	457	978	883	9143	—	2743	2412	—	29.6	0.6	—	483 (41.0)	—	—
Kotynia et al. (2018)	1	G-5ϕ12	150	400	379	2200	—	900	565	—	30.2	0.99	—	1091 (51.5)	—	—
	2	G-3ϕ16	150	400	377	2200	—	900	603	—	28.8	1.07	—	1091 (51.5)	—	—
	3	G-3ϕ18	150	400	376	2200	—	900	763	—	28.8	1.35	—	1091 (51.5)	—	—
	4	G-4ϕ16	150	400	377	2200	—	900	804	—	30.5	1.42	—	1091 (51.5)	—	—
	5	G-4ϕ18	150	400	376	2200	—	900	1018	—	28.8	1.80	—	1091 (51.5)	—	—
	6	G-3ϕ12/2ϕ12	150	400	368	2200	—	900	565	—	31.7	1.02	—	1091 (51.5)	—	—
	7	G-3ϕ18/2ϕ18	150	400	367	2200	—	900	1018	—	31.7	1.85	—	1091 (51.5)	—	—
Al-Hamrani et al. (2021)	1	B-ρ_1-2.5-250	200	300	235	2550	250	590	684	158	44.5	1.45	0.32	1177 (49.5)	1000 (50.0)	700
	2	B-ρ_1-2.5-350	200	300	235	2550	350	590	684	158	44.5	1.45	0.23	1177 (49.5)	1000 (50.0)	700
	3	B-ρ_1-3.5-350	200	300	235	2550	350	825	684	158	44.5	1.45	0.23	1177 (49.5)	1000 (50.0)	700
	4	B-ρ_1-3.5-250	200	300	235	2550	250	825	684	158	44.5	1.45	0.32	1177 (49.5)	1000 (50.0)	700
	5	B-ρ_2-3.5-250	200	300	232	2550	250	825	1005	158	44.5	2.17	0.32	1110 (46.5)	1000 (50.0)	700
	6	B-ρ_2-2.5-250	200	300	232	2550	250	590	1005	158	44.5	2.17	0.32	1110 (46.5)	1000 (50.0)	700
	7	B-ρ_2-2.5-350	200	200	232	2550	350	590	1005	158	44.5	2.17	0.23	1110 (46.5)	1000 (50.0)	700
	8	B-ρ_2-3.5-350	200	300	232	2550	350	825	1005	158	44.5	2.17	0.23	1110 (46.5)	1000 (50.0)	700
	9	NS-ρ_2-3.5	200	300	232	2550	—	825	1005	—	44.5	2.17	—	1110 (46.5)	—	—
	10	NS-ρ_2-2.5	200	300	232	2550	—	590	1005	—	44.5	2.17	—	1110 (46.5)	—	—
	11	NS-ρ_1-2.5	200	300	235	2550	—	590	684	—	44.5	1.45	—	1177 (49.5)	—	—
Current study	1	DBM9-41C	320	740	670	3000	300	1350	1684	404	47	0.78	0.41	1337 (56.7)	1153 (53.1)	723
	2	DBM10-41C	320	740	670	3000	300	1350	1684	404	47	0.78	0.41	1337 (56.7)	1153 (53.1)	723

*Each group in Gross et al. (2003) comprises three identical specimens; there are 30 specimens in total.

why Tables 2 and 3 include extensive information needed to successfully use the available design methods.

The specimens' names listed in column C3 of Table 2 refer to the original studies and were kept the same for cross-reference. In this database, the specimens' depths varied from 200 to 1000 mm. This range of depths will allow the accuracy of models to be checked to capture the size effect. Similarly, the ratio of longitudinal reinforcement covered a wide range, from 0.45 to 2.56%.

Predictions of current models

Of the 93 specimens assembled in the database, 72 contained no transverse reinforcement, and 21 were transversely reinforced with GFRP stirrups. The specimens without GFRP stirrups were used to evaluate the accuracy of the predicted concrete contribution in shear using the models. All the models listed in Table 1 were used to calculate the shear strength, denoted as V_r. These predicted strengths were compared against the experimentally determined shear values. It should be noted that all the experimental shear strengths listed in Table 3 include the self-weight of the beams. The predicted-to-experimental shear strength ratios for the specimens without and with transverse reinforcement are plotted in Fig. 1 and 2, respectively. To determine the stirrups' contribution to shear resistance, the bend strengths of FRP stirrups listed in column 16 (C16) of Table 2 were used, and no strain limits were specified.

Table 3—Selected test results of beams

Paper	No.	Name	*d*, mm	*a*/*d*	Failure mode	Longitudinal bar type	Failure load, kN	Shear, kN	Crack angle
Gross et al. (2003)	1	FRP-1a-26-NS	226	4.0	Shear	GFRP (sand-coated)	78.20	40.94	—
	2	FRP-1b-26-NS					77.57	40.63	—
	3	FRP-1c-26-NS					76.26	39.97	—
	4	FRP-2a-26-NS	226	4.0	Shear	GFRP (sand-coated)	68.94	35.90	—
	5	FRP-2b-26-NS					66.65	34.75	—
	6	FRP-2c-26-NS					63.49	33.17	—
	7	FRP-3a-26-NS	226	4.0	Shear	GFRP (sand-coated)	71.42	37.55	—
	8	FRP-3b-26-NS					80.49	42.09	—
	9	FRP-3c-26-NS					88.93	46.31	—
	10	FRP-4a-26-NS	226	4.0	Shear	GFRP (sand-coated)	91.48	47.95	—
	11	FRP-4b-26-NS					89.69	47.06	—
	12	FRP-4c-26-NS					90.59	47.51	—
	13	FRP-5a-26-NS	224	4.0	Shear	GFRP (sand-coated)	86.51	45.30	—
	14	FRP-5b-26-NS					89.92	47.00	—
	15	FRP-5c-26-NS					90.29	47.20	—
	16	FRP-6a-26-NS	224	4.0	Shear	GFRP (sand-coated)	94.18	48.93	—
	17	FRP-6b-26-NS					87.98	45.83	—
	18	FRP-6c-26-NS					84.42	44.10	—
	19	FRP-1a-26-HS	226	4.0	Shear	GFRP (sand-coated)	83.12	43.20	—
	20	FRP-1b-26-HS					75.51	39.39	—
	21	FRP-1c-26-HS					76.00	39.63	—
	22	FRP-2a-26-HS	226	4.0	Shear	GFRP (sand-coated)	68.93	35.68	—
	23	FRP-2b-26-HS					70.72	36.58	—
	24	FRP-2c-26-HS					65.01	33.72	—
	25	FRP-3a-26-HS	224	4.0	Shear	GFRP (sand-coated)	69.97	36.30	—
	26	FRP-3b-26-HS					69.37	36.00	—
	27	FRP-3c-26-HS					71.48	37.06	—
	28	FRP-4a-26-HS	224	4.0	Shear	GFRP (sand-coated)	78.05	40.65	—
	29	FRP-4b-26-HS					87.10	45.17	—
	30	FRP-4c-26-HS					92.80	48.02	—
Ashour (2006)	1	Beam 1	167	4.0	Shear	GFRP (sand-coated)	25	13.2	—
	2	Beam 3	212	3.1	Shear	GFRP (sand-coated)	35	18.4	—
	3	Beam 5	263	2.5	Shear	GFRP (sand-coated)	50	26.1	—
	4	Beam 7	167	4.0	Shear	GFRP (sand-coated)	35	18.2	—
	5	Beam 9	212	3.1	Shear	GFRP (sand-coated)	55	28.4	—
	6	Beam 11	263	2.5	Shear	GFRP (sand-coated)	60	31.1	—
El-Sayed et al. (2006a)	1	CN-1	326	3.1	Shear	CFRP (sand-coated)	155	81.5	—
	2	GN-1	326	3.1	Shear	GFRP (sand-coated)	141	74.5	—
	3	CN-2	326	3.1	Shear	CFRP (sand-coated)	208	108	—
	4	GN-2	326	3.1	Shear	GFRP (sand-coated)	120	64	—
	5	CN-3	326	3.1	Shear	CFRP (sand-coated)	249	128.5	—
	6	GN-3	326	3.1	Shear	GFRP (sand-coated)	155	81.5	—

As shown in Fig. 1, the strength ratios for beam specimens without transverse reinforcement were found to be 0.57, 1.02, 0.72, and 0.86, with a COV of 20%, 23%, 17%, and 15%, using the ACI 440.1R-15, CSA S806-12, CSA S6:19, and Bentz et al. (2010) models, respectively. Likewise, the strength ratios, plotted in Fig. 2, for beam specimens with

Table 3 (cont.)—Selected test results of beams

El-Sayed et al. (2006b)	1	CN-1.7	326	3.1	Shear	CFRP (sand-coated)	249	128.5	—
	2	GN-1.7	326	3.1	Shear	GFRP (sand-coated)	155	81.5	—
	3	CH-1.7	326	3.1	Shear	CFRP (sand-coated)	260	134	—
	4	GH-1.7	326	3.1	Shear	GFRP (sand-coated)	174	91	—
	5	CH-2.2	326	3.1	Shear	CFRP (sand-coated)	174	178	—
	6	GN-2.2	326	3.1	Shear	GFRP (sand-coated)	115.5	119.5	—
Bentz et al. (2010)	1	L05-0	937	3.25	Shear	GFRP (sand-coated)	239	135	—
	2	M05-0	438	3.48	Shear	GFRP (sand-coated)	167	86	—
	3	S05-0	194	3.93	Shear	GFRP (sand-coated)	108	54.5	—
	4	L05-1	937	3.25	Shear	GFRP (sand-coated)	388	237	—
	5	L05-2	937	3.25	Flexural rupture	GFRP (sand-coated)	461	246	—
	6	L20-0	857	3.56	Shear	GFRP (sand-coated)	435	232	—
	7	M20-0	405	3.77	Shear	GFRP (sand-coated)	272	138	—
	8	S20-0	188	4.05	Shear	GFRP (sand-coated)	147	74	—
	9	L20-1	857	3.56	Shear	GFRP (sand-coated)	850	500	—
	10	M20-1	405	3.77	Shear	GFRP (sand-coated)	303	154	—
	11	L20-2	857	3.56	Flexural Crushing	GFRP (sand-coated)	1350	690	—
Johnson and Sheikh (2016)	1	JSC32-NT	575	2.92	Shear	GFRP (ribbed)	308	164.7	45
	2	JSV40-NT	575	2.92	Shear	GFRP (sand-coated)	327	174.2	41
	3	JSC32-22B	575	2.92	Shear	GFRP (ribbed)	774	397.7	44
	4	JSC32-40B	575	2.92	Flexure-shear	GFRP (ribbed)	901	461.2	49
	5	JSC32-50B	575	2.92	Flexure-shear	GFRP (ribbed)	1095	558.2	56
	6	JSV40-22B	575	2.92	Shear	GFRP (sand-coated)	749	385.2	51
	7	JSV40-40B	575	2.92	Shear	GFRP (sand-coated)	895	458.2	49
	8	JSV40-50B	575	2.92	Flexure-shear	GFRP (sand-coated)	1067	544.2	52
Khodaie (2018)	1	S6-0.12-2A	146	3.1	Shear	GFRP (sand-coated)	—	36.9	—
	2	S6-0.12-3A	146	3.1	Shear	GFRP (sand-coated)	—	26.3	—
	3	S3-0.12-1A	292	3.1	Shear	GFRP (sand-coated)	—	19.2	—
	4	S3-0.12-2A	292	3.1	Shear	GFRP (sand-coated)	—	17.9	—
	5	S1-0.12-1A	883	3.1	Shear	GFRP (sand-coated)	—	154	—
	6	S1-0.12-2B	883	3.1	Shear	GFRP (sand-coated)	—	151	—
Kotynia et al. (2018)	1	G-5ϕ12	379	2.39	Shear	GFRP (ribbed)	—	34.3	40
	2	G-3ϕ16	377	2.39	Shear	GFRP (ribbed)	—	31.7	35
	3	G-3ϕ18	376	2.39	Shear	GFRP (ribbed)	—	38.6	46
	4	G-4ϕ16	377	2.39	Shear	GFRP (ribbed)	—	34.8	41
	5	G-4ϕ18	376	2.39	Shear	GFRP (ribbed)	—	38.2	51
	6	G-3ϕ12/2ϕ12	368	2.44	Shear	GFRP (ribbed)	—	34.8	47
	7	G-3ϕ18/2ϕ18	367	2.39	Shear	GFRP (ribbed)	—	47.7	41

transverse reinforcement were found to be 1.34, 0.87, 1.10, and 0.93, with a COV of 22%, 23%, 26%, and 17%, respectively, for these four models.

This shows that the ACI procedure is conservative in predicting concrete contribution to shear resistance. This can be attributed to the omission of shear carried along the crack through aggregate interlock. Moreover, the ACI equation ignores the size effect of the beams, which is why higher COV were observed. The GFRP stirrups' contribution to shear resistance in ACI 440.1R-15 is based on a 45-degree truss model, which makes the ACI prediction unconservative. As shown in Fig. 2, the average predicted-to-experimental ratio was 1.34. The trend demonstrates that the 45-degree truss model, in combination with static estimates of the concrete contribution, is responsible for the high strength estimates.

In summary, ACI provisions in calculating the concrete contribution to overall shear resistance neglect the size effect, aggregate interlock, and aggregate cleaving. Therefore,

Table 3 (cont.)—Selected test results of beams

Al-Hamrani et al. (2021)	1	B-ρ_1-2.5-250	235	2.5	Shear	BFRP (sand-coated)	—	119.7	45
	2	B-ρ_1-2.5-350	235	2.5	Shear	BFRP (sand-coated)	—	70.8	48
	3	B-ρ_1-3.5-350	235	3.5	Shear	BFRP (sand-coated)	—	57.7	44
	4	B-ρ_1-3.5-250	235	3.5	Shear	BFRP (sand-coated)	—	89.9	40
	5	B-ρ_2-3.5-250	232	3.5	Flexure-shear	BFRP (sand-coated)	—	92.7	38
	6	B-ρ_2-2.5-250	232	2.5	Shear	BFRP (sand-coated)	—	123.8	35
	7	B-ρ_2-2.5-350	232	2.5	Shear	BFRP (sand-coated)	—	87.5	43
	8	B-ρ_2-3.5-350	232	3.5	Shear	BFRP (sand-coated)	—	65.8	45
	9	NS-ρ_2-3.5	232	3.5	Shear	BFRP (sand-coated)	—	54.7	40
	10	NS-ρ_2-2.5	232	2.5	Shear	BFRP (sand-coated)	—	88.4	48
	11	NS-ρ_1-2.5	235	2.5	Shear	BFRP (sand-coated)	—	61	45
Current study	1	DBM9-41C	670	2.01	Shear	GFRP (sand-coated)	958.7	487.7	54
	2	DBM10-41C	670	2.01	Shear	BFRP (sand-coated)	936.2	476.0	51

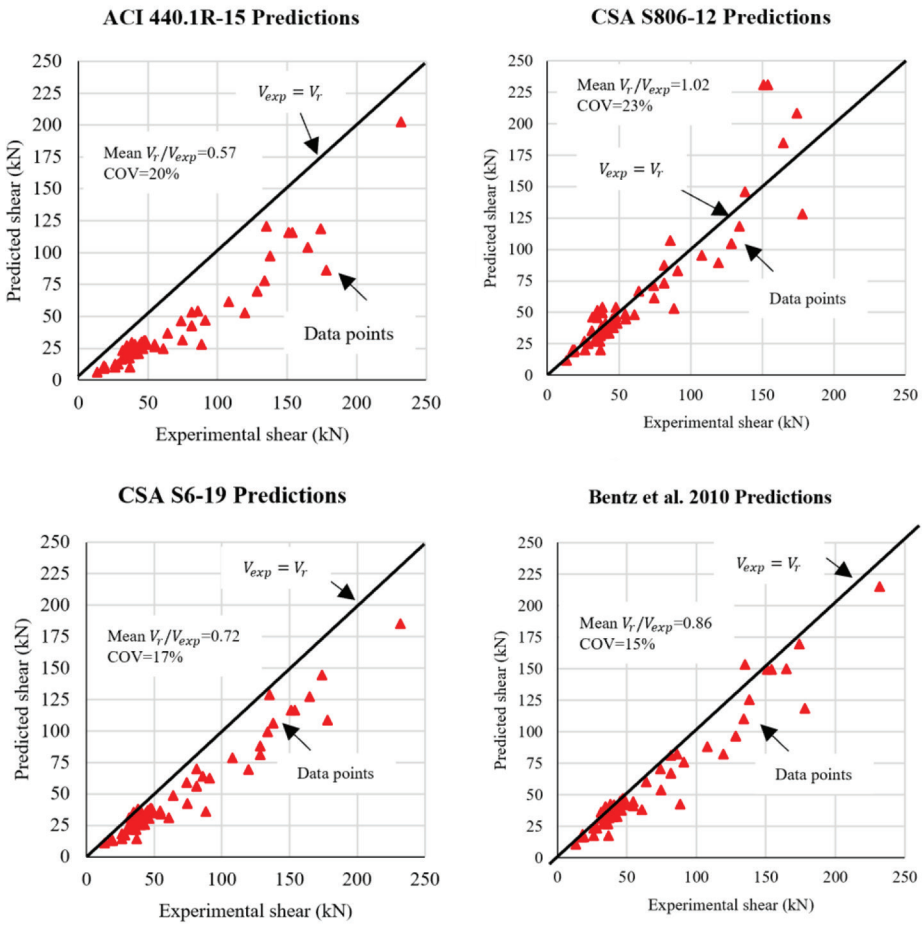


Fig. 1—Predicted-to-experimental shear strength values for GFRP-RC beam specimens without transverse reinforcement. (Note: 1 kN = 0.2248 kip.)

for members without shear reinforcement, estimates of strength are conservative. The contribution of transverse reinforcement assuming the 45-degree truss model results in an unconservative estimate because the beams with GFRP longitudinal reinforcement experience higher rotation of diagonal struts and provide steeper crack angles.

On average, CSA S806-12 predictions to estimate the concrete contribution to shear resistance were reasonably accurate, with a strength ratio of 1.02 but a high COV of 23%. This higher variation in predictions makes the model less reliable. In some specimens, the predicted-to-experimental strength ratios were higher than 1.5. The strength ratio for beam specimens with transverse stirrups using this method was 0.87, with a COV of 23.3%. In general, the method underestimated the shear resistance that can be attributed to the 0.4 factor in the numerator of the V_s equation.

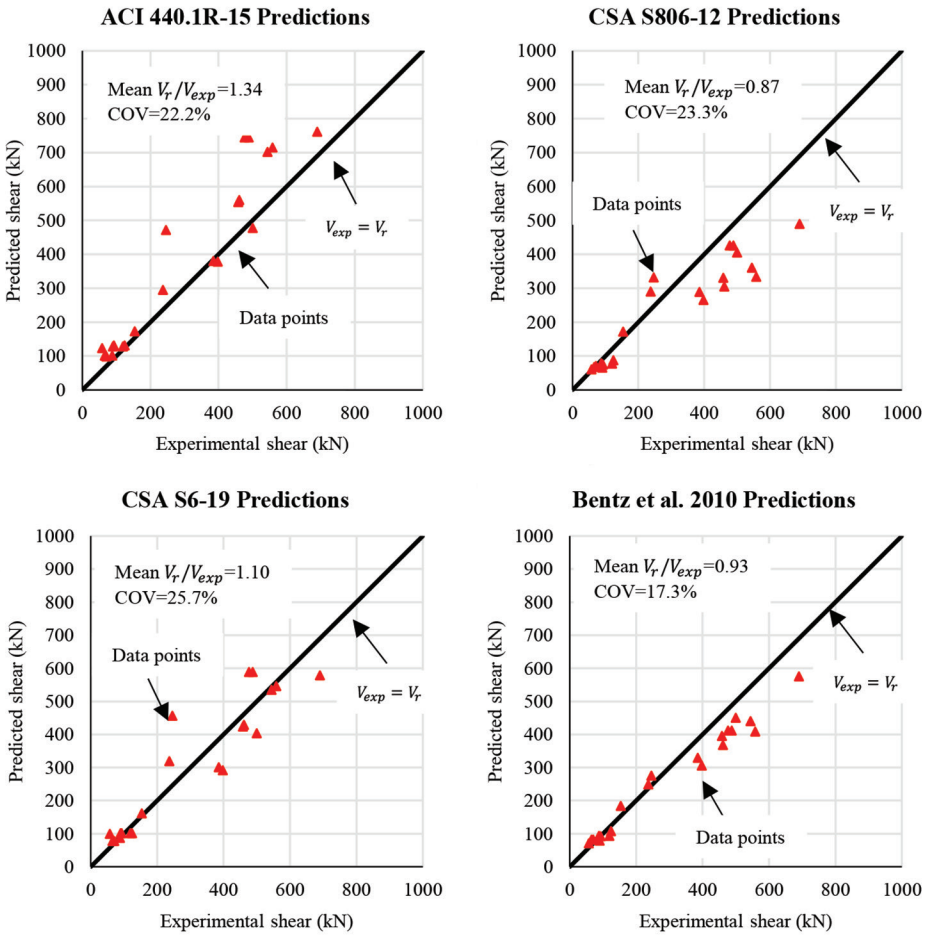


Fig. 2—Predicted-to-experimental shear strength values for GFRP-RC beam specimens with transverse reinforcement. (Note: 1 kN = 0.2248 kip.)

The CSA S6:19 method for concrete contribution underestimated the shear resistance, with a strength ratio of 0.72, as shown in Fig. 1. This is because the equations for concrete contribution were developed using the MCFT, which was originally developed for steel-reinforced members. The V_c in CSA S6:19 is thus suitable for lower values of middepth strains, which happen in steel-reinforced members. However, in the case of GFRP members, middepth strains can be significantly higher than those in steel-reinforced members, and the linear relation for the β-factor ([0.4/1] + 1500ε_x) would overestimate the crack widths at higher strains, resulting in lower shear strength predictions. On the other hand, a strain limit of 0.003 at the middepth location limits the angle of principal compression to 50 degrees, which in actual beam tests with GFRP reinforcement has been observed to be higher. Due to this upper limit on the angle of principal compression, the predicted strength for stirrups' contribution was found to be unsafe, with a strength ratio of 1.10.

Finally, the Bentz et al. (2010) model yielded the most accurate predictions among these four models. To incorporate the behavior of GFRP-RC members, Bentz et al. (2010) made two main changes to MCFT-based shear provisions. First, the relation for the β-factor was revised, and a nonlinear relation was proposed to accurately estimate the crack width at higher strain values; second, the strain limit of 0.003 was removed from the equations. As highlighted earlier, the average strength ratios using the Bentz et al. (2010) model were 0.86 and 0.93 for beam specimens without and with FRP transverse reinforcement, respectively. The COV was approximately 15.4% and 17%, respectively, the least among the companion models. However, the ratio of predicted-to-experimental shear capacity varied from a maximum of 1.17 to a minimum of 0.47, leaving room for further improvements. The approach to address the β-factor and remove the strain limit of 0.003 appears to be rational, considering the extensive data and the observations made during the tests. An effort is, however, needed to bring the mean strength ratio closer to 1.0 and reduce the COV as much as possible. Based on these points, the MCFT formulation is revisited in this study, and a few changes are proposed to fill the gaps identified.

Development and areas of improvement for FRP reinforcement

Vecchio and Collins (1986) developed the MCFT to predict the shear behavior of cracked steel-RC elements. Using the test results of concrete panels in pure shear and published aggregate interlock tests (Walraven 1981), an iterative procedure was developed to predict the shear behavior

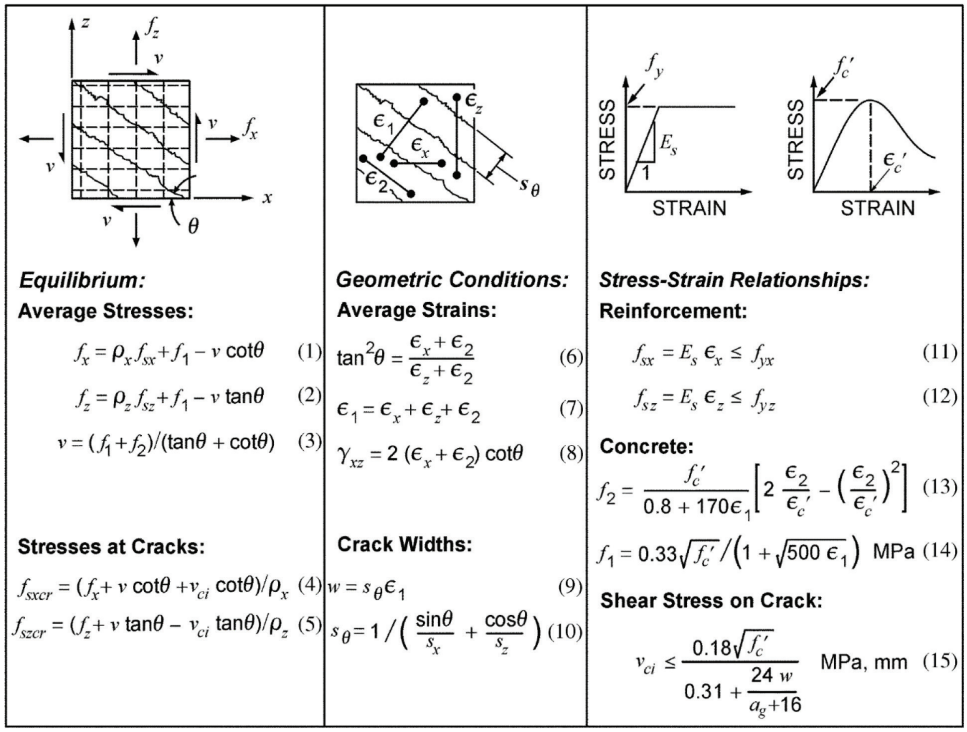


Fig. 3—Equations of MCFT (Vecchio and Collins 1986).

of steel-RC elements. The basic model used the 15 equations listed in Fig. 3. These equations can be solved simultaneously to predict the shear behavior.

To use the MCFT for the design codes, a simplified approach was developed to calculate the shear strength of steel-RC elements. The basic equation presented by Bentz et al. (2006) to estimate the concrete contribution toward shear resistance is as follows

$$V_c = \underbrace{\left(\frac{0.4}{1+1500\varepsilon_x}\right)}_{\beta'}\underbrace{\left(\frac{1300}{1000+s_{xe}}\right)}_{C_s'} b_w d_v \sqrt{f_c'} \qquad (4)$$

and the effective crack spacing parameter, s_{xe}, can be found using the following relation

$$\underbrace{s_{xe} = \frac{31.5d}{16 + a_g}}_{C_a'} \qquad (5)$$

The formulation of the previous V_c equation included the completion of the following three steps:

Step 1—The 15 equations of the MCFT were solved first to obtain the β′ factor shown in Eq. (4). The procedure to solve these equations is revisited in this study and is summarized in the flowchart shown in Fig. 4.

The β′ factor was obtained by estimating the crack width and then substituting the crack width relation in Eq. (15) of the MCFT, shown in Fig. 3. To estimate the crack width, an aggregate size of 19 mm and effective crack spacing of 300 mm were assumed in the analysis. Figure 5 shows the crack widths estimated by solving the MCFT equations for different middepth strain values. It was found that for steel-reinforced members, a linear approximation to crack width can be used, as the middepth strains are usually lower than 0.001 and rarely exceed 0.002. This linear relation of crack width, $w = 0.2 + 1000\varepsilon_x$, was plugged into Eq. (15) of the MCFT in Fig. 3 and simplified to obtain the β′ factor.

Step 2—To extend the application of Eq. (4) for different aggregate sizes, a modification factor (highlighted as C_a' in Eq. (5)) was developed.

Step 3—Finally, to account for different crack spacings, a modification factor, C_s', was incorporated into Eq. (4). This factor was developed by repeating the iterative process listed in Fig. 4 with different effective crack spacings, and the results were divided by those for s_{xe} = 300 mm. The development of the C_s' factor is discussed in Bentz and Collins (2006). As shown in Fig. 6, it was found that the C_s' was slightly different at different middepth strains, but because the strains in steel-reinforced members are in the range of 0.001 to 0.002, an average approximation of the C_s' factor was assumed ignoring the effect of middepth strains. This cannot be ignored for the FRP-reinforced members due to higher strains.

Equation (4) was found to successfully capture the shear behavior of steel-reinforced members. However, in the case of FRP reinforcement, much higher longitudinal and middepth strains can be expected, and the linear approximation in Fig. 5 would highly overestimate the crack width and result in conservative estimates.

Hoult et al. (2008) revised the steel-based shear provisions and updated Eq. (4) for FRP reinforcement. A nonlinear approximation, as shown in Fig. 5, was assumed for the MCFT results. This nonlinear approximation of crack width

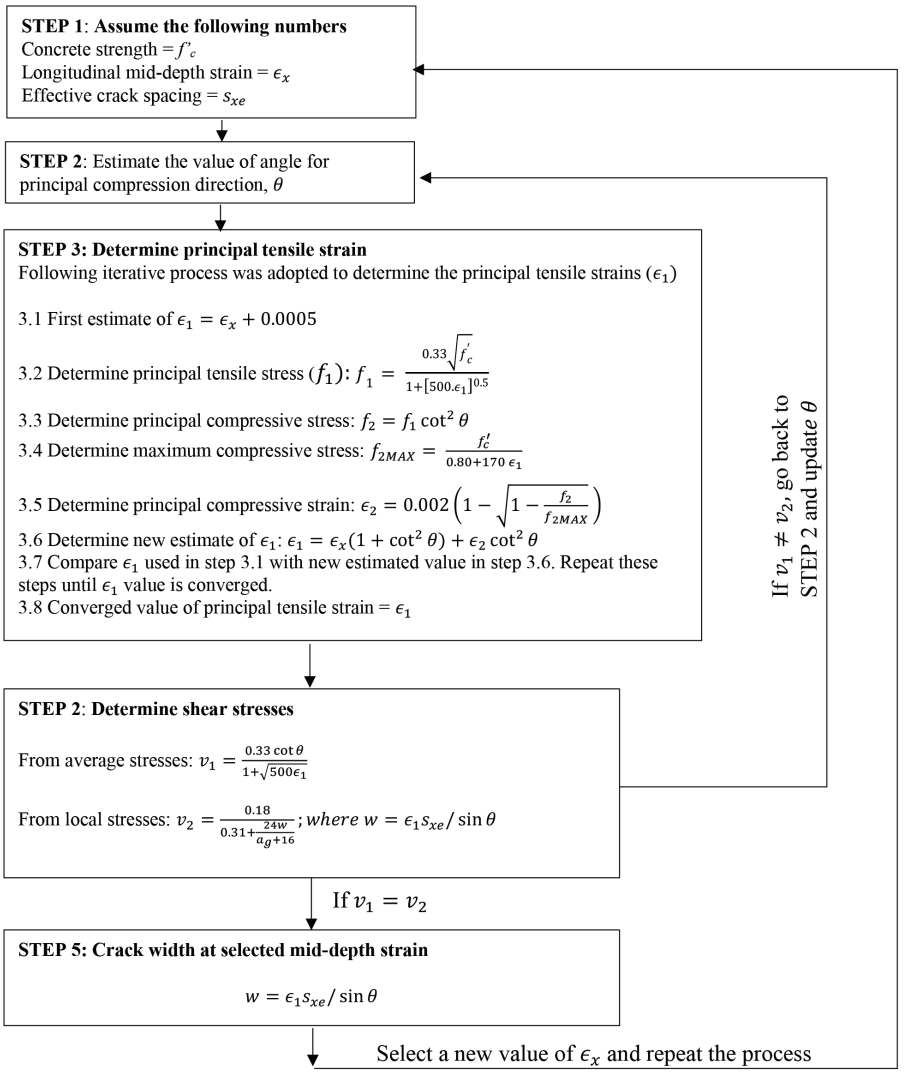


Fig. 4—Procedure for using MCFT equations to predict shear capacity.

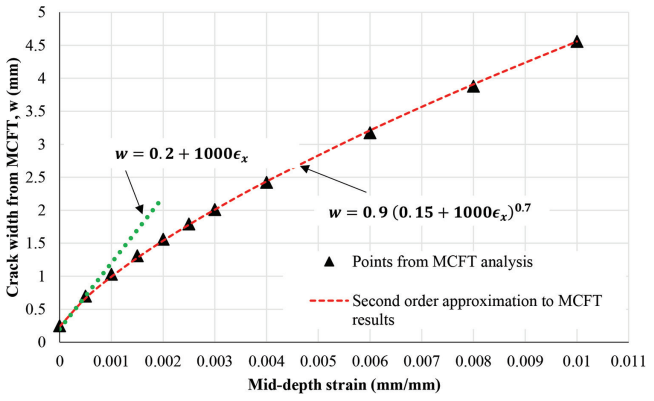


Fig. 5—Estimate of diagonal crack width using MCFT equations. (Note: 1 mm = 0.0394 in.)

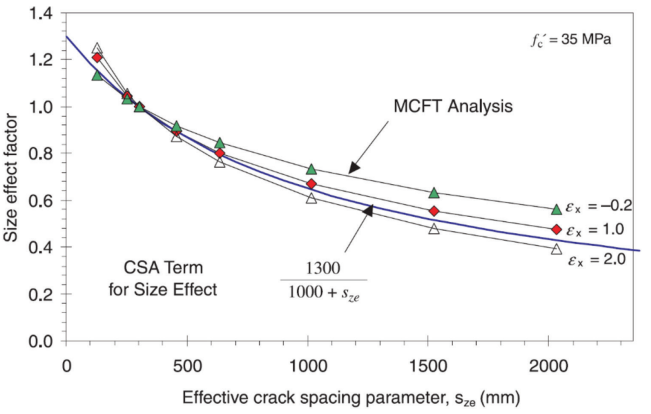


Fig. 6—Determining size factor (Bentz and Collins 2006).

was substituted in Eq. (15) (in Fig. 3) of the MCFT equations to get the updated β′ factor.

$$\beta' = \left(\frac{0.30}{0.5 + (1000\varepsilon_x + 0.15)^{0.7}}\right) \quad (6)$$

The updated equation, presented by Hoult et al. (2008), to find the concrete contribution for RC members longitudinally reinforced with FRP bars is as follows

$$(V_{c\text{–Hoult et al. 2008}}) = \left(\frac{0.30}{0.5 + (1000\varepsilon_x + 0.15)^{0.7}}\right)\left(\frac{1300}{1000 + s_{xe}}\right)\sqrt{f'_c}\,b_w d_v \quad (7)$$

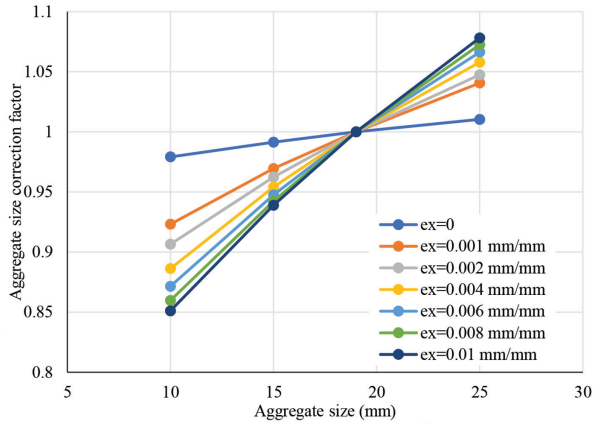


Fig. 7—Aggregate size correction factor. (Note: 1 mm = 0.0394 in.)

Later, Bentz et al. (2010) and Johnson (2014) used Eq. (7) to simulate the concrete contribution to shear strength in various tests and found that although the accuracy of the predictions by using this nonlinear equation (Eq. (3)) was improved, the relation still needed further improvement. It is important to note here that Hoult et al. (2008) updated the β′ factor to account for the effect of higher middepth strains, but the C_s' and C_a' factors were kept the same as originally developed for steel members in Bentz and Collins (2006). As shown in Fig. 6, the middepth strain effect can be ignored for lower strain values for the size factor; however, it is necessary to extend the formulation of crack spacing and aggregate size factors for higher strains and account for any changes in the behavior. Thus, the current study extended the MCFT equations for higher strain values and separately investigated the effects of modification factors on shear strength predictions.

PROPOSED MODEL

The model proposed in the current study to predict the shear contribution of beams longitudinally reinforced with FRP bars is generalized as follows

$$V_c = \beta C_s C_a b_w d\sqrt{f_c'} \tag{8}$$

The β-factor is the same as proposed by Hoult et al. (2008) and can be calculated using Eq. (9).

$$\beta = \left(\frac{0.3}{0.5 + (1500\varepsilon_x + 0.15)^{0.7}}\right) \tag{9}$$

To use the model for different member depths and aggregate sizes, two factors, C_a and C_s, are introduced in Eq. (8). Contrary to the C_s' and C_a' factors, which were coupled together in the original formulation of CSA equations by Bentz et al. (2006), these factors in the proposed model are calculated independently. This was deemed necessary to separately investigate the effects of different aggregate sizes and crack spacings on shear predictions.

To account for different aggregate sizes, the iterative process listed in Fig. 4 was repeated with different aggregate sizes, and the results were divided by those for a_g = 19 mm.

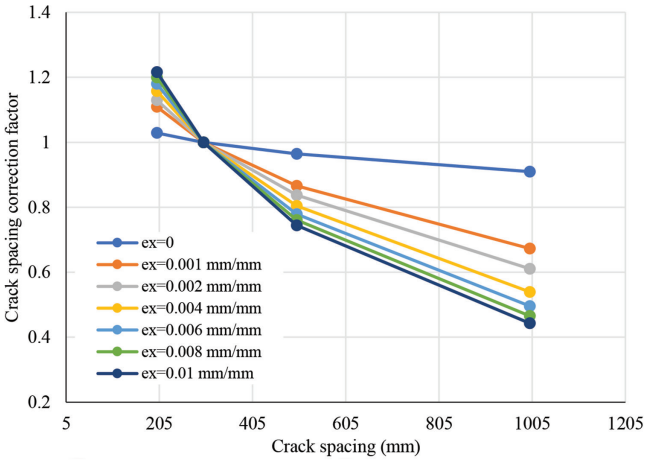


Fig. 8—Crack spacing correction factor.

The effect of different aggregate sizes on the normalized shear strength is plotted in Fig. 7, where it can be seen that the normalized shear strength increases with the increasing size of the aggregate. Additionally, as expected, the rate of the increase was found to be dependent on the middepth strain values. As shown in Fig. 7, the slope of each line varies based on the middepth strain level. Therefore, the modification factor, C_a, was derived to incorporate the effect of both aggregate size and strain value.

This two-dimensional variation in the modification factor as a function of aggregate size and the middepth strain was captured with the help of Eq. (10), which was statistically derived using the data points plotted in Fig. 7. The detailed procedure to derive Eq. (10) is provided in Appendix A.*

$$C_a = \frac{60 + a_g(0.5 + 90\varepsilon_x)}{60 + 19(0.5 + 90\varepsilon_x)} \tag{10}$$

A similar procedure was adopted to incorporate the effect of different crack spacings, and the variation in normalized shear strength with different crack spacings and middepth strain levels is plotted in Fig. 8.

Again, a two-dimensional equation was developed to successfully capture the variation depicted in Fig. 8.

$$C_s = \frac{600}{600 + (s_x - 300)(0.5 + 70\varepsilon_x)} \tag{11}$$

The crack spacing parameter, s_x, in the previous equations is the horizontal spacing of diagonal cracks and was taken as equal to the effective depth 0.90d or effective shear depth d_v of the beams for steel-reinforced members. However, for the FRP reinforcement, this assumption results in an inaccurate estimate of the spacing of shear cracks, especially when there is no transverse reinforcement. This is mostly due to the various surface treatments of the FRP bars. It was found that different surface conditions affect the bonding behavior of FRP bars, and hence, the cracking pattern changes.

*The Appendix is available at **www.concrete.org/publications** in PDF format, appended to the online version of the published paper. It is also available in hard copy from ACI headquarters for a fee equal to the cost of reproduction plus handling at the time of the request.

Zakaria et al. (2011) proposed the following equations to estimate the shear crack spacing.

$$S_{m\theta} = \frac{1}{\frac{\sin\theta}{S_{mx}} + \frac{\cos\theta}{S_{my}}} \quad (12)$$

$$S_{mx} = 2\left(c_x + \frac{S_x}{10}\right) + k_1 k_2 \frac{d_{bx}}{\rho_x} \quad (13)$$

$$S_{my} = 2\left(c_s + \frac{S_y}{10}\right) + k_1 k_2 \frac{d_{by}}{\rho_y} \quad (14)$$

The shear crack spacing, $S_{m\theta}$ is calculated by the spacing of vertical cracks (S_{mx}) and the spacing of horizontal cracks (S_{my}) with the consideration of the shear crack angle (θ). These parameters are physically illustrated in Fig. 9. After calculating the inclined spacing, Masukawa (2012) found that the crack spacing parameter (s_x) can be found using Eq. (15)

$$s_x = \sin\theta S_{m\theta} \quad (15)$$

In the case of no transverse reinforcement, Eq. (12) to (15) can be simplified to the following relation, which can be used to find the crack spacing, s_x, to determine the C_s factor in Eq. (11).

$$s_x = S_{mx} = 2\left(c_x + \frac{S_x}{10}\right) + k_1 k_2 \frac{d_{bx}}{\rho_x} \quad (16)$$

where ρ_x is the ratio of longitudinal reinforcement to the effective concrete area and is determined by $A_f/(2.5(h - d)b_w)$; k_2 is taken as 0.25; and k_1 represents the bond characteristics of the longitudinal reinforcing bar. Kharal and Sheikh (2014) suggested the following k_1 values for different types of FRP bars.

$$k_1 = \begin{cases} \text{0.25 for GFRP Bar A} \\ \text{(helically wrapped with light sand coating on surface)} \\ \text{0.2 for GFRP Bar V} \\ \text{(heavily sand-coated bars)} \\ \text{0.3 for GFRP Bar C} \\ \text{(ribs on the surface)} \end{cases} \quad (17)$$

For members with stirrups, it is observed that the spacing of the diagonal cracks will typically be less than 300 mm (Bentz et al. 2010; Johnson 2014). Therefore, the crack spacing parameter (s_x) was conservatively taken as 300 mm in this study. The stirrup contribution to shear resistance can be determined using the following equation

$$V_s = \frac{A_{fv} f_{fv} d_v}{s} \cot(\theta) \quad (18)$$

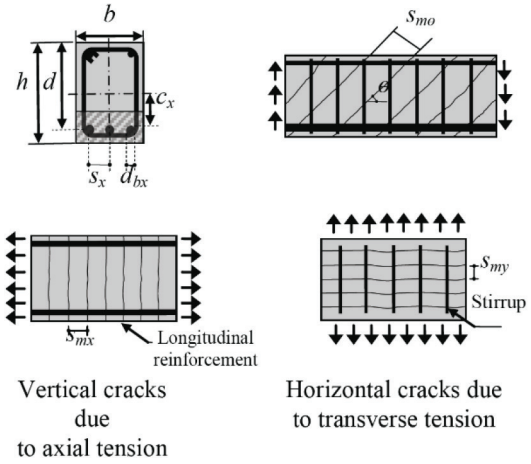


Fig. 9—Crack parameters (Zakaria et al. 2011).

where θ is the angle of principal compression. As highlighted in Bentz et al. (2006), the conservative approach for determining θ is to consider the value of θ at which the MCFT predicts that V_c has its maximum contribution to the strength, and this can easily be done by repeating the iterative process listed in Fig. 4 and taking the s_x as 300 mm in the formulation. This iterative process was conducted in the current study, and the following nonlinear relation is proposed to better predict the angle of principal compression for FRP-RC members at higher middepth strains.

$$\theta = \left(\frac{21{,}700\varepsilon_x + 31}{310\varepsilon_x + 1}\right)\left(0.88 + \frac{s_x}{2500}\right)\left(\frac{152 - a_g}{133}\right) \quad (19)$$

The foregoing relation takes into account the effect of higher strains and the different aggregate sizes. For members with minimum transverse reinforcement, s_x can be taken as 300 mm.

Summary and accuracy of proposed model

The proposed model to predict the shear strength of FRP-RC members is summarized in Fig. 10. The accuracy of the proposed model was evaluated by predicting the shear strengths of the 93 specimens assembled in the database. Predicted versus experimental shear strength values are plotted in Fig. 11. The proposed model yielded predicted-to-test strength ratios of 0.96 and 1.00 for the beam specimens without and with transverse reinforcement, respectively. The COV also improved, and the proposed model resulted in COV of 13% and 15.6%, respectively. All the predicted values plotted in Fig. 11 have been tabulated in Appendix B, which also provides the values of all theoretical parameters. It is evident that the changes suggested in the proposed model successfully captured the behavior of FRP-RC beams both without and with GFRP transverse reinforcement.

CONCLUSIONS

Understanding the behavior of fiber-reinforced polymer (FRP)-reinforced concrete (RC) members subjected to shear is challenging because of several factors: higher strains due to a lower modulus of FRP, different bond behavior of different types of FRP bars, and uncertainties in accurately

$$V_r = V_c + V_s$$

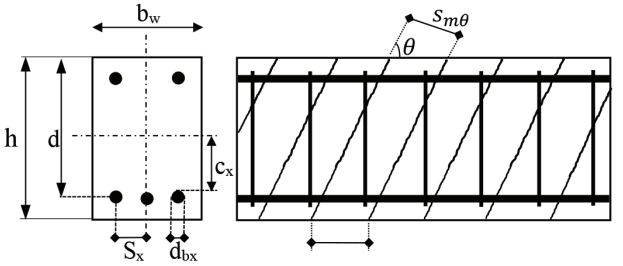
$$V_c = \beta . C_s . C_a . b_w d \sqrt{f'_c}$$

$$\beta = \left(\frac{0.3}{0.5 + (1500\epsilon_x + 0.15)^{0.7}}\right)$$

$$C_s = \frac{600}{600 + (s_x - 300)(0.5 + 70\epsilon_x)}$$

$$C_a = \frac{60 + a_g(0.5 + 90\epsilon_x)}{60 + 19(0.5 + 90\epsilon_x)}$$

$$\epsilon_x = \frac{\left(\frac{M_f}{d_v}\right) + V_f - V_P + 0.5N_f - A_P f_{p0}}{2E_f A_f + E_P A_P}$$



Note: V_P, N_f, E_P, A_P, *and* $A_P f_{p0}$ *correspond to prestress and axial loading and are taken as zero in the current study.*

$$s_x = 2\left(c_x + \frac{S_x}{10}\right) + 0.25k_1\frac{d_{bx}}{\rho_x} \leq d_v$$

$$k_1 = 0.2\ (sand\ coated\ bars); 0.25(helically\ wrapped\ bars); or\ 0.30(ribbed\ bars)$$

$$\rho_x = A_f/(2.5(h-d)b_w)$$

$$s_x = 300\ mm\ for\ members\ with\ minimum\ transverse\ reinforcement$$

$$V_s = \frac{A_{fv} f_{fv} d_v}{s}\cot(\theta)$$

$$\theta = \left(\frac{21700\epsilon_x + 31}{310\epsilon_x + 1}\right)\left(0.88 + \frac{s_x}{2500}\right)\left(\frac{152 - a_g}{133}\right)$$

Fig. 10—Summary of proposed model.

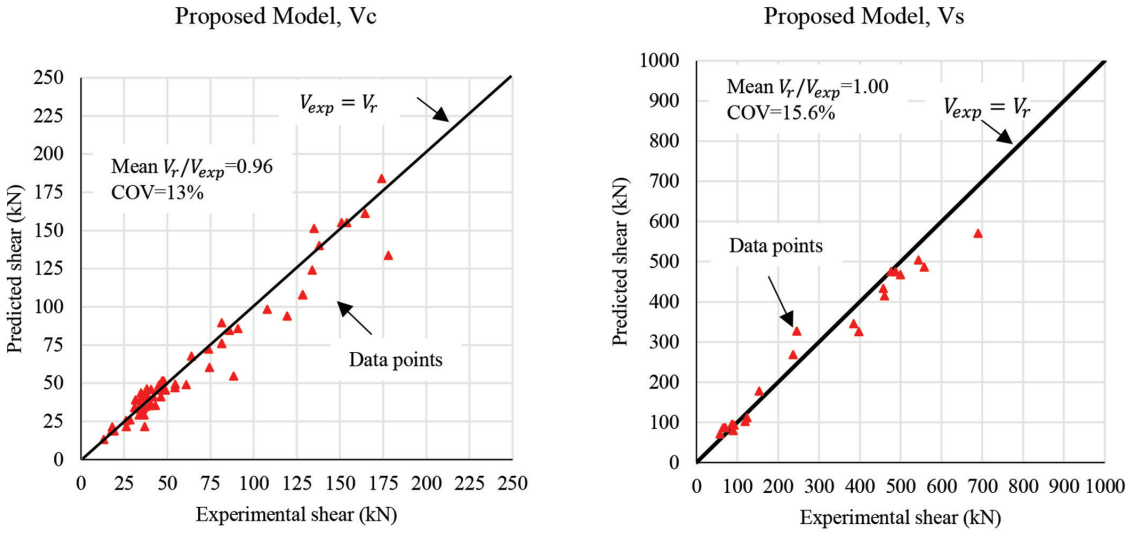


Fig. 11—Predictions made by proposed model. (Note: 1 kN = 0.2248 kip.)

determining the bend strength of glass FRP (GFRP) stirrups. This paper revised Modified Compression Field Theory (MCFT)-based shear provisions, and several suggestions were made to increase the accuracy of predictions for FRP-RC elements. The following concluding remarks can be made from the current analysis:

1. It was found that with increasing crack spacing, which is a function of beam depth, shear strength decreased, and the rate at which shear strength decreased was dependent on the middepth strain levels. A modification factor to account for this effect was developed, which improved the accuracy of the predictions.

2. It was also observed that by increasing the aggregate size, shear strength increased, and the rate of the increase was also found to be dependent on the middepth strain levels.

3. The proposed model significantly improved the accuracy of MCFT-based shear provisions for FRP-RC members available in the literature.

4. The proposed model provided more reliable and consistent results than any of the shortlisted four models. The proposed model yielded a predicted-to-experimental strength ratio of 0.96 and 1.00 for FRP-RC beam specimens without and with GFRP stirrups. The coefficient of variation (COV) was approximately 13% and 15.6%, respectively.

AUTHOR BIOS

Jahanzaib *is a Research Assistant in the Department of Civil and Mineral Engineering at the University of Toronto, Toronto, ON, Canada, where he completed his PhD in civil engineering. His research interests include the effect of climate change on glass fiber-reinforced polymer (GFRP)-reinforced concrete (RC) structures and the fire and shear behavior of GFRP-RC members.*

Shamim A. Sheikh, *FACI, is a Professor of civil and mineral engineering at the University of Toronto. He is past Chair and a member of Joint ACI-ASCE Committee 441, Reinforced Concrete Columns, and a member of ACI Committee 374, Performance-Based Seismic Design of Concrete Buildings. His research interests include earthquake resistance and seismic upgrade of concrete structures, confinement of concrete, and the use of fiber-reinforced polymer (FRP) in concrete structures.*

NOTATION

A_f	=	area of longitudinal FRP reinforcement
A_{fv}	=	area of FRP shear reinforcement
a	=	length of shear span of beam
b_w	=	beam width
d	=	effective depth of beam cross section
d_{bx}	=	diameter of longitudinal bars
d_v	=	effective shear depth (greater of $0.9d$ or $0.72h$)
E_f	=	elastic modulus of longitudinal FRP straight bar reinforcement
f_c'	=	concrete compressive strength
f_{cr}	=	concrete cracking strength
f_{fb}	=	bend strength of GFRP stirrups
f_{fu}	=	ultimate strength of FRP straight bars
f_{fv}	=	usable stress for FRP stirrups
h	=	beam overall depth
k	=	ratio of depth of neutral axis to effective depth
M_f	=	factored moment at critical shear section
n_f	=	modular ratio
r	=	bend radius
S_x	=	spacing between longitudinal bars
s	=	spacing of stirrups
s_x	=	crack spacing parameter used in proposed model
s_{xe}	=	crack spacing parameter
V_c	=	shear strength provided by concrete
V_f	=	factored shear at critical shear section
V_r	=	shear capacity of GFRP-RC beam
V_s	=	shear strength provided by FRP shear reinforcement
ϵ_x	=	middepth strain
θ	=	angle of compression
ρ_f	=	reinforcement ratio

REFERENCES

ACI Committee 440, 2015, "Guide for the Design and Construction of Structural Concrete Reinforced with Fiber-Reinforced Polymer (FRP) Bars (ACI 440.1R-15)," American Concrete Institute, Farmington Hills, MI, 88 pp.

Al-Hamrani, A.; Alnahhal, W.; and Elahtem, A., 2021, "Shear Behavior of Green Concrete Beams Reinforced with Basalt FRP Bars and Stirrups," *Composite Structures*, V. 277, Dec., Article No. 114619. doi: 10.1016/j.compstruct.2021.114619

Ashour, A. F., 2006, "Flexural and Shear Capacities of Concrete Beams Reinforced with GFRP Bars," *Construction and Building Materials*, V. 20, No. 10, Dec., pp. 1005-1015. doi: 10.1016/j.conbuildmat.2005.06.023

Bentz, E. C., and Collins, M. P., 2006, "Development of the 2004 Canadian Standards Association (CSA) A23.3 Shear Provisions for Reinforced Concrete," *Canadian Journal of Civil Engineering*, V. 33, No. 5, May, pp. 521-534. doi: 10.1139/l06-005

Bentz, E. C.; Massam, L.; and Collins, M. P., 2010, "Shear Strength of Large Concrete Members with FRP Reinforcement," *Journal of Composites for Construction*, ASCE, V. 14, No. 6, Dec., pp. 637-646. doi: 10.1061/(ASCE)CC.1943-5614.0000108

Bentz, E. C.; Vecchio, F. J.; and Collins, M. P., 2006, "Simplified Modified Compression Field Theory for Calculating Shear Strength of Reinforced Concrete Elements," *ACI Structural Journal*, V. 103, No. 4, July-Aug., pp. 614-624.

Bywalski, C.; Drzazga, M.; Kamiński, M.; and Kaźmierowski, M., 2020, "A New Proposal for the Shear Strength Prediction of Beams Longitudinally Reinforced with Fiber-Reinforced Polymer Bars," *Buildings*, V. 10, No. 5, May, Article No. 86. doi: 10.3390/buildings10050086

CSA A23.3:19, 2019, "Design of Concrete Structures," CSA Group, Toronto, ON, Canada, 301 pp.

CSA S6:19, 2019, "Canadian Highway Bridge Design Code," CSA Group, Toronto, ON, Canada, 1182 pp.

CSA S806-12 (R2021), 2012, "Design and Construction of Building Structures with Fibre-Reinforced Polymers," CSA Group, Toronto, ON, Canada, 201 pp.

El-Sayed, A. K.; El-Salakawy, E. F.; and Benmokrane, B., 2006a, "Shear Strength of FRP-Reinforced Concrete Beams without Transverse Reinforcement," *ACI Structural Journal*, V. 103, No. 2, Mar.-Apr., pp. 235-243.

El-Sayed, A. K.; El-Salakawy, E. F.; and Benmokrane, B., 2006b, "Shear Capacity of High-Strength Concrete Beams Reinforced with FRP Bars," *ACI Structural Journal*, V. 103, No. 3, May-June, pp. 383-389.

Gross, S. P.; Yost, J. R.; Dinehart, D. W.; Svensen, E.; and Liu, N., 2003, "Shear Strength of Normal and High Strength Concrete Beams Reinforced with GFRP Bars," *Proceedings of the International Conference on High Performance Materials in Bridges*, A. Azizinamini, A. Yakel, and M. Abdelrahman, eds., Kona, Hawaii, pp. 426-437.

Hoult, N. A.; Sherwood, E. G.; Bentz, E. C.; and Collins, M. P., 2008, "Does the Use of FRP Reinforcement Change the One-Way Shear Behavior of Reinforced Concrete Slabs?" *Journal of Composites for Construction*, ASCE, V. 12, No. 2, Apr., pp. 125-133. doi: 10.1061/(ASCE)1090-0268(2008)12:2(125)

Johnson, D. T. C., 2014, "Investigation of Glass Fibre Reinforced Polymer (GFRP) Bars as Internal Reinforcement for Concrete Structures," PhD thesis, Department of Civil and Mineral Engineering, University of Toronto, Toronto, ON, Canada, 453 pp.

Johnson, D. T., and Sheikh, S. A., 2016, "Experimental Investigation of Glass Fiber-Reinforced Polymer-Reinforced Normal-Strength Concrete Beams," *ACI Structural Journal*, V. 113, No. 6, Nov.-Dec., pp. 1165-1174. doi: 10.14359/51689017

Kharal, Z., and Sheikh, S. A., "Tension Stiffening and Cracking Behavior of GFRP Reinforced Concrete," *ACI Structural Journal*, V. 114, No. 2, Mar.-Apr. 2017, pp 299-310

Khodaie, S., 2018, "Meso-Scale Simulation of Size-Dependent Shear Behavior in Glass Fiber Reinforced Polymer Reinforced Concrete Beams without Stirrups," doctoral dissertation, College of Engineering and Computing, University of South Carolina, Columbia, SC, 231 pp.

Kotynia, R.; Kaszubska, M.; and Barros, J. A. O., 2018, "Shear Behavior of Steel or GFRP Reinforced Concrete Beams Without Stirrups," *High Tech Concrete: Where Technology and Engineering Meet – Proceedings of the 2017* fib *Symposium, held in Maastricht, The Netherlands, June 12-14, 2017*, D. A. Hordijk and M. Luković, eds., Springer, Cham, Switzerland, pp. 769-777. doi: 10.1007/978-3-319-59471-2_90

Masukawa, J., 2012, "Degradation of Shear Performance of Beams due to Bond Deterioration and Longitudinal Bar Cutoffs," PhD thesis, Department of Civil and Mineral Engineering, University of Toronto, Toronto, ON, Canada, 353 pp.

Razaqpur, A. G., and Isgor, O. B., 2006, "Proposed Shear Design Method for FRP-Reinforced Concrete Members without Stirrups," *ACI Structural Journal*, V. 103, No. 1, Jan.-Feb., pp. 93-102.

Vecchio, F. J., and Collins, M. P., 1986, "The Modified Compression-Field Theory for Reinforced Concrete Elements Subjected to Shear," *ACI Journal Proceedings*, V. 83, No. 2, Mar.-Apr., pp. 219-231.

Walraven, J. C., 1981, "Fundamental Analysis of Aggregate Interlock," *Journal of the Structural Division*, ASCE, V. 107, No. 11, Nov., pp. 2245-2270. doi: 10.1061/JSDEAG.0005820

Zakaria, M.; Ueda, T.; and Wu, Z., 2011, "Evaluating and Proposing Prediction Models of Shear Crack Width in Concrete Beams," *Journal of Japan Society of Civil Engineers, Ser. E2 (Materials and Concrete Structures)*, V. 67, No. 2, pp. 245-263.

ACI STRUCTURAL JOURNAL TECHNICAL PAPER

Title No. 121-S68

Assessment of Use of Steel Bars with Unintended High Strength in Tied Columns

by Muhammad Masood Rafi and Muhammad Saad Khan

This paper presents the details of the analyses which were conducted to study the effects of steel reinforcing bars with unintended high strength on the behaviors of reinforced concrete (RC) columns. The influence of these bars on the column strength and strength-reduction factors were investigated. The former was studied with the help of column axial load-moment interaction diagrams, while a reliability analysis was carried out for the latter. Four different column cross sections reinforced with reinforcement ratios varying from 1 to 4% were included in the analysis. Other variables included concrete compressive and reinforcing bar yield strengths. The effects of the aforementioned variables were also considered on the development length of the reinforcing bars in tension and compression. It was found that the use of reinforcing bars with unintended high strength could change column behavior to compression-controlled at a lesser axial load level, which is accompanied by a reduction in the curvature capacity. Modifications have been suggested to control the negative effects of unintended high strength of bars on the column behavior and bar development length. Strength-reduction factors for RC sections ranging from compression-controlled to tension-controlled regions have also been proposed, which differ from those suggested by the prevalent code of practice.

Keywords: curvature; moment capacity; Monte Carlo simulation; reinforced concrete columns; strength-reduction factor; tensile strain.

INTRODUCTION

Reinforced concrete (RC) is a prevalent construction practice in several regions of the world, including Pakistan. An RC member's performance depends on the quality control methods followed for concrete and reinforcing bar production. The need of steel reinforcing bars in RC arises owing to the concrete's low tensile strength. These bars are produced following manufacturing standards, which ensure quality control in production. The design recommendations for RC in design codes assume that steel reinforcing bars comply with these manufacturing standards.

ASTM A615/A615M-05a[1] and BS 4449:1997 [2] are generally followed in manufacturing hot-rolled deformed bars and cold-twisted ribbed steel reinforcing bars, respectively, in Pakistan. The design of RC structures is conducted using ACI 318-08.[3] The yield (f_y) and ultimate (f_u) strengths of the bar have been recommended as 420 and 620 MPa (60 and 90 ksi), respectively, by ASTM A615.[1] On the other hand, BS 4449[2] recommends f_y and f_u as 460 and 497 MPa (67 and 72 ksi), respectively, for Grade 460B bars. Rafi et al.[4] analyzed the data of 2400 hot-rolled deformed and 2200 cold-twisted ribbed bars of diameters ranging from 10 to 40 mm (0.4 to 1.6 in.). These authors reported that the bars complying with the aforementioned standards could provide f_y greater than 750 MPa (110 ksi), which is substantially higher than the recommended strength. Because the use of these unintended high-strength bars in the design of flexural members was found to alter the failure mode from ductile to brittle, Rafi et al.[4] proposed modifications in the existing design provisions of ACI 318-08[3] for flexural members reinforced with these bars.

Columns in RC frame structures not only support the axial load but are also the main lateral force-resisting elements. In addition, eccentrically applied axial load on a column causes a bending moment. Failure of columns can create serious issues in load resistance and (in worst cases) can even lead to the collapse of a structure. It is, therefore, essential that the behaviors of columns reinforced with locally manufactured bars are investigated to understand the differences between the actual and the assumed behavior in the design code.

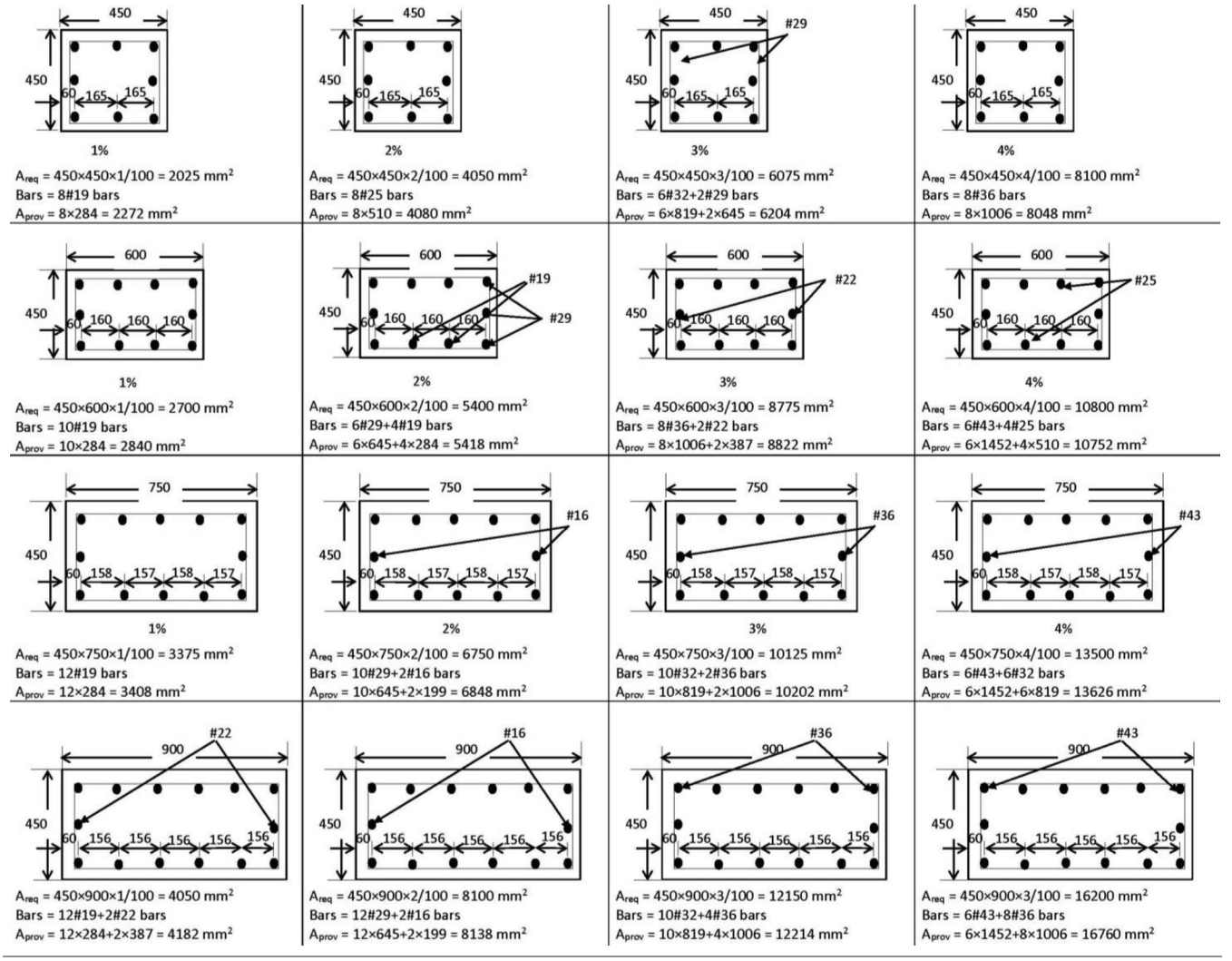
Further, an adequate bond between concrete and steel bars is needed to transfer the stresses to the embedded bars. The tension force applied to the bar is resisted by the bond stress. As a result, an appropriate development length of the bar is needed in the design of RC flexural members to ensure that some length of the bar is left in the concrete after its yielding to avoid bond strength failure. Besides other properties of concrete and reinforcing bars, bond strength is also influenced by the yield strength of the bar, and bars with larger f_y require longer development lengths.

This paper presents the studies that were conducted to investigate the effects of unintended reinforcing bar strength (available in the construction industry in Pakistan) on the behaviors of columns and the development length of the bar. Reliability-based calibration of strength-reduction factors recommended by ACI 318-08[3] for eccentrically loaded columns has also been carried out. Reliability analysis is a useful method to address uncertainties associated with design procedures suggested by the design codes.[5-8] The Monte Carlo method was employed for determining the strength-reduction factors for the beam-column. This is an effective method for solving probabilistic problems using statistical properties of known variables.[9,10]

Only short RC columns were included in the analysis, and the effects of slenderness on column behavior are beyond the

ACI Structural Journal, V. 121, No. 5, September 2024.
MS No. S-2023-047.R1, doi: 10.14359/51740852, received July 11, 2023, and reviewed under Institute publication policies. Copyright © 2024, American Concrete Institute. All rights reserved, including the making of copies unless permission is obtained from the copyright proprietors. Pertinent discussion including author's closure, if any, will be published ten months from this journal's date if the discussion is received within four months of the paper's print publication.

Table 1—Details of columns



scope of the analysis presented in this paper. Further, square and rectangular tied columns have been analyzed and circular cross section and/or spiral reinforcement are not considered, although the framework presented can be extended to incorporate these parameters. Finally, the effects of confinement on the concrete compressive strength are also not taken into account. The studies presented in this paper are in continuation to those conducted by Rafi et al.[4] Based on the analysis of the aforementioned behaviors, design recommendations have been proposed to reduce the negative influence of the bars on the design conducted by ACI 318-08.[3]

RESEARCH SIGNIFICANCE

The low strength of concrete in tension is augmented by steel reinforcing bars. Reference is generally made by the design codes to the reinforcing bar manufacturing standards, and both these are applied in conjunction. A deviation from the set of principles prescribed by the reinforcing bar manufacturing standard could impact design procedures that need to be carefully studied for the uncompromised safety of human beings. This paper aims to assess the validity and effectiveness of ACI 318-08[3] in the context of reinforcing bars made from ship plates and ingots. Although the presented study has been conducted in the context of Pakistan, the issue is relatively global. For example, Kankam[11] reported that 80,000 tons (2240 lb) of steel scrap is recycled annually in Ghana for use in steel reinforcing bar production. Further, Kankam and Adom-Asamoah[12] observed brittle failure of the under-reinforced beams reinforced with bars made of scrap material. Therefore, the results presented in this paper may apply to other parts of the world where similar construction practices exist.

METHODOLOGY OF WORK

Load-moment interaction diagram

The analysis of the column was carried out by determining the load-moment interaction diagram using a computer program. The effects of f_y larger than 420 MPa (60 ksi) on the column behavior are studied using different cross sections, concrete strengths (f_c), and reinforcement ratios (ρ). The overall scheme of work is summarized in Table 1. It is noted in Table 1 that four commonly used tied column cross sections were included in the analysis, which included 450 x 450, 600 x 450, 750 x 450, and 900 x 450 mm (18 x 18, 24 x 18, 30 x 18, and 36 x 18 in.). The aspect ratios of these cross sections ranged from 1 to 2, which is similar to

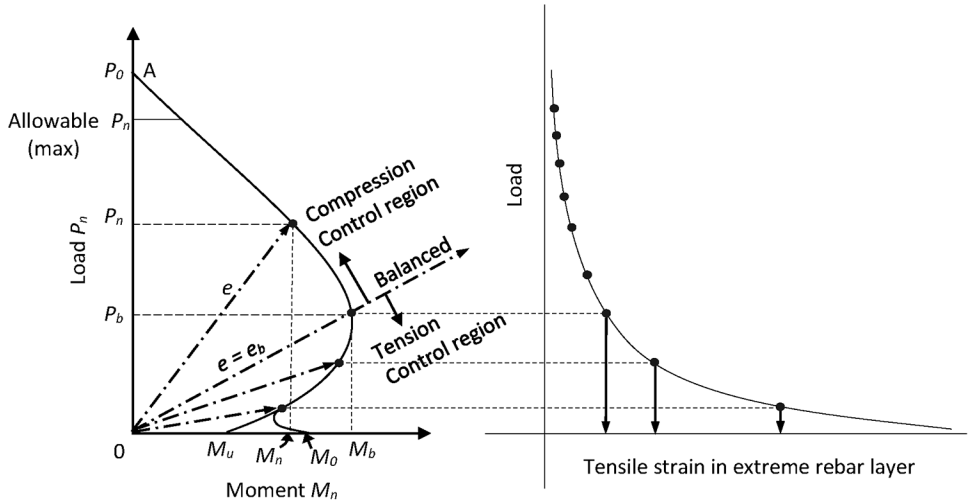


Fig. 1—Typical variations of axial load with: (a) moment; and (b) tensile strain in extreme reinforcing bar layer.

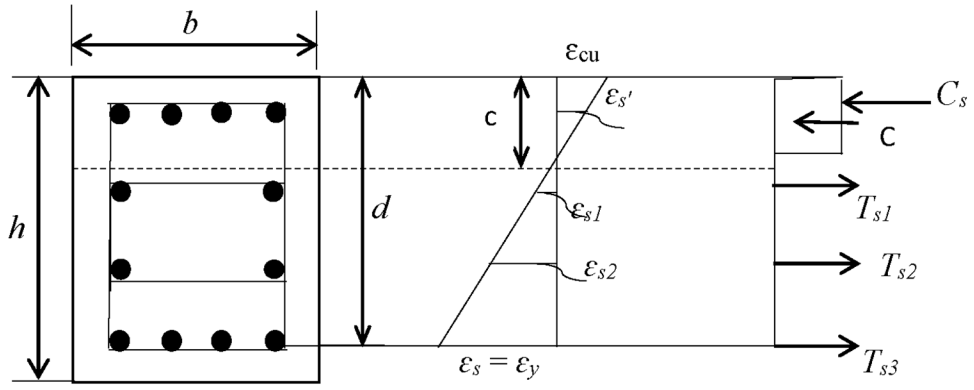


Fig. 2—Typical column cross section.

the tied columns analyzed by Szerszen et al.[13] The reinforcement ratio in these columns varied from 1 to 4%. Note that the diameters of the bars were selected to ensure that the number of the bars in a given column remains the same at all ρ values, and provided (A_{prov}) and required (A_{req}) areas of the steel bars are close to each other. Three values of f_c were employed, which included 21, 28, and 35 MPa (3000, 4000, and 5000 psi). Based on the reported f_y up to 770 MPa (112 ksi) by Rafi et al.[4] for the available steel reinforcing bars, four f_y values of 420, 550, 650, and 750 MPa (60, 80, 94, and 110 ksi) were considered in the analysis. These values cover the spectrum of f_y scatter in the upper region (higher than 420 MPa [60 ksi]) of the normal distribution curve, with a mean value of 550 MPa (80 ksi) reported by Rafi et al.[4]

Figure 1 illustrates a typical axial load-moment interaction diagram for a beam-column. A balanced condition on this diagram is represented by the balanced axial load (P_b) and balanced moment (M_b). This condition is reached when concrete compressive strain (ε_c) in an unconfined state reaches $\varepsilon_{cu} = 0.003$[14] simultaneously with a steel strain (ε_s) equal to yield strain ($\varepsilon_y = f_y/E_s$) in the extreme tensile reinforcement, where E_s is the elastic modulus of steel reinforcing bar. The balanced eccentricity (e_b) is determined as M_b/P_b.

The region of the load-moment interaction diagram above the balanced point is referred to as a compression-controlled region, which is characterized by increasing axial load and decreasing moment. Column failure in this region occurs by crushing of concrete on the compression side with $\varepsilon_c = 0.003$, while steel stress (f_s) is less than f_y. This region ends at P_n(max), which is $0.8P_o$ and $0.85P_o$ for tied and spirally reinforced columns, respectively.[14] Note that P_o is the pure axial load point (Fig. 1), which represents a large axial load acting at the plastic centroid of the column without any moment.

The region below the balanced point is tension-controlled, which is characterized by a small axial load at large eccentricity caused by a large moment. Tension steel bars yield before crushing of concrete ($\varepsilon_c < 0.003$) in this region. The point where the section is subjected to a bending moment (M_o) with zero axial loads is referred to as a pure flexure point. The failure in this case is similar to a beam.

Axial load (P_n) and moment (M_n) at any point on the curve (Fig. 1) are determined using Eq. (1) and (2), respectively, which can be obtained by considering strain compatibility and force equilibrium for an RC section, as shown in Fig. 2

$$P_n = C + C_S - T \tag{1}$$

$$M_n = (T + C_S)\left(d - \frac{h}{2}\right) + C\left(\frac{h}{2} - \frac{\beta c}{2}\right) \tag{2}$$

where $C = 0.85f_c 0.85cb$; $C_s = A_s(f_s - 0.85f_c)$; $T = A_s f_s$; $f_s = E_s\varepsilon_s$; $\varepsilon_s = \varepsilon_{cu}[(d - c)/c]$; and A_s and f_s are the area and stress of reinforcing bars in tension, respectively. Note that Bae and Bayrak[15] have proposed modifications in the compressive stress block parameters for ACI 318-19,[14] which apply to both normal and high-strength concrete.

The curvature (φ) of the cross section is calculated by Eq. (3)

$$\varphi = \varepsilon_{cu}/c \tag{3}$$

Development length

ACI 318-19[14] recommends Eq. (4) and (5) for the calculation of the development length of the bar in tension (l_{dt}) and compression (l_{dc}), respectively

$$l_{dt} = K d_b \frac{f_y}{\sqrt{f_c}} \tag{4}$$

$$l_{dc} = \frac{d_b f_y}{4\sqrt{f_c}} \geq 0.04 d_b f_y \tag{5}$$

where $K = (9/10)(\alpha\beta\gamma\lambda/[(c_b + K_{tr})/d_b)]$; α is the reinforcement location factor = 1.0; β is the coating factor = 1.0; γ is the reinforcement size factor and is taken as 0.8 for up to No. 19 (No. 6) bar and 1.0 for No. 22 (No. 7) and larger-diameter bars; λ is the lightweight aggregate concrete factor = 1.0 for normalweight concrete; c_b is the smaller of spacing or cover dimension; d_b is the diameter of the bar; K_{tr} is the transverse reinforcement index = $A_{tr}f_y/10sn$; A_{tr} is the total cross-sectional area of all transverse reinforcement placed at a spacing of s; and n is the number of bars to be developed

The data of f_y reported by Rafi et al.[4] were employed to study their effects on the bar development length both in tension and compression. d_b varied from No. 13 to 32 (No. 4 to 10) bar, whereas f_c varied from 21 to 50 MPa (3000 to 7000 psi).

Reliability analysis for eccentrically loaded columns

Probability-based analyses were carried out to obtain reliability indexes and strength-reduction factors for the eccentrically loaded columns. The employed approach is well documented in the existing literature and has been applied by different researchers such as Szerszen et al.,[13] Szerszen and Nowak,[16] and Zhang,[17] to mention a few of them.

The limit state design procedure of ACI 318-19[14] describes the general condition for failure to occur as given by Eq. (6)

$$R - Q \leq 0 \tag{6}$$

where R and Q are the resistance and load effect, respectively. The difference between R and Q provides the safety margin.

Strength-reduction (ϕ) and load amplification (γ) factors are used in Eq. (6) by ACI 318-19[14] in accordance with the ultimate limit state design method to ensure the safety of design elements, which for a beam-column can be written as Eq. (7)

$$\phi P \geq \gamma Q \tag{7a}$$

$$(\phi P_n, \phi M_n) \geq (P_u, M_u) \tag{7b}$$

R is a function of the material strength property factor (designated as f_M), geometric property factor (designated as f_G), and professional factor (designated as f_P).[5] The factor f_M considers statistical variations in the strength and elastic modulus of concrete and steel reinforcing bars. The factor f_G considers statistical variations in concrete cross-section dimensions (width, height, and effective depth) due to fabrication errors, and the area of steel reinforcing bars, whereas the factor f_P represents statistical variations in the nominal resistance of the RC cross section associated with design calculations.

Rafi et al.[4] reported that variations of R/Q are better represented by a log-normal distribution of the probability of failure. As a result, the reliability index (β) for the failure limit state (Eq. (6)) was calculated using Eq. (8)[6]

$$\beta = \frac{\ln\left(R_m / Q_m\right)}{\sqrt{V_R^2 + V_Q^2}} \tag{8}$$

where R_m and Q_m are the mean of R and Q, respectively; and V_R and V_Q are the coefficients of variation of R and Q, respectively.

The factor ϕ is determined by Eq. (9)

$$\phi = \frac{1 - \left(\frac{\sigma_R}{\sqrt{\sum(\sigma Q_i^2) + \sigma_R^2}}\right)\beta V_R}{\nu_R} \tag{9}$$

where σ_Q and σ_R are the standard deviation of load and resistance, respectively; i is the load type; and ν_R is the ratio between the nominal to mean value of strength-reduction factor and is taken as 0.95, as suggested by Sutrisno et al.[18]

Given the statistical variations in f_M, f_F, and f_P, the statistical bias coefficient (ξ) and V for each of these are required to determine R. Note that $\xi = R_m/R_u$, where R_u is the design strength. Because the statistical data of mean and standard deviation for the aforementioned factors are unavailable in Pakistan,[4] reliance has been made on the values of ξ and V reported in the existing literature.

Table 2 summarizes the values of ξ and V for the three types of factors mentioned earlier. The mean concrete strength (f_{cm}) was calculated from Eq. (10), as suggested by Rafi et al.[4] for determining ξ for concrete strength

$$f_{cm} = 0.675f_c + 1.1 \leq 1.15f_c \tag{10}$$

where f_c is 28-day concrete compressive strength in ksi. The value of V (taken as 0.18 in Table 2) for concrete and ξ and V for f_y were taken as from Rafi et al.[4]

In the absence of locally available data, the ξ and V values for the concrete cross section were taken from Ellingwood

Table 2—Summary of statistical parameters

Material properties[4]						Geometrical properties					
Concrete, MPa (psi)			Steel, MPa (ksi)			Cross section[6]		Steel area[13]		Professional factor[13]	
Nominal f_c	ξ	V	Nominal f_y	ξ	V	ξ	V	ξ	V	ξ	V
21 (3000)	1.04	0.18	420 (60)	1.187	0.15	1.005	0.04	1.00	0.06	1.00	0.08
28 (4000)	0.95	0.18									
35 (5000)	0.89	0.18									

et al.[6] On the other hand, these values for the area of steel reinforcing bars and for the professional factor were selected from Szerszen et al.[13] and are given in Table 2.

The loading combinations for strength design suggested by ACI 318-08[3] are given by Eq. (11) to (15), which were employed to calculate the design action for the considered limit state

$$Q_u = 1.2D + 1.6L \quad (11)$$

$$Q_u = 1.2D + 1.6L + 0.5S \quad (12)$$

$$Q_u = 1.2D + 0.5L + 1.6S \quad (13)$$

$$Q_u = 1.2D + 0.5L + 0.5S + 1.6W \quad (14)$$

$$Q_u = 1.2D + 0.5L + 0.2S + 1.0E \quad (15)$$

where Q_u is the factored load; and D, L, S, W, and E are the dead, live, snow, wind, and earthquake loads, respectively.

The values of ξ and V for S, W, and E were taken from the literature,[6,16,19] which are as follows: dead load: ξ = 1.05, V = 0.10; live load: ξ = 1.0, V = 0.25; snow load: ξ = 0.82, V = 0.26; wind load: ξ = 0.78, V = 0.37; and earthquake load: ξ = 0.66, V = 0.56.

Each of the load combinations given by Eq. (11) to (15) were calculated for a range of $D/(D + L)$ (designated as η) ratios (varying from 0.1 to 1.0). The contribution of S, W, and E was taken as $0.5D$ each, as suggested by Szerszen and Nowak.[16] The range of geometric (Table 1) and material properties for the investigated column sections described earlier was used for determining their nominal axial load versus moment curves.

The variable nature of material strength, cross-sectional dimensions, and inaccuracies associated with design equations require that their randomness is considered in the design to make it more reliable. This can be done by using a large database from experimental testing, which is not only expensive, but also requires a considerably long time. Simulation techniques provide an alternative to this. The Monte Carlo method was employed for increasing the size of the data set of load and resistance. This method is a powerful reliability analysis tool that is based on the generation of a specific number of sets of random variables and executing the same number of analyses using the generated variables. It has been employed by various researchers for determining solutions to a variety of problems in civil engineering.[10,13,17,20-25]

The values of f_c, f_y, f_P, b, h, and ρ were randomly sampled to analyze 10,000 cross sections, and the results were determined as load-moment interaction curves. The resistance data were extracted at eccentricity values chosen to cover both the compression-controlled and tension-controlled regions of the interaction diagram. ε_s in the extreme reinforcing bar layer on the tension side (Fig. 1) was also determined at these eccentricity values. As a result, 10,000 values of resistance were obtained at each eccentricity and corresponding ε_s that were stored for further analysis.

The previously determined nominal load-moment interaction diagrams were factored using ϕ recommended by ACI 318-08,[3] and the factored resistance was equated to Q_u given by Eq. (11) to (15) at all the selected eccentricity values. Q_u was decomposed into respective load components (D, L, S, E, and W) for a given load combination (Table 3). This decomposition was carried out for η values ranging from 0.1 to 1.0. Different load components were sampled 10,000 times from their respective distributions, and Q values at the selected eccentricities were extracted and stored. The load and resistance data, and their statistical variations, were used in Eq. (8) and (9) to obtain ϕ values, which were employed to generate plots of surfaces formed by the interaction of ϕ, ε_s, and η.

RESULTS AND DISCUSSION

Effects on column design

Figure 3 shows typical plots of the load-moment interaction diagram for a few of the analyzed column sections included in Table 1. It is seen in Fig. 3 that P_b reduces with an increase in f_y. The behaviors of all the analyzed columns are similar in this respect. It is evident from the plots in Fig. 3 that the column behavior changes to a compression-controlled section at a lower load level as compared to the level assumed in the design, considering f_y = 420 MPa (60 ksi). At the same time, the flexural capacity for the tension-controlled response of the column increases. The axial strength of the column also increases at higher f_y. This increase is, however, limited by ε_{cu} (taken as 0.003), which is exhausted at f_y = 550 MPa (80 ksi).[3] The moment capacity for a compression-controlled response is not affected significantly by an increase in f_y, especially after a load of nearly $P_0/2$. For a tension-controlled response, the column carries an axial tensile load much earlier as f_y is increased. Further, the decrease in P_b with an increase in ρ is rapid at higher f_y, and P_b was an axial tension in some cases.

Figure 4 shows typical load-curvature relations for a few of the analyzed column sections. It is seen that the curvature of the column reduces with an increase in f_y beyond 420 MPa

Table 3—Decomposed load types

Load type	Eq. (11)	Eq. (12)	Eq. (13)	Eq. (14)	Eq. (15)
Dead	$\frac{Q}{1.2+1.6\left(\frac{1}{\eta}-1\right)}$	$\frac{Q}{1.2+1.6\left(\frac{1}{\eta}-1\right)+0.5(0.5)}$	$\frac{Q}{1.2+0.5\left(\frac{1}{\eta}-1\right)+1.6(0.5)}$	$\frac{Q}{1.2+0.5\left(\frac{1}{\eta}-1\right)+0.5(0.5)+1.6(0.5)}$	$\frac{Q}{1.2+0.5\left(\frac{1}{\eta}-1\right)+0.2(0.5)+1.0(0.5)}$
Live	$\frac{\left(\frac{1}{\eta}-1\right)Q}{1.2+1.6\left(\frac{1}{\eta}-1\right)}$	$\frac{\left(\frac{1}{\eta}-1\right)Q}{1.2+1.6\left(\frac{1}{\eta}-1\right)+0.5(0.5)}$	$\frac{\left(\frac{1}{\eta}-1\right)Q}{1.2+0.5\left(\frac{1}{\eta}-1\right)+1.6(0.5)}$	$\frac{\left(\frac{1}{\eta}-1\right)Q}{1.2+0.5\left(\frac{1}{\eta}-1\right)+0.5(0.5)+1.6(0.5)}$	$\frac{Q}{1.2+0.5\left(\frac{1}{\eta}-1\right)+0.2(0.5)+1.0(0.5)}$
Snow	—	$\frac{(0.5)Q}{1.2+1.6\left(\frac{1}{\eta}-1\right)+0.5(0.5)}$	$\frac{(0.5)Q}{1.2+0.5\left(\frac{1}{\eta}-1\right)+1.6(0.5)}$	$\frac{(0.5)Q}{1.2+0.5\left(\frac{1}{\eta}-1\right)+0.5(0.5)+1.6(0.5)}$	$\frac{(0.5)Q}{1.2+0.5\left(\frac{1}{\eta}-1\right)+0.2(0.5)+1.0(0.5)}$
Wind	—	—	—	—	—
Earthquake	—	—	—	—	$\frac{(0.5)Q}{1.2+0.5\left(\frac{1}{\eta}-1\right)+0.2(0.5)+1.0(0.5)}$

(60 ksi). Because this reduction is not anticipated in the design by the designers, it can have serious implications on the ductility demand of a column during the seismic excursion. For example, the curvature ductility of a 450 x 450 mm (18 x 18 in.) column section with f_c = 21 MPa (3000 psi) and ρ = 1% subjected to P_n = 600 kN (135 kip) reduces to 1.20 from 2.48 (nearly 52% reduction) if f_y is increased from 420 to 750 MPa (60 to 110 ksi), respectively. Further, the reduction in the ultimate curvature is higher for f_y up to 550 MPa (80 ksi). Thereafter, change in ultimate curvature with f_y is marginal.

It becomes evident in the previous that control on the balanced point is needed to avoid undesirable behavior of columns, which could endanger the safety of building occupants. This requires an evaluation of those parameters that influence column behavior with respect to its axial load-moment interaction diagram.

To study the effects of h and f_c on the column behavior, the axial load-moment interaction diagrams were normalized to dimensionless quantities. The moment has been normalized by dividing it by the product of f_c, A_g, and h, while the axial load is normalized by dividing it by the product of f_c and A_g. Figure 5 illustrates typical examples of normalized load-moment interaction diagrams at two values of f_c for all column sections included in this study to demonstrate the effects of changing h of the column on its behavior. It is seen in Fig. 5 that (except for a small variation in the normalized P_b) the behaviors of all the column sections are similar for the same f_c, f_y, and ρ. The maximum difference in the normalized P_b comes out to be 0.04%, which is insignificant. This is an indication that the influence of h on the column behavior is negligible in the context of the issue highlighted due to the unintended use of high-strength reinforcing bars.

Figure 6 illustrates the influence of f_c on the normalized P_b of the analyzed column sections at a couple of f_y values. The data of two column sections have been presented at all the three employed f_c values due to the similarity of behaviors of the analyzed columns. It is seen in Fig. 6 that the normalized P_b increases with f_c at the same value of f_y, while the normalized moment is reduced. These results are an indication that column behavior is influenced by the change in f_c at higher f_y values.

Figure 7 illustrates the influence of ρ on P_b of the analyzed column sections at different f_y values. The data of all analyzed column sections have been presented at a few selected values of f_c due to the similarity of behaviors. The values of P_b have been normalized to P_b for f_y = 420 MPa (60 ksi) (P_{b420}) in Fig. 7. It is seen that the normalized P_b at the same ρ reduces with increasing f_y, and this reduction becomes higher at larger ρ values. Once again, the behaviors of all the column sections are similar in this respect. It can be inferred that P_b is influenced by ρ as f_y is increased beyond 420 MPa (60 ksi).

The influence of ρ on normalized P_b (P_b/P_{b420}) is studied further by considering the change in the normalized P_b between two consecutive values of f_y. This indicated that the difference in normalized P_b between two consecutive values of f_y remains similar at the same value of ρ. For example, this difference was found to be 0.204 and 0.189 for a change

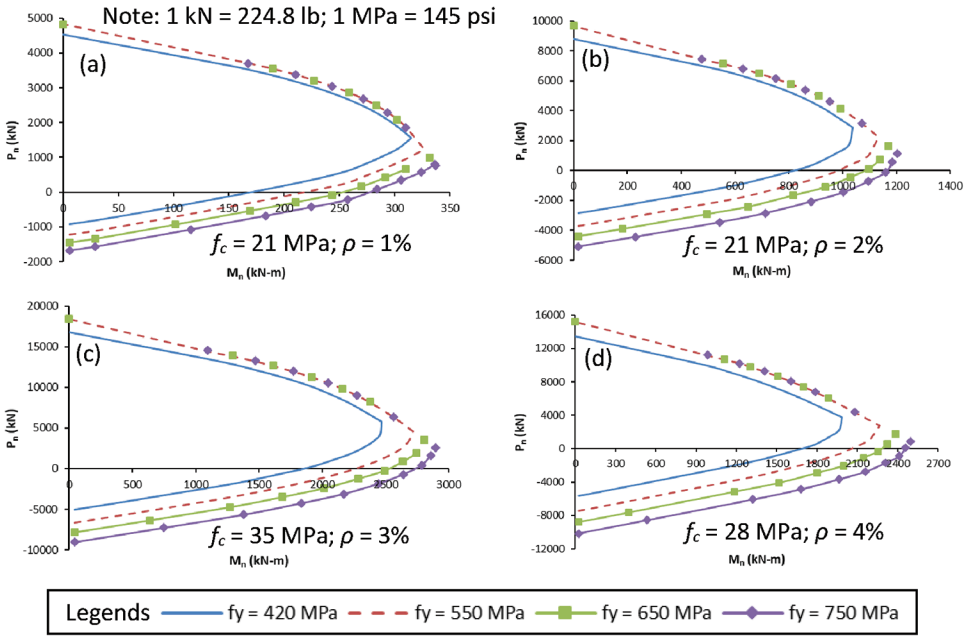


Fig. 3—Load-moment interaction diagram for column section: (a) 450 x 450 mm (18 x 18 in.); (b) 450 x 750 mm (18 x 30 in.); (c) 450 x 900 mm (18 x 36 in.); and (d) 450 x 750 mm (18 x 30 in.).

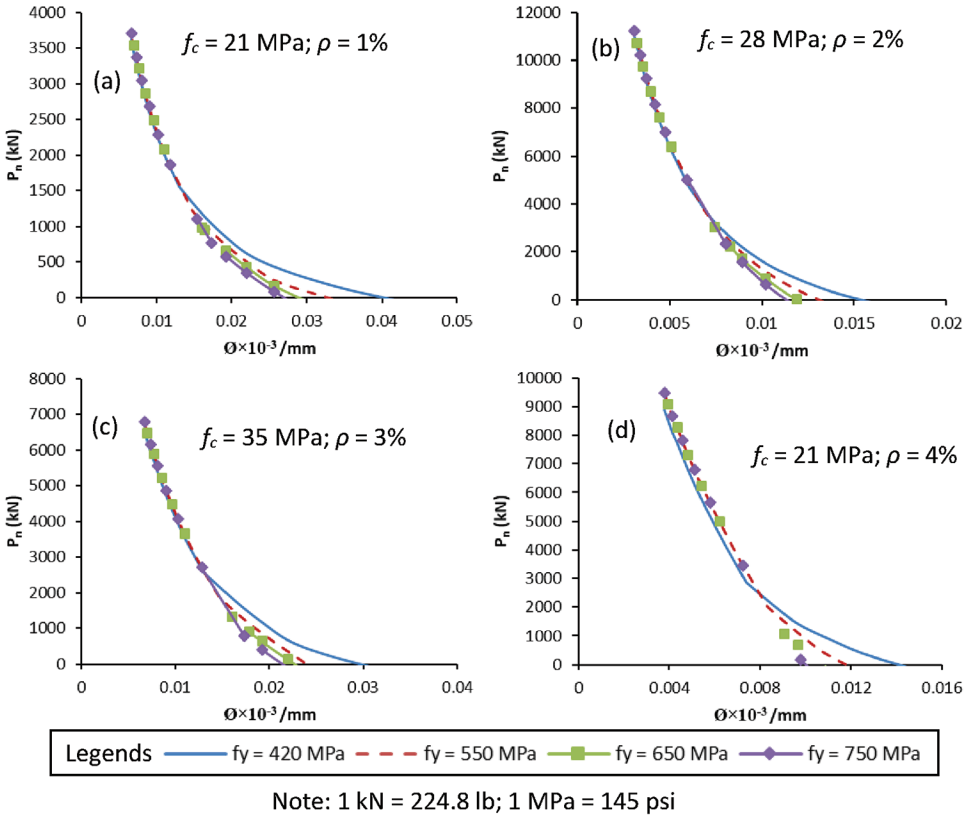


Fig. 4—Load-curvature diagram for column section: (a) 450 x 450 mm (18 x 18 in.); (b) 450 x 900 mm (18 x 36 in.); (c) 450 x 600 mm (18 x 24 in.); and (d) 450 x 750 mm (18 x 30 in.).

in f_y from 420 to 550 MPa (60 to 80 ksi) and from 550 to 650 MPa (80 to 94 ksi), respectively, for a 450 x 750 mm (18 x 30 in.) cross section with f_c = 35 MPa (5000 psi) and ρ = 3%. This behavior was found to be independent of the column section, as can be expected from Fig. 5. Therefore, an average value of P_b/P_{b420} at each of the ρ was determined.

These data were plotted graphically versus $\rho/\sqrt{f_c}$, as shown in Fig. 8. A regression analysis of the data in Fig. 8 provided the relationship between these parameters, which is given by Eq. (16)

$$P_b = \left[1 + 4.42\left(\frac{\rho}{\sqrt{f_c}}\right)^{0.5}\right] \times P_{b420} \quad (16)$$

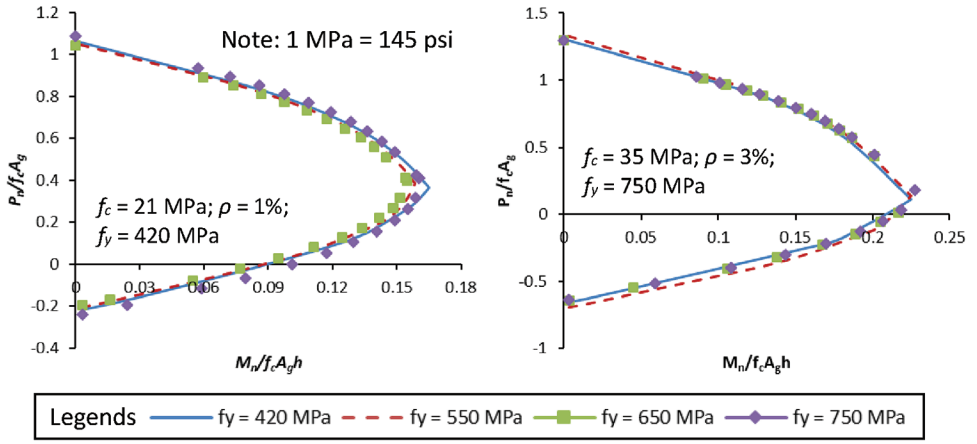


Fig. 5—Effects of section depth on normalized axial load-moment interaction diagram.

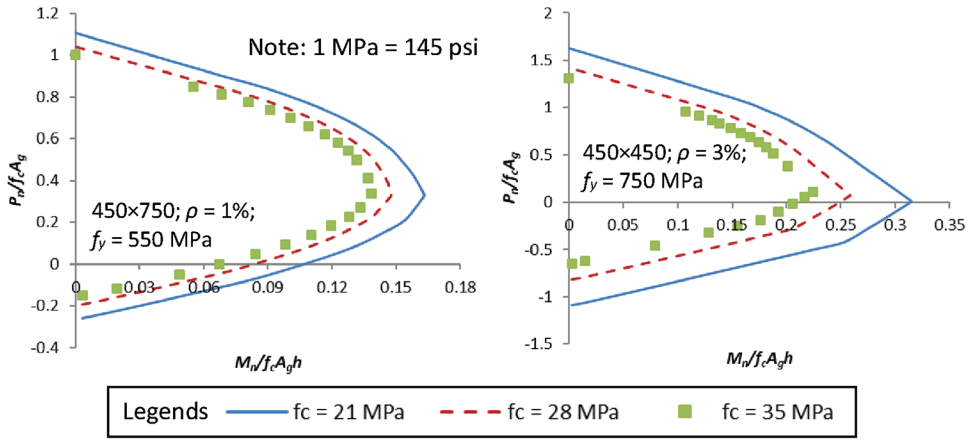


Fig. 6—Effects of concrete strength on normalized axial load-moment interaction diagram.

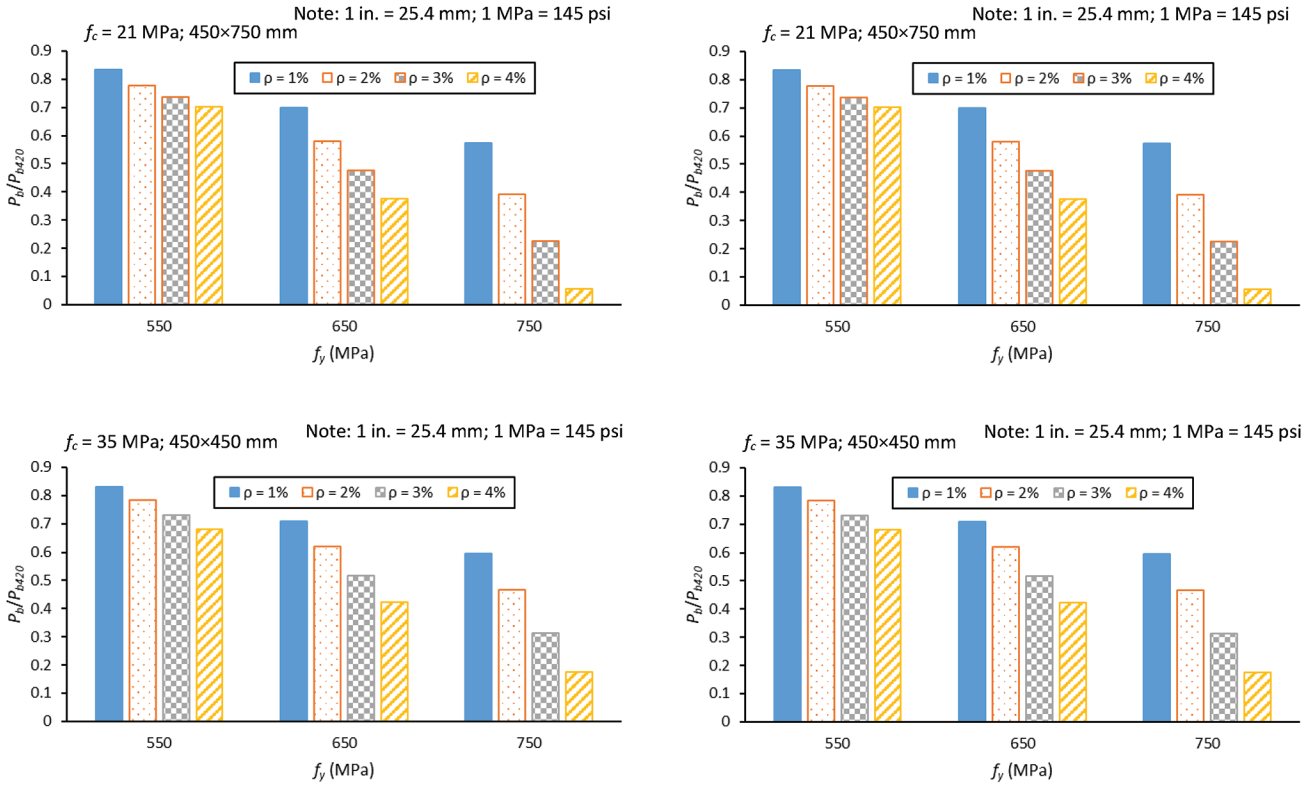


Fig. 7—Variations in normalized balanced axial load with yield strength.

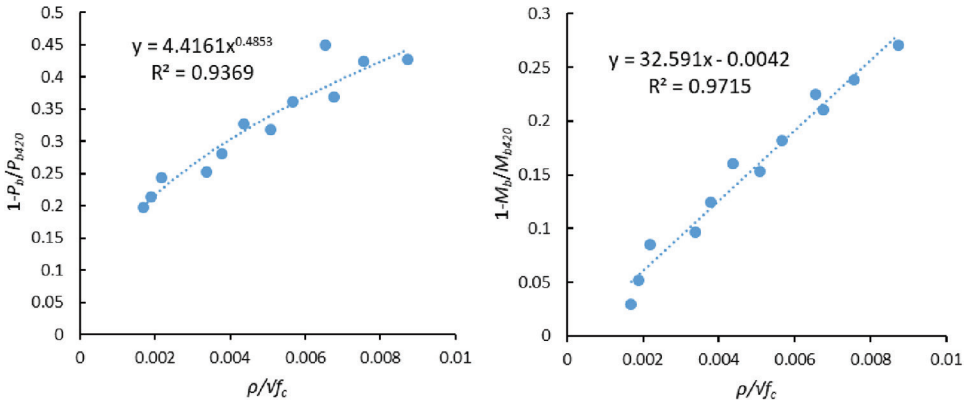


Fig. 8—Relationship of parameters for determining correction factor.

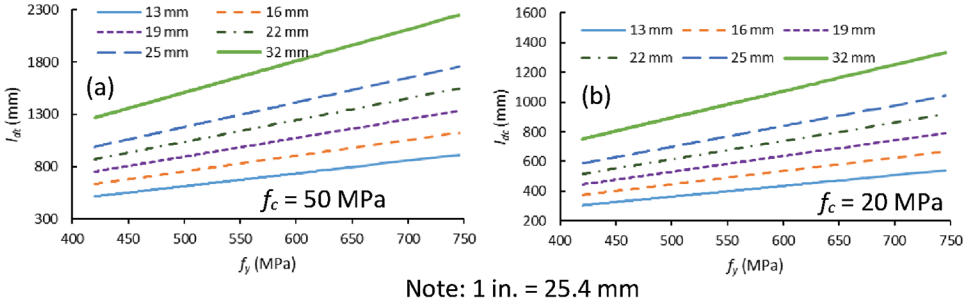


Fig. 9—Variations in development length with reinforcing bar yield strength: (a) tension; and (b) compression.

A very high correlation coefficient for Eq. (16) ($R^2 = 0.94$ is seen in Fig. 8. It is proposed that P_b is determined by using Eq. (16), which can be manifested as Eq. (17) in terms of the balanced neutral axis (Fig. 2) for establishing the balanced point (Fig. 1).

$$c_b = \left[1 + 4.42\left(\frac{\rho}{\sqrt{f_c}}\right)^{0.5}\right] \times c_{b420} \quad (17)$$

Following the aforementioned approach, a relation of M_b/M_{b420} with $\rho/\sqrt{f_c}$ is also illustrated in Fig. 8. A regression analysis of the data in Fig. 8 is provided from the relation given by Eq. (18) ($R^2 = 0.972$)

$$M_b = \lambda \times M_{b420} \quad (18)$$

where $\lambda = [1 + 32.6(\rho/\sqrt{f_c'}) - 1/238]$.

The moment values calculated from Eq. (2) are proposed to be divided by the factor λ (Eq. (19)) to provide control on the increase in the moment due to the unintended use of high-strength reinforcing bars in construction

$$M_n = \frac{1}{\lambda}\left[(T + C_s)\left(d - \frac{h}{2}\right) + C\left(\frac{h}{2} - \frac{\beta c}{2}\right)\right] \leq M_{b420} \quad (19)$$

As a typical example of the application of the aforementioned proposed method, consider a 450 x 450 mm (18 x 18 in.) column with f_c = 28 MPa (4000 psi) and ρ = 1%. The capacity of this column for f_y = 420 MPa (60 ksi) is M_n = 330 kN·m (244 kip·ft) and P_n = 1200 kN (270 kip). If the same column is accidentally reinforced with reinforcing bars of unintended f_y as 550 MPa (80 ksi), P_n reduces to 815 kN (183 kip) for the same M_n = 330 kN·m (244 kip·ft). This undesirable situation can be controlled with the help of Eq. (17) and (19). The use of these equations requires that the column section is increased to 450 x 600 mm (18 x 24 in.), which provides M_n = 405 kN·m (299 kip·ft) at P_n = 1200 kN (270 kip) for f_y = 420 MPa (60 ksi) at ρ = 1%. Alternatively, ρ provided could be increased to 1.5% for the same 450 x 450 mm (18 x 18 in.) column section, yielding M_n = 345 kN·m (255 kip·ft) at P_n = 1200 kN (270 kip). Both these sections also provide M_n larger than 330 kN·m (244 kip·ft) at P_n = 1200 kN (270 kip) if reinforced with unintended f_y = 550 MPa (80 ksi).

Effect on development length

Figure 9 illustrates typical plots of the effects of f_y on l_{dt} and l_{dc} for different diameters of reinforcing bars. As can be expected from Eq. (4) and (5), development length increases with f_y and decreases with f_c for the same diameter of the reinforcing bar. The data plotted in Fig. 9 indicate the need of introducing an appropriate modification factor in Eq. (4) and (5) to account for the unintended high f_y values (larger than 420 MPa [60 ksi]) during construction. A factor α is proposed herein for use in Eq. (4) and (5), which can be written as Eq. (20) and (21), respectively

$$l_{dt} = \alpha K d_b \frac{f_y}{\sqrt{f_c}} \quad (20)$$

$$l_{dc} = \frac{\alpha d_b f_y}{4\sqrt{f_c}} \geq 0.04\alpha d_b f_y \quad (21)$$

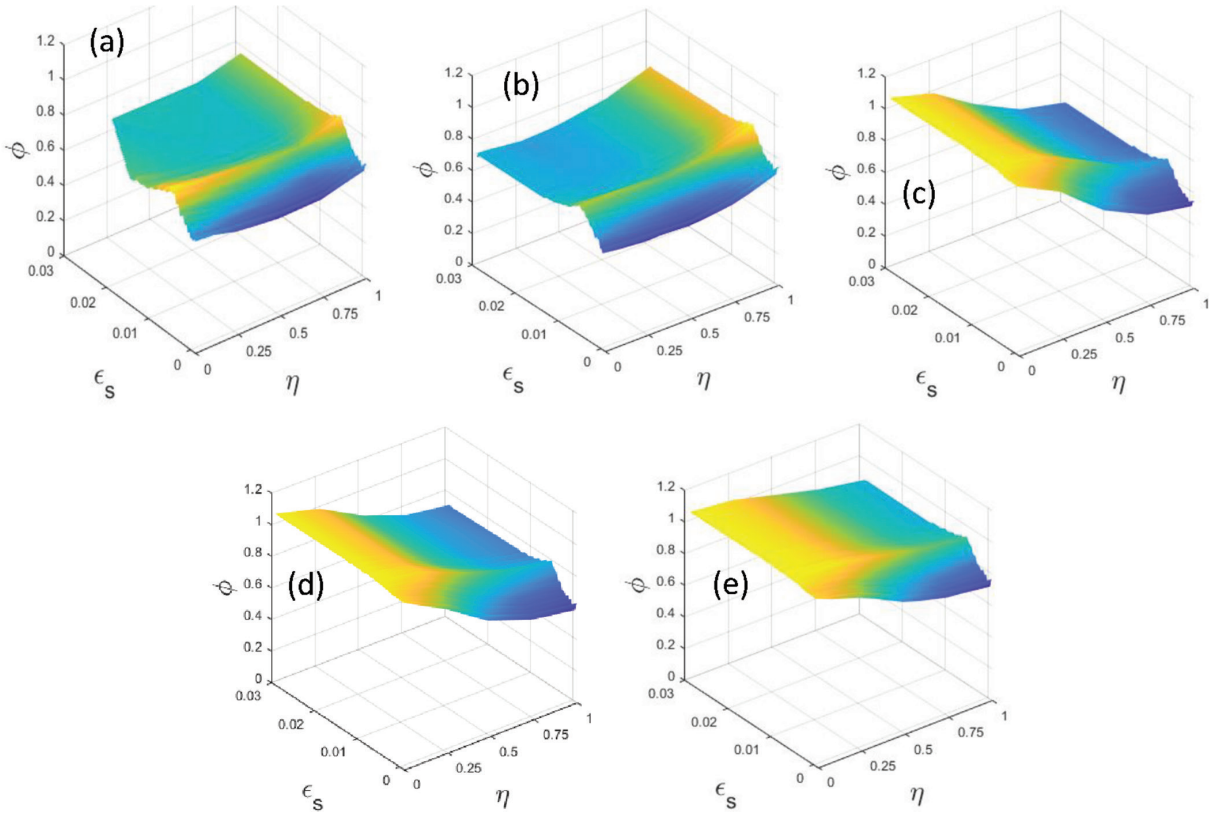


Fig. 10—Reliability surface for column reinforced with 2% reinforcement ratio: (a) Eq. (11); (b) Eq. (12); (c) Eq. (13); (d) Eq. (14); and (e) Eq. (15).

The value of α was determined considering the maximum increase in the development length of the bar of a given diameter. The maximum increase was 78% at f_y = 750 MPa (110 ksi) as compared to f_y = 420 MPa (60 ksi). Nearly parallel curves of different diameter bars in Fig. 9 signifies that this increase is insensitive to the reinforcing bar diameter. These data indicate that the development length in the design requires a nearly 78% increase for the types of bars employed. These findings are similar to those reported by Rafi et al.[4] related to the influence of f_y on the rotation capacity of RC beams. Taking a corollary from the 50% increase in the rotation capacity suggested by Rafi et al.,[4] the same increase in the development length is proposed herein, implying α = 1.5.

Strength-reduction factor

Three-dimensional surface plots were obtained for all the employed ρ values (1 to 4%) and load combinations (Eq. (11) to (15)). A typical example of these surfaces for all the employed load combinations at ρ = 2% is illustrated in Fig. 10. The plots of surfaces at other ρ values are similar to those in Fig. 10. It is seen that ϕ values increase with η at each ε_s for Eq. (11) and (12) and decrease for Eq. (13) to (15). This type of behavior can be explained (first) based on higher inherent variation in snow, wind, and earthquake loadings, as indicated by their higher *V* values. In addition, because the quantification of these aforementioned load types is dependent on the dead load quantity, increasing values of η result in increased variability in the total load quantity due to higher individual load factors for *S*, *W*, and *E* in the load combinations. This causes a reduction in ϕ for the loading combinations given by Eq. (13) to (15).

Figure 11 illustrates the variations of ϕ with η at different ε_s values. The plots at ρ = 2% are shown in Fig. 11 as a typical example. The bands of variations have been formed by joining the upper and lower values of ϕ over the full range of η values at a given ε_s for each load combination. It is seen in Fig. 11 that variations in ϕ with η at each ε_s are small for the load combinations given by Eq. (11) and (12). On the other hand, the variability in ϕ is large, with η at each ε_s for the remaining load combinations, resulting in wide bands of variations in ϕ. Further, the thickness of the band of variability in ϕ values reduces considerably at $\varepsilon_s \geq 0.005$ for load combinations given by Eq. (13) to (15).

Based on the previous, an average value of ϕ over the full range of η at the same ε_s was determined for the load combinations given by Eq. (11) and (12) at each ρ. Figure 12 illustrates the curves of average ϕ values at each ρ as a function of ε_s. It is seen that variations in ϕ with ρ are negligible at the same ε_s. This is contrary to the findings reported by Szerszen et al.,[13] as these authors reported that the reliability index is highly sensitive to ρ. Based on the negligible variations of the data of ϕ with ρ at each strain, an average value of ϕ is determined and is presented in Fig. 12. A comparison of the average curve is also made with the ϕ values proposed by ACI 318-08.[3] It is seen that the average ϕ = 0.62 for the compression-controlled section is smaller, as suggested by ACI 318-08.[3] Further, ϕ increases linearly to 0.81 at ε_s = 0.005, which is the endpoint of the transition zone.[3] The constant ϕ plateau in the tension-controlled region ends at

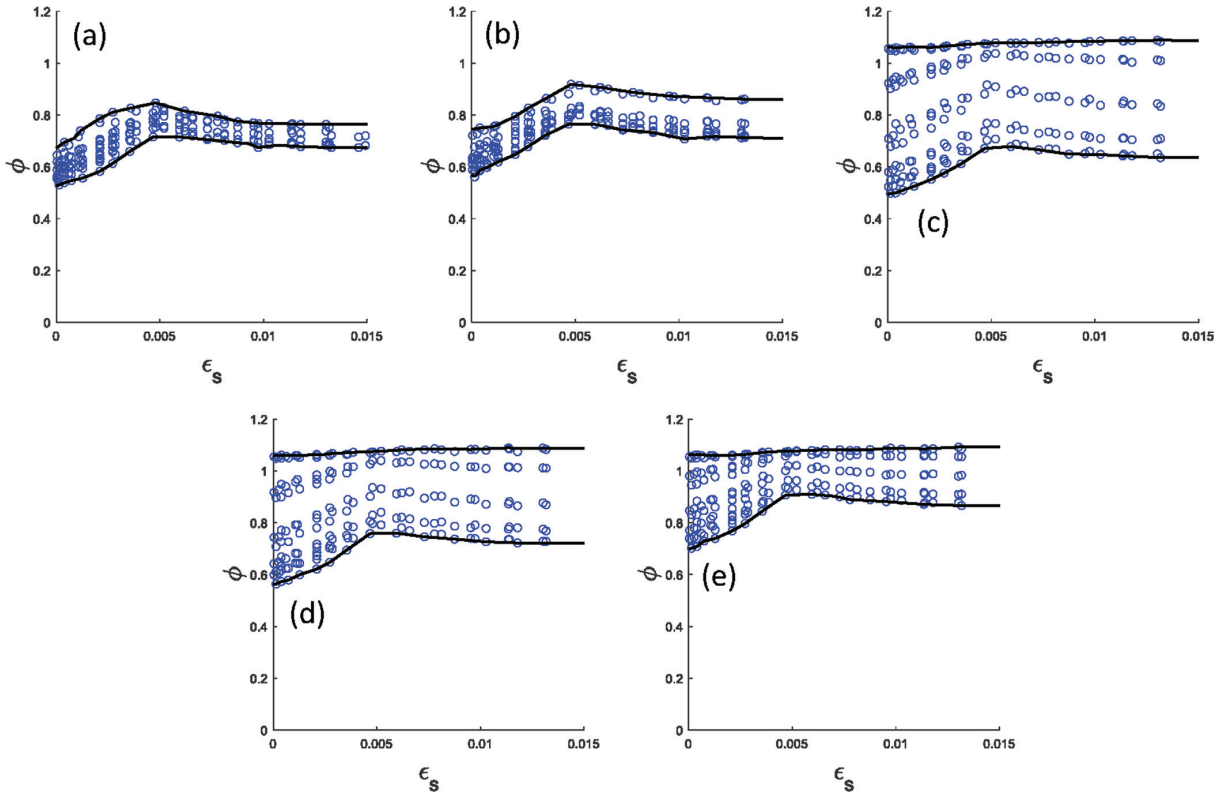


Fig. 11—Strength-reduction factor for column reinforced with 2% reinforcement ratio in function of tensile strain and load ratio: (a) Eq. (11); (b) Eq. (12); (c) Eq. (13); (d) Eq. (14); and (e) Eq. (15).

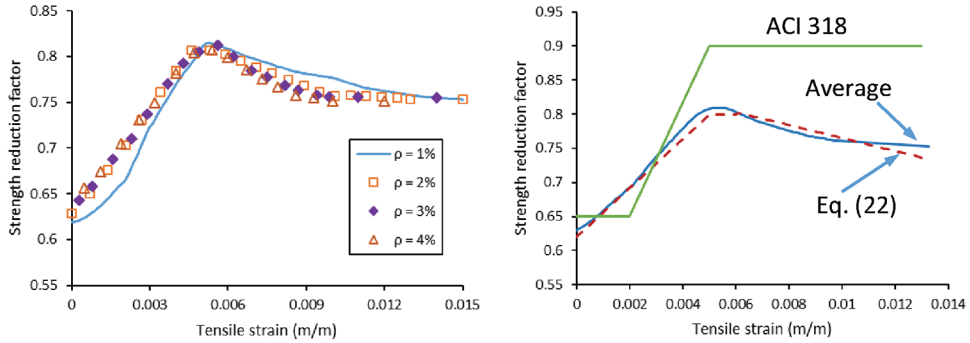


Fig. 12—Variations in strength-reduction factor versus tensile strain.

ε_s = 0.006, followed by a linearly decreasing trend. Note that Rafi et al.[4] reported ϕ as 0.60 and 0.80 for the compression-controlled and tension-controlled sections, respectively, which are similar to those found in this paper. The small differences could be attributed to the reason that the method of analysis employed by Rafi et al.[4] did not include statistical variation in the load. Further, because control on the drift demand of the structure is likely to limit the value of ε_s in the tension-controlled region, the value of ϕ may be taken as constant for the under-reinforced sections, neglecting the decreasing trend of the last branch in Fig. 12. Nevertheless, the following model is suggested for the calculation of ϕ (Eq. (22)) from the average curve in Fig. 12

$$\phi = 36\varepsilon + 0.62 \text{ for } \varepsilon \le 0.005 \quad (22a)$$

$$\phi = 0.80 \text{ for } 0.005 \le \varepsilon \le 0.006 \quad (22b)$$

$$\phi = -10\varepsilon + 0.86 \text{ for } \varepsilon \ge 0.006 \quad (22c)$$

The resulting curve from Eq. (22) is also shown in Fig. 12, which compares well with the average curve.

CONCLUSIONS

The analytical behaviors of concrete beam-columns reinforced with steel reinforcing bars with unintended high strength are studied in this paper. The effects of these bars on the strength and strength-reduction factors of the column and development length requirements of the reinforcing bar were analyzed. The following conclusions can be drawn from the presented study in this paper:

1. The use of steel reinforcing bars with unintended high tensile strength could affect the column behavior by changing it from tension-controlled to compression-controlled at a lesser axial load level compared to the load considered in the design. This also reduces the curvature capacity, affecting

the column ductility. This type of behavior is influenced by the concrete strength and reinforcement ratio, while it was independent of the cross-sectional dimensions.

2. Larger development lengths in tension and compression are required as the tensile strength of the bar increases for avoiding failure of bond strength.

3. Necessary modifications in the design calculations have been suggested as Eq. (17), (19), (20), and (21) to address the issues related to the change in column response from tension-controlled to compression-controlled and to avoid bond failure.

4. Strength-reduction factors have been proposed for a reinforced concrete (RC) section behavior ranging from pure compression to a purely flexural behavior (Eq. (22)).

AUTHOR BIOS

Muhammad Masood Rafi *is a Professor and Chair in the Department of Earthquake Engineering at NED University of Engineering and Technology, Karachi, Sindh, Pakistan, and is the Editor-in-Chief of the* NED University Journal of Research*. His research interests include seismic analysis and retrofitting of reinforced concrete (RC) and masonry structures, finite element analysis of RC structures, fire resistance of concrete structures, post-earthquake fire, behavior of fiber-reinforced polymer (FRP)-reinforced concrete structures, deflection of concrete structures, experimental analysis of RC structures, recycling of concrete, and disaster management and risk reduction.*

Muhammad Saad Khan *is a Lecturer in the Department of Civil Engineering at NED University of Engineering and Technology. His research interests include image processing, recycled concrete, numerical modeling, and reversed-cyclic behavior of reinforced concrete members.*

DECLARATION OF CONFLICTING INTERESTS

The author(s) declare(s) that there is no conflict of interest.

REFERENCES

1. ASTM A615/A615M-05a, "Standard Specification for Deformed and Plain Carbon-Steel Bars for Concrete Reinforcement," ASTM International, West Conshohocken, PA, 2005.

2. BS 4449:1997, "Specification for Carbon Steel Bars for Reinforcement of Concrete," British Standards Institution, London, UK, 1997.

3. ACI Committee 318, "Building Code Requirements for Reinforced Concrete (ACI 318-08) and Commentary (ACI 318R-08)," American Concrete Institute, Farmington Hills, MI, 2008, 473 pp.

4. Rafi, M. M.; Lodi, S. H.; and Nizam, A., "Chemical and Mechanical Properties of Steel Rebars Manufactured in Pakistan and Their Design Implications," *Journal of Materials in Civil Engineering*, ASCE, V. 26, No. 2, 2014, pp. 338-348. doi: 10.1061/(ASCE)MT.1943-5533.0000812

5. Ravindra, M. K., and Galambos, T. V., "Load and Resistance Factor Design for Steel," *Journal of the Structural Division*, ASCE, V. 104, No. 9, Sept. 1978, pp. 1337-1353.

6. Ellingwood, B.; Galambos, T. V.; MacGregor, J. G.; and Cornell, C. A., "Development of a Probability Based Load Criterion for American National Standard A58: Building Code Requirements for Minimum Design Loads in Buildings and Other Structures," NBS Special Publication 577, National Bureau of Standards, Washington, DC, 1980, 222 pp.

7. Nowak, A. S., and Collins, K. R., *Reliability of Structures*, CRC Press, Boca Raton, FL, 2013, 407 pp.

8. Iatsko, O., and Nowak, A. S., "Load and Resistance Factors for Concrete Bridges and Buildings," *Dennis Mertz Symposium on Design and Evaluation of Concrete Bridges*, SP-340, A. S. Nowak and H. Nassif, eds., American Concrete Institute, Farmington Hills, MI, 2020, pp. 19-31.

9. Grant, L. H.; Mirza, S. A.; and MacGregor, J. G., "Monte Carlo Study of Strength of Concrete Columns," *ACI Journal Proceedings*, V. 75, No. 8, Aug. 1978, pp. 348-358.

10. Cardoso, J. B.; de Almeida, J. R.; Dias, J. M.; and Coelho, P. G., "Structural Reliability Analysis Using Monte Carlo Simulation and Neural Networks," *Advances in Engineering Software*, V. 39, No. 6, 2008, pp. 505-513. doi: 10.1016/j.advengsoft.2007.03.015

11. Kankam, C. K., "Bond Strength of Reinforcing Steel Bars Milled from Scrap Metals," *Materials & Design*, V. 25, No. 3, 2004, pp. 231-238. doi: 10.1016/j.matdes.2003.09.011

12. Kankam, C., and Adom-Asamoah, M., "Strength and Ductility Characteristics of Reinforcing Steel Bars Milled from Scrap Metals," *Materials & Design*, V. 23, No. 6, 2002, pp. 537-545. doi: 10.1016/S0261-3069(02)00028-6

13. Szerszen, M. M.; Szwed, A.; and Nowak, A. S., "Reliability Analysis for Eccentrically Loaded Columns," *ACI Structural Journal*, V. 102, No. 5, Sept.-Oct. 2005, pp. 676-688.

14. ACI Committee 318, "Building Code Requirements for Reinforced Concrete (ACI 318-19) and Commentary (ACI 318R-19) (Reapproved 2022)," American Concrete Institute, Farmington Hills, MI, 2019, 624 pp.

15. Bae, S., and Bayrak, O., "Stress Block Parameters for High-Strength Concrete Members," *ACI Structural Journal*, V. 100, No. 5, Sept.-Oct. 2003, pp. 626-636.

16. Szerszen, M. M., and Nowak, A. S., "Calibration of Design Code for Buildings (ACI 318): Part 2—Reliability Analysis and Resistance Factors," *ACI Structural Journal*, V. 100, No. 3, May-June 2003, pp. 383-391.

17. Zhang, T., "Partial Material Strength Reduction Factors for ACI 318," master's thesis, The University of Western Ontario, London, ON, Canada, 2017.

18. Sutrisno, W.; Piscesa, B.; and Irmawan, M., "Strength Reduction Factor of Square Reinforced Concrete Column Using Monte Carlo Simulation," *Journal of Civil Engineering*, V. 35, No. 2, 2020, pp. 50-56. doi: 10.12962/j20861206.v35i2.8657

19. Israel, M.; Ellingwood, B.; and Corotis, R., "Reliability-Based Code Formulations for Reinforced Concrete Buildings," *Journal of Structural Engineering*, ASCE, V. 113, No. 10, 1987, pp. 2235-2252. doi: 10.1061/(ASCE)0733-9445(1987)113:10(2235)

20. Benjamin, J. R., and Cornell, C. A., *Probabilidad y Estadística en Ingeniería Civil*, McGraw Hill, México City, Mexico, 1981.

21. Ang., A., and Tang, W. H., *Probability Concepts in Engineering Planning and Design. Vol. II*, John Wiley & Sons, Inc., New York, 1984.

22. Hong, H. P., "Risk Analysis and Decision Making in Engineering (CEE 4458A)," The University of Western Ontario, London, ON, Canada, 2015.

23. Marinilli, A., "Simplified Stochastic Analysis of Reinforced Concrete Frames under Seismic Loads," *14th World Conference on Earthquake Engineering* (14WCEE), Beijing, China, Oct. 12-17, 2008.

24. Lutomirski, T. A.; Nowak, A. S.; and Lutomirska, M., "Strength Reduction Factor for Circular Reinforced Concrete Columns," *ACI Structural Journal*, V. 119, No. 4, July 2022, pp. 303-310. doi: 10.14359/51734653

25. Baji, H., "Calibration of the FRP Resistance Reduction Factor for FRP-Confined Reinforced Concrete Building Columns," *Journal of Composites for Construction*, ASCE, V. 21, No. 3, 2017, p. 04016107. doi: 10.1061/(ASCE)CC.1943-5614.0000769

ACI STRUCTURAL JOURNAL TECHNICAL PAPER

Title No. 121-S69

Experimental Study on Scale Effect of Eccentrically Compressed Reinforced Concrete Columns Strengthened with Carbon Fiber-Reinforced Polymer

by Jianhui Si, Yuan Zhou, Zhaobao Zeng, Kai Li, Jiannan Hu, Zewei Liu, and Xinchao Ding

Strictly following the similarity principle of specimen size, eccentricity, and carbon fiber-reinforced polymer (CFRP) strengthening layers, three groups of reinforced concrete square columns with different scales were designed. Experimental studies on eccentric compression of unstrengthened columns and CFRP-strengthened columns were carried out. The failure characteristics of specimens of various sizes were obtained, as well as the bearing capacity, ductility coefficient, lateral deflection, CFRP, and steel bar strain were analyzed. The test results showed an improved ductility, stiffness, and bearing capacity of eccentrically compressed reinforced concrete columns, strengthened with CFRP. However, the strengthening effect is inversely proportional to the size of the specimen and has a more obvious size effect.

Keywords: carbon fiber-reinforced polymer (CFRP) strengthened columns; reinforced concrete square column; size effect; small eccentric compression.

INTRODUCTION

Due to various natural disasters, the increase in the service life of a building, and other factors, the safety of the structure has been reduced. The obvious solution is to demolish and rebuild, but it is very expensive for the economy and increasingly harmful to the waste of resources and the environment. Strengthening is a viable option for ensuring the safety of the structure.[1,2] Carbon fiber-reinforced polymer (CFRP) is widely used in structural strengthening and building repair fields because of its light weight, high strength, fatigue resistance, and relatively simple construction.[3-6] CFRP can effectively constrain the lateral deformation of a concrete column, putting it in a three-dimensional (3-D) compression state. Thus, the strength and ductility of columns are improved as a concrete column failure, and longitudinal reinforcement yield is delayed.[7-10] Lin et al.[11] designed eight CFRP-confined rectangular reinforced concrete columns by controlling the load eccentricity, bending direction, and CFRP thickness. The test results showed that the axial ultimate bearing capacity decreases with the increase in load eccentricity. The plane section assumption is still valid for CFRP-confined rectangular concrete columns subjected to eccentric loads. Lam et al.[12] carried out an experimental study on the compression performance of ultra-high-performance concrete (UHPC) confined by CFRP. Based on the research results, the prediction equations of compressive strength and ultimate strain of UHPC confined by CFRP are proposed. Al-Rousan[13] established a CFRP composite-confined circular reinforced concrete column model. They found that the ultimate axial strength increases and the ultimate displacement increases slightly with the rise of CFRP layers. With a more in-depth understanding of CFRP, researchers have conducted several studies on prestressed CFRP-confined concrete columns.[14-19] Lu et al.[20] designed 10 prestressed CFRP-strengthened reinforced concrete square columns for axial compression performance tests. The analysis of the experimental results showed that the greater the prestress degree and the wrapping range, the stronger the restraint of the core concrete. Wang et al.[21] investigated nine columns with varying axial compression ratios, prestress levels, CFRP layers, and prestressed CFRP wrapping areas. They found that the increase in prestress level greatly influenced the stiffness and horizontal bearing capacity of columns. Janke et al.[22] tested 45 cylindrical confined specimens and comparison specimens under axial, eccentric, single, and cyclic loading to confirm the beneficial effects of confined prestress on the residual bearing capacity of concrete.

Guo et al.[23] proposed a CFRP hoop-confined concrete stress-strain model to study the influence of specimen size on the axial compression performance of the cylinder wrapped with a CFRP ring. To study the relationship between the number of CFRP layers and size, Zhou et al.[24] conducted uniaxial compression tests on concrete cylinders using the number of CFRP layers as a variable and analyzed the parameters such as uniaxial compressive strength, peak strain, and so on, and found that there was a significant scaling effect for concrete cylinders with different confinement ratios. Besides, Zhou et al.[25] compared the results with test results of small specimens when studying the axial compression performance of large-size cylindrical concrete confined by prestressed CFRP. Wang et al.[26] produced 23 concrete square columns confined in varying sizes of CFRP. The size of the specimens, theoretical lateral CFRP confining pressure, and other factors were divided into 10 groups. The experimental results analyzed that the angular strain decreased with the increased specimen size. The effective strain factor model of CFRP considering scale effect is proposed. Furthermore, the heterogeneity of concrete is an essential factor causing the

ACI Structural Journal, V. 121, No. 5, September 2024.
MS No. S-2023-082.R6, doi: 10.14359/51740854, received March 25, 2024, and reviewed under Institute publication policies. Copyright © 2024, American Concrete Institute. All rights reserved, including the making of copies unless permission is obtained from the copyright proprietors. Pertinent discussion including author's closure, if any, will be published ten months from this journal's date if the discussion is received within four months of the paper's print publication.

Table 1—Test parameters

Specimen number	Section size, mm	Quantity	Height, mm	Cover thickness, mm	Eccentricity, mm	Layers of CFRP
ES0	100 x 100	3	300	15	19	0
ES1	100 x 100	3	300	15	19	1
EM0	200 x 200	3	600	30	38	0
EM2	200 x 200	3	600	30	38	2
EL0	300 x 300	3	900	45	57	0
EL3	300 x 300	3	900	45	57	3

scale effect. Jin et al.[27] considered the interaction between the heterogeneity of concrete and CFRP and further studied the influence of size on CFRP-confined concrete columns based on experiments and simulations.

The literature shows that CFRP-confined axially compressed concrete columns have a certain size effect. In practical engineering, reinforced concrete columns are subjected to eccentric compression. Therefore, for the first time, the authors investigated the scale effect test of using CFRP to reinforce eccentric compression columns.

RESEARCH SIGNIFICANCE

CFRP is a lightweight, high-strength, fatigue-resistant, and relatively simple construction material that is widely used in structural reinforcement and building restoration. It is able to restrain the lateral deformation of concrete columns in a three-way compressed state, delaying the destruction of concrete and the yielding of longitudinal reinforcement, thus improving the strength and ductility of the column. In actual engineering, reinforced concrete columns are basically under eccentric compression, so the first experimental study on the scaling effect of CFRP-reinforced eccentric compression columns was carried out.

TEST DESIGN

Specimen design

Most of the current experimental studies are mainly based on small-size confined concrete columns, and the proposed prediction models and design specifications do not consider the influence of size effects, which may lead to deviations and safety hazards in the research and design of confined concrete columns. Three sizes of specimens were designed: 100 x 100 x 300 mm, 200 x 200 x 600 mm, and 300 x 300 x 900 mm.

Eighteen reinforced concrete square columns were prepared for the experiment, and they were divided into three groups according to the size of the components. To reduce the contingency and discreteness of the test, there are three CFRP-strengthened columns and unstrengthened columns of different sizes in each group. The eccentricity, number of layers of CFRP, and size of the components are the design parameters of the experiment. The eccentricity increases in proportion to the size: 19, 38, and 57 mm, respectively. The specimen number is ECX, where E represents eccentric compression, and C is the cross-sectional size. From small to large are S, M, and L. X is the layers of CFRP, which are 0, 1, 2, and 3. Table 1 shows the detailed parameters of the test specimens.

Specimen strengthening

Because CFRP is soft, the angle of the columns was smoothed using an angle grinder to avoid CFRP damage at the sharp point of the specimens. Then the concrete columns were cleaned with sandpaper, mixed epoxy resin, and curing agent in the proportion of 2:1, evenly spread on the surface of the concrete columns. CFRP was pasted on the concrete columns surface and surrounded by a circle. The overlap length of the front and rear was 150 mm; thus, the surface was completely wrapped. A layer of epoxy resin adhesive was coated on the surface, and the CFRP was fully impregnated by cylinder rolling. This operation was repeated until the required number of layers of CFRP was completed. The width of the CFRP was 300 mm. A layer in EM2 and EL3 must be wrapped using multiple CFRP with a lap length of 10 mm.

Material mechanical properties

The specimens were made of commercial concrete from the same batch and strength grade of C30. Mechanical properties of three groups (three test blocks in each group) of cube specimens with a side length of 150 mm were tested based on the standard method in GB 50010-2010.[28] The average compressive strength of standard-size concrete cubes measured was 37.86 MPa. The longitudinal bars and stirrups adopt different strength grades of steel bars in which the longitudinal bars are HRB400 steel bars, and the stirrups are HRB335 steel bars. The mechanical properties of steel bars are measured using the Standard Test Method for Concrete Structures,[29] as measured by the electronic tensile testing machine of the steel bars, with the specific parameters listed in Table 2. The first-class CFRP with a width of 300 mm is used to facilitate the test, and the results submitted by the manufacturer obtain its mechanical properties. Table 3 presents the details.

Test device and measurement content

The device used in the test is a 500 ton servo hydraulic long-column testing machine in the Structural Laboratory of Xi'an University of Technology, as shown in Fig. 1. Before the test, dry powder for plastering of strengthened columns (to observe the development of cracks) and the eccentric load were applied using two single-hinge bearings placed at both ends of the specimen. Calibration of eccentricity and single-hinge support by infrared rays ensure that applied load and eccentricity are in a straight line. The load and displacement of the concrete column were collected and monitored by data collection equipment connected to the

Table 2—Reinforcement parameters

Part	Grade	Size, mm	YS, MPa	UTS, MPa
Longitudinal reinforcement	HRB400	φ = 8	482.12	709.56
	HRB400	φ = 16	441.19	637.96
	HRB400	φ = 25	459.93	642.16
Stirrup	HRB335	φ = 6	364.16	513.61
	HRB335	φ = 8	384.22	552.73
	HRB335	φ = 10	390.96	540.26

Table 3—Material parameters

Type	Tensile strength, MPa	Elasticity modulus, GPa	Elongation, %	Thickness, mm
CFRP	3520	268	1.77	0.167

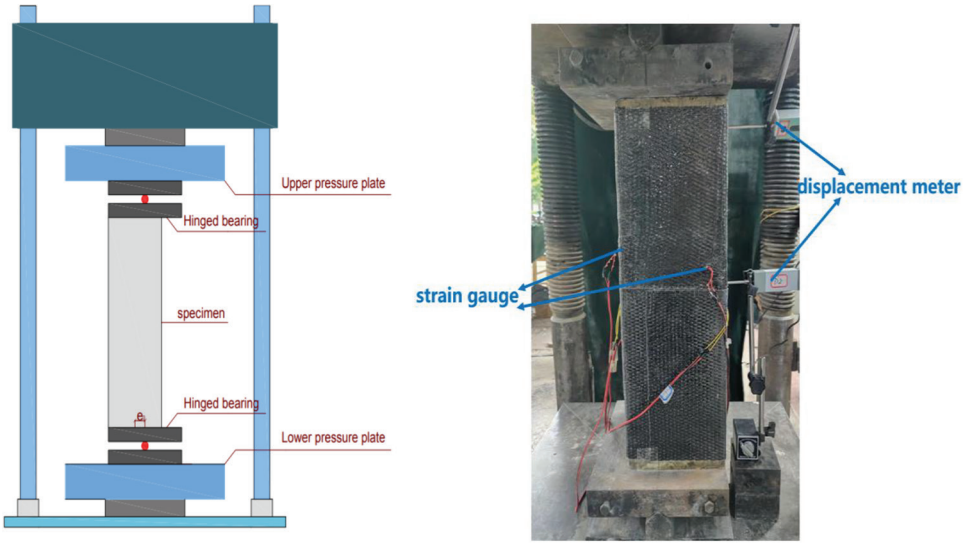


Fig. 1—Test device diagram.

long-column testing machine during the eccentric loading process. Strain gauges were placed in the middle of the reinforcement and concrete columns in the near and far eccentric areas, including the measuring point position of CFRP, which was consistent with that of the concrete column. Displacement meters were placed in the upper and middle of the concrete column to measure its lateral deflection. The structural design drawing of the component and the schematic diagram of the measuring points are shown in Fig. 2.

Test plan

The test loading method was divided into two steps. First, based on load-displacement loading mode. Each 10% of the predicted ultimate load is divided into one level. For each level load for 3 minutes, the data were collected. The loading rate of each level varies due to the different estimated ultimate loads caused by the various sizes of the components, ranging from 0.2 to 0.4 and 0.6 kN/s. After reaching 80% of the ultimate load, displacement-controlled loading was adopted with loading rates of 0.1, 0.2, and 0.3 mm/min. When the load drops to 70% of the ultimate load, stop loading is a failure sign.

EXPERIMENTAL OBSERVATIONS

As shown in Fig. 3, the failure modes of unstrengthened columns of various sizes are relatively similar. At the beginning of loading, there was no obvious change in these specimens. When the load reached 50% of the ultimate bearing capacity, cracks appeared in the corner of the concrete column near the eccentric area. As the load increased, microcracks developed and extended, and cracks appeared on the concrete column side. Near the ultimate bearing capacity, the cracks extended to the middle of the concrete column near the eccentric area, and the crack penetration and width increased gradually. With the sound of sporadic concrete column fragmentation, the load appeared to have a "cliff-like" decline, and the concrete column was suddenly crushed. The concrete column protective layer fell off, and some concrete fell off. The crack width reached the maximum, and the end of the concrete column near the eccentric side was crushed. The damage was relatively sudden and was classified as brittle damage.

Unlike the unstrengthened columns, the failure shape of the strengthened columns was significantly changed after loading, and the concrete column damage was more serious. Figures 4 and 5 show the details of the damage. At

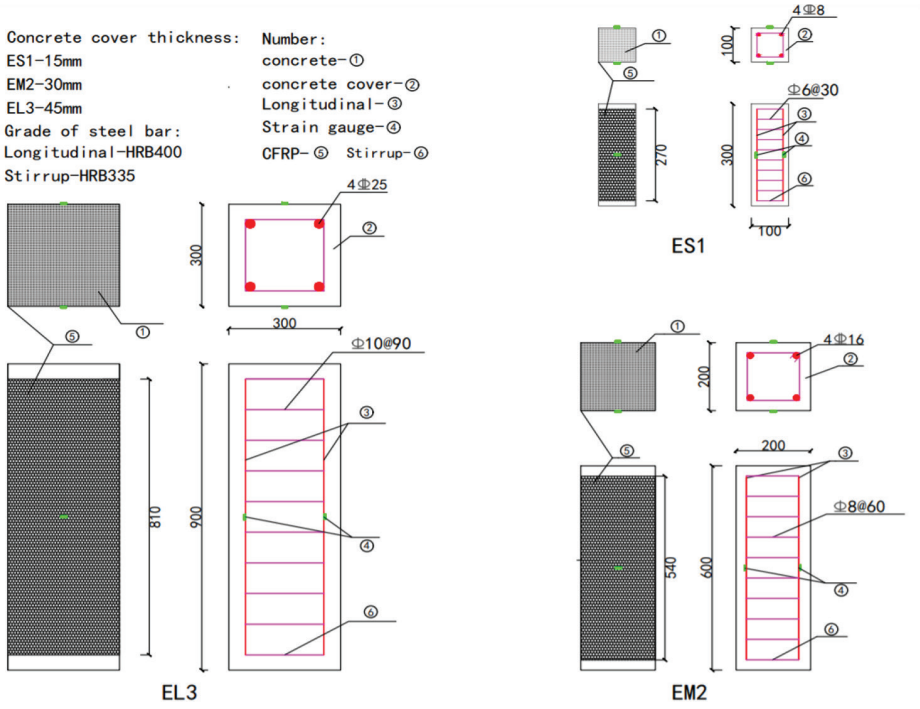


Fig. 2—Drawing of structural design and measuring point layout.

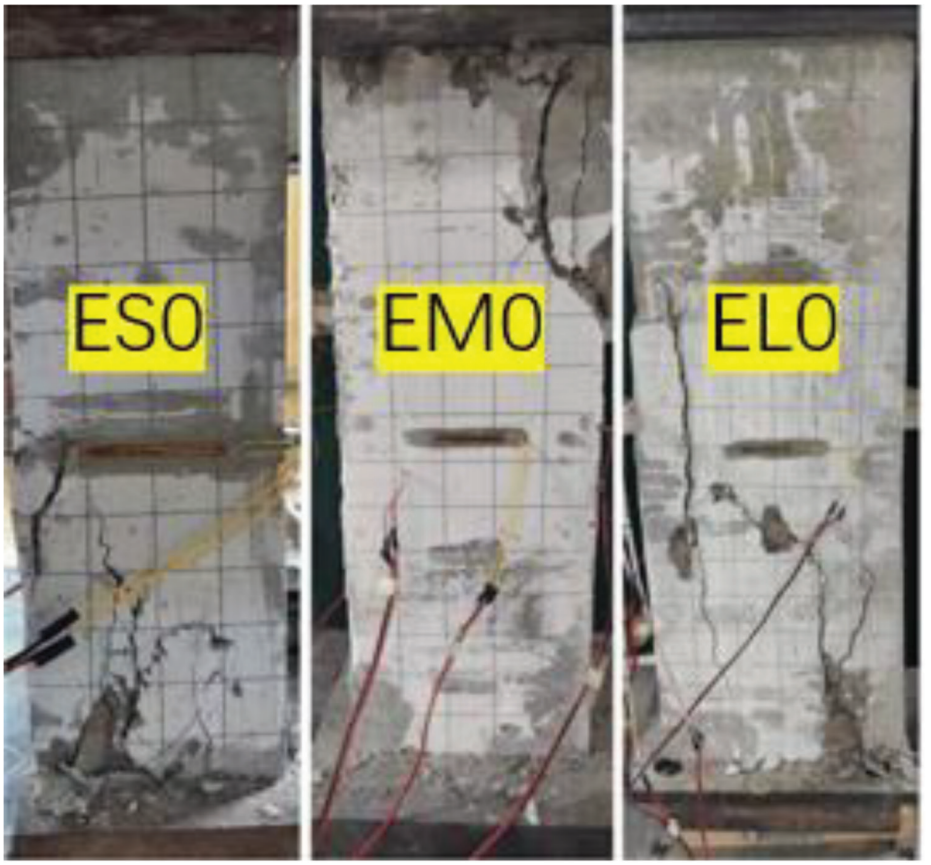


Fig. 3—Typical failure modes of unstrengthened columns.

the initial loading stage, the lateral deflection of the CFRP-strengthened columns was small, the load-displacement curve grew linearly, and the columns were in the elastic stage. As the load reached 70% of the ultimate bearing capacity, cracking sounds of fragments began to appear, and the concrete column became bent. As the lateral deflection of the concrete column increased, the lateral restraint of CFRP was continuously strengthened to prevent cracks from forming. When the load reached ultimate bearing capacity, CFRP provided a restraining force to keep the structure under



Fig. 4—Typical failure modes of CFRP-strengthened columns.



Fig. 5—Local failure pattern of CFRP-strengthened columns.

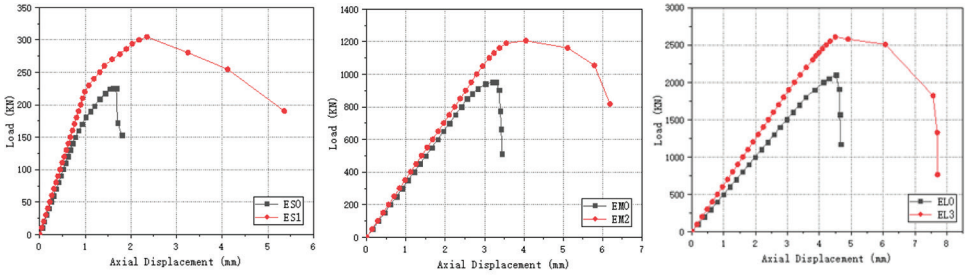


Fig. 6—Load-axial displacement curve.

pressure, while the columns' deflection increased significantly. When the load continued to drop, the CFRP strain continued to increase, and the specimen could still withstand the axial load. After that, the sound became denser, and the CFRP was gradually torn, which further reduced the appearance of dull explosions. The concrete near the eccentric area of the column was crushed, and a little concrete of the column fell off. The CFRP was pulled off at the corners, and the axial load was greatly reduced. Observing the wrapped CFRP, the bonding between the second and third CFRP layers was complete without peeling. Local wrinkles appeared due to the columns' deformation in the middle of the CFRP. CFRP-strengthened columns had more significant deformation and buckling of the bars near the eccentric side compared to unstrengthened columns.

Table 4—Test results of strengthened concrete columns by eccentric loading CFRP composite materials

Specimen number	Ultimate load, kN	Ultimate load increase, %	Lateral deflection, mm	Peak deflection, mm	Limit displacement, mm
ES0	228.5	—	0.994	0.956	1.8
ES1	307.5	34.57	6.801	1.169	5.36
EM0	963.5	—	0.894	0.832	3.44
EM2	1223.5	26.98	5.482	1.460	6.19
EL0	2101.4	—	0.822	0.772	4.67
EL3	2609.6	24.23	4.590	2.54	7.71

Table 5—Displacement ductility coefficient

Specimen	Δ_y, mm	Δ_u, mm	μ
ES1	1.566	3.986	2.545
EM2	3.404	5.832	1.713
EL3	4.234	6.653	1.583

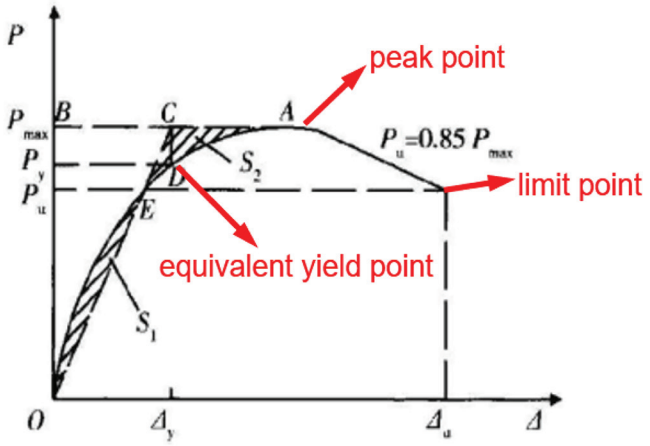


Fig. 7—Calculation diagram based on equivalent elastic-plastic energy method.

TEST RESULTS AND ANALYSIS

Analysis of bearing capacity

The ultimate bearing capacity of each size of CFRP-strengthened column and the unstrengthened columns were considered as the average value of a group of test pieces to reduce the influence of error, contingency, and dispersion. Table 4 shows the results of each group of test pieces.

The test results show that the average ultimate bearing capacity of ESO, EM0, and ELO under eccentric load are 228.5, 963.5, and 2101 kN. The ultimate bearing capacity of ES1, EM2, and EL3 under the strengthening of CFRP are improved to varying degrees: 307.5, 1223.5, and 2609 kN, respectively, and the ultimate bearing capacity is increased by 34.57, 26.98, and 24.23%, respectively, as shown in the unstrengthened columns of Table 4. CFRP strengthened concrete columns can improve the load-bearing capacity and ductility of the columns. The reason is that the lateral pressure provided by the CFRP constrains the deformation of concrete columns under uniaxial stress, so the columns are in a three-way compression state, and the strengthening effect is significant. Even if the number of layers, eccentricity, stirrup spacing, and steel bar diameter of CFRP are increased proportionally to the increase in size, the strengthening effect still decreases to some extent as the size of the columns increases because the larger the cross-sectional area of concrete column, the lower the constraint of CFRP on the concrete in the core area.

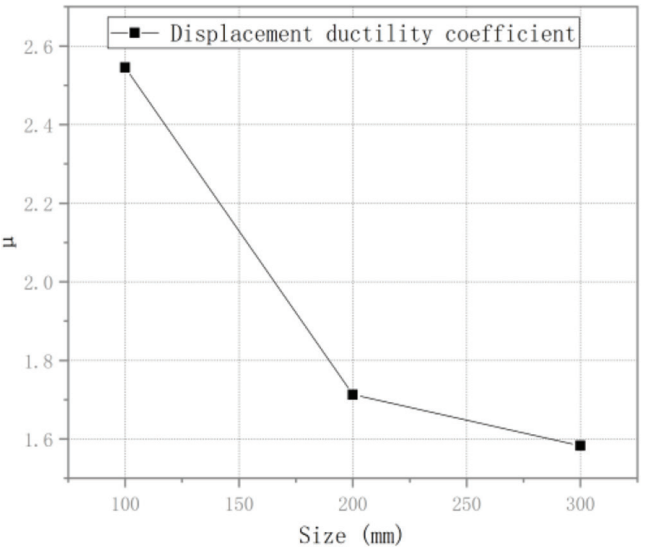


Fig. 8—Displacement ductility coefficient-load curve.

Load-axial displacement curve analysis

Figure 6 depicts the load-axial displacement curve of the unstrengthened columns and the CFRP-strengthened columns. At the beginning of test loading, the contrast columns are in the elastic stage. The load that the specimen could work under in a short period of time drops rapidly after being loaded to the ultimate load. The axial displacement change between the failure and ultimate load points is very small, resulting in cliff-type sliding and brittle failure.

The elastic stage of the CFRP-strengthened columns is longer than the unstrengthened columns, which can usually reach approximately 75% of the ultimate load. The maximum axial displacement increased significantly. The unstrengthened columns from small to large are 1.80, 3.44, and 4.67 mm, and the CFRP-strengthened columns are 5.46, 6.19, and 7.71 mm, with an increase of 203.3, 79.9, and 65.1%. Simultaneously, the slope of the load-axial displacement curve of the strengthened columns is larger than that of the unstrengthened columns, indicating that the stiffness of the specimens is significantly enhanced after CFRP strengthens the columns. As the load increases, the specimens enter the elastoplastic stage, deformation increases, and the restraint effect of CFRP increases so that the slope of the curve does

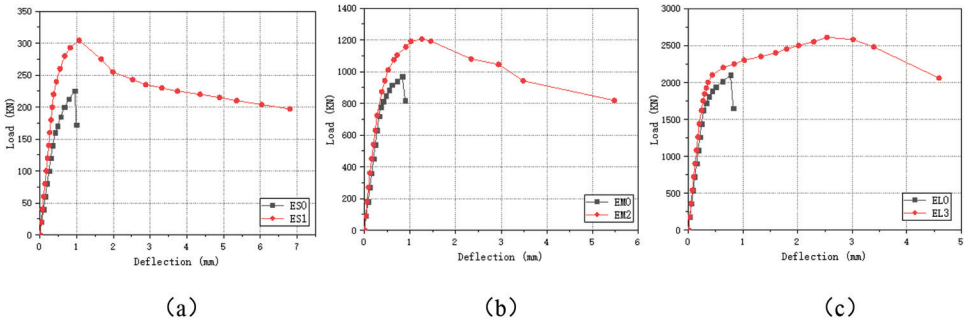


Fig. 9—Load-deflection curves for lateral displacement.

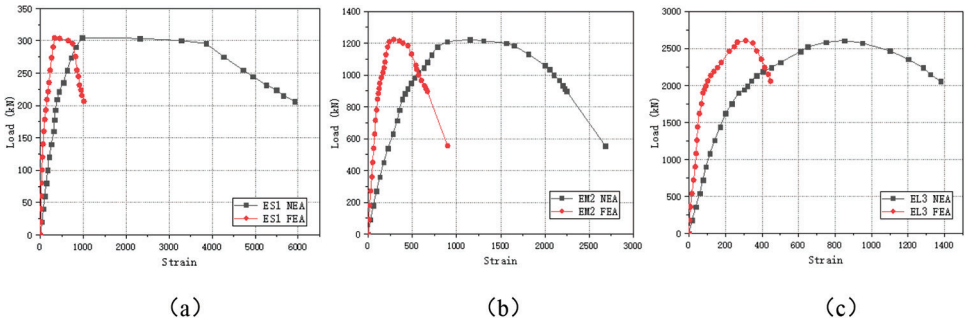


Fig. 10—Load-strain curves of CFRP sheet.

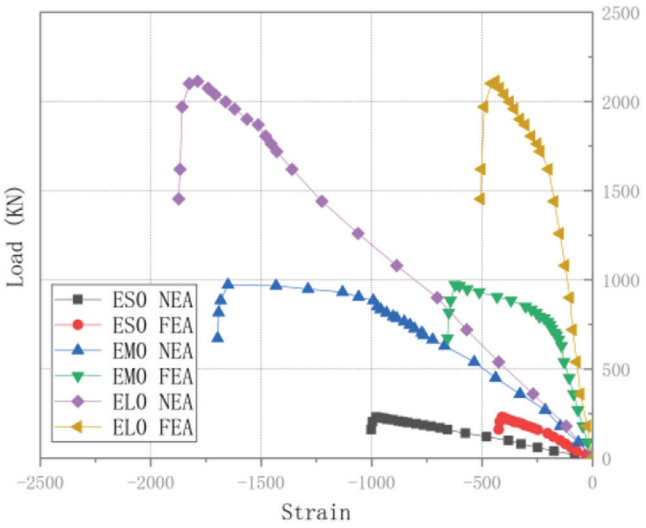


Fig. 11—Load-strain curves of column strengthened with CFRP.

not reduce significantly. However, the slope of the curve of the unstrengthened columns is relatively gentle, and the growth rate of axial displacement is increased. When the ultimate bearing capacity is reached, the concrete column suffers severe damage, reducing its mechanical properties and bonding concrete and steel bars. The load then begins to decrease, and the curve of the CFRP-strengthened columns gradually decreases. With the increase in axial displacement, the core concrete is crushed, the CFRP is gradually torn, and the constraining force of the core area is reduced, resulting in a faster decline in the bearing capacity of the CFRP-strengthened columns and a steeper curve. Compared with the unstrengthened columns under the same load, the concrete columns strengthened with CFRP have increased axial displacement, resulting in severe concrete column damage. The ductility of the specimen is significantly improved so that the structure has better safety.

Displacement ductility coefficient

The displacement ductility coefficient can reflect the macroscopic ductility of the columns. The larger the displacement ductility coefficient, the stronger the deformability of the structural columns and vice versa. The ductility coefficient μ is defined as the ratio of the ultimate displacement Δ_u to the yield displacement Δ_y, as presented in the following formula (1)

$$\mu = \Delta_u/\Delta_y \quad (1)$$

The load displacement of an ideal elastoplastic structure has an obvious yield point, so the yield displacement and yield load of the component can be easily determined. The equivalent elastoplastic energy method is frequently used to determine the yield point for the load-displacement curve without an obvious yield point. It is based on energy equivalence to convert the actual skeleton curve into an ideal elastoplastic curve for calculation. As shown in Fig. 7, the point corresponding to 85% of the peak load in the curve is E. The straight-line BA formed by the connection of point E and origin O intersects at point C, the displacement corresponding to the abscissa of point C is Δ_y, and Δ_u is the displacement corresponding to the peak load dropping 15% when the load-displacement curve is in the descending section. Table 5 depicts the results based on calculation. The displacement ductility coefficient decreases gradually with the increase in component size, showing a certain size effect, as shown in Fig. 8.

Table 6—Relevant calculation parameter values

Specimen	N, kN	σ_{s1}, N/mm^2	σ_{s2}, N/mm^2	ε_b	$f_{c,k}$, N/mm^2	$f_{cc,k}$, N/mm^2	$(f_{cc,k}/f_{cc}) - 1$	$(f_{cc,k}/f_{c,k}) - 1$
ES0	228.5	200.2	84.9	0.462	43.59	—	0.689	0.0094
ES1	307.5	1264.4	406.8	0.607	—	44.00		
EM0	963.5	339.3	131.2	0.479	45.03	—	0.776	0.0278
EM2	1223.5	646.6	212.0	0.569	—	46.28		
EL0	2101.4	374.6	101.1	0.471	43.03	—	0.860	0.1264
EL3	2609.6	477.2	156.4	0.543	—	48.47		

Load-deflection curve analysis

Figure 9 depicts the load-deflection (lateral displacement) curve of unstrengthened and CFRP-strengthened columns. In the figure, the ordinate is the eccentric load, and the abscissa is the deflection. During the loading process, the middle and upper parts of the specimens will produce certain deformation, so the deflection of specimens is the difference between the deflection of the middle and upper parts.

According to the load-deflection curve, the slope of the curve is large in the early stage of the test, and the deflection increases slowly. When the load reaches approximately 60% of the actual peak load, the slopes of the curves of ES0, ES0, and EL0 begin to decrease, and the deflection starts to increase rapidly. ES1, EM2, and EL3 were strengthened by CFRP, and the stiffness of the columns increased, limiting lateral deformation. So, the lateral deflection growth at $0.6N_u$ is gentler than that of the unstrengthened columns. When the load is $0.75N_u$, the CFRP has a certain degree of damage, and the deflection increases rapidly. Compared with ES0, the maximum deflection of EM0 and EL0 was decreased by 12.97 and 19.25%, while the maximum deflection of EM2 and EL3 decreased by 19.38 and 32.5% compared with ES1. Concrete defects are unavoidable because it is a heterogeneous material. According to statistical theory, the larger the component, the more internal defects it contains, and the more easily the concrete column can be damaged. As a result, the maximum deflection decreases as the size of the CFRP-strengthened and unstrengthened columns grows. The peak deflections of ES1, EM2, and EL3 were increased by 22.28%, 75.48%, and 228.93%, respectively, compared with ES0, EM0, and EL0. Compared with ES0, the peak deflections of EL3 and EM2 are increased by 24.89% and 117.80%, respectively. In summary, CFRP-strengthened concrete columns can improve the plastic deformation capacity of columns. The increase rate of the peak deflection improves significantly as the number of CFRP layers increases. However, the load decreases rapidly with the increase in specimen size, and the maximum deflection decreases. Compared with the specimen with fewer strengthening layers of CFRP, the specimen shows certain brittleness. For the same load, the deflection is smaller than that of the unstrengthened column, which improves the safety reserve of the structure.

STRAIN ANALYSIS

Strain of carbon fiber-reinforced polymer

The lateral constraint force increases with the deformation of concrete columns for CFRP-strengthened columns, so the lateral constraint provided by CFRP belongs to the passive constraint. Before CFRP tears, the deformation of the columns is coordinated with the deformation of CFRP, and the deformation of the concrete section and its restraint can be understood from the hoop strain of CFRP.

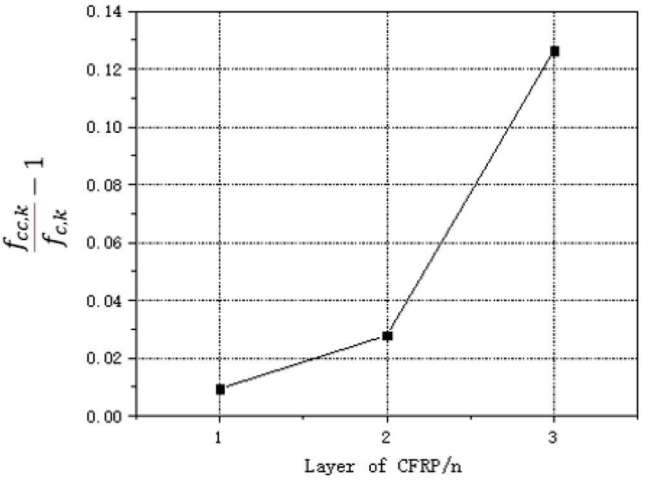


Fig. 12—Relationship between relative strength of confined concrete and layer of CFRP.

Figure 10 shows the load-strain curve of CFRP-strengthened columns. The ordinate is the load, and the abscissa is the CFRP strain measured by strain gauges placed in the middle of the near eccentric area (NEA) and the far eccentric area (FEA) of the columns. During the entire loading process, all CFRPs are in tension, as shown in Fig. 9. In the initial loading stage, the concrete column deforms less before cracks, has little effect on CFRP extrusion, and hardly participates in the work. However, as the load increases, the continuous development of microcracks and the penetration lead to more significant deformation of the concrete column. CFRP restrains the lateral deformation of the column and has a greater restraint on the core concrete. Simultaneously, the CFRP generates a hoop tensile force, which causes the CFRP to be deformed under the tension. When the load reaches the peak, the concrete column fails, CFRP provides the binding force, and the load-bearing capacity does not appear to slide down the cliff, allowing the component to continue to bear the load. When it fails, the strain of CFRP is much smaller than its ultimate tensile strain, and the use rate is low. Besides, the peak strain of the NEA and FEA decreases with the increase in specimen size because a large concrete column has more defects, and the local stress is transferred to the external CFRP by bonding, and the stress concentration and uneven distribution lead to faster failure

of the column. In summary, the small concrete column can fully play the tensile strength and deformability of CFRP.

Reinforcing bar strain

To analyze the size effect of CFRP-strengthened concrete columns more deeply, the strains of steel bars in the columns before and after CFRP reinforcement were compared. Figures 11(a) and (b) are the load-strain curves of the unstrengthened and the CFRP-strengthened columns. Both the NEA and FEA are under compression contrary to CFRP. When strengthened and unstrengthened columns of various sizes reach their ultimate bearing capacity, the steel bars in the NEA yield first, followed by the ES1 steel bars in the FEA. The maximum and peak strains of ES1, EM2, and EL3 were increased, with the maximum strain near the eccentric area increasing by 531.5, 90.5, and 27.3%, and the maximum peak strain increasing by 12.2, 49.5, and 3.7%. Although the steel bars in the remote eccentric areas of EM2 and EL3 did not yield, the strain also increased significantly, improving the effective use rate of the steel bars.

The results obtained from the measurements show that the compressive strain of the steel bars near the eccentric area of ES1 is the largest, and the compressive strain increases as the restraint level increases. The hoop effect of CFRP prevents longitudinal steel bars from buckling.

Constrained concrete strength

To calculate the constrained concrete strength of CFRP to strengthen reinforced concrete square columns, the following three assumptions need to be satisfied: the concrete compression section conforms to the plane sections assumption, the tensile strength of the concrete is not included, and the CFRP and the concrete deformation are coordinated. Under the premise of this assumption, according to GB 50608-2010,[30] the formula for calculating the design value of constrained concrete strength is as Eq. (2)

$$f_{cc} = f_c + 3.5E_f t_f/R(k_{s\sigma} - 6.5/\beta_j)\varepsilon_{ru} \quad (2)$$

ε_{ru} is the design value of the CFRP hoop limit strain in the confined concrete column; $k_{s\sigma}$ is the stress section shape factor; β_j is the constraint stiffness parameter; E_f is the elastic modulus of CFRP; t_f is the thickness of CFRP; R is the geometric parameter; and f_c is the compressive strength of concrete.

For rectangular sections, R and $k_{s\sigma}$ should be calculated according to Eq. (3) and (4)

$$R = 0.5\sqrt{(b^2 + h^2)} \quad (3)$$

Notation: b and h are the length and width of the section of the specimen.

$$k_{s\sigma} = \left(1.25\frac{r_c}{b} + \frac{r_c}{h} + 0.33\right)\left(\frac{h}{b}\right)^{0.4} \quad (4)$$

Notation: r_c is the chamfering radius of the rectangular section and the rounded rectangular section.

The axial force of the specimen is the sum of the axial force of the concrete and the axial force of the steel bar.[31] Therefore, the calculation formulas of the ultimate compressive strength $f_{cc,k}$ of confined concrete and the ultimate compressive strength of unconstrained concrete $f_{c,k}$ can be calculated according to Eq. (5) and (6)

$$f_{cc,k} = \frac{N - \Sigma^m{}_{i=1}\sigma_{si}A_{si}}{\alpha_1 bx} \quad (5)$$

$$f_{c,k} = \frac{N - f_y{}'A_s{}' + \sigma_s A_s}{\alpha_1 bx} \quad (6)$$

Notation: N is the ultimate bearing capacity; σ_{si} is stress of longitudinal reinforcement at layer I of the section; A_{si} is the the total area of section i longitudinal reinforcement; x is the height of the compression area; α_1 is equivalent coefficient; f_y' is yield strength of reinforcement near eccentric area; A_s' is cross-sectional area of reinforcement near eccentric area; σ_s is stress of longitudinal reinforcement in the FEA; and A_s is cross-sectional area of the steel bar in the FEA

$$\varepsilon_b = \frac{\beta_1}{1 + \frac{f_y}{E_s\varepsilon_{cc,u}}} \quad (7)$$

In Eq. (7): ε_b is the height of the relative limit compression zone; $\varepsilon_b = x/h_0$,x is the height of the limit pressure zone; h_0 is the effective height of the section, which is the distance from the edge on one side of the section with the larger compressive stress to the resultant force of the longitudinal reinforcement on the other side of the section; f_y is the tensile strength of longitudinal reinforcement; E_s is the elastic modulus of the reinforcement; and $\varepsilon_{cc,u}$ is the ultimate compressive strain of CFRP-confined concrete, the relevant calculated values are shown in Table 6.

The relationship between the relative strength of confining concrete $f_{cc,k}/f_{c,k} - 1$, and the number of CFRP layers is shown in Fig. 12. The test results show that the strength of the confined concrete increases with the increase in the number of CFRP layers. Compared with the design value of the restrained concrete strength calculated in the engineering application technical standard of fiber-reinforced composite materials, the restrained concrete strength calculated according to the test results is higher. It can be seen that the formula given by the specification is very conservative.

CONCLUSIONS

In this research, an eccentric loading test was carried out on 18 reinforced concrete columns, and the following conclusions can be drawn:

1. Carbon fiber-reinforced polymer (CFRP) can effectively restrain the lateral deformation of concrete columns, create the structure in a state of three-way stress, and increase the axial displacement and lateral deflection to a certain extent, and the plastic deformation of the structure can be improved.

2. For CFRP-strengthened concrete columns, the bearing capacity of ES1, EM2, and EL3 increased by 34.97%,

26.98%, and 24.23%, respectively, and the strengthening with CFRP effect was significant. After reaching the ultimate bearing capacity, the bearing capacity curve did not show a "cliff-cut" decline, and the ductility was significantly improved.

3. The strain of the steel bar inside the concrete column was significantly improved after the CFRP constraint. The maximum strain in the near eccentric area (NEA) was increased by 531.5%, 90.5%, and 27.3%, and the maximum peak strain was increased by 12.2%, 49.5%, and 3.7%, respectively. CFRP strengthening can improve the use rate of steel bars.

4. Although CFRP has good tensile strength, the failure strain is lower when it is pasted with large-size columns, and it can fully use its mechanical properties when working with small-size columns.

5. As the size of the strengthened columns increases, its displacement ductility coefficient decreases, while ultimate bearing capacity, maximum strain of CFRP, maximum strain, and maximum deflection of unstrengthened columns are reduced compared with the increase in unstrengthened columns, and there is an obvious size effect.

6. Confined concrete strength increases with the size of the specimen. It is much larger than the design value of the specification, and there is sufficient safety reserve in the engineering design.

CONFLICT OF INTEREST

The authors declare no conflict of interest.

DATA AVAILABILITY STATEMENT

All the authors do not have any possible conficts of interest.

ORCID

Jianhui Si https://orcid.org/0000-0003-4846-4886.

Funding information: Natural Science Foundation of Shaanxi Province, Grant/Award Number: 2021JM-332.

AUTHOR BIOS

Jianhui Si *is a Professor at Xi'an University of Technology, Xi'an, China. He received his BSc in construction engineering, his MSc in structural engineering, and his PhD in hydrostructural engineering from Xi'an University of Technology in 1999, 2004, and 2009, respectively. His research interests include concrete structure theory, structural optimization and simulation analysis, and structural strengthening and repair.*

Yuan Zhou *received his bachelor's degree in civil engineering from Luoyang Institute of Science and Technology, Luoyang, China, in 2021, and is currently pursuing his master's degree in civil engineering at Xi'an University of Technology, with a focus on optimization and reinforcement of concrete structures.*

Zhaobao Zeng *received his BS in civil engineering from Jiujiang University, Jiujiang, China, in 2020, and his MS in civil engineering from Xi'an University of Science and Technology in 2023. His research interests include the optimization and reinforcement of concrete structures.*

Kai Li *received his bachelor's degree in civil engineering from Yan'an University, Yan'an, China, in 2019, and his master's degree in civil engineering from Xi'an University of Science and Technology in 2023. His research interests include the optimization and reinforcement of concrete structures.*

Jiannan Hu *received his BSc in civil engineering from Shaanxi University of Technology, Hanzhong, China, in 2020, and his MSc in civil engineering from Xi'an University of Technology in 2023. His research interests include the optimization and reinforcement of concrete structures.*

Zewei Liu *received his bachelor's degree in civil engineering and his master's degree in civil engineering from Xi'an University of Technology in 2020 and 2023, respectively. His research interests include the optimization and reinforcement of concrete structures.*

Xinchao Ding *is a Licensed Engineer with the Northwest Survey and Design and Research Institute of China Electric Construction Co., Ltd. His research interests include the optimization and reinforcement of concrete structures.*

ACKNOWLEDGMENTS

The writers gratefully acknowledge the support for this work, which was funded by Natural Science Foundation of Shaanxi Province (Grant No. 2021JM-332).

REFERENCE

1. Teng, J. G.; Chen, J. F.; Smith, S. T.; and Lam, L., *FRP Strengthened RC Structures*, John Wiley & Sons, Inc., New York, 2012.

2. Zhou, Y.; Chen, X.; Wang, X.; Sui, L.; Huang, X.; Guo, M.; and Hu, B., "Seismic Performance of Large Rupture Strain FRP Retrofitted RC Columns with Corroded Steel Reinforcement," *Engineering Structures*, V. 216, 2020, p. 110744. doi: 10.1016/j.engstruct.2020.110744

3. Wang, D.; Wang, Z.; Smith, S. T.; and Yu, T., "Seismic Performance of CFRP-Confined Circular High-Strength Concrete Columns with High Axial Compression Ratio," *Construction and Building Materials*, V. 134, 2017, pp. 91-103. doi: 10.1016/j.conbuildmat.2016.12.108

4. Moghtadernejad, N.; Jamshidi, M.; Maheri, M. R.; and Keong, C. K., "Repair of Post-Heated Short Rectangular Reinforced Concrete Columns with FRP Jackets," V. 34, *Structures*, 2021, pp. 4269-4283.

5. Mohammed, A. A.; Manalo, A. C.; Ferdous, W.; Zhuge, Y.; Vijay, P. V.; and Pettigrew, J., "Experimental and Numerical Evaluations on the Behaviour of Structures Repaired Using Prefabricated FRP Composites Jacket," *Engineering Structures*, V. 210, 2020.

6. Zhao, J.; Si, C.; Ren, W.; Zhang, X.; and Sun, Y., "Experimental and Numerical Studies on Seismic Performance of Rectangular Concrete Columns Reinforced by CFRP Bars with Different Ratios and Positions," *Structures*, V. 32, 2021, pp. 237-253.

7. Yan, L., and Chouw, N., "Natural FRP Tube Confined Fibre Reinforced Concrete under Pure Axial Compression: A Comparison with Glass/Carbon FRP," *Thin-Walled Structures*, V. 82, 2014, pp. 159-169. doi: 10.1016/j.tws.2014.04.013

8. Widiarsa, I. B. R., and Hadi, M. N. S., "Performance of CFRP Wrapped Square Reinforced Concrete Columns Subjected to Eccentric Loading," *Procedia Engineering*, V. 54, 2013, pp. 365-376.

9. Kusumawardaningsih, Y., and Hadi, M. N. S., "Comparative Behaviour of Hollow Columns Confined with FRP Composites," *Composite Structures*, V. 93, No. 1, 2010, pp. 198-205.

10. Nematzadeh, M.; Mousavimehr, M.; Shayanfar, J.; and Omidalizadeh, M., "Eccentric Compressive Behavior of Steel Fiber-Reinforced RC Columns Strengthened with CFRP Wraps: Experimental Investigation and Analytical Modeling," *Engineering Structures*, V. 226, 2021, Article No. 111389.

11. Lin, G.; Zeng, J. J.; Teng, J. G.; and Li, L. J., "Behavior of Large-Scale FRP-Confined Rectangular RC Columns under Eccentric Compression," *Engineering Structures*, V. 216, 2020, p. 110759. doi: 10.1016/j.engstruct.2020.110759

12. Lam, L.; Huang, L.; Xie, J.-H.; and Chen, J.-F., "Compressive Behavior of Ultra-High Performance Concrete Confined with FRP," *Composite Structures*, V. 274, 2021, p. 274.

13. Al-Rousan, R., "Behavior of Circular Reinforced Concrete Columns Confined with CFRP Composites," *Procedia Manufacturing*, V. 44, 2020, pp. 623-630. doi: 10.1016/j.promfg.2020.02.247

14. Qiang, W.; Bailin, L. I.; Lu, C.; and Zhang, Z., "Square Column When the Loss of Prestress of Prestressed CFRP Reinforced Concrete," *Building Science*, V. 4, No. 3, 2020, pp. 57-64.

15. Feng, L.; Ying, L.; and Lujian, T., "Analysis and Finite Element Simulation of Mechanical Properties of Prestressed Carbon Fiber Reinforced Concrete Rectangular Bias Columns," *Engineering Construction*, V. 49, No. 9, 2017, pp. 14-20.

16. Donghui, C., and Yanhong, Y., *Journal of Building Science and Engineering*, V. 34, No. 4, 2017, pp. 34-40.

17. Lu, C.; Wei, F.; Wang, Q.; Liu, C.; and Li, Z., "Experimental Study on Axial Compression Performance of Reinforced Concrete Short Square

Section Columns Reinforced with Prestressed Carbon Fiber Cladding," *Industrial Building*, V. 47, No. 5, 2017, pp. 171-178.

18. Donghui, C.; Yannan, Y.; and Xu, Y., *Journal of Building Science and Engineering*, 2013, V. 30, No. 1, pp. 25-31.

19. Zhai, A.; Sun, M.; Ji, C.; Chen, S.; and Wang, C., *Journal of Hydraulic and Building Engineering*, 2013, V. 11, No. 1, pp. 31-36.

20. Lu, C.-L.; Xiao, Y.-P.; Wang, Q.; and Zhu, W.-X., "Study on Axial Compressive Properties of RC Square Columns Strengthened with Prestressed CFRP Sheets, *Structures*, V. 27, 2020, pp. 2011-2024.

21. Wang, Q.; Lv, J.; Lu, C.; and Zhu, W., "Experimental Study on Seismic Performance of Square RC Columns Strengthened with Multi-Layer Prestressed CFRP Fabric," *Journal of Building Engineering*, V. 45, 2022, pp. 45.

22. Janke, L.; Czaderski, C.; Ruth, J.; and Motavalli, M., "Experiments on the Residual Load-Bearing Capacity of Prestressed Confined Concrete Columns," *Engineering Structures*, V. 31, No. 10, 2009, pp. 2247-2256. doi: 10.1016/j.engstruct.2009.04.006

23. Guo, Y.-C.; Gao, W.-Y.; Zeng, J.-J.; Duan, Z.-J.; Ni, X.-Y.; and Peng, K.-D., "Compressive Behavior of FRP Ring-Confined Concrete in Circular Columns: Effects of Specimen Size and a New Design-Oriented Stress-Strain Model," *Construction and Building Materials*, V. 201, 2019, pp. 350-368. doi: 10.1016/j.conbuildmat.2018.12.183

24. Zhou, J.; Bi, F.; Wang, Z.; and Zhang, J., "Experimental Investigation of Size Effect on Mechanical Properties of Carbon Fiber Reinforced Polymer (CFRP) Confined Concrete Circular Specimens," *Construction and Building Materials*, V. 127, 2016, pp. 643-652. doi: 10.1016/j.conbuildmat.2016.10.039

25. Zhou, C.; Siha, A.; Qiu, Y.; and Pan, Q., "Experimental Investigation of Axial Compressive Behavior of Large-Scale Circular Concrete Columns Confined by Prestressed CFRP Strips," *Journal of Structural Engineering*, ASCE, V. 145, No. 8, 2019, p. 04019070. doi: 10.1061/(ASCE)ST.1943-541X.0002351

26. Wang, D. Y.; Wang, Z. Y.; Smith, S. T.; and Yu, T., "Size Effect on Axial Stress-Strain Behavior of CFRP-Confined Square Concrete Columns," *Construction and Building Materials*, V. 118, 2016, pp. 116-126. doi: 10.1016/j.conbuildmat.2016.04.158

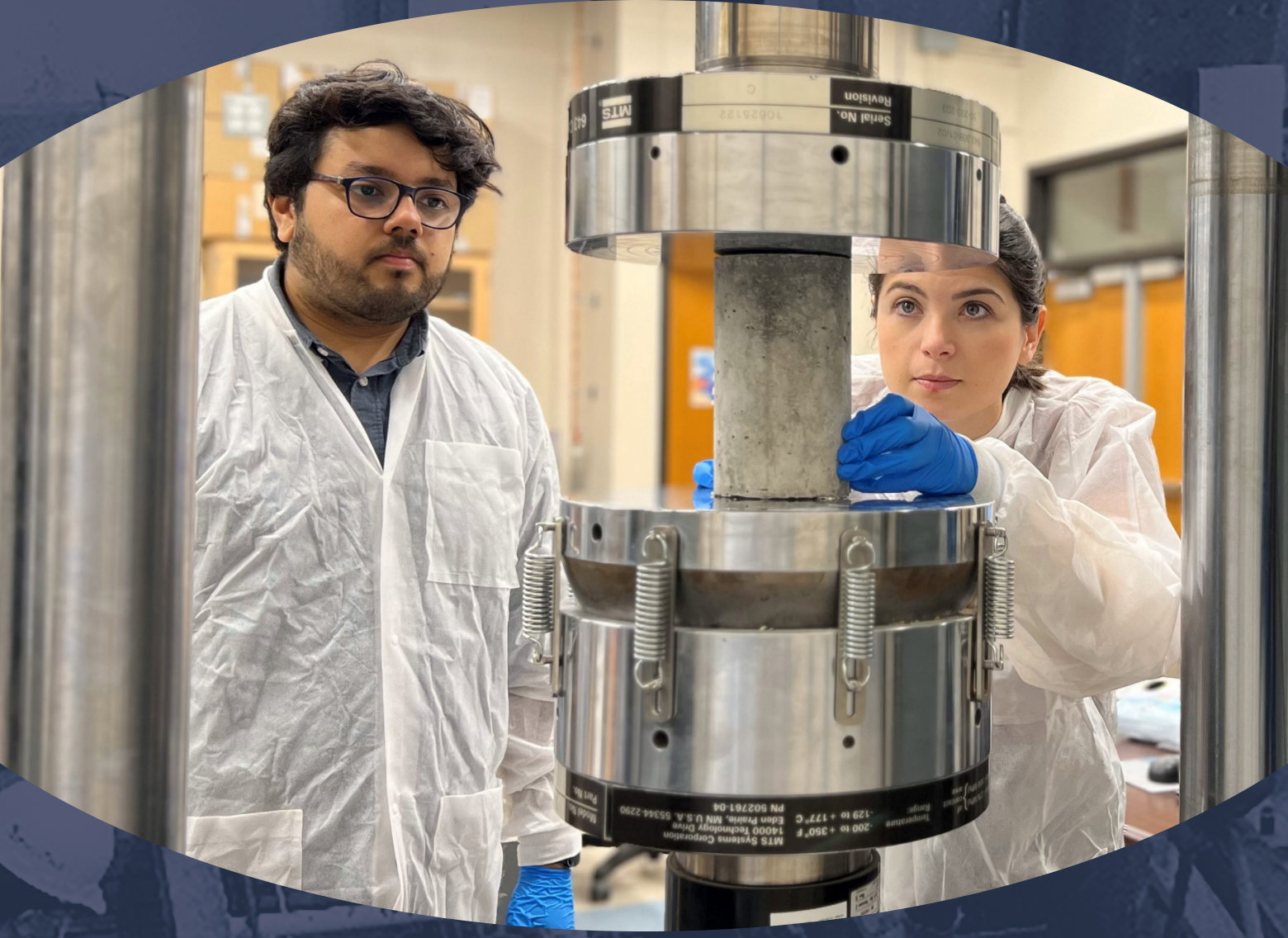
27. Jin, L.; Chen, H.; Wang, Z.; and Du, X., "Size Effect on Axial Compressive Failure of CFRP-Wrapped Square Concrete Columns: Tests and Simulations," *Composite Structures*, V. 254, 2020, p. 254 doi: 10.1016/j.compstruct.2020.112843

28. GB 50010-2010, "Code for Design of Concrete Structures," Ministry of Housing and Urban-Rural Development of the People's Republic of China, Beijing, China, 2010.

29. GB/T 50152-2012, "Standard Test Method for Concrete Structures," Ministry of Housing and Urban-Rural Development of the People's Republic of China, Beijing, China, 2012.

30. GB 50608-2010, "Technical Code for Infrastructure Application of FRP Composites," Ministry of Housing and Urban-Rural Development of the People's Republic of China, Beijing, China, 2010.

31. Jiaru, Q.; Lirong, C.; and Dongliang, Z., "Concrete Column Stirrup Constraint at the Center of the Compression Performance," *Journal of Tsinghua University*, Natural Science Edition, 2002, pp. 1369-1373.



Calling all researchers in the concrete industry:

CRC'S 2025 REQUEST FOR PROPOSALS IS NOW OPEN.

The CRC seeks to advance the concrete industry through the funding of concrete research projects that further the knowledge and sustainability of concrete materials, construction, and structures.

Proposals must be endorsed by at least one ACI Technical Committee.

aci Foundation
Building the Future

ACIFOUNDATION.ORG/RESEARCH

APPLY TODAY

ACI STRUCTURAL JOURNAL TECHNICAL PAPER

23-092

Study on Seismic Damage Model of Fly Ash Foamed Concrete Wall

by Yunhong Hao, Hongze Wang, Yupeng Zhao, Chakelehan, and Yong Shi

Firstly, the proposed static test was carried out on eight fly ash foamed concrete walls with different axial compression ratios μ and steel ratios ρ. Secondly, the quantitative analysis method of wall damage was proposed based on the crack development theory, and the real damage index was proposed. Then, through theoretical analysis and curve fitting, two kinds of seismic damage models—energy method and Park-Ang-W—were proposed, and the damage values were calculated to compare with the real damage values. Finally, the Park-Ang-W model was used to analyze the parameter expansion of 16 Abaqus wall models with different axial compression ratios μ and steel ratios ρ. The results show that the damage evaluation index based on crack development theory can effectively reflect the damage of fly ash foamed concrete walls. The accuracy of the energy method model is not high at the low number of cycles, and the error is less than 20% at the high number of cycles. The Park-Ang-W model has an error of approximately 10% at a high number of cycles, which better reflects the true damage of the specimen. The axial compression ratio μ has little effect on the wall damage, with a maximum effect range of 6.7%. Increasing the reinforcement ratio can effectively reduce the wall damage, with a maximum effect range of 12.6%. The results of the study provide a theoretical basis for the future application of fly ash foamed concrete in construction projects.

Keywords: axial compression ratio; damage parameter; fly ash foamed concrete; seismic damage model; shear wall; steel ratio.

INTRODUCTION

At present, environmental protection is an important research direction in the field of civil engineering, especially in external wall insulation.[1-3] In recent years, commonly used thermal insulation materials, such as polystyrene boards and rock wool boards, have good thermal insulation properties, but the construction waste generated is irreversible pollution of the environment.[4,5] Foamed concrete is widely used in construction projects as a non-load-bearing component due to its light weight, sound insulation, and good heat preservation.[6-9] In addition, the closed pores inside the foamed concrete play an important role in dissipating seismic energy.[10-12] This provides very favorable conditions for foamed concrete as a component integrating thermal insulation and load-bearing. However, at present, foamed concrete still has the disadvantages of low strength and high brittleness, which bring great obstacles to the popularization and application of foamed concrete as a load-bearing component.[13-16] In particular, how to prevent brittle fracture of materials with brittle characteristics from occurring in the event of internal damage has become an urgent problem.

There is no calculation method for quantitatively analyzing the internal damage of components, but only a rough classification of the different stages of damage in terms of appearance. Even at the same stage, the damage to the component varies considerably.[17-19] It is also difficult to accurately determine the internal damage of a component from its exterior alone. In addition, it is neither safe nor economical to define the damage only based on the appearance of seismic components. The seismic damage model can better reflect the real damage condition of components, and it is more convenient and faster to calculate the damage directly in the calculation, which is the main method to study the damage of components.[20-22] The existing seismic damage model is derived from the Park-Ang model proposed in 1983, but the model is only applicable to columns, and some of the parameters do not apply to walls.[23-25] The shear-wall structure is currently the main structural form of high-rise buildings. As the main vertical energy-consuming member, the internal damage and destruction of the wall are significant to the building structure. Although some scholars have studied the seismic damage modeling of walls, several important parameters, such as the energy-consuming capacity and loading and unloading stiffness of walls, have not been considered in the model. This will lead to a huge error between the calculation results and the actual process.[26-28] Therefore, it is now also necessary to propose a seismic damage model for walls.

Based on the previously mentioned issues, this paper proposes a calculation method for quantitatively calculating the actual damage to the wall and an actual damage index for measuring the damage, aiming to accurately calculate it under the action of loads. Subsequently, the energy method model and the Park-Ang-W model are proposed to calculate the damage value of the wall through theoretical calculation and numerical fitting. Finally, eight foamed concrete walls with different axial compression ratios and steel ratios and 16 Abaqus models were tested using the proposed static test to verify the accuracy of the two models in damage calculation. Based on the calculation results, the influence laws of different axial compression ratios μ and steel ratios ρ on the damage of walls were derived.

ACI Structural Journal, V. 121, No. 5, September 2024.

MS No. S-2023-092.R5, doi: 10.14359/51740855, received March 25, 2024, and reviewed under Institute publication policies. Copyright © 2024, American Concrete Institute. All rights reserved, including the making of copies unless permission is obtained from the copyright proprietors. Pertinent discussion including author's closure, if any, will be published ten months from this journal's date if the discussion is received within four months of the paper's print publication.

Table 1—Specimen design

No. of specimen	Size of walls, mm	Size of wire mesh, mm	Axial compression ratio μ	Thickness of C-section steel, mm	Steel ratio ρ
SJ-1	1500 x 1000 x 200	ϕ4@100	0	0	0
SJ-2	1500 x 1000 x 200	ϕ4@100	0.1	0	0
SJ-3	1500 x 1000 x 200	ϕ4@100	0.2	0	0
SJ-4	1500 x 1000 x 200	ϕ4@100	0.3	0	0
SJ-5	1500 x 1000 x 200	ϕ4@100	0	1	0.004
SJ-6	1500 x 1000 x 200	ϕ4@100	0	2	0.008
SJ-7	1500 x 1000 x 200	ϕ4@100	0.3	1	0.004
SJ-8	1500 x 1000 x 200	ϕ4@100	0.3	2	0.008

RESEARCH SIGNIFICANCE

First, the proposed damage value calculation method provides a quantitative analysis method for wall damage under seismic action. Second, the seismic damage model is a guide for the application of fly ash foamed concrete walls in engineering. Finally, the research results are important for the future large-scale promotion of fly ash foamed concrete walls.

EXPERIMENTAL PROGRAM

Specimen design

Eight fly ash foamed concrete wall specimens were fabricated. The wall frames were made of 4 mm cold-drawn steel wire mesh and cold-formed thin-walled C-beams. The strength and stability of the walls met the requirements of the design code. The parameters selected in the test were axial compression ratio μ and steel ratio ρ. The specific design parameters of the wall are shown in Table 1, and the reinforcement construction is shown in Fig. 1. The density of the fly ash foamed concrete was 12 kN/m^3. The standard value of cubic compressive strength was 15.4 MPa, which was close to the strength of C15 ordinary concrete. The cold-drawn steel wire mesh was made of Q195 steel, and the measured tensile strength was 278 MPa. The cold-formed thin-walled C-beam was made of Q235, and the measured tensile strength was 341 MPa.

Loading device and loading system

The loading device is shown in Fig. 2. The axial load is applied at the top using a hydraulic jack with a measuring range of 2000 kN. In the horizontal direction, a horizontal load is applied using an electro-hydraulic servo actuator. The bottom of the specimen was secured to the loading frame with four 30 mm diameter bolts to ensure that the wall would not slide during loading. The loading system is shown in Fig. 3; the loading mode was load-displacement mixed loading.[29,30] The specimen was controlled by a load of 10 kN per stage before yielding and a displacement of 0.25 times the yield displacement per stage after yielding. When the maximum load for a given stage of the cycle dropped below 85% of the peak load, the test was stopped, and the specimen was declared damaged.[31,32]

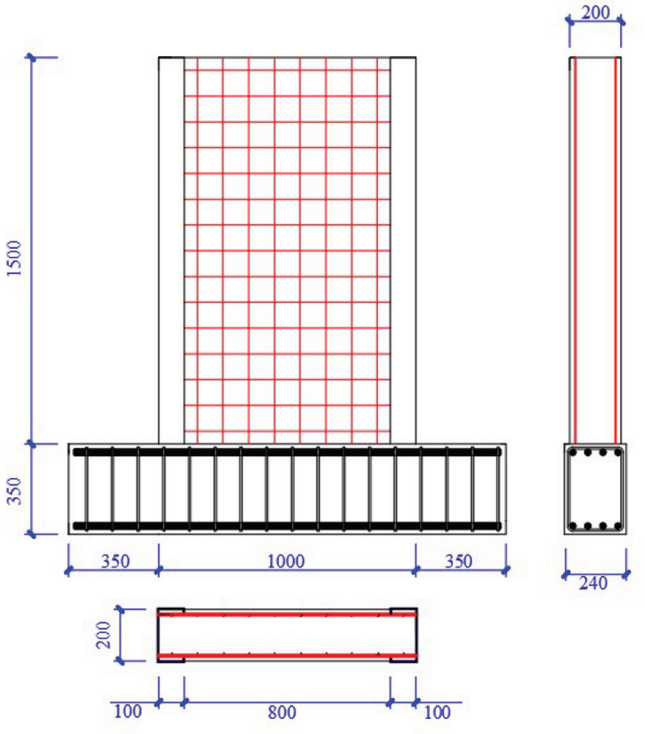


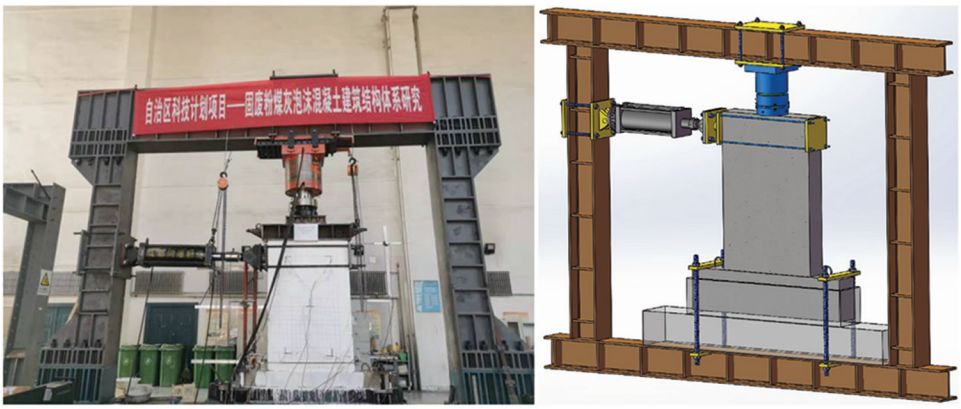
Fig. 1—Wall size and reinforcement construction.

ESTABLISHMENT OF SEISMIC DAMAGE MODEL

Indexes of true damage of specimens

It is generally believed that the damage degree of the wall is related to the length of the crack.[33-35] Based on the research results of foamed concrete members, it was found that the damage degree of walls is related not only to the extension length of cracks but also to their width.[15,36,37] In particular, the length and width of the largest main crack determine the damage inside the wall.[38-40] Based on this, this paper proposes a damage index to measure the damage to the wall under seismic action, which is expressed by the damage parameter D_i. The calculation principle of the damage index is shown in Fig. 4. The formula of the damage parameter D_i is shown in Eq. (1)

$$D_i = \frac{\sum_{i=1}^{n} l_{p,i} \cdot \left(\frac{b_{p,i} + b_{p,i+1}}{2}\right) + \sum_{j=1}^{n} l_{r,j} \cdot \left(\frac{b_{r,j} + b_{r,j+1}}{2}\right)}{B \cdot \max(b_{p,i}, b_{r,j})} \quad (1)$$



(a)Loading device (b)Loading device model

Fig. 2—Loading device.

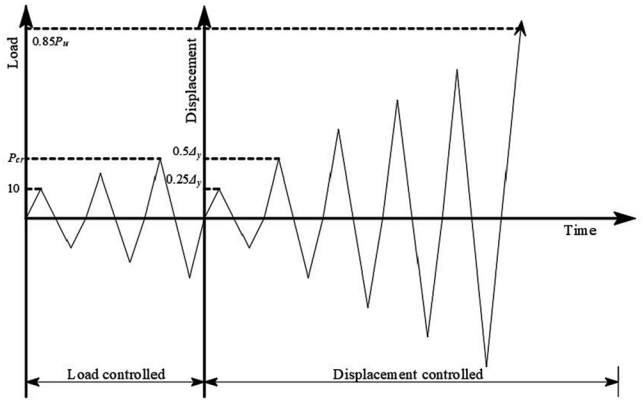


Fig. 3—Reversed cyclic loading history.

where $l_{p,i}$ and $l_{r,j}$ are the maximum main crack lengths of the specimen in compression and tension, respectively; $b_{p,i}$ and $b_{r,j}$ are the maximum principal crack widths of Δ_t specimens at intervals during compression and tension, respectively; Δ_t is an arbitrary time length, and the smaller the value, the higher the precision; θ_1 and θ_2 represent the angle between the maximum principal crack and the horizontal plane in compression and tension; and B is taken as the height of the wall section.

Energy method model

The first seismic damage model proposed in this paper is the energy method model. The damage parameter D_i is calculated as the ratio of damage dissipation energy to the total energy of the input member. The calculation method is shown in Fig. 5. The member in Fig. 5 can be regarded as an ideal thermodynamic system from the beginning to the end of loading, in which the internal energy of the input system is equal to the work done by the external force on the member. In addition, the energy in this system consists of three components—that is, elastic deformation energy, plastic deformation energy, and damage dissipation energy, namely

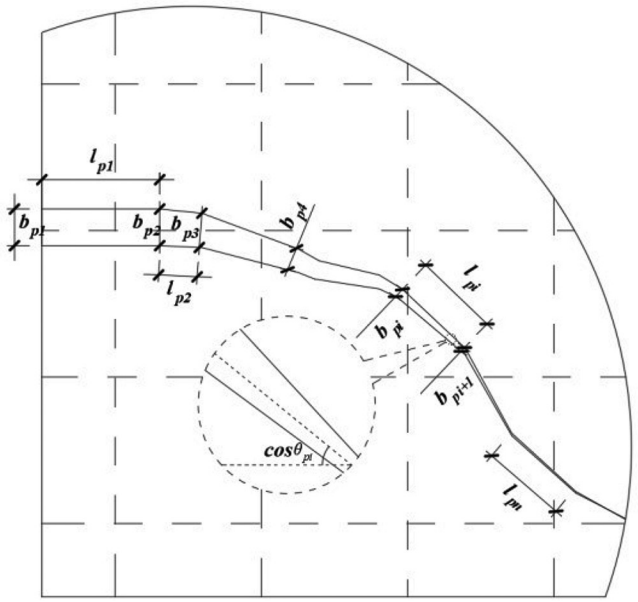


Fig. 4—Schematic diagram of damage index.

$$E = W = \Delta_i \cdot P_i = K_0 \cdot \Delta_i^2 = W_{ei} + W_{pi} + W_{Di} \quad (2)$$

For the calculation of elastic deformation energy W_{ei}, it can be seen from the figure that it is the sum of area S_{CDE} and S_{GHI}. The integral of the two curves can be obtained as follows

$$W_{ei} = \int_{\Delta_{ei}}^{\Delta_{pi}+\Delta_{ei}} f_2(\Delta) \cdot d(\Delta) + \int_{-\Delta_{pi}-\Delta_{ei}}^{-\Delta_{pi}} f_1(\Delta) \cdot d(\Delta) \quad (3)$$

$$W_{pi} = \int_{0}^{\Delta_{pi}+\Delta_{ei}} f_1(\Delta) \cdot d\Delta + \int_{-\Delta_{pi}-\Delta_{ei}}^{0} f_2(\Delta) \cdot d\Delta - W_{ei} \quad (4)$$

Finally, the calculation formula of the damage parameter D_i in the energy method model is

$$D_i = \frac{W_{Di}}{E} = \frac{K_0 \cdot \Delta_i^2 - W_{ei} - W_{pi}}{K_0 \cdot \Delta_i^2} = 1 - \frac{W_{ei} - W_{pi}}{K_0 \cdot \Delta_i^2} \quad (5)$$

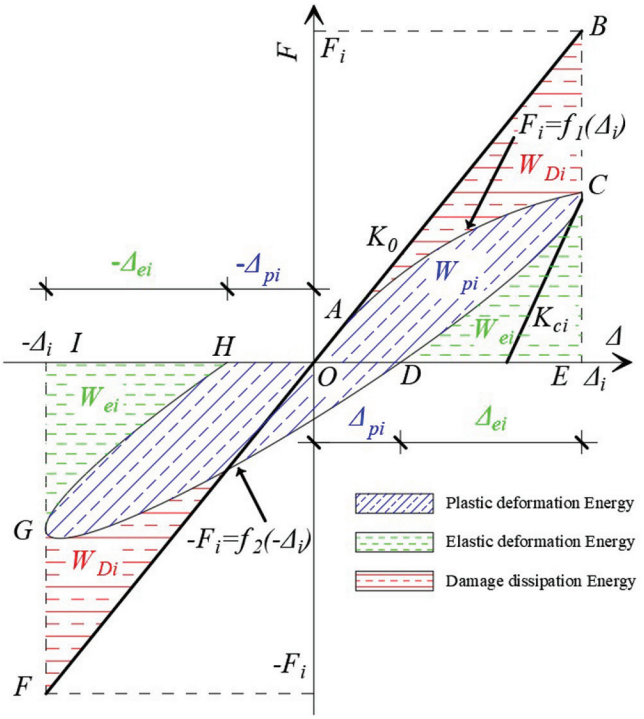


Fig. 5—Schematic diagram of energy distribution.

Park-Ang Model

The Park-Ang model is the most widely used seismic damage model,[41,42] and the calculation formula mainly consists of two parts. The first part is the damage caused to the member at the peak load point of each stage of the hysteresis loop. The second part is the damage caused by energy loss during the loading and unloading process of each stage of the hysteresis loop. The concrete calculation formula is shown in Eq. (6)

$$D_i = \frac{\delta_{im}}{\delta_u} + \beta \cdot \frac{\int dE_i}{Q_y \cdot \delta_u} \tag{6}$$

where δ_{im} is the maximum displacement of members in the i-th hysteresis loop; δ_u is the ultimate horizontal displacement of the member under horizontal monotonic load; $\int dE_i$ is the area of the i-th hysteresis loop; Q_y is the yield load of the member under horizontal monotonic load; and β is the energy dissipation factor of the component, which is calculated according to the following formula

$$\beta = (-0.447 + 0.073\lambda + 0.24\eta_0 + 0.314\rho_1) \times 0.7\rho_v \tag{7}$$

where λ is the shear-span ratio of the component ($1.7 \le \lambda \le 3$); η_0 is the axial compression ratio of the member ($\eta_0 \ge 0.2$); ρ_1 is the ratio of longitudinal reinforcement ($\rho_1 \ge 0.75\%$); and ρ_v is the stirrup ratio.

Park-Ang-W model

Although the Park-Ang model is the most widely used seismic damage model at present, it has some problems. First, the model is mainly applied to ordinary concrete columns, and the parameters, such as shear-span ratio and stirrup ratio, have little reference value for walls, but the parameters related to stiffness and stiffness degradation are not involved. Second, the function does not converge when the displacement is 0 and δ_u. Finally, some parameters in the model are determined by low cycle and static load tests, respectively, which greatly increases the workload.[43] Based on the Park-Ang model and considering stiffness degradation during component reloading and stiffness damage during tension-compression unloading, a two-parameter seismic damage model for walls, the Park-Ang-W model, is proposed in this paper. The model considers that the main cause of wall damage is the change in loading and unloading stiffness and energy dissipation capacity under each level of repeated load. The damage of the specimen before loading is 0. As the displacement of the specimen tends to the limit displacement δ_u, the damage parameter of the member tends to 1. The expression of the damage parameter D_i is

$$D_i = \left(2 - \frac{K_i + K_{ri}}{K_0}\right)^{\alpha} + \left(\frac{\int dE_i}{Q_y \cdot \delta_u}\right)^{\beta} \tag{8}$$

where K_i is the stiffness of the specimens under the first cycle; K_0 is the initial stiffness of the specimens without damage; and K_{ri} is the unloading stiffness of the specimen under cycle i. The calculation of $\int dE_i$ assumes that the area of the forward and reverse hysteresis curves is the same, and the calculation formula is

$$\int dE_i = \int_{-\delta_{ui}}^{\delta_{ui}} L_1 \cdot d\delta - \int_{-\delta_{ui}}^{\delta_{ui}} L_2 \cdot d\delta = \int_0^{\delta_{ui}} (L_2 - L_1) \cdot d\delta \tag{9}$$

α and β are first-order polynomials of steel ratio ρ and axial compression ratio μ, respectively.

$$\left.\begin{matrix}\alpha \\ \beta\end{matrix}\right\} = \begin{cases} A\mu + B\rho + C \\ D\mu + E\rho + F \end{cases} \tag{10}$$

To better understand the damage calculation method and damage model proposed in this paper, the research methods and ideas are shown in Fig. 6.

CALCULATION OF REAL DAMAGE VALUE D_i

Calculation of damage index

According to the development of cracks during the quasi-static test of the wall, the cracks are shown in Fig. 7. Lines of different colors represent the expansion and extension of cracks at different cycles. The maximum principal fracture direction and horizontal plane angles are between 30 and 45 degrees. The crack length increased with the increase in the axial compression ratio, especially the length of the maximum main crack. When the axial compression ratio μ was 0.2, a penetrating crack formed at the main crack of maximum tension and compression. With the increase in the steel ratio, the maximum crack length of the specimens decreased significantly. This indicates that C-type steel can effectively limit the propagation and development of cracks.

The true damage value D_i of the specimens calculated from Eq. (1) is shown in Fig. 8. The trend of the overall damage

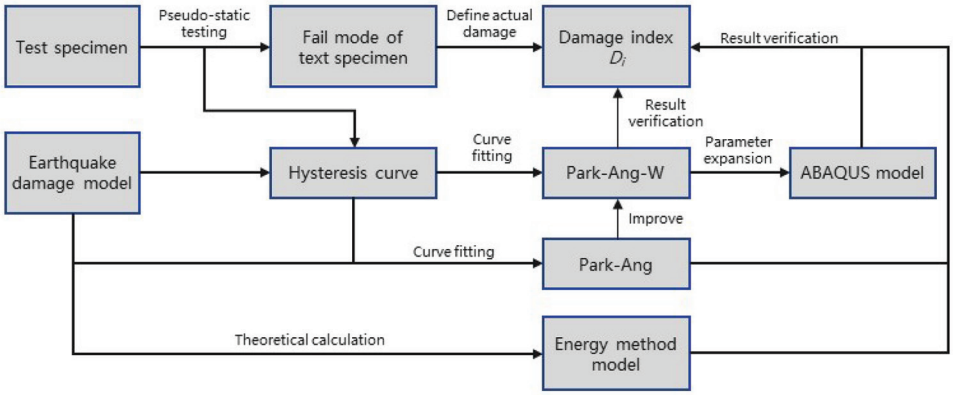


Fig. 6—Technology roadmap.

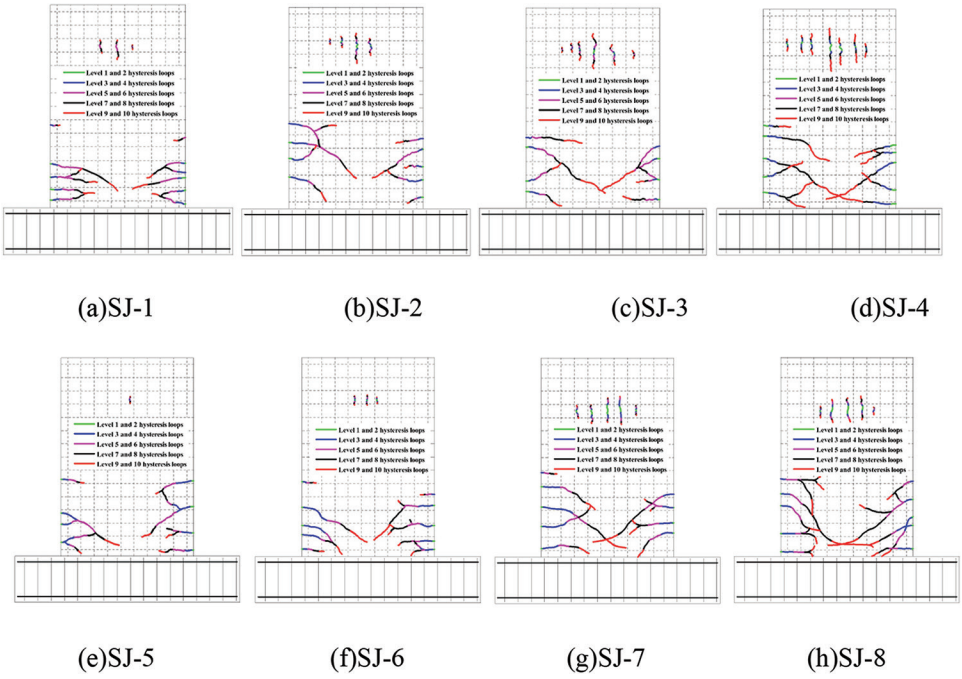


Fig. 7—Diagram of fracture development.

degree curve of the specimens is the same, and the damage amount of each specimen is close, with the maximum range within 12%. The specimen with the largest amount of damage was SJ-4. The damage value reached 0.89 when the axial compression ratio μ = 0.3 and steel ratio ρ = 0. SJ-6 was the specimen with the smallest amount of damage. The damage value was 0.79 when the axial compression ratio μ = 0.3 and ρ = 0.008.[44]

Damage value D_i of Park-Ang-W model

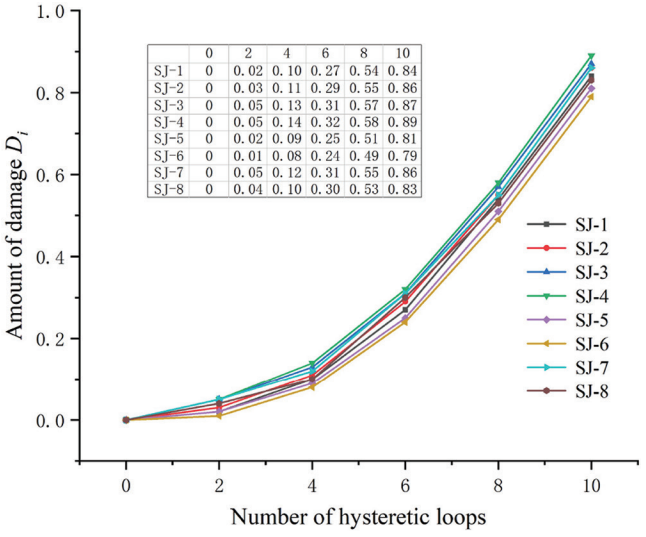
The hysteresis curves of the eight specimens obtained from the tests are shown in Fig. 9. The calculated parameters in the model are given in tables, where Δ_{im} is the ultimate displacement of the specimen at the i-th cycle; K_i is the loading stiffness of the specimen at the i-th cycle, and the value is determined by the peak load and peak displacement in this cycle; K_{ri} is the unloading stiffness of the specimen at the i-th cycle, and its value is determined by calculating peak load, displacement, post-unloading load, and displacement in this cycle; $\int dE_i$ is the area of the i-th hysteresis ring, and the calculation formula is shown in Eq. (9); E_1 and E_2 are the first two terms of Eq. (9), respectively, representing the curve integral of the two curves; Δ_u is the maximum displacement of the specimen in the pseudo-static test; Q_y is the yield load of the specimen; and K_0 is the initial stiffness of the specimen without yield, which is determined according to the peak load and peak displacement of a cycle. Equations (8) and (10) are used to fit the curves of eight parameters according to the test results. The fitting formula is shown in Eq. (11). Due to the multi-parameter fitting, the fitting results cannot be displayed on the image. The coefficient of determination $R^2 = 0.9214$ of the fitting curve can be obtained. The fitting value agrees well with the actual damage value. For the hysteresis curve of any given specimen, the two parameters, axial compression ratio μ and steel ratio ρ, can be used to calculate the damage value D_i using Eq. (11).

$$D_i = \left(2 - \frac{K_i + K_{ri}}{K_0}\right)^{-1.66\mu - 12.11\rho + 1.38} + \left(\frac{\int dE_i}{Q_y \cdot \Delta_u}\right)^{10.7\mu - 30.44\rho + 0.97} \tag{11}$$

VERIFICATION OF SEISMIC DAMAGE MODEL

Test verification

The calculated damage value D_i is compared with the actual damage value D_i according to the three seismic damage models described previously; the comparison results are shown in Fig. 10. As a whole, the trend of the damage curves of the three seismic damage models is the same as that of the real damage value curves, and all of them are quadratic function curves. The results prove that the proposed damage model has a high correlation with the true damage value. The damage curves of the three seismic damage models fit the true damage curves from low to high in the order of the energy method model, Park-Ang model, and Park-Ang-W model. According to the comparison between the energy method model curve and the real damage value curve, the error becomes smaller and smaller with the increase in the number of hysteresis loops, and the error of all specimens is approximately 10% in the 10th cycle. However, the error was large in the second to sixth cycles. The main reason was because the damage degree of the specimen was small in the first few cycles, and the error was caused by insufficient precision in the comparison. Another reason is the error caused by inaccurate measurement results in the actual measurement process of specimen cracks. When comparing the Park-Ang model curve with the real damage value curve, the calculation error of the damage value after the sixth hysteresis loop is generally between 5 and 25%, and the accuracy still cannot meet the requirements. According to the comparison between the curve of the Park-Ang-W model and the real damage value curve, the error can reach approximately 10% in the sixth cycle. With the increase in the number of cycles, the error becomes smaller and smaller. By the 10th cycle, the error is less than 5%. This shows that the Park-Ang-W model has high computational accuracy and can better reflect the damage of the specimen after many cycles.



	0	2	4	6	8	10
SJ-1	0	0.02	0.10	0.27	0.54	0.84
SJ-2	0	0.03	0.11	0.29	0.55	0.86
SJ-3	0	0.05	0.13	0.31	0.57	0.87
SJ-4	0	0.05	0.14	0.32	0.58	0.89
SJ-5	0	0.02	0.09	0.25	0.51	0.81
SJ-6	0	0.01	0.08	0.24	0.49	0.79
SJ-7	0	0.05	0.12	0.31	0.55	0.86
SJ-8	0	0.04	0.10	0.30	0.53	0.83

Fig. 8—Specimen damage value D_i.

Numerical simulation verification of Park-Ang-W model

Because the calculation of the damage value of the Park-Ang-W model is based on the fitting of test results, the question of whether the relationship between the model damage value and the real damage value has universal applicability needs to be further explored. In this paper, the finite element software Abaqus is used to analyze the damage of fly ash foamed concrete walls, and the influence of the axial compression ratio μ and steel ratio ρ on the damage of the

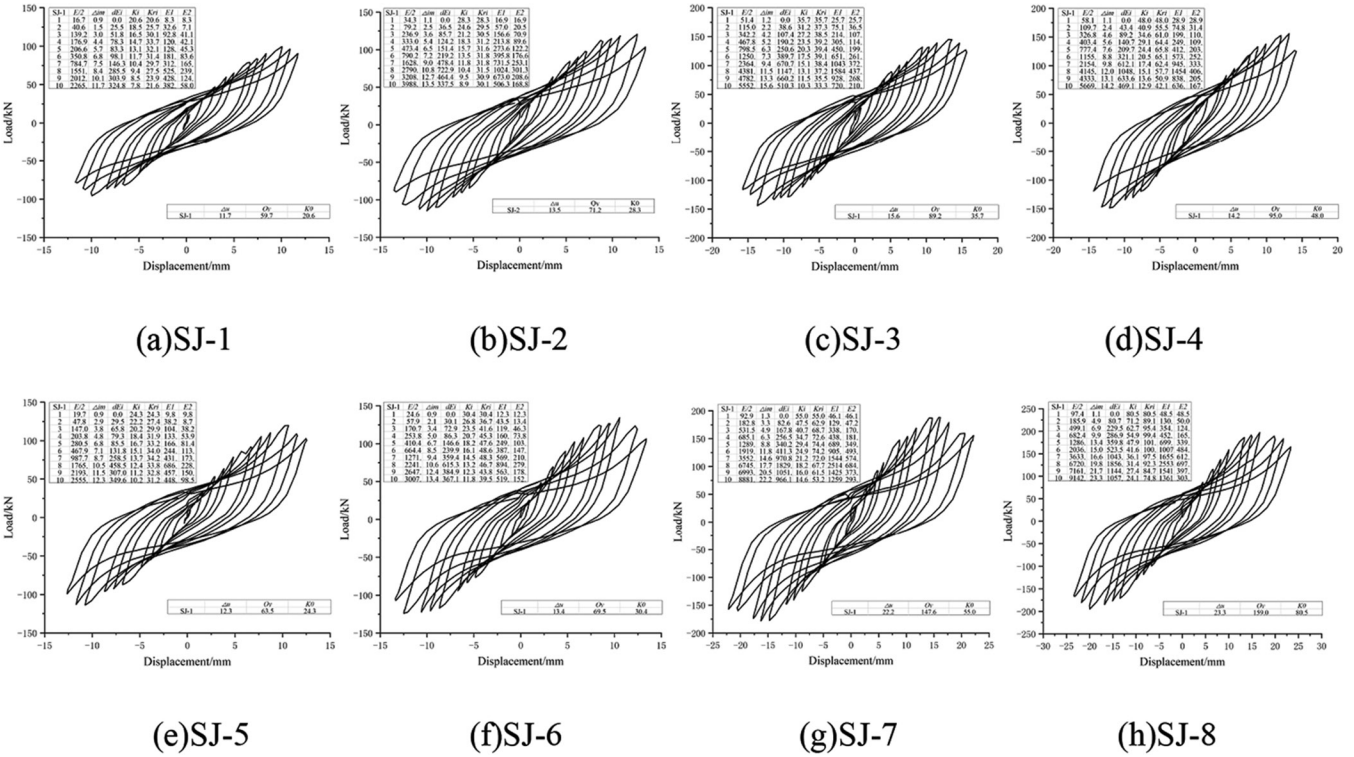


Fig. 9—Hysteresis curves of specimens.

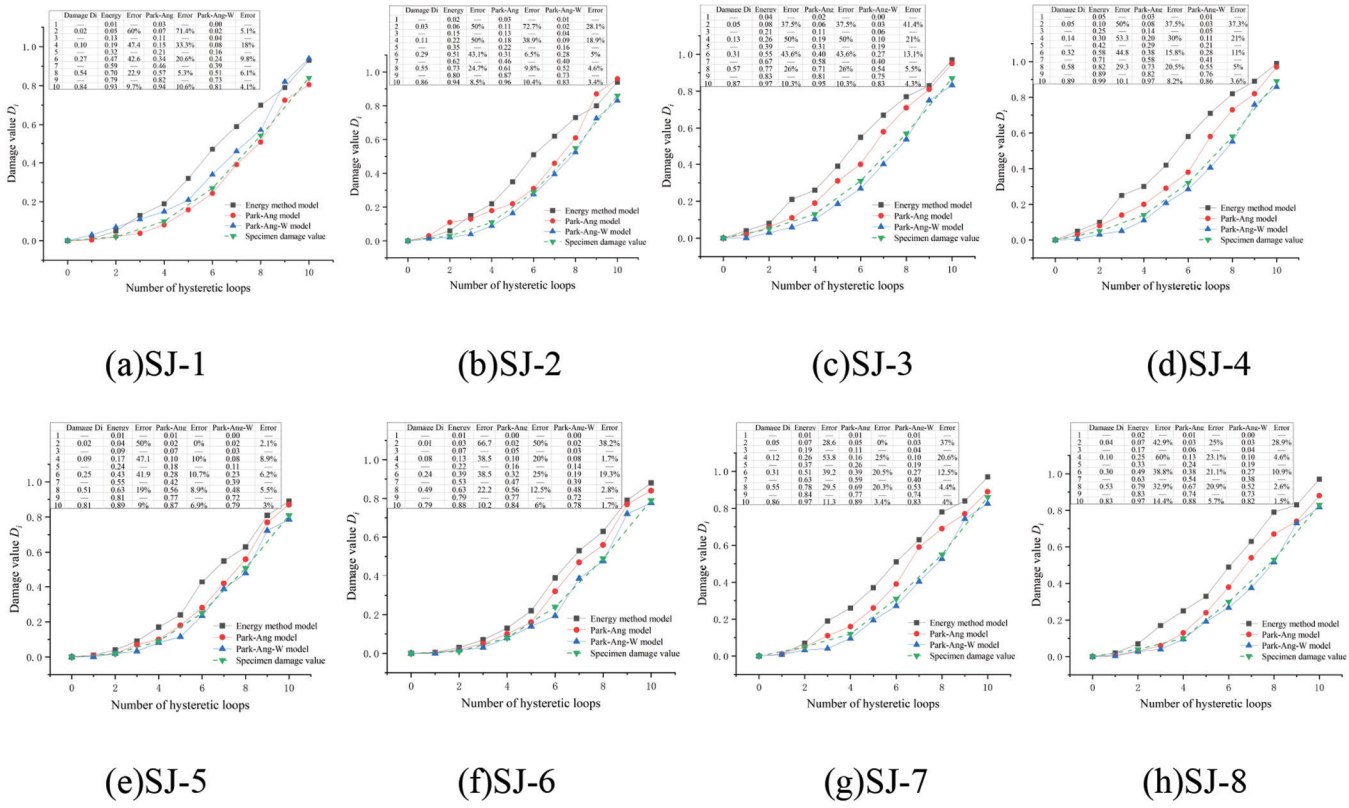


Fig. 10—Comparison of damage values calculated by different models with real damage values.

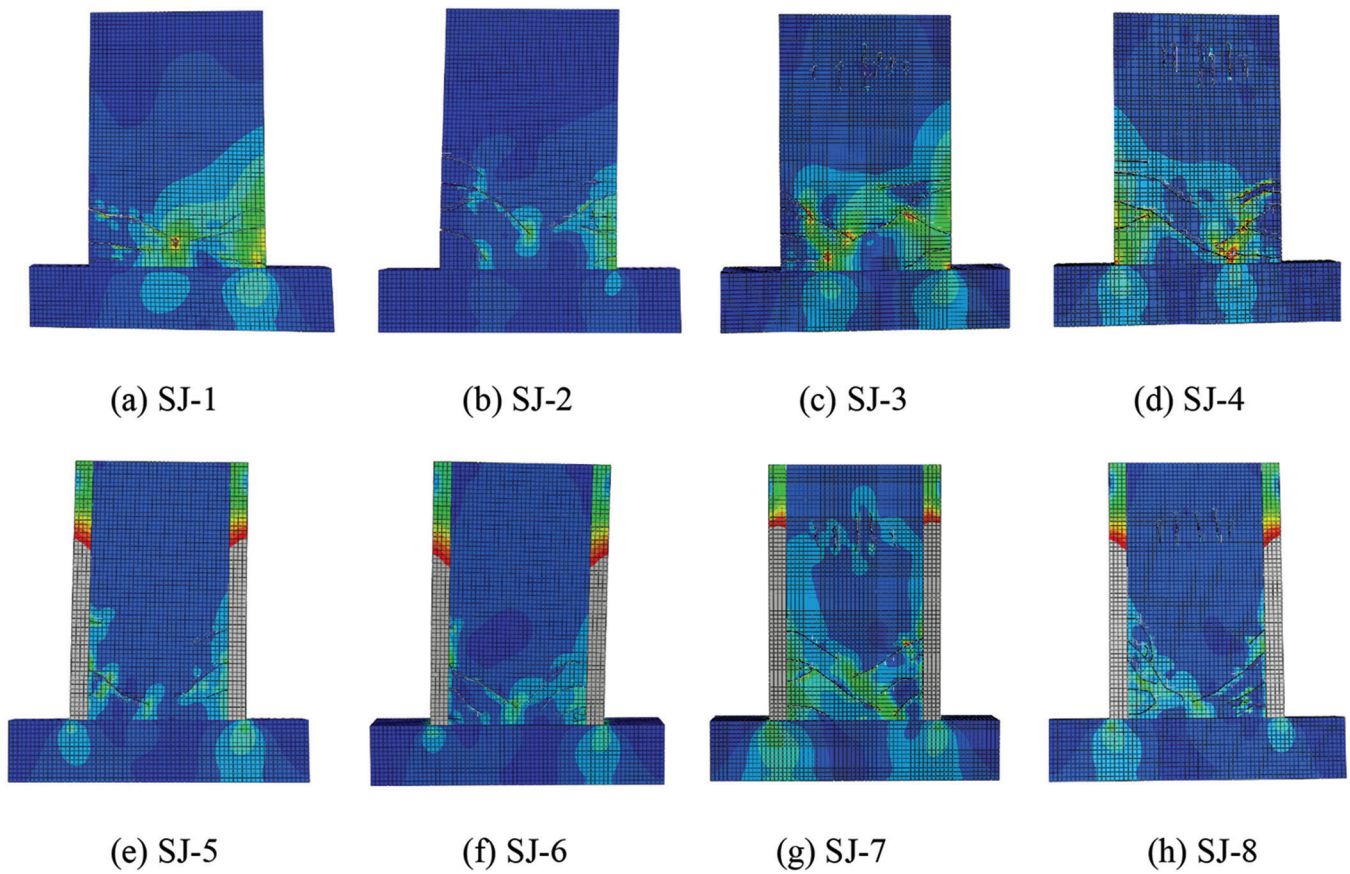


Fig. 11—Diagram of simulated fracture distribution.

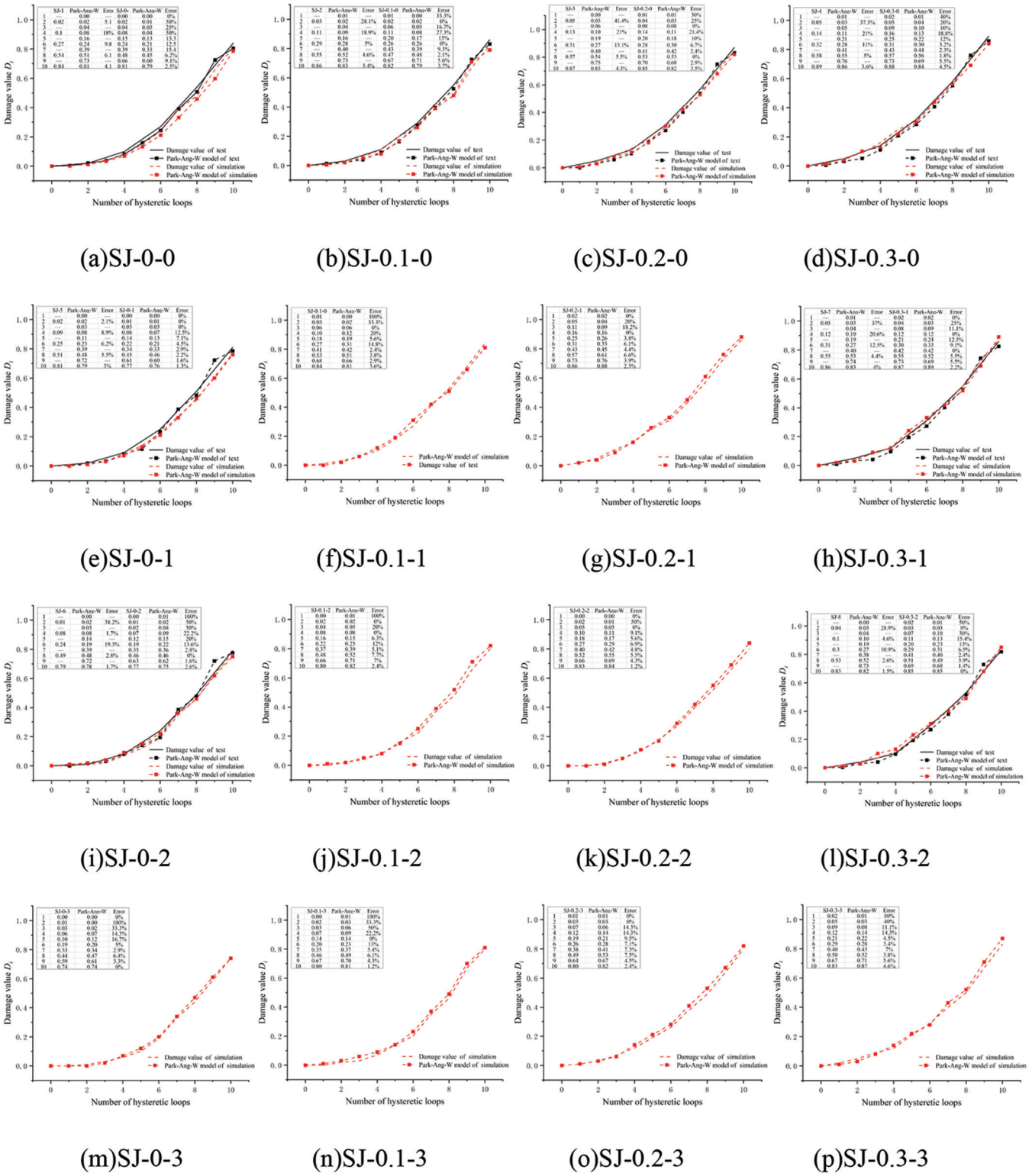


Fig. 12—Numerical simulation verification of damage value of Park-Ang-W model.

walls is studied. The constitutive model of foamed concrete is based on the concrete damage plasticity (CDP) model.[44,45] The three-fold line model is used for the constitutive model of steel.[46] The loading system adopts quasi-static loading.

The failure modes and crack development of the specimens under loading are shown in Fig. 11. The simulated crack distributions of the specimens are all along bending-shearing diagonal cracks of 30 to 45 degrees. The length and width of the cracks are in agreement with the test results. This indicates that the Abaqus software can effectively simulate the failure and cracking of the wall.

The Park-Ang-W model damage values of 16 walls were verified by the Abaqus model mentioned previously. The specimen number is represented by SJ-a-b, where "a" stands for axial compression ratio, and "b" stands for wall thickness of Type C steel. The axial compression ratio is 0, 0.1, 0.2,

and 0.3, respectively. The wall thickness of C-section steel is 0 mm, 1 mm, 2 mm, and 3 mm, and the corresponding ratio is 0, 0.004, 0.008, and 0.012, respectively. The comparison between the damage value of the Park-Ang-W model simulated by Abaqus and the real damage value of the model specimen is shown in Fig. 12. According to the results of the overall curve of 16 specimens, the damage of the wall gradually increases with the axial compression ratio μ increase, but the influence range is small. When the axial compression ratio μ is 0.3, it only increases by 6.7% compared to when the axial compression ratio is 0. The damage to the wall decreases gradually with the steel ratio ρ increase. When the wall thickness of C-type steel is 0.3, the damage value of the wall decreases by 12.3% compared to when the wall thickness is 0. This indicates that increasing the steel distribution ratio is more effective for reducing seismic damage to walls. From the comparison of the real damage value and simulated damage value, the maximum error is 5.1%. This indicates that the simulation results are in good agreement with the actual test results. According to the comparison between the simulated damage value and the damage value of the Park-Ang-W model, the error in the first four cycles is still relatively large, generally above 15%. However, after reaching the fourth cycle, the error is relatively small, generally less than 10%. By the 10th cycle, the maximum error is only 4.6%. This is consistent with the results of the experiment. In general, the calculation results of the Park-Ang-W model are not accurate enough when the number of cycles is less than four, but the calculation results are more accurate when the number of cycles is higher, which can reflect the real damage situation of the wall.

CONCLUSIONS

Based on the crack development theory, a method for calculating the true damage value of walls is proposed. Then, two seismic damage models for walls are proposed by theoretical calculation and experimental analysis. Finally, eight test specimens and 16 numerical simulation specimens were used to verify the damage values of the two models. The following results are obtained:

1. The method for calculating the damage value of the wall can effectively calculate the damage caused by the repeated loading of the specimen.

2. The error between the damage value obtained by the energy method model and the true damage value is large when the number of cycles is two to four, and the error is approximately 10% when the 10th cycle is reached. The maximum damage value D_i of the model is 0.99.

3. The error between the Park-Ang-W model damage value and the actual damage value can reach approximately 10% in the sixth cycle and even higher accuracy in the high cycle. The maximum damage value D_i of the model is 0.86. The Park-Ang-W model can better reflect the actual damage to the wall.

4. The finite element simulation results of Abaqus agree well with the test results, and the error is generally approximately 10%. When the axial compression ratio μ increased, the wall damage increased by 6.7%. When the steel ratio ρ increased, the wall damage was reduced by 12.3%. Reducing the axial compression ratio has little effect on the damage to the wall, and increasing the steel distribution ratio has a significant effect on the damage to the wall.

AUTHOR BIOS

Yunhong Hao *is a Professor at Inner Mongolia University of Technology, Hohhot, Inner Mongolia, China, where he received his BS, MS, and PhD in civil engineering in 2005, 2013, and 2018, respectively. His research interests include the properties of concrete materials and concrete impact.*

Hongze Wang *is a PhD Student at Inner Mongolia University of Technology, where he received his BS and MS in civil engineering in 2016 and 2020, respectively. His research interests include the seismic design of concrete structures and wall components.*

Yupeng Zhao *is a PhD Student at Inner Mongolia University of Technology, where he received his BS and MS in civil engineering in 2020. His research interests include the design of foamed concrete walls.*

Chakelehan *is a PhD Student at Inner Mongolia University of Technology, where he received his BS and MS in civil engineering in 2020. His research interests include the seismic performance of foamed concrete walls.*

Yong Shi *is a Professor at Inner Mongolia University of Technology, where he received his BS, MS, and PhD in civil engineering in 2004, 2010, and 2021, respectively. His research interests include the properties of concrete materials and concrete impact.*

REFERENCES

1. Hao, H.; Bi, K.; Chen, W.; Pham, T. M.; and Li, J., "Towards Next Generation Design of Sustainable, Durable, Multi-Hazard Resistant, Resilient, and Smart Civil Engineering Structures," *Engineering Structures*, V. 277, 2023, Article No. 115477. doi: 10.1016/j.engstruct.2022.115477

2. Stanojević, A. D.; Milošević, M. R.; Milošević, D. M.; Turnšek B. A. J.; and Jevremović L. L., "Developing Multi-Criteria Model for the Protection of Built Heritage from the Aspect of Energy Retrofitting," *Energy and Buildings*, V. 250, 2021, Article No. 111285. doi: 10.1016/j.enbuild.2021.111285

3. Kruger, J.; Cho, S.; van den Heever, M.; Bester, F.; van Rooyen, A.; and van Zijl, G., "Nanotechnology for Improved Three-Dimensional Concrete Printing Constructability," *ACI Materials Journal*, V. 118, No. 6, Nov. 2021, pp. 19-28.

4. Platt, S. L.; Walker, P.; Maskell, D.; Shea, A.; Bacoup, F.; Mahieu, A.; Zmamou, H.; and Gattin, R., "Sustainable Bio & Waste Resources for Thermal Insulation of Buildings," *Construction and Building Materials*, V. 366, 2023, Article No. 130030. doi: 10.1016/j.conbuildmat.2022.130030

5. Ma, S.; Tan, S.; Pan, Y.; and Gu, Y., "Experimental Study on Fiber-Reinforced Ceramsite Concrete Composite Wall Panel and Correction of Seismic Damage Model," *Structures*, V. 59, 2024, Article No. 105805. doi: 10.1016/j.istruc.2023.105805

6. Song, Q.; Bao, J.; Xue, S.; Zhang, P.; and Mu, S., "Collaborative Disposal of Multisource Solid Waste: Influence of an Admixture on the Properties, Pore Structure and Durability of Foam Concrete," *Journal of Materials Research and Technology*, V. 14, 2021, pp. 1778-1790. doi: 10.1016/j.jmrt.2021.07.075

7. Raj, A.; Sathyan, D.; and Mini, K. M., "Physical and Functional Characteristics of Foam Concrete: A Review," *Construction and Building Materials*, V. 221, 2019, pp. 787-799. doi: 10.1016/j.conbuildmat.2019.06.052

8. Allouzi, R.; Al Qatawna, A.; and Al-Kasasbeh, T., "Lightweight Foamed Concrete Mixture for Structural Use," *ACI Materials Journal*, V. 117, No. 3, May 2020, pp. 99-109.

9. Zhang, Y.; Li, Y.; Fan, W.; and Dias-da-Costa, D., "Seismic Damage and Assessment Model Analysis of Prestressed Segmental Bridge Columns," *Structures*, V. 38, 2022, pp. 797-807. doi: 10.1016/j.istruc.2022.02.018

10. Dunn, T. P. A.; van Zijl, G. P. A. G.; and van Rooyen, A. S., "Investigating a Reinforced Lightweight Foamed Concrete Walling System for Low-Rise Residential Buildings in Moderate Seismic Regions," *Journal of Building Engineering*, V. 20, 2018, pp. 663-670. doi: 10.1016/j.jobe.2018.09.011

11. Koyama, A.; Suetsugu, D.; Fukubayashi, Y.; and Mitabe, H., "Experimental Study on the Dynamic Properties of Rigid Polyurethane Foam in Stress-Controlled Cyclic Uniaxial Tests," *Construction and Building Materials*, V. 321, 2022, Article No. 126377. doi: 10.1016/j.conbuildmat.2022.126377

12. Xu, Z.; Chen, Z.; Osman, B. H.; and Yang, S., "Seismic Performance of High-Strength Lightweight Foamed Concrete-Filled Cold-Formed Steel

Shear Walls," *Journal of Constructional Steel Research*, V. 143, 2018, pp. 148-161. doi: 10.1016/j.jcsr.2017.12.027

13. Lu, Y.; Hu, X.; Yang, X.; and Xiao, Y., "Comprehensive Tests and Quasi-Brittle Fracture Modeling of Light-Weight Foam Concrete with Expanded Clay Aggregates," *Cement and Concrete Composites*, V. 115, 2021, Article No. 103822. doi: 10.1016/j.cemconcomp.2020.103822

14. Gencel, O.; Bayraktar, O. Y.; Kaplan, G.; Benli, A.; Martínez-Barrera, G.; Brostow, W.; Tek, M.; and Bodur, B., "Characteristics of Hemp Fibre Reinforced Foam Concretes with Fly Ash and Taguchi Optimization," *Construction and Building Materials*, V. 294, 2021, Article No. 123607. doi: 10.1016/j.conbuildmat.2021.123607

15. Song, Y., and Lange, D. A., "Crushing Behavior and Crushing Strengths of Low-Density Foam Concrete," *ACI Materials Journal*, V. 117, No. 2, Mar. 2020, pp. 43-52.

16. Fu, Z.; Gao, R.; and Li, Y., "Measuring Seismic Resilience of Building Portfolios Based on Innovative Damage Ratio Assessment Model," *Structures*, V. 30, 2021, pp. 1109-1126. doi: 10.1016/j.istruc.2021.01.041

17. Malkeshi, F.; Banazadeh, M.; and Serajzadeh, S. A., "Micro-Finite Element Damage Modeling in Steel Plate Shear Walls," *Journal of Constructional Steel Research*, V. 170, 2020, Article No. 106074. doi: 10.1016/j.jcsr.2020.106074

18. Peng, S.; Wang, J.; Yao, Y.; Min, T.; Li, C.; Luo, L.; Zhu, Y.; Wen, X.; and Zhou, M., "A Modified *Park-Ang* Model for Seismic Damage Assessment of Recycled Aggregate Concrete-Filled Square Steel Tube Columns," *Case Studies in Construction Materials.*, V. 17, 2022, Article No. e01692. doi: 10.1016/j.cscm.2022.e01692

19. Lee, N.-L., "Application of Two-Stage Evaluation and Optimization Update Methods for the Structural Damage Detection of a Portal Beam Structure," *Structures*, V. 29, 2021, pp. 684-690. doi: 10.1016/j.istruc.2020.11.035

20. Xingxing, W.; Wei, W.; Jihong, Y.; and Yutian, W., "Seismic Damage Model for Gypsum Board-to-CFS Stud Screw Connections Considering Ground Motion Duration," *Engineering Structures*, V. 280, 2023, Article No. 115688. doi: 10.1016/j.engstruct.2023.115688

21. Wang, N., and Huang, X., "Global Damage Model for the Seismic Reliability Analysis of a Base-Isolated Structure," *Structures*, V. 34, 2021, pp. 4892-4907. doi: 10.1016/j.istruc.2021.10.059

22. Peng, S.; Xiong, Z.; and Zeng, X.-G., "A Restoring Force Model for CFRP Seismic-Damaged RACFST Columns: Theoretical, Experimental, and Simulation Analysis," *Structures*, V. 40, 2022, pp. 273-283. doi: 10.1016/j.istruc.2022.04.017

23. Ghosh, S.; Datta, D.; and Katakdhond, A. A., "Estimation of the Park–Ang Damage Index for Planar Multi-Storey Frames Using Equivalent Single-Degree Systems," *Engineering Structures*, V. 33, No. 9, 2011, pp. 2509-2524. doi: 10.1016/j.engstruct.2011.04.023

24. Ranjani, I. S., and Ramamurthy, K., "Relative Assessment of Density and Stability of Foam Produced with Four Synthetic Surfactants," *Materials and Structures*, V. 43, No. 10, 2010, pp. 1317-1325. doi: 10.1617/s11527-010-9582-z

25. Dong, J.; Bai, Y.; Liu, Y.; Cong, X.; and Shen, C., "Seismic Damage Assessment of New Type Prefabricated Concrete Frame Joints," *Journal of Constructional Steel Research*, V. 215, 2024, Article No. 108553. doi: 10.1016/j.jcsr.2024.108553

26. Dong, Y.-R.; Xu, Z.-D.; Zeng, K.; Cheng, Y.; and Xu, C., "Seismic Behavior and Cross-Scale Refinement Model of Damage Evolution for RC Shear Walls," *Engineering Structures*, V. 167, 2018, pp. 13-25. doi: 10.1016/j.engstruct.2018.03.096

27. Choi, Y.; Park, D.; Kim, S.; and Hong, J.-W., "Seismic Performance of Crack-Damaged Masonry Wall Structures via Shaking Table Tests," *Structures*, V. 45, 2022, pp. 2272-2291. doi: 10.1016/j.istruc.2022.09.120

28. Gorji Azandariani, A.; Gholhaki, M.; and Gorji Azandariani, M., "Assessment of Damage Index and Seismic Performance of Steel Plate Shear Wall (SPSW) System," *Journal of Constructional Steel Research*, V. 191, 2022, Article No. 107157. doi: 10.1016/j.jcsr.2022.107157

29. Zhang, J.; Zhao, Y.; Li, X.; Li, Y.; and Dong, H., "Experimental Study on Seismic Performance of Recycled Aggregate Concrete Shear Wall with High-Strength Steel Bars," *Structures*, V. 33, 2021, pp. 1457-1472. doi: 10.1016/j.istruc.2021.05.033

30. Sivaguru, V., and Rao, G. A., "Strength and Behavior of Reinforced Concrete Squat Shear Walls with Openings under Cyclic Loading," *ACI Structural Journal*, V. 118, No. 5, Sept. 2021, pp. 235-250.

31. Xiao, C.; Zhu, A.; Li, J.; and Li, Y., "Experimental Study on Seismic Performance of Embedded Steel Plate-HSC Composite Shear Walls," *Journal of Building Engineering*, V. 34, 2021, Article No. 101909. doi: 10.1016/j.jobe.2020.101909

32. Hao, Y.; Wang, H.; Qin, L.; Sun, H.; Zhao, Y.; and kelehan, C., "Experimental and Numerical Study on Seismic Performance of Prefabricated New Fly Ash Foam Concrete Structure," *Soil Dynamics and Earthquake Engineering*, V. 178, 2024, Article No. 108462. doi: 10.1016/j.soildyn.2024.108462

33. Zhang, J.; Liu, X.; and Yang, Q., "A Unified Elasto-Viscoplastic Peridynamics Model for Brittle and Ductile Fractures under High-Velocity Impact Loading," *International Journal of Impact Engineering*, V. 173, 2023, Article No. 104471. doi: 10.1016/j.ijimpeng.2022.104471

34. Zhang, J.; Yang, Q.; and Liu, X., "Peridynamics Methodology for Elasto-Viscoplastic Ductile Fracture," *Engineering Fracture Mechanics*, V. 277, 2023, Article No. 108939. doi: 10.1016/j.engfracmech.2022.108939

35. As'ad, S.; Mukahar; and Sukiman, M., "Investigation on Wall Crack Damage and Its Proposed Repair Method," *Procedia Engineering*, V. 54, 2013, pp. 165-175. doi: 10.1016/j.proeng.2013.03.016

36. Li, J.; Chen, Z.; and Chen, W., "Axial Load-Bearing Capacities of Pre-Cast Self-Insulation Walls Made by Foam Concrete," *Structures*, V. 27, 2020, pp. 1951-1961. doi: 10.1016/j.istruc.2020.08.001

37. Jiang, N.; Ge, Z.; Guan, Y.; Zuo, Z.; Zhang, H.; Ling, Y.; and Šavija, B., "Experimentally Validated Meso-Scale Fracture Modelling of Foamed Concrete," *Theoretical and Applied Fracture Mechanics*, V. 122, 2022, Article No. 103631. doi: 10.1016/j.tafmec.2022.103631

38. Dhasindrakrishna, K.; Ramakrishnan, S.; Pasupathy, K.; and Sanjayan, J., "Collapse of Fresh Foam Concrete: Mechanisms and Influencing Parameters," *Cement and Concrete Composites*, V. 122, 2021, Article No. 104151. doi: 10.1016/j.cemconcomp.2021.104151

39. Rezaie, A.; Godio, M.; and Beyer, K., "Investigating the Cracking of Plastered Stone Masonry Walls under Shear–Compression Loading," *Construction and Building Materials*, V. 306, 2021, Article No. 124831. doi: 10.1016/j.conbuildmat.2021.124831

40. Montaser, W. M.; Shaaban, I. G.; Zaher, A. H.; Khan, S. U.; and Sayed, M. N., "Structural Behaviour of Polystyrene Foam Lightweight Concrete Beams Strengthened with FRP Laminates," *International Journal of Concrete Structures and Materials*, V. 16, No. 1, 2022, Article No. 59.

41. Kalateh-Ahani, M., and Amiri, S., "A Park-Ang Damage Index-Based Framework for Post-Mainshock Structural Safety Assessment," *Structures*, V. 33, 2021, pp. 820-829. doi: 10.1016/j.istruc.2021.04.039

42. Carrillo, J.; Oyarzo-Vera, C.; and Blandón, C., "Damage Assessment of Squat, Thin and Lightly-Reinforced Concrete Walls by the Park & Ang Damage Index," *Journal of Building Engineering*, V. 26, 2019, Article No. 100921. doi: 10.1016/j.jobe.2019.100921

43. Fan, Y.; Wang, Y.; Ge, J.; and Ai, B., "Seismic Damage and Evaluation Analysis of Joints in Enhanced-Performance Recycled Aggregate Concrete Frame," *Structures*, V. 37, 2022, pp. 1157-1164. doi: 10.1016/j.istruc.2022.01.065

44. Bakhti, R.; Benahmed, B.; Laib, A.; and Alfach, M. T., "New Approach for Computing Damage Parameters Evolution in Plastic Damage Model for Concrete," *Case Studies in Construction Materials.*, V. 16, 2022, Article No. e00834. doi: 10.1016/j.cscm.2021.e00834

45. Hao, Y.; Wang, H.; Qin, L.; Hou, Y.; and Shi, Y., "Dynamic Characteristics and Response Analysis of a New Type of Prefabricated Fly Ash Foam Concrete Structure," *Structures*, V. 57, 2023, Article No. 105074. doi: 10.1016/j.istruc.2023.105074

46. Behzadi-Sofiani, B.; Gardner, L.; and Wadee, M. A., "Behaviour, Finite Element Modelling and Design of Cruciform Section Steel Columns," *Thin-Walled Structures*, V. 182, Part A, 2023, Article No. 110124. doi: 10.1016/j.tws.2022.110124

ACI STRUCTURAL JOURNAL TECHNICAL PAPER

Title No. 121-S71

Failure Analysis of Reinforcing Semi-Grouted Sleeve Node Connection

by Jingshuang Zhang, Ruihan Qin, Fei Lv, Yonghua Shu, and Yanqing Wu

In this paper, uniaxial tensile testing of semi-grouted sleeve connectors was carried out by controlling the amount of expansive agent in the grout material. The effects of different steel bar diameters and anchorage depths on the failure mode, bearing capacity, and surface strain of sleeve connectors were studied. It is found that there are three failure modes in the specimens—namely, steel bar pullout failure, steel bar slip failure, and screw thread failure. The expansion characteristics of the grout material can partially compensate for the lack of compressive strength. Based on the analysis of the ultimate bearing capacity of different specimens, a design method to prevent the slip failure of the semi-grouted sleeve is proposed. The addition of 5 to 11% expansive admixture can reduce the circumferential strain of the casing from the steel bar anchorage location to the grouting end by 28.57 to 125.30%, with no impact on the longitudinal strain variation pattern. As the depth of steel bar anchorage increases, the expansive effect of the steel bar anchorage and casing longitudinal strain gradually surpasses the shrinkage effect, while the shrinkage effect at the grouting end of the casing gradually outweighs the expansive effect. With an increase in steel bar diameter, the longitudinal strain at the grouting end of the casing only decreases by 1.75% and 2.10%, essentially having no significant impact.

Keywords: bearing capacity; grout material; reinforcement connection; semi-grouted sleeve; stress-strain; uniaxial tension.

INTRODUCTION

The reliability of steel bar connections in precast nodes in prefabricated concrete structural buildings plays a crucial role in ensuring the integrity and seismic performance of the structural system.[1,2] Steel bar sleeve connections are currently widely used and relatively mature techniques in steel bar connection technology. Compared to traditional steel bar connection methods, they offer more flexibility and convenience in construction.[3,4]

The research and application of steel bar sleeve connections have a history of several decades. In 1968, American structural engineer Alfred A. Yee invented the steel bar sleeve, and applied it in the construction of the 38-story Ala Moana Hotel frame structure building in Honolulu, HI. Due to its excellent performance, it quickly garnered widespread attention and research among scholars.[5-7] Hayashi et al.[8,9] found, through uniaxial tensile and cyclic loading tests on joints, that the position of the sleeve shear key and grout thickness do not affect the ultimate bearing capacity of the joint. Lamport[10] discovered through comparative tests on different grout strengths that the ultimate bearing capacity of grout sleeve joints varies with the square root of the grout strength. Sayadi et al.[11] found that increasing the sleeve length and steel bar anchorage length can enhance the bond strength and ultimate bearing capacity of the joint. Ling et al.[12,13] conducted uniaxial tensile tests on sleeves by controlling parameters such as anchorage length and sleeve diameter, providing calculation formulas to evaluate the structural performance of the connection specimens. Wu et al.[14] conducted monotonic tensile and uniaxial cyclic tensile tests on specimens with 36 different grout ages and steel bar types. The study revealed that the failure mode of the sleeve primarily depends on the relative magnitudes of the ultimate bond strength and the tensile force corresponding to the ultimate strength of the steel bar. Han and Huang[15] found that the confinement stress of the sleeve was unevenly distributed along the bond length, with higher confinement stress in the central bonding region compared to the ends. During the yielding stage, the confining stress and bond strength increase with the yield strength of the steel bar.

In summary, scholars have conducted extensive research on the mechanical performance of fully grouted sleeves. Under different parameter conditions, the forces transmitted between the steel bar-grout material-steel bar sleeve vary, leading to changes in the strain on the sleeve surface.[16-18] Semi-grouted sleeves, as an improved sleeve connection method, feature relatively smaller dimensions, convenient construction, and easier assurance of construction quality.[19,20]

RESEARCH SIGNIFICANCE

Whether the failure modes of semi-grouted and fully grouted sleeves are the same, how the precompressive stress induced by grout material expansion affects the sleeve failure modes, and whether it is possible to predict the failure modes of semi-grouted sleeves through a certain method have not yet received sufficient research attention.

Therefore, experiments were conducted using high-strength non-shrinkage cement-based sleeve grout material, with grout material expansion agent, anchorage depth of steel bar, and steel bar diameter as variable parameters to study and analyze the failure modes, bearing capacity, and stress-strain variations on the surface of the semi-grouting sleeve. The safety and reliability issues of semi-grouted sleeve connection points were investigated, aiming to provide data references for research on semi-grouted sleeves.

ACI Structural Journal, V. 121, No. 5, September 2024.

MS No. S-2023-143.R3, doi: 10.14359/51740856, received March 30, 2024, and reviewed under Institute publication policies. Copyright © 2024, American Concrete Institute. All rights reserved, including the making of copies unless permission is obtained from the copyright proprietors. Pertinent discussion including author's closure, if any, will be published ten months from this journal's date if the discussion is received within four months of the paper's print publication.

Table 1—Semi-grouted sleeve technical parameters

Sleeve mode	l, mm	l_1, mm	l_2, mm	l_3, mm	l_4, mm	D_1, mm	D_2, mm	d, mm
GT20	211	175	28	136	30	42	32.5	20
GT22	230	191	30.5	151	30	45	35.0	22
GT25	256	215	33	175	30	50	38.5	25

Note: l is length of semi-grouted sleeve; l_1 is anchorage length of steel bar; l_2 is depth of threaded hole; l_3 is distance between grouting hole and slurry outlet hole; l_4 is position of grouting hole; D_1 is outer diameter of semi-grouted sleeve; D_2 is internal diameter of semi-grouted sleeve; and d is diameter of steel bar. Material of sleeve: structural alloy steel, tensile strength is 600 MPa, yield strength is 355 MPa, and percentage elongation after fracture is 16%.

Table 2—Physical properties of grout

Grouting material	HCSA doping, %	Flow degree, mm		Compressive strength, MPa			Vertical expansion rate, %
		Initial	30 minutes	1 day	3 days	28 days	Difference between 24 hours and 3 hours
G1	5	347	331	56.7	65.9	84.4	0.10
G2	8	362	347	56.6	71.8	105.9	0.15
G3	11	364	339	63.5	78.4	70.4	0.23

Table 3—Steel material properties

Diameter, mm	A, %	R^o_{eL}, MPa	R^o_m, MPa	R^o_{eL}/R_{eL}	R^o_m/R^o_{eL}
20	26.2	485	649	1.21	1.34
22	26.6	481	639	1.20	1.33
25	26.8	459	633	1.15	1.38

Note: A is elongation of steel bar after break; R^o_{eL} is measured yield strength of steel bar; R^o_m is measured tensile strength of steel bar; and R_{eL} is standard value of yield strength of steel bar.

EXPERIMENTAL DESIGN

Specimen design

The experiment involved the design of 27 types of connection specimens, with the research parameters being grout material expansion agent dosage (5, 8, and 11%), steel bar anchorage depth (5d, 7d, and 8d), and steel bar diameter (20, 22, and 25 mm). The steel bar sleeves chosen were JM series semi-grouted sleeve, with different diameter steel bars corresponding to the respective types of semi-grouted sleeves. The steel bar sleeve structure and technical parameters are shown in Fig. 1 and Table 1.

Material properties

The experiment used a self-made high-strength non-shrink cement-based sleeve grout material. The water-cement ratio (w/c) of the grout material was 0.26, with a plastic expansion agent dosage of 0.03% and a sand-cement ratio of 1.0; in addition, 5% silica fume, 0.5% water reducer, and 5% fly ash were added while controlling the amount of high-performance calcium sulfoaluminate (HCSA). In accordance with the requirements of JG/T 408-2019,[21] tests were conducted on the flowability, compressive strength (on 40 x 40 x 160 mm samples), and vertical expansion rate of the self-made grout material, with the test results shown in Table 2. Hot-rolled deformed steel bars with diameters of 20, 22, and 25 mm were used in the experiment. Different diameter steel bars were paired with corresponding types of steel bar sleeves. The steel bar properties are detailed in Table 3.

Test content and methods

To investigate the influence of the strain on the sleeve surface as the stress on the steel bar surface changes during loading, resistance strain gauges were attached to the steel bar surface and the steel bar sleeve surface before loading the specimens. The strain data on the steel bar sleeve surface were collected, and data collection stopped when the strain gauges on the steel bar surface broke or detached. The location of the strain gauges is shown in Fig. 2.

The experiment used a 1000 kN hydraulic universal testing machine (Fig. 3(a)) and conducted uniaxial tensile tests according to JGJ 107-2016.[22] The loading sequence was 0 → maximum tensile force (recording ultimate tensile bearing capacity) → failure, with a loading rate of 25 mm/min. When loading to the failure (steel bar fracture, steel bar slip) of the steel bar sleeve, stop loading. A static resistance strain gauge was used to collect the sleeve surface strain data (Fig. 3(b)).

Studies have shown that eccentricity of the steel bar can lead to differences in strain on both sides of the steel bar sleeve surface, and can also affect the tensile displacement of the joint's ultimate axial force.[23,24] To avoid the influence of steel bar eccentricity on the sleeve connection specimens, and to prevent disturbance to the connecting steel bar during the grouting process, the steel bar with threaded ends was first screwed into the sleeves and fixed on the panel during the specimen fabrication process. Subsequently, the steel bar at the grouting end was manually aligned and then secured using self-tapping screws.

EXPERIMENTAL RESULTS AND ANALYSIS

Destruction pattern

In the uniaxial tensile test, three failure modes were observed: steel bar fracture failure, steel bar slip failure, and screw thread failure. For steel bar fracture failure (Fig. 4(a)), the fracture of the steel bar occurred in the middle section away from the threaded or grouted end. This indicates that the ultimate tensile strength of the sleeve connection segment is higher than that of the grouting end and threaded end, with the weakest point of the specimen located at the two end steel bars. During the loading process of the specimen, as the load

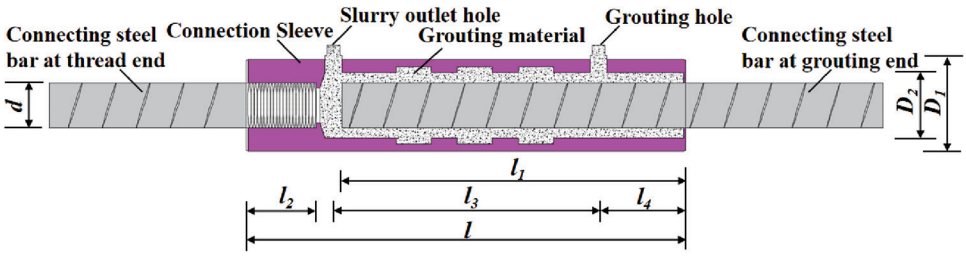


Fig. 1—Semi-grouted sleeve structure.

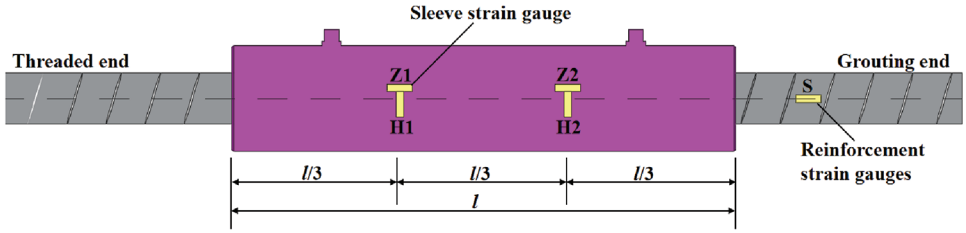


Fig. 2—Position diagram of strain gauge.



(a) Universal testing machine (b) Static resistance strain gauge

Fig. 3—Test apparatus.

increased, cracks appeared in the grout material at the grouting end and continuously extended outward, finally falling off in a cone shape. Although the specimen had failed, the grouting material and the anchoring steel bar were still bonded together without any apparent signs of pullout, indicating that the bond force between the grout material and the steel bar was still playing a role before the specimen failed. In Specimen T20-G1-7d, the steel bar fractured at the thread connection point, which was due to inadequate thread processing, leading to the incomplete insertion of the thread steel bar into the steel bar sleeve. The load was only transmitted by the screwed-in part, reducing the load-transfer area and causing it to become the weak point of the specimen.

For steel bar slip failure (Fig. 4(b)), cracks appeared on the bonding surface between the steel bar and the grout material, the concrete interlocking teeth between the steel bar rib sheared off, and the conical wedge action lost its effect. The steel bar separated from the grout material, and there was also a small amount of grout material between the transverse ribs of the steel bar. This indicates that the failure of the specimen was due to the load reaching the ultimate bond strength between the grout material and the steel bar, which is classified as a steel bar scraping plough pullout failure. It is worth noting that in all specimens, there were no instances of the steel bar sleeve being pulled apart or the grout material and anchored steel bar being pulled out as a whole.

For screw thread failure (Fig. 4(c)), this failure mode should not exist. From the figure, it can be observed that the steel thread was flattened. The authors believe this is a result of failed steel bar thread processing, rather than a typical failure phenomenon. Referring to the uniaxial tensile test results, Specimen T22-G1-7d failed when the load reached 126.5 kN. By comparing the yield loads of Specimens T20-G1-7d and T25-G1-7d, it can be surmised that at the point of failure of Specimen T22-G1-7d, the connector was still in the elastic phase.

Through analysis, it was determined that the failure mode of the sleeve connection depends on the ultimate tensile strength of the specimen and the ultimate bond strength between the steel bar and grout material. That is, when the ultimate tensile strength of the specimen is less than the ultimate bond strength between the steel bar and grout material, the specimen failure is by steel bar fracture; when the ultimate tensile strength of the specimen is greater than the ultimate bond strength between the steel bar and grout material, the specimen failure is by steel bar slip. It is imperative to

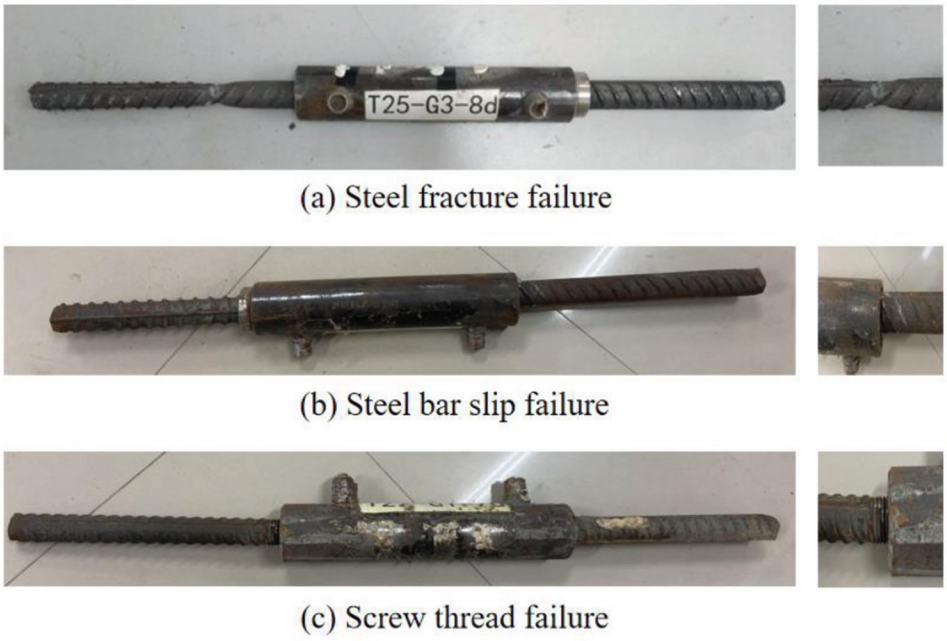


Fig. 4—Sleeve failure mode.

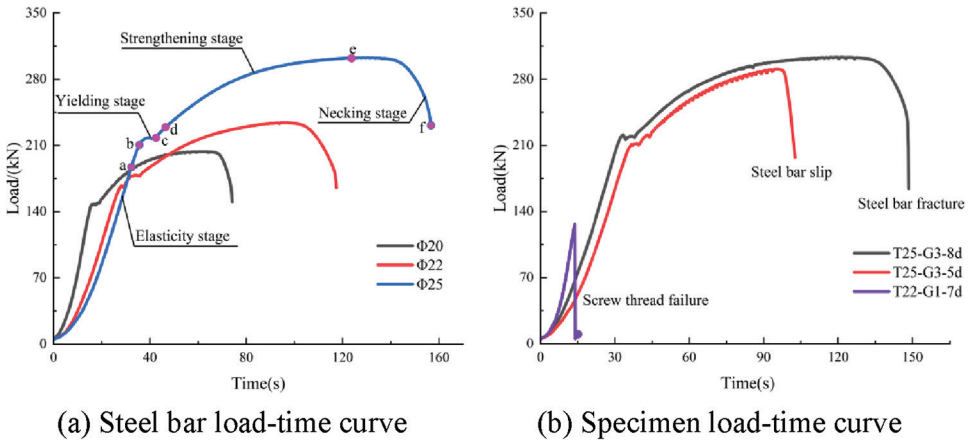


Fig. 5—Uniaxial tensile test load-time curve.

ensure the machining quality of the sleeve thread and steel bar thread to prevent steel bar failure in the thread section and steel bar slip failure.

Load-bearing capacity analysis

Through the uniaxial tensile test, it was observed that the variation law of the steel bar sleeve connectors is similar to that of the steel bar; it can be divided into four stages: the elasticity stage, the yielding stage, the strengthening stage, and the necking stage. In instances where the specimen experienced steel bar slip failure, the steel bar did not reach the ultimate tensile strength, and thus failed to meet the requirements for connection effectiveness.[25-27] Figure 5 shows the load-time curves of the steel bar and three typical failure modes of connectors: T25-G3-8d (steel bar fracture failure), T25-G3-5d (steel bar slip failure), and T22-G1-7d (screw thread failure). The results of the uniaxial tensile tests are shown in Table 4.

Except for Specimens T20-G1-7d and T22-G1-7d, four specimens experienced steel bar slip failure, while the rest exhibited steel bar fracture failure, indicating that most of specimens had met the use requirements. As the anchoring depth increases, there is a decreasing trend in the bond strength of the specimens. For example, in Specimen T22-G2, as the anchorage depth increased from 5*d* to 7*d*, the bond strength at the point of failure decreased by 28.52%; with an increase from 7*d* to 8*d*, the bond strength decreased by 12.63%. It was found that when failure occurs between the yielded portion of the steel bar and the grout material, stress redistribution occurs between the anchored steel bar and grout material, leading to the bonding force decreasing. As the anchorage depth increases, the average bond stress value along the radial direction of the steel bar decreases.

The ratio of the measured ultimate tensile strength of the connection specimens to the standard ultimate tensile strength of the steel bar is greater than 1.10, indicating that the sleeve connector under the grout material has a large safety design allowance. Even though the compressive strength of the grout material falls below the standard requirements when the HCSA content is 11%, the steel bar sleeve still meets the requirements for use. This suggests that

Table 4—Unidirectional tensile test results

ID	P_y, kN	P_u, kN	$\tau_{b,max}$, MPa	f_{mst}/f_{stk}	Failure mode
T20-G1-8d	140.7	199.1	>19.81	1.17	Steel bar fracture
T20-G1-7d	148.0	204.2	>23.23	1.20	Steel bar fracture
T20-G1-5d	147.3	203.4	>32.39	1.20	Steel bar fracture
T22-G1-8d	173.5	238.8	>19.64	1.16	Steel bar fracture
T22-G1-7d	—	126.5	>11.89	0.62	Screw thread failure
T22-G1-5d	173.1	239.2	>31.48	1.17	Steel bar fracture
T25-G1-8d	220.5	304.9	>19.42	1.15	Steel bar fracture
T25-G1-7d	211.1	297.7	>21.67	1.12	Steel bar fracture
T25-G1-5d	—	291.0	29.66	1.10	Steel bar slip
T20-G2-8d	140.6	199.7	>19.87	1.18	Steel bar fracture
T20-G2-7d	148.6	202.6	>23.04	1.19	Steel bar fracture
T20-G2-5d	147.2	200.8	>31.97	1.18	Steel bar fracture
T22-G2-8d	168.2	233.8	>19.23	1.14	Steel bar fracture
T22-G2-7d	166.9	234.2	>22.01	1.14	Steel bar fracture
T22-G2-5d	166.6	234.0	>30.79	1.14	Steel bar fracture
T25-G2-8d	—	301.0	>18.90	1.12	Steel bar fracture
T25-G2-7d	214.9	302.8	>22.04	1.14	Steel bar fracture
T25-G2-5d	200.0	296.7	30.68	1.14	Steel bar slip
T20-G3-8d	141.0	201.0	>20.00	1.19	Steel bar fracture
T20-G3-7d	139.0	200.2	>22.77	1.18	Steel bar fracture
T20-G3-5d	138.7	198.7	31.64	1.17	Steel bar slip
T22-G3-8d	168.9	235.4	>19.36	1.15	Steel bar fracture
T22-G3-7d	169.9	236.0	>22.18	1.15	Steel bar fracture
T22-G3-5d	166.7	233.8	>30.77	1.14	Steel bar fracture
T25-G3-8d	220.0	302.6	>19.27	1.14	Steel bar fracture
T25-G3-7d	208.6	295.9	>21.54	1.12	Steel bar fracture
T25-G3-5d	209.9	290.6	29.62	1.10	Steel bar slip

Note: P_y is load at yield of connected specimen; P_u is ultimate tensile load of connected specimen; and $\tau_{b,max}$ is ultimate bond strength of connected specimen. When connector is broken by steel bar, the ultimate bonding force takes the ultimate tensile load P_u; f_{mst} is the measured ultimate tensile strength of the connection specimen, $f_{mst} = P_u/[\pi(d/2)^2]$; f_{stk} is standard value of ultimate tensile strength of steel bar, 540 MPa.

the expansive properties of the grout material can, to some extent, compensate for the insufficient compressive strength.

According to Fig. 6, it can be observed that the anchorage depth and the strength of the grout material do not significantly impact the ultimate tensile strength of the sleeve connector. However, with an increase in steel bar diameter, the ultimate bearing capacity of the specimens shows a linear growth trend. This indicates that when the specimens experience fracture failure, the ultimate bearing capacity of the specimens primarily depends on the ultimate tensile strength of the steel bar. When using the G2 grout material, the ultimate tensile strength of the specimens is higher than the other two types. By fitting the collected data (Fig. 7), the relationship between the ultimate tensile strength and the steel bar diameter was obtained

$$P_u = 1.11d_b^2 - 30.32d_b + 361.72 \quad (1)$$

$$R^2 = 0.9984 \quad (2)$$

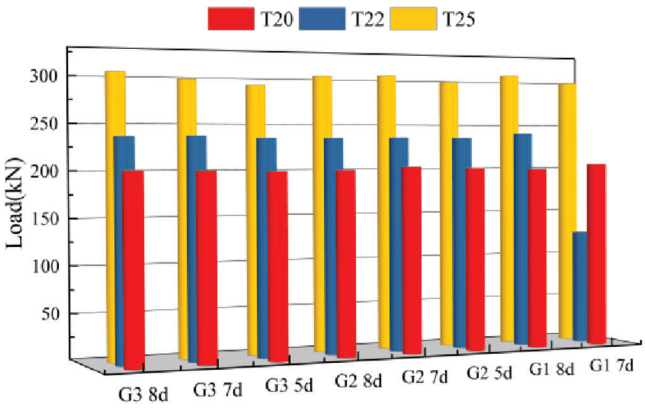


Fig. 6—Sleeve ultimate bearing capacity influence trend.

The slip failure of the specimen depends on the bond strength between the steel bar and the grout material $\tau_{b,max}$[28]

$$\tau_{b,max} = P_{b,exp}/(\pi \cdot d_b \cdot l_b) \quad (3)$$

Table 5—Values of constant *k*

ID	T20-8d	T20-7d	T20-5d	T22-8d	T22-7d	T22-5d	T25-8d	T25-7d	T25-5d
G1	2.2	2.5	3.5	2.1	1.3	3.4	2.1	2.4	3.2
G2	1.9	2.2	3.1	1.9	2.1	3.0	1.8	2.1	2.9
G3	2.4	2.7	3.8	2.3	2.6	3.7	2.3	2.6	3.5

where $P_{b,exp}$ is the ultimate strength between steel bar and grout material; d_b is the diameter of the connecting steel bar; and l_b is the anchorage depth of the steel bar. Einea et al.[29] found that the ultimate bond strength $\tau_{b,max}$ between steel bar and grout material can be approximated

$$\tau_{b,max} = k \cdot \sqrt{f_c} \quad (4)$$

where k is a constant; and f_c is the compressive strength of the grout. Substituting Eq. (3) into Eq. (4), the following can be obtained

$$P_{b,exp} = k \cdot \pi \cdot d_b \cdot l_b \cdot \sqrt{f_c} \quad (5)$$

If it is assumed that all specimens experience steel bar slip failure, then substituting the data from Table 4 into Eq. (5) yields a constant k, as shown in Table 5. When designing steel bars of different diameters or anchorage depths, the corresponding k value can be selected within the respective range, calculating the ultimate bond strength between the steel bar and the grout material. This calculation can be compared with the experimental strength to avoid steel bar slip failure in the connection components.

In the test results, because most of the connections did not experience steel bar slip failure, the k value of the specimens with tensile failure of steel bars in this paper is relatively conservative. In the next step, more tests with different steel bar diameters can be carried out to determine the accurate k value.

Effect of grouting material on surface strain of sleeve

From Fig. 8(a), it is evident that the circumferential strain variations on the surface of the steel bar sleeve connector using different grout materials exhibit a consistent pattern, showing nonlinear growth with increased load. The strain at point H1 is greater than the strain at point H2, indicating a gradual reduction in sleeve strain from the deep anchorage of the reinforcement toward the grouting end. The strain at these two points decreases by 65.54%, 28.57%, and 54.84% for the three grout materials, respectively. The difference in strain between points H1 and H2 is minimal for the G2 grout material, suggesting a more uniform distribution of circumferential strain when using G2. The circumferential strain development on the surface of the sleeve using the G3 grout material progresses most rapidly. The reason is that when the sleeve connector is tensile, the mechanical bite force between the steel rib and grout material forms a cone wedge action[30-32] to produce radial component force. These radial forces offset the precompression stress generated during the grout material hardening process. When the stress value exceeds the strength of the grout material, the expansion

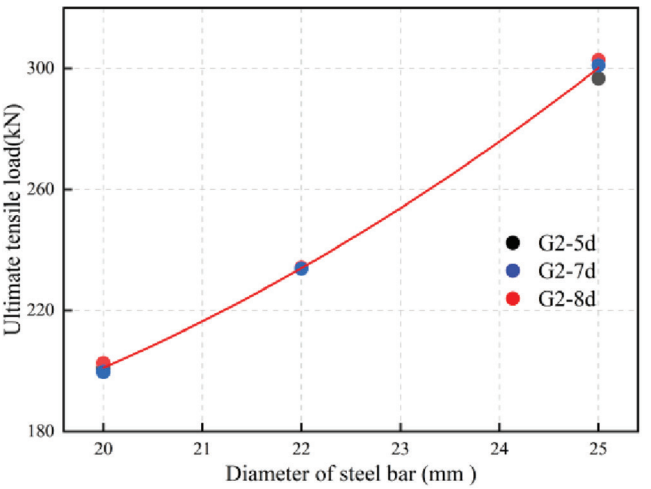
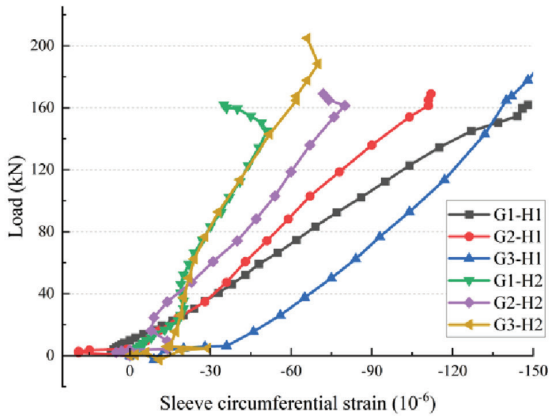
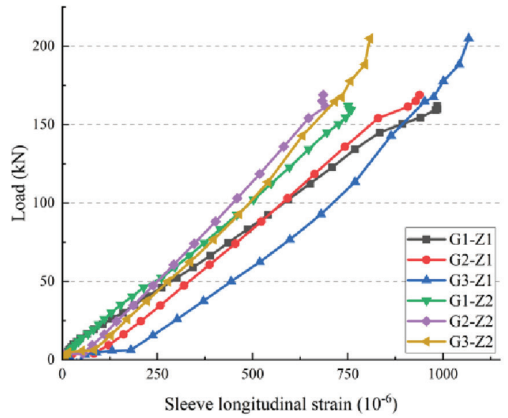


Fig. 7—Fitting of ultimate bearing capacity.

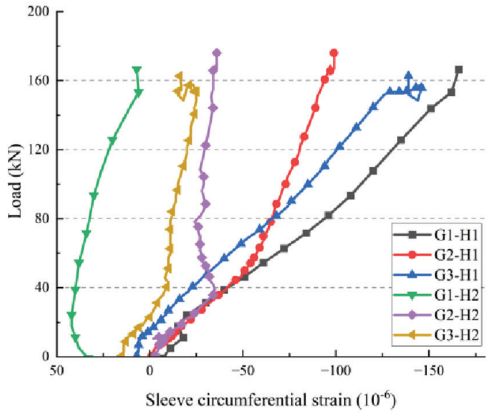
cracking of the grout material occurs—the rib squeezes the grout material to produce a radial displacement, resulting in a gradual increase in wall strain. This process continues until the steel bar slip leads to the disappearance of the "cone wedge" effect, or the steel bar is pulled off to stop loading. Despite the higher precompression stress generated during the hardening process, the strength of the G3 grout material is lower than that of G1 and G2 due to the excessive inclusion of HCSA. Consequently, with increasing load, the circumferential strain of the G3 grout material consistently exceeds that of the other two materials, with a maximum circumferential strain of up to -155×10^{-6}. In the T25 sleeve type, the circumferential strains of the three grout materials at points H1 to H2 decreased by 125.30%, 63.64%, and 82.88%, respectively. Combining the strain curve in Fig. 8(c), it is observed that the circumferential strain of the G2 grout material is lower than that of the G3 grout material at point H1. This indicates that the excessive inclusion of expansion agents has an adverse effect on the circumferential strain of the sleeve connector surface. Due to being farther away from the load concentration area, point H2 experiences lower radial forces, resulting in minimal crack expansion in the surrounding grout material. Therefore, the influence of the grout material on the strain at point H2 is relatively minor, while point H1 represents the critical section for the semi-grouted sleeve connector. From Fig. 8(b) and (d), it can be observed that the longitudinal strains on the surface of the sleeve connector are tensile strains, increasing linearly with the applied load. With an increase in the inclusion of expansion agents, the strain of the G3 grout material specimens surpasses that of G1 and G2. The change in strain from point Z1 to point Z2 is approximately 25% for all cases, indicating that the dosage of the expansion agent does not affect the variation trend of longitudinal strain. However, it does have



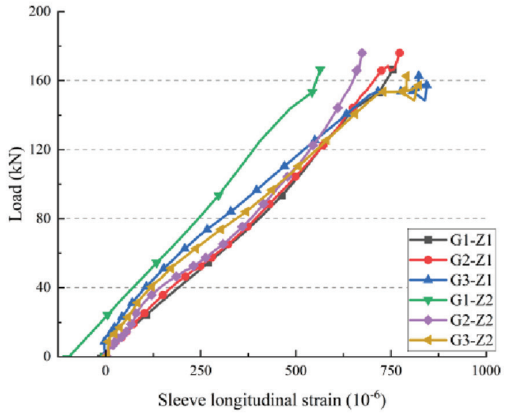
(a) Specimen T20-8d circumferential strain



(b) Specimen T20-8d longitudinal strain



(c) Specimen T25-8d circumferential strain



(d) Specimen T25-8d longitudinal strain

Fig. 8—Surface strain of different grouting material sleeves.

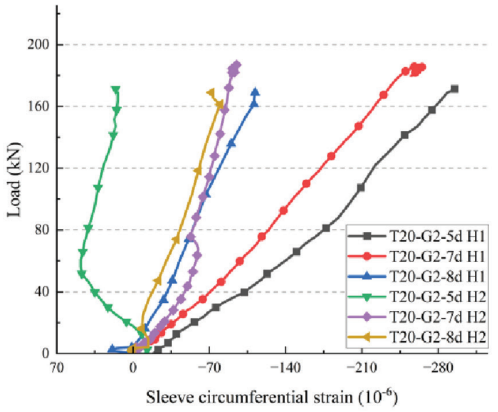
an adverse effect on the actual value of the longitudinal strain.

Effect of anchorage depth on sleeve surface strain

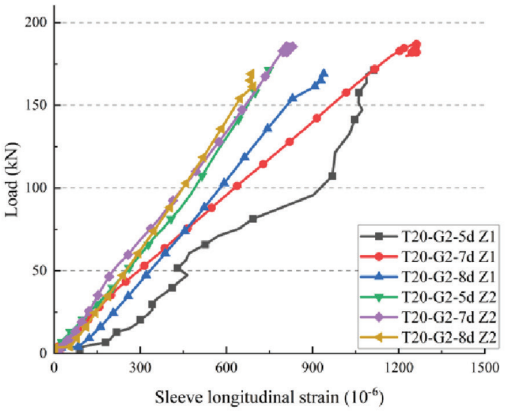
From Fig. 9(a), it is evident that as the anchorage depth increases, the circumferential strain on the sleeve surface gradually diminishes. Simultaneously, the disparity between points H1 and H2 decreases, reduced by 105.42%, 64.75%, and 35.71% for varying anchorage depths, indicating an enhancement in the specimen's resistance to deformation. The reason for this is that as the anchorage depth of the steel bar increases, the contact area between the steel bar and the grouting material increases, and at the same time, the mechanical bite force between the steel rib and the grouting material also increases, consequently enhancing the connector's stiffness. During the loading process, the circumferential strains at point H1 are all compressive strains, while the strains at point H2 transition from tensile strains to compressive strains with the increase in anchorage depth. This phenomenon arises from the circumferential expansion effect exerted on the steel bar sleeve during loading due to the shear expansion of the grout material, as well as the circumferential shrinkage effect induced by the Poisson effect when the specimen is subjected to tension.[33-35] When the shrinkage effect surpasses the expansion effect, the sleeve surface strain is a compressive strain. With the increase in anchorage depth, the expansion effect at point H1 gradually exceeds the shrinkage effect, while the shrinkage effect at point H2 gradually surpasses the expansion effect. In Fig. 9(c), a similar phenomenon is observed, where the strain difference between points H1 and H2 decreases by 157.49%, 126.00%, and 88.49%, respectively. When the anchorage depth reaches 7*d* and 8*d*, the circumferential strain at point H2 for T25-G3 is nearly zero, indicating that at this point, the shrinkage effect and expansion effect essentially cancel each other out. From Fig. 9(b) and (d), it can be observed that the longitudinal strains on the sleeve surface are all tensile strains, showing linear growth. The strain at points Z1 and Z2 for the T20 specimen decreases by 141 × 10^{-6} and 162 × 10^{-6}, respectively, while for the T25 specimen, they decrease by 373 × 10^{-6} and 353 × 10^{-6}, respectively. This decrease suggests that with the increase in anchorage depth, the shrinkage effect inside the steel bar sleeve gradually surpasses the expansion effect.

Effect of steel bar diameter on sleeve surface strain

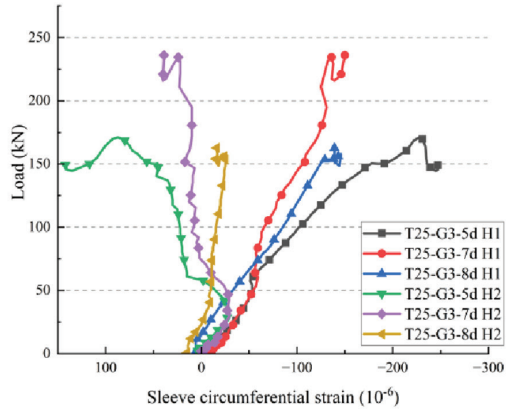
From Fig. 10(a), it is evident that the circumferential strains of the specimens are all compressive strains. For Specimen T20-G2-8d, the circumferential strain at point H1 is –112 × 10^{-6}, which is 13.13% greater than that of Specimen T25-G2-8d. At point H2, the circumferential strain



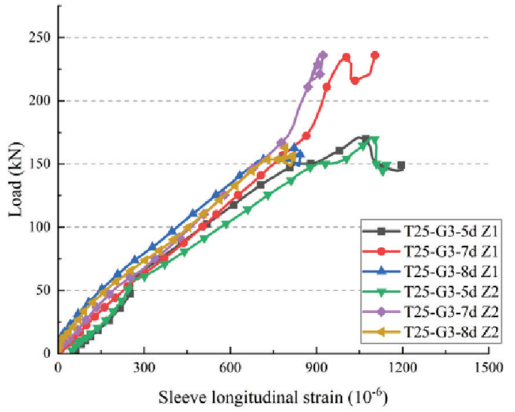
(a) Specimen T20-G2 circumferential strain



(b) Specimen T20-G2 longitudinal strain



(c) Specimen T25-G3 circumferential strain



(d) Specimen T25-G3 longitudinal strain

Fig. 9—Surface strain of sleeves with different anchorage depths.

is –72 × 10^{-6}, which is 50% greater than that of Specimen T25-G2-8d. With the increase in steel bar diameter, the circumferential strain on the steel bar sleeve surface gradually decreases. In Fig. 10(c), a similar phenomenon can also be observed. There are two main reasons for this phenomenon. First, with the increase in steel bar diameter, the amount of grout material needed to be injected into the sleeve increases, leading to an increase in the stiffness of the specimen and enhancing its ability to resist deformation. Second, with the increase in steel bar diameter, the bonding surface area between the steel bar and the grout material increases, leading to an enhancement in the chemical bonding force, frictional force, and mechanical bite force between them. From Fig. 10(b) and (d), it can be seen that the longitudinal strains of the specimens are all tensile strains. With the increase in steel bar diameter, the longitudinal strains on the sleeve gradually decrease. However, for the T20-G2-8d and T25-G2-8d specimens, the strains at point Z2 only decreased by 1.75% and 2.1%, respectively. The small magnitude of this change indicates that the steel bar diameter does not significantly affect the longitudinal strains at the grouting end of the sleeve.

CONCLUSIONS

This study investigated the failure modes, bearing capacity, and stress-strain variations on the surface of semi-grouted sleeves through the uniaxial tensile test, using a self-made high-strength non-shrink cement-based grout material. The variables considered in the study were the grout material expansion agent (5%, 8%, and 11%), steel bar anchorage depth (5*d*, 7*d*, and 8*d*), and steel bar diameter (20, 22, and 25 mm). The conclusions are as follows.

1. The semi-grouted sleeve exhibits three distinct failure modes: steel bar fracture failure, steel bar slip failure, and screw thread failure. When the ultimate tensile strength of the specimen is less than the ultimate bond strength between the steel bar and the grout material, the specimen failure is by steel bar fracture; when the ultimate tensile strength of the specimen is greater than the ultimate bond strength between the steel bar and the grout material, the specimen failure is by steel bar slip. The unqualified processing of sleeve and steel bar thread will lead to the failure of the steel bar in the thread section and screw thread failure.

2. Under different variable parameters, the ratio of the measured ultimate tensile strength of the connection specimen to the standard value of the steel bar's ultimate tensile strength is greater than 1.10. The expansion properties of the grout material can, to some extent, compensate for the insufficient compressive strength. For slip failure, the established relationship between bond strength, grout material strength, steel bar diameter, and anchorage depth can estimate the

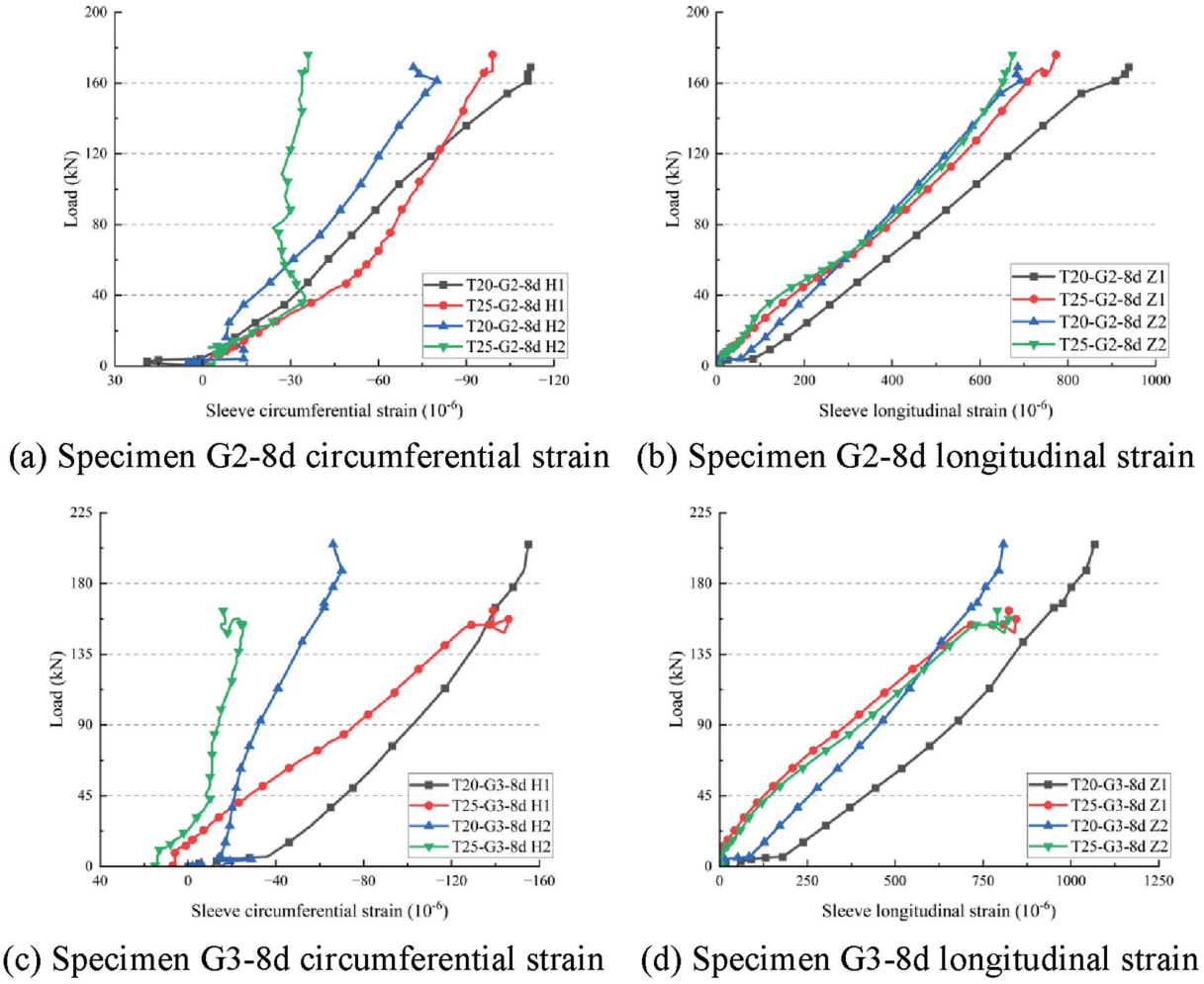


Fig. 10—Surface strain of sleeves with different steel bar diameters.

ultimate bond strength of the steel bar and the grouting material during the slip failure.

3. By comparing the circumferential strain and longitudinal strain of the steel bar sleeve under different expansion agent dosages, it was found that the circumferential strain of the sleeve gradually decreases from the steel bar anchorage depth to the grouting end, with a reduction range of 28.57% to 125.30%. An appropriate amount of expansion can improve the circumferential stress distribution of the steel bar sleeve. The longitudinal strain variations of the sleeve remain at approximately 25%, and the dosage of the expansion agent does not affect the variation trend of the longitudinal strain. But an excessive amount of expansion agent can increase the longitudinal strain values.

4. By comparing the circumferential strain and longitudinal strain of the sleeve at different anchorage depths, it was observed that as the anchorage depth increases, the expansive effect on the circumferential strain in the middle part of the sleeve and the longitudinal strain of the sleeve gradually exceeds the shrinkage effect. At the grouting end of the steel bar sleeve, the shrinkage effect gradually surpasses the expansive effect.

5. By comparing the circumferential strain and longitudinal strain of the sleeve at different steel bar diameters, it was found that increasing the steel bar diameter reduces the surface strain of the sleeve. However, it has almost no effect on the longitudinal strain at the grouting end—the specimen only exhibited reductions of 1.75% and 2.10%.

6. In this study, only the uniaxial tensile test was carried out on the semi-grouted sleeve. In the next step, high-stress repeated tension and compression tests can be carried out to study the connection performance of the steel bar sleeve under more complex stress states.

AUTHOR BIOS

JingShuang Zhang *is a Professor at Anhui University of Science and Technology, Huainan, China, where he received his PhD in 2014 and is a national specialty trainer in civil engineering. His research interests include concrete structures and new construction materials.*

Ruihan Qin *is a Master's Student at Anhui University of Science and Technology. His research interests include concrete structures.*

Fei Lv *is a Master's Student at Anhui University of Science and Technology. His research interests include concrete structures.*

Yonghua Shu *is a Master's Student at Anhui University of Science and Technology. His research interests include new construction materials.*

Yanqing Wu *is a Master's Student at Anhui University of Science and Technology. His research interests include new construction materials.*

REFERENCES

1. Henriques, J.; Raposo, J. M.; Silva, L. S.; and Neves, L. C., "Tensile Resistance of Steel-Reinforced Anchorages: Experimental Evaluation," *ACI Structural Journal*, V. 110, No. 2, Mar.-Apr. 2013, pp. 239-249. doi: 10.14359/51684404

2. Shi, J. J.; Hu, G. F.; Zhang, X. F.; Zhang, H. J.; Chen, W. H.; and Yang, B., "Current Status of Application of Grouting Quality Inspection Methods for Assembled Concrete Building Sleeves," *Building Structure*, V. 49, 2019, pp. 545-549. doi: 10.19701/j.jzjg.2019.S2.101 (in Chinese)

3. Liu, L. I., and Xiao, J. Z., "Research Progress of Grouting Connection of Steel Sleeve," *Journal of Building Structures*, V. 44, No. 1, 2023, pp. 235-247. doi: 10.14006/j.jzjgxb.2022.0165 (in Chinese)

4. Ling, J. H.; Abd Rahman, A. B.; Ibrahim, I. S.; and Hamid, Z. A., "Behaviour of Grouting Pipe Splice under Incremental Tensile Load," *Construction and Building Materials*, V. 33, 2012, pp. 90-98. doi: 10.1016/j.conbuildmat.2012.02.001

5. Wang, C., and Chan, T. M., "Seismic Design and Parametric Study of Steel Modular Frames with Distributed Seismic Resistance," *Thin-Walled Structures*, V. 182, Part B, 2023, Article No. 110325. doi: 10.1016/j.tws.2022.110325

6. Lu, Z. W.; Huang, J.; Li, Y. B.; Dai, S. B.; Peng, Z.; Liu, X.; and Zhang, M., "Mechanical Behaviour of Grouting Sleeve Splice under Uniaxial Tensile Loading," *Engineering Structures*, V. 186, 2019, pp. 421-435. doi: 10.1016/j.engstruct.2019.02.033

7. Huang, Y.; Zhu, Z. G.; Huang, D.; Yi, W. J.; and Zhang, R., "Experimental Study on Static Tension Stretching of Grouting Connections of Semi-Grouting Sleeve," *Journal of South China University of Technology*, V. 44, No. 2, 2016, pp. 26-32. doi: 10.3969/j.issn.1000-565X.2015.02.005

8. Hayashi, Y.; Shimizu, R.; Nakatsuka, T.; and Suzuki, K., "Bond Stress-Slip Characteristic of Reinforcing Bar in Grouting-Filled Coupling Steel Sleeve," *Journal of Structural and Construction Engineering*, V. 59, No. 462, 1994, pp. 131-139. doi: 10.3130/aijs.59.131_3

9. Hayashi, Y.; Nakatsuka, T.; Miwake, I.; and Suzuki, K., "Mechanical Performance of Grout-Filled Coupling Steel Sleeves under Cyclic Loads," *Journal of Structural and Construction Engineering*, V. 496, No. 62, 1997, pp. 91-98. doi: 10.3130/aijs.62.91_3

10. Lamport, W. B., "Ultimate Strength of Grouting Pile-to-Sleeve Connections," PhD dissertation, The University of Texas at Austin, Austin, TX, 1988.

11. Sayadi, A. A.; Abd. Rahman, A. B.; Sayadi, A.; Bahmani, M.; and Shahryari, L., "Effective of Elastic and Inelastic Zone on Behavior of Glass Fiber Reinforced Polymer Splice Sleeve," *Construction and Building Materials*, V. 80, 2015, pp. 38-47. doi: 10.1016/j.conbuildmat.2015.01.064

12. Ling, J. H.; Rahman, A. B. A.; Mirasa, A. K.; and Hamid, Z. A., "Performance of Cs-Sleeve under Direct Tensile Load: Part I: Failure Modes," *Malaysian Journal of Civil Engineering*, V. 20, No. 1, 2008, pp. 89-106. doi: 10.11113/mjce.v20.15759 (in Malaysian)

13. Ling, J. H.; Rahman, A. B. A.; and Ibrahim, I. S., "Feasibility Study of Grouting Splice Connector under Tensile Load," *Construction and Building Materials*, V. 50, No. 1, 2014, pp. 530-539. doi: 10.1016/j.conbuildmat.2013.10.010

14. Wu, S. B.; Lin, F.; and Wang, T., "Experimental Study on the Effect of Age and Reinforcement Type on the Force Performance of Reinforcement Sleeve Grouting Connections," *Building Structures*, V. 43, No. 14, 2013, pp. 77-82. doi: 10.19701/j.jzjg.2013.14.016 (in Chinese)

15. Han, B., and Huang, Y., "Experimental Study on Bond Performance between Rebar and Grout and Confinement Effects of Grouting Sleeve Connections," *Construction and Building Materials*, V. 354, 2022, p. 129088. doi: 10.1016/j.conbuildmat.2022.129088

16. Ma, J. F.; Bai, G. L.; Liang, L. L.; Wang, L.; and Su, N. F., "Mechanical Behavior of Semi-Grouting Sleeve and Steel Bar Connection," *Structural Concrete*, V. 24, No. 4, 2023, pp. 5299-5313. doi: 10.1002/suco.202200529

17. Chen, D.; Wu, Z. X.; Bao, Y.; Ding, S. P.; Shao, Y.; and Xu, T., "Experimental Study on Mechanical Properties of Half-Grouted Sleeve Connections with Grouted Defects," *Buildings*, V. 12, No. 11, 2022, pp. 1807-1834. doi: 10.3390/buildings12111807

18. Reardon, E. J.; James, B. R.; and Abouchar, J., "High Pressure Carbonation of Cementitious Grout," *Cement and Concrete Research*, V. 19, No. 3, 1989, pp. 385-399. doi: 10.1016/0008-8846(89)90028-8

19. Belleri, A., and Riva, P., "Seismic Performance and Retrofit of Precast Concrete Grouting Sleeve Connections," *PCI Journal*, V. 57, No. 1, 2012, pp. 97-109. doi: 10.15554/pcij.01012012.97.109

20. Seo, S. Y.; Nam, B. R.; and Kim, S. K., "Tensile Strength of the Grout-Filled Head-Splice-Sleeve," *Construction and Building Materials*, V. 124, 2016, pp. 155-166. doi: 10.1016/j.conbuildmat.2016.07.028

21. JG/T 408-2019, "Sleeve Grout for Reinforcing Steel Connections," Ministry of Housing and Urban-Rural Development of the People's Republic of China, Beijing, China, 2019.

22. JGJ 107-2016, "Technical Specification for Mechanical Splicing of Steel Reinforcing Bars," Ministry of Housing and Urban-Rural Development of the People's Republic of China, Beijing, China, 2016.

23. Chen, J. W.; Wang, Z. W.; and Ju, S. L., "Experimental Study and Numerical Simulation of the Tensile Performance of Semi-Grouting Sleeve Reinforcement with Eccentric Connection," *Journal of Building Structures*, V. 41, 2020, pp. 160-171. doi: 10.14006/j.jzjgxb.2020.S2.0019 (in Chinese)

24. Li, M.; Pan, Z. H.; Wan, Q. Y.; Si, Q.; and Sun, Y. G., "Study on the Force Performance of Grouting Sleeve Connection Considering the Effect of Eccentricity," *Jiangsu Keji Daxue Xuebao. Ziran Kexue Ban*, V. 33, No. 6, 2019, pp. 99-105. doi: 10.11917/j.issn.1673-4807.2019.06.015

25. Alias, A.; Zubir, M. A.; Shahid, K. A.; and Abd. Rahman, A. B., "Structural Performance of Grouting Sleeve Connectors with and without Transverse Reinforcement for Precast Concrete Structure," *Procedia Engineering*, V. 53, 2013, pp. 116-123. doi: 10.1016/j.proeng.2013.02.017

26. Huang, Y.; Zhu, Z. G.; Naito, C. J.; and Yi, W. J., "Tensile Behavior of Half-Grouted Sleeve Connections: Experimental Study and Analytical Modeling," *Construction and Building Materials*, V. 152, 2017, pp. 96-104. doi: 10.1016/j.conbuildmat.2017.06.154

27. Yan, Q. S.; Chen, T. Y.; and Xie, Z. Y., "Seismic Experimental Study on a Precast Concrete Beam-Column Connection with Grout Sleeves," *Engineering Structures*, V. 155, 2018, pp. 330-344. doi: 10.1016/j.engstruct.2017.09.027

28. Untrauer, R. E., and Henry, R. L., "Influence of Normal Pressure on Bond Strength," *ACI Journal Proceedings*, V. 62, No. 5, May 1965, pp. 577-586. doi: 10.14359/7711

29. Einea, A.; Yamang, T.; and Tadros, M. K., "Grout-Filled Pipesplices for Precast Concrete Construction," *PCI Journal*, V. 40, No. 1, 1995, pp. 82-93. doi: 10.15554/pcij.01011995.82.93

30. Zhao, W. P., and Xiao, J. Z., "Ontological Model of Bond Slip between Ribbed Reinforcement and Concrete," *Engineering Mechanics*, V. 28, No. 4, 2011, pp. 164-171. doi: CNKI:SUN:GCLX.0.2011-04-028 (in Chinese)

31. Wu, T.; Liu, Q. W.; Cheng, R.; and Liu, X., "Experimental Study on the Performance of Grouting Connection of Steel Sleeve and Analysis of Stress in the Cylinder Wall," *Engineering Mechanics*, V. 34, No. 10, 2017, pp. 68-75. doi: CNKI:SUN:GCLX.0.2017-10-010 (in Chinese)

32. Xu, T. F.; Li, Q. W.; Zhao, E. D.; Ding, J. C.; and Zhan, Y. L., "On the Early-Age Bond-Slip Behavior of an Eccentric Bar Embedded in a Grouting Sleeve," *Engineering Structures*, V. 190, 2019, pp. 160-170. doi: 10.1016/j.engstruct.2019.04.020

33. Liu, C.; Pan, L. F.; Liu, H.; Tong, H. W.; Yang, Y. B.; and Chen, W., "Experimental and Numerical Investigation on Mechanical Properties of Grouting-Sleeve Splices," *Construction and Building Materials*, V. 260, 2020, p. 120441. doi: 10.1016/j.conbuildmat.2020.120441

34. Zheng, Y. F., "Research on GDPS Grouting Sleeve Reinforcement Connection Technology," dissertation, Southeast University, Nanjing, China, 2016. (in Chinese)

35. Zhao, Y.; Zou, R. B.; Ding, T.; and Xiao, J. Z., "Experimental Study of the Shear Behaviour of Concrete-Grout-Concrete Joints," *Journal of Building Engineering*, V. 43, 2021, p. 103095. doi: 10.1016/j.jobe.2021.103095

ACI STRUCTURAL JOURNAL TECHNICAL PAPER

Title No. 121-S72

Prestressing Analysis of Large Three-Dimensional Systems and Prestress Management

by Hiroshi Nishio, Yosuke Yagi, and Yasuaki Ishikawa

A three-dimensional (3-D) finite element method for prestressing and seating analysis has been developed. This method improves the accuracy of the results obtained using the widely adopted initial stress method and enables calculation of the seating loss effect, which is the final stress prediction of prestressing. Its application for large numbers of indeterminate-order structures is shown by comparing its calculation results with two-dimensional (2-D) conventional analysis, as well as with observed strain results for cables of an existing 462 m, six-span continuous bridge. With these considerations, a new management method of prestressing for jack force-diverting systems where the prestressing force does not focus uniquely on a design section was developed so that constructed prestressed concrete structures can be well-secured to comply with design objectives.

Keywords: friction loss; large-scale prestressed concrete (PC) structure; prestressing analysis; prestressing management; set loss; three-dimensional (3-D) finite element method (FEM) analysis.

INTRODUCTION

The three-dimensional (3-D) finite element method (FEM) analysis of prestressing is usually performed with the initial stress method, as found in software programs such as Abaqus and DIANA. However, this method has fundamental shortcomings, such as cable rigidity affecting the accuracy of calculations and setting common joints between cables, and concrete does not allow relative slip between the two, although slip is a known phenomenon. DIANA has provided a remedy in which the rigidity of cables is made ineffective during prestressing and retrieved after grouting. In contrast, Abaqus ignores these deficiencies by assuming that their effects are negligibly small.

These findings were reviewed in a previous paper[1] that pointed out that the stress error amounts to several tens of percent of the actual values when the relative rigidity ratio between concrete and cables becomes large.

This study developed a more direct method to obtain the prestressing load for concrete that can overcome the aforementioned deficiencies of the initial stress method and also developed an improved analysis method for seating loss that gives more accurate results than the initial stress method adopted in software such as DIANA.[2]

The developed method also makes possible the calculation of pulled-out cable lengths from anchorage plates at prestressing, the value of which is used for prestressing management in a more advanced manner. Then, the applicability of the developed prestress calculation method for a large degree-of-freedom system, including the calculation of stress variation at the seating stage of prestressing, is shown with observed stresses for an actual elevated s-curved bridge having a length of 462 m. The results obtained for 3-D reaction forces and moments for piers and box girders are considered to be important design variables for this type of bridge but cannot be determined using a two-dimensional (2-D) frame analysis, although the use of 2-D frame analysis is currently specified in the standards for bridge construction in Japan[3] for a treated s-curved multi-span bridge.

Basing on the results obtained in this study, an advanced management method for prestressing is proposed.

RESEARCH SIGNIFICANCE

The developed 3-D FEM was applied to prestressing analysis of an existing six-span curved prestressed concrete (PC) bridge 462 m long, and the results of the examination assured its applicability to general cases of prestressing analysis of any 3-D structures with an arbitrary cable layout. Based on these results, this paper proposes a more accurate prestressing management method, which is expected to contribute to improved PC construction quality.

THEORETICAL CONSIDERATION OF PRESTRESSING AND SEATING ANALYSIS

The prestressing cable force exerted on concrete is given directly by the differential of the cable force along its length, which improves the accuracy of the initial stress method for prestressing analysis and seating loss analysis for final prestress prediction.

Prestressing analysis

The cable force vector $\boldsymbol{T}$ that acts on concrete depends on the cable configuration and is expressed generally as

$$\boldsymbol{T}(\theta,s) = T(\theta,s) \cdot \boldsymbol{n} \tag{1}$$

The force vector $\boldsymbol{f}$ acting on concrete is the variation of the cable force and given in differential form as

$$\boldsymbol{f} = \frac{\partial \boldsymbol{T}(\theta,s)}{\partial s} = \frac{\partial T(\theta,s) \cdot \boldsymbol{n}}{\partial s}$$
$$= \frac{\partial T(\theta,s)}{\partial s} \cdot \boldsymbol{n} + T(\theta,s)\frac{\partial \boldsymbol{n}}{\partial s} = \boldsymbol{S} + \boldsymbol{Z} \tag{2}$$

ACI Structural Journal, V. 121, No. 5, September 2024.
MS No. S-2023-170.R2, doi: 10.14359/51740857, received February 29, 2024, and reviewed under Institute publication policies. Copyright © 2024, American Concrete Institute. All rights reserved, including the making of copies unless permission is obtained from the copyright proprietors. Pertinent discussion including author's closure, if any, will be published ten months from this journal's date if the discussion is received within four months of the paper's print publication.

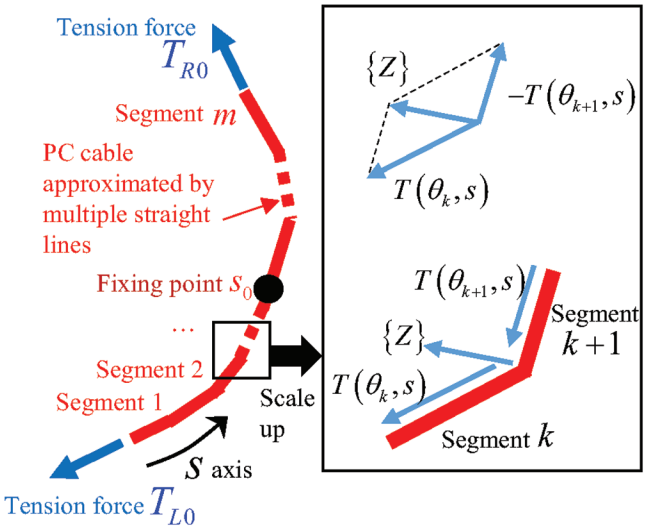


Fig. 1—Approximation of curved PC cable by multiple straight lines.

where

$$\boldsymbol{S} = \frac{\partial T(\theta,s)}{\partial s} \cdot \boldsymbol{n} \tag{3}$$

and

$$\boldsymbol{Z} = T(\theta,s)\frac{\partial \boldsymbol{n}}{\partial s} \tag{4}$$

where $\boldsymbol{n}$ is the directional normal along the coordinate s of the cable configuration. The first term on the right-hand side of Eq. (2) is the frictional force, and the second term is the pseudo-centripetal force.

To treat these forces numerically, a PC cable with a curved configuration in 3-D space is approximated by multiple straight lines and modeled as a series of line groups composed of m line segments, as shown in Fig. 1, the length of which depends on the required solution accuracy. The length of m line segments is generally not equally divided, and it is necessary to divide it depending on the PC cable curvature radius. In a domain where the curvature radius is small, it is necessary to increase the number of divisions and use a small line segment length. Note that both ends of each line segment need not be on the surface of solid elements of concrete. Let coordinate s along the line segment be taken from the left end of the PC steel, and let θ_k be the sum of the angles formed by line segments $k+1$ from the left contacting end, where the angle is measured clockwise. Then, Eq. (3) is reduced to

$$\{S\} = \frac{\partial T(\theta_k,s)}{\partial s}\{n_k\} \tag{5}$$

where $\{n_k\}$ denotes the unit vector for the direction of the line segment k. When an angle change occurs between line segment k and line segment $k+1$, as shown in Fig. 2, the pseudo-centripetal force $\{Z\}$ in Eq. (4) is reduced to

$$\{Z\} = T(\theta_k,s)\{n_k\} - T(\theta_{k+1},s)\{n_{k+1}\} \tag{6}$$

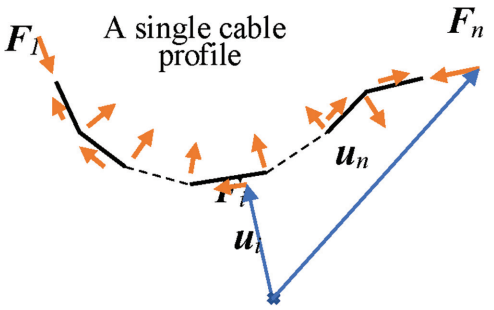


Fig. 2—Forces equivalent to prestressing effect.

This force is converted to the nodal force for 3-D elements by applying the virtual work principle.

Error norm of discretized joint forces

Forces working on concrete with cable prestressing are reactions in concrete that occur against the jack pulling, frictional, and pseudo-centripetal forces, as shown in Fig. 2. These forces are always self-balancing for every cable; therefore, the forces and the moments satisfy the following equations in each cable

$$\sum \boldsymbol{F}_i = 0, \sum \boldsymbol{F}_i \times u_i = 0 \tag{7}$$

where $\boldsymbol{F}_i$ is the combined jack, frictional, and other forces; and $\boldsymbol{u}_i$ may be measured from any point in space.

Now, in the construction of an actual bridge, several hundred cables would be used with prestressing forces of 1000 to 3000 kN for each cable. When the FEM calculation is applied, these forces, which are reacting to the cable forces, are converted to nodal forces of elements and denoted as

$$N_x, N_y, N_z \tag{8}$$

for each joint of the elements through which cables pass. Though the equation should satisfy

$$\sum N_{x,i} = 0, \sum N_{y,i} = 0, \sum N_{z,i} = 0$$

and

$$\sum(yN_z - zN_y) = 0, \sum(zN_x - xN_z) = 0, \sum(xN_y - yN_x) = 0 \tag{9}$$

this is not the case, and errors always exist

$$\sum N_x = \Delta_x, \sum N_y = \Delta_y, \sum N_z = \Delta_z$$
$$\sum(yN_z - zN_y) = \Delta_{mx}, \sum(zN_x - xN_z) = \Delta_{my}, \sum(xN_y - yN_x) = \Delta_{mz} \tag{10}$$

Therefore, the error norms are defined as

$$N_{rm}N_x = \frac{\Delta_x}{\sum|N_x|}, \quad N_{rm}N_y = \frac{\Delta_y}{\sum|N_y|}, \quad N_{rm}N_z = \frac{\Delta_z}{\sum|N_z|}$$

$$N_{rm}M_x = \frac{\Delta_{mx}}{\sum|(yN_z - zN_y)|}$$

$$N_{rm}M_y = \frac{\Delta_{my}}{\sum|(zN_x - xN_z)|}$$

$$N_{rm}M_z = \frac{\Delta_{mz}}{\sum|(xN_y - yN_z)|} \quad (11)$$

Depending on the magnitude of the error norm, redistribution of the nodal force should be considered, and its limit may be given by the required calculation accuracy. However, the limits of error norm may be set at approximately 10^{-3} to 10^{-5} in general cases. In the following discussion, the error norm is found to be below 10^{-3} in all cases, and no redistribution of the nodal forces is performed.

Seating loss analysis

Seating loss analysis requires calculating pulled-out cable lengths at the ends, where cable extension and concrete deformation calculations are necessary.

To obtain the pulled-out cable lengths from anchor plates at the left and right ends, it is necessary to consider deformation of concrete along the cable profile as well as the amount of PC steel extension, as shown in Fig. 3. Pulled-out cable lengths at both ends are expressed by the following equations, where the lengths at the left and right ends are denoted as Δl_L and Δl_R, respectively

$$\Delta l_L = \Delta l_{L,cab} - \Delta l_{L,con} \quad (12a)$$

$$\Delta l_R = \Delta l_{R,cab} - \Delta l_{R,con} \quad (12b)$$

where the subscripts *cab* and *con* denote components of the pulled-out length attributed to PC cable extension and concrete deformation, respectively.

The left and right pulled-out lengths for a PC cable can be expressed by the following equations, respectively, by the path integral of the strain generated in the PC cable along the cable length starting from the unmovable fixing point to the left or right end

$$\Delta l_{L,cab} = \int_0^{s_0} \frac{T(\theta_k, s)}{EA} ds \quad (13a)$$

$$\Delta l_{R,cab} = \int_{s_0}^{l_{end}} \frac{T(\theta_k, s)}{EA} ds \quad (13b)$$

where EA is the axial stiffness of the PC cable; s_0 is the unmovable fixing point of a cable; and l_{end} is the total cable length.

In addition, the left and right pulled-out cable length components due to concrete contraction are expressed by Eq. (14a) and (14b), respectively, by the path integral of concrete strain components along the PC cable from the unmovable fixing point s_0 to the left or right end

$$\Delta l_{L,con} = \int_0^{s_0} \varepsilon_c ds \quad (14a)$$

$$\Delta l_{R,con} = \int_{s_0}^{l_{end}} \varepsilon_c ds \quad (14b)$$

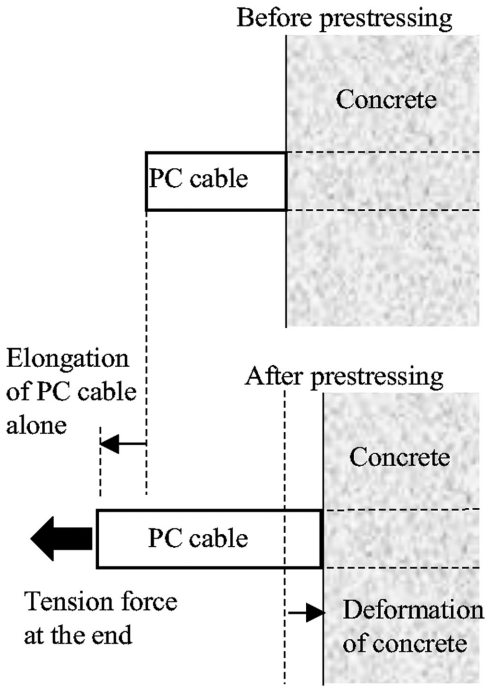


Fig. 3—Pulled-out PC cable length including concrete.

where ε_c is a normal strain component for concrete in the direction along the PC cable and is expressed by Eq. (15) using the concrete strain tensor ε_{ij} and the component n_i of the unit vector $\{n_k\}$.

$$\varepsilon_c = \varepsilon_{ij} n_i n_j \quad (15)$$

Let q_L and q_R be the seating length values for the left and right ends, respectively, for a PC cable due to anchor seating. The solution for the problem requires the iterations given as follows.

In the first step, these deformations are assumed to be composed of components of the PC cable extension alone. From Eq. (13), q_L and q_R can be expressed as

$$q_L = \int_0^{s_0} \frac{T(\theta_k, s)}{EA} ds \quad (16a)$$

$$q_R = \int_{s_0}^{s_{max}} \frac{T(\theta_k, s)}{EA} ds \quad (16b)$$

In writing Eq. (16a) and (16b), the tension force relief at both ends may be different and accompanied by arbitrary anchor-seating magnitudes. If the tension force at the fixing point is given as T_{s0}, the tension force distribution due to the anchor-seating reliefs can be expressed by the following expressions from Eq (1)

$$T(\theta_k, s) = \begin{cases} T_{s_0} \cdot e^{\mu\theta_k + \lambda s} & s \le s_0 \\ T_{s_0} \cdot e^{\mu\theta_{m-k} + \lambda(s_{max} - s)} & s > s_0 \end{cases} \quad (17)$$

It should be noted that the fixing point position for Eq. (17) will be generally different from that for the tensioning process. Substitution of Eq. (17) into Eq. (16) yields two unknown variables, T_{s_0} and s_0, for the given values of

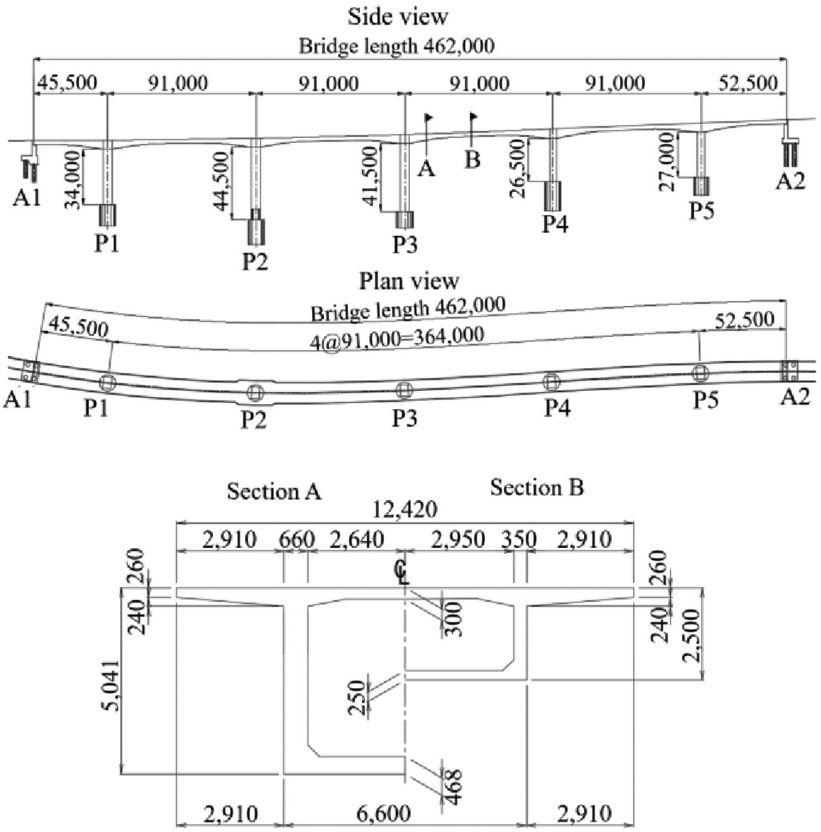


Fig. 4—General view of target existing continuous viaduct. (Note: Units are in mm.)[4]

Eq. (16). The obtained T_{s_0} and s_0 are used to find the equivalent nodal force due to the anchor-seating loss in the same way as described in the previous section. After solving the global stiffness equation, the new concrete contraction deformation is recalculated in the same way as described in the previous section, and then the pulled-out lengths for the PC cable are updated using the following equations

$$\Delta l_{L,con} = q_L + \Delta l_{L,con} \tag{18a}$$

$$\Delta l_{R,con} = q_R + \Delta l_{R,con} \tag{18b}$$

This process is repeated until the deformation converges.

It should be noted that a new friction coefficient at the seating stage should be identified, even when holding the superposition assumption of cable force derivation at this stage.

So far, the cable forces are considered to correspond to those on the concrete. Therefore, the rigidity of the cables is not considered in the FEM stiffness calculation. However, to calculate the stress after seating, it is necessary to consider the cable stiffness in the cases of full or partial bonding to concrete. Such an unbonded prestressing analysis is another theoretical problem and is under study by the authors.

SIMULATION BY PROPOSED 3-D FEM OF EXISTING CONTINUOUS VIADUCT AT PRESTRESSING AND COMPARISON WITH CONVENTIONAL CALCULATION RESULTS

Overview of existing viaduct and outline of study

Figure 4 shows the shape, longitudinal view, and plan view of the existing bridge. The total length is 462 m, and the curved section is approximately 12 m away from the straight line connecting A1 and A2 at the point of greatest curvature. An elevation difference of approximately 5 m exists between A1 and A2 due to a longitudinal gradient. Table 1 shows the dimensions of the bridge.

The specific response for this bridge was studied assuming simultaneous prestressing of all the external cables placed between A1 and A2 to compare the results of the proposed method, conventional analysis, and actual measurements. Prestressing cables with built-in optical fibers in the external cables[4,5] were specially arranged between P2 and P4 and between P1 and P2, and the tension force of the cables was measured. These cable forces observed at prestressing and after seating were compared with the calculated results.

Figure 5 shows a diagram of the analysis model for the proposed method and a part of the discretization. Table 2 shows the parameters used for the analysis. Because the bridge draws a gentle s-curve on the plane and has a gentle upward slope from A1 to A2, the arrangement of the prestressing cables is not symmetric. In the analysis by the proposed method, the whole bridge (462 m long, six spans) was faithfully discretized, as shown in Fig. 5. Therefore, it was a large degree-of-freedom analysis with 257,566 elements, 367,271 nodes, and 1,101,813 degrees of

Table 1—Overview of target existing continuous viaduct

Bridge type	PC box-girder bridge
Structural form	Six-span continuous rigid-frame viaduct
Bridge length	462.000 m (road center)
Span length	44.500 + 4 @ 91.000 + 51.500 m (structural center)
Width	12.800 to 15.300 m
Effective width	5.565 + 5.565 to 6.815 + 6.815
Bridge alignment	Longitudinal gradient: +3.007% (L = 470.000 m)
	Cross slope: 1.886 to 6.000%
	Plane figure: A = 400 to 450 m (clothoid) to R = 900 m (arc)

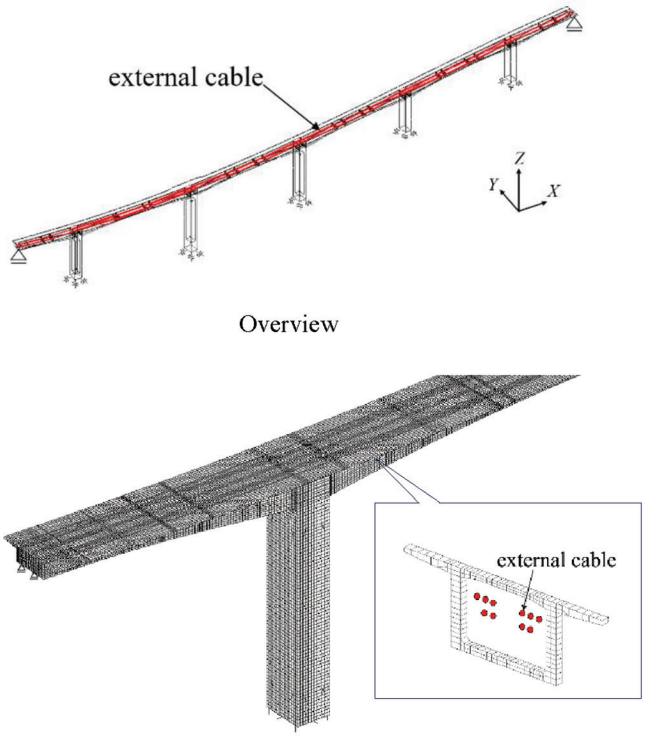


Fig. 5—Analysis model for proposed method.

freedom. The calculation time was approximately 2 hours with a processor at 3.70 GHz, with 128 GB of installed random-access memory (RAM). It is noted that the calculation time was relatively short because the prestressing analysis was linear.

Bridge deformation and stress distribution due to simultaneous prestressing of all external cables

Prestressing load on concrete—As shown in Fig. 6 and Table 3, the five sets of external cables are arranged to extend over two span lengths in each set and overlap at every span. The number of cables in each set and the prestressing forces are shown in Table 3; the total tension force was approximately 96,000 kN.

Table 2—Parameters used for analysis

Young's modulus	Concrete (superstructure)	31,000 N/mm^2
	Concrete (substructure)	28,000 N/mm^2
	Prestressing cable (from mill sheet)	194,150 N/mm^2
Coefficient of friction	Per length	0/m
	Per angle	0.3/rad
Analysis model	Number of nodes	367,271
	Number of elements	257,566

Table 3—Overview of external cable arrangement

Cable position		A1 to P2	P1 to P3	P2 to P4	P3 to P5	P4 to A2
Cable piece		6	6	4	6	6
Final prestressing, kN/piece	A1 side	3254.6				
	A2 side	3254.6				
Coefficient of friction	μ	0.3				
	λ	0				
Pulled-out length at anchorage, mm	A1 side	5.0				
	A2 side	5.0				

As an example of discrete prestressing load derivation, one cable out of four at the span P2 to P4, the profile of which is shown in Fig. 7, was selected, and the frictional load in the x-direction and centripetal load in the y- and z-directions were calculated when prestressing with a jack force of 3254.6 kN was applied at both ends, as shown in Fig. 8, to demonstrate the characteristics of this method. It should be noted that it is difficult to determine these values using the initial stress method. These prestressing loads are shown along the cable profile in such a manner that slack is removed from the curved profile length to form a straight line. The load peaks are at diaphragm wall locations inside the box-section girder because the cable is an external cable. This figure shows that the prestressing force applies a rather peculiar load that acts on the bridge horizontally in both the x- and y-directions, as well as vertically. Therefore, the bridge response depends on these forces and deforms accordingly. In addition, the loads shown in Fig. 8 and the jack force of 3254.6 kN at both ends make up the total prestressing load, and their summed values are equal to the summed reaction forces at the pier bases.

Deformation and sectional stress—The actual prestressing timing differs for each cable, but the analysis by the conventional calculation of prestressing was performed assuming simultaneous prestressing of all sets of cables. Here, it is noted that the conventional method, as described in the present paper, denotes the method actually used in the design and documented in the design of the bridge analyzed herein, the model of which is a 2-D frame analysis with the initial strain method. The theoretical manual for the software used is referred to as UC-BRIDGE[6] or PCBOX-II.[7]

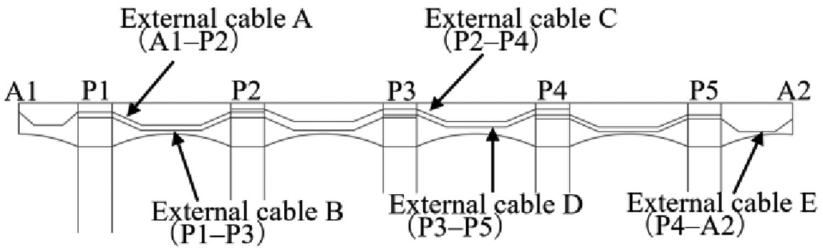


Fig. 6—Schematic diagram of external cable layout.

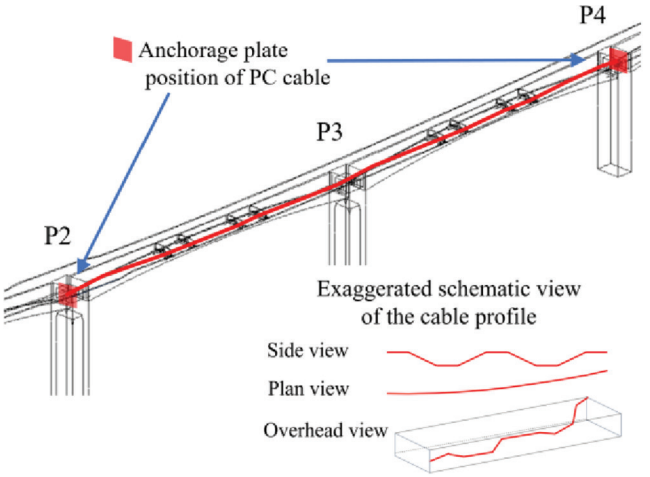


Fig. 7—Analysis model of P2 to P4 external cable prestressing.

Therefore, the calculated results are first compared with the 2-D frame analysis results, using the same parameters in both cases, such as the friction coefficient and Young's modulus of the materials.

Table 4 compares the calculated sectional forces, and Table 5 compares the displacement results. Though a difference exists in the displacements in the x- and z-directions, the most striking difference between the two methods is the displacement in the y-direction, which is normal to the bridge axis. The conventional calculation does not provide this information because it is a 2-D calculation. It is interesting that the deformation makes an inverted s-curve in the horizontal plane, which is reasonable.

Similarly, Fig. 9(b), (d), and (e) provide information that is not obtained in a conventional 2-D calculation. Because the prestressing cable profile has a nearly s-shaped curve in the direction of the bridge axis, a pseudo-centripetal positive horizontal force is acting on it, which is followed by the negative horizontal pseudo-centripetal force. Therefore, Fig. 9(b) shows that the piers are deflecting in the reverse s-curve direction; the reaction force directions in Fig. 9(b) show them at the base of each pier. Figure 9(d) also shows the 3-D effect of the prestressing—that is, the moment around the x-axis—which does not appear in the 2-D conventional calculation.

Figure 9(c) shows the uplifting force acting on the piers due to prestressing, which can be calculated by both the conventional and proposed methods. However, the prestressing induction that uplifts the structures is a rather peculiar external force. These indications show that, in

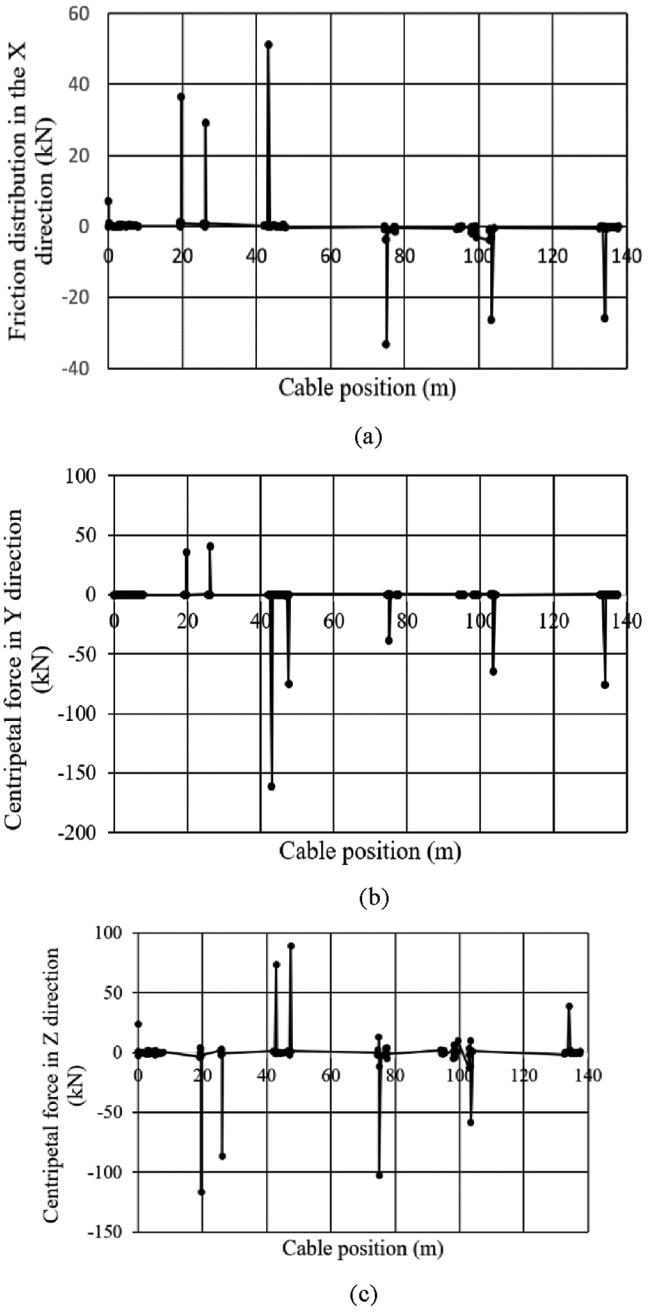
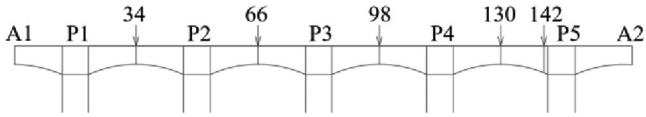


Fig. 8—(a) Friction distribution in x-direction; (b) centripetal force in y-direction; and (c) centripetal force in z-direction.

general, 3-D effects can never be neglected for curvilinear bridge shapes.

A sectional force comparison is shown in Table 4. The table shows the characteristics of the results, including that

Table 4—Comparison of cross-sectional forces calculated by conventional analysis and proposed method for prestressing of all external cables (sectional force)

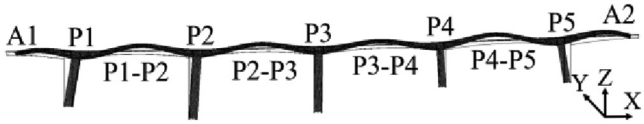


Section	Sectional force	Proposed method	Conventional method	Conventional/ Proposed	Section	Sectional force	Proposed method	Conventional method	Conventional/ Proposed
A1	Reaction force R_x, kN	0	—	—	130	Axial force N, kN	–35,458	–34,136	0.96
	Reaction force R_y, kN	0	—	—		Shear force (vertical) S2, kN	8	369	46.13
	Reaction force R_z, kN	–508	–577	1.14		Shear force (lateral) S3, kN	1770	—	—
	Moment M_x, kN·m	713	—	—		Torsional moment M1, kN·m	117	—	—
	Moment M_y, kN·m	–122	—	—		Bending moment M2, kN·m	–12,659	–14,270	1.13
	Moment M_z, kN·m	0	—	—		Bending moment M3, kN·m	–1604	—	—
34	Axial force N, kN	–35,245	–33,525	0.95	142	Axial force N, kN	–34,835	–34,194	0.98
	Shear force (vertical) S2, kN	–310	–320	1.03		Shear force (vertical) S2, kN	–1724	–719	0.42
	Shear force (lateral) S3, kN	–143	—	—		Shear force (lateral) S3, kN	–2773	—	—
	Torsional moment M1, kN·m	120	—	—		Torsional moment M1, kN·m	4121	—	—
	Bending moment M2, kN·m	–12,530	–13,932	1.11		Bending moment M2, kN·m	75,683	80,222	1.06
	Bending moment M3, kN·m	5320	—	—		Bending moment M3, kN·m	1301	—	—
66	Axial force N, kN	–28,231	–26,613	0.94	A1	Reaction force R_x, kN	0	—	—
	Shear force (vertical) S2, kN	–398	–113	0.28		Reaction force R_y, kN	0	—	—
	Shear force (lateral) S3, kN	–560	—	—		Reaction force R_z, kN	–96	–152	1.58
	Torsional moment M1, kN·m	–221	—	—		Moment M_x, kN·m	–48	—	—
	Bending moment M2, kN·m	10,886	12,459	1.14		Moment M_y, kN·m	0	—	—
	Bending moment M3, kN·m	–1610	—	—		Moment M_z, kN·m	0	—	—
98	Axial force N, kN	–28,223	–26,619	0.94					
	Shear force (vertical) S2, kN	–15	–90	6.00					
	Shear force (lateral) S3, kN	1021	—	—					
	Torsional moment M1, kN·m	130	—	—					
	Bending moment M2, kN·m	–10,099	–11,845	1.17					
	Bending moment M3, kN·m	100	—	—					

cross-sectional torsion is automatically generated in the analysis by the proposed method, in addition to the two components of cross-sectional bending moment around the y-axis and the z-axis. Furthermore, the shear force is calculated in two directions of the cross section in the proposed 3-D analysis, while the shear force is only in one direction and the bending moment is only around the y-axis in the conventional analysis. Therefore, the amount of information is completely different. It may be appropriate to add that the ground rigidity at the base of each pier is given with equivalent spring element rigidity with the values of ground spring rigidity given in the 2-D calculation. The use of spring elements is simply due to the code's functional limits.

Table 4 shows the values of the shear force and torsional moment at the girder cross sections numbered 34, 66, 98, 130, and 142 to emphasize the 3-D effect in the stress calculation, where the predominant sectional force causes bending. The difference in the resulting shear force between the proposed analysis and the conventional analysis in these cross sections is large, and the proposed analysis gives a larger shear force. However, the value itself is small and may not be the determining factor for sectional dimensions. The vertical shear force S2 in cross section number 142 obtained by the proposed method appears larger than that obtained by the conventional method. The authors cannot argue whether the proposed method is more or less secure than the conventional method based on this fact alone because the direction of the shear force due to prestress is opposite to that of the shear force due to the dead load and live load, and the overall load effect is not considered here. In contrast, this is considered to be an example suggesting that the proposed analysis method can improve the accuracy of PC structure designs in the future. From a design point of view, there are cases where a large amount of information is meaningless, but regardless, due consideration must be given to the axial force, two-directional shear forces, bending moment around two axes, and torsional moment acting on the cross section in the case of a curved bridge design. Moreover, it is suggested that these cross-sectional forces can be control index values in structural design.

Table 5—Comparison of displacements calculated by proposed method and conventional analysis for prestressing of all external cables (displacement in mm)



		Proposed analysis		Conventional analysis		Conventional/Proposed	
Direction	Axial	Vertical	Horizontal	Axial	Vertical	Axial	Vertical
A1	28.5	–0.4	3.4	22.0	0	0.77	0
P1	22.7	0	0.2	19.0	0	0.84	—
P1 to P2	18.0	19.6	0.7	13.5	20.8	0.75	1.06
P2	11.5	0	2.6	8.3	0	0.72	—
P2 to P3	7.0	17.2	4.1	3.9	18.9	0.56	1.10
P3	2.1	0	2.9	–0.5	0	–0.24	—
P3 to P4	–3.4	15.4	2.0	–4.9	18.4	1.44	1.19
P4	–6.9	0	0.3	–9.5	0	1.38	—
P4 to P5	–15.3	20.7	–0.6	–15.0	23.1	0.98	1.12
P5	–18.8	0	–1.1	–20.6	0	1.10	—
A2	–25.9	–0.7	–3.5	–24.0	0	0.93	0

In general, in any cross section, the axial force obtained using the conventional method is as small as approximately 90% of that using the proposed method, and the bending moment for the conventional analysis around the y-axis, M2, is always larger by approximately 10% than that for the proposed method. The reason for these tendencies may be the fact that the stiffness of the pier is smaller in the analysis by the proposed method due to the shear deformation effect, while the conventional method neglects this effect, resulting in stiffer pier deformational characteristics. This is observed in the displacement characteristics in the longitudinal direction. The displacement in the longitudinal direction is 30% larger at location A1 and 13% larger at location A2 in the proposed analysis; that is, the contraction of the upper box girder 462 m long is larger.

As for another trend of a larger bending moment, at almost all sections in Table 4 for the proposed method, with respect to the conventional calculation, the small deflection at every span center in the proposed calculation method may be related, as observed in Table 5. Further investigation of these phenomena is not discussed here and may be treated in future papers.

The one characteristic result to point out is that the bending moment around the z-axis, M3, exceeds the bending moment around the y-axis, M2, by 50% in section number 34, for which the conventional analysis gives no information, because M3 does not exist in the conventional calculation. The other characteristic point is that the torsional moment, M_x, is calculated in the proposed method, while in the conventional analysis, it is not. On this point, the Japan highway bridge design standard[3] specifies that it should be calculated in special cases by 3-D grid analysis using only the dead load of the bridge surface and live loads. However, the Japan bridge design standard[3] refers to this point as follows: "According to previous specifications, it is said that the effect of torsional moment due to live loads on straight single girders and T-girders is small, and it is not necessary to consider torsional moment. However, recent inspection results have confirmed cases of cracks occurring in bulkheads, etc., regardless of whether they are straight girders or curved girders, or regardless of cross-sectional dimensions, etc. and for which the influence of torsional moment cannot be denied. Therefore, the current design standard specifies that the torsional moment caused by live loads should be taken into consideration, as a principle of structural design."

Considering the previous results and requirements, the authors believe that the proposed method will be a more powerful tool for detailed structural analysis of prestressing large PC structures with a complex and arbitrary geometry.

OBSERVATION OF STRAIN DISTRIBUTION IN CABLES AND PULLED-OUT LENGTHS OF CABLES AT PRESTRESSING

Observation of strain distribution in cables between piers P2 and P4

As discussed earlier, the PC cable stress calculation is essentially the same in either calculation method because the following equation is used for cable stress calculation, and the same friction coefficients are used

$$\frac{\partial T}{\partial s} = \left(\mu \frac{\partial \theta}{\partial s} + \lambda\right) T \tag{19}$$

where T, s, and θ are the cable force, the length measured along the cable profile, and the directional angle change of the cable profile, respectively; and μ and λ are friction coefficients for the angle change and length change, respectively. However, the pulled-out cable length has scarcely been discussed in the past because it is affected by concrete contraction during prestressing. The initial stress method

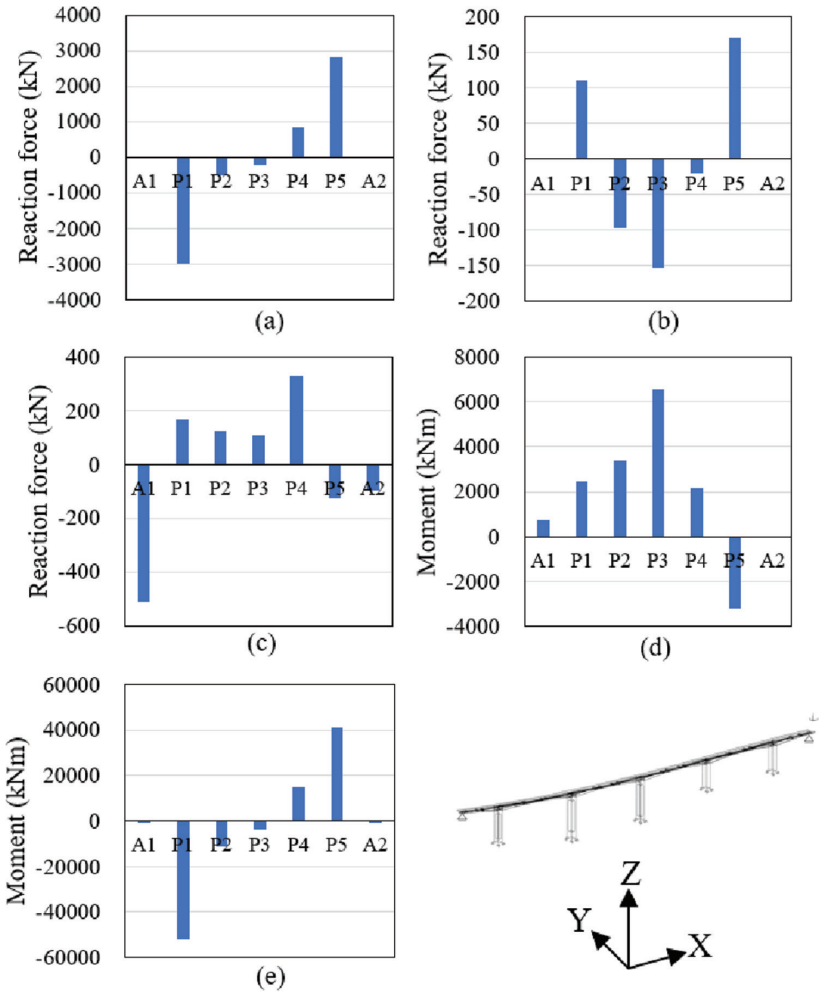


Fig. 9—(a) Axial ground reaction forces; (b) perpendicular ground reaction forces; (c) vertical ground reaction forces; (d) moment about bridge axis; and (e) moment perpendicular to bridge axis.

adopted in many types of software does not allow iteration of initial strain settings, even though the originally assumed initial strain cannot ensure a given pulled-out length after calculating the stress for related components. In contrast, the proposed method theoretically accounts for the seating loss mechanism and explains the measured strain distribution. Two cases of cable strain measurement for the bridge considered in the present study are discussed herein.

Strain measurement for cables was carried out for prestressing between piers P2 and P4. Similarly, the cable strain between P1 and P2 was measured with a similar embedded device. The difference between the two is that the cables between P2 and P4 are external cables and are surrounded by air for most of their length; therefore, the friction loss for the stress is mainly due to the angle change at the diaphragm wall in the span, while the cables between P1 and P2 are enclosed within the span, where friction loss occurs along their whole length. Figure 7 shows the cable profile between P2 and P4.

Table 6 shows the analysis conditions. Figures 10(a) and (b) show a comparison between the measured tension force in the prestressing cable and the analysis value. In Fig. 10, the cable where strain is measured is an external cable that is surrounded by air, except at the pier head and the diaphragm wall section. Despite the fact that the cable is surrounded by air, the measured strain varies in these exposed cable sections, which may not be reasonable. This seems to be due to a device error, and it limits the accuracy of the measurement. If these fluctuations are ignored, the calculation and measurement results are in good agreement when the friction coefficients are assumed to be $\mu = 0.3$ and $\lambda = 0.003$, and the pulled-out length in Table 7 is almost the same as the measured length. Seating analysis has rarely been discussed in the past. As shown in Fig. 10(a), the target bridge provides data for the strain distribution after seating, which indicates that the strain relief zone is extended over the whole span with a length of over 91 m, and this observation is quite contrary to the basic assumptions of the Japan highway standard[3] or DIANA manual, which assume a mirror inversion relief line of prestressing at a certain level that is determined so that the integrated strain value becomes a stipulated seating value. Note that at this stage, in prestressing design, it is necessary to identify critical sections where the stress becomes a maximum and a minimum along the span length of concern. The results show that these locations are completely different from those considered by the designer, which means that it is necessary to improve the seating analysis. For this purpose, a method must be used that can simulate the general seating stress distribution. Here, it is attempted to apply Eq. (19) with slight modification of the

Table 6—Analysis conditions (P2 to P4)

Item	Value	Remarks
Young's modulus	194,150 N/mm^2	From average of mill sheets
Prestressing force at end	3472.37 kN	From final tension of 40.7 MPa in prestressing management diagram, considering 1% of jack internal friction loss
Coefficient of friction	In air: λ = 0/m μ = 0/rad In concrete: λ = 0.003/m μ = 0.3/rad	From this study
Pulled-out length at anchorage	P2 side: 11.6 mm P4 side: 11.6 mm	From this study

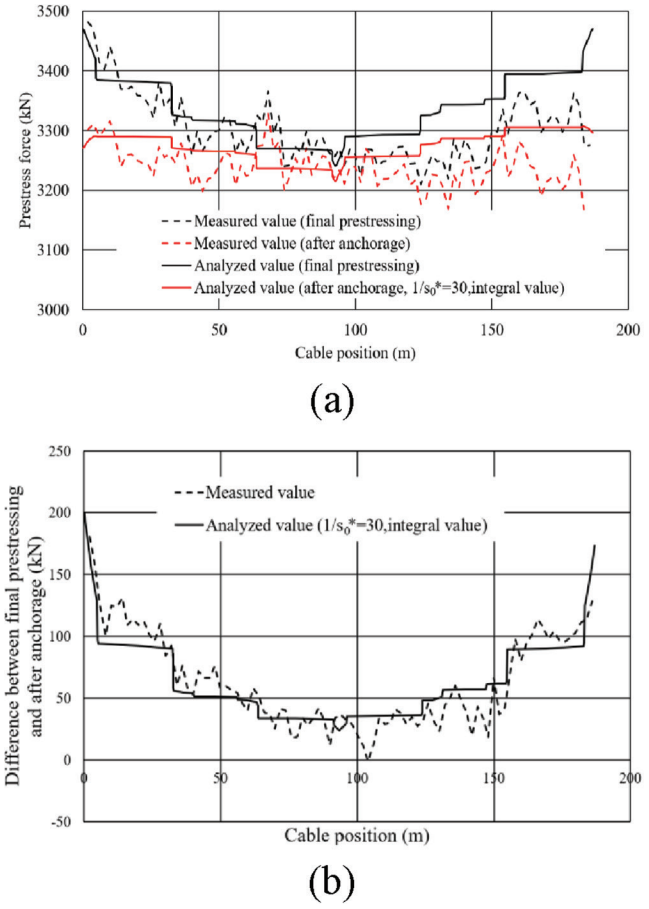


Fig. 10—(a) Comparison of measured and analysis values for prestressing force; and (b) comparison of measured and analysis values for difference between final prestressing and after anchorage (in cables between piers P2 and P4).

friction factors, assuming the superposition of much larger friction coefficients. The results are shown in Fig. 10(b). Note that the strain data represent the relieved portion of the total strain upon consideration that the observed total strain in the P2 to P4 side has some irregularity. The results show good agreement with the observed strain data, which suggests that stress relief for prestressing cables after seating may be possible with this analysis method.

Table 7—Comparison of PC cable pulled-out length (P2 to P4)

One side	Starting side	Measured value	613 mm
		Calculated value	604 mm
	Ending side	Measured value	610 mm
		Calculated value	619 mm
Both sides (total)		Measured value	1222 mm
		Calculated value	1223 mm

Herein, it may be necessary to elaborate on the assumption adopted in this seating analysis. The assumption is that the cable force is expressed at seating as follows

$$T = T_0 \cdot e^{-\mu\theta\left(\frac{s}{s_0^*}\right)-\lambda\left(\frac{s}{s_0^*}\right)} \quad (20)$$

where the original length s for the cables is normalized by s_0^* to express the contact point density, where s_0^* = 1 m in the original equation at prestressing and decreases at the seating stage according to the increase in its density. For the seating analysis of the P2 to P4 cables, s_0^* = 1/30 m was adopted. In other words, the contact length index s_0^* was taken as 3.33 cm.

Observation of strain distribution in cables between P1 and P2

For the strain measurement between P1 and P2, shown in Fig. 11, prestressing of this internal cable involved connecting the cantilever tip. This span connection is the last step in the closure of all spans, and the pulled-out length for the prestressing cables is affected by the structural rigidity of the entire bridge. The measured prestressing force for the PC cable during prestressing and after seating is shown in Fig. 12. The prestressing force on the P2 side appears to be larger than that on the P1 side. However, according to the prestressing management chart used during construction, the same prestressing force was introduced on both the left and right sides, and the difference between the measured values and the actual values is most likely due to the fact that the part of the PC cable arrangement that causes angle changes on the P1 side is not identical to that on the P2 side, or it is due to measurement error. It should also be noted that prestressing relief at seating occurred over the entire length of the PC cable, which is 36.08 m long, and the prestressing loss in the center of the PC cable was almost equal to that at the anchorage end.

The PC steel specifications used in the analysis are shown in Table 8. Young's modulus values were taken from the mill certificate issued by the material manufacturer to be aligned with on-site prestressing management records.

The measured values of the pulled-out length of the cable and the results calculated by the proposed method are shown in Table 9. The total calculated pulled-out length for the PC steel agrees well with the measured value.

A comparison of the PC cable force at prestressing and after seating between the observed values and the calculated values assuming friction coefficients of μ = 0.055 and λ = 0.0005 and the same contact length index s_0^* of 3.33 cm is

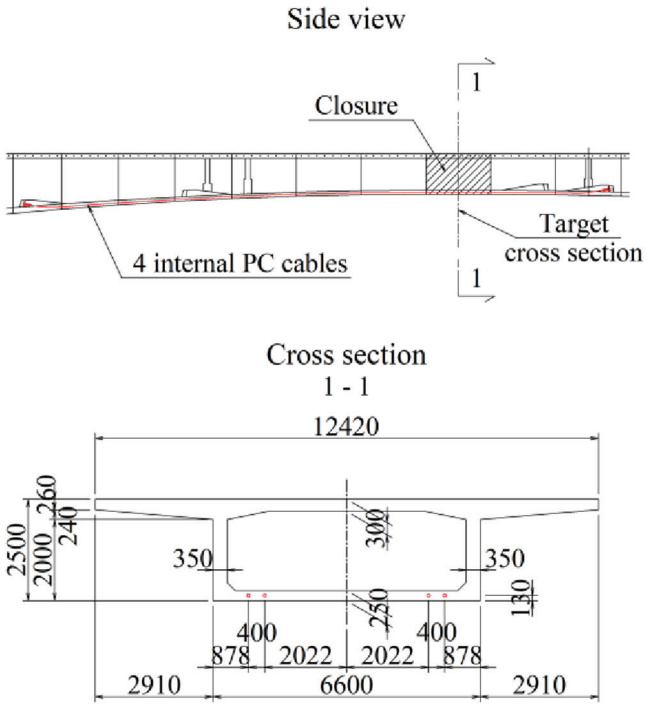


Fig. 11—Internal PC cables layout of P1 to P2 span for closure. (Note: Units are in mm.)

shown in Fig. 12. These results show almost perfect agreement between the observed and calculated strain values.

The original friction coefficients that should be adopted at prestressing need to be discussed in more detail. However, this remains a topic for future work.

IMPROVEMENT OF PRESTRESSING MANAGEMENT

Prestressing management in force-diverting systems

The induced prestress in large-scale structures is, in most cases, dependent on its indeterminate order because the jack prestressing force is distributed to related structural components to which the jack stressing component is connected.

Current management of prestressing in Japan adopts the jack pressure and pulled-out length for a cable from an anchor plate as the control indexes for prestressing, though practices outside Japan seem to adopt jack pressure alone.

The pulled-out length criterion, $\Delta_s + \Delta_c$, is the sum of the cable elongation and concrete contraction. However, concrete contraction Δ_c cannot be calculated yet using the tools presently available. Therefore, a certain amount of error always exists in the current calculations because the current management method neglects this factor, and the rigidity of cables less than the actual values is specified in a rather obscure form in the Japan Road Association standard.[3]

The concrete deformation due to prestressing, Δ_c is expressed as

$$\Delta_c = \int_{s_0}^{s} \varepsilon_c \, ds \tag{21}$$

where integration is carried out along the cable profile to the end point, starting from the unique unmovable point where the concrete and cable have no relative slip. The method

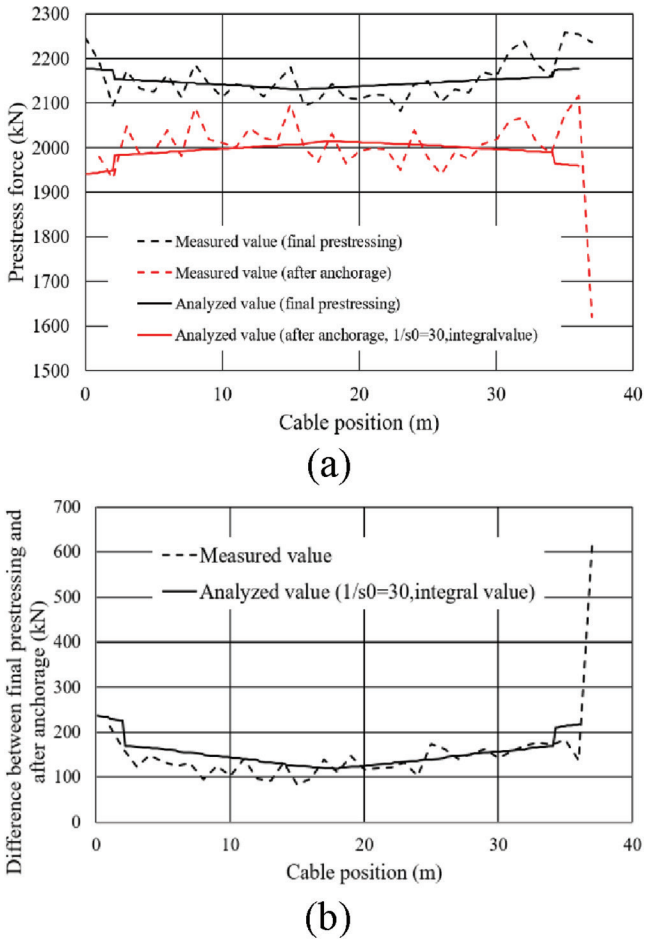


Fig. 12—(a) Comparison of measured and analysis values for prestressing force; and (b) comparison of measured and analysis values for difference between final prestressing and after anchorage (in cables between piers P1 and P2).

Table 8—Analysis conditions (P1 to P2)

Item	Value	Remarks
Young's modulus	191,900 N/mm^2	From average of mill sheets
Prestressing force at end	2177.13 kN	From final tension of 40.0 MPa in prestressing management diagram, considering 1% of jack internal friction loss
Coefficient of friction	In concrete: λ = 0.0005 1/m μ = 0.055 1/rad	From this study
Pulled-out length at anchorage	P2 side: 8.6 mm P4 side: 8.6 mm	From this study

Table 9—Comparison of PC cable pulled-out length (P1 to P2)

One side	Starting side	Measured value	120 mm
		Calculated value	107 mm
	Ending side	Measured value	122 mm
		Calculated value	138 mm
Both sides (total)		Measured value	242 mm
		Calculated value	245 mm

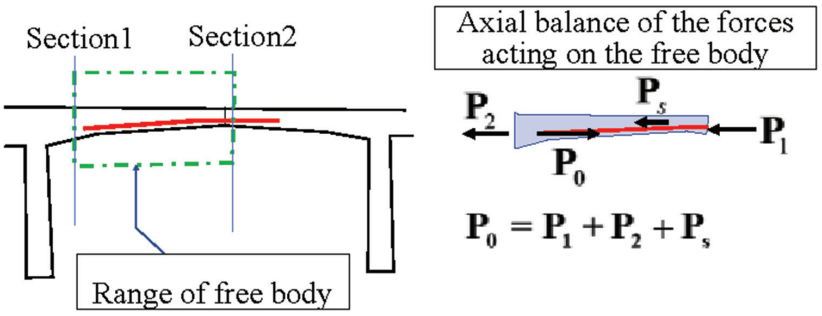


Fig. 13—Conceptual diagram of P1 to P2 prestressing force.

proposed in a previous paper[1] enabled the calculation of this contraction, and the pulled-out length can be correctly calculated and used for prestressing management.

Diverting prestressing force in actual six-span elevated bridge

As already discussed, the prestressing force branches off toward several components in indeterminate structures, as is shown for the target bridge, and the design jack prestressing force is not concentrated entirely in a design section. This situation is examined for an actual six-span bridge.

The prestressing force to close the span between piers P1 and P2 was examined by determining how much of the jack prestressing force is actually transferred to the closing section with respect to the design closing force. As shown in Fig. 13, the jack prestressing force P_0 is expressed as

$$P_0 = P_1 + P_2 + P_s = P_1 + \beta P_0 + (1 - e^{-\mu\theta - \lambda s})P_0 \quad (22)$$

where P_1, P_2, and P_s are the closing force at the closing section, the diverting force that acts on neighboring components, and the frictional force consumed between the jack point and the closing section, respectively; and the value β is a sensitivity factor, which is the ratio of the diverting force P_2 that acts on neighboring components having a jack prestressing force P_0. For this bridge, the closing cables for the span between P1 and P2 are set in two sections, with four cables per section. The total force for four cables is

$$P_0 = 8708.4 \text{ kN}$$

and the calculated values are

$$P_1 = 7853.7 \text{ kN}, P_2 = 380.2 \text{ kN}, P_s = 474.5 \text{ kN}$$

using the respective friction coefficients

$$\lambda/\mu = 0.0636, \mu = 0.055, \lambda = 0.0035$$

P_2 is the portion of the jack force transferred to neighboring components, which are subjected to 4.4% of the jack prestressing force. Adding up the frictional loss from P_2 and P_s shows that almost 10% of the jack prestressing force is not used for the closing span, and approximately 90% of the jack prestressing force acts as the closing force. This is an assumed force distribution, which depends on the assumed rigidity of the base ground and pier and the friction coefficients, and there is no assurance that all the parameters in the calculation are correct. Among these parameters, the one most likely to vary is the ground rigidity, which changes to half or twice the assumed value rather easily. Therefore, it is proposed that the effect should be closely examined for proper prestressing management. There are at least three major parameters—β, μ, and λ—that affect the accuracy of the working force at a design section, and determining the sensitivity of the parameter β to the ground rigidity may be most important and has been performed for the target bridge.

The sensitivity to β is defined in this study such that the β value varies when the ground rigidity changes within the range of +50% to –50% of the design value. Therefore, numerical prestressing experiments were performed while multiplying the design value of the ground rigidity twice by a factor of 1/1000. The results are shown in Fig. 14 and 15.

In Fig. 14, the horizontal axis is the number of multipliers for the assumed ground rigidity, and the vertical axis is the concrete contraction at the jack point. In Fig. 15, the horizontal axis is the number of multipliers for the assumed ground rigidity, and the vertical axis is the β value.

The β value with the assumed ground rigidity is given by

$$\beta = 380.2 \text{ kN}/8708.4 \text{ kN} = 0.044 = 4.4\%$$

Figure 15 shows that when the ground rigidity changes from approximately 1.5 times to 0.5 times, the β values only exhibit a small variation of 0.042%. Thus, the sensitivity to ground rigidity variation in this case is only 4.2%, which indicates that it does not much affect prestressing force transfer to the design section in this case. This is an indication that the ground is hard enough, and changing the rigidity to half of the initial value will affect the prestressing force at the section by only 4.2%. The ground on which the bridge was constructed seems to have rather high soil rigidity, and it can be safely assumed that a variation in the assumed ground rigidity by approximately 1.5 or 0.5 times the initial value does not affect the prestressing force applied to the closing section.

Proposed prestressing management

Prestressing management is a kind of remote management for introducing force to a cross section several tens of meters away from a jack point, during which the frictional jack force is reduced. Moreover, for structures with a large number of indeterminate orders, the jack prestressing force is diverted to many structural components, and identification of the force transferred to the design cross section depends

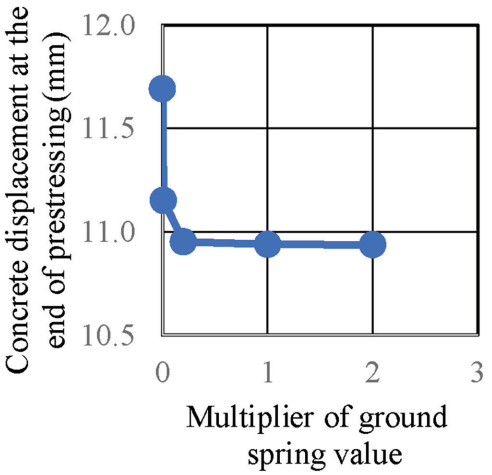


Fig. 14—Sensitivity of concrete displacement to ground rigidity.

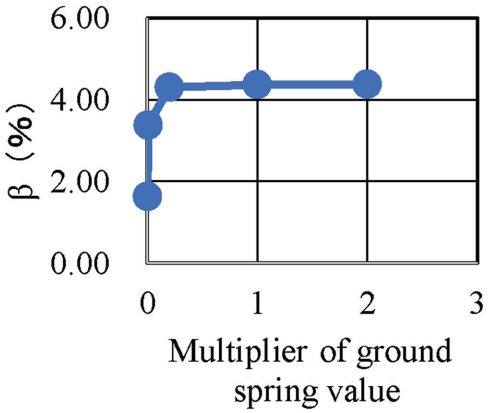


Fig. 15—Sensitivity of ground spring value β to ground rigidity multiplier.

on the accuracy of the analytical calculation. Based on these considerations, the proposals for improving the management of prestressing are as follows:

1. The sensitivity of the β value to ground rigidity is first examined. However, if other factors influence the ground rigidity, then a sensitivity study must be carried out for these factors as well.

2. A prestressing management chart is drawn with a horizontal axis that is the pulled-out length for the cable from the anchor plate, $\Delta_s + \Delta_c$, while the vertical axis is the jack pressure—that is, the prestressing force. In the chart, a stop line for prestressing is drawn. This line is directly affected by the β value, because the prestressing force acting at the target section P_1 is

$$P_1 = \xi P_0$$
$$\xi = e^{-\mu\theta-\lambda s} - \beta \quad (23)$$

as shown conceptually in Fig. 16.

3. The measured slope of the pulled-out length for the cable is matched with the chart slope to determine the specific μ and λ values.

4. The value of ξ may be estimated by an appropriate strain measurement device in the upper and lower box slabs.

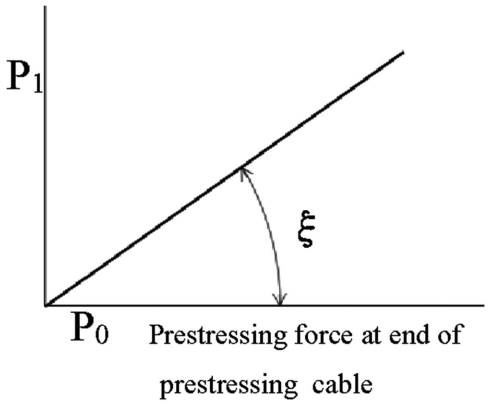


Fig. 16—Conceptual diagram of influence factor.

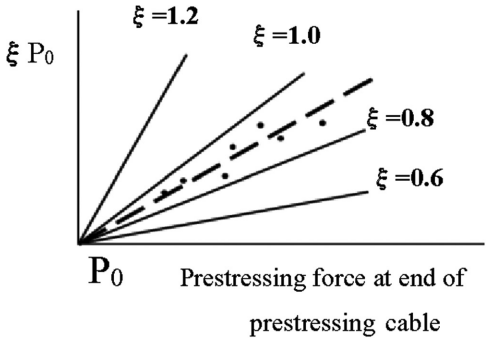


Fig. 17—Conceptual diagram of β identification.

5. If the estimated ξ is outside the limit range, then β should be reestimated from Fig. 17.

Therefore, the prestressing management chart is almost similar to the current chart commonly used.[8] However, the value of β should be written in the chart with μ and λ.

For variations in the β value outside the limit range, the standard should specify how to cope with this situation.

CONCLUSIONS

To extend a study reported in a previous paper,[1] the developed three-dimensional (3-D) finite element method (FEM) was enhanced to compare its theoretical basis with that for the initial strain method. The resulting FEM was applied to a prestressing calculation for an existing six-span, 462 m long bridge, and the observed strain distribution in the cables was compared with the calculated values even after the seating stage, which showed that the current seating loss analysis needs major revision. Based on the results obtained, a new prestressing management method was proposed to ensure the reliability of constructed prestressed concrete (PC) structures.

AUTHOR BIOS

Hiroshi Nishio *is the former Representative Director and Executive Vice President of ABE NIKKO KOGYO CO., LTD. He received his master's degree in engineering from Tohoku University, Sendai, Japan.*

Yosuke Yagi *is an Executive Officer at Fuji P.S Corporation. He received his BS from Meijo University, Nagoya, Japan.*

Yasuaki Ishikawa *is a Professor at Meijo University. He received his DrEng from Nagoya University, Nagoya, Japan. His research interests include the mechanical behavior of prestressed concrete structures and its numerical simulation.*

ACKNOWLEDGMENTS

This study was conducted as part of the research activities of the LECOM Study Group. Thanks are due to T. Tanabe, Professor Emeritus of Nagoya University, and the study group members T. Endo, Professor Emeritus of Tohoku Gakuin University, and Y. Sasaki of the Japan Ministry of Land, Infrastructure, Transport and Tourism. Thanks are also due to H. Osawa, K. Temamoto, and N. Sogabe, Kajima Corporation, for providing valuable data, including optical fiber measurement data. Finally, thanks go to Y. Imai of Fuji Consultants for providing information on overseas prestressing management.

NOTATION

$\boldsymbol{F}_i$ = jack, frictional, and other forces
$N_{rm}N_x$, $N_{rm}N_y$, $N_{rm}N_z$, $N_{rm}M_x$, $N_{rm}M_y$, $N_{rm}M_z$ = error norm
N_x, N_y, N_z = nodal forces of elements
P_s = frictional force consumed between jack point and closing section
P_0 = jack prestressing force
P_1 = closing force at closing section
P_2 = diverting force that acts on neighboring components
s = length measured along cable profile
T = cable force and directional angle change for cable profile
$\boldsymbol{u}_i$ = measured from any point in space
β = sensitivity factor for diverting force P_2 acting on components' neighboring jack with prestressing force P_0
Δ_c = sum of all concrete contraction
Δ_s = sum of all cable elongation
γ = shear strain of section
λ = frictional coefficient for length change
μ = frictional coefficient for angle change
θ = directional angle change for cable profile
ξ = sensitivity factor for closing force at closing section P_1 acting on components' neighboring jack with prestressing force P_0

REFERENCES

1. Ishikawa, Y., and Watanabe, K., "A Numerical Study on the Accuracy of Prestressing Analysis with Initial Strain Method," The 79th JSCE Annual Meeting Proceedings, Japan Society of Civil Engineers, Tokyo, Japan, 2024.

2. Ishikawa, Y.; Nishio, H.; and Yagi, Y., "Development on New 3DFEM Analytical Method and Management in Prestressing Process for PC Structures," *Journal of Japan Society of Civil Engineers*, V. 79, No. 10, 2023, Article No. 23-00003. doi: 10.2208/jscejj.23-00003

3. Japan Road Association, "Specification for Highway Bridges Part III Concrete Bridges," Tokyo, Japan, 2017.

4. Okubo, K.; Imai, M.; Sogabe, N.; Nakaue, S.; Chikiri, K.; and Niwa, J., "Development of the Measuring Method for PC-Tensile Force Distribution by Optical Fiber Applicable to Control of Prestressing and Maintenance of PC Structures," *Journal of Japan Society of Civil Engineers Ser. E2 (Materials and Concrete Structures)*, V. 76, No. 1, 2020, pp. 41-54. doi: 10.2208/jscejmcs.76.1_41

5. Nagumo, H.; Mouri, K.; Morita, Y.; Sogabe, N.; Imai, M.; and Sato, T., "Construction of Tsukidate Viaduct Superstructure as Part of Reconstruction Assistance Road," *Bridge and Foundation Engineering*, V. 50, No. 12, 2016, pp. 5-10.

6. FORUM8, "UC-BRIDGE," Version 10, FORUM8 Co., Ltd., Tokyo, Japan, 2023.

7. JIP Techno Science Corporation, "PCBOX-II," Version 2018.5.8, Tokyo, Japan, 2018.

8. Ishii, T.; Kikuchi, A.; and Itaya, H., "Consideration on Effectiveness of Elongation Measurement System for Prestressing Using Image Processing Technology," *Proceedings of the 29th Symposium on Developments in Prestressed Concrete of Japan Prestressed Concrete Institute*, 2020, pp. 453-456.

ACI STRUCTURAL JOURNAL TECHNICAL PAPER

Title No. 121-S73

Dowel Bar Contribution to Bond Deterioration under Cyclic Loading

by Edom A. Zewdie, Chikako Fujiyama, and Koichi Maekawa

This research delves into the performance of dowels in reinforced concrete joints, highlighting the crucial role of subgrade reaction in providing firm support for dowel bars. The experimental analysis conducted on jointed specimens loaded below their dowel capacity revealed permanent deformations. The examination discerned a gradual extension of cracks emanating from the joint interface, attributing their initiation to bond deterioration under cyclic loading conditions. This research encompasses diverse variables, including dowel arrangements, bar sizes, types, confinement levels, bond conditions, and section size, offering a comprehensive exploration of factors influencing this different joint behavior.

Keywords: bond deterioration; crack; cyclic shear; dowel; joint interface; premature failure; splitting failure.

INTRODUCTION

In reinforced concrete structures, joints serve as a critical shear transfer zone. Joint interfaces alter between flat (smooth/very smooth), rough crack, or mechanically interlocking. These interfaces are due to the connection of precast concrete construction, jointed concrete pavements, retrofitted concrete columns, the interface between old and new concrete, flexural-shear cracks formed in ultimate limit states, and so on. Researchers[1-3] indicate that the shear transfer mechanism across joint interfaces is the contribution of mechanical interlocking, aggregate interlocking, axial confining stress, bar pullout displacement, bar pullout force, concrete resistance, and dowel action. These mechanisms coexist and have demonstrated interdependence. Their interaction depends on the number of reinforcements crossing the interface, bar size, reinforcement bar property, and strength of concrete. Overall contribution is difficult to obtain by simple superposition; hence, a wide range of shear models and scatter of experimental results exist.

The shear transfer mechanism according to Maekawa et al.,[2] is summarized in Fig. 1. Herein, displacement δ caused by the shear load is refrained by the normal stress and shear stresses along the two directions. Normal stresses are induced normal to the crack plane due to the resistance of the aggregate interlocking effect. This aggregate interlocking is responsible for the crack widening at the interface. Due to the crack widening, the bar is displaced, and tension is created on the bar. This pullout tension force is resisted by the compressive force. The crack opening not only depends on the degree of roughness, but also on the level of axial confinement and the controlling mechanism of this axial confinement. Parallel to the crack plane, shear stress resistance is due to dowel action and concrete resistance to shear. For flat (very smooth) interfaces, shear capacity is governed by dowel strength. In the absence of dowels, it is reported[1] that reinforced concrete (RC) joints behave in a brittle manner with joint slips less than 0.05 mm (0.00197 in.). It is considered that ductility is exhibited in the presence of dowels and failure occurs at larger slips of 0.5 to 1.5 mm (0.02 to 0.05 in.).[1]

The ultimate shear capacity of RC joints depends on the failure criterion imputed to section property and loading conditions. According to researchers,[2,4] there are three governing modes of failures for RC joint interfaces. Failure mode 1 is due to concrete spalling and plastic hinge formation; this is initiated due to the plastic hinge at a certain location away from the joint interface. Mode 2 is due to insufficient cover provision, leading to weak and strong mechanisms. In a weak mechanism, failure is due to the inability of the cover to resist the tensile stress developed when the bar pushes the concrete cover. The strong mechanism is where the bar is pushed against the concrete core, and no splitting is expected to occur. The final mode of failure is when the joint interface is flat. In this case, the shear capacity of the joint depends on the dowel strength of the bars. Herein, the pullout of reinforcing bars is negligible, and strength depends on the dowel strength of the bars.

The contribution of dowel action is overlooked due to the difficulty in exploring its contribution. This is caused because of the difficulty in quantitatively measuring shear force transferred by the integration of the different components. Embedded bars in concrete experiments are used to investigate critical dowel load and concrete subgrade stiffness. This concrete subgrade reaction is detrimental to the accurate relationship between the deflection, bar strain, and concrete local fracturing. The Timoshenko[5] beam on elastic foundation analogy is adopted; some suggested a uniform stress distribution under the bars, and others[4] took the bearing capacity of the subgrade stiffness to be several times higher than the uniaxial compressive strength of concrete. Thus, both critical dowel capacity and concrete subgrade stiffness are empirically formulated. Despite the differences in the subgrade stiffness of the supporting concrete, critical dowel load predictions[1,4,6] are similar.

The aforementioned cases already made the shear transfer mechanism complex. Most experiments consider

ACI Structural Journal, V. 121, No. 5, September 2024.

MS No. S-2023-180.R3, doi: 10.14359/51740858, received February 6, 2024, and reviewed under Institute publication policies. Copyright © 2024, American Concrete Institute. All rights reserved, including the making of copies unless permission is obtained from the copyright proprietors. Pertinent discussion including author's closure, if any, will be published ten months from this journal's date if the discussion is received within four months of the paper's print publication.

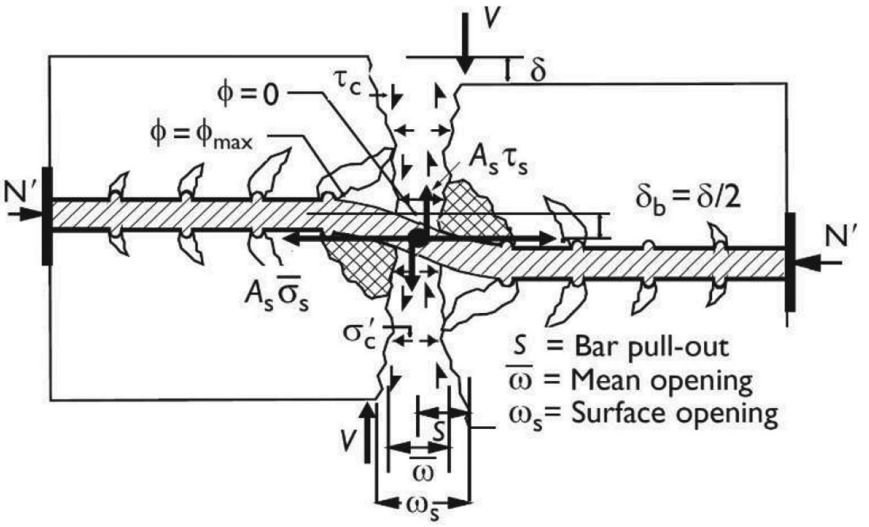


Fig. 1—Summary of shear-transfer mechanism.[2]

monotonically loaded specimens. Cyclic loading is considered in some cases, but is limited to addressing dowel stiffness degradation after plastic hinge formation. In this research, a loading condition less than the critical and design dowel capacity is cyclically applied. Concrete deterioration is observed under this cyclic loading. This cyclic degradation strongly affected bond loss and finally led to splitting cracks, joint deteriorations, and plastic hinge formation.

RESEARCH SIGNIFICANCE

Experimental investigations and the performance of existing structures exhibit considerable variation. For instance, in jointed concrete pavements, bridge corbels, deep beams, and piles, cases of early concrete deterioration under service conditions are observed. Structural members with no axial confining pressure are experimentally simulated in this research. An experimental investigation to address the effect of cyclic loading degradation on the section's capacity is considered. Stepwise, incremental cyclic loads beginning from less-than-critical dowel load are applied to the specimens. Under these conditions, failure criteria for the specimens are studied and presented in this paper. Herein, the initiation of failure due to the debonding of bar and concrete is duly given attention. This information is important for the prediction of RC structures' performance under cyclic loading.

The durability of joints in RC structures is notably influenced by cyclic shear loading. Precise predictions of the shear transfer behavior enable accurate estimation of structures' remaining life, enhancing structural performance and facilitating the development of ultra-high-performance construction materials. Consequently, it contributes to enhancing the performance of joints, increasing safety against collapse, and creates opportunities for the implementation of engineered materials.

TEST PROGRAM

Despite rigorous experimental investigations, the intensity and behavior of loading experienced on existing structures is different from the laboratory mockups. Experiments of different arrangements can facilitate the investigation of different governing criteria. The experimental layout for an embedded bar under shear loading depends on the objective and factors affecting it. In general, it can be categorized into loads directly applied to the dowel and loads applied to the concrete unit. In this investigation, jointed specimens with two very smooth joints are constructed. A load is applied to the center unit of these jointed specimens (Fig. 2). The applied load is resisted by two steel plate supports near the very smooth interface. Hence, the load is transferred to the supports by the two dowel actions on the left and right.

Rectangular RC beams are prepared with two flat (very smooth) joint interfaces. Test specimens (Fig. 2) consisted of three concrete units crossed with reinforcing bars. At the joint interfaces, polytetrafluoroethylene sheets are placed to avoid any frictional stress transfer between the units. The length of embedment of the dowel bars extends all the way through the three concrete units. The embedment lengths used are 600 and 300 mm (24 and 11.81 in.). Specimens of different bar types, bar sizes, cross section sizes, confinement types, and bond conditions are organized as shown in Fig. 2. In Fig. 2, Beams 1, 1R, and 2 are specimens made with a single embedded bar. Beams 1 and 1R are RC sections embedded with deformed bars (bars with lugs), while Beam 2 is an RC section made with a plain bar. Beams 3 and 4 are RC sections with different bar sizes and concrete cross section sizes, respectively. Beams 4 and 8 are twice the size of Beam 1, and the length of the loading plate (L) is altered (Fig. 1) from 150 to 250 mm (6 to 9.9 in.). In addition, the embedded length of the bar for Beam 8 is 300 mm (11.81 in.). Confined specimens (Beams 5 and 6) are constructed by using spiral stirrups. For Beams 5 and 6, two different stirrup arrangements are used. In Beam 5, active confinement with direct contact of longitudinal and stirrups is adopted, whereas Beam 6 has passive confinement with no direct contact in the longitudinal and stirrups. In Beam 7, the reinforced bar is lapped with rubber of 1 mm (0.0394 in.) thick into 10 layers. This removes the bond in the rubber-covered region and creates a weak subgrade stiffness. In all the specimens, the center unit is 300 mm

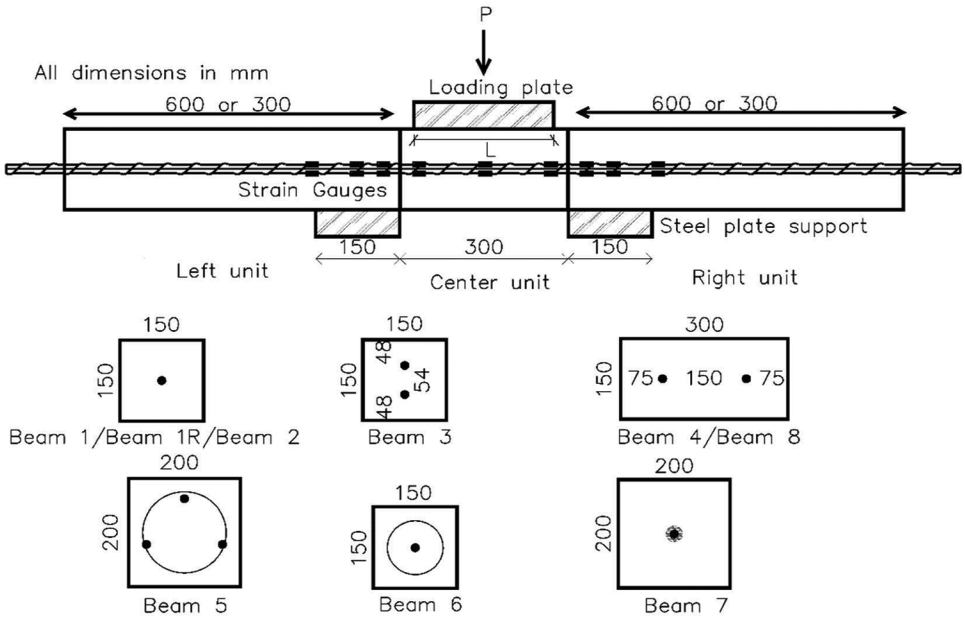


Fig. 2—Specimen layout and dimensions.

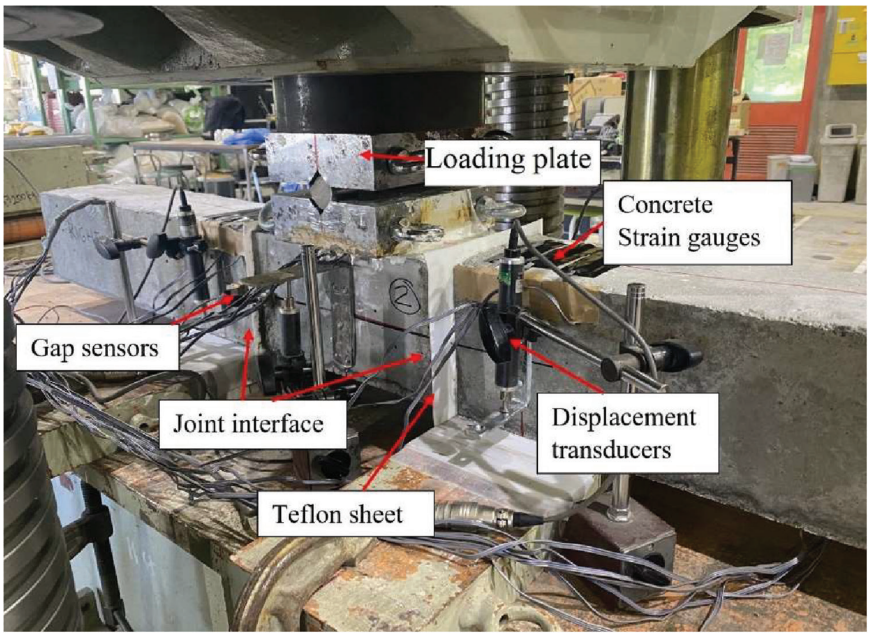


Fig. 3—Experiment setup and measuring instruments.

(11.81 in.) in longitudinal length. The left and right units are each 600 mm (24 in.) long for all the specimens except Beam 8. Details of the specimens' dimensions, loading plate, and bar arrangement are presented in Fig. 2.

To measure strain variation on the reinforcing bar and local strain variation between different locations on the reinforcement bar, strain gauges are mounted (Fig. 2). These strain gauges are placed *D* distances from the joint interfaces. The Beam 8 reinforcing bar is installed with no strain gauges. With the exception of Beams 1 and 2, in all the other specimens, concrete strain gauges are placed at the surface of both the left and right units near the joints. In addition, displacement transducers and gap sensors are used to measure relative vertical displacements (δ) and joint openings, respectively (Fig. 3). The displacement transducers are placed at the center and support to measure the joint displacement of the vertical slip due to the cyclic shear. The gap sensors installed at the joint interfaces are placed to measure opening due to the cyclic shear load.

Materials

Very smooth concrete joints at the interface are achieved by casting the center units first and then performing a subsequent casting of left and right units after sufficient curing. Concrete cylindrical specimens are sampled for each mixture, and compressive strength is described in Table 1. All concrete blocks are made of ordinary portland cement with a maximum size crushed aggregate of 20 mm (0.79 in.). The specimens are cast and air-cured in the laboratory, covered with plastic. For Beam 8, only mortar grout is used to cast

Table 1—Concrete properties

Specimen	Longitudinal bar size, mm	Stirrup bar size, mm	f_{yk}, MPa	Left unit	Center unit	Right unit
				Compressive strength, MPa		
Beam 1	16	—	400	29	37	29
Beam 1R	16	—	400	65	54	65
Beam 2	16	—	400	39	36	39
Beam 3	13	—	385	37	57	37
Beam 4	16	—	400	45	57	43
Beam 5	13	8	385	49	57	43
Beam 6	16	8	400	48	57	48
Beam 7	16	—	400	42	57	42
Beam 8	16	—	400	64	78	64

Table 2—Dowel capacity of specimens

Specimen	f_{yk}, MPa	D_u, kN	$D_{u,d}$, kN	Description
Beam 1	400	36	27	Control specimen
Beam 1R	400	49	37	Lower load level, higher compressive strength
Beam 2	400	40	30	Round bar
Beam 3	385	57	43	Two bars with a smaller diameter
Beam 4	400	87	67	Double cross section size
Beam 5	385	85	65	Active confinement
Beam 6	400	46	35	Passive confinement
Beam 7	400	—	—	No bond, rubber lapped, and monotonic loading
Beam 8	400	106	82	Double cross section size, mortar mixture, highest compressive strength, short embedment length, and no strain gauges

the specimens. The concrete compression tests on 200 mm (7.9 in.) height x 100 mm (3.9 in.) diameter cylindrical specimens were carried out before or after all test series. The mortar compression test samples are taken by using 100 mm (3.9 in.) height x 50 mm (2 in.) diameter cylindrical specimens. Sixteen and 13 mm (0.62 and 0.51 in.) longitudinal bars of 400 and 385 MPa (58 and 56 ksi) strength are used, respectively (Table 1).

Loading

To set the loading criteria, the critical dowel capacity and design capacity of the section were computed. Dowel capacity equations, according to Vintzēleou and Tassios[4] and Randl,[1] are used to calculate the capacity of the section. The dowel capacity for each section is computed based on Eq. (1) and (2). The critical dowel load (Eq. (1)) and design dowel capacity (Eq. (2)) of the beams are presented in Table 2. For computation of the critical dowel load, the lowest compressive strength from the three units is selected. All specimens except Beam 7 are subjected to cyclic loading. The cyclic loading applied to the joints is less than the dowel capacity of the sections presented in Table 2. The loading history adopted for each of the specimens is presented in Fig. 4. The load amplitude and the number of cycles applied to each of the sections vary. This is due to manual control of the speed dial and load indicator gauge to maintain controlled loading conditions. While maintaining precise control over the load amplitude during the successive loading proves challenging, cyclic loading is applied, accompanied by a gradual increase in load amplitude after a series of cycles

$$D_u = 1.3D^2\sqrt{f_{ck}f_{yk}} \quad (1)$$

$$D_{u,d} = D^2\sqrt{f_{ck}f_{yk}} \quad (2)$$

where D_u is critical dowel capacity; D_{ud} is design dowel capacity; D is reinforcing bar diameter; f_{ck} is the characteristic compressive strength of concrete; and f_{yk} is the characteristic yield strength of the reinforcing bar.

EXPERIMENTAL RESULTS AND DISCUSSION

Bond deterioration

The cyclic load applied at the center unit of the specimens results in progressive damage of the jointed specimen. This progressive damage starts at the joint interface and gradually progresses to the surface of the specimen. Figure 4 shows the load-displacement relationship of the specimens herein; it is observed that the beams undergo cyclic concrete degradation. A residual displacement is present after each cycle of loading. The sum of the residual deformation added after each cycle gives the cumulative damage of the section (Fig. 5). In the computation of this residual deformation (cumulative damage), the initial damage in the section due to the initial loading is not considered. In this initial loading stage, some bedding error is observed, which could be due

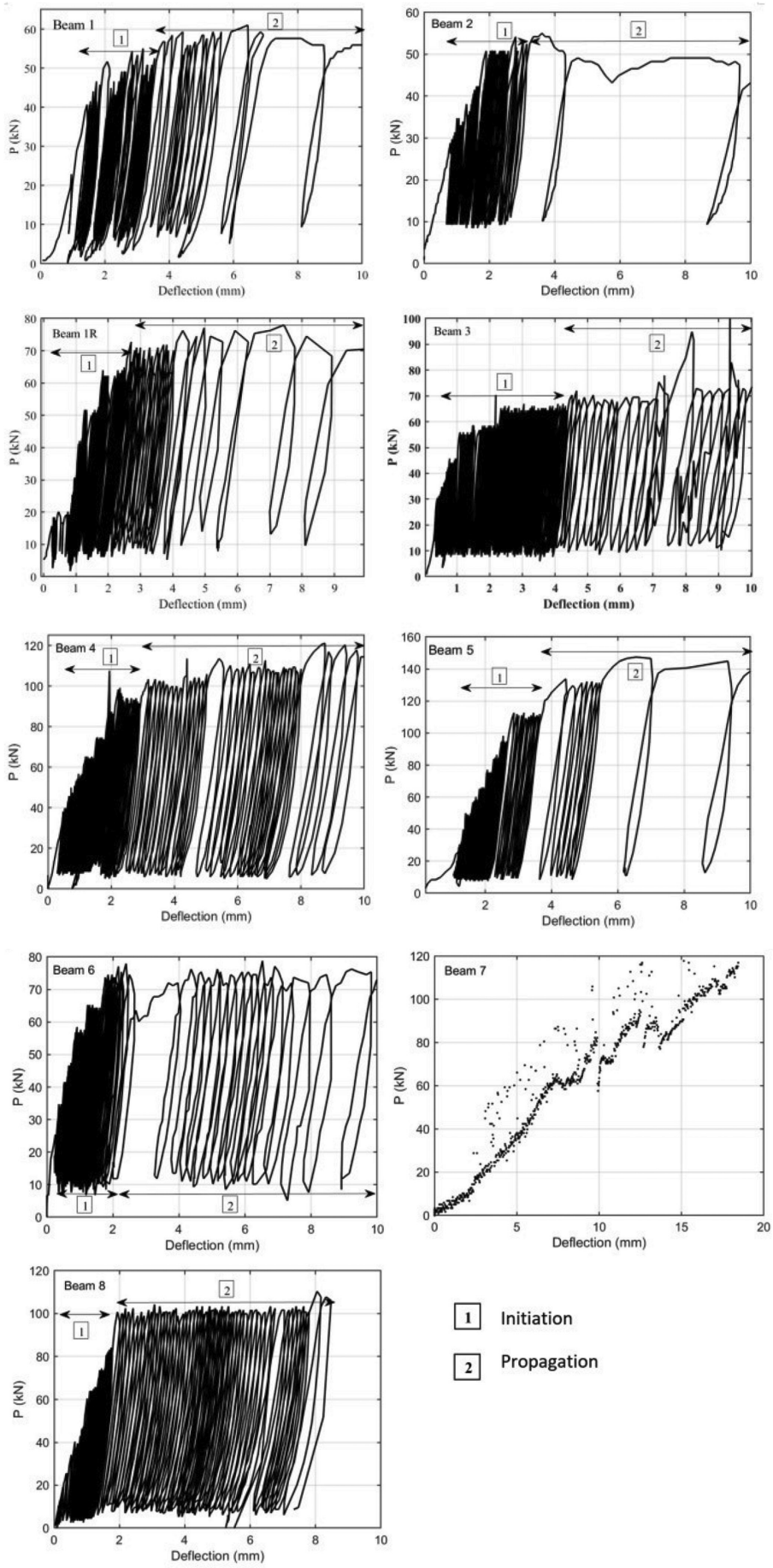


Fig. 4—Experiment results of specimens.

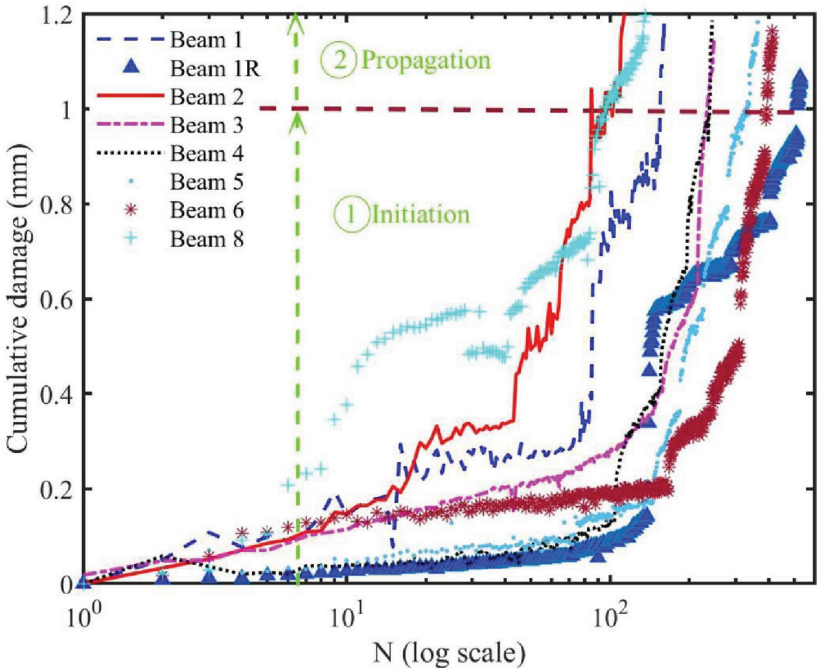


Fig. 5—Rate of damage of specimens.

to the strain gauge protective layers. These layers are applied to protect the strain gauge from moisture and damage while casting the concrete. The bedding error observed reduces when the layers are reduced and tightly placed. The section with no strain gauge (Beam 8) also confirms that such errors do not appear without the layers. The cumulative damage versus the number of repetitive cycle loading (N) for each specimen is plotted in Fig. 5. The damage rate of the specimens is found to have exponential growth (Fig. 5). The rate of damage presented in Fig. 5 shows that damage is highly incremental even if the load is less than the expected dowel capacity. The plasticity of the sections observed in Fig. 4 is attributed to concrete degradation. This has led to premature failure due to concrete degradation in the experimental specimens (Fig. 6).

The patterns of the load-deflection diagram can be grouped in two. The first category, where the rate of damage is low and there is congestion in the load deflection diagram, is categorized as the crack initiation stage. The second category, where there is significant plasticization, is categorized as the crack propagation stage. Concrete degradation on the crack propagation stage depends upon the different tested parameters. The crack propagation stage is different under the different tested conditions. As the load-deflection curve for the specimens in Fig. 4 showed a variation in the propagation stage, the observed crack propagation and fracture behavior for the specimens are also different. The crack initiation stage is the initial cause of the progression of a crack in the later stage. During the initiation stage, bond deterioration occurs, playing a crucial role in the subsequent progression of cracks in later stages.

Unconfined sections with deformed bars (Beams 1, 1R, 3, and 4) displayed splitting cracks at the top and bottom face of the specimen. This splitting failure originated from the bar at the position of the joint interface (Fig. 6). The surface splitting observed on Beams 1 and 3 progresses throughout the length of the specimen. This crack propagates along the bar axis. On the contrary, the splitting crack observed on Beam 4 does not follow the bar axis, but moves toward the edge of the specimen (Fig. 6). Damage of the section with plain bars (Beam 2) shows that the section collapses with side cracks and no splitting failures (Fig. 6). Figure 4 shows that the section displays progressive damage of concrete under cyclic loading below its capacity. The contribution of bar lugs under the cyclic load application can be understood by comparing Beams 1 and 2. For the crack propagation stage, the specimen with a plain bar shows significant deflection, leading to collapse. The strain values at 2D for the plain bars are higher as compared to Beam 1 (Fig. 7). Thus, Beam 1's fatigue capacity is increased due to the presence of bar lugs (Fig. 8).

Confined sections (Beams 5 and 6) displayed concrete deterioration near the joint interface (Fig. 5). In Fig. 4 and 5, confinement is shown to lengthen the crack initiation stage. Thus, increased fatigue performance is obtained. The propagation stage for Beams 5 and 6 is different due to the different confinement techniques applied. In both the specimens, the concrete deterioration is close to the joint interface. The strain gauge reading for these specimens confirms the existence of bond loss. The cyclic loading also resulted in cyclic strain increments, which is responsible for the bond loss. The bond loss near the joint face is responsible for the plastic hinge formation of the bars. This stage is accompanied with significant crack propagation near the joint interfaces.

Beam 8 displays early concrete deterioration near the joint interface (Fig. 6). No strain gauge is placed in this specimen, thus confirming the bond deterioration is not caused due to the strain gauge adhesives. Figure 4 shows cyclic loading also resulted in cyclic damage, which is responsible for the bond loss. This stage is accompanied by significant crack

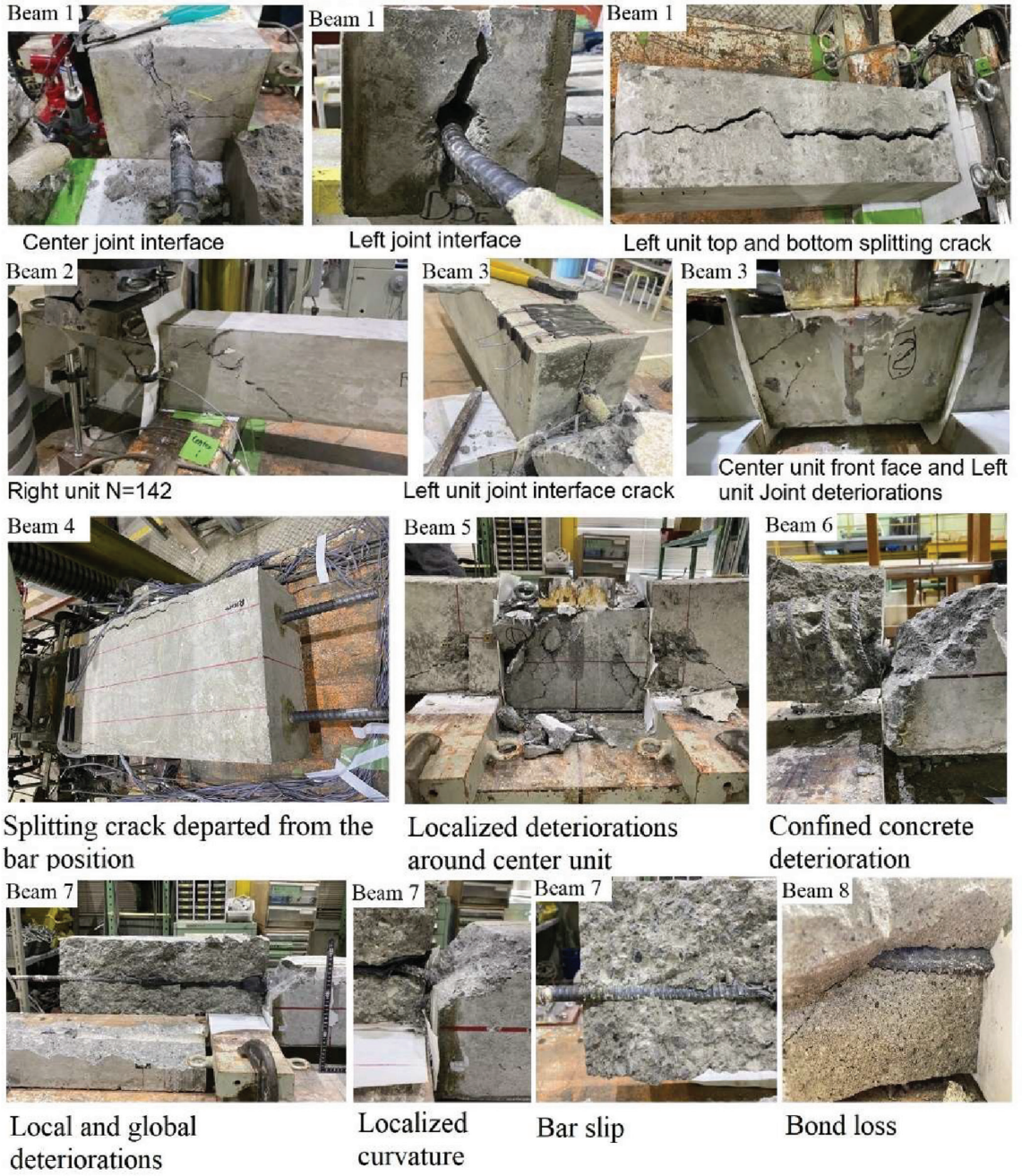


Fig. 6—Premature section failures observed on specimens.

propagation near the joint interfaces. Even if the capacity of the section increased by doubling the section (Beam 1) and the compressive strength of the specimen increased by using mortar grout only, the section deteriorates fast (Fig. 8).

The load-deflection curves for all the specimens show almost parallel loading and unloading curves. This implies that the stiffness of the section is not affected by the cyclic loading. As shown in Fig. 4 with the stiffness not being affected, the cyclic deterioration progressed. According to Timoshenko's[5] beam on elastic foundation theory, the continuous reaction of the foundation is proportional to the deflection. This constant is defined as subgrade stiffness and is the reaction per unit length when deflection is equal to unity. In this experiment, constant k values are obtained. But a permanent deformation exists; thus, the experimental RC sections fail to agree with the beam on elastic foundation theory. This can be attributed to the subgrade's brittle behavior.

The joint deteriorations observed in the specimens initiate due to local bond loss at the joint interfaces (Fig. 6). The bond failures at the beginning of cyclic load applications are captured from the strain gauge readings shown in Fig. 7. The strain reading on the top and bottom surface of the bar shows strain reading of the bar at the bar and concrete boundary. In this figure, it can be observed that the strain gauges placed close to the joint faces (that is, 600 and 900 mm [24 and 36 in.]) recorded a higher value. The strain value reading reduces as the position shifts farther away from the joint faces. Although the strain value reduces as the distance moves further from the joint interface, the measured strain

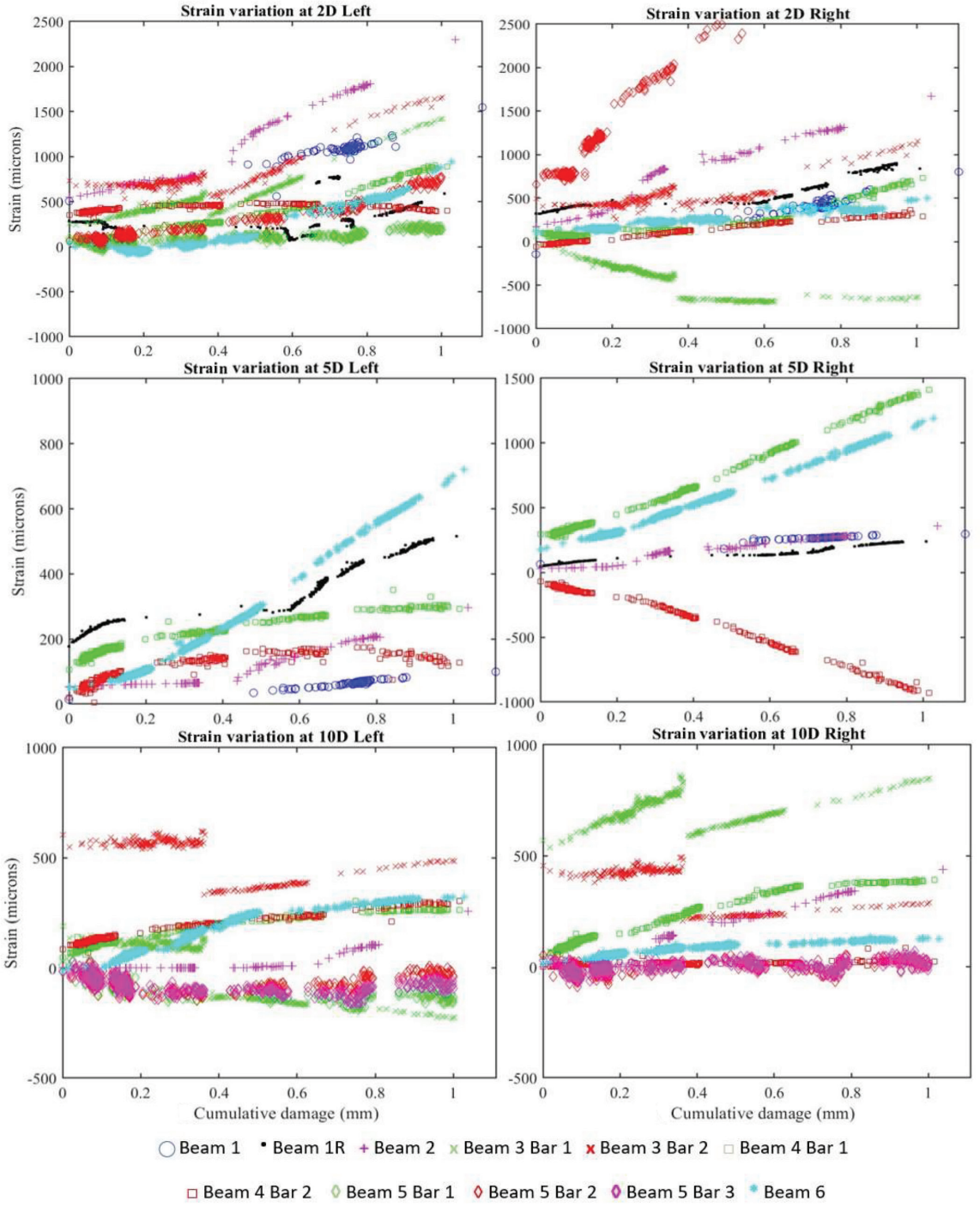


Fig. 7—Strain gauge readings of specimens at 1 mm (0.0394 in.) cumulative damage.

values on each location are incremental (Fig. 7). In addition, the strain values at the same location are different for the left and right units of the specimen. For specimens with more than one bar, the strain values at specific locations are not equal. This variation can be due to the internal stress distribution within the section and the redistribution of loads between the left and right units. In general, the strain readings of the specimens both at 2*D*, 5*D*, and 10*D* demonstrate that the sections undergo bond deterioration propagating from the joint face (Fig. 7). Bond degradation was recorded in investigations by Moradi et al.[7] and Maekawa and Qureshi[3] where the bond deterioration zone is the resulted because of the curvature formation under combined axial and shear loading conditions. Even though no direct axial load is applied to the specimens, similar behavior is observed in the set of experiments conducted.

Figure 8 illustrates the cycle endurance of each specimen under varying applied load levels. The applied load is normalized by its dowel capacity and considering that the load is distributed to both left and right units, the capacities computed in Table 2 are doubled. A comparative analysis is conducted with the control unit (Beam 1) to examine the influence of load level, bar size, confinement conditions, cross section size and compressive strength on the interfacial properties of joints during both the initiation and propagation stage. As explained earlier, the initiation stage is attributed to

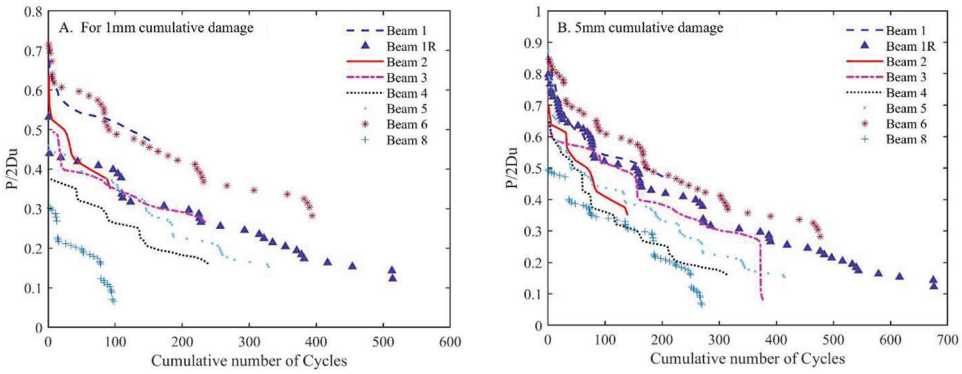


Fig. 8—Number of cycles specimens withstand for 1 and 5 mm (0.0394 and 0.1979 in.) cumulative damage, respectively; normalized load with critical dowel capacity.

the bond deterioration stage. The impact of load levels can be examined through the analysis of Beams 1 and 1R. Beam 1 experiences higher load amplitude during initial cycles, whereas Beam 1R is subjected to lower load amplification at the early stage of the cycle. As depicted in Fig. 8, in both the initiation and propagation stages, applying higher amplitude loading has demonstrated a reduction in fatigue life, while lower amplitude has exhibited an extension of fatigue life. The influence of bar types can be evaluated through the examination of Beams 1 and 2. Figure 8 distinctly illustrates that deformed bars (bar lugs) exhibit enhanced fatigue performance when compared to plain bars. The assessment of bar size is conducted through the study of Beam 3, revealing that adopting a smaller bar size leads to an early bond deterioration stage (Fig. 8(a)). Conversely, employing smaller bar sizes results in a higher fatigue life during the propagation stage (Fig. 8(b)). The issue of confinement can be addressed by looking into Beams 5 and 6. In the initiation stage, passive confinement (Beam 6) increases the fatigue life whereas active confinement has not so much improved the fatigue life. In the propagation stage, both confinement cases improve the fatigue life. Additionally, the effects of cross section increase and higher compressive strength are addressed using Beams 4 and 8 respectively. The size effect (Beam 4) has shown to shorten the fatigue life at both stages. Similarly, the mortar specimen (higher compressive strength) negatively impacts the fatigue life.

In Fig. 8, the slope of each specimen (except Beam 8) exhibits similar characteristics and hence poses similar fatigue rates. Upon scrutinizing the fatigue rate, a discernible trend in the slope of the graph is observed, excluding Beams 2 and 8, during the initiation stage. In the propagation stage, it can be generally fitted onto a similar slope, with the exception of Beam 2. Consequently, despite the variability in amplitude loading, a similarity in the sections is obtained based on fatigue resistance. The significant drop in fatigue rate for Beam 8 is attributed to coarse aggregate distribution in the mixture.[8]

Curvature formation

The examination of bond effects on curvature formation involves the careful selection of specimens—namely Beams 1, 2, and 7—as integral components of the investigation process. The selection of these three beams is intended to illustrate the influence of varying bond conditions on the degradation of concrete sections. Beam 7 is built to have a no-bond zone; this is done by covering the bar with rubber. In addition, the bar is on elastic subgrade due to the presence of layered rubber underneath the bar. Beam 7 is subjected to monotonic loading up to failure. The specimen showed a splitting crack at the top and bottom face; in addition, a significant slip of the end of the bar is also observed[9] (Fig. 6). The impact of such bond loss on the curvature formation can be understood from Fig. 9. Herein, the curvature value at 2*D* from the joint face is computed for Beams 1, 2, and 7. These values are compared with the theoretical curvature according to beam theory. The curvature of the section shown in Fig. 9 is computed when the section is loaded with half of its dowel capacity. In the case of Beam 7, the critical dowel capacity of Beam 1 can be considered. The effect of bond loss is shown to increase the curvature value. Beam 7 exhibits a higher curvature value, followed by Beam 2, where plain bars are used. Beam 1 has a lower curvature as compared to Beams 7 and 2. The formation of curvature plays an important role in the propagation stage. After the bond deterioration stage the crack propagation stage rampantly progresses through the section when plain bars are used. This crack propagation is attributed to the localized kinking (bending) of the bars (Fig. 6).

SUMMARY AND CONCLUSIONS

Experimental investigations of the joint interface under different conditions of confinement and bar arrangement are carried out. The cyclic load *P* applied to the center unit causes bond deterioration. This bond deterioration causes concrete deterioration in the specimens before any of the specimens reach the dowel capacity. Hence, joints are the crucial area that significantly reduces expected performance structures. The performance of joints depends on the confinement of the longitudinal bar. The provision of stirrups retards the formation of splitting cracks and lengthen the fatigue life. The following concluding remarks are made.

1. The cyclic shear force applied to the joints causes bond deterioration causing premature concrete deterioration.

2. When subjected to loads less than the dowel capacity, incremental plasticity due to concrete damage is observed in the jointed specimens.

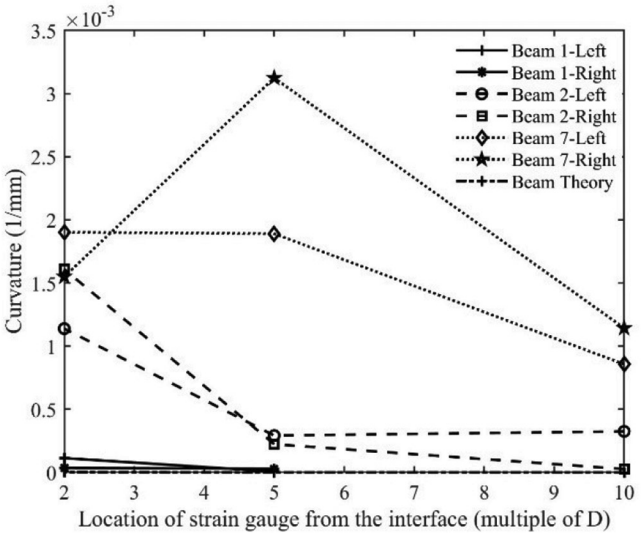


Fig. 9—Curvature distribution for different bond conditions.

3. The type of joint concrete deterioration depends on the confinement type, bar size, and load level.

4. For the unconfined sections, cracking occurs at the joint interface both below and above the bars, resulting in splitting cracks on the top and bottom surfaces of the specimens.

5. Confined sections exhibit concrete deterioration near the joint interface.

6. The curvature of the bar near the joint interface depends on the bond condition of the joint and the type of bar.

7. In this investigation, incremental deformation within the section identifies that a beam on an elastic foundation may not function for modeling dowel action under cyclic conditions.

AUTHOR BIOS

ACI member **Edom A. Zewdie** *is a PhD Candidate at Yokohama National University, Yokohama, Japan. She received her BSc and MSc in civil engineering from Addis Ababa University, Addis Ababa, Ethiopia, in 2013 and 2015, respectively. Her research interests include working on the shear-transfer mechanism due to dowel bars, focusing on the failure mechanism arising from bond degradation.*

Chikako Fujiyama *is a Professor at Yokohama National University. She received her BSc from Kyoto University, Kyoto, Japan, and MSc and PhD in civil engineering from The University of Tokyo, Tokyo, Japan. Her research interests include the mechanics of steel-concrete composite structures under cyclic loads and material development of geopolymer concrete.*

ACI member **Koichi Maekawa** *is an Emeritus Professor at The University of Tokyo and a Visiting Professor at Yokohama National University. He received his BSc, MSc, and PhD in civil engineering from The University of Tokyo. His research interests include multi-scale modeling of reinforced concrete structures both in mechanical and durability aspects.*

ACKNOWLEDGMENTS

The first author is grateful to the Monbukakusho (Ministry of Education, Culture, Sports, Science and Technology of the Japanese Government) for sponsoring postgraduate studies.

NOTATION

A_s	=	area of reinforcement bar
D	=	reinforcement bar diameter
D_u	=	critical dowel capacity
D_{ud}	=	design dowel capacity
f_{ck}	=	characteristics compressive strength
f_{yk}	=	characteristic *s* yield strength
N'	=	axial load or confining pressure
S	=	bar pullout displacement
V	=	shear force
δ	=	vertical deflection or shear displacement
δ_b	=	bar deflection
Φ	=	curvature of reinforcement bar
Φ_{max}	=	maximum curvature of reinforcement bar
τ_c	=	shear stress of concrete
τ_s	=	shear stress of reinforcement bar
σ_c	=	compressive stress developed on crack
σ_s	=	normal stress at reinforcement bar
$\overline{\omega}$	=	mean crack opening
ω_s	=	surface crack opening

REFERENCES

1. Randl, N., "Design Recommendations for Interface Shear Transfer in *fib* Model Code 2010," *Structural Concrete*, V. 14, No. 3, 2013, pp. 230-241. doi: 10.1002/suco.201300003

2. Maekawa, K.; Okamura, H.; and Pimanmas, A., *Non-Linear Mechanics of Reinforced Concrete*, CRC Press, London, UK, 2003, pp. 385-431.

3. Maekawa, K., and Qureshi, J., "Computational Model of Reinforcing Bar Embedded in Concrete Under Combined Axial Pullout and Transverse Displacement," *Doboku Gakkai Rombunshuu*, V. 31, No. 538, 1996, pp. 227-239. doi: 10.2208/jscej.1996.538_227

4. Vintzēleou, E. N., and Tassios, T. P., "Mathematical Models for Dowel Action Under Monotonic and Cyclic Conditions," *Magazine of Concrete Research*, V. 38, No. 134, 1986, pp. 13-22. doi: 10.1680/macr.1986.38.134.13

5. Timoshenko, S., *Strength of Materials, Part II: Advanced Theory and Problems*, third edition, D. Van Nostrans Company, Inc., 1956, 563 pp.

6. Vintzeleou, N., and Tassios, T. P., "Behavior of Dowels under Cyclic Deformations," *ACI Structural Journal*, V. 84, No. 1, Jan.-Feb. 1987, pp. 18-30.

7. Moradi, A. R.; Soltani, M.; and Tasnimi, A. A., "A Simplified Constitutive Model for Dowel Action Across RC Cracks," *Journal of Advanced Concrete Technology*, V. 10, No. 8, 2012, pp. 264-277. doi: 10.3151/jact.10.264

8. Zewdie, E.; Fujiyama, C.; and Maekawa, K., "Performance of Precast Concrete Joints in Cyclic Shear By Using Prepacked Concrete," *Journal of Japan Concrete Institute*, V. 45, 2023.

9. Zewdie, E., and Maekawa, K., "Failure and Limit States of Precast Concrete Joints Under Low Cycle Shear," *Proceedings of the 14th* fib *International PhD Symposium in Civil Engineering*, Rome, Italy, 2022, pp. 81-88

ACI STRUCTURAL JOURNAL TECHNICAL PAPER

Title No. 121-S74

Effect of Mechanical Splice to Seismic Performance of Precast Column-Foundation Connection

by Wei Zhang and Deuckhang Lee

Identifying plastic hinge property is one of key the factors in successful modeling and subsequent seismic performance evaluation of precast concrete (PC) moment frame systems. Tight mechanical splices are also essentially required in precast connections, and its residual slip can greatly affect the plastic hinge length and finally the emulative performance level of PC seismic force-resisting system (SFRS). However, most of the existing models are not directly applicable in current forms to estimate the plastic hinge length of precast connections with mechanical splices. To address the effects of the residual slip induced in the mechanically spliced reinforcement system and its nonuniform stiffness due to splicing device (or coupler), a detailed nonlinear finite element (FE) analysis model was developed in this study, where plasticity-based constitutive models and a unique connector element were adopted for concrete and mechanically spliced reinforcements, respectively. Existing test results of column-foundation connections were used to verify the analytical approach. On this basis, a robust macro modeling method was also proposed for nonlinear cyclic analysis of PC moment frame systems with mechanical splices in this study. It appears that the magnitude of the residual slip in mechanical splices can greatly undermine the lateral stiffness, energy dissipation capacity, and equivalent viscous damping ratio of PC moment connections, and the proposed macro modeling approach can reasonably capture their behavioral characteristics.

Keywords: energy dissipation; equivalent viscous damping; mechanical splice; performance; precast concrete; residual slip; seismic; stiffness.

INTRODUCTION

Plastic deformation inevitably concentrates in the vicinity of precast moment connections with large inelastic curvatures, and it subsequently accompanies localized damage, such as severe cracking, crushing and spalling of concrete, in the so-called plastic hinge region.[1,2] Over the past decades, extensive researches have been conducted on the nonlinear analysis of precast concrete (PC) structures, and on this basis, a high level of accuracy in the sectional analysis of flexural members has been achieved with clear theoretical backgrounds.[3,4] Given that the sectional response of the plastic hinge region is in a form of curvature response, the corresponding member response can be obtained by using the plastic hinge length (L_p). Therefore, a reasonable estimation of the plastic hinge length is the key in successfully modeling the lateral load-drift response and conducting proper seismic performance evaluation of the precast seismic force-resisting systems (SFRS). Various empirical expressions are available in literature to estimate the plastic hinge length of conventional reinforced concrete (RC) members. Some of widely adopted expressions[5-16] are chosen and summarized in Appendix A (Table A1). On this basis, key influential factors can be identified, and these include the diameter (d_b) and yield strength of longitudinal reinforcement (f_y), and the section size (h). It also infers that the plastic hinge length (L_p) usually ranges from $0.25h$ to $1.0h$.

On the other hand, for PC members to be used as a part of the SFRS as specified in the codes,[17,18] the emulative connection details are essentially required to guarantee a comparable seismic performance to a conventional RC monolithic system. However, it seems that the existing empirical expressions of plastic hinge length need to be modified to reflect the effects of relatively large diameter and correspondingly high axial rigidity of mechanical couplers (splicing devices) used to connect two adjacent reinforcements. These mechanical splicing devices barely deform under tension due to relatively higher local axial stiffness, which usually results in reduced curvatures in the splice region, as depicted in Fig. 1. As said, the reduced curvature could lead to shorter plastic hinge length. Besides, existing studies[17-19] indicated that the connection properties of mechanical splicing devices are susceptible in some cases to poor quality control during their production and installation process, which makes the effects of mechanical splices on lateral drift behavior and plastic hinge more complex due to residual slips (RS) induced between splicing device and connecting reinforcements.

To this end, this study aims to develop a robust nonlinear finite element (FE) analysis model to investigate the cyclic response and plastic hinge mechanism of connections in precast moment frame systems. FE models were built upon a continuum plasticity-based damage model of concrete materials. Two-node connector elements with only tensile translational degree-of-freedom (DOF) are addressed to simulate the tensile behavior of a mechanically spliced reinforcement system. Because only a single plastic hinge is expected to be developed in the column-foundation connection system, precast column-foundation connection test results were intentionally chosen from the literature[20] for verifications. Then, the analytical model was verified by comparing with existing test results. Because the plastic hinge length is essentially required to convert the curvature response obtained from sectional analysis to member response expressed in a form of rotational response, the effects of plastic hinge length and residual slip in mechanical splices are reflected in the analytical models. Finally, a simple energy-based macro nonlinear modeling method is

ACI Structural Journal, V. 121, No. 5, September 2024.

MS No. S-2023-183.R5, doi: 10.14359/51740859, received February 10, 2024, and reviewed under Institute publication policies. Copyright © 2024, American Concrete Institute. All rights reserved, including the making of copies unless permission is obtained from the copyright proprietors. Pertinent discussion including author's closure, if any, will be published ten months from this journal's date if the discussion is received within four months of the paper's print publication.

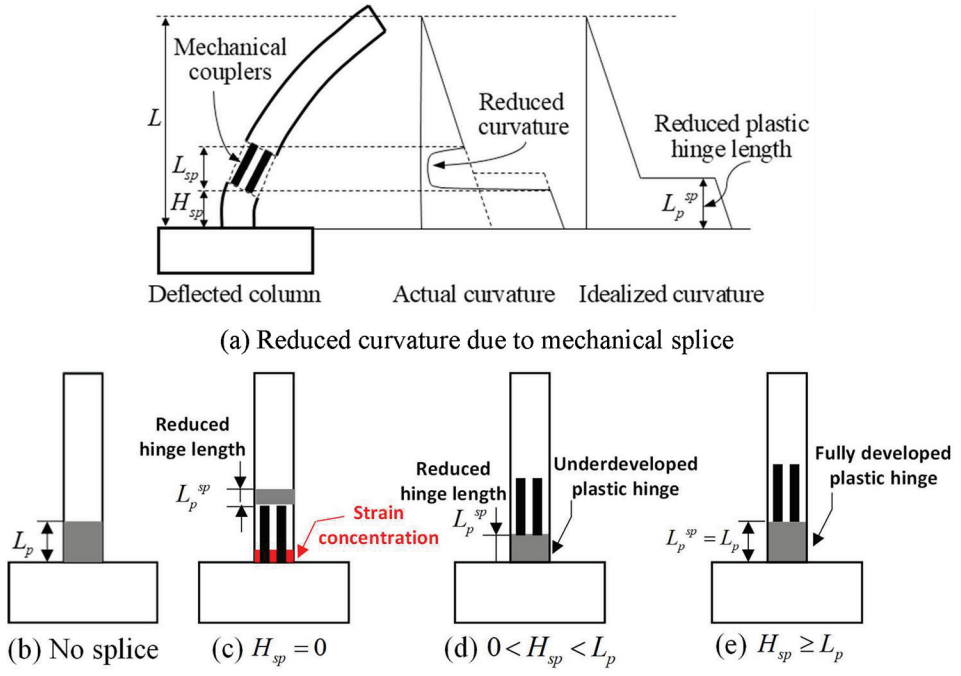


Fig. 1—Effect of mechanical splice on plastic hinge length.

proposed and verified for performance-based seismic design of a new precast moment frame system and seismic performance evaluation of existing precast buildings with mechanically spliced precast connections.

RESEARCH SIGNIFICANCE

PC members are usually connected by mechanical splices. The seismic performance and emulation level of precast building systems significantly depend on the local stiffness of the splicing device and the tightness of the splicing performance, as indicated by the level of its residual slip. This study focuses on identifying the plastic hinge mechanism of PC moment connections for proper modeling and subsequent accurate seismic performance evaluation. To achieve this, a detailed nonlinear FE analysis model was developed using plasticity-based material models, softened contact models, and unique connector elements. Furthermore, a robust macro modeling method is proposed for nonlinear cyclic analysis. The study highlights the detrimental effects of residual slip in mechanical splices on the lateral stiffness, energy-dissipation capacity, and equivalent viscous damping ratio of precast moment connections.

FINITE ELEMENT APPROACH

Existing test results for verifications

A nonlinear FE analysis model is developed in this study to estimate the cyclic responses of RC and PC column-foundation connection specimens, where the joint region between column and foundation was monolithically cast for RC connections, while precast connections were mechanically spliced between reinforcements extended from precast column and RC foundation. Test results reported in Guan et al.[20] are employed to verify the nonlinear FE analysis model because they reported all the key test observations, such as the measured plastic hinge length, energy dissipations, and equivalent viscous damping ratio (ζ_{eq}). Both the RC and PC columns had the same geometric and dimensional properties, as presented in Fig. 2(a) and (b), respectively. The total length of the column member was 2115 mm (83.2 in.), and its section size was 450 mm (17.7 in.) in both the height and width. The lower column was reinforced by typical closed hoops with spacing of 100 mm (3.9 in.), while the hoop spacing of the upper column was 200 mm (7.8 in.). The diameter of stirrups was D10 (No. 3). There were eight longitudinal reinforcements in the column section, and dowel reinforcements were directly connected to the foundation for the RC specimen, as shown in Fig. 2(a). For the PC specimen, the reinforcement from the column and foundation were connected by using the typical grouted mechanical couplers, as shown in Fig. 2(b). Note that an ultra-high-performance concrete (UHPC) prefabricated jacket was applied to the coupler region to prevent buckling failure of couplers (splicing devices) and also to replace the formwork. Except for the presence of the mechanical splices, RC and PC had the same material properties. The compressive strength of the concrete for column and foundation were measured at 31.8 and 40.6 MPa (4.6 and 5.8 ksi), respectively. The yield and tensile strengths of the hoops were 542.0 and 634.7 MPa (78.6 and 92.0 ksi), respectively, while those for the longitudinal reinforcements were 413.3 and 580.3 MPa (59.9 and 84.1 ksi), respectively. The spliced reinforcements can be considered as Type 2 mechanical splice specified in ACI 318-19,[17] according to the original source.[20]

Finite element modeling

To conduct the nonlinear FE analysis, three-dimensional (3-D) models were first built in the ABAQUS FEA platform[21] for the aforementioned RC and PC specimens, and those are presented in Fig. 2(c) and 2(d), respectively. For concrete elements, a 3-D brick element with a single Gauss

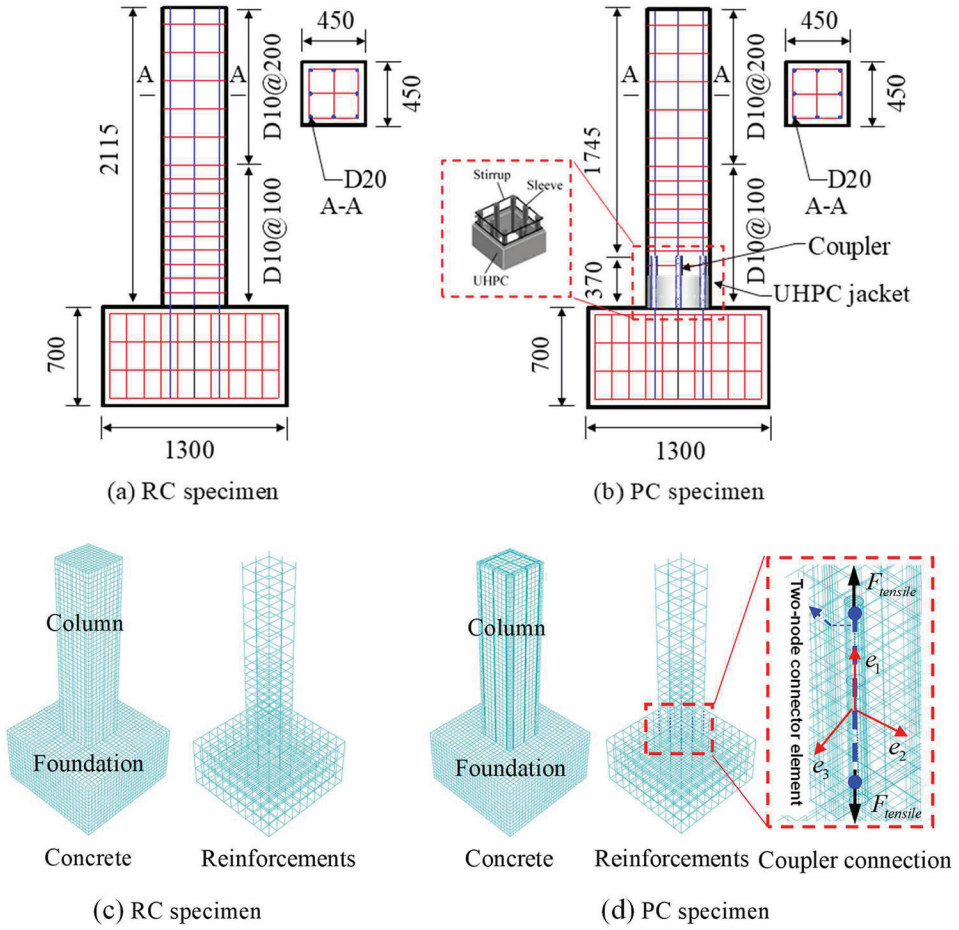


Fig. 2—Test specimens and FE models of column-foundation connection. (Note: 1 mm = 0.039 in.)

integration point located in the center of the element was adopted. Because the concrete element could be subject to high levels of compressive strain, an hourglass control formulation was predefined to improve the accuracy of nonlinear iterative computations. For reinforcing elements, two-node uniaxial truss element was adopted. Regarding the mechanical splices of the PC specimen, most of the previous studies[22-24] employed typical FE analysis by using 3-D solid elements to directly model the grout-type mechanical splices, where bond behaviors have to be defined between mechanical splicing devices, grout matrix, and two connecting reinforcing bars. However, it is a great challenge to accurately characterize the bond between them, and the interaction between mechanical splicing devices and the surrounding concrete is also of great concern. Such intensively complicated surface-to-surface contacts related to the mechanical splices inevitably lead to convergence issues, according to Zhang et al.[24] Hence, this study intentionally used the simple but robust two-node connector elements to quantitively address the connection behavior of mechanical splices in the FE analysis so that their axial force-elongation response (F-u_1 relationship in Fig. 3) can be explicitly defined in the FE model (refer to Fig. 2(d)). In this way, the computational efficiency can be greatly improved as well. These two-node connector elements are single-degree-of-freedom (SDOF) elements along the axial translation, and this translation direction needs to be predefined in a local coordinate system, as shown in Fig. 2(d) and 3(c).

In the FE models, there are three key interactions to be defined: the reinforcement-surrounding concrete interaction; concrete-to-concrete contact at junction between column and foundation (that is, surface-to-surface contact); and also axial force-elongation response for the mechanically spliced reinforcement system modeled through two-node elements, where the elongation (u_1) is a relative deformation between the two end nodes of the connecting reinforcements. Figure 3 shows the schematic descriptions of the three interactions. The truss element for the reinforcements (Nodes A-B) is basically embedded in concrete element, as shown in Fig. 3(a). When Node A is located on a-b-c-d face, its DOFs are intentionally constrained to Nodes a, b, c, and d with appropriate weight factors being determined based on the geometrical location of Node A in the concrete element, and vice versa for Node B. The concrete surface-to-surface contact at the joint between column and foundation is achieved by detecting the clearance between them (two surfaces). Normally, a hard contact condition could lead to sudden stress increase when zero clearance is detected, which usually makes it difficult to obtain stable convergence in the numerical analysis. To mitigate the stress bump, a softened contact with the smoothed exponential pressure-overclosure relationship was applied, as shown in Fig. 3(b). For axial force-elongation response of a mechanically spliced reinforcement system (F-u_1), the relative deformation (u_1) between the two end nodes of the connecting reinforcements

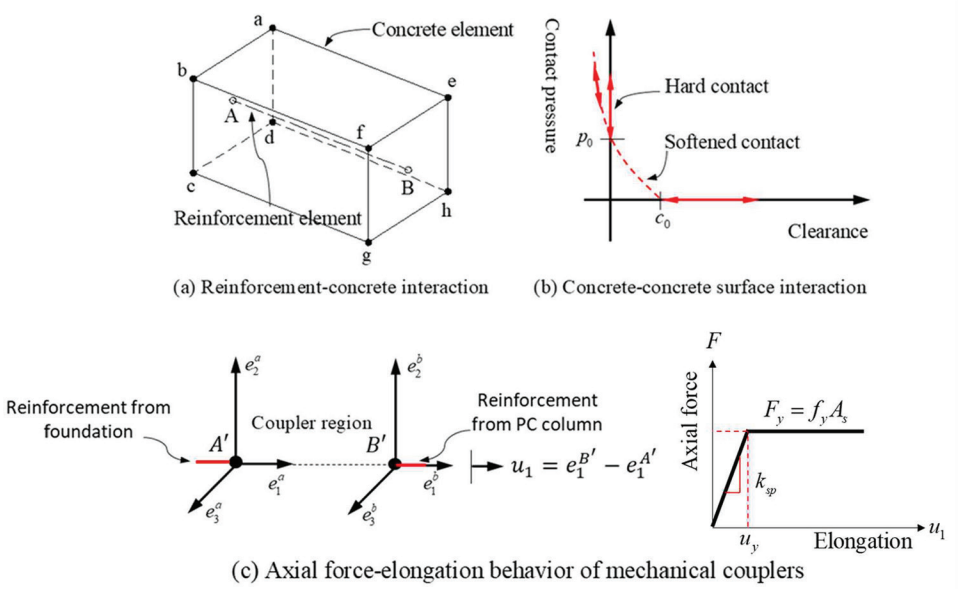


Fig. 3—Key interactions in FE modeling.

(refer to Fig. 3(c)) should be first detected. Then its axial response can be expressed, as follows

$$F = k_{sp}u_1 \tag{1}$$

where k_{sp} is the tensile stiffness of a mechanically spliced reinforcement system (that is, coupler region). Note that the detailed process to derive the tensile stiffness (k_{sp}) is to be presented in the subsequent section. In addition, no rotational DOF is allowed for this two-node connector element, which reflects the rigid behavior of couplers to flexure.

The mechanical behavior of concrete was modeled through a continuum and plasticity-based damage model. It assumes that the dominant concrete failure mechanisms are set by tensile cracking and compressive crushing. The evolution of the failure surface is controlled by two hardening variables (equivalent plastic strains ε_t^{pl} and ε_c^{pl}), and those are defined as the residual strains under tension and compression loading due to the damage of concrete. Therefore, these equivalent plastic strains can be linked to failure mechanisms, and more details can be found elsewhere.[25] The damaged concrete leads to degradation of the elastic stiffness, which can be characterized by two tension and compression damage parameters, d_t and d_c. The relationship between the damage parameters and equivalent plastic strains are expressed, as follows

$$\sigma_t = (1 - d_t)E_0(\varepsilon_t - \varepsilon_t^{pl}) \tag{2}$$

$$\sigma_c = (1 - d_c)E_0(\varepsilon_c - \varepsilon_c^{pl}) \tag{3}$$

where E_0 is the initial (undamaged) stiffness of concrete. Under cyclic loadings, the degradation mechanisms of concrete are more complex, where it involves the opening and closing of existing cracks. It is experimentally observed that there is some recovery of the elastic stiffness as the drift increases during the cyclic loading test. Therefore, for cyclic loading, the reduction of elastic modulus is given in terms of a scalar degradation expression, as follows

$$E = (1 - s_t d_c)(1 - s_c d_t)E_0 \tag{4}$$

where s_t and s_c are the functions of the stress state that are introduced to consider the stiffness recovery effects associated with stress reversals, which can be defined as follows

$$s_t = 1 - \omega_t \gamma(\sigma_{11});\ 0 \le \omega_t \le 1 \tag{5}$$

$$s_c = 1 - \omega_c(1 - \gamma(\sigma_{11}));\ 0 \le \omega_c \le 1 \tag{6}$$

$$\gamma(\sigma_{11}) = \begin{cases} 1, & \sigma_{11} > 0 \\ 0, & \sigma_{11} < 0 \end{cases} \tag{7}$$

where ω_t and ω_c are the weight factors related to the recovery level of the tensile and compressive stiffness upon load reversal; and $\sigma_{11} > 0$ and $\sigma_{11} < 0$ denote the tensile and compressive regimes of the loading cycle, respectively. The stress-strain curves of reinforcements were adopted from the test results. Some of the key modeling parameters for concrete materials, reinforcements, and mechanical couplers are summarized in Appendix B* (Tables B1 and B2). It should be noted that the UHPC jacket of the PC specimen was assumed to be fully elastic, and no damage parameter was assigned because it had much larger strength than other concrete materials and remained undamaged (elastic) during the test. Moreover, the tensile stiffness of mechanical couplers was derived from the analytical models in later section. The test setup, loading protocol, and boundary conditions were in line with the actual conditions reported in Guan et al.[20]

*The Appendix is available at **www.concrete.org/publications** in PDF format, appended to the online version of the published paper. It is also available in hard copy from ACI headquarters for a fee equal to the cost of reproduction plus handling at the time of the request.

The nonlinear FE analysis results are presented and compared with the test results in Fig. 4. It can be seen that the overall cyclic responses including the loading, unloading, and reloading stiffness matched very well with the test results, which indicates that the concrete damaged plasticity model can well capture the stiffness degradation and recovery mechanisms of concrete under cyclic loadings. In addition, the peak points of the reaction force at each cycle also coincided well with the test results for both RC and PC specimens. Based on the validated FE analysis approach, the plastic hinges featured by compression damage parameter are also compared with the test specimens, as shown in Fig. 5(a) and (b). From the observations made from the experiments, the region with spalling of concrete cover was considered as the plastic hinge region, which was featured by the high compression damage parameter 0.9 in the FE models. For the RC specimen, the average plastic hinge length was measured at 345 mm (13.5 in.) from the test, while that from FE model was 330 mm (12.9 in.), as shown in Fig. 5(a). Besides, the strain distributions along longitudinal reinforcements were also extracted and presented in Fig. 5(a), where it clearly shows that the strain responses within the plastic hinge region are much higher than those outside the plastic region. For the PC specimen, the plastic hinge length was decreased to 315 mm (12.4 in.) in an average sense due to the reduced curvature in the region of mechanical couplers, as shown

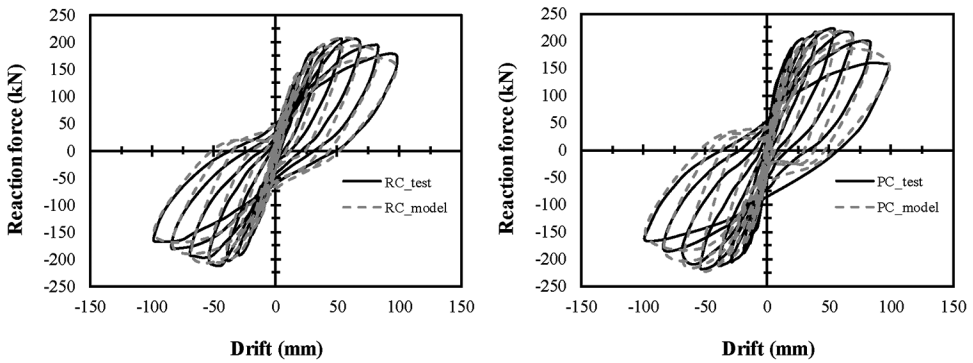


Fig. 4—Cyclic response of test specimens and analysis results. (Note: 1 kN = 0.225 kip; 1 mm = 0.039 in.)

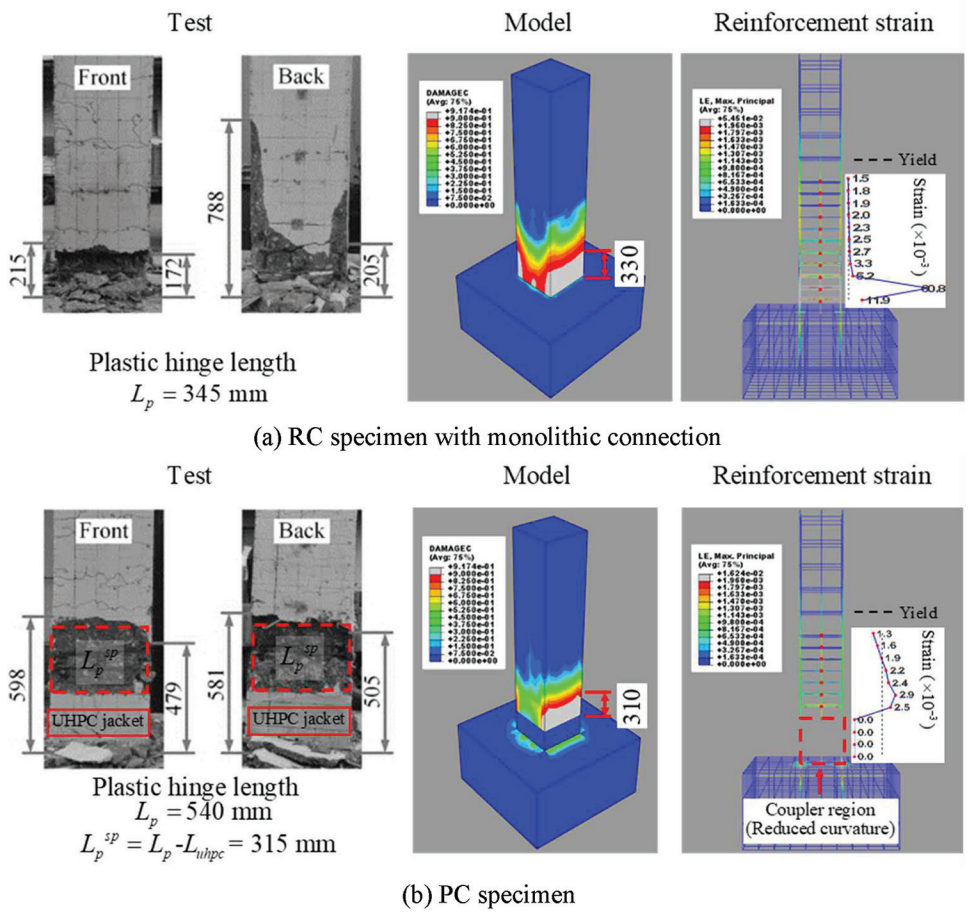


Fig. 5—Plastic response of test specimens. (Note: 1 mm = 0.039 in.)

in Fig. 5(b). This behavioral feature was also well captured by the FE analysis, as also shown in Fig. 5(b), where the plastic hinge length was 310 mm (12.2 in.), and also the reinforcement showed lower strains within the plastic hinge compared to the RC specimen. These results indicate that the FE model can capture the plastic hinge behavior of those test specimens with reasonable accuracy.

Effect of local stiffness of mechanical splice device

The flexural rotation of a column member consists of two parts—that is, linear-elastic rotation (θ_e) before the formation of plastic hinge and plastic rotation (θ_p) after the formation of plastic hinge. Hence, the total column rotation (θ_{tot}) can be expressed, as follows

$$\theta_{tot} = \theta_e + \theta_p = \phi_y(L/2) + (\phi_u - \phi_y)L_p \tag{8}$$

where ϕ_y and ϕ_u are the yielding and ultimate curvatures, respectively. Regarding the base length of the plastic hinge of RC column (L_p), several existing empirical expressions are already available, as presented in Appendix A. However, for precast connections, the effect of the locally higher axial stiffness of the mechanically spliced region should be considered in estimating the plastic hinge length (L_p^{sp}). Note that the base length of plastic hinge (L_p) is defined for no splice condition, and the plastic hinge length (L_p^{sp}) considers the effect of the mechanical coupler device. The reduced plastic hinge length of the mechanically spliced region (L_p^{sp}) in the precast connection is mainly affected by the length and location of splicing device (L_{sp} and H_{sp}), as shown in Fig. 1, and also its rigid length factor (β), which reflects the relative rigidity of the mechanical splicing device (that is, the coupler) to two connecting reinforcements.[26] Note that the introduction of the rigid length factor (β) is to quantify the rigid length of mechanical couplers, which can be expressed as βL_{sp}, then the rest of the coupler region ($L_{cr} - \beta L_{sp}$) can be assumed to deform as the bar region, as shown in Fig. 6(a). Therefore, when the spliced reinforcement system is under tension, only the deformable portion ($L_{cr} - \beta L_{sp}$) of the coupler region, where $L_{cr} = L_{sp} + 2d_b$ (refer to Fig. 6(a)) contributes to the overall elongation of the mechanically spliced reinforcement system. For example, when β is zero, the whole coupler device experiences the same strain as the reinforcing bars, while the whole splicing device contributes no deformation when β is 1.0. Based on the strain of the

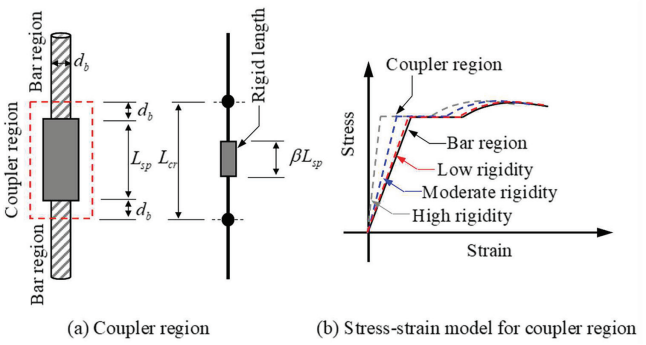


Fig. 6—Stress-strain relationship in mechanically spliced reinforcement system.

reinforcing bar (that is, the bar region in Fig. 6), the effective strain of the coupler region (ε_{sp}) can be approximated based on Tazarv and Saiidi,[26] as follows

$$\varepsilon_{sp} = \frac{\Delta}{L_{cr}} = \frac{L_{cr} - \beta L_{sp}}{L_{cr}}\varepsilon_s \tag{9}$$

where L_{cr} is the length of the coupler region taken as $L_{sp} + 2d_b$; ε_s is the strain of the reinforcing bar; and Δ is the elongation of the coupler region. From Eq. (9), the elongation of the coupler region (Δ) can be estimated as follows

$$\Delta = (L_{cr} - \beta L_{sp})\varepsilon_s \tag{10}$$

Because the yielding and necking inevitably occur at the reinforcing bar (that is, bar region) outside the coupler device in tension, the force-elongation relationship of the coupler region at yielding can be expressed as follows

$$F_y = f_y A_s = k_{sp}\Delta = k_{sp}(L_{cr} - \beta L_{sp})\varepsilon_s \tag{11}$$

where f_y and A_s are the yield strength and area of reinforcing bar, respectively; and k_{sp} is the tensile stiffness of the coupler region, which can be rewritten according to Eq. (11) as follows

$$k_{sp} = \frac{f_y A_s}{(L_{cr} - \beta L_{sp})\varepsilon_s} \tag{12}$$

Equation (12) can also be expressed in the form of the elastic modulus to define the stress-strain relationship for a sectional response, as follows

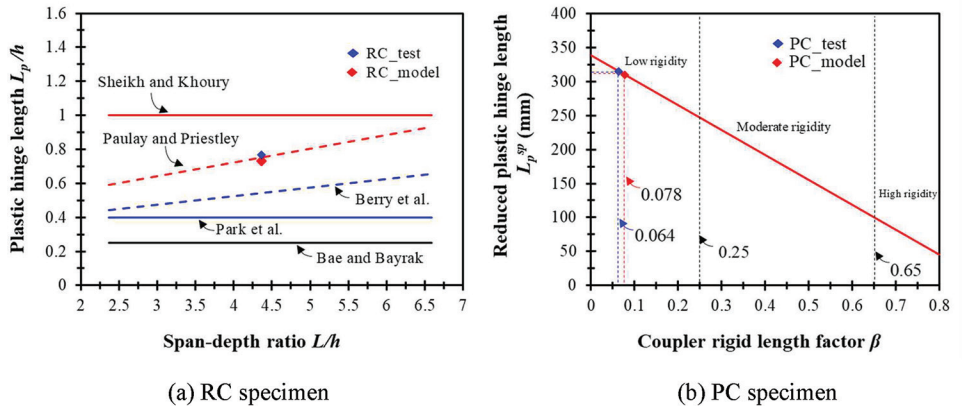
$$E_{sp} = \frac{f_y}{\varepsilon_{sp}} = \frac{f_y}{\left(\frac{L_{cr} - \beta L_{sp}}{L_{cr}}\right)\varepsilon_s} \tag{13}$$

where E_{sp} is the elastic modulus of coupler region. With this relationship, the tensile stiffness (k_{sp}) or elastic modulus (E_{sp}) of the coupler region can be determined with the given material properties of reinforcing bar (for example, f_y, A_s, and ε_s) and rigid length factor (β). The higher the rigid length factor (β), the higher the expected tensile stiffness in the coupler region. The low rigid length factor indicates the stress-strain relationship in the coupler region approaches to that of the naked reinforcement with no splicing device (that is, bar region or bare bar), as shown in Fig. 6(b), where the gray dashed curve represents the stress-strain relationship of the coupler region with high rigidity, while the blue and red ones represent those with moderate and low rigidity, respectively. According to Tazarv and Saiidi,[26] it is recommended that the reduced plastic hinge length (L_p^{sp}) of the precast connection with a mechanical splice can be expressed as follows

$$L_p^{sp} = L_p - \left(1 - \frac{H_{sp}}{L_p}\right)\beta L_{sp} \le L_p \tag{14}$$

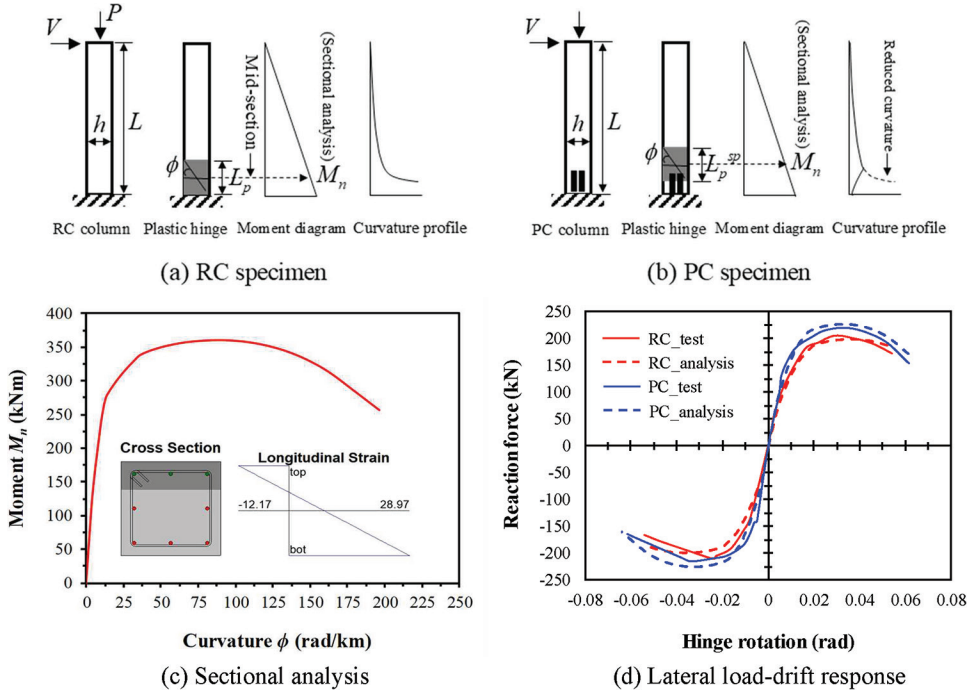
where the term of $1 - H_{sp}/L_p$ reflects the location effect of couplers, which is also considered in the analytical model

of Lee et al.[27] The effect of coupler location is demonstrated in Fig. 1(b) to 1(e) for better understanding. When there is no splice, the plastic hinge is to be developed at base, as presented in Fig. 1(b). If the reinforcements are mechanically spliced at the junction between the column and foundation, as shown in Fig. 1(c), strain concentration occurs, and it leads to reduced strain above the mechanical couplers. As a result, the plastic hinge length above the couplers is inevitably reduced. If the mechanical couplers are moved up to some distance from the base but still within the range of base plastic hinge length (L_p), as shown in Fig. 1(d), the plastic hinge still can not fully develop, consequently, the plastic hinge length with mechaical splices (L_p^{sp}) is lower than the base length of plastic hinge (L_p). If the mechanical couplers are located beyond the base length of plastic hinge (L_p), the plastic hinge can be fully developed, the plastic hinge length with mechaical splices (L_p^{sp}) is the same as the base length of plastic hinge (L_p), as shown in Fig. 1(e). From Eq. (14), the β value can be traced back by using the test results. Figure 7(a) shows the comparison of some of the existing empirical plastic hinge length expressions as listed in Appendix A to the test results. It shows that Paulay and Priestley's expression[10] ($L_P = 0.08z + 0.022f_y d_b$) matches the best with the test and modeling results of the plastic hinge length in this study, where z is the distance from critical section to point of contraflexure. Based on Paulay and Priestley's expression for the base length of plastic hinge under no splice condition (L_p), the corresponding plastic hinge length (L_p^{sp}) and coupler rigid length factor (β) of the PC connection were reversely estimated by using Eq. (14). Figure 8(b) shows the effect of the relative rigidity provided by the mechanical couplers. It can be seen that the rigid length factor (β) is quite low for the test specimens reported in Guan et al.,[20] which indicates that the stress-strain relationship in the coupler region is similar to that of bar region. With the plastic hinge length (L_p^{sp}) and rigid length factor (β) determined, the tensile stiffness of the splicing system (k_{sp}) can be estimated according to Eq. (12), and this estimated stiffness was employed to define the axial



(a) RC specimen (b) PC specimen

Fig. 7—Plastic hinge length of test and analytical results. (Note: 1 mm = 0.039 in.)



(a) RC specimen (b) PC specimen

(c) Sectional analysis (d) Lateral load-drift response

Fig. 8—Lateral responses of column-foundation connections. (Note: 1 kN = 0.225 kip; 1 mm = 0.039 in.)

force-slip response in the previous FE model as indicated in Eq. (1).

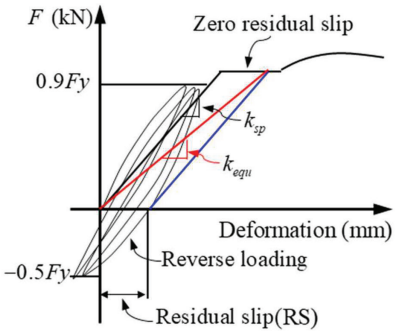
Figures 8(a) and (b) illustrate the lateral load-drift responses of RC and PC columns, respectively. For the RC column, the plastic hinge forms nearby the column base, where the curvature concentrated, as shown in Fig. 8(a). However, for the PC connection, the plastic hinge region is elevated away from the base due to the presence of couplers at the junction of column and foundation, where the curvature in the coupler region is clearly smaller in magnitude due to the locally higher rigidity provided by the mechanical splicing device (coupler), as shown in Fig. 8(b). Within the plastic hinge region, as mentioned previously, uniform inelastic curvature can be assumed, and thus the sectional response at the middle of the plastic hinge can be chosen to represent the overall flexural response of the plastic hinge region. On this basis, the sectional flexural response of the column member can be converted into the lateral load-rotation response based on Eq. (8). Figures 8(c) and (d) show the moment-curvature curve obtained from the sectional analysis of the midsection in the plastic hinge length. Then the curvature can be converted into the corresponding rotation through Eq. (8). The moment can be also converted into the reaction force, as follows

$$V = M_n / L_c \tag{15}$$

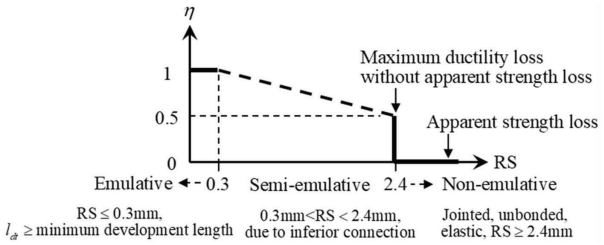
where L_c is the distance from column tip to midsection of plastic hinge region. The comparisons of the lateral load-drift responses for both the RC and PC connections are presented in Fig. 8(d), where it can be seen that the analytical curves agreed well with the test results.

Effect of residual slip and corresponding emulative level

The splicing performance of a mechanical coupler is critical in the seismic performance and emulative level of precast SFRS. Therefore, the design codes of structural concrete in many countries set strict requirements on the performance of mechanical couplers under cyclic loadings. In terms of the strength, Type 2 mechanical splice requires the test results should satisfy 1.25 times the yield strength ($1.25f_y$) and tensile strength (f_u). While for the RS, ISO 15835-2:2009[28] stipulates the testing method and performance criteria for the mechanical splices to be used in seismic regions, as shown in Fig. 9(a). Note that standards[29,30] in Korea, Japan, and other countries are also quite similar to each other. The testing should be kept within the elastic limit with an upper bound of $0.9f_y$ in tension and a lower bound of $0.5f_y$ in compression for the first 20 cycles. It is required that the RS after cyclic testing should be less than 0.3 mm (0.01 in.) to ensure an emulative connection, and this allowable slip is also adopted in Korean and Japanese standards.[29,30] However, no clear background is available regarding the slip limit of 0.3 mm (0.01 in.). In addition, the effects of the residual slip of mechanical couplers on the seismic performances including energy dissipation capacity, viscous damping ratio, and plastic hinge are still not clearly identified. The primary effect of the RS is the



(a) Low-cycle loading testing of mechanically-spliced reinforcement



(b) Emulation level defined from residual slip

Fig. 9—Effect of residual slip on emulation level of spliced reinforcement connection. (Note: 1 kN = 0.225 kip; 1 mm = 0.039 in.)

delayed yielding of connection as marked by the blue line in Fig. 9(a). Consequently, compared to those without RS, the equivalent stiffness of the mechanically spliced reinforcement system with RS (k_{equ}) is lower, as marked by the red line in Fig. 9(a). Equation (12) gives the tensile stiffness of the coupler region without RS (k_{sp}), from which the equivalent stiffness of the coupler region with RS (k_{equ}) can be expressed by reflecting the RS, as follows

$$k_{equ} = \frac{f_y A_s}{(L_{cr} - \beta L_{sp})\varepsilon_s + \mathrm{RS}} \tag{16}$$

Equation (16) can also be expressed in the form of a stress-strain relationship for the sectional analysis (that is, moment-curvature analysis), as follows

$$E_{equ} = \frac{f_y}{\frac{L_{cr} - \beta L_{sp}}{L_{cr}}\varepsilon_s + \frac{\mathrm{RS}}{L_{cr}}} \tag{17}$$

where E_{equ} is the equivalent elastic modulus of the coupler region with RS. To investigate the effect of the magnitudes of RS on the system responses of the precast moment frames, a parametric study was conducted by using the nonlinear FE analyses of PC column-foundation connections with various levels of RS ranging from 0.3 to 9.6 mm (0.01 to 0.32 in.). Note that the yield strength of the spliced reinforcement systems was kept constant. In addition, the coupler rigid length factor (β) of the PC connection is assumed to be the same with the value presented previously in Fig. 7(b).

Figure 10 shows the cyclic behavior of the PC column-foundation connections with different levels of RS. It

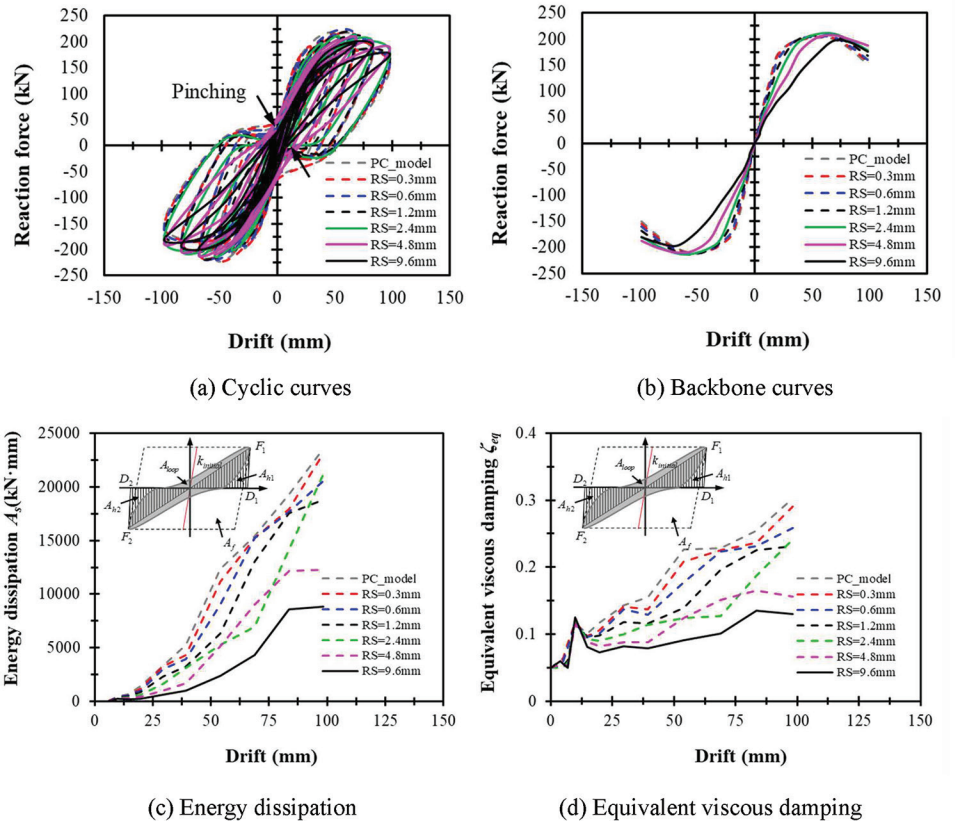


Fig. 10—Effect of RS on cyclic response. (Note: 1 kN = 0.225 kip; 1 mm = 0.039 in.)

appears that the pinching behavior of the PC column under cyclic loading gets more severe as the magnitude of the RS increases, as shown in Fig. 10(a). This pinching behavior becomes more obvious when the residual slip exceeds 0.3 mm (0.01 in.). In addition, the initial stiffness of the PC column also decreases as the RS increases, as shown in Fig. 10(b). This is because the equivalent stiffness of couplers (k_{equ}) decreases with increasing RS, as shown in Fig. 9(a). The energy dissipation defined by the enclosed area of loops (A_{loop}) and equivalent viscous damping (EVD) ratio (ζ_{eq}) calculated as $\zeta_{eq} = 0.05 + A_{loop}/[2\pi(A_{h1} + A_{h2})]$ are also remarkably reduced, as shown in Fig. 10(c) and (d). Approximately, losses of 4.1%, 14.7%, 23.6%, 20.1%, 48.5%, and 57.0% in the EVD ratio (ζ_{eq}) are observed for the cases with RS of 0.3. 0.6, 1.2, 2.4, 4.8 and 9.6 mm (0.01, 0.02, 0.04, 0.08, 0.16, and 0.32 in.), at ultimate state, respectively. This result indicates that RS less than 0.3 mm (0.01 in.) can be considered as the emulative connection. As shown in Fig. 9(b), when the RS is larger than 0.3 mm (0.01 in.) but less than 2.4 mm (0.08 in.), the connection can be referred to as the semi-emulative connection, because the ultimate energy dissipation and corresponding EVD loss are approximately 20%, as presented in Fig. 10(c) and (d). However, if the RS is greater than 2.4 mm (0.08 in.), the ultimate EVD loss could reach more than 50%, and the peak strength is also significantly degraded. Thus, the connection with the RS greater than 2.4 mm (0.08 in.) should be considered as the non-emulative connection, and it shall be prohibited in its application alone as an SFRS. Moreover, because the equivalent stiffness with residual slip (k_{equ}) also increases with the rigid length factor (β) as indicated in Eq. (16), the initial stiffness of the PC connection system can be proportional to β.

The relative deformations (that is, elongation) were measured at 20.36, 19.51, 19.48, 18.76, 17.43, 17.23, and 15.37 mm (0.80, 0.77, 0.76, 0.74, 0.69, 0.68, and 0.61 in.), respectively. All of them clearly exceeded their elongation at yielding (u_y, refer to Fig. 3(c)), which were 0.77, 1.07, 1.37, 1.97, 3.17, 5.57, and 10.37 mm (0.03, 0.04, 0.05, 0.07, 0.11, 0.19, and 0.35 in.) for the parametric analysis cases with various magnitudes of the residual slip level (0.0, 0.3. 0.6, 1.2, 2.4, 4.8 and 9.6 mm [0, 0.01, 0.02, 0.04, 0.08, 0.16, and 0.32 in.]), respectively. It can be seen that all the cases are clearly yielded, and thus the plastic hinge can be formed for all the cases. Note that the elongation at yielding can be computed from the Table B2 in Appendix B (that is, the yield force divided by tensile stiffness, F_y/k_{sp}, as presented in Fig. 3(c)). The plastic hinges of the PC columns with various RS obtained from the analyses are presented in Appendix C (Fig. C1), where it appeared that the peak strain value increases due to the delayed yielding as the residual slip increases. However, it also shows the marginal influence on the plastic hinge length, which indicates that the plastic hinge length can be reduced when the rigidity of mechanical splices is higher than that of bar region.

MACRO MODELING APPROACH

In previous sections, the effects of the RS on the cyclic response and plastic hinge mechanism of PC connections with the mechanical splices were explored and discussed in detail. However, such a nonlinear FE analysis approach is too complex and computationally costly to be used in

nonlinear static and dynamic analyses of precast building systems. Thus, a simple and practical energy-based macro modeling approach is developed and presented in this study.

The key strategy of the macro modeling approach is depicted in Fig. 11, where a zero-length rotational spring element is adopted to reflect the plastic behavior in a lumped manner. This zero-length rotational spring element was set to be located at the mid-section of plastic hinge length estimated from Eq. (14), as shown in Fig. 11(a). The lateral response of a PC column-foundation connection can be obtained from the sectional analysis and Eq. (8), from which the sectional response can be converted into the rotational behavior at the member level. Note that the sectional analysis of a plastic hinge section should consider the effect of the stress-strain relationship of the coupler region (refer to Eq. (13) and (17)). After determining the overall lateral behavior (backbone curve), the hysteretic behavior is to be defined, as shown in Fig. 11(b). This hysteretic rule is basically defined by four featured points on the backbone curve (that is, yield point, peak point, ultimate displacement point, and fracture point), and the pinching coefficient ($\alpha_{pinching}$) is also required to define the points where reloading begins. To derive the pinching coefficient ($\alpha_{pinching}$) and corresponding hysteresis rule, the energy dissipation (that is, the enclosed area, A_{loop}) at the ultimate displacement point (usually defined by displacement at 20% of strength degradation) should be determined, and the energy dissipation (A_{loop}) can be rewritten as follows

$$A_{loop} = (\zeta_{eq} - 0.05)[2\pi(A_{h1} + A_{h2})] \tag{18}$$

where ζ_{eq} is the EVD ratio, which can be taken as $\zeta_0 + A_{loop}/[2\pi(A_{h1} + A_{h2})]$; and ζ_0 is the elastic damping ratio, usually taken as 0.05 (5%). Meanwhile, at the ultimate displacement point, the enclosed area (A_{loop}) can be calculated by assuming the unloading stiffness (k_u) remains the same as the elastic secant stiffness (k_e), as follows

$$A_{loop} = \left[\begin{array}{c}\left(\dfrac{M_{y1}\theta_1 + M_{y2}\theta_2 + (\theta_1 + \theta_2)2\alpha_{pinching}}{2}\right) - \\ \left(\theta_1 - \dfrac{M_{y1}}{k_e}\right)\dfrac{M_{y2}\alpha_{pinching}}{2} \\ \left(\theta_2 - \dfrac{M_{y2}}{k_e}\right)\dfrac{M_{y1}\alpha_{pinching}}{2}\end{array}\right] - \frac{M_{y1}^2 + M_{y2}^2}{2k_e} \tag{19}$$

where M_{y1} and M_{y2} are the yield flexural strengths in the positive and negative direction, respectively; θ_1 and θ_2 are the rotations at the ultimate displacement points in the positive and negative direction, respectively; and $\alpha_{pinching}$ is the pinching point where reloading begins. From Eq. (18) and (19), the relationship between the pinching coefficient ($\alpha_{pinching}$) and EVD ratio (ζ_{eq}) can be derived as follows

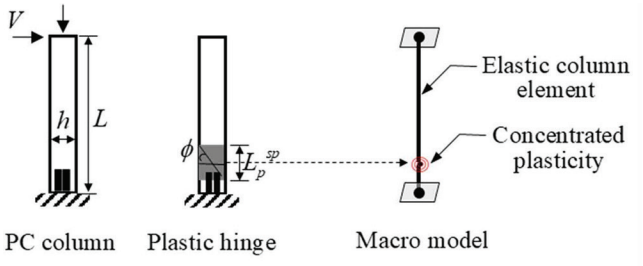
$$\alpha_{pinching} = \frac{\left[\begin{array}{c}2\pi(\zeta_{eq} - 0.05)(M_{y1}\theta_1 + M_{y_2}\theta_2) + \\ (M_{y1}^2 + M_{y2}^2)/k_e\end{array}\right]}{\begin{array}{c}-(M_{y1}\theta_1 + M_{y2}\theta_2) \\ M_{y1}\theta_1 + M_{y_2}\theta_2 - M_{y1}\theta_2 - \\ M_{y2}\theta_1 + 2M_{y1}M_{y2}/k_e\end{array}} \tag{20}$$

Equation (20) indicates that the pinching coefficient ($\alpha_{pinching}$) is a function of EVD (ζ_{eq}), yield flexural strengths (M_{y1} and M_{y2}), ultimate rotations (θ_1 and θ_2), and elastic secant stiffness (k_e). Once the yield point, ultimate displacement point, and the EVD at the ultimate displacement point are determined, the pinching coefficient ($\alpha_{pinching}$) can be easily identified. In this way, the pinching behavior is well reflected in the proposed macro modeling approach by using the EVD ratio, ζ_{eq}.

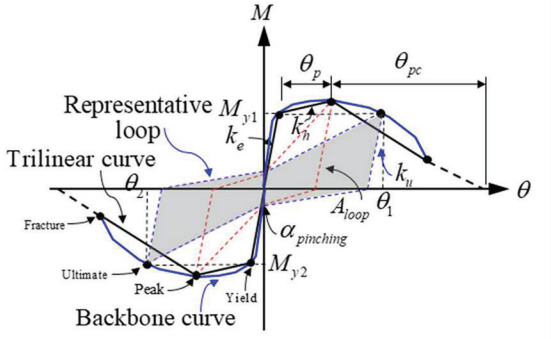
From previous studies,[31-34] a general relationship between the ductility ratio (μ) and EVD ratio (ζ_{eq}) can be obtained. Hwang[35] proposed a statistical EVD-ductility relationship in a semi-empirical manner by analyzing various earthquake-induced ground motions, as follows

$$\zeta_{eq} = \zeta_0 + 1/3\pi\left(\frac{\mu - 1}{\mu}\right)\mu^{0.58} \tag{21}$$

This EVD-ductility relationship is compared in Fig. 12 with the test and analytical results presented in the previous sections. It clearly confirms that the EVD ratio (ζ_{eq}) has a strong correlation with the ductility (μ). Note that the larger RS is, the lower the stiffness is expected. Thus, the ductility inevitably decreases, and it makes the ultimate EVD ratio decreased, as shown in Fig. 12(b). With this relationship, the whole hysteretic behavior can be determined after identifying the four feature points on backbone curve and ultimate ductility ratio. A detailed computational procedure is

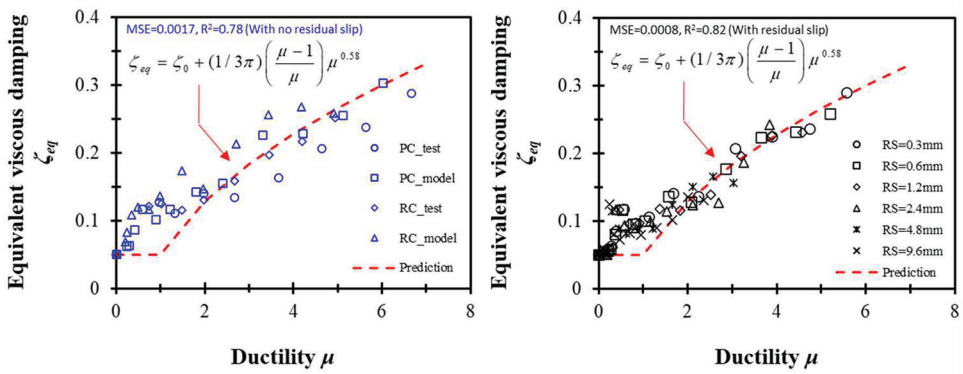


(a) Idealized plastic hinge in macro model



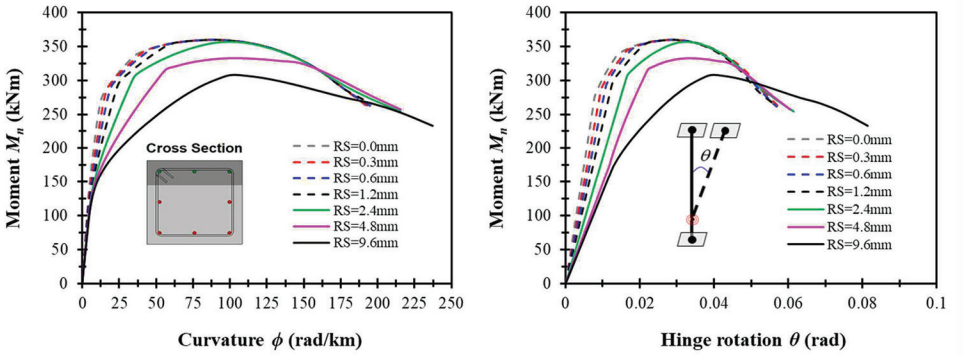
(b) Hysteretic rules

Fig. 11—Macro modeling approach of precast connections.



(a) Results without residual slip (b) Results with residual slip

Fig. 12—EVD ratio of test specimens and analytical results.



(a) Sectional analyses (b) Moment-rotation responses

Fig. 13—Moment-rotation relationships of plastic hinge with various RS. (Note: 1 kN = 0.225 kip; 1 mm = 0.039 in.)

Table 1—Macro modeling parameters

Specimen ID	M_{y1}/M_{y2}, kN·m	M_{p1}/M_{p2}, kN·m	M_{u1}/M_{u2}, kN·m	M_{f1}/M_{f2}, kN·m	k_e, kN·m·rad^{-1}	k_h, kN·m·rad^{-1}	θ_p, rad	θ_{pc}, rad	μ	$\alpha_{pinching}$, kN·m
RS = 0.0	287.7	359.6	287.7	256.3	30,700	3657	0.0197	0.0989	5.59	105
RS = 0.3	287.7	359.6	287.7	256.9	25,996	3867	0.0186	0.1004	4.77	83
RS = 0.6	287.7	359.6	287.7	261.4	23,250	4196	0.0171	0.0999	4.20	66
RS = 1.2	287.7	359.6	287.7	265.8	20,699	4630	0.0155	0.1013	3.68	51
RS = 2.4	285.4	356.7	285.4	254.3	17,058	4463	0.0160	0.0997	3.19	36
RS = 4.8	266.1	332.6	266.1	257.2	15,125	4377	0.0152	0.1223	3.32	37
RS = 9.6	246.7	308.3	246.7	233.4	15,104	2700	0.0228	0.1743	4.71	70

Note: 1 kN = 0.225 kip; 1 mm = 0.039 in.; M_y is yield point; M_p is peak point; M_u is ultimate displacement point; M_u is fracture point; k_e is elastic secant stiffness; k_h is strain hardening stiffness; θ_p is rotation of strain hardening; θ_{pc} is post-peak rotation; μ is ultimate ductility ratio; $\alpha_{pinching}$ is residual strength at which reloading begins.

presented in Appendix D (Fig. D1) to demonstrate how the energy-based macro modeling process can be made.

Figure 13 shows the sectional analysis results and corresponding moment-rotation responses of the column-foundation connections with various levels of RS. Based on these moment-rotation responses and the EVD ratio defined from Eq. (21), the lateral drift and hysteretic responses can be estimated. Some of the key modeling parameters are summarized in Table 1. The nonlinear analyses were conducted on OpenSees platform,[36] where the column was modeled by using force-based beam-column element, and the plastic hinge was modeled through zero-length element for which the ModIMKPinching material model[1] was adopted (refer to Table 1). The macro modeling results are compared with the nonlinear FE analyses in Fig. 14(a) to 14(g). It can be seen that the macro models provided reasonable estimations compared to the nonlinear FE analysis results. In addition, the EVD ratios estimated from the macro models are compared with those estimated from Eq. (21) in Fig. 14(h), where the strong correlations can be still found between EVD ratio and ductility. It indicates that the initial stiffness of the connections decreases as the RS increases. Subsequently, the corresponding ductility inevitably decreases, and it finally triggers the decrease in EVD ratio and cyclic performance of the precast connections.

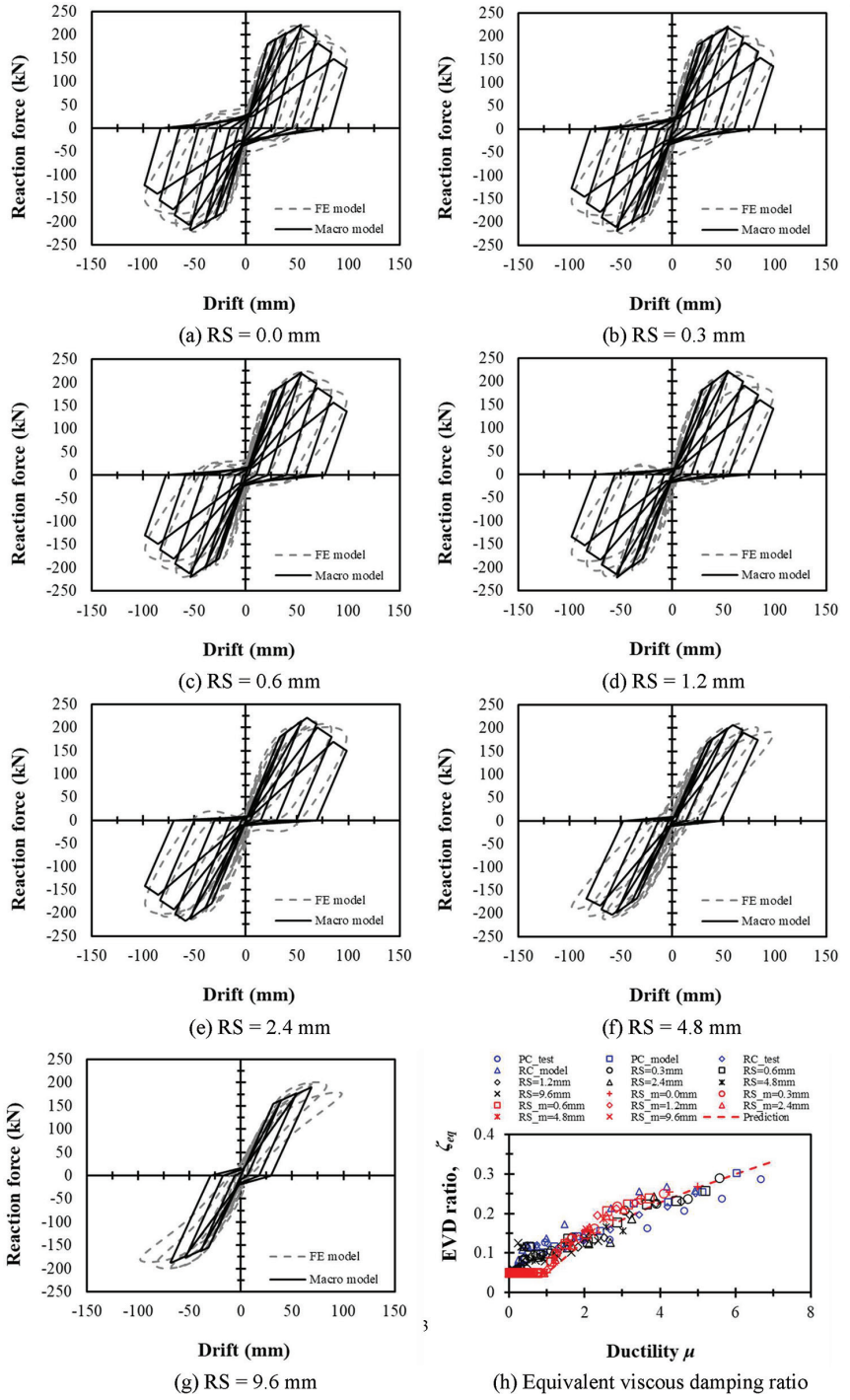


Fig. 14—Comparisons of FE analysis results and macro models. (Note: 1 kN = 0.225 kip; 1 mm = 0.039 in.)

CONCLUSIONS

To identify the effect of residual slip (RS) on the plastic hinge mechanism and corresponding emulative level of precast connections, this study developed a robust nonlinear finite element (FE) analysis method and macro modeling method. The existing test results were used to verify the proposed approaches. On this basis, the following conclusions can be drawn:

1. The continuum plasticity-based damage model of concrete can well reflect the damage evolution and plastic hinge formation in precast connection regions. The two-node connector element with only tensile translational degree of freedom (DOF) developed in this study is very useful to model the rigid mechanical couplers.

2. For lateral responses of precast column (PC)-foundation connection, it appeared that the presence of rigid mechanical couplers can reduce the plastic hinge length, and it is mainly affected by the length of couplers, distance of couplers from foundation, and coupler rigid length factor, which reflects the relative rigidity of couplers to connecting reinforcements.

3. The residual slip of mechanically spliced reinforcement system leads to delayed yielding of connection, which lowers its equivalent tensile stiffness, and consequently reduces the initial lateral stiffness of the PC column-foundation

connections. In addition, the energy dissipation capacity and equivalent viscous damping of the PC connections can be significantly reduced when RS exceeds 0.3 mm (0.01 in).

4. Equivalent viscous damping (EVD) increases with ductility, but the RS reduces the lateral stiffness, and it subsequently reduces the EVD by decreasing the ultimate ductility ratio. Based on the relationship between EVD and ductility, an energy-based macro modeling method was developed to reasonably account for the effects of RS of mechanical couplers in the PC column-foundation connections.

5. Based on the investigation of this study, it is recommended that the mechanical splice should better keep a distance of the base length of plastic hinge (L_p) from the critical section to allow the full development of plastic hinge in a mechanically spliced precast connection. If the mechanical splice is designed immediately next to the critical section, small-size splice devices are recommended to mitigate the detrimental effect of locally higher stiffness. In addition, the RS of mechanical splice should be strictly limited within 0.3 mm (0.01 in.).

AUTHOR BIOS

Wei Zhang *is a Postdoctoral Faculty Fellow in the School of Civil Engineering at Changsha University of Science and Technology, Changsha, China. He recieved his PhD in architectural engineering from Chungbuk National University, Cheongju, Korea. His research interests include shear, flexural, and seismic responses of reinforced concrete structures.*

ACI member **Deuckhang Lee** *is an Associate Professor in the Department of Architectural Engineering at Chungbuk National University. He is a member of Joint ACI-ASCE Subcommittees 445-E, Shear and Torsion – Torsion, and 445-F, Interface Shear. His research interests include shear and torsion in structural concrete, and seismic analysis and design of precast and prestressed concrete structures.*

ACKNOWLEDGMENTS

This work was supported by the National Research Foundation of Korea (NRF) grant funded by the Korea government (MSIT) (No. RS-2023-00209647).

REFERENCES

1. Ibarra, L. F.; Medina, R. A.; and Krawinkler, H., "Hysteretic Models that Incorporate Strength and Stiffness Deterioration," *Earthquake Engineering & Structural Dynamics*, V. 34, No. 12, 2005, pp. 1489-1511. doi: 10.1002/eqe.495

2. Won, D. H.; Han, T.; Kim, S.; Park, W.-S.; and Kang, Y. J., "Transverse Reinforcement for Confinement at Plastic Hinge of Circular Composite Hollow RC Columns," *Computers and Concrete*, V. 17, No. 3, 2016, pp. 387-406. doi: 10.12989/cac.2016.17.3.387

3. Zhang, W.; Lee, D.; Kim, S. H.; Ju, H.; and Lee, C. J., "Seismic Performance of Precast Wide Beam-Column Connections with Asymmetrical Anchorage Reinforcement Details," *Engineering Structures*, V. 275, 2023, p. 115237. doi: 10.1016/j.engstruct.2022.115237

4. Lee, D.; Zhang, W.; Kang, S. M.; and Kang, T. H. K., "Seismic Performance of Precast Shear Wall Systems and Connection Details for Underground Structures," *Journal of Structural Engineering*, V. 149, No. 6, 2023, p. 04023069. doi: 10.1061/JSENDH.STENG-11888

5. Baker, A. L. L., *Ultimate Load Theory Applied to the Design of Reinforced and Prestressed Concrete Frames*, Concrete Publications Ltd., London, UK, 1956.

6. Sawyer, H. A., "Design of Concrete Frames For Two Failure Stages," *Flexural Mechanics of Reinforced Concrete*, SP-12, American Concrete Institute, Farmington Hills, MI, 1965, pp. 405-437.

7. Corley, W. G., "Rotational Capacity of Reinforced Concrete Beams," *Journal of the Structural Division*, V. 92, No. 5, 1966, pp. 121-146. doi: 10.1061/JSDEAG.0001504

8. Mattock, A. H., "Discussion of "Rotational Capacity of Hinging Regions in Reinforced Concrete Beams," *Journal of the Structural Division*, V. 93, No. 2, 1967, pp. 519-522. doi: 10.1061/JSDEAG.0001678

9. Priestley, M. J. N., and Park, R., "Strength and Ductility of Concrete Bridge Columns Under Seismic Loading," *ACI Structural Journal*, V. 84, No. 1, Jan.-Feb. 1987, pp. 61-76.

10. Paulay, T., and Priestley, M. J. N., *Seismic Design of Reinforced Concrete and Masonry Buildings,* John Wiley & Sons, Inc., New York, 1992.

11. Sheikh, S. A., and Khoury, S. S., "Confined Concrete Columns with Stubs," *ACI Structural Journal*, V. 90, No. 4, July-Aug. 1993, pp. 414-431.

12. Coleman, J., and Spacone, E., "Localization Issues in Force-Based Frame Elements," *Journal of Structural Engineering*, ASCE, V. 127, No. 11, 2001, pp. 1257-1265. doi: 10.1061/(ASCE)0733-9445(2001)127:11(1257)

13. Park, R.; Priestley, M. J. N.; and Gill, W. D., "Ductility of Square-Confined Concrete Columns," *Journal of the Structural Division*, V. 108, No. 4, 1982, pp. 929-950. doi: 10.1061/JSDEAG.0005933

14. Panagiotakos, T. B., and Fardis, M. N., "Deformations of Reinforced Concrete Members at Yielding and Ultimate," *ACI Structural Journal*, V. 98, No. 2, Mar.-Apr. 2001, pp. 135-148.

15. Bae, S., and Bayrak, O., "Plastic Hinge Length of Reinforced Concrete Columns," *ACI Structural Journal*, V. 105, No. 3, May-June 2008, pp. 290-300.

16. Berry, M. P.; Lehman, D. E.; and Lowes, L. N., "Lumped-Plasticity Models for Performance Simulation of Bridge Columns," *ACI Structural Journal*, V. 105, No. 3, May-June 2008, pp. 270-279.

17. ACI Committee 318, "Building Code Requirements for Structural Concrete (ACI 318-19) and Commentary (ACI 318R-19) (Reapproved 2022)," American Concrete Institute, Farmington Hills, MI, 2019, 624 pp.

18. ASCE/SEI 7-22, "Minimum Design Loads and Associated Criteria for Buildings and Other Structures," American Society of Civil Engineers, Reston, VA, 2022, 800 pp.

19. Zhang, W.; Lee, D.; Lee, C.; Zhang, X.; and Ikechukwu, O., "Bond Performance of SFRC Considering Random Distributions of Aggregates and Steel Fibers," *Construction and Building Materials*, V. 291, 2021, p. 123304. doi: 10.1016/j.conbuildmat.2021.123304

20. Guan, D.; Chen, Z.; Liu, J.; Lin, Z.; and Guo, Z., "Seismic Performance of Precast Concrete Columns with Prefabricated UHPC Jackets in Plastic Hinge Zone," *Engineering Structures*, V. 245, 2021, p. 112776 doi: 10.1016/j.engstruct.2021.112776

21. Smith, M., *ABAQUS/Standard User's Manual*, Dassault Systems Simulia Corp, Providence, RI, 2009.

22. Ding, M.; Xu, W.; Wang, J.; Chen, Y.; Du, X.; Fang, R.; Huang, X.; and Sun, H., "Plastic Hinge Regions of prefabricated Concrete Columns with Grouted Sleeves and Simplified Calculation Method for Plastic Hinge Length," *Structures*, V. 43, 2022, pp. 710-725. doi: 10.1016/j.istruc.2022.06.081

23. Hung, H. H.; Sung, Y. C.; Lin, K. C.; Jiang, C. R.; and Chang, K. C., "Experimental Study and Numerical Simulation of Precast Segmental Bridge Columns with Semi-Rigid Connections," *Engineering Structures*, V. 136, 2017, pp. 12-25. doi: 10.1016/j.engstruct.2017.01.012

24. Zhang, W.; Lee, D. H.; Lee, W. J.; Kim, M. S.; and Park, J. Y., "Effect of Cast-in-Place Beams on Seismic Performance of Precast Shear Walls," *ACI Structural Journal*, V. 120, No. 1, Jan. 2023, pp. 89-102. doi: 10.14359/51737231

25. Zhang, W.; Lee, D. H.; Ikechukwu, O.; and Okonkwo, M., "Nonlinear Shear Analysis of Corroded Reinforced Concrete Beams Considering Bond Mechanism," *ACI Structural Journal*, V. 118, No. 6, Nov. 2021, pp. 47-61. doi: 10.14359/51732996

26. Tazarv, M., and Saiidi, M. S., "Seismic Design of Bridge Columns Incorporating Mechanical Bar Splices in Plastic Hinge Regions," *Engineering Structures*, V. 124, 2016, pp. 507-520. doi: 10.1016/j.engstruct.2016.06.041

27. Lee, D. H.; Kang, T. H. K.; Ju, H.; Moon, S. W.; and Yang, I. S., "Seismic Performance of Reinforced Concrete Column-Foundation Connections with Combo-Type Mechanical Splices," *ACI Structural Journal*, V. 116, No. 5, Sept. 2019, pp. 173-186. doi: 10.14359/51716766

28. ISO 15835-2, I., "Steels for the Reinforcement of Concrete-Reinforcement Couplers for Mechanical Splices of Bars-Part 2: Test Methods," International Organization for Standardization, Geneva, Switzerland, 2009, 11 pp.

29. KDS 41 1700, "Building Seismic Design: Standard," Architectural Institute of Korea, Seoul, Korea, 2019, 123 pp.

30. JSCE Guidelines for Concrete, "Standard Specifications for Concrete Structures," Japan Society of Civil Engineers, Tokyo, Japan, 2007, 469 pp.

31. Zhang, Q.; Wei, Z. Y.; Gong, J. X.; Yu, P.; and Zhang, Y. Q., "Equivalent Viscous Damping Ratio Model for Flexure Critical Reinforced Concrete Columns," *Advances in Civil Engineering*, V. 2018, 2018, pp. 1-15. doi: 10.1155/2018/4802075

32. Augusto, H.; Castro, J. M.; Rebelo, C.; and da Silva, L. S., "Ductility-Equivalent Viscous Damping Relationships for Beam-to-Column

Partial-Strength Steel Joints," *Journal of Earthquake Engineering*, V. 23, No. 5, 2019, pp. 810-836. doi: 10.1080/13632469.2017.1342290

33. Rodrigues, H.; Varum, H.; Arêde, A.; and Costa, A., "A Comparative Analysis of Energy Dissipation and Equivalent Viscous Damping of RC Columns Subjected to Uniaxial and Biaxial Loading," *Engineering Structures*, V. 35, 2012, pp. 149-164. doi: 10.1016/j.engstruct.2011.11.014

34. Mohebkhah, A., and Tazarv, J., "Equivalent Viscous Damping for Linked Column Steel Frame Structures," *Journal of Constructional Steel Research*, V. 179, 2021, p. 106506. doi: 10.1016/j.jcsr.2020.106506

35. Hwang, J., "Evaluation of Equivalent Linear Analysis Methods of Bridge Isolation," *Journal of Structural Engineering*, ASCE, V. 122, No. 8, 1996, pp. 972-976. doi: 10.1061/(ASCE)0733-9445(1996)122:8(972)

36. McKenna, F.; Fenves, G. L.; and Scott, M. H., *Open System for Earthquake Engineering Simulation*, University of California, Berkeley, Berkeley, CA, 2000.

ACI STRUCTURAL JOURNAL TECHNICAL PAPER

Title No. 121-S75

Uniaxial Compressive Behavior of Fiber-Reinforced Rubberized Recycled Concrete Column

by Md. Shahjalal, Kamrul Islam, Mohammad Tiznobaik, M. Shahria Alam, and Raquib Ahsan

The concrete industry is increasingly adopting the production of environmentally sustainable green concrete. Using recycled coarse aggregate (RCA) produced from demolished concrete infrastructures and waste tire-derived crumb rubber (CR) in the concrete mixture provides a sustainable construction practice and can enhance structural performance. This study investigates the uniaxial compressive behavior of concrete columns composed of RCA, CR, and polypropylene (PP) fiber. A total of 26 columns 150 x 150 x 950 mm in size were tested under uniaxial compression loading. Test parameters included longitudinal reinforcement ratio (0, 1.4, and 2.0%), tie spacing (75 and 150 mm), CR content (0, 5, 10, and 15% of the volume of natural fine aggregate), and percentage of PP fiber (0 and 0.5% of the volume of the total mixture) with 30% RCA replacement (by weight of natural coarse aggregate). The compressive behavior, failure mechanism, influence of longitudinal and transverse reinforcement, dilation, ductility, and toughness were examined. This study demonstrated that incorporating fiber into the concrete made with RCA and CR waste materials improved the axial capacity, resulting in fiber-reinforced rubberized recycled concrete (FRRC) columns with enhanced ductility and toughness. These findings support the development of sustainable concrete for structural columns, justifying their applicability to existing design codes.

Keywords: axial capacity; concentric column; crumb rubber (CR); ductility; failure mode; polypropylene (PP) fiber; recycled coarse aggregate (RCA).

INTRODUCTION

Sustainability is one of the primary concerns in this twenty-first century. Concrete industries and scientific communities are devoting much effort to improving the sustainability of civil engineering structures. Approximately 25 billion tons per year of concrete is produced worldwide, for which nearly 13 billion tons per year of natural aggregates are required.[1] According to Wang et al.,[2] the demand for natural aggregates will be doubled within two or three decades. Another challenge is the use of demolished concrete waste. For example, in Europe and China, the construction and demolished waste (CDW) generation rate is approximately 0.45 and 0.20 billion tons per year, respectively.[3] So far, most of this waste is dumped into landfills. However, part of CDW can be recycled and used in concrete as an aggregate, and these recycling facilities are spreading and becoming available in most parts of the world.[4] Replacing the coarse aggregate up to 30% usually has no detrimental effect on the concrete.[5-11] The use of recycled coarse aggregate (RCA) is approved by ACI Committee 555[12] and CSA A23.1-14/A23.2-14.[13]

According to Grammelis et al.,[14] almost 3 billion tons of tires reach the end of their useful life, and it is anticipated that it will reach nearly 5 billion by 2030. The rubber particles have structural potential. Rubberized concrete (RuC) provides higher ductility[15] and energy absorption capacity[16,17] and enhances resistance to cracking and spalling of concrete.[18,19] However, the inclusion of RCA and crumb rubber (CR) decreases concrete's compressive, tensile, and flexural strengths. Incorporating different fibers into the concrete mixture can mitigate the negative influence of RCA and CR.[3,10] This study will reuse these potential waste materials (RCA and CR) along with fibers in reinforced concrete (RC) columns.

Choi and Yun[5] tested 17 square columns 400 x 400 mm in size with different types, qualities, and quantities of recycled aggregates under compressive loading. It was found that the axial capacity for columns with RCA decreased by almost 6 to 8% compared to the control natural aggregate concrete (NAC) columns. The ductility and crack patterns of the recycled aggregate concrete (RAC) columns were almost identical to those of traditional RC columns. Zhou et al.[20] found that similar to the natural aggregate columns, recycled concrete columns also possessed an obvious elastic stage, crack stage, and fracture stage under eccentric loading. Ajdukiewicz and Kliszczewicz[21] reported that, although the differences in the load-bearing capacity between NAC and RAC columns can be disregarded, the difference in deformability should be contemplated. Breccolotti and Materazzi[22] performed a reliability analysis of RC columns made with RCA and suggested a proper modification of the resistance factor of concrete.

Son et al.[23] tested 12 RuC columns 200 x 300 x 1600 mm in size. A slightly lower axial load-carrying capacity was found compared to the conventional column. However, the curvature ductility increased up to 90%. Besides, RuC columns could undergo lateral deformation over two times more than conventional columns. Hassanli et al.[24] used fiber-reinforced polymer (FRP) wrapping and an expansive agent in RuC columns to increase the strength. The confinement effect of RuC was found to be much higher than NAC due to the incompressible property of rubber, with a Poisson's ratio of approximately 0.5.

ACI Structural Journal, V. 121, No. 5, September 2024.
MS No. S-2023-194.R1, doi: 10.14359/51740860, received February 6, 2024, and reviewed under Institute publication policies. Copyright © 2024, American Concrete Institute. All rights reserved, including the making of copies unless permission is obtained from the copyright proprietors. Pertinent discussion including author's closure, if any, will be published ten months from this journal's date if the discussion is received within four months of the paper's print publication.

Table 1—Properties of materials

Variables	NCA	RCA	NFA	CR	Cement	PP fiber	Reinforcing steel		
							Steel 8 mm Ø	Steel 10 mm Ø	Steel 12 mm Ø
Nominal maximum size, mm	19.0	19.0	4.75	4.75	—	—	—	—	—
Bulk specific gravity (SSD)	2.82	2.59	2.59	1.12	—	—	—	—	—
Bulk specific gravity (OD)	2.81	2.51	2.55	—	2.95	0.91	—	—	—
Absorption capacity, %	0.33	2.97	1.40	1.10	—	—	—	—	—
Fineness modulus	6.73	6.73	2.48	3.12	—	—	—	—	—
Tensile strength f_t, MPa	—	—	—	—	—	480	—	—	—
Elastic modulus E, GPa	—	—	—	—	—	7.0	210	213	227
Yield strength f_y, MPa	—	—	—	—	—	—	441	451	484
Ultimate strength f_u, MPa	—	—	—	—	—	—	553	543	558
Yield strain ε_z, mm/mm	—	—	—	—	—	—	0.00209	0.00211	0.00212

Note: SDD is saturated surface dry; OD is oven dry.

Based on the preceding review, it was found that both the RCA and CR decreased the axial capacity of columns but exhibited superior performance in terms of ductility, dilation, and lateral deformability of columns. The addition of fibers into the concrete mixtures may further enhance the properties of columns containing recycled materials. Limited research has been conducted on the compressive behavior of fiber-reinforced concrete columns.[25] For instance, Raza et al.[25] investigated the behavior of fiber-reinforced (steel fiber and polypropylene [PP] fiber) concrete columns that had glass FRP (GFRP) bars as structural reinforcement. The study focused on enhancing the columns' behavior by introducing fiber content into the concrete mixture. The experimental results revealed that though the GFRP columns showed lower axial capacity (8.68%) than those of fiber-reinforced steel-RC columns, the GFRP columns provided higher ductility (19.71%) than the fiber-reinforced steel-RC columns. However, almost similar failure modes were observed for both types of columns.

The existing literature suggests that most of the past studies investigated the individual effect of RCA, CR, or fiber on the compressive behavior of columns. To the authors' knowledge, no study has been conducted on their combined effect in columns. Thus, this study focuses on the combined effect of RCA, CR, and PP fiber on different compressive behaviors of RC columns under uniaxial compression loading. The main objective of this study is to evaluate the compressive behavior of concrete columns using these potential waste materials (RCA and CR) along with PP fiber.

RESEARCH SIGNIFICANCE

All past studies that investigated the individual effect of RCA, CR, and PP fiber on the compressive behavior of RC columns[5,23,25] or their combined effects were limited to concrete cylinders or beams.[3,10,11,26] This research aims to investigate their combined effect on RC columns' responses. The failure modes of this new type of fiber-reinforced rubberized recycled concrete (FRRC) were examined. The axial capacity, deflection characteristics, dilation ratio, toughness, ductility, and code comparison with ACI 318-19[27] and CSA A23.3:19[28] were also investigated. The RCA and CR were used as potential waste materials to develop sustainable concrete for columns. The findings of this study demonstrate that although RCA and CR decreased the axial capacity of columns, the inclusion of fiber increased it. In addition, the fiber brought about a drastic change in the failure mode. The FRRC columns showed more ductile phenomena with no significant separation of concrete cover. They also provided a higher toughness and ductility value. In summary, this study helps create sustainable concrete for application in structural columns and justifies their applicability to the existing design codes.

EXPERIMENTAL INVESTIGATION

Materials

The concrete mixtures were prepared using natural coarse aggregate (NCA), natural fine aggregate (NFA), CR, portland composite cement (PCC), and PP fiber. The RCA was collected from an old, demolished structure by crushing it into four sizes (19, 12.5, 9.5, and 4.75 mm) using a crusher machine. After that, they were washed three times to dispel the impurities that adhered to their surface. The CR was produced by shredding discarded tires collected from the local market using a shredder machine with a nominal maximum size of 4.75 mm. The PP fiber had a length of 12 mm and was imported from China. The specifications of the PP fiber presented in Table 1 were provided by the company. Mild steel reinforcing bars were selected for both longitudinal and transverse reinforcement. The properties of each material were determined following their respective ASTM International standards and are listed in Table 1.

Concrete mixture proportions

Nine different concrete mixtures were prepared with a design compressive strength of 30 MPa. The overall amount of cement and the water-cement ratio (w/c) remained constant at 456 kg/m^3 and 0.45, respectively. Also, the replacement level for RCA was set at 30% of the NCA's weight. The NFA was replaced with CR in 5, 10, and 15% proportions by volume. In addition, the PP fibers were included in the

Table 2—Concrete mixture designs per cubic meter

Scheme	Batch code	RCA, %	CR, %	PP fiber, %	Coarse aggregate, kg		Fine aggregate, kg		PP fiber, kg	Slump, mm	f_c', MPa		f_t, MPa	E, GPa	f_r, MPa	ν
					NCA	RCA	NFA	CR			28 days	56 days	56 days	56 days	56 days	56 days
NAC	CC	0	0	0	979.6	—	731.4	—	—	165	42.87	47.27	3.46	25.0	5.07	0.22
RAC	RC_0	30	0	0	685.7	293.9	731.4	—	—	150	36.08	41.73	3.29	20.0	5.04	0.24
RRC	RC_5	30	5	0	685.7	293.9	694.8	15.9	—	130	33.83	38.50	3.25	19.8	4.35	0.25
	RC_{10}	30	10	0	685.7	293.9	658.3	31.8	—	90	30.50	35.07	3.05	18.5	4.03	0.27
	RC_{15}	30	15	0	685.7	293.9	621.7	47.7	—	75	24.00	28.33	2.52	12.5	3.92	0.30
FRC	RC_0F	30	0	0.5	685.7	293.9	731.4	—	4.55	85	43.57	48.37	3.69	28.5	6.06	0.20
FRRC	RC_5F	30	5	0.5	685.7	293.9	694.8	15.9	4.55	75	39.60	43.73	3.34	21.7	4.72	0.23
	$RC_{10}F$	30	10	0.5	685.7	293.9	658.3	31.8	4.55	60	33.28	38.48	3.21	19.3	4.68	0.24
	$RC_{15}F$	30	15	0.5	685.7	293.9	621.7	47.7	4.55	50	31.17	35.67	2.94	14.6	4.42	0.27

Note: NAC is natural aggregate concrete/control; RAC is recycled aggregate concrete; RRC is rubberized recycled concrete; FRC is fiber-reinforced recycled concrete; FRRC is fiber-reinforced rubberized recycled concrete; f_c' is compressive strength; f_t is tensile strength; E is modulus of elasticity; f_r is flexural strength; ν is Poisson's ratio.

concrete mixture at 0.5% of the total concrete volume. The mixture proportions of the materials per cubic meter are presented in Table 2.

Design and fabrication of specimens

Twenty-six square columns were fabricated according to ACI 318-19,[27] each with a cross section of 150 x 150 mm and a height of 950 mm. All the columns were scaled down to one-third of their original size due to the capacity and vertical clearance of the testing machine. All the columns were short columns considering the slenderness ratio of 11 (that is, $kl_u/r = 11$), which is less than 22 as per ACI 318-19.[27] The support conditions were considered as both ends fixed. The mixing procedure of CR and PP fiber in the concrete mixture was adopted from the previous works by the authors.[3,10] All the specimens were moist-cured beneath a layer of wet jute fibers for approximately 28 days, a common practice of curing for different structural elements in Bangladesh.

The columns were designed with haunched column heads 250 x 250 x 100 mm in size. This modification to the column end design was made to prevent the possibility of premature failure due to high stress concentration in the column end areas. Eighteen columns were reinforced with a 1.4% longitudinal reinforcement ratio (four reinforcing bars of 10 mm diameter), and four columns were reinforced with a 2.0% longitudinal reinforcement ratio (four reinforcing bars of 12 mm diameter). The columns with longitudinal reinforcement complied with the minimum amount of longitudinal reinforcement (1%) and the maximum tie spacing mandated by ACI 318-19.[27] For these 22 columns, 8 mm diameter steel bars were used as transverse reinforcement. The lowest-size normal-strength reinforcement available in the local market in Bangladesh is an 8 mm deformed steel bar. The remaining four columns were unreinforced (plain concrete) to verify the contribution of concrete to the axial capacity of columns.

Two tie spacings of 75 and 150 mm center-to-center distance were selected. The 150 mm tie spacing corresponds to the smallest lateral dimension, which is required to attain the maximum strength of the concrete core. The other spacing, 75 mm, was selected as the viewpoint of seismic provisions of the Bangladesh National Building Code (BNBC) 2020.[29] According to BNBC 2020, the minimum tie spacing should be one-half of the smallest cross-sectional dimension of the column, which complies with ACI 318-19.[27] A 25 mm spacing was provided at the end zones of the columns to provide additional lateral support to avoid premature failure in these areas. However, at these end zones, there was a chance of sieving fresh concrete with a maximum aggregate size of 19 mm. Thus, extra care was taken during the casting period to ensure the presence of small-size aggregates in these regions. Regarding the concrete cover, a 25 mm cover was maintained from each face of the columns. The detailed test matrix is provided in Table 3, and the reinforcement detailing of columns is presented in Fig. 1(a). Eighty-one concrete cylinders were cast to determine various mechanical properties of concrete, such as compressive strength (f_c'), modulus of elasticity (E), and Poisson's ratio (ν). Moreover, 27 dog-bone-shaped specimens and 27 prism beams were cast to quantify tensile strength (f_t) and flexural strength (f_r), respectively. These properties of concrete are compiled in Table 2.

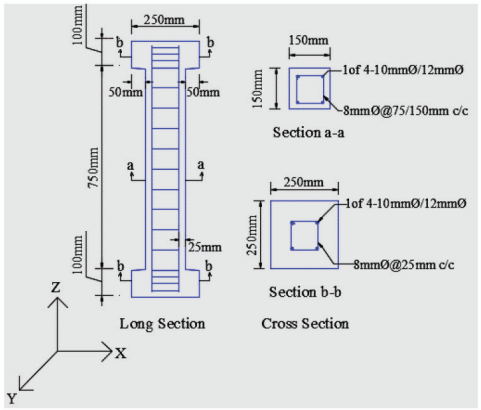
Test setup and procedure

Various mechanical properties of concrete were determined by following their respective ASTM International standards. All column specimens were tested at 56 days under uniaxial loading up to concrete crushing using a 1000 kN capacity universal testing machine (UTM). A displacement-controlled loading rate of 0.1 mm/min was applied during testing. A digital data acquisition system was used to record data during the whole test program. Four linear variable displacement transducers (LVDTs) were used at the midheight of the columns to measure the lateral displacement. The readings for longitudinal/axial and transverse strains of reinforcement and concrete columns were collected using strain gauges. The crack formation and corresponding loads were meticulously recorded. A pair of high-definition video cameras was used to record the failure patterns of column specimens at different loading levels. The total instrumental plan of the test setup is shown in Fig. 1(b).

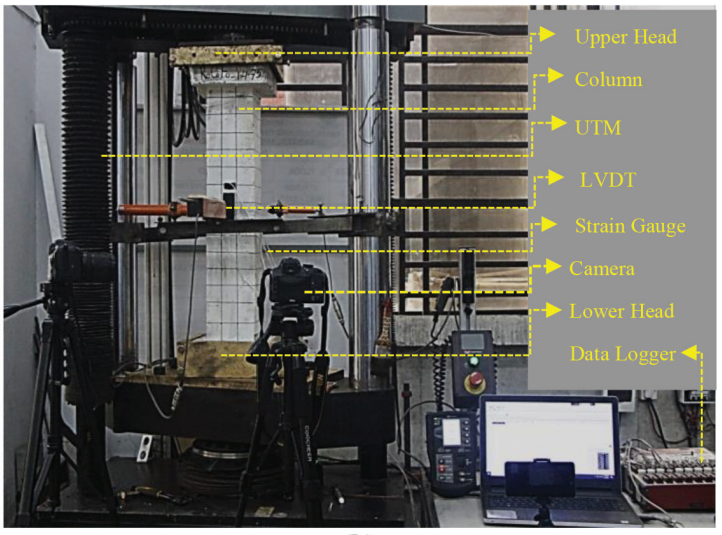
Table 3—Test matrix

SN	Scheme	Column code	Longitudinal reinforcement		Transverse reinforcement
			Detaining	ρ, %	
1	NAC	CC_NR-0	—	—	—
2	RRC	RC_{15}_NR-0			
3	FRC	RC_0F_NR-0			
4	FRRC	$RC_{15}F$_NR-0			
5	NAC	CC_LR-75	4 to 10 mmφ	1.4	8 mmφ@75 mm center-to-center
6	RAC	RC_0_LR-75			
7	RRC	RC_5_LR-75			
8		RC_{10}_LR-75			
9		RC_{15}_LR-75			
10	FRC	RC_0F_LR-75			
11	FRRC	RC_5F_LR-75			
12		$RC_{10}F$_LR-75			
13		$RC_{15}F$_LR-75			
14	NAC	CC_LR-150	4 to 10 mmφ	1.4	8 mmφ@150 mm center-to-center
15	RAC	RC_0_LR-150			
16	RRC	RC_5_LR-150			
17		RC_{10}_LR-150			
18		RC_{15}_LR-150			
19	FRC	RC_0F_LR-150			
20	FRRC	RC_5F_LR-150			
21		$RC_{10}F$_LR-150			
22		$RC_{15}F$_LR-150			
23	NAC	CC_HR-150	4 to 12 mmφ	2.0	8 mmφ@150 mm center-to-center
24	FRRC	RC_5F_HR-150			
25		$RC_{10}F$_HR-150			
26		$RC_{15}F$_HR-150			

Note: RC_XF_NR/LR/HR-Y: R means 30% RCA replacement; C is CR; $_X$ is percentage of CR replacement; F is 0.5% of PP fiber; NR is no longitudinal reinforcement ratio; LR is 1.4% longitudinal reinforcement ratio; HR is 2.0% longitudinal reinforcement ratio; Y is tie spacing; and CC is conventional concrete.



(a)



(b)

Fig. 1—(a) Reinforcement configuration of columns; and (b) test setup.



Fig. 2—Failure mode of different columns. (Note: RC$_X$F_NR/LR/HR-Y: R means 30% RCA replacement; C is CR; $_X$ is percentage of CR replacement; F is 0.5% of PP fiber; NR is no longitudinal reinforcement ratio; LR is 1.4% longitudinal reinforcement ratio; HR is 2.0% longitudinal reinforcement ratio; Y is tie spacing; and CC is conventional concrete.)

EXPERIMENTAL RESULTS AND DISCUSSION

Cracking and failure mode

The post-failure view of different tested columns is represented in Fig. 2. Distinct failure modes were observed based on the inclusion of RCA, CR, fiber, or transverse reinforcement spacing. In general, the failure mechanism of column specimens containing fiber (fiber-reinforced recycled concrete [FRC] and FRRC) progressed as follows: 1) concrete cracking and then yielding of the longitudinal reinforcing bars; 2) minor spalling of concrete cover; and, finally, 3) buckling of the reinforcing bars. On the contrary, the specimens without any fiber (NAC, RAC, and rubberized recycled concrete [RRC]) exhibited the same pattern,

except for a large concrete spalling in the second stage. The concrete core was also damaged significantly.

Figures 2(a) to (i) display the crack pattern of the columns containing 1.4% longitudinal reinforcement with 75 mm tie spacing. In the NAC column (CC_LR-75) and RAC column (RC_0_LR-75), as the axial load increased, cracking initiated at the midheight of the columns and then propagated toward the heads. The concrete cover spalled off after the yielding of the longitudinal reinforcing bars. With the further increase in axial load, the longitudinal reinforcing bars eventually buckled upon failure. For the RRC columns (RC_5_LR-75, RC_{10}_LR-75, and RC_{15}_LR-75), the concrete cover spalling was comparatively lower than the RAC and NAC columns. However, some distinct cracking lines were observed. The propagation of these cracking lines represents the shear failure mode in RRC columns. Furthermore, a higher crack length was visualized. On the contrary, minor concrete cover separation occurred in the FRC (RC_0F_LR-75) and FRRC columns (RC_5F_LR-75, RC_{10}F_LR-75, and RC_{15}F_LR-75). A zigzag failure pattern was observed. The enhancement of bridging capacity due to fiber resisted a well-defined crack width. Besides, the crack length was comparatively lower than that of RRC columns. No distinct shear failure mode was observed.

Figures 2(j) to (r) illustrate the failed specimens of columns containing 1.4% longitudinal reinforcement with 150 mm tie spacing. Upon reaching the peak load, the large tie-spaced (150 mm) NAC, RAC, and RRC columns failed suddenly, accompanied by an explosive noise. Excessive buckling of the steel reinforcing bars was observed. The axial load dropped almost immediately after reaching the peak point, without any prior warning. The column specimens experienced failure in the entire upper half. However, the FRC and FRRC column specimens followed ductile failure mode with minor concrete spalling. The failure modes were nearly identical to the 75 mm-spaced columns. The cracking lines followed a zigzag pattern. Besides, no visible buckling of the longitudinal reinforcement occurred. However, the FRRC column containing a higher percentage of CR (15%) provided a larger crack width than the column containing lower CR content. Thus, the brittle failure of the column with significant concrete spalling can be minimized by incorporating fiber content into the concrete mixture.

The crack patterns of columns with a high longitudinal reinforcement percentage (2.0%) are shown in Fig. 2(s) to (v). Fewer cracks were observed on the surface of the columns compared to the low-reinforcement-percentage (1.4%) columns. From the failure mode of unreinforced plain concrete columns (Fig. 2(w) to (z)), it was observed that the fiber-reinforced plain columns (RC_0F_NR-0 and RC_{15}F_NR-0**)** exhibited gradual damage, while the NAC (CC_NR-0) and RRC columns (RC_{15}_NR-0) provided a brittle failure. The RRC specimen (RC_{15}_NR-0) simply broke into two pieces without giving any prior warning after reaching its peak load. Thus, a shear failure mode was detected in the RRC specimen, whereas the FRC and FRRC specimens exhibited a more ductile phenomenon. A significant difference in the post-peak behavior of FRC and FRRC specimens was observed compared to the RRC specimen, which is evident in the load-deformation responses of plain concrete columns.

Load-deformation responses

The load-deformation curves of different RC columns are taken from the UTM and presented in Fig. 3. The peak load varies depending on the inclusion of RCA, CR, and fiber content, along with the longitudinal reinforcement ratio and tie spacing. The load-deformation curves are divided into three stages. The first stage refers to the behavior up to the peak load. This pattern is almost identical to the plain concrete column, as depicted in Appendix A.* Besides, the behavior of this stage is almost similar for all columns as there is no significant effect of materials/longitudinal reinforcement/transverse reinforcement in this stage. The load-deformation curve of this stage up to the first cracking represents the elastic limit. In this segment, the columns were uncracked. After increasing the load, small hairline cracks were generated, and the columns were gradually entered into the inelastic segment, which extended up to the peak load. In this segment, the steel yielded. The second stage started after reaching the columns at the peak point and finished before the beginning of concrete spalling. The hairline cracks started to form within the concrete cover, culminating in gradual spalling, which reduced the cross-sectional area and subsequently led to a decrease in axial stress. A significant difference was observed in this phase between the columns with and without fiber. The FRC and FRRC columns exhibited a distinct path, whereas this segment was very short for the NAC, RAC, and RRC columns. These columns (NAC, RAC, and RRC) experienced a rapid drop in axial load after reaching their ultimate point. However, increasing the percentage of CR content in FRRC columns increased the length of the second stage, thus exhibiting a more ductile behavior. Moreover, transverse reinforcement played a significant role in this phase. Thus, a notable difference was observed among the load-deformation curves of the columns with 75 and 150 mm tie spacing. This stage was not so distinct for the curves of the columns containing 150 mm tie spacing due to the comparatively lower confinement effect. The confinement effect of transverse reinforcement characterized the third phase. This phase began with the spalling of the concrete cover and ended with the complete failure of the column. In the third stage, the curves associated with the larger tie-spaced columns went straight down after reaching the ultimate point, and the load dropped abruptly, whereas the curves of the lower tie-spaced columns provided a more ductile phenomenon. Regarding materials effect, it was seen that for NAC, RAC, and RRC columns with up to 5% CR content, the curves did not exhibit the second stage and directly entered the third stage by providing the concrete spalling immediately after passing the peak load. On the contrary, in the FRC and FRRC columns, especially those containing higher CR content, the load dropped gradually in the descending portion of the load-deformation curves.

*The Appendix is available at **www.concrete.org/publications** in PDF format, appended to the online version of the published paper. It is also available in hard copy from ACI headquarters for a fee equal to the cost of reproduction plus handling at the time of the request.

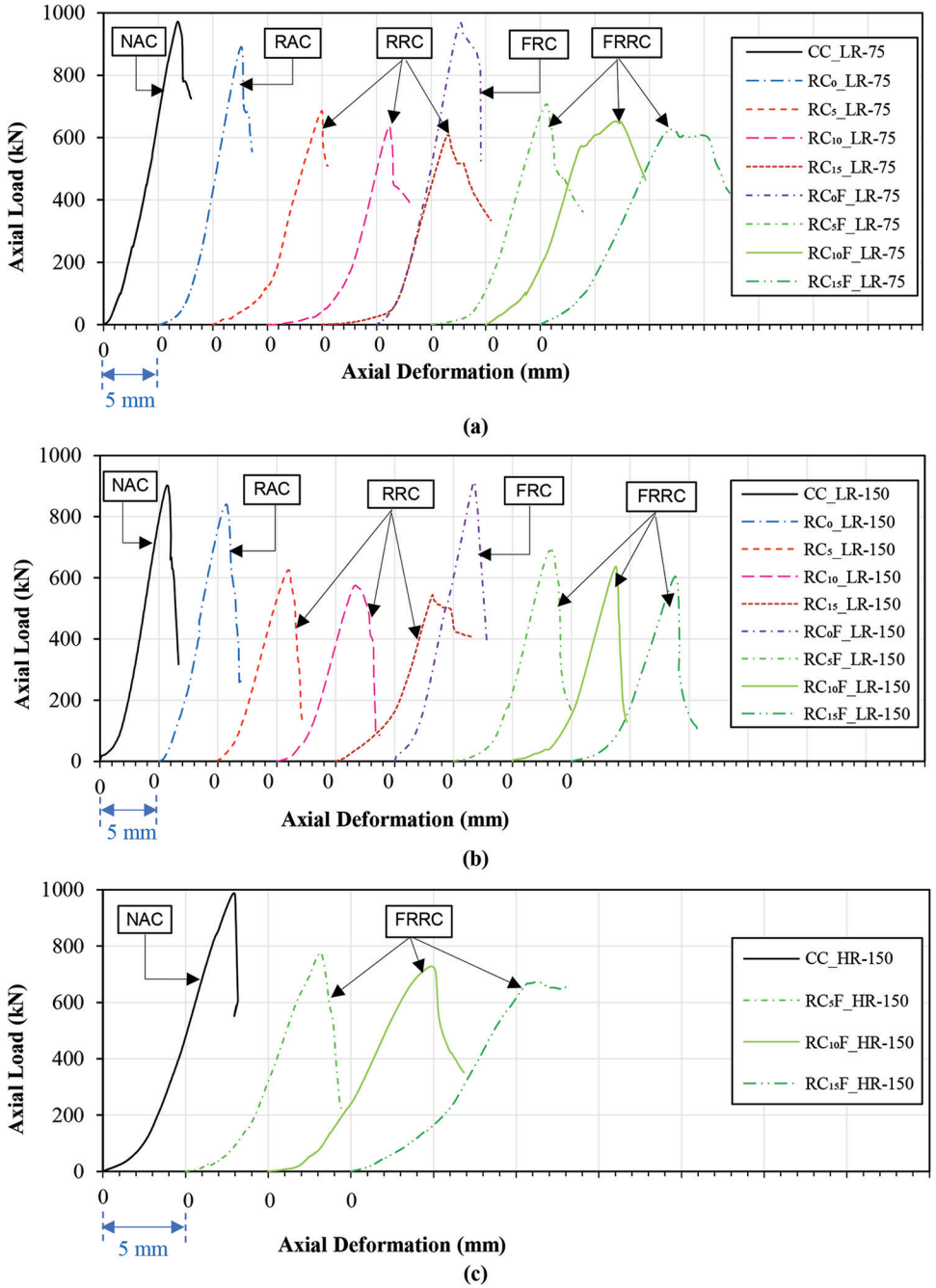


Fig. 3—Load-deformation relationship of RC columns: (a) ρ = 1.4% with 75 mm tie spacing; (b) ρ = 1.4% with 150 mm tie spacing; and (c) ρ = 2.0% with 150 mm tie spacing.

For these columns, distinct second and third stages were observed.

Axial deformation characteristics

Table 4 summarizes the test results of all column specimens. The table shows that the deformation capacity increases with the increasing CR content. For instance, in the columns with a longitudinal reinforcement ratio of 1.4% and tie spacing of 75 mm, the deformations corresponding to the peak load were 7.60, 9.98, 11.19, and 11.56 mm for 0, 5, 10, and 15% CR content, respectively. As rubber is a soft material with a lower elastic modulus, RuC will deform more than conventional concrete. However, including fiber content in the RAC and RRC columns further increased the deformation capacity of columns by 1.1, 6.0, 6.4, and 3.5% compared to the corresponding column with no fiber, respectively. The bridging action of fiber can enhance the deformation capacity of the concrete. The same phenomenon is observed with the ultimate deformation, as shown in Table 4.

As expected, the 150 mm tie-spaced columns exhibited comparatively lower deformation capacity than the 75 mm tie-spaced columns. Regarding RAC and RRC columns, approximately 25, 39.8, 40.3, and 28.8% lower deformation capacity was found, corresponding to the peak load for 150 mm tie-spaced columns compared to the 75 mm tie-spaced columns with 0, 5, 10, and 15% CR content, respectively. This reduction was 12.1% for the FRC column and 20.9, 26.4, and 26.2%, respectively, for the FRRC

Table 4—Test results of uniaxial compression test of different RC column specimens

Scheme	Column code	P_{Peak}, kN	$P_{F\text{-}Crack}$, kN	$P_{\Delta u}$, kN	Δ_{Peak}, mm	$\Delta_{F\text{-}Crack}$, mm	Δ_u, mm	μ	Toughness, kN·mm
NAC	CC_LR-75	971.7	449.1	724.7	6.79	3.95	8.02	1.83	3202
RAC	RC_0_LR-75	891.2	301.7	555.5	7.60	4.34	8.59	1.79	2510
RRC	RC_5_LR-75	685.7	147.7	509.6	9.98	4.90	10.52	2.06	2537
	RC_{10}_LR-75	636.1	51.4	390.8	11.19	5.41	13.03	2.12	2596
	RC_{15}_LR-75	608.1	24.0	334.1	11.56	5.89	15.48	2.21	3529
FRC	RC_0F_LR-75	968.3	384.9	525.8	7.68	4.31	9.55	2.20	3221
FRRC	RC_5F_LR-75	707.2	47.3	361.7	10.58	3.98	13.89	2.80	3364
	RC_{10}F_LR-75	652.1	97.0	464.1	11.91	3.72	14.65	3.66	4741
	RC_{15}F_LR-75	626.4	68.7	422.0	11.97	3.26	17.35	4.90	5535
NAC	CC_LR-150	902.0	416.1	317.2	5.73	3.42	6.66	1.74	2315
RAC	RC_0_LR-150	840.6	404.5	260.4	5.70	3.42	6.93	1.77	2297
RRC	RC_5_LR-150	625.8	306.6	130.2	6.01	3.41	7.18	1.89	2025
	RC_{10}_LR-150	575.1	218.3	85.1	6.68	3.85	8.74	2.02	2144
	RC_{15}_LR-150	545.0	141.2	401.1	8.23	4.63	11.64	2.14	2317
FRC	RC_0F_LR-150	913.9	497.2	385.4	6.75	4.30	7.83	1.82	2690
FRRC	RC_5F_LR-150	688.8	175.4	150.6	8.37	4.49	10.23	2.02	2324
	RC_{10}F_LR-150	636.6	41.5	128.8	8.77	3.19	10.72	2.82	2417
	RC_{15}F_LR-150	604.3	52.0	91.9	8.83	3.06	10.91	2.96	2548
NAC	CC_HR-150	987.5	847.2	588.0	7.93	6.83	8.07	1.17	3073
FRRC	RC_5F_HR-150	776.1	154.7	218.7	8.13	3.82	9.46	2.25	2563
	RC_{10}F_HR-150	727.9	136.9	351.3	9.88	3.8	11.8	2.73	3164
	RC_{15}F_HR-150	671.9	141.2	309.3	11.21	4.55	14.24	3.02	4677

Note: P_{Peak} is peak axial load; $P_{F\text{-}Crack}$ is load corresponding to first crack; $P_{\Delta u}$ is load at failure point; Δ_{Peak} is deformation corresponding to peak axial load; $\Delta_{F\text{-}Crack}$ is deformation corresponding to first crack; Δ_u is deformation corresponding to failure point; μ is ductility.

columns. With a higher tie spacing, the columns cannot resist higher deformation; rather, they reach their peak points or failure points by providing a lower deformation capacity. On the other hand, the increase in the longitudinal reinforcement ratio positively impacts deformation capacity. The deformation capacity corresponding to the peak load of the columns with a 2.0% longitudinal reinforcement ratio increased from 5.73 to 7.93 mm, 8.77 to 9.88 mm, and 8.83 to 11.21 mm for 0, 10, and 15% CR content, respectively, compared to the 1.4% longitudinal reinforcement ratio. However, for 5% CR content, deformation capacity decreased slightly (<3%). Thus, it can be concluded that incorporating CR content can help increase the axial deformation capacity, which can be further improved by adding fiber content.

Axial load-carrying capacity

Table 4 presents the axial load-carrying capacity of different column specimens. Overall, it can be seen that RAC, RRC, and FRRC columns provide lower axial capacity. However, it mostly depends on the percentage of CR content, longitudinal reinforcement ratio, and tie spacing. The capacity decreases with an increase in CR content. For instance, the axial load capacity of the RAC column with a longitudinal reinforcement ratio of 1.4% and 75 mm tie spacing decreased by 8.3%. For RRC columns, it decreased by 29.4, 35.5, and 37.4% for 5, 10, and 15% CR content, respectively. This lower capacity can be attributed to the insufficient adhesion and smooth surfaces of CR particles, which weakens the interfacial transition zone (ITZ),[3] and the hydrophobic nature of CR particles, which increases porosity in concrete.[30] Moreover, due to the presence of two different types of materials at the ITZ (CR is hydrophobic, and cement paste is ionic), they cannot mix effectively.[30] Son et al.[23] also found a decreasing pattern in axial capacity for CR content. However, the inclusion of 0.5% PP fiber in the same mixtures (RC_0F_LR-75, RC_5F_LR-75, RC_{10}F_LR-75, and RC_{15}F_LR-75) slightly increased the axial capacity by 8.7, 3.1, 2.5, and 3.0%, respectively, compared to the corresponding column without fiber. Fiber forms an effective bridge between the aggregate and cement paste and can change the failure mode from brittle to ductile by limiting the crack propagation and improving the aggregate interlock across failure planes.[10] However, though the FRRC columns exhibited higher axial capacity than the RRC columns, the effect of CR was still prominent in FRRC columns, thus demonstrating lower capacity than the control one. Similarly, for the columns with 150 mm tie spacing, the reduction percentages were 6.8% for the RAC column and 30.6, 36.2, and 39.6% for the RRC columns, respectively. The incremental percentages due to fiber content were 8.7% for the FRC column and 10.1, 10.7, and 10.9% for the FRRC columns, respectively, compared to the corresponding

column with no fiber. This is consistent with the compressive testing results of concrete cylinders, as presented in Table 2. One interesting observation is that for the RAC column, the axial capacity with 75 mm tie spacing was 91.7% of that for the 75 mm tie-spaced NAC column and 93.2% for the 150 mm tie spacing. Thus, the reduction percentages of axial capacity due to RCA were very close at both tie spacings, which is expected. Regarding the tie spacing effect, on average, 6.2% lower capacity is obtained with a 150 mm tie-spaced column compared to a 75 mm tie-spaced column because of the lower confinement of concrete. On the other hand, increasing the longitudinal reinforcement ratio from 1.4 to 2.0% increased the axial capacity by 9.5% for the NAC column and by 12.7, 14.3, and 11.2% for FRRC columns, corresponding to 5, 10, and 15% CR content.

Strain in concrete and reinforcement

The midpoint lateral deformations for different surfaces of column specimens and the typical axial load-strain curves are presented in Appendix B. The locations of the strain gauges and the LVDTs are presented in Fig. 1(b). The points on the negative side of the graphs indicate compression, whereas the points on the positive side indicate tension. Regarding lateral deformation, each column experienced either tension or compression on specific faces. In terms of strain, the longitudinal strain gauges were subjected to compressive force, while the transverse strain gauges were subjected to either tensile or compressive force.

Appendix C implies that the steel yields before the concrete crushes. As the strain in the longitudinal reinforcing bar of all columns at peak load is greater than the yield strain of the reinforcing bar, ε_z (presented in Table 1), and less than the concrete strain, it is thus concluded that the steel yields before the concrete crushes. The failure in all specimens resulted from the buckling of the steel reinforcing bars rather than the core concrete crushing. Comparing the longitudinal compressive strain of concrete on two different sides of the columns, it was found that all the tested columns deformed in either the z-x or z-y plane. The pattern of all the curves presented in Appendix B is identical and independent of RCA, CR, PP fiber, longitudinal reinforcement ratio, or tie spacing. As a result, it is evident that the test protocol, specimen preparation, and materials used were all well-controlled.

The lateral deformation capacity and concrete strain increase with the increase in CR content, and they further increase after including PP fibers. On the other hand, increasing the longitudinal reinforcement ratio decreases the lateral deformation capacity. In terms of strains in reinforcing bars, the steel bars in a higher CR content column experienced a higher strain (both longitudinal and transverse) compared to the column containing a lower percentage of CR content. The addition of fibers slightly decreased both the longitudinal strain (3% on average) and transverse strain (10% on average) of the reinforcement, which is shown in Appendix C. As fibers make the concrete stiffer, the fiber-reinforced concrete can withstand higher loads than RuC. Thus, incorporating fibers comparatively increases the concrete's contribution to axial capacity and decreases the load on steel; subsequently, the reinforcement experiences a relatively lower strain.

Contribution of concrete to axial capacity

Table 5 summarizes the steel reinforcing bars and concrete contribution to the axial capacity of different column specimens. The table reports the following results for each column: peak axial load, P_{peak}; the load carried by the reinforcing bars, $P_{S\text{-}peak}$ (calculated by multiplying the cross-sectional area of longitudinal reinforcing bars by the yield strain and modulus of elasticity of the reinforcing bars); the ratio between the load carried by the reinforcing bars and the peak load, $P_{S\text{-}peak}/P_{peak}$; the load carried by the concrete, $P_{C\text{-}peak}$ (calculated as the difference between P_{peak} and $P_{S\text{-}peak}$); the ratio between the load carried by the concrete and the peak load, $P_{C\text{-}peak}/P_{peak}$; and the normalized load carried by the concrete, $P_{C\text{-}peak}/f_c'A_c$.

Table 5 shows that in the control columns and RAC columns with 75 mm tie spacing, the $P_{C\text{-}peak}/f_c'A_c$ value was approximately 0.80, which is close to the value of 0.85 defined in ACI 318-19.[27] However, for RRC, FRC, and FRRC specimens, this ratio varies from 0.55 to 0.77 depending on the percentage of CR and fiber, tie spacing, and longitudinal reinforcement ratio. This indicates the inadequacy of the existing equation of the NAC columns when applied to these new types of concrete. The contribution of concrete to axial capacity ($P_{C\text{-}peak}/P_{peak}$) decreased gradually with an increasing percentage of CR content. Besides, increasing the tie spacing can further decrease the concrete contribution and thus increase the steel contribution to axial capacity. For the RAC and RRC specimens, the concrete contribution varied from 76.8 to 84.1% of the peak load for 75 mm tie-spaced columns and 74.1 to 83.2% for 150 mm tie-spaced columns. However, incorporating the fiber can slightly increase the concrete contribution and decrease the load on steel. For the FRC and FRRC specimens, the concrete contribution varied from 77.4 to 85.4% for 75 mm tie-spaced columns and 76.6 to 84.5% for 150 mm tie-spaced columns.

With increasing the longitudinal reinforcement ratio, the contribution of load carried by concrete decreased, and the steel contribution increased. The load carried by the longitudinal reinforcement fell within the range of 20.5 to 23.4% of the peak load for the FRRC columns containing $\rho = 1.4\%$, whereas for the columns with $\rho = 2.0\%$, it varied from 28.1 to 32.4%. The contribution of concrete to axial capacity is also validated regarding plain concrete columns; the summary of the test results is presented in Appendix D. The variation in concrete contribution, as calculated from strain gauge data and plain concrete data, is lower than 16%.

Volumetric strain (ε_v)

Examining the volumetric response allows the behavior of confined concrete to be understood.[31,32] Volumetric strain ε_v is defined as $\varepsilon_v = \varepsilon_a + 2\varepsilon_l$. Herein, ε_a is the axial strain, and ε_l is the lateral strain of the column. It should be emphasized that a positive volumetric strain signifies the volume expansion of the column, while a negative value indicates contraction. All columns in this study have undergone volume expansion.

Table 5—Summary of concrete and steel contribution to axial capacity of RC columns

Scheme	Column code	P_{peak}, kN	$P_{S\text{-}peak}/P_{peak}$, %	$P_{C\text{-}peak}$, kN	$P_{C\text{-}peak}/P_{peak}$, %	$P_{C\text{-}peak}/f_c'A_c$, %
NAC	CC_LR-75	971.7	14.5	830.5	85.5	79.2
RAC	RC_0_LR-75	891.2	15.9	749.9	84.1	81.0
RRC	RC_5_LR-75	685.7	20.6	544.4	79.4	63.7
	RC_{10}_LR-75	636.1	22.2	494.8	77.8	63.6
	RC_{15}_LR-75	608.1	23.2	466.8	76.8	74.3
FRC	RC_0F_LR-75	968.3	14.6	827.0	85.4	77.1
FRRC	RC_5F_LR-75	707.2	20.0	565.9	80.0	58.3
	RC_{10}F_LR-75	652.1	21.7	510.8	78.3	59.8
	RC_{15}F_LR-75	626.4	22.6	485.1	77.4	61.3
NAC	CC_LR-150	902.0	15.7	760.8	84.3	72.5
RAC	RC_0_LR-150	840.6	16.8	699.4	83.2	75.5
RRC	RC_5_LR-150	625.8	22.6	484.5	77.4	56.7
	RC_{10}_LR-150	575.1	24.6	433.9	75.4	55.8
	RC_{15}_LR-150	545.0	25.9	403.7	74.1	64.2
FRC	RC_0F_LR-150	913.9	15.5	772.6	84.5	72.0
FRRC	RC_5F_LR-150	688.8	20.5	547.5	79.5	56.4
	RC_{10}F_LR-150	636.6	22.2	495.3	77.8	58.0
	RC_{15}F_LR-150	604.3	23.4	463.0	76.6	58.5
NAC	CC_HR-150	987.5	22.1	769.5	77.9	73.8
FRRC	RC_5F_HR-150	776.1	28.1	558.1	71.9	57.9
	RC_{10}F_HR-150	727.9	30.0	509.9	70.0	60.1
	RC_{15}F_HR-150	671.9	32.4	453.9	67.6	57.7

Note: P_{peak} is peak axial load; $P_{S\text{-}peak}$ is load carried by reinforcing bars; $P_{C\text{-}peak}$ is load carried by concrete; f_c' is compressive strength of concrete; A_c is cross-sectional area of concrete.

The volumetric strain, ε_v, of different columns is illustrated in Appendix E. The initial slope of all curves closely aligns with $(1 - 2\nu)\varepsilon_a$, corresponding to the elastic condition.[31,32] Herein, ν is the Poisson's ratio of concrete, which is found from the compression test of concrete cylinders (Table 2), and ε_a is the axial strain of concrete columns, which is found from the strain gauges used in columns.

The volumetric strain curve of plain concrete columns is almost close to the perfectly elastic curve. However, these curves deviate from the perfectly elastic curve for the RC columns. The larger tie-spaced columns show a comparatively higher volumetric strain than the smaller ones. Besides, the curve rapidly reaches the failure point for the columns with larger tie spacing. On the other hand, in the case of smaller tie spacing, the curves are more stable. The lower tie spacing offers a lateral restraint against the cracked concrete core, further delaying the crack development. It was also seen that the volumetric strain of RRC columns is comparatively higher than that of RAC columns. The same case also occurs for FRC and FRRC columns. The columns containing a higher reinforcement ratio provided a lower volumetric strain and a more stable curve than the lower reinforcement ratio.

Ductility (μ)

The displacement ductility is the ratio of the axial deformation of the column under an axial load up to 85% of the peak axial load on the descending portion of the load-deformation curve, that is, $\Delta_{0.85}$ to the axial deformation up to the elastic portion, Δ_y.[5,33] Table 4 presents the ductility values of different columns. Overall, it was observed that the RRC and FRRC columns exhibited comparatively higher ductility than that of the control column. However, the ductility of the RAC columns was almost similar to that of NAC columns. With an increase in the CR content, the ductility value increased, and it further increased after including fiber content in the concrete mixtures. For the RRC columns with a longitudinal reinforcement ratio of 1.4% and a tie spacing of 75 mm, the ductility value increased by 12.3, 15.7, and 20.2% for 5, 10, and 15% CR content, respectively, compared to the control column. After adding 0.5% PP fiber, the ductility value increased by almost 1.52, 1.99, and 2.67 times for 5, 10, and 15% CR content, respectively, compared to that of the control specimen, which is approximately 35.7, 72.2, and 122.3% higher than that of the corresponding RRC specimens. The same trend is also observed for the 150 mm tie-spaced columns. Fiber can withstand load against higher deformation after its yield point because it helps create a strong bridge within the denser concrete matrix on each side of the fracture. Additionally, fiber works as a barrier to

the crack propagation and establishes a strong link between the aggregate and cement paste. Thus, the ductility value increases and alters the failure mode by restricting crack propagation and improving aggregate interlock along the failure planes.

Due to the lower confinement effect of the 150 mm tie-spaced columns, the ductility value slightly decreased (up to 8%) for RRC specimens compared to the 75 mm tie-spaced columns. However, for FRRC specimens, it decreased by up to 39.7%. This lower ductility of larger tie-spaced columns also affects the failure mechanism. The larger tie-spaced columns failed suddenly, providing no significant warning compared to the smaller ones. However, no significant difference was observed in ductility after increasing the longitudinal reinforcement ratio from 1.4 to 2.0%.

Toughness

The toughness value is quantified by summing up the area under the axial load versus the axial deformation curve up to 85% of the peak axial load on the descending portion[34]; this is summarized in Table 4. Overall, it can be seen that the RRC columns exhibit comparatively lower toughness than that of the control specimens. However, adding fiber content to the concrete mixture improves the toughness value. For RRC columns with a longitudinal reinforcement ratio of 1.4% and a tie spacing of 75 mm, the toughness value decreased by 20.8 and 18.9% for 5 and 10% CR content and then increased by 10.2% for 15% CR content compared to the control specimen. From the load-deformation curves (Fig. 3), it is observed that the axial capacity of RRC specimens decreases with increasing CR content, but the deformation capacity increases gradually compared to the control columns. Thus, the area under the load-deformation curve for RRC columns containing up to 10% CR content was lower than the control specimens. However, this area gradually increased with increasing CR content. For 15% CR content, it exhibited a higher toughness value than that of the control one because of the incremental tendency of deformation capacity with an increase in the CR content. After adding 0.5% PP fiber in RAC and RRC mixtures, the toughness value increased almost 1.01, 1.05, 1.48, and 1.73 times for 0, 5, 10, and 15% CR content, respectively, compared to the control specimen, which was approximately 28.3, 32.6, 82.6, and 56.8% higher than that of the corresponding RAC and RRC specimens. The same trend is observed for the 150 mm tie-spaced columns, as presented in Table 4. Comparing the 75 and 150 mm tie-spaced columns, it is observed that the toughness value of the larger tie-spaced columns decreased significantly. The reduction was almost 8.5% for the RAC specimen, and 20.2, 17.4, and 34.4% for the RRC specimens containing 5, 10, and 15% CR content, respectively. For the FRC specimen, it was reduced by 16.5%, and for the FRRC specimens, the reduction percentage was approximately 30.9, 49.0, and 54.0% for 5, 10, and 15% CR content, respectively. On the other hand, an improved toughness value was achieved by increasing the longitudinal reinforcement ratio from 1.4 to 2.0%. For the FRRC columns with $\rho = 2.0\%$, the toughness value increased by approximately 10.3, 30.9, and 83.5% compared to $\rho = 1.4\%$ for 5, 10, and 15% CR content, respectively.

Dilation ratio (λ)

The dilation ratio (λ) is the ratio between the transverse strain (ε_l) and the axial strain (ε_a) of the column under any specific axial load.[5,31] The dilation ratio versus axial strain of different column specimens is presented in Appendix F, and the dilation ratio corresponding to the peak load (λ_p) for different columns is presented in Fig. 4. The dilation ratio for all the RC columns ranges from 0.10 to 0.33 up to the peak load. For plain concrete columns, it varies between 0.10 to 0.30. In most cases, the dilation ratio increases with increasing the axial strain or axial load. Figures 4(a) and (b) show that the λ_p value increases with increasing CR content, which indicates improved deformability and energy absorption capacity. On the contrary, the inclusion of fiber makes the concrete stiff, decreasing the λ_p value. The λ_p value for the 75 mm tie-spaced RAC column containing a 1.4% longitudinal reinforcement ratio was 0.24, and for the RRC columns, this value was 0.26, 0.27, and 0.29 for 5, 10, and 15% CR content, respectively. For the FRC column, this value was 0.23, and for the FRRC columns, these ratios are 0.25, 0.26, and 0.28, respectively. Figure 4(c) illustrates that the λ_p value increases as the tie spacing increases. In contrast, the increase in the longitudinal reinforcement ratio shows the opposite trend. Besides, Fig. 4(d) interprets that the plain concrete columns exhibit a comparatively lower λ_p value than the RC columns.

Code provision for ultimate capacity

Figure 5 depicts that the existing equations can accurately predict the nominal capacity of uniaxially loaded conventional columns and RAC columns but overestimate the capacities of RRC, FRC, and FRRC columns. The equations overestimate by up to 40% depending on the percentage of CR, fiber content, tie spacing, and longitudinal reinforcement ratio. As previously mentioned, the $P_{C\text{-}peak}/f_c'A_c$ value varied from 0.55 to 0.77 for RRC and FRRC specimens, affecting their axial capacity prediction. Thus, the existing equations need to be further modified by incorporating the effect of CR and fiber before using them for RRC and FRRC columns. Two new equations have been proposed in the current study. The equations are formulated based on the conventional axial capacity equation for normal RC columns, which is the sum of concrete and steel contributions. For RRC and FRRC columns, as the effect of incorporating all these materials (RCA, CR, and PP fiber) simultaneously is simply the sum of the individual effects of incorporating each, their individual effect is considered in the equations. CR reduces the axial capacity of concrete, and thus, the last term of the equations is considered negative. In addition, the reduction factor has been changed to incorporate these materials' effects. Equation (1) is for columns without fiber (RRC columns), and Eq. (2) is for columns with fiber (FRRC columns).

Proposed equation for RCA with CR (without fiber)

$$P_0 = 0.72f_c'(A_g - A_s) + f_yA_s - \frac{CR}{0.00020} \quad (1)$$

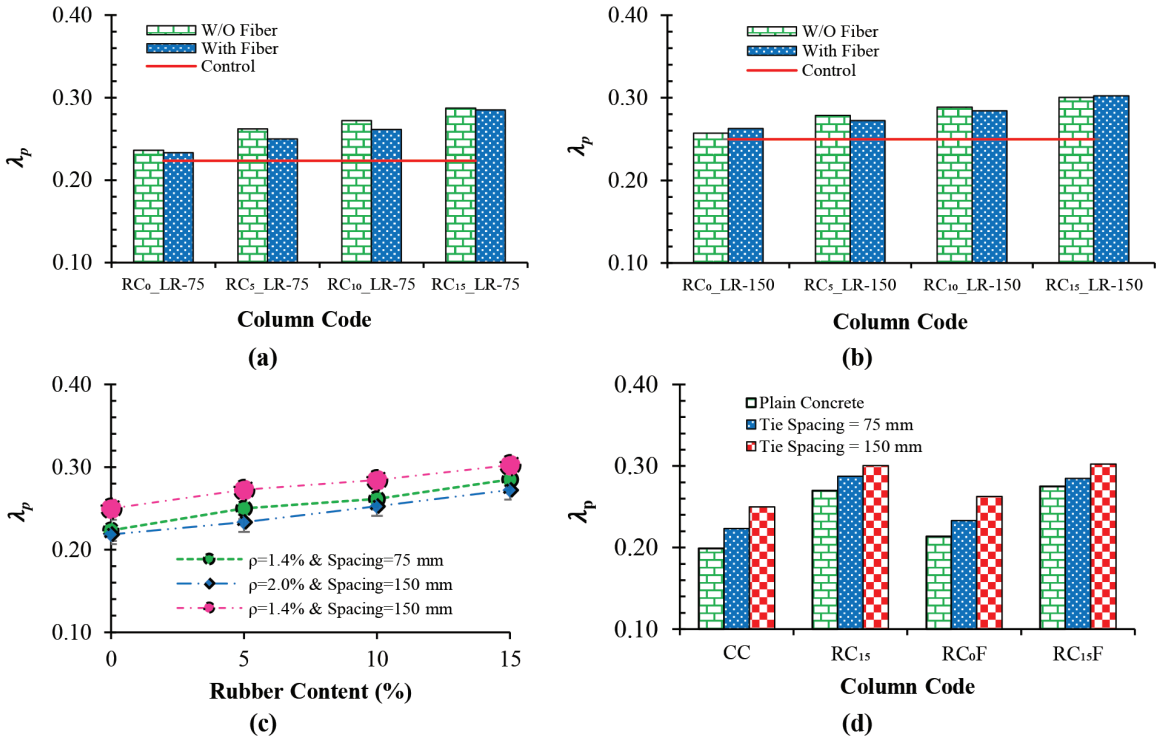


Fig. 4—Variation in dilation ratio corresponding to peak load (λ_p) for different RC columns: (a) ρ = 1.4% with 75 mm tie spacing; (b) ρ = 1.4% with 150 mm tie spacing; (c) comparison of columns with ρ = 1.4% and ρ = 2.0%; and (d) comparison of RC columns with plain concrete column.

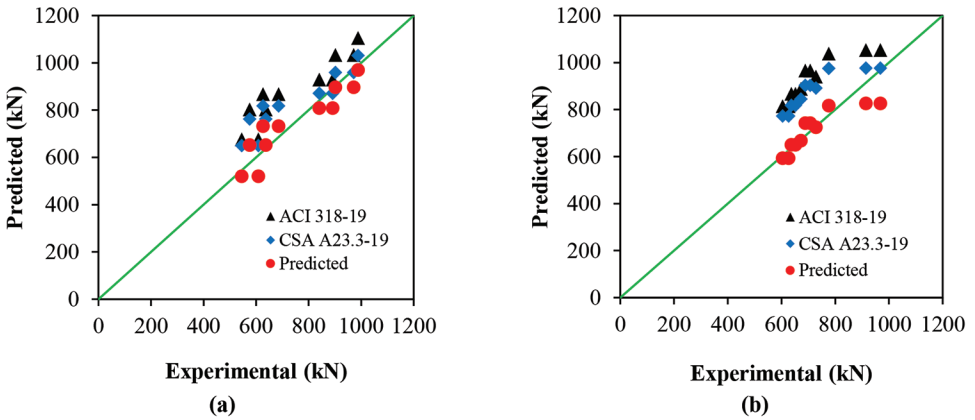


Fig. 5—Comparison of nominal axial loads to experimental loads: (a) without fiber; and (b) with fiber combinations.

Proposed equation for RCA with CR (with fiber)

$$P_0 = 0.64f_c'(A_g - A_s) + f_yA_s - \frac{CR}{0.00028} \quad (2)$$

where P_0 is the nominal peak axial load in N; f_c' is the compressive strength of concrete in MPa; A_g is the gross area of the column in mm^2; A_s is the total area of longitudinal reinforcement in mm^2; f_y is the yield strength of the longitudinal reinforcement in MPa; and CR is the volumetric percentage of crumb rubber. It should be emphasized that the proposed equations are applicable for a range of CR content from 0 to 15% with an RCA and PP fiber of 30% and 0.5%, respectively. Although a limited amount of test data has been used to develop the proposed equations, further research needs to be conducted through experimental and numerical studies to validate the applicability of the proposed equations with a wider range of input variables. Figure 5 shows that the proposed equations can predict the axial capacity of RRC and FRRC columns with good accuracy (<10% variation). The coefficients of determination (R^2) are found to be 0.990 and 0.995, and the coefficients of variation (COV) are 9.33 and 7.11% for the RRC and FRRC columns, respectively.

LIMITATIONS AND FUTURE RESEARCH DIRECTIONS

1. Due to the laboratory constraint and vertical clearance of the testing machine, all the column specimens were constructed considering a length scale factor of one-third. However, large-scale columns varying in reinforcing bar size and strength should be tested in the future.

2. A detailed numerical parametric study should be conducted in the future before regularizing the use of this hybrid concrete.

3. Future research should focus on investigating the seismic behaviors of RRC and FRRC columns through shake-table testing.

4. Because the columns were tested under concentric loading conditions, considering interior columns, their behavior under eccentric loading conditions should also be investigated.

5. Various durability properties of this new hybrid concrete should also be investigated before implementing it in real construction projects.

CONCLUSIONS

The main findings of this study can be stated as follows:

1. For 75 mm tie-spaced natural aggregate concrete (NAC) and recycled aggregate concrete (RAC) columns, extensive concrete spalling occurred, whereas minor spalling occurred in rubberized recycled concrete (RRC) and fiber-reinforced rubberized recycled concrete (FRRC) columns. However, in 150 mm tie-spaced RRC columns, almost half of the entire column was damaged, providing significant concrete crushing with excessive buckling of the reinforcing bars. In contrast, FRRC columns exhibited more ductile phenomena with minor separation of concrete cover. Columns with a higher reinforcement ratio (2.0%) exhibited a higher crack-resisting capacity.

2. The axial deformation corresponding to the peak load increased with increasing crumb rubber (CR) content up to 70 and 76% for 75 mm tie-spaced RRC and FRRC columns compared to the control specimen. For 150 mm tie-spaced columns, it increased by up to 44% and 54%, respectively.

3. The axial capacity decreased after including CR content up to 37.4 and 35.5% for RRC and FRRC columns with 75 mm tie spacing and 39.6 and 33.0% for 150 mm tie-spaced columns. However, FRRC columns exhibited a comparatively higher axial capacity than RRC columns. Besides, increasing the longitudinal reinforcement ratio from 1.4 to 2.0% resulted in an average 10% increase in axial capacity.

4. The reduction factor for RRC and FRRC specimens varied from 0.55 to 0.74 and 0.56 to 0.77, respectively, depending on the percentage of CR, tie spacing, and longitudinal reinforcement ratio, which needs modification.

5. The NAC and RAC columns exhibited almost similar ductility, which increased after including CR and fiber content. Up to 167 and 70% higher ductility was found in 75 and 150 mm tie-spaced FRRC columns, depending on the percentage of CR content. No significant variation in ductility was observed due to changes in the longitudinal reinforcement ratio.

6. The toughness value of RRC columns was reduced with 5 and 10% CR content compared to the control specimen but exhibited an increase with 15% CR content. However, all the FRRC columns exhibited a higher toughness value, increasing up to 73% and 16% for 75 mm and 150 mm tie-spaced columns, respectively, depending on the percentage of CR content.

This study demonstrated that incorporating fiber into the concrete made with recycled coarse aggregate (RCA) and CR waste materials improved the axial capacity, resulting in FRRC columns with enhanced ductility and toughness. These findings support the development of sustainable concrete for structural columns, justifying its applicability to existing design codes.

AUTHOR BIOS

ACI member **Md. Shahjalal** *is a PhD Student in the Department of Civil Engineering at the University of Calgary, Calgary, AB, Canada. He received his BSc from the Military Institute of Science and Technology (MIST), Dhaka, Bangladesh, and his MSc from Bangladesh University of Engineering and Technology (BUET), Dhaka, Bangladesh. He was a Lecturer in the Department of Civil Engineering at MIST. His research interests include concrete materials and analysis, and design and testing of reinforced concrete structures.*

ACI member **Kamrul Islam** *is a Doctoral Candidate in the Department of Civil, Geological and Mining Engineering at Polytechnique Montréal, Montréal, QC, Canada. He received his MSc from the University of Alberta, Edmonton, AB, Canada, in 2012. He is a member of ACI Committee 341, Performance-Based Seismic Design of Concrete Bridges, and Joint ACI-ASCE Committee 343, Concrete Bridge Design. His research interests include earthquake engineering, seismic behavior of structural systems, sustainable construction materials, and biomechanics.*

ACI member **Mohammad Tiznobaik** *is a Lecturer in the School of Engineering at The University of British Columbia (UBC) Okanagan, Kelowna, BC, Canada. He received his master's degree and PhD from the University of Manitoba, Winnipeg, MB, Canada. His research interests include the analysis, design, and testing of reinforced concrete structures; cementitious materials; and the durability of concrete. He received the ACI Wason Medal for Materials Research in 2020.*

ACI member **M. Shahria Alam** *is a Tier-1 Principal's Research Chair in Resilient and Green Infrastructure in the School of Engineering at UBC Okanagan and the Director of the Green Construction Research and Training Centre (GCRTC) at UBC. He received his PhD from the University of Western Ontario, London, ON, Canada. He is Chair of Joint ACI-ASCE Committee 441, Reinforced Concrete Columns, and ACI Subcommittee 341-C, Earthquake Resistant Bridges-Retrofit.*

Raquib Ahsan *is a Professor in the Department of Civil Engineering at BUET. He is the former Director of the BUET-Japan Institute of Disaster Prevention and Urban Safety (BUET-JIDPUS). He received his PhD from The University of Tokyo, Tokyo, Japan.*

ACKNOWLEDGMENTS

The authors would like to convey their sincere thanks and gratitude to the lab technicians of the Concrete Lab and SM Lab of BUET and MIST. Special thanks to the BUET and MIST authorities for giving the financial support.

REFERENCES

1. Mohammed, T. U.; Hasnat, A.; Awal, M. A.; and Bosunia, S. Z., "Recycling of Brick Aggregate Concrete as Coarse Aggregate," *Journal of Materials in Civil Engineering*, ASCE, V. 27, No. 7, July 2015, p. B4014005. doi: 10.1061/(ASCE)MT.1943-5533.0001043

2. Wang, B.; Yan, L.; Fu, Q.; and Kasal, B., "A Comprehensive Review on Recycled Aggregate and Recycled Aggregate Concrete," *Resources, Conservation and Recycling*, V. 171, Aug. 2021, Article No. 105565. doi: 10.1016/j.resconrec.2021.105565

3. Hossain, F. M. Z.; Shahjalal, M.; Islam, K.; Tiznobaik, M.; and Alam, M. S., "Mechanical Properties of Recycled Aggregate Concrete Containing Crumb Rubber and Polypropylene Fiber," *Construction and Building Materials*, V. 225, Nov. 2019, pp. 983-996. doi: 10.1016/j.conbuildmat.2019.07.245

4. AECOM, "Technical Assistance Consultant's Report on People's Republic of China: Construction and Demolition Waste Management and Recycling," AECOM Asia Company Limited, Hong Kong, Apr. 2018, 272 pp.

5. Choi, W.-C., and Yun, H.-D., "Compressive Behavior of Reinforced Concrete Columns with Recycled Aggregate under Uniaxial Loading,"

Engineering Structures, V. 41, Aug. 2012, pp. 285-293. doi: 10.1016/j.engstruct.2012.03.037

6. Alam, M. S.; Slater, E.; and Billah, A. H. M. M., "Green Concrete Made with RCA and FRP Scrap Aggregate: Fresh and Hardened Properties," *Journal of Materials in Civil Engineering*, ASCE, V. 25, No. 12, Dec. 2013, pp. 1783-1794. doi: 10.1061/(ASCE)MT.1943-5533.0000742

7. Huda, S. B., and Alam, M. S., "Mechanical and Freeze-Thaw Durability Properties of Recycled Aggregate Concrete Made with Recycled Coarse Aggregate," *Journal of Materials in Civil Engineering*, ASCE, V. 27, No. 10, Oct. 2015, p. 04015003. doi: 10.1061/(ASCE)MT.1943-5533.0001237

8. Limbachiya, M. C.; Leelawat, T.; and Dhir, R. K., "Use of Recycled Concrete Aggregate in High-Strength Concrete," *Materials and Structures*, V. 33, No. 9, Nov. 2000, pp. 574-580. doi: 10.1007/BF02480538

9. Etxeberria, M.; Vázquez, E.; Marí, A.; and Barra, M., "Influence of Amount of Recycled Coarse Aggregates and Production Process on Properties of Recycled Aggregate Concrete," *Cement and Concrete Research*, V. 37, No. 5, May 2007, pp. 735-742. doi: 10.1016/j.cemconres.2007.02.002

10. Shahjalal, M.; Islam, K.; Rahman, J.; Ahmed, K. S.; Karim, M. R.; and Billah, A. H. M. M., "Flexural Response of Fiber Reinforced Concrete Beams with Waste Tires Rubber and Recycled Aggregate," *Journal of Cleaner Production*, V. 278, Jan. 2021, Article No. 123842. doi: 10.1016/j.jclepro.2020.123842

11. Shahjalal, M.; Islam, K.; Ahmed, T.; and Ahsan, R., "Mechanical Characterization of Fiber-Reinforced Rubberized Recycled Concrete," *Construction and Building Materials*, V. 412, Jan. 2024, Article No. 134799. doi: 10.1016/j.conbuildmat.2023.134799

12. ACI Committee 555, "Removal and Reuse of Hardened Concrete (ACI 555R-01)," American Concrete Institute, Farmington Hills, MI, 2002, 26 pp.

13. CSA A23.1-14/A23.2-14, "Concrete Materials and Methods of Concrete Construction/Test Methods and Standard Practices for Concrete," CSA Group, Toronto, ON, Canada, 2014, 690 pp.

14. Grammelis, P.; Margaritis, N.; Dallas, P.; Rakopoulos, D.; and Mavrias, G., "A Review on Management of End of Life Tires (ELTs) and Alternative Uses of Textile Fibers," *Energies*, V. 14, No. 3, Feb. 2021, Article No. 571. doi: 10.3390/en14030571

15. Ismail, M. K., and Hassan, A. A. A., "Performance of Full-Scale Self-Consolidating Rubberized Concrete Beams in Flexure," *ACI Materials Journal*, V. 113, No. 2, Mar.-Apr. 2016, pp. 207-218. doi: 10.14359/51688640

16. Shahjalal, M.; Islam, K.; Ahmed, K. S.; Tamanna, K.; and Alam, M. S., "Mechanical Characterization of Rubberized Fiber Reinforced Recycled Aggregate Concrete for Bridge Barriers," *Proceedings of IABSE-JSCE Joint Conference on Advances in Bridge Engineering-IV*, A. F. M. S. Amin, Y. Okui, and A. R. Bhuiyan, eds., Dhaka, Bangladesh, Aug. 2020, pp. 379-388.

17. Shahjalal, M.; Hossain, F. M. Z.; Islam, K.; Tiznobaik, M.; and Alam, S., "Experimental Study on the Mechanical Properties of Recycled Aggregate Concrete Using Crumb Rubber and Polypropylene Fiber," *Proceedings of CSCE Annual Conference 2019: Growing with Youth*, Montréal, QC, Canada, June 2019, pp. 2603-2612.

18. Moustafa, A., and ElGawady, M. A., "Dynamic Properties of High Strength Rubberized Concrete," *Eco-Efficient and Sustainable Concrete Incorporating Recycled Post-Consumer and Industrial Byproducts*, SP-314, M. L. Nehdi, ed., American Concrete Institute, Farmington Hills, MI, 2017, pp. 3.1-3.22.

19. Ismail, M. K., and Hassan, A. A. A., "Shear Behaviour of Large-Scale Rubberized Concrete Beams Reinforced with Steel Fibres," *Construction and Building Materials*, V. 140, June 2017, pp. 43-57. doi: 10.1016/j.conbuildmat.2017.02.109

20. Zhou, J. H.; He, H. J.; Meng, X. H.; and Huan, S., "Experimental Study of Recycled Concrete Columns under Large Eccentric Compression," *Earth and Space 2010: Engineering, Science, Construction, and Operations in Challenging Environments*, G. Song and R. B. Malla, eds., Honolulu, HI, Mar. 2010, pp. 531-538.

21. Ajdukiewicz, A. B., and Kliszczewicz, A. T., "Comparative Tests of Beams and Columns Made of Recycled Aggregate Concrete and Natural Aggregate Concrete," *Journal of Advanced Concrete Technology*, V. 5, No. 2, 2007, pp. 259-273. doi: 10.3151/jact.5.259

22. Breccolotti, M., and Materazzi, A. L., "Structural Reliability of Eccentrically-Loaded Sections in RC Columns Made of Recycled Aggregate Concrete," *Engineering Structures*, V. 32, No. 11, Nov. 2010, pp. 3704-3712. doi: 10.1016/j.engstruct.2010.08.015

23. Son, K. S.; Hajirasouliha, I.; and Pilakoutas, K., "Strength and Deformability of Waste Tyre Rubber-Filled Reinforced Concrete Columns," *Construction and Building Materials*, V. 25, No. 1, Jan. 2011, pp. 218-226. doi: 10.1016/j.conbuildmat.2010.06.035

24. Hassanli, R.; Youssf, O.; Vincent, T.; Mills, J. E.; Manalo, A.; and Gravina, R., "Experimental Study on Compressive Behavior of FRP-Confined Expansive Rubberized Concrete," *Journal of Composites for Construction*, ASCE, V. 24, No. 4, Aug. 2020, p. 04020034. doi: 10.1061/(ASCE)CC.1943-5614.0001038

25. Raza, A.; Ali, B.; and Aslam, H. M. U., "Axial Performance of Hybrid Fiber Reinforced Concrete Columns Having GFRP Longitudinal Bars and Spirals," *Journal of Building Engineering*, V. 35, Mar. 2021, Article No. 102017. doi: 10.1016/j.jobe.2020.102017

26. Shahjalal, M.; Islam, K.; Batool, F.; Tiznobaik, M.; Hossain, F. M. Z.; Ahmed, K. S.; Alam, M. S.; and Ahsan, R., "Fiber-Reinforced Recycled Aggregate Concrete with Crumb Rubber: A State-of-the-Art Review," *Construction and Building Materials*, V. 404, Nov. 2023, Article No. 133233. doi: 10.1016/j.conbuildmat.2023.133233

27. ACI Committee 318, "Building Code Requirements for Structural Concrete (ACI 318-19) and Commentary (ACI 318R-19) (Reapproved 2022)," American Concrete Institute, Farmington Hills, MI, 2019, 624 pp.

28. CSA A23.3:19, "Design of Concrete Structures," CSA Group, Toronto, ON, Canada, 2019, 301 pp.

29. BNBC 2020, "Bangladesh National Building Code," Ministry of Housing and Public Works, Dhaka, Bangladesh, 2020, 2464 pp.

30. Xie, J.; Fang, C.; Lu, Z.; Li, Z.; and Li, L., "Effects of the Addition of Silica Fume and Rubber Particles on the Compressive Behaviour of Recycled Aggregate Concrete with Steel Fibres," *Journal of Cleaner Production*, V. 197, Part 1, Oct. 2018, pp. 656-667. doi: 10.1016/j.jclepro.2018.06.237

31. De Luca, A.; Matta, F.; and Nanni, A., "Behavior of Full-Scale Glass Fiber-Reinforced Polymer Reinforced Concrete Columns under Axial Load," *ACI Structural Journal*, V. 107, No. 5, Sept.-Oct. 2010, pp. 589-596.

32. Tobbi, H.; Farghaly, A. S.; and Benmokrane, B., "Concrete Columns Reinforced Longitudinally and Transversally with Glass Fiber-Reinforced Polymer Bars," *ACI Structural Journal*, V. 109, No. 4, July-Aug. 2012, pp. 551-558.

33. Pessiki, S., and Pieroni, A., "Axial Load Behavior of Large-Scale Spirally-Reinforced High-Strength Concrete Columns," *ACI Structural Journal*, V. 94, No. 3, May-June 1997, pp. 304-313.

34. Zhao, J.; Xu, P.; and Fan, C., "An Investigation of the Toughness and Compressive Toughness Index of Steel Fiber Reinforced Concrete," *Journal of Building Structures*, V. 12, No. 4, 1991, pp. 44-51.

ACI STRUCTURAL JOURNAL TECHNICAL PAPER

Title No. 121-S76

Tensile Behavior of Small Screw Anchors under Cyclic Crack Openings

by Chandani Chandra Neupane, Jessey Lee, Tilak Pokharel, Hing-Ho Tsang, and Emad Gad

Small-sized anchors (typically 6 mm [0.24 in.]) are commonly used for nonstructural applications. There has been increasing demand for seismic performance of fastenings for nonstructural applications; however, there have been no 6 mm (0.24 in.) size screw anchors with seismic prequalification for large crack width. This study investigated the feasibility of small-sized screw anchors to perform under tension loading in crack widths of up to 0.8 mm (0.03 in.). Tension tests were conducted in cracked concrete with varying crack widths (0.3, 0.5, and 0.8 mm [0.01, 0.02, and 0.03 in.]) under monotonic, pulsating, and varying crack width load protocol. Based on the findings of this study, 6 mm (0.24 in.) screw anchors exhibited load drop and slip behavior in large crack width during the residual capacity test, even for anchors with a deeper embedment. Finite element analysis was conducted to investigate the feasibility of a larger-sized thread width to perform in 0.8 mm (0.03 in.) crack width.

Keywords: anchorage in concrete; experimental study; finite element analysis; nonstructural application; screw anchors; seismic performance.

INTRODUCTION

ACI 355.2,[1] ACI 355.4,[2] EOTA EAD 330232-01-0601,[3] and EOTA EAD 330499-01-0601[4] detail the prequalification requirements of fasteners under seismic actions. Australia has also recently introduced seismic prequalification and design requirements in AS 5216:2021,[5] which are consistent with requirements in the European Assessment Documents (EADs).[3,4]

There are two seismic performance categories of fasteners—namely, C1 and C2 in EADs[3,4]—with C2 prequalification requirements being more stringent than C1. For both the C1 and C2 seismic performance categories, prequalification of fasteners in cracked concrete is required. A fastener that has C2 prequalification automatically satisfies the requirement for C1 prequalification. The C1 performance category requires tests in a static crack with a crack width (Δw) of 0.5 mm (0.02 in.), whereas the C2 performance category requires tests in both static and dynamic cracks with a maximum Δw up to 0.8 mm (0.03 in.). The prequalification requirements in ACI 355.2[1] and ACI 355.4[2] are equivalent to the C1 seismic performance category, whereas another seismic performance category (ASPC 2), which is similar to C2 in Europe, is approved by the International Code Council Evaluation Service (ICC-ES) in its acceptance criteria (AC510) in the United States.[6]

In Europe, fasteners prequalified for seismic applications require a European Technical Assessment (ETA) with approval for the C1 or C2 seismic performance category, depending on the intended application. The requirements for fastenings with C1 or C2 performance categories are assigned depending on the seismicity level of a region and site amplification (according to EN 1992-4:2018[7] in Europe, AS 5216:2021[5] in Australia, and ACI 318-19[8] in the United States). The C2 seismic performance category is typically required for high seismic hazard zones or buildings of higher importance levels such as hospitals. In EN 1992-4,[7] there is a further distinction for seismic performance requirements for fasteners based on their application in nonstructural or structural connection (particularly for importance classes II and III, and in low seismic hazard zones). However, such distinction is not provided in AS 5216[5] and the seismic requirement for fastenings is the same, irrespective of the fastener's application in nonstructural or structural fixing. Further, both EN 1992-4 and AS 5216 require C2 performance category for nonstructural applications, for high-importance class buildings (importance level IV/4). The motivation of this study is driven by the introduction of AS 5216:2021[5] in Australia, where nonstructural applications in buildings with higher importance class and/or higher seismicity will require a C2. Before the introduction of AS 5216:2021, for example, the Royal Adelaide Hospital in Australia used the C1 prequalified 6 mm (0.24 in.) screw anchors,[9] which will not be qualified under the new requirements.

Small-sized fastenings (typically 6 mm [0.24 in.]) are usually used for supporting cable trays, air-conditioning ducts, pipes, and so on. Such fasteners are typically prequalified for static and quasi-static loading only. A single building may require the installation of a large number of fasteners. For example, the Royal Adelaide Hospital uses over 60,000 numbers of 6 mm (0.24 in.) screw anchors for nonstructural applications.[9] At present, 8 mm (0.31 in.) and larger-sized fasteners from different manufacturers are prequalified for C2 requirements. However, using larger-sized screw anchors would lead to a higher cost and additional installation time. The seismic prequalification of redundant fasteners is not yet covered by AS 5216[5] and EN 1992-4.[7]

In an earlier study, Hoehler and Eligehausen[10] considered uniform amplitude crack cycles (n = 10) with a crack width of 0.8 mm (0.03 in.) to take into account crack opening and closing due to moment reversal during seismic events. The authors conducted experimental investigation with headed studs and different types of post-installed anchors including screw anchors (diameter = 20 mm [0.79 in.]) in the test

ACI Structural Journal, V. 121, No. 5, September 2024.
MS No. S-2023-234.R1, doi: 10.14359/51740862, received February 27, 2024, and reviewed under Institute publication policies. Copyright © 2024, American Concrete Institute. All rights reserved, including the making of copies unless permission is obtained from the copyright proprietors. Pertinent discussion including author's closure, if any, will be published ten months from this journal's date if the discussion is received within four months of the paper's print publication.

member with four crack planes. In another study, Hoehler and Eligehausen[11] investigated the behavior of anchors under tension cycling at near ultimate loads considering the effects of cycling frequency and cycling pattern. The study by Hoehler and Eligehausen[11] recommended restricting single cycling frequency and stepwise increasing load cycling pattern. A maximum target crack width of 0.8 mm (0.03 in.) was considered in the study, where the authors tested expansion anchors together with 12 mm (0.47 in.) diameter screw anchors. To realistically evaluate the seismic performance of different post-installed anchors, Mahrenholtz et al.[12] considered stepwise increasing load cycles (n = 36) and Mahrenholtz et al.[13] used stepwise increasing cyclic crack (n = 32 and 41) protocols in seismic testing. Concrete test members with a single crack plane were used for crack cycling tests,[13] whereas comparatively, large wedge split slabs with multiple crack planes were used for reference tests and load cyclic tests.[10,12,13] Maximum target crack widths of 0.5 and 0.8 mm (0.02 and 0.03 in.) were considered in their studies. Screw anchors were not considered for load cyclic tension tests in Mahrenholtz et al.,[12] whereas screw anchors with a diameter of 16 mm (0.63 in.) were tested in crack cyclic tests in Mahrenholtz et al.[13] The technical background of the development of the forward ordered stepwise increasing load cycles (n = 75) and crack cycles (n = 59) protocol for the C2 performance category of simulated seismic tests in the current European guideline is discussed in Mahrenholtz et al.[14] These unified protocols consider two performance levels—namely, serviceability and suitability levels—by evaluating anchor behavior in moderate crack width (Δw = 0.5 mm [0.02 in.]) and maximum considered crack width (Δw = 0.8 mm [0.03 in.]), respectively. All screw anchors tested in these studies[10,11,13] performed well under seismic conditions and exhibited pullout or combined concrete cone and pullout failure mode.

There are a few studies[10,11,13] that evaluated the seismic performance of fasteners including screw anchors, but they did not cover the seismic performance of small-sized (6 mm [0.24 in.]) screw anchors. Currently, some of these small concrete screw anchors from different manufacturers are prequalified for C1 seismic performance category. To date, there has been no reported research on the performance of small screw anchors in large crack widths.

Driven by a clear need to identify seismic performance for small-sized fastenings in nonstructural applications due to speed of installation and economic considerations, this research conducted an experimental investigation of small screw anchors in 0.8 mm (0.03 in.) crack width as required by C2 seismic performance category. There are different types of post-installed anchors; however, this study only investigates the performance of concrete screw anchors as they are commonly used for nonstructural applications, and they have better performance under seismic loadings compared to other types of nonstructural fastenings such as direct actuated fasteners and drop-in anchors. A total of 19 anchor tests were conducted to verify the results obtained from the developed test setup. Additionally, 23 anchor tests were conducted in 0.8 mm (0.03 in.) crack width for small screw anchors. The test results were evaluated in terms of sustained loads and crack cycles, failure mode, load-displacement behavior, ultimate failure load, and displacement. Further, the relationship of screw thread profiles and crack width size is discussed in this paper. Finally, finite element analyses were conducted to simulate the screw anchor behavior.

RESEARCH SIGNIFICANCE

This research addresses the open question of the performance of small-sized anchors that are widely used in nonstructural applications in large crack width conditions (in particular, 0.8 mm [0.03 in.] crack width as required in C2 seismic prequalification), which is a design requirement for sites with higher seismicity and buildings with higher-importance class. The significance of the study entails the limitations of small screw anchors under cyclic loading and crack cycling. Further investigations into the thread size of screw anchors were conducted for better performance in large crack widths, which may help to develop new anchor products.

EXPERIMENTAL INVESTIGATION

The experimental investigation in this study consists of two test series. The first test series was conducted to validate the seismic test setup (the first of its kind in Australia). Once the test result from the first series of tests was validated against published data, the second test series was conducted to investigate the performance of small-sized (6 mm [0.24 in.]) screw anchors in 0.8 mm (0.03 in.) crack width considering the requirements for C2.

Screw anchors and concrete test members

Figure 1 shows all the screw anchors tested in this experimental study. For the first test series, 12 mm (0.47 in.) concrete screws (refer Fig. 1) with C1 and C2 seismic prequalification, with nominal depth (h_{nom}) of 100 mm (3.94 in.) were tested. For the second test series, 6 mm (0.24 in.) concrete screws (S1 and S2; refer to Fig. 1) from

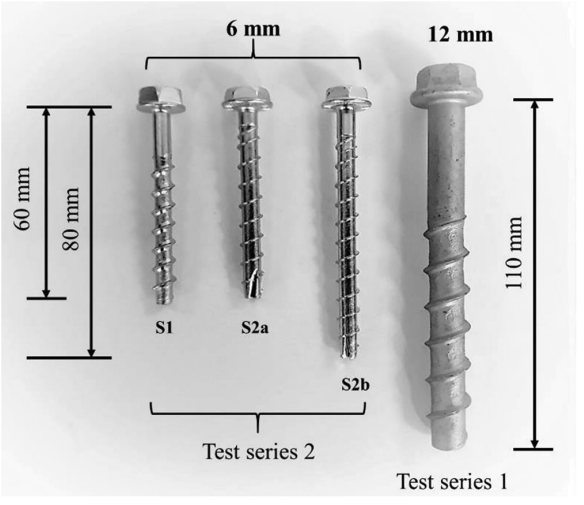


Fig. 1—Screw anchors tested in this study. 12 mm (0.47 in.) screw anchor was used for test series 1 and 6 mm (0.24 in.) screw anchors from two manufacturers (S1 and S2) with different embedment depths (a and b) were used for test series 2. (Note: 1 mm = 0.0394 in.)

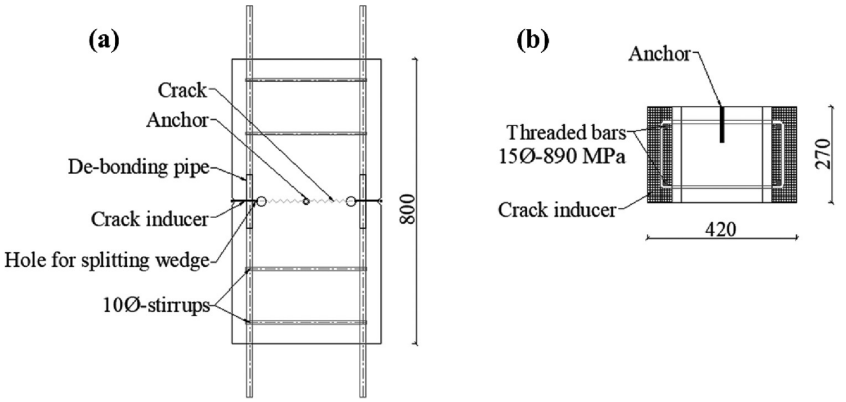


Fig. 2—Concrete test member: (a) top view; and (b) cross-sectional view at midsection. (Note: Dimensions in mm; 1 mm = 0.0394 in.)

two different manufacturers were considered. Screw anchors with comparable properties (embedment depth, size) and prequalification were selected. Both types of 6 mm (0.24 in.) screw anchors investigated in this study are prequalified for the C1 performance category in accordance with EAD 330232-01-0601.[3] Additional tests were carried out considering deeper embedment (S2b; refer Fig. 1). Installation was conducted as per instructions in product prequalification documents. The thread size and profile may differ from manufacturer to manufacturer for same-sized screw anchors and is discussed later in this paper.

A concrete test member was designed to allow the formation and control of crack as per the requirements of EAD 330232-01-0601.[3] The total gross cross-section area (A_g) of the member was 0.1134 m^2 (175.77 in.^{2}) ($B \times H$ = 420 mm × 270 mm [16.5 in. × 10.6 in.]) and the longitudinal reinforcement ratio (ρ) was 0.0062. Figure 2 shows the concrete test member used for testing. Four 15 mm (0.59 in.) diameter threaded bars[15] with a steel grade of 890/1080 were used as longitudinal reinforcement. The threaded bars were connected to fixing plates using nuts with matching threads. Two stirrups were used on each side of the member. External conduits (outside diameter 25 mm [0.98 in.]) were used to position splitting wedges. Plastic pipes of inner diameter 19 mm (0.75 in.) were used to debond concrete and reinforcing bar in 75 mm (2.95 in.) length on each side from the middle of the member (expected crack plane). To help and guide crack formation at the middle of the member throughout the plane, 2 mm (0.08 in.) thick steel plates were used as a crack inducer (Fig. 2(b)).

Concrete with a design characteristic compressive strength of 25 MPa (3625 psi) was used. Concrete test members were cast in three batches and stored in a lab until the time of testing. Test members with the same dimensions and details were used in reference tests and all other seismic tests—including crack cycling tests to avoid the influence of concrete test members on the performance of fasteners. A fastener was tested on both sides of the concrete test member because the depth of the test member is large enough (that is, depth of test member/2 > 1.5h_{ef}) except for crack cycling tests. The concrete member was significantly damaged after the crack cycling test and thus the test could not be conducted on the other side of the member. Concrete cylinders of 100 x 200 mm (3.94 x 7.87 in.) (diameter x height) were cast together with the concrete test members and tested to obtain compressive strength during anchor tests in accordance with AS 1012.9.[16] The mean concrete compressive strength was 31.5 MPa (4568 psi) in C1 and 28.8 MPa (4177 psi) in C2 tests for 12 mm (0.47 in.) screw anchor and 29.0 MPa (4206 psi) for 6 mm (0.24 in.) screw anchor tests in this study.

Test requirements, setup, and procedure

Testing conditions, requirements, assessment criteria, and loading history as per EAD 330232-01-0601[3] were used for the performance evaluation of fasteners under tension loading considering C1 and C2 seismic performance categories. Table 1 shows the key requirements for tensile tests with the assessment criteria for seismic prequalification of post-installed anchors. The loading histories for C1 and C2 tension tests are presented in Fig. 3. Criteria for C1 assessment include completion of cycling history and ultimate capacity requirements, while the C2 assessment evaluates in terms of load-displacement characteristics, displacement limits, coefficient of variation (cv) in capacity, and displacement in addition to the completion of cycling history with the ultimate capacity requirement. In a single test, more than a 5% temporary drop in load and/or greater than 10% displacement slip at peak load is not acceptable for the C2 seismic performance category before 70% of peak load. The scatter of displacement at 50% of ultimate load with cv more than 40% is not acceptable for the C2 performance category in residual capacity tests (without considering displacement occurred during the cycling phase). Similarly, the scatter of ultimate capacity with a cv of more than 30% is not acceptable for the C2 performance category.

Only a single anchor was tested in a crack plane for all the tension tests. Test members from the same batch of concrete casting were used for the reference tests and the corresponding tension tests, which reduced the normalization of test results when calculating the loading requirement.

A hairline crack was generated in the test specimen by hammering splitting wedges into sleeves before the test specimen was placed in the rig developed. Both splitting wedges were hammered at the same time to help the formation of consistent crack in a single crack plane. Then, the test

Table 1—Tension tests key requirements, conditions, and assessment criteria for seismic prequalification of post-installed fasteners as per EAD 330232-01-0601

Seismic performance category	Test ID[a]	Tension tests	Concrete strength	Crack width, mm (Δw)[b]	Load[c]	Key assessment criteria			
						Load capacity[d]	Load reduction factor α[e]	Scatter[f]	Reduction factor for scatter, β[g]
C1	C1.1	PT	C20/25	0.5	$N_{eq} = 0.5N_{u,m}$	$N_{u,m,C1} \geq 160\%N_{eq}$	$\alpha_{N,C1} = N_{eq,req}/N_{eq}$ $\alpha_{N,C1}{}^{\delta} = N_{u,m,C1}/160\%N_{eq}$	—	—
C2	C2.1a	RT	C20/25	0.8	—	$N_{u,m,C2.1a} \geq 0.8N_{u,m}{}^{*}$	$\alpha_{C2.1a} = N_{u,m,C2.1a}/0.8N_{u,m}{}^{*}$	$CV(\delta(0.5N_{u,m,C2.1a}) \leq 40\%$ $CV(N_u) \leq 30\%$	$\beta_{CV,C2.1a} = 1/(1 + (CV(N_{u,m,c2.1a})\text{-}20) \times 0.03)$
	C2.1b		C50/60			$N_{u,m,C2.1b} \geq 0.8N_{u,m}{}^{\#}$	$\alpha_{C2.1b} = N_{u,m,C2.1b}/0.8N_{u,m}{}^{\#}$	$CV(\delta(0.5N_{u,m,C2.1b}) \leq 40\%$ $CV(N_u) \leq 30\%$	$\beta_{CV,C2.1b} = 1/(1 + (CV(N_{u,m,c2.1b})\text{-}20) \times 0.03)$
	C2.3	PT	C20/25	$0.5\ (\leq 0.5\ N/N_{max})$ $0.8\ (> 0.5N/N_{max})$	$N_{max} = 0.75N_{u,m,C2.1a}$	$N_{u,m,C2.3} \geq 0.9N_{u,m,C2.1a}$	$\alpha_{C2.3a} = N_{max,req,1}/N_{max}$ $\alpha_{C2.3b} = N_{max,req,2}/N_{max}$ $\alpha_{C2.3c} = N_{u,m,C2.3}/0.9N_{u,m,C2.1a}$	$CV(\delta(0.5N_{u,m,C2.3}) \leq 40\%$ $CV(N_u) \leq 30\%$	$\beta_{CV,C2.3} = 1/(1 + (CV(N_{u,m,c2.3})\text{-}20) \times 0.03)$
	C2.5	CT	C20/25	$0.1 \leq \Delta w \leq 0.5$ (N_{w1}) $0.6 \leq \Delta w \leq 0.8$ (N_{w2})	$N_{w1} = 0.4N_{u,m,C2.1a}$ $N_{w2} = 0.5N_{u,m,C2.1a}$	$N_{u,m,C2.5} \geq 0.9N_{u,m,C2.1a}$	$\alpha_{C2.5a} = N_{w2,req,1}/N_{w2}$ $\alpha_{C2.5b} = N_{w2,req,2}/N_{w2}$ $\alpha_{C2.5c} = N_{u,m,C2.5}/0.9N_{u,m,C2.1a}$	$CV(\delta(0.5N_{u,m,C2.5}) \leq 40\%$ $CV(N_u) \leq 30\%$	$\beta_{CV,C2.5} = 1/(1 + (CV(N_{u,m,c2.5})\text{-}20) \times 0.03)$

[a]Test series number as per EAD 330232-01-0601.

[b]Increase in crack width after initial hairline crack.

[c]Maximum or constant fastener load, normalization required if concrete strength is different than reference tests.

[d]Ultimate load capacity, if condition is fulfilled reduction factor $\alpha = 1$.

[e]Reduction factor to consider cyclic load reduction to avoid fastener failure during cycles (α_{C1}, $\alpha_{C2.3a}$, and $\alpha_{C2.5a}$), to meet maximum service level displacement limit of $\delta_m(0.5N/N_{max}) \leq 7$ mm ($\alpha_{C2.3b}$ and $\alpha_{C2.5b}$), to consider ultimate load requirement (α_{C1}, $\alpha_{C2.3c}$, and $\alpha_{C2.5c}$).

[f]$CV(\delta(0.5N_{u,m}) \leq 40\%$ in tension tests does not apply if $\delta(0.5N_{u,m}) \leq 0.4$ mm.

[g]Reduction factor to consider large scatter of ultimate failure load if $CV(N_u) \leq 20\%$ reduction factor $\beta = 1$.

Note: PT is pulsating tension; RT is reference tension; CT is tension with varying crack widths (crack cycling); CV is coefficient of variation; δ is displacement of fastener; $N_{u,m}$ is mean tension capacity from reference tests in cracked concrete ($\Delta w = 0.3$ mm); $N_{u,m}{}^{*}$ is mean tension capacity from maximum crack width and large hole diameter tests ($\Delta w = 0.5$ mm); $N_{u,m}{}^{\#}$ is mean tension capacity from maximum crack width and small hole diameter tests ($\Delta w = 0.5$ mm); $\alpha_{N,C1}{}^{\delta}$ is reduction factor if fastener completes cycle but does not fulfill capacity requirement; $\alpha_{C2.1} = \min(\alpha_{C2.1a}; \alpha_{C2.1b})$; $\alpha_{C2.3} = \min(\alpha_{C2.3a}; \alpha_{C2.3b}) \times \alpha_{C2.3c}$, $\alpha_{C2.5} = \min(\alpha_{C2.5a}; \alpha_{C2.5b}) \times \alpha_{C2.5c}$, $\alpha_{N,C2} = \alpha_{C2.1} \times \min(\alpha_{C2.3}; \alpha_{C2.5})$; $\beta_{CV,C2.1} = \min(\beta_{CV,C2.1a}; \beta_{CV,C2.1b})$; $\beta_{CV,N,C2} = \min(\beta_{CV,C2.1}; \beta_{CV,C2.3}; \beta_{CV,C2.5})$.

member was mounted between an actuator and the specimen supporting system (Fig. 4). A horizontal servo-controlled actuator with a capacity of 500 kN (112 kip) (both tension and compression) with 150 mm (5.9 in.) stroke was mounted in the actuator support system (Fig. 4). The actuator was used to generate static crack or dynamic crack based on the corresponding test program. Roller supports were used to support the member in the vertical direction. The actuator support system and the specimen support system were connected to a strong floor using high-strength threaded rods and super nuts. The theoretical background and details about test setup development were presented in Neupane et al.[17]

A hole was drilled with a four-cutter drill bit according to the manufacturer installation instructions (MII) in the prequalification document. Then, the hole was cleaned as per the instructions. Prior to the installation of the fastener into the drilled hole, the crack generated was confirmed using a borescope to ensure the fastener would be located in the crack plane over the effective load-transfer length. Anchor was installed in generated hairline crack as per the MII and the required installation torque was applied using a calibrated torque wrench. Then, tension loading was applied using a vertical 100 kN (22.5 kip) servo-controlled actuator. Figure 4 shows a schematic diagram and pictures of the setup used in the tests. The clearance of the support frame was large enough (that is, 500 mm [19.7 in.] > $4h_{ef}$) to avoid the interference of the concrete cone.

Displacement transducers were installed in both the concrete member and at the top of the anchor (Fig. 4(a) and (c)). Horizontal transducers in the concrete test member were used to measure and monitor/control crack width, whereas the vertical transducer at the top of anchor was to measure anchor displacement during loading. Two additional vertical linear variable differential transformers (LVDTs) on each side of the slab were installed to monitor the test member displacement in the vertical direction during the tension test. The average of the crack width measurement values from the two LVDTs on each side of the slab was considered as the required crack width (Δw) during testing, as the LVDTs were located at a distance equal to the effective embedment depth from the top surface of the test member. The load applied and the displacement measured by the LVDTs were controlled/monitored and recorded during the testing by a data acquisition system as per specific test requirements.

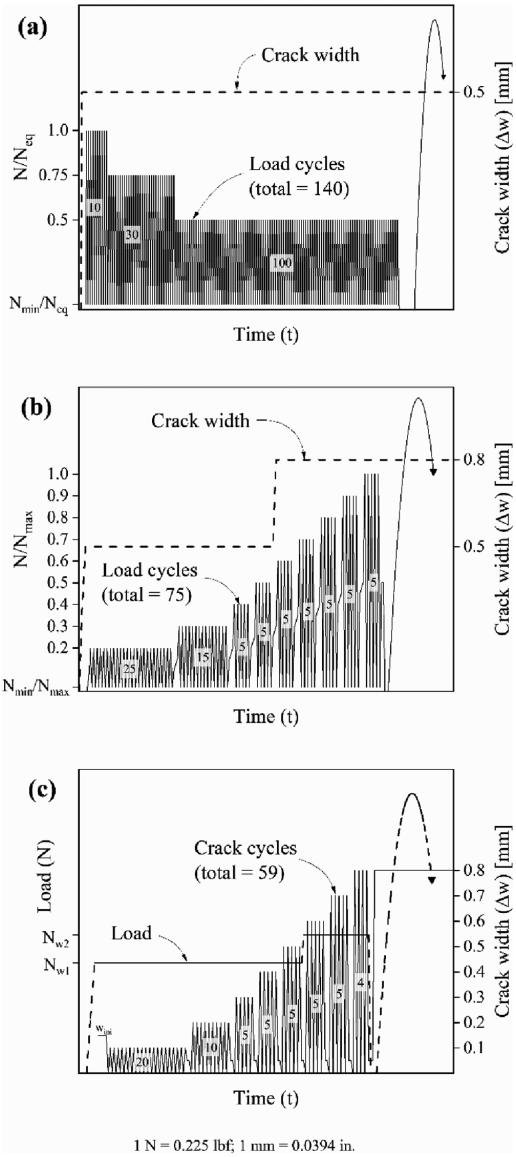


Fig. 3—Load history (redrawn as per EAD 330232-01-0601[3]): (a) pulsating tension test (C1); (b) pulsating tension test (C2); and (c) tension load with crack cycling test (C2).

EXPERIMENTAL RESULTS AND DISCUSSION

Validation of test results

Validation tests were conducted considering monotonic/reference tests (RT), pulsating tension tests (PT), and tension with varying crack widths tests (CT) as per testing requirements of C1 and C2 seismic performance categories. Additional reference tests were conducted to calculate the loading requirement for pulsating tension for the C1 category.

Table 2 summarizes key results from the validation tests. All the fasteners tested for seismic tension tests for C1 and C2 performance categories successfully completed the respective loading cycles. Pulsating tension tests were completed with a maximum required load of 20.6 and 19.4 kN (4.6 and 4.4 kip) for C1 and C2, respectively. However, it was necessary to reduce the sustained load (N_{w2}) twice (up to $N_{w2,\text{reduced}}$ = 70% of N_{w2} resulting load reduction factor = 0.70) to achieve a minimum of two tests in which all crack cycles were completed successfully for the tension with varying crack width tests. Residual capacity tests were conducted after the successful completion of cyclic tests. All the specimens failed by pullout failure in the residual capacity tests. Only one screw anchor, out of five tests, failed in concrete cone failure in the reference tests with a crack width (Δw) of 0.3 mm (0.01 in.).

Figure 5 illustrates the load-displacement behavior obtained from seismic tension tests considering C1 and C2 performance categories. Overall, they showed similar load-displacement behavior for test repeats. In both pulsating tension and crack cycling tests, the displacement at the end of the serviceability level was less than the limiting displacement ($\delta_{N,lim}$ = 7 mm [0.28 in.]). In the case of pulsating tension tests of the C2 category, the displacement of the screw increased significantly in the first cycle after opening the crack width up to 0.8 mm (0.03 in.). The displacement of the screw anchor at 50% of peak failure load was generally less than or equal to 0.4 mm (0.015 in.) in all seismic validation tests. In the case of displacement more than 0.4 mm (0.015 in.), scatter of displacement was less than 40% (maximum up to 19.2%). In pulsating tests and crack cycling tests, the anchor displacements ($\delta(N_u)$) were always greater than the displacements of corresponding reference tests ($\delta(N_{u,r})$), which resulted in a ratio of $\delta(N_u)/\delta(N_{u,r})$ greater than 1.

The required residual capacity for the seismic pulsating test series for the C1 category is 160% (33 kN [7.4 kip]) of the applied cyclic load. The mean residual capacity obtained from the test series was approximately 150% (30.9 kN [6.9 kip]) only ($N_{u,m}/N_{u,m,r}$ = 75%, applied cyclic load = 50% of $N_{u,m,r}$), resulting in a reduction factor of 0.94. This may be caused by the high tensile capacity resulting from the reference test. On the other hand, the required residual capacity for pulsating tension test and crack cycling test series for the C2 category is at least 90% (23.3 kN [5.2 kip]) of the capacity obtained from the corresponding reference test. The mean residual capacity obtained from the test series was approximately 9% and 11% more than the reference test for pulsating tension tests and crack cycling tests, respectively. It shows that load and crack cycling did not affect the load-carrying capacity of screw anchors at a large crack width. Further, the scatter of ultimate loads was less than 20% (maximum up to 14%) in all test series. The mean residual capacity for tests with crack width (Δw) 0.8 mm (0.03 in.) (C2 category) was less as compared to capacity with crack width (Δw) 0.5 mm (0.02 in.) (C1 category). This result is consistent with the findings of past research.[12] Further, variation in residual capacity was high in tests with large crack widths.

Table 3 depicts the comparison of key results from the experiment with the published values in the prequalification document (ETA) for the same screw anchor. The capacity of the screw anchor as per the prequalification document was compared with the normalized capacity against 20 MPa (2900 psi) concrete compressive strength obtained from the experiment. The values were normalized to the square root of compressive strength according to EAD 330232-01-0601.[3] Because nonseismic tests were out of the scope of this study, only seismic reduction factors (if any) calculated

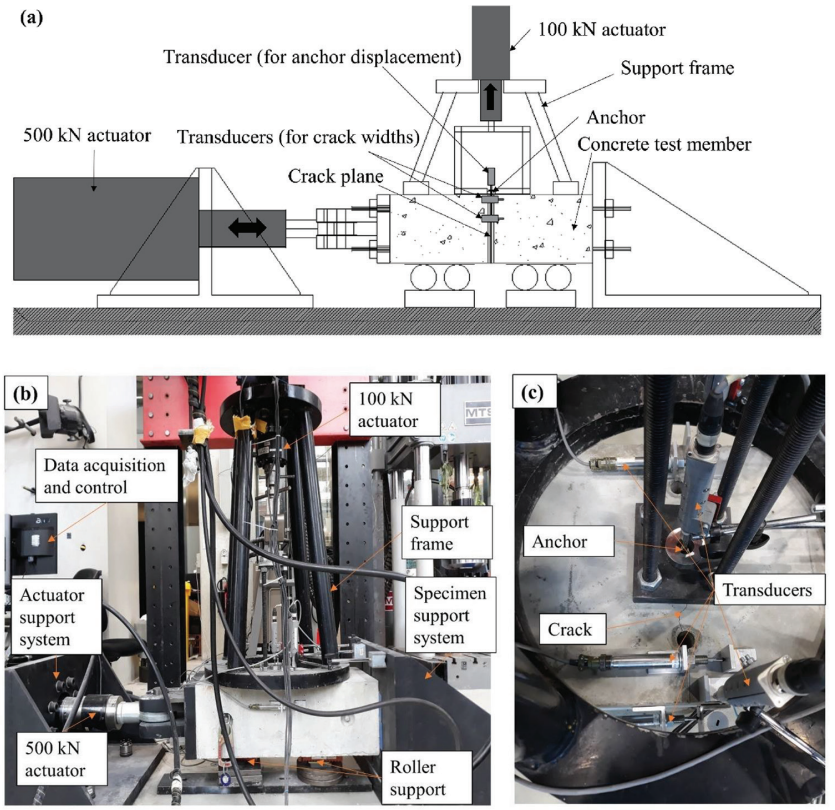


Fig. 4—Seismic tension test setup: (a) schematic view; (b) side view; and (c) top view. (Note: 1 kN = 0.225 kip.)

Table 2—Results of validation tests for 12 mm (0.47 in.) screw anchor with 100 mm (3.94 in.) nominal depth

Seismic performance category	Tests	Target max. crack width, mm (Δw)	No. of tests	Sustained load, N_{w2} (kN)	Failure mode	Displacement during cycle, mm, with Δw		Average pullout capacity, kN			Average pullout displacement, mm			
						δ(0.5)	δ(0.8)	$N_{u,m}$	cv	$N_{u,m}/N_{u,m,r}$	δ(0.5$N_{u,m}$)	cv[a]	δ(N_u)	δ(N_u)/δ($N_{u,r}$)
—	RT	0.3	5	—	PO[b]	—	—	41.2	3.7	—	0.32	—	2.74	—
C1	PT	0.5	3	—	PO	1.75	—	30.9	5.2	0.75	0.11	—	3.64	1.33
C2	RT	0.8	3	—	PO	—	—	25.9	14.0	—	0.52	19.2	2.76	—
	PT	0.8	3	—	PO	0.45	2.21	28.2	13.0	1.09	0.11	—	3.34	1.21
	CT	0.8	2	13.0	Failure during cycling									
		0.8	1	10.4	Failure during cycling									
		0.8	2	9.1	PO	0.50	1.40	28.8	—	1.11	0.15	—	3.20	1.16

[a]cv not considered if displacements at 50% of peak failure load are less than or equal to 0.4 mm.

[b]One anchor failed in concrete cone failure mode. As ultimate load from concrete cone failure is in similar range (within 3%) as pullout failure, they have been considered together. If removing concrete-cone failure, average results would be 41.4 kN instead of 41.2 kN.

Note: cv is coefficient of variation (%), calculated for more than three test repeats only; δ(0.5) and δ(0.8) = displacements at last cycle with crack width of 0.5 mm and 0.8 mm, respectively; $N_{u,m}$ is mean ultimate failure load; $N_{u,m,r}$ is mean ultimate failure load from corresponding reference tests; δ(0.5$N_{u,m}$) is displacement at 50% of mean ultimate failure load from residual capacity tests (only displacement in residual capacity tests neglecting displacements occurred during cyclic load/crack); PO is pullout failure; 1 mm = 0.0394 in.; 1 kN = 0.225 kip.

based on the conducted test series were considered for the calculation of the experimental characteristic value. For the C1 performance category, the characteristic tension resistance obtained from the experiment was approximately 9% more as compared to values in the prequalification document. For the C2 performance category, the characteristic value obtained from the reference tests (Δw = 0.8 mm [0.03 in.]) was considered to be on the conservative side as an alternative to the characteristic value from "maximum crack width and large hole diameter" and "maximum crack width and small hole diameter" tests (Δw = 0.5 mm [0.02 in.]). The crack cycling test was the governing test in terms of tension resistance due to the load reduction factor of 0.7 and was approximately 11% more as compared to the value in the prequalification document. The anchor displacement obtained from the experiment at the serviceability and ultimate levels were 12% and 6% less (experiment: 0.50 mm and 2.21 mm [0.020 and 0.087 in.], prequalification document: 0.57 and 2.36 mm [0.022 and 0.093 in.]) than the corresponding value in the prequalification document. Hence, the validation test results showed that the capacity

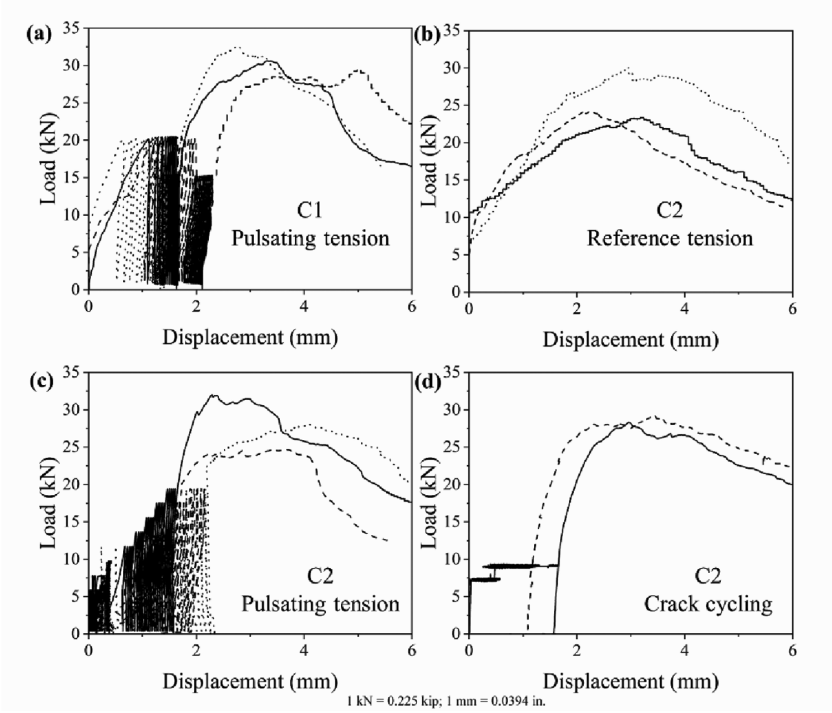


Fig. 5—Load-displacement behavior of 12 mm (0.47 in.) screw anchor under: (a) C1 seismic performance category, pulsating tension, and C2 seismic performance category; (b) reference tension; (c) pulsating tension; and (d) tension load with crack cycling (different lines represent results from test repeats).

Table 3—Comparison of characteristic capacity of 12 mm (0.47 in.) screw anchor

Seismic performance category	Experimental results			Published value in prequalification (PQ) document			$N_{ch,exp}/N_{ch,PQ}$	$\delta(0.5)_{exp}/\delta(0.5)_{PQ}$	$\delta(0.8)_{exp}/\delta(0.8)_{PQ}$
	Characteristic tension $N_{ch,exp}$, kN	Displacement $\delta(0.5)_{exp}$, mm	Displacement $\delta(0.8)_{exp}$, mm	Characteristic tension $N_{ch,PQ}$, kN	Displacement $\delta(0.5)_{PQ}$, mm	Displacement $\delta(0.8)_{PQ}$, mm			
C1	26.9	—	—	24.6	—	—	1.09	—	—
C2	7.9	0.50	2.21	7.1	0.57	2.36	1.11	0.88	0.94

Note: 1 mm = 0.0394 in.; 1 kN = 0.225 kip.

values are within a reasonable range when compared with values in the prequalification document.

Test results of small (6 mm [0.024 in.]) screw anchors

Seismic tests were conducted on 6 mm (0.024 in.) screw anchors considering crack cycling tests as per one of the C2 testing requirements. This test is considered because it was the governing test in the validation tests series and a similar conclusion was drawn by Mahrenholtz et al.[14] The performance of two 6 mm (0.024 in.) screw anchors (namely, S1 and S2a) from two different manufacturers were investigated. Both concrete screws were prequalified for the C1 performance category and tested with a nominal embedment depth of 55 mm (2.2 in.). Screw anchors (S2b) were also tested with a deeper embedment (that is, nominal embedment depth = 75 mm [3 in.]) under pulsating tension and crack cycling. Additional reference tests of the C2 category with low-strength concrete was conducted to calculate and compare the loading requirement and for performance evaluation. Table 4 summarizes the key results obtained from the seismic tests.

Sustained load and crack cycles—The load at the fixing point shall be limited during the design of redundant fasteners, assuring load distribution and transmission through the nonstructural systems (Fig. 6). Limiting values of design load as per AS 5216:2021[5] is 2 or 3 kN (0.45 or 0.67 kip) per fixing point for 3 and ≥4 number of fixing points, respectively, in the system. Hence, a sustained load (N_{w2}) of 2 kN (0.45 kip) was applied as a trial in the first set of testing to gauge. However, the screw anchor (S1) did not complete all 59 cycles. It was necessary to reduce the sustained load (N_{w2}) three times (to N_{w2} = 0.5 kN [0.11 kip]) to get a minimum of two tests in which all crack cycles were completed successfully. For S2, 0.5 kN (0.11 kip) sustained load was selected to compare against the performance of S1. The results showed that the performance of S2 with 0.5 kN (0.11 kip) exhibited similar behavior as S1. Hence, further testing with a greater sustained load was not conducted. All fasteners tested with the sustained load (N_{w2}) of 0.5 kN (0.11 kip) successfully completed all crack cycles of the test series. However, the small sustained load resulted in a very small load reduction factor equal to 0.11 for screws with deeper embedment (S2-6-75). Residual capacity tests were conducted after the successful completion of crack cycles

Table 4—Results of seismic tests for 6 mm (0.24 in.) screw anchors

Seismic performance category	Screw anchor ID	Tests	Target maximum crack width, mm (Δw)	No. of tests	Sustained load, N_{w2}, kN	Failure mode	Displacement during cycle, mm with Δw		Average pullout capacity, kN			Average pullout displacement, mm			
							$\delta(0.5)$	$\delta(0.8)$	$N_{u,m}$	cv	$N_{u,m}/N_{u,m,r}$	$\delta(0.5N_{u,m})$	cv[a]	$\delta(N_u)$	$\delta(N_u)/\delta(N_{u,r})$
C2	S1-6-55	RT	0.8	2	—	PO	—	—	2.2	—	—	0.23	—	1.14	—
		CT	0.8	1	2.0	Failure during cycling									
			0.8	1	1.0	Failure during cycling									
			0.8	2	0.8	Failure during cycling[b]									
			0.8	2	0.5	PO	0.38	0.73	2.6	—	1.18	0.06	—	2.14	1.88
	S2a-6-55	CT	0.8	2	0.5	PO	0.29	0.44	5.7	—	—	0.54	—	1.93	—
	S2b-6-75	RT	0.8	5	—	PO	—	—	9.2	20.7	—	0.52	66.7	1.92	—
		PT	0.8	3	—	PO	0.03	0.55	8.5	22.6	0.92	0.33	103.0	2.26	1.17
		CT	0.8	5	0.5	PO	0.23	0.39	8.7	26.9	0.95	0.36	122.6	2.04	1.06

[a]cv not considered if displacements at 50% of peak failure load is less than or equal to 0.4 mm.

[b]All or at least an anchor failure during cycling.

Note: cv is coefficient of variation (%), calculated for more than three test repeats only; $\delta(0.5)$ and $\delta(0.8)$ are displacements at last cycle with crack width of 0.5 mm and 0.8 mm, respectively; $N_{u,m}$ is mean ultimate failure load; $N_{u,m,r}$ is mean ultimate failure load from corresponding reference tests; $\delta(0.5N_{u,m})$ is displacement at 50% of mean ultimate failure load from residual capacity tests (only displacement in residual capacity tests neglecting displacements occurred during cyclic load/crack); PO is pullout failure; 1 mm = 0.0394 in.; 1 kN = 0.225 kip.

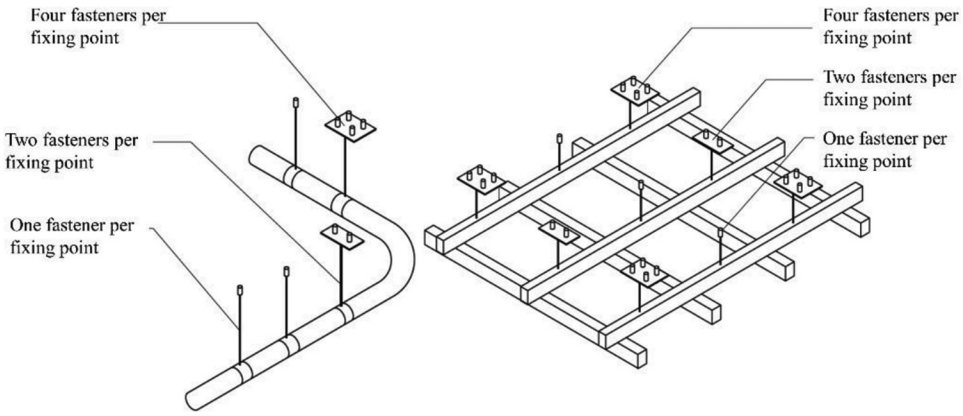


Fig. 6—Example of redundant nonstructural systems with different number of fixing points (AS 5216[5]).

for all tests. Load drop and slip behavior were observed before ultimate failure in some of the residual capacity tests, which is discussed later in the paper.

Failure mode—All the tested 6 mm (0.24 in.) screw anchors failed by pullout failure mode during the residual capacity tests of different seismic test series. A similar failure mode was observed in past research[10,13] for larger-sized screw anchors during seismic tests. Figure 7 shows the typical pullout failure mode during the seismic tests. There was very little or no concrete damage in the anchorage area except pulling out of anchor (with screw threads full of concrete dust) from the hole. The anchor failed in pullout failure mode when it did not complete all cycles and also failed during crack cycling.

Load-displacement behavior—Although the anchor failed during the crack cycling phase for S1-6-55 with sustained load (N_{w2}) from 2 to 0.8 kN (0.45 to 0.18 kip), improved performance was achieved in each reduction of sustained load in terms of completed cycles, corresponding crack width, and displacement. Load-displacement graphs from reference tests, pulsating tension tests, and crack cycling tests with a sustained load of 0.5 kN (0.11 kip) are illustrated in Fig. 8. All screw anchors completed the crack cycles successfully with 0.5 kN (0.11 kip) maximum sustained load. Further, the screw anchors completed the pulsating load cycles successfully with a 2 kN (0.45 kip) maximum load.

During the residual capacity phase of the tests for both screw products (S1-6-55 and S2a-6-55), the load dropped significantly before ultimate failure. A similar load drop was also recorded in the case of a longer screw anchor (S2b-6-75) in crack cycling tests (Fig. 8(f)). The load-displacement graphs from reference tension tests are comparable with residual capacity tests for the same concrete screw. In a reference test, uncontrolled slip of anchor happened at small load as well (Fig. 8(d)). For the tested 6 mm (0.24 in.) screw anchors, nearly 8% load drop and slip with greater than 18% of displacement occurred in some tests during the test series, which is not acceptable for C2. Further, load-displacement behavior from these test series showed very high variability for 6 mm (0.24 in.) screw anchors. This variability may

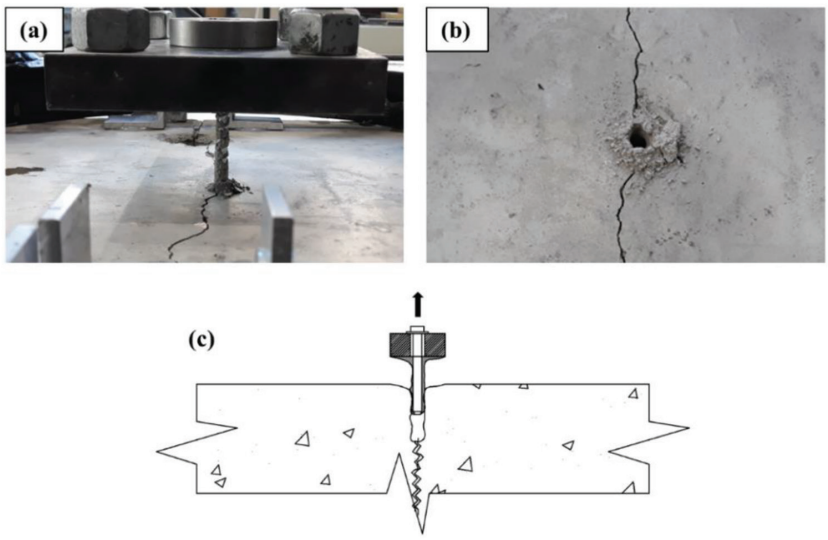


Fig. 7—Typical pullout failure mode. Photos of pullout failure from experiment: (a) side view; (b) top view; and (c) schematic representation of pullout failure mode.

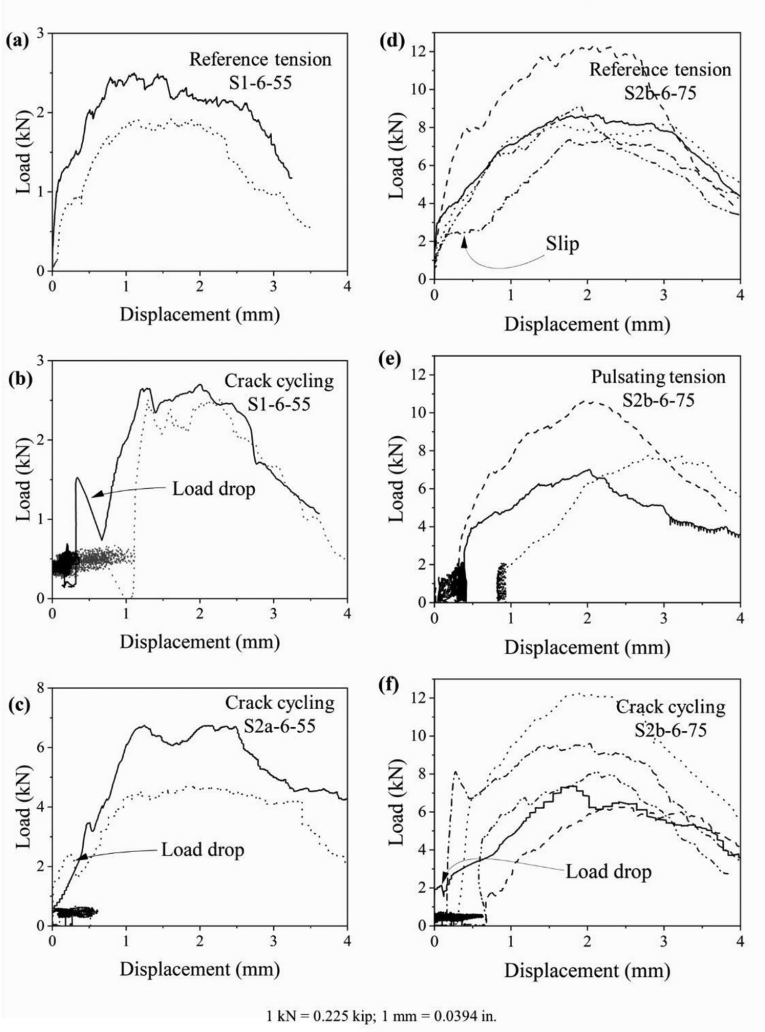


Fig. 8—Load-displacement behavior of 6 mm (0.24 in.) screw anchors under C2 seismic performance category: (a) reference tension (S1-6-55); (b) tension load with crack cycling (S1-6-55); (c) tension load with crack cycling (S2a-6-55); (d) reference tension (S2b-6-75); (e) pulsating tension (S2b-6-75); and (f) tension load with crack cycling (S2b-6-75) (different lines represent results from test repeats).

be due to the large crack width requirement in the loading protocol as compared to the size of the screw and very low level of sustained load. Additionally, any small changes in test parameters could cause notable variations in load and displacement due to the small values of each of them. Similar to the validation test series, during pulsating tension tests, the displacement increased significantly after opening the crack width to 0.8 mm (0.03 in.).

Displacement—The mean displacement of anchor after the completion of serviceability level cycles was 0.38 and 0.29 mm (0.015 and 0.011 in.) whereas, after the completion of ultimate level cycles, was 0.73 and 0.44 mm (0.029 and 0.017 in.) in crack cycling tests for S1-6-55 and S2a-6-55, respectively. In the case of screws with deeper embedment (S2b-6-75), displacements at the serviceability level (0.23 mm [0.009 in.]) and the ultimate level (0.39 mm [0.015 in.]) were less as compared to the same type of anchor with shallow embedment. The displacements at the end of load/crack cycles with crack width 0.5 mm (0.02 in.) were always less than the limiting displacement ($\delta_{N,lim}$ = 7 mm [0.28 in.]) for the serviceability level. The displacements of the screw anchor (S2b-6-75) at 50% of peak failure load were more than 0.4 mm (0.016 in.) in the seismic tests. In such cases, there was a huge scatter of displacement with a cv up to 122.6% in residual capacity tests of crack cycling tests. This is mainly due to small values (with average displacement = 0.36 mm [0.014 in.]) and high variability in test repeats. In pulsating tension and crack cycling tests, the total anchor displacements $\delta(N_u)$ were always greater than the displacements that occurred during the corresponding reference tests $\delta(N_{u,r})$, which resulted in a ratio of $\delta(N_u)/\delta(N_{u,r})$ greater than 1. The displacement ratio $\delta(N_u)/\delta(N_{u,r})$ ranges between 1.06 and 1.88 for 6 mm (0.24 in.) screw anchors. In some tests, the anchor displacement during the cycling phase was minimal due to the very low sustained load and did not have significant permanent displacement after completion of cycles.

Ultimate failure load—The required residual capacity from the pulsating tension and crack cycling tests is at least 90% of the capacity obtained from the corresponding reference test. The failure load obtained from the test series was approximately 18% more than reference test for S1-6-55. In contrast, the load was approximately 92% in pulsating tension and 95% in crack cycling tests as compared to the corresponding reference tests for S2b-6-75. Similar results were observed in literature with higher[11] or lower[10,13] failure loads in load/crack cycling tests as compared to corresponding reference tests. In both cases, it shows that crack cycling does not affect the load-carrying capacity of screw anchors at large crack widths. With the same nominal embedment depth, the residual capacity of S2 screw anchors was higher than S1 screw anchors. The ultimate failure load between test repeats has high variation due to the sensitivity of screw threads' engagement with large crack widths in the reference tests, pulsating tension tests, and crack cycling tests. This variability may be due to the large crack width requirement in the loading protocols as compared to the size of the screw and small value of loads. For example, the scatter of ultimate loads was more than 20%, resulting in a reduction factor due to large scatter. Greater values of residual capacity may be due to high variability in the test series in terms of the ultimate load. This point may be further supported by the finding that the mean capacity of S2b-6-75 was more comparable than S1-6-55, where the number of tests repeats increased to five instead of two.

CRACK WIDTH, ENGAGING THREAD, AND BEARING AREA

Based on the experimental study conducted, the 6 mm (0.24 in.) concrete screws investigated in this study did not meet all the necessary requirements for the tension tests stipulated in the C2 performance category. The tested 6 mm (0.24 in.) screw anchors (S1 and S2) were already prequalified for the C1 performance category. These screw anchors in their larger 8 mm (0.31 in.) size have approval for the C2 performance category. Hence, a comparison is made between 6 and 8 mm (0.24 and 0.31 in.) screw anchors to investigate further considering bearing area on concrete and actual thread engagement width with respect to crack width in concrete.

Table 5—Thread profile and parameters of screw anchors

Thread details		Screw type/product			
		S1		S2	
Profile					
Parameters, mm	Size	6	8	6	8
	Anchor nominal diameter d_o	6	8	6	8
	Cutting diameter of drill bit $d_{cut} \leq$	6.4	8.45	6.4	8.45
	Core diameter d_k	5.1	7.1	5.85	7.85
	Threaded outer diameter d_t	7.5	10.6	7.85	10.3
	Thread width $((d_t - d_k)/2)$	1.2	1.75	1	1.225

Note: 1 mm = 0.0394 in.

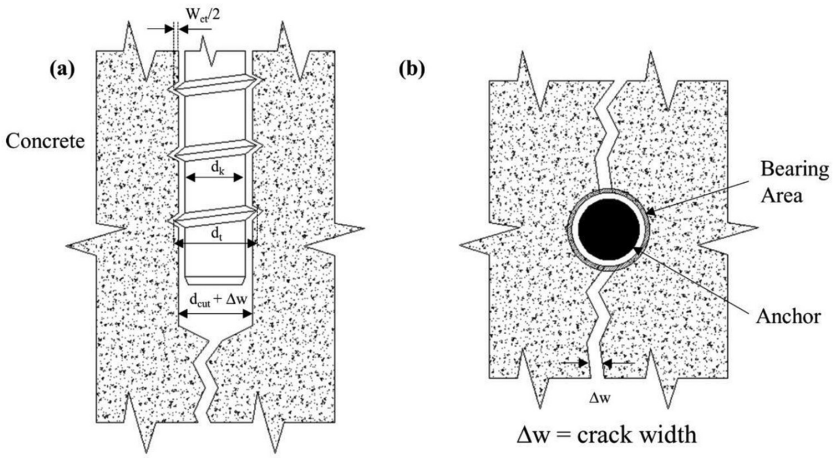


Fig. 9—Typical schematic diagram with: (a) side view; and (b) top section view of screw anchor in cracked concrete showing engaging thread and bearing area section in concrete.

Table 5 presents the thread profile and thread parameters of both 6 and 8 mm (0.24 and 0.31 in.) screws (S1 and S2). All the parameters are taken from the respective prequalification document, which were verified by measuring the thread of screw anchors. The measured values of thread parameters were within ±0.05 mm and ±0.10 mm (±0.002 in. and ±0.004 in.) tolerance for 6 and 8 mm (0.24 and 0.31 in.) screw anchors. When comparing thread profile and thread width, the two screw products (S1 and S2) have very different thread details and different values of thread widths. Screw anchor located in a crack has a reduced bearing area of thread flanks as compared to uncracked concrete, resulting in a reduction of the anchor capacity and stiffness.[18] Hence, the actual thread of the screw that engages in the concrete and the total bearing area (contact area) will play a more important part during seismic tests in cracked concrete. The thread engagement width ($w_{et} = d_t - d_{cut} - \Delta w$) of the screw anchor was calculated considering the thread outer diameter (d_t), cutting diameter (d_{cut}), and maximum crack width (Δw). Figure 9 shows the typical schematic diagram of screw anchor in cracked concrete with actual engaging thread and bearing sectional area of screw threads in concrete. Maximum crack width (Δw) is the key difference between C1 (Δw = 0.5 mm [0.02 in.]) and C2 (Δw = 0.8 mm [0.03 in.]) seismic performance category.

Figure 10 illustrates the correlation of the bearing section area with engaged thread width by maximum crack width ratio ($w_{et}/\Delta w$). Bearing area and $w_{et}/\Delta w$ for screws with C1 prequalification are higher than that with C2 prequalification, showing the clear effect of maximum crack width for both screw sizes and products. Further, 8 mm (0.31 in.) screws have higher values of bearing area and $w_{et}/\Delta w$ than 6 mm (0.24 in.) screws due to the increase in anchor diameter. S2 screw anchors have a greater bearing area and $w_{et}/\Delta w$ as compared to S1 for 6 mm (0.24 in.). This aligns with the results of experimental work on 6 mm (0.24 in.) screw anchors, where S2 screw anchors performed better than S1. In contrast, S1 screw anchors have greater bearing area and $w_{et}/\Delta w$ as compared to S2 for 8 mm (0.31 in.). Interestingly, all considered prequalified anchors have $w_{et}/\Delta w$ ratio greater than 1 for both the C1 and C2 categories. These prequalified

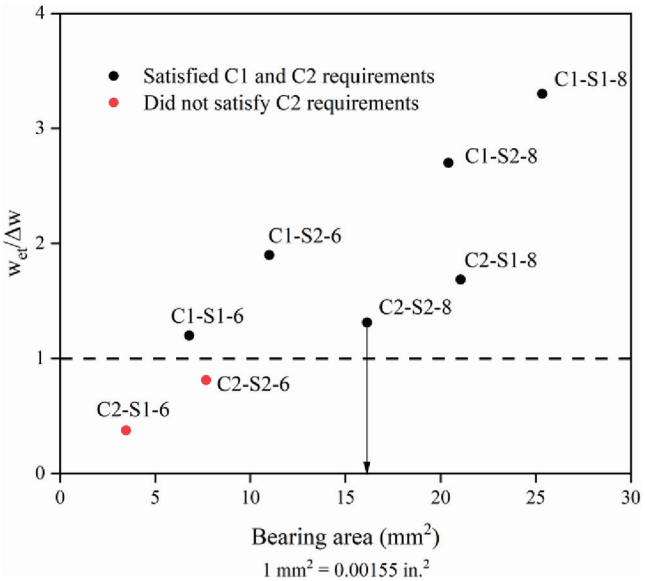


Fig. 10—Bearing area correlated with engaging thread width by crack width ratio (name of each point is given to represent performance category, manufacturer, and nominal size of screw anchor).

anchors have $w_{et}/\Delta w$ of at least 1.20 and 1.31 for the C1 and C2 performance categories, respectively. In terms of bearing area, 8 mm (0.31 in.) screw anchors have at least 16.12 mm² (0.025 in.²). Only 6 mm (0.24 in.) screw anchors (S1 and S2) from both manufacturers have a value lesser than 1 for $w_{et}/\Delta w$ for the C2 category as shown in Fig. 10, showing a lesser thread engagement width which resulted in inadequate performance under crack cycling for 0.8 mm (0.03 in.). This point got further support as the test results on 6 mm (0.24 in.) screw anchors in this study did not meet some of the C2 performance requirements.

FINITE ELEMENT ANALYSIS

Test results and analytical investigation show that screw anchor performance is dependent on engagement thread width. Hence, further investigation to check the effect of thread engagement—the comprehensive three-dimensional (3-D) finite element model—was developed using

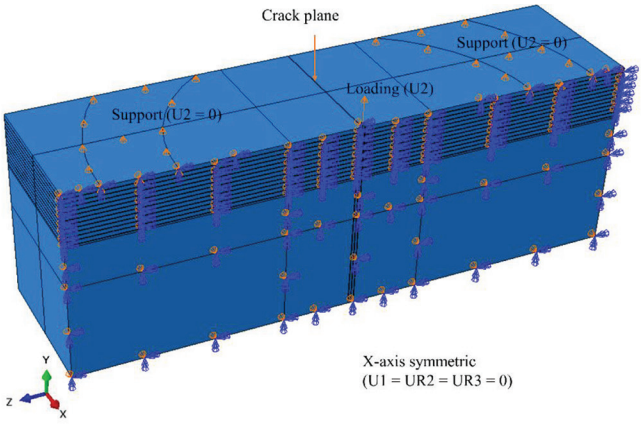


Fig. 11—Finite element model with boundary conditions.

Abaqus software developed by Dassault Systemes.[19] The finite element model was validated by comparing predictions with test results and was further used to investigate screw behavior, ultimate failure load, and failure mode with increased thread width.

Finite element model

In the finite element model, the concrete damage plasticity (CDP) model was used for concrete, and elastic behavior was used for the anchor. At the concrete-anchor interface, hard contact was used in the normal direction and Coulomb friction with a frictional coefficient of 0.5 was used in the tangential direction. Displacement loading was applied at the top of anchor and surface, where reaction support contacts the concrete, and was restrained in the vertical direction. Further, crack was defined in the crack plane by considering the physical gap of thickness equal to the crack width. Neupane et al.[20] conducted a comprehensive finite element analysis considering different thread profiles of screw anchors. It was observed that the acceptable results (within 4% in ultimate load and 10% in displacement) could be achieved using a simplified model with circular cylindrical thread. Hence, threads of screw anchor were simplified into circular cylindrical in the models instead of complex spiral threads. The finite element model was developed considering half geometry by taking advantage of symmetrical conditions (Fig. 11). To further save computational resources, finer mesh (up to 0.1 mm [0.004 in.]) was used for screw anchor, and concrete in anchorage region, while relatively coarse mesh (up to 10 mm [0.394 in.]) was used for concrete away.

Concrete compressive strength, tensile strength, modulus of elasticity, and Poisson's ratio of 29.8 MPa, 3.47 MPa, 27,103 MPa, and 0.2 (4322 psi, 503 psi, 3931 ksi, and 0.2), respectively, were used in finite element analysis. These material properties for concrete were average values obtained from experimental material testing. A fracture energy value of 79 N/m (0.45 lbf/in.) was used, which was calculated as recommended by Abaqus.[19] The value of CDP parameters of dilation angle (ψ) = 20, yield surface shape factor (K_c) = 2/3, eccentricity (ϵ) = 0.1, stress ratio (σ_{b0}/σ_{c0}) = 1.16, and viscosity (μ) = 0 are used for the models.[19,20] Concrete stress-strain relationship under compression was defined based on Carreira and Chu.[21] In the relationship, linear behavior of up to 40% of the ultimate stress was taken into account.[22] The yield stress and fracture energy were used to define the tensile behavior of concrete. Modulus of elasticity and Poisson's ratio of 210,000 MPa (30,458 ksi) and 0.3, respectively, were used for steel.

Finite element analysis results and discussion

To validate the finite element model, a comparison was made with experimental results for 12 and 6 mm (0.47 and 0.24 in.) screw anchors in 0.8 mm (0.03 in.) crack width. Figures 12(a) and (b) show the comparison of load-displacement behavior, which showed that the model was able to capture experimental behavior reasonably well. However, the predicted value is slightly higher than the average ultimate load (experiment: 9.2 kN [2.1 kip], FEA: 11.7 kN [2.6 kip]) in the case of 6 mm (0.24 in.) screw anchors, as experimental results have high variability for the small-sized anchor. Finite element analysis showed that screw threads engaged with concrete after load was applied, leading to local concrete crushing (shown in the first low peak), followed by concrete cracking near the thread engaged area. Starting with uniform distribution in the screw anchor, the bottom threads had more concentrated stress before observing failure in concrete. The cracking pattern visualized by analysis matched with the experimentally observed pullout failure mode (Fig. 12(c)).

Using the validated finite element model, additional analysis was conducted with increased thread width by 0.4 mm (0.016 in.), which will increase the screw outer diameter by 10%. Figure 12(d) presents the analysis results with different values of engaged thread for the 6 mm (0.24 in.) screw anchor (S2b-6-75). The ultimate failure load slightly increased after increasing the engaged thread width. It can be observed that for the 6 mm (0.24 in.) size of screw, increasing thread size up to 0.4 mm did not result in a significant effect in terms of ultimate load and failure mode. Furthermore, load-displacement behavior with increased thread size was very similar. Hence, for 6 mm (0.24 in.) screw anchor, an increase in thread width slightly increased the screw capacity; however, it is uncertain that the small-sized screw anchor will work in cracked concrete in large crack width. Furthermore, there is a possibility that the finite

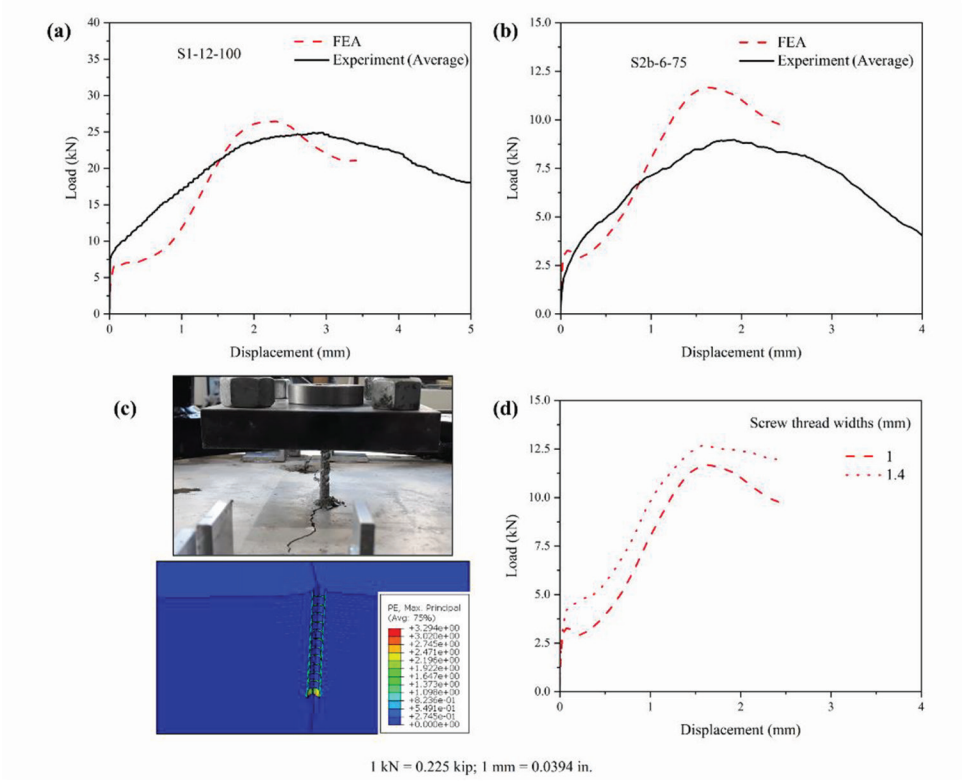


Fig. 12—Finite element analysis (FEA) results. Experiment versus FEA load-displacement behavior of screw anchor in cracked concrete of 0.8 mm (0.03 in.) crack width: (a) S1-12-100; (b) S2b-6-75; (c) failure mode observed in experiment versus simulated crack pattern from FEA (S2b-6-75); and (d) comparison of load-displacement behavior of screw anchor (S2b-6-75) with increased thread width.

element model could not accurately capture the effects of increasing the thread size.

Modification of screw geometry needs experimental confirmation—mainly to ensure the acceptable load-displacement behavior in test repeats as required by prequalification documents. This study can serve as a starting point for the fastener industry for future product development and experimental verification. Furthermore, practical applications should also be considered because an increase in the undercut width or any change in the geometry of the screw can cause installation difficulty.[23,24]

CONCLUSIONS

Experimental study was conducted for the prequalified 12 mm (0.47 in.) screw anchor under tension loading for validation of the seismic test setup considering both C1 and C2 performance categories. Using the validated testing setup, an experimental investigation was carried out for 6 mm (0.24 in.) screw anchors in cracked concrete with large crack width (Δw = 0.8 mm [0.03 in.]) under seismic tension loading considering both static and dynamic cracks. Prequalified screw anchors (nominal embedment depth = 55 mm [2.2 in.]) for the C1 category from two manufacturers (S1 and S2) were tested to assess performance in different products. Additional tests considering deeper embedment (nominal embedment depth = 75 mm [3 in.]) were conducted using screw anchor S2b. The performance of the 6 mm (0.24 in.) screw anchors was evaluated in terms of ultimate failure load, failure mode, anchor displacement, and load-displacement behavior with highly demanding C2 performance category requirements. Both types of 6 mm screw anchors completed crack cycles with a sustained load of 0.5 kN (0.11 kip) but load drop and slip behavior were observed during some residual capacity tests. Further, displacement values at 50% of the ultimate failure load were largely scattered exceeding the 40% limit for coefficient of variation (cv), as prescribed in EOTA EAD 330232-01-0601.[3] The 6 mm (0.24 in.) screw anchors being tested in this study do not pass some of the requirements and hence are deemed not suitable for the C2 performance category.

Given the next size up (8 mm [0.31 in.]) of the screw anchor types investigated in this study are prequalified for C2 performance category, the thread details of 6 and 8 mm (0.24 and 0.31 in.) screw anchors from the two different manufacturers were analyzed in terms of the ratio of its engaging thread width by maximum crack width ratio ($w_{et}/\Delta w$) and bearing area. For both types of screw anchors, the 8 mm (0.31 in.) size, which is prequalified for C2 performance, has $w_{et}/\Delta w$ greater than 1 when compared to both C1 and C2 categories' crack width requirements. However, 6 mm (0.24 in.) anchors for the C2 category have $w_{et}/\Delta w$ less than 1, showing the presence of less engaged thread in concrete due to a larger crack width, which may lead to unsatisfactory performance.

Based on experimental investigation and evaluation, it was found that 6 mm (0.24 in.) screw anchors did not meet the requirements of the C2 performance category with a temporary load drop (>5%) and slip behavior (>10%) observed in

some of the reference tests and crack cycling tests. Based on the available evidence, screw anchors of 8 mm size from the same manufacturers hold C2 seismic prequalification. Further, finite element analyses were conducted to examine the effect of engaged thread width of screw anchors in cracked concrete and results showed a slight increase (approximately 9%) in ultimate load with minimal influence in terms of load-displacement behavior for screw anchors with increased thread width by 0.4 mm (0.016 in.). This reinforced the experimental findings of small-sized screw anchors exhibiting slip behavior in concrete with large crack widths.

The conclusions made in this study are based on the experimental findings and might not be applicable to all screws/manufacturers. However, given that the applications for these 6 mm (0.24 in.) screw anchors is for redundant nonstructural applications, further research may investigate less stringent prequalification requirements given the redundancy in the system.

AUTHOR BIOS

Chandani Chandra Neupane *is a Structural Engineer at Allfasteners in Melbourne, Australia. He received his BEng in civil engineering from Tribhuvan University, Kirtipur, Nepal; his MEng in structural engineering from Asian Institute of Technology (AIT), Pathum Thani, Thailand; and his PhD in civil engineering from Swinburne University of Technology, Melbourne, Australia. His research interests include post-installed anchorage in concrete and finite element analysis.*

Jessey Lee *is a Senior Lecturer and Deputy Chair in the Department of Civil and Construction Engineering and the Training and Development Manager at the Australian Engineered Fasteners and Anchors Council (AEFAC) at the Swinburne University of Technology. She received her BEng (Hons) and PhD from the University of Melbourne, Melbourne, Australia. Her research interests include steel connections, fastenings to concrete, modular construction, and nonconforming building products.*

Tilak Pokharel *is an AEFAC National Technical Manager at the Swinburne University of Technology. He received his BEng from Tribhuvan University; his MEng from the University of Tokyo, Tokyo, Japan; and his PhD from the University of Melbourne. His research interests include finite element modeling, steel and composite construction, anchorage, and earthquake-resistant design.*

Hing-Ho Tsang *is a Professor and the Chair of Civil and Structural Engineering at the University of Dundee, Dundee, Scotland, UK. He received his BEng (Hons) and PhD from the University of Hong Kong, Hong Kong. His research interests include seismic design and analysis of anchors in concrete and design of anchors in external devices for enhancing seismic performance.*

Emad Gad *is a Professor and Dean of the School of Engineering at Swinburne University of Technology. He received his BEng (Hons) from Monash University, Melbourne, Australia, and his PhD from the University of Melbourne. His research interests include structural dynamics, steel construction and connections, experimental techniques, and finite element modeling.*

ACKNOWLEDGMENTS

The authors extend their sincere gratitude to lab technicians at Smart Structures Laboratory at Swinburne University of Technology, Melbourne, Australia, and the support of all The Australian Engineered Fasteners and Anchors Council (AEFAC) members.

REFERENCES

1. ACI Committee 355, "Post-Installed Mechanical Anchors in Concrete—Qualification Requirements and Commentary (ACI-CODE-355.2-22)," American Concrete Institute, Farmington Hills, MI, 2022, 102 pp.

2. ACI Committee 355, "Qualification of Post-Installed Adhesive Anchors in Concrete and Commentary (ACI CODE-355.4-19(21)) (Reapproved 2021)," American Concrete Institute, Farmington Hills, MI, 2021, 51 pp.

3. EAD 330232-01-0601, "Mechanical Fasteners for Use in Concrete," European Organisation for Technical Assessment, Brussels, Belgium, 2019. 122 pp.

4. EAD 330499-01-0601, "Bonded Fasteners for Use in Concrete," European Organisation for Technical Assessment, Brussels, Belgium, 2018, 115 pp.

5. AS 5216:2021, "Design of Post-Installed and Cast-In Fastenings in Concrete," Standards Australia, Sydney, NSW, Australia, 2021, 128 pp.

6. AC510, "Seismic Qualification of Post-Installed Anchors in Concrete," International Code Council Evaluation Service, Brea, CA, 2020, 29 pp.

7. EN 1992-4:2018, "Eurocode 2: Design of Concrete Structures—Part 4: Design of Fastenings for Use in Concrete," British Standards Institution, London, UK, 2018.

8. ACI Committee 318, "Building Code Requirements for Structural Concrete (ACI 318-19) and Commentary (ACI 318R-19) (Reapproved 2022)," American Concrete Institute, Farmington Hills, MI, 2019, 624 pp.

9. "The New Royal Adelaide Hospital, Adelaide—A Complete Hilti Solution for Highly Specified Electrical Fastenings," https://www.hilti.com.au/content/hilti/A2/AU/en/engineering/design-center/anchor-systems/jobsite-references/royal-adelaide-hospital.html. (last accessed Aug. 7, 2024)

10. Hoehler, M. S., and Eligehausen, R., "Behavior and Testing of Anchors in Simulated Seismic Cracks," *ACI Structural Journal*, V. 105, No. 3, May-June 2008, pp. 348-357.

11. Hoehler, M. S., and Eligehausen, R., "Behavior of Anchors in Cracked Concrete under Tension Cycling at Near-Ultimate Loads," *ACI Structural Journal*, V. 105, No. 5, Sept.-Oct. 2008, pp. 601-608.

12. Mahrenholtz, P.; Eligehausen, R.; Hutchinson, T. C.; and Hoehler, M. S., "Behavior of Post-Installed Anchors Tested by Stepwise Increasing Cyclic Load Protocols," *ACI Structural Journal*, V. 113, No. 5, Sept.-Oct. 2016, pp. 997-1008. doi: 10.14359/51689023

13. Mahrenholtz, C.; Eligehausen, R.; Hutchinson, T. C.; and Hoehler, M. S., "Behavior of Post-Installed Anchors Tested by Stepwise Increasing Cyclic Crack Protocols," *ACI Structural Journal*, V. 114, No. 3, May-June 2017, pp. 621-630. doi: 10.14359/51689431

14. Mahrenholtz, P.; Wood, R. L.; Eligehausen, R.; Hutchinson, T. C.; and Hoehler, M. S., "Development and Validation of European Guidelines for Seismic Qualification of Post-Installed Anchors," *Engineering Structures*, V. 148, 2017, pp. 497-508. doi: 10.1016/j.engstruct.2017.06.048

15. Dywidag Tie-Rod System, https://dywidag.com/products/dywidag-tie-rod-system. (last accessed Aug. 7, 2024)

16. AS 1012.9:2014, "Methods of Testing Concrete Method 9: Compressive Strength Tests—Concrete, Mortar and Grout Specimens," Standards Australia, Sydney, NSW, Australia, 2014, 12 pp.

17. Neupane, C. C.; Lee, J.; Pokharel, T.; Tsang, H. H.; and Gad, E., "Development of Seismic Test Set-Up for Fasteners in Australia," Australian Earthquake Engineering Society Virtual Conference, Richmond, VIC, Australia, 2020.

18. Eligehausen, R.; Mallée, R.; and Silva, J. F., *Anchorage in Concrete Construction*, Ernst & Sohn, Berlin, Germany, 2006.

19. Abaqus, user documentation, Dassault Systèmes, Vélizy-Villacoublay, France, 2022.

20. Neupane, C. C.; Lee, J.; Pokharel, T.; Tsang, H. H.; and Gad, E., "Experimental and Numerical Investigation of Screw Anchors in Large Crack Width," *Engineering Structures*, V. 300, 2024, p. 117150. doi: 10.1016/j.engstruct.2023.117150

21. Carreira, D. J., and Chu, K. H., Stress-Strain Relationship for Plain Concrete in Compression," *ACI Journal Proceedings*, V. 82, No. 6, Nov.-Dec. 1985, pp. 797-804.

22. Mirza, O., and Uy, B., "Behaviour of Composite Beam-Column Flush End-Plate Connections Subjected to Low-Probability, High-Consequence Loading," *Engineering Structures*, V. 33, No. 2, 2011, pp. 647-662. doi: 10.1016/j.engstruct.2010.11.024

23. Olsen, J.; Pregartner, T.; and Lamanna, A. J., "Basis for Design of Screw Anchors in Concrete," *ACI Structural Journal*, V. 109, No. 4, July-Aug. 2012, pp. 559-568.

24. Tarawneh, A. N.; Saleh, E. F.; and Majdalaweyh, S. A., "Reliability Assessment and Strength Reduction Factor Calibration for Screw Anchors Concrete Breakout," *ACI Structural Journal*, V. 119, No. 2, Mar.-Apr. 2022, pp. 113-122.

ACI STRUCTURAL JOURNAL TECHNICAL PAPER

Title No. 121-S77

Numerical Modeling of Squat Reinforced Concrete Shear Walls with High-Strength Materials

by Robert D. Devine, Steven M. Barbachyn, Yahya C. Kurama, and Ashley P. Thrall

This paper presents a numerical study that simulates the behavior of squat reinforced concrete (RC) shear walls with high-strength reinforcing steel and high-strength concrete. The finite element models are critically evaluated based on previous experiments of four deep-beam specimens and four squat shear-wall specimens with varied material strengths, base moment-to-shear ratios, and section shapes (rectangular and flanged). Monotonic lateral load analyses provided reasonable predictions of the peak lateral strength for squat walls tested under reversed-cyclic loading. However, reversed-cyclic models were necessary for more accurate predictions of the cyclic lateral load versus drift behavior, including cracking, stiffness degradation, lateral load-resistance mechanism, peak strength and corresponding drift, and energy dissipation. Importantly, the model predictions for specimens using high-strength materials were as good as or better than those using normal-strength materials with the same base moment-to-shear ratio. Thus, the use of higher-strength materials did not negatively impact the ability of the models to predict wall behavior.

Keywords: deep beams; high-strength concrete (HSC); high-strength steel reinforcement; low aspect ratio; nonlinear finite element modeling; shear design; shear walls; stocky walls.

INTRODUCTION

This paper presents the nonlinear finite element (FE) modeling and analysis of squat reinforced concrete (RC) shear walls (wall height-to-length aspect ratio, $h_w/l_w \leq 2.0$, where h_w is the wall height and l_w is the wall length) with high-strength concrete (HSC) and high-strength reinforcing steel (HSR). Structural design engineers often use code-based analytical methodologies and equations (for example, ACI 318-19 [ACI Committee 318 2019]) to approximate the initial lateral stiffness and strength of squat RC shear walls. While these analytical approaches were developed based on empirical data, numerous numerical and experimental studies have demonstrated significant scatter and often gross overpredictions of the wall stiffness and strength (Sozen and Moehle 1993; Farrar et al. 1993; ASCE 1994; Luna et al. 2015; Gulec and Whittaker 2011; Barbachyn et al. 2017a; Farvashany et al. 2008).

Compared with analytical methods, nonlinear numerical FE models can provide more reliable predictions for the lateral load behavior of squat RC shear walls. However, these models are much more complicated than closed-form analytical approaches and require significant engineering expertise. Guidelines for the nonlinear FE modeling of squat shear-wall structures with HSC and HSR based on measured test data are especially limited in the literature.

Toward developing this guidance, this paper presents the FE modeling and analysis of four deep-beam specimens that were tested under monotonic lateral loading and four squat shear-wall specimens that were tested under reversed-cyclic lateral loading (Devine et al. 2018, 2020; Barbachyn et al. 2020). Both monotonic and cyclic FE models were developed and compared with the measured data. The deep beam specimens were designed with reinforcement to represent the web regions of squat RC walls. The specimens used high-strength materials (HSM) with concrete compressive strength, f_c', of approximately 15 ksi (103 MPa) and specified reinforcement yield strength, f_{sy}, of 100 ksi (689 MPa; ASTM A1035/A1035M [2020] Grade 100 [690]), normal-strength materials (NSM; f_c' of approximately 6 ksi [41.4 MPa] and f_{sy} of 60 ksi [413 MPa; ASTM A706/A706M (2016) Grade 60 (420)]), and combinations of HSM and NSM.

RESEARCH SIGNIFICANCE

Squat RC shear walls are common primary lateral load-resisting members in low-rise buildings in seismic regions as well as in safety-related construction, such as buildings in nuclear power plants. The design of the shear walls is critical to the safety and cost-efficiency of these buildings. Squat RC walls stand to especially benefit from HSR and HSC because the lateral load design for these structures is governed mainly by strength, with reduced demands for ductility, which is compatible with the reduced strain capacities of HSM. The lateral load behavior of squat shear walls with HSM has been investigated experimentally. However, research on the numerical modeling of these structures is still limited. The current paper contributes to the knowledge base regarding: 1) monotonic pushover FE analyses, which are more commonly used for structural design purposes; and 2) reversed-cyclic analyses. Different from previous research focused mostly on the lateral strength, this paper evaluates the models for other important structural behaviors, such as the diagonal-cracking strength, load-deflection behavior up to peak load, and energy dissipation. Ultimately, comparisons between the numerical predictions and experimental data contribute to a deeper behavioral understanding and better numerical modeling of squat shear-wall structures with HSC and HSR.

ACI Structural Journal, V. 121, No. 5, September 2024.

MS No. S-2023-266.R3, doi: 10.14359/51740863, received March 28, 2024, and reviewed under Institute publication policies. Copyright © 2024, American Concrete Institute. All rights reserved, including the making of copies unless permission is obtained from the copyright proprietors. Pertinent discussion including author's closure, if any, will be published ten months from this journal's date if the discussion is received within four months of the paper's print publication.

BACKGROUND

Existing literature on the FE modeling of squat shear walls with HSC and/or HSR is limited. Iwashita et al. (1991) developed three-dimensional (3-D) nonlinear numerical models to predict the lateral strength and displacement capacity of squat flanged RC shear walls with HSR and HSC. These models used layered concrete shell elements, embedded isotropic reinforcing bar shell elements, and linear spring elements between the wall base and the foundation to simulate base rotation. The models provided accurate predictions for the lateral strength and corresponding drift, though the stiffness after shear-induced cracking was overpredicted.

Palermo and Vecchio (2003) developed concrete and steel constitutive material models for the numerical analysis of squat and slender RC walls using a compression-field analysis approach. These material models were verified (Palermo and Vecchio 2004) in monotonic and cyclic two-dimensional (2-D) FE analyses of two flanged squat wall test specimens, including HSR. The 2-D models, which significantly simplified the 3-D flanged wall footprint, provided accurate predictions for the lateral strength of the specimens, though failure was predicted at smaller displacements than measured. The monotonic pushover analyses provided reasonable results for lateral strength, but the cyclic analyses were more accurate in predicting the measured behavior.

Extensive investigations were conducted by Gulec et al. (2008, 2009) to predict the lateral strength of squat RC walls using 2-D FE analyses in VecTor2 (Wong et al. 2013). These studies evaluated both rectangular walls and walls with boundary members using databases of 120 rectangular wall specimens and 247 specimens with barbell or flanged cross sections, including walls with HSR. For most cases of the three types of wall geometries, the predicted lateral strengths were within 10% of the measured values (Gulec and Whittaker 2011).

Farvashany et al. (2008) developed 3-D FE models in Ansys to predict the lateral strength of squat RC shear walls with normal-strength concrete (NSC) and HSC. The results provided a mean test-to-predicted strength ratio of 1.02 for a database of 75 walls. Similar to other studies, the predicted displacement at failure was typically smaller than the measured displacement. Using this model, Farvashany (2017) analyzed the lateral strength of 243 simulated walls with varying concrete strength, height-length aspect ratio (h_w/l_w), applied axial load, and vertical and horizontal reinforcement ratios.

Syed and Gupta (2015) used FE models in Abaqus to investigate the seismic fragility of RC shear walls in nuclear power plants, focusing on uncertainties in material parameters. A study by Barbachyn et al. (2017a) was the first to systematically investigate the effectiveness of HSC and/or HSR in increasing the lateral strength of squat RC walls. In this study, which focused on walls with rectangular cross sections, a 2-D FE model in VecTor2 (Wong et al. 2013) was evaluated using a database of previously tested squat walls with HSM in the literature, providing a mean measured-to-predicted strength ratio of 0.97 for the data set. To evaluate the effects of HSC and HSR on the lateral strength of squat rectangular walls, Barbachyn et al. (2017a) conducted a parametric investigation using VecTor2 models of 64 non-nuclear building walls and 128 nuclear building walls with varied height, length, thickness, concrete strength, steel strength, vertical reinforcement ratio, and normalized base moment-to-shear ratio, $M_b/(V_b l_w)$, where M_b and V_b are the applied base moment and base shear, respectively.

Another numerical study by Barbachyn et al. (2017b) investigated the reduction in total reinforcing bar weight and total wall construction cost normalized by the lateral strength of squat rectangular RC shear walls, again determined by 2-D VecTor2 models. The parametric investigation included 1536 nuclear building shear walls and 768 non-nuclear building walls, varying the same aforementioned parameters and the ratio of horizontal reinforcement ratio to vertical reinforcement ratio.

Epackachi and Whittaker (2018) conducted a parametric study to investigate the effects of height-to-length aspect ratio, reinforcement ratio, and axial load on the lateral load behavior of lightly reinforced, squat shear walls using an FE model in LS-DYNA that was validated with data from 22 wall tests. Nagender et al. (2019) developed FE models of six RC walls with aspect ratios of 1, 1.25, and 1.5, studying stiffness reduction, lateral strength, ductility, failure pattern, and energy dissipation. Wang et al. (2022) developed a novel biaxial concrete FE model in Abaqus and validated it against a database of 32 RC wall test specimens with aspect ratios below 1.5. Petrone et al. (2021) implemented an FE-based model in OpenSees using novel isoparametric elements coupled with layered sections and a novel plane-stress plastic-damage concrete material model to simulate the in-plane nonlinear static and dynamic behavior of RC walls. This model was validated against experimental walls with aspect ratios varying between 0.4 and 2.3. More recently, Chandra and Teng (2022) developed a strut-and-tie model to predict the lateral strength of squat RC shear walls. This study used nonlinear FE analyses in ATENA to determine the depth of the compression zone at the bottom of the wall.

OVERVIEW OF FE MODELING

The structural analysis software ATENA-GiD (Version 5.7.0, Build 17436; Červenka et al. 2018) was used for the nonlinear FE analyses presented in this paper. The numerical predictions were compared with the measured behavior of four deep-beam specimens tested under monotonic lateral loading (Devine et al. 2018) and four shear-wall specimens tested under reversed-cyclic lateral loading (Barbachyn et al. 2020; Devine et al. 2020).

Deep-beam specimen model features

The 2-D FE models of the four deep beam test specimens (DB1, DB2, DB3, and DB4) described in Devine et al. (2018) were developed. Figure 1 depicts the test setup and model geometry. The beams featured combinations of NSM and HSM, as listed in Table 1. All the concrete material properties (elastic modulus E_c, compressive strength f_c', and tensile strength f_t) and reinforcing steel properties (elastic modulus E_s and yield strength f_y) are measured results from

materials testing performed according to ASTM International standards, as described in more detail in Devine (2020). All four beams had rectangular cross sections representative of slices from the length of a prototype squat shear wall and were designed with the same amount and layout of reinforcing bars. This facilitated direct comparisons of lateral load behavior among specimens for which material strengths were the only varied parameters. Reinforcing bars in the longitudinal direction (that is, the horizontal direction in the as-tested cantilever beam configuration) and transverse direction (that is, the vertical direction in the cantilever configuration) were uniformly distributed with a ratio of ρ_s = 0.83%. The specimens were loaded monotonically with a normalized base moment-to-shear ratio, $M_b/(V_b h_b)$, of 0.5, where h_b is the beam depth.

Different FE mesh sizes were investigated as part of a mesh refinement study, limiting the aspect ratio of the elements to 2:1 in all regions. A mesh with a target element size of approximately 1 x 1 in. (25.4 x 25.4 mm) was ultimately used in the nonlinear regions of the model, while larger elements (up to 4 in. [102 mm]) were used in the linear-elastic regions of the foundation to improve computational efficiency.

Table 1—Deep-beam material properties

Material property	DB1 (NSC/NSR)	DB2 (NSC/HSR)	DB3 (HSC/NSR)	DB4 (HSC/HSR)
E_c, ksi	6060	6040	7430	7270
f_c', ksi	7.28	6.91	14.6	15.3
f_t, ksi	0.451	0.514	1.03	0.862
E_s, ksi	27,400	28,100	27,400	28,100
f_y, ksi	69.0	132	69.0	132
ρ_s, %	0.83	0.83	0.83	0.83

Note: Ec is measured elastic modulus of concrete from 3 x 6 in. (76.2 x 152.4 mm) cylinders; f_c' is measured compressive strength of concrete from 3 x 6 in. (76.2 x 152.4 mm) cylinders; f_t is measured tensile strength of concrete from 3 x 6 in. (76.2 x 152.4 mm) cylinders; E_s is measured elastic modulus of primary vertical and horizontal reinforcement; f_y is measured yield strength of primary vertical and horizontal reinforcement; ρ_s is provided reinforcement ratio in vertical and horizontal directions; 1 ksi = 6.89 MPa.

Shear-wall specimen model features

FE models of the four shear-wall test specimens described in Barbachyn et al. (2020) and Devine et al. (2020) were developed. Even though these specimens were tested under reversed-cyclic lateral loading, analyses were conducted under monotonic and reversed-cyclic loading to investigate the ability of monotonic analyses to adequately predict behavior. This is important because monotonic analyses require significantly reduced computational time and, therefore, are easier to use in practice.

Figure 2 depicts the test setup and general model geometry for the rectangular (W1, W2, and W3) and flanged (W4F) walls. Table 2 lists the material properties for the specimens, with W1 featuring NSM and a reinforcement ratio of ρ_s = 1.8% for the primary vertical and horizontal bars, and W2, W3, and W4F using HSM with ρ_s = 0.83%. All the concrete and steel material properties are measured results from material testing (Devine 2020). The specimens were loaded with a base moment-to-shear ratio, $M_b/(V_b l_w)$, of 0.5 for W1 and W2 and 0.75 for W3 and W4F. Specimens W1, W2, and W3 included rectangular penetrations, while W4F was a solid wall with no penetrations.

Two-dimensional FE models were developed for the rectangular wall specimens W1, W2, and W3. The target mesh size within the wall region was selected as approximately 3 in. (76.2 mm) based on a mesh refinement study, recommendations from ATENA-GiD documentation (Kabele et al. 2010), and previous FE modeling studies of squat RC walls (Wong et al. 2013; Barbachyn et al. 2017a; Gulec 2009), while also limiting the aspect ratio of the elements to a maximum of 2. A 3-D FE model was developed for Specimen W4F to better capture the effect of the flanges. Only one-half of the specimen was modeled based on symmetry

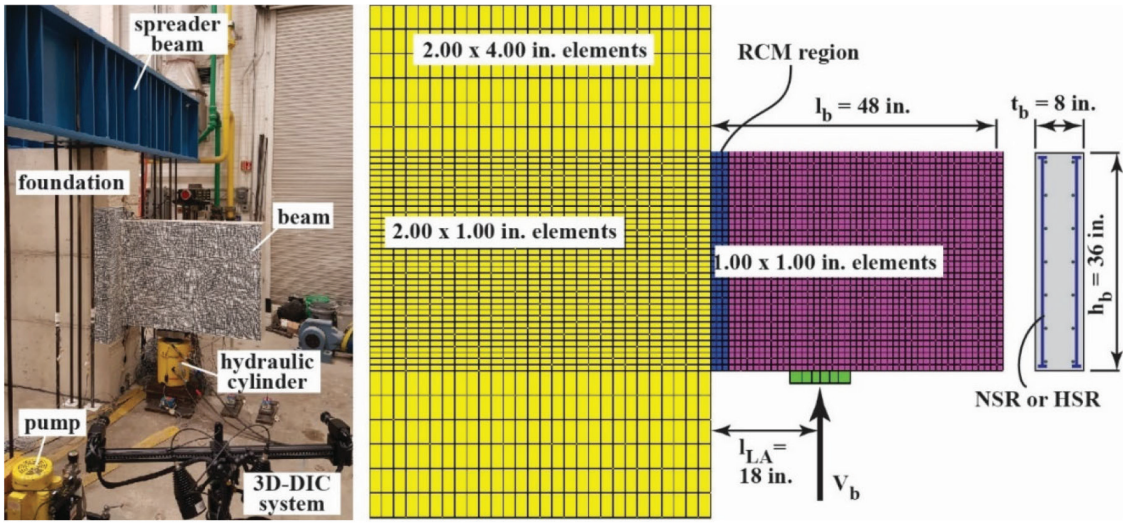


Fig. 1—Deep beam specimens: (a) test setup (adapted from Devine et al. [2018]); and (b) 2-D model geometry. (Note: 1 in. = 25.4 mm.)

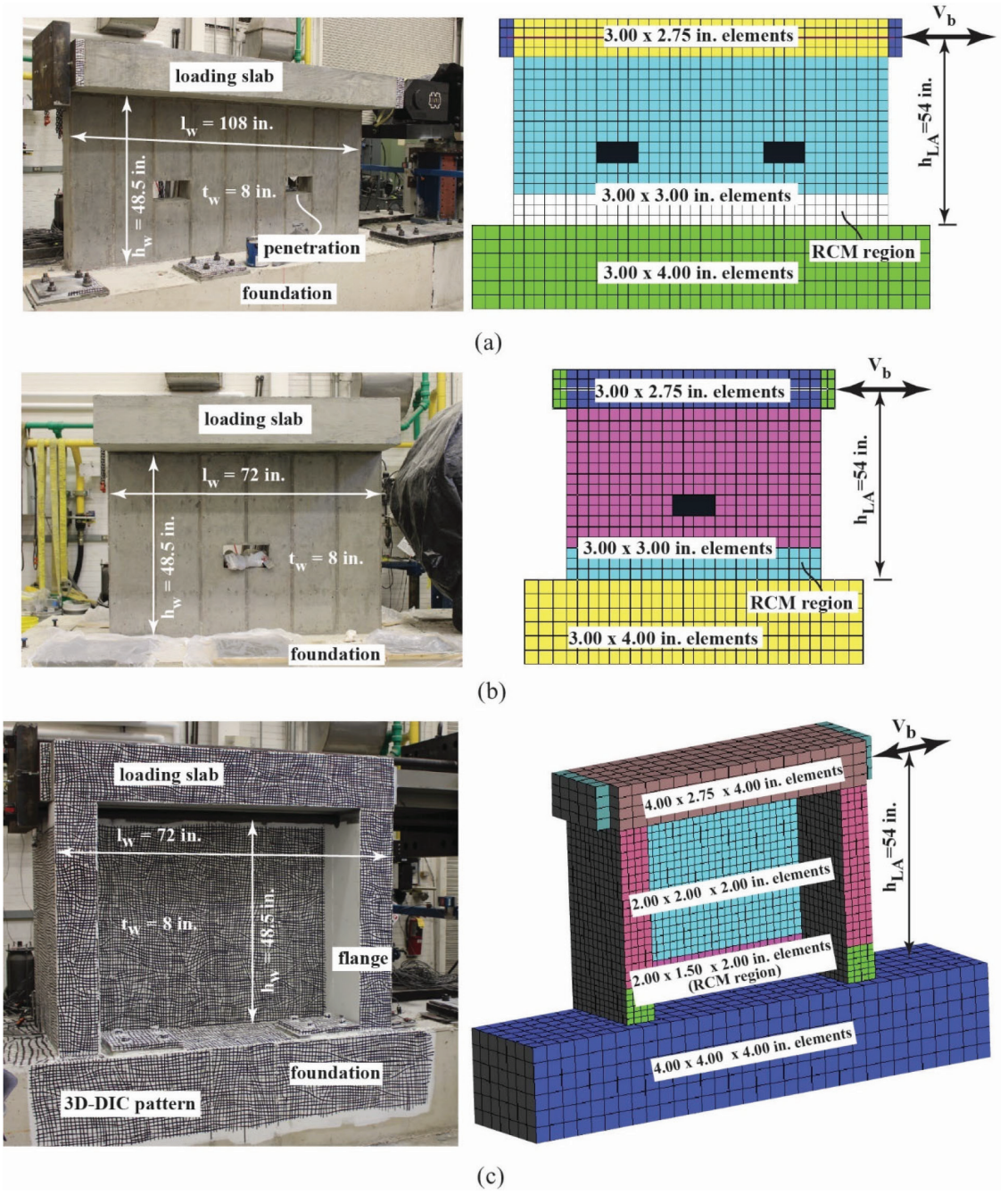


Fig. 2—(Left) Test setup (adapted from Devine et al. [2020] and Barbachyn et al. [2020]); and (right) model geometry: (a) W1 and W2; (b) W3; and (c) W4F. (Note: 1 in. = 25.4 mm.)

with respect to the vertical plane through the centerline of the wall web thickness to reduce computation expense. In the web and flange regions, the target mesh dimensions were approximately 2 in. (50.8 mm), while also limiting the aspect ratio of the elements to a maximum of 2 based on a mesh refinement study. Larger elements (up to 4 in. [102 mm]) were used in the foundation of all four wall specimens to improve computational efficiency.

Element types

All the models used isoparametric elements integrated with Gauss methods. The 2-D four-node quadrilateral plane-stress element type in ATENA-GiD was used to model the foundation, beam, wall, load application slab, and load application plates in the deep-beam and rectangular shear-wall specimens. To capture the behavior of the flanges, 3-D eight-node hexahedral brick elements with smeared reinforcement were used for the wall web and flanges in Specimen W4F. The reinforcing bars in the deep-beam and rectangular shear-wall specimens were modeled using discrete two-node one-dimensional (1-D) embedded truss elements. Assuming perfect bond, the reinforcement element nodes were embedded within the concrete elements by making their displacements kinematically dependent on the surrounding concrete element nodes. Geometric nonlinearity was incorporated in all the element types.

All the deep-beam and shear-wall specimens included a cold construction joint between the specimen and the

Table 2—Shear-wall material properties

Material property	W1 (NSC/NSR)	W2 (HSC/HSR)	W3 (HSC/HSR)	W4F (HSC/HSR)
E_c, ksi	6470	6970	6770	6540
f_c', ksi	6.95	14.8	14.2	14.0
f_t, ksi	0.832	1.10	1.04	1.12
E_s, ksi	27,300	28,200	28,200	28,100
f_y, ksi	72.5	122	122	125
ρ_s, %	1.8	0.83	0.83	0.83

Note: E_c is measured elastic modulus of concrete from 3 x 6 in. (76.2 x 152.4 mm) cylinders; f_c' is measured compressive strength of concrete from 3 x 6 in. (76.2 x 152.4 mm) cylinders; f_t is measured tensile strength of concrete from 3 x 6 in. (76.2 x 152.4 mm) cylinders; E_s is measured elastic modulus of primary vertical and horizontal reinforcement; f_y is measured yield strength of primary vertical and horizontal reinforcement; ρ_s is provided reinforcement ratio in vertical and horizontal directions; 1 ksi = 6.89 MPa.

foundation. However, interface elements (that is, elements that model contact interactions between two surfaces) were not included at the beam-to-foundation or wall-to-foundation joints of the models. This is because interface elements require significant calibration to provide accurate results and are not expected to be practical for engineers to use in design. As such, the models were not able to capture any base slip or gap opening behavior at beam-to-foundation or wall-to-foundation cold joints of the test specimens.

Boundary conditions and applied loads

The nodal displacements at the bottom of the foundation for each model were fixed in all directions. For the 3-D model of the flanged Specimen W4F, the nodal displacements on the vertical plane dividing the specimen in half through the web mid-thickness were also fixed in the out-of-plane direction to simulate the symmetric boundary provided by the other half of the specimen.

Each model included the self-weight of the RC and miscellaneous attachments to the specimen (for example, loading plates). In the wall models, the prestress forces in the horizontal actuator-to-specimen clamping rods were also included. However, the clamping of the specimen foundation to the laboratory strong floor was not modeled because the induced stresses were deemed unlikely to affect the beam or wall specimen behavior.

The monotonic and reversed-cyclic analyses were performed by prescribing displacements to a node at the center of the load application plate in each specimen. For the reversed-cyclic analyses, each shear-wall model was subjected to either 11 or 12 displacement cycles. The applied cycle displacements were adjusted to match the measured peak cycle drifts from each experiment (Devine 2020) at the location of the hydraulic actuator. Each peak target displacement was achieved in 20 analysis steps, resulting in a total of 80 steps in each reversed cycle. The default full Newton-Raphson solution method in ATENA-GiD (Červenka et al. 2018) was used to conduct the nonlinear analyses.

Table 3—Concrete material model parameters

Parameter	Value
Advanced tension parameters	
Fracture energy G_f, kip/in.	1.20×10^{-3}
Tension stiffening factor *TS*	0.05
Fixed/rotating crack coefficient, *FR*	1.0 for FCM regions; 0.0 for RCM regions
Maximum aggregate size d_{agg}, in.	0.5
Shear factor S_F	5
Crack spacing minimum cs_{min}, in.	5
Advanced compression parameters	
Stress at onset of nonlinear behavior f_{co}, ksi	$-2.1f_t$
*Strain at compressive strength ε_{cp}	–0.002 to –0.003 for NSC; –0.0025 to –0.0035 for HSC
Plastic strain at compressive strength ε_c^p	$\varepsilon_{cp} - f_c'/E_c$
Critical compression displacement w_d, in.	–0.0875 for NSC; –0.0425 for HSC
Compressive strength reduction limit factor due to cracking r_c	1.0
Other parameters	
Eccentricity	0.52
Return direction of plastic-flow multiplier β	0
Specific concrete material weight, lb/ft^3	145

*Value of ε_{cp} = –0.0025 was ultimately used for both NSC and HSC in this research.

Note: 1 ksi = 6.89 MPa; 1 kip = 4.45 kN; 1 in. = 25.4 mm; 1 lb/ft^3 = 16.0 kg/m^3.

MATERIAL MODELS

Linear-elastic material model properties

The foundations, load application plates, and shear-wall load application slabs behaved essentially in the linear-elastic range during the experiments. As such, these components were all modeled using the elastic-isotropic material models in ATENA-GiD. For steel, the elastic modulus, E_s, was defined as 29,000 ksi (199,948 MPa), and the Poisson's ratio was taken as 0.30. For concrete, the measured test day elastic modulus, E_c, was used (Barbachyn et al. 2020; Devine et al. 2020), with a Poisson's ratio of 0.20 (ATENA-GiD default for concrete).

Nonlinear concrete material model properties

The nonlinear fracture-plastic model in ATENA-GiD, which combines constitutive models for the compression (plastic) and tension (fracture) behavior of concrete, was used to model the concrete in the beam regions of the deep-beam specimens and web and flange regions of the shear-wall specimens. The compressive strength, f_c', and tensile strength, f_t, were taken as the measured specimen test day properties. Table 3 summarizes some of the other concrete material model input values (Devine 2020), with key parameters depicted in Fig. 3 (Červenka et al. 2018).

The concrete compression plasticity model in ATENA-GiD uses a failure surface (Menétrey and Willam 1995) defined by four parameters based on the experimental work of

van Mier (1986): 1) stress at which nonlinear behavior begins, f_{co}; 2) plastic strain at compressive strength, ε_c^p; 3) critical compression displacement, w_d; and 4) compressive strength reduction limit factor due to cracking, r_c. On the post-peak descending branch of the compression stress-strain curve, equivalent plastic strains are transformed into displacements through a crush-band length scale factor, which is characterized by the FE size. The critical compression displacement, w_d, quantifies the displacement at which the compression stress degrades to zero. The concrete plasticity model includes two additional parameters: 1) "eccentricity," which controls the shape of the concrete failure surface; and 2) the return direction of the plastic-flow multiplier, β, which controls the volumetric change of concrete during crushing.

The concrete fracture model in ATENA-GiD uses a smeared-crack formulation and crack-band model, where the cracking behavior is described by a Rankine failure criterion and exponential tension-softening model (Červenka et al. 2018). In concrete with reinforcement, tension stresses do not immediately degrade to zero upon cracking. Instead, the tension softening (that is, tension stress degradation after cracking) is controlled by the fracture energy, G_f, and tension-stiffening factor, *TS* (Hordijk 1991). To define the fracture behavior of concrete, four other material model parameters are defined: 1) fixed/rotating crack coefficient, *FR*; 2) maximum aggregate size, d_{agg}, for modeling aggregate interlock; 3) shear factor, S_F; and 4) crack spacing minimum, cs_{min}.

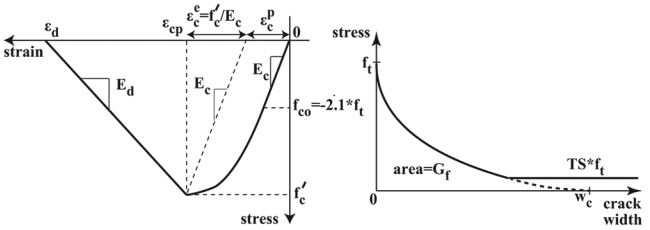


Fig. 3—Concrete model (adapted from Červenka et al. [2018]): (a) compression stress versus strain; and (b) tension stress versus crack opening.

A crack is formed in the model when the maximum principal stress in the concrete exceeds f_t. The fixed/rotated crack coefficient, *FR*, defines how the crack orientation changes with the principal stress directions. *FR* = 1.0 identifies a fixed-crack model (FCM) (Červenka 1985), where the orientation, or angle, of the cracks is set based on the maximum principal stress direction at crack initiation. As such, the principal stress directions in an element after cracking do not need to be orthogonal to the crack orientation, which requires shear stress transfer over the crack interface. *FR* = 0.0 identifies a rotating-crack model (RCM) (Vecchio and Collins 1986), where the orientation of opened cracks updates to coincide with the normal direction to the maximum principal stresses. In this case, no shear stress needs to be transferred across the crack interfaces.

Values of *FR* between 0 and 1 may be used, allowing cracks to rotate until a designated crack width, after which the crack orientation is fixed. In the models described in this paper, the FCM (that is, *FR* = 1.0) was used for each specimen, with the exception of the 9.00 in. (228.6 mm) height (calculated as, $h_{LA}/6$) and 3.00 in. (76.2 mm) length (calculated as, $l_{LA}/6$) directly adjacent to the foundation cold-joint interface of the shear-wall and deep beam models, respectively (RCM regions in Fig. 1 and 2). The shear-wall regions adjacent to the foundation cold-joint interface (that is, over a height of 9.00 in. [228.6 mm] at the wall base) were modeled with the RCM (that is, *FR* = 0) because preliminary cyclic analyses showed that the use of FCM elements at the wall base severely weakened the shear capacity of these regions and caused the models to predict considerably lower peak lateral strengths.

Nonlinear steel reinforcement material model properties

The reinforcing steel in the deep beam and shear-wall specimens was modeled using a multiline stress-strain law in ATENA-GiD, including linear-elastic, yield plateau, and strain-hardening regions. Figures 4(a) and (b) depict the measured and corresponding multilinear stress-strain models for selected normal-strength reinforcing steel (NSR) and HSR. Between five and seven points, not including the origin, were used to capture the measured behavior of the

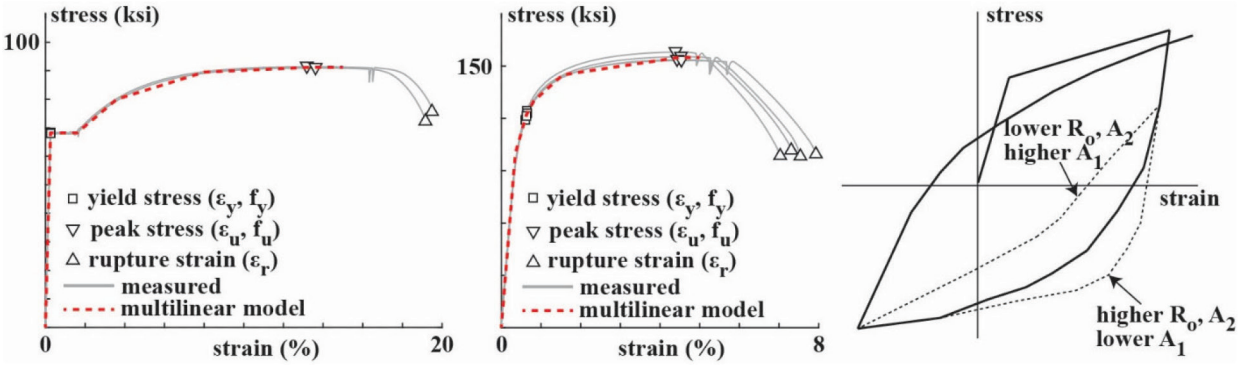


Fig. 4—Multilinear reinforcement models: (a) No. 4 Grade 60; (b) W2/W3 No. 4 Grade 100; and (c) hysteretic behavior (adapted from Červenka et al. [2018]). (Note: 1 ksi = 6.89 MPa.)

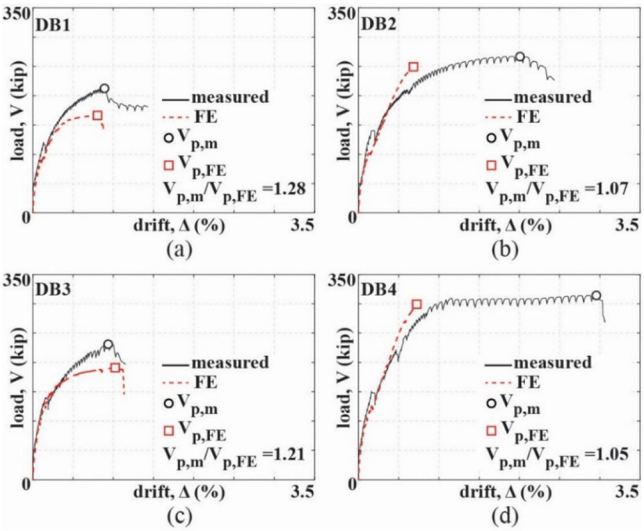


Fig. 5—Predicted and measured monotonic lateral load-drift behaviors: (a) DB1; (b) DB2; (c) DB3; and (d) DB4. (Note: 1 kip = 4.45 kN.)

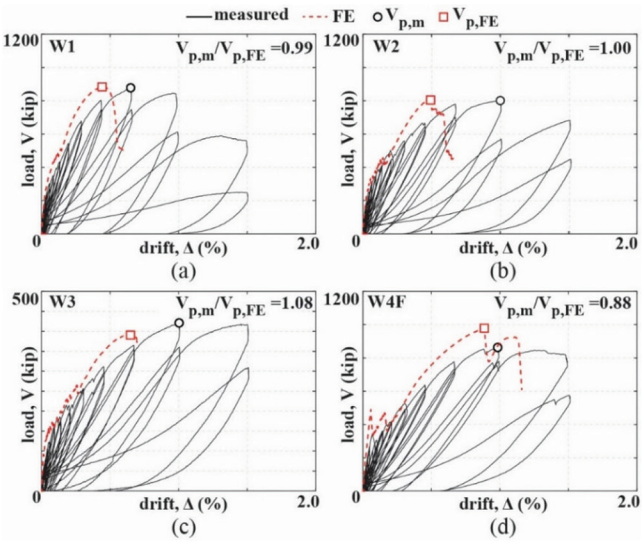


Fig. 6—Predicted monotonic and measured cyclic (first quadrant) lateral load-drift behaviors: (a) W1; (b) W2; (c) W3; and (d) W4F.

different reinforcement sizes, grades, and heat up to the peak stress point. For the 2-D models of the deep beams and rectangular shear walls, whose behaviors were predominately in-plane, no out-of-plane reinforcement (that is, crossties) was modeled. The out-of-plane crossties were modeled in the 3-D models of Specimen W4F. This reinforcement remained in the linear-elastic range because the out-of-plane deformations perpendicular to the wall web or flange were minimal.

For the cyclic models, the hysteretic behavior of the reinforcing steel, depicted in Fig. 4(c), was defined by three parameters in ATENA-GiD: R_o = 20, A_1 = 18.5, and A_2 = 0.15, based on Menegotto and Pinto (1973) and Filippou et al. (1983). The R_o parameter governs the initial shape of the curved transition of the steel stress-strain behavior between load reversals, and A_1 and A_2 control the modification of the R_o parameter with increased strain reversals.

The reinforcement in the deep beam and rectangular wall specimens was modeled as discrete reinforcing bars. The web and flange reinforcing bars in Specimen W4F were modeled as smeared reinforcement due to difficulties in attaining a convergent solution given the significant releases of energy from diagonal cracking when using discrete reinforcement. Specifically, the normalized shear stress at diagonal cracking was much greater in Specimen W4F (approximately $5\sqrt{f_c'}$) than in the other shear-wall specimens (ranging between $1.85\sqrt{f_c'}$ and $3.25\sqrt{f_c'}$). During an analysis step where diagonal cracking occurs, the FE model must redistribute the stresses to find an accurate state of equilibrium between the applied load and the internal concrete and reinforcement stress resultants. By using smeared reinforcement, the bar spacing was idealized as infinitely small, which allowed the reinforcement stresses to be determined at all concrete cracks instead of at discrete bar locations, improving numerical stability.

MONOTONIC ANALYSIS RESULTS

Figures 5 and 6 present the monotonic lateral load versus drift analysis results of the deep-beam and shear-wall specimens, respectively. Because the wall specimens were tested under reversed-cyclic lateral loading, only the first quadrant of the measured behavior of each wall (that is, the initial loading direction) was used to compare with the monotonic analysis result. As discussed earlier, the ability of the monotonic analyses to predict the behavior of the cyclically tested

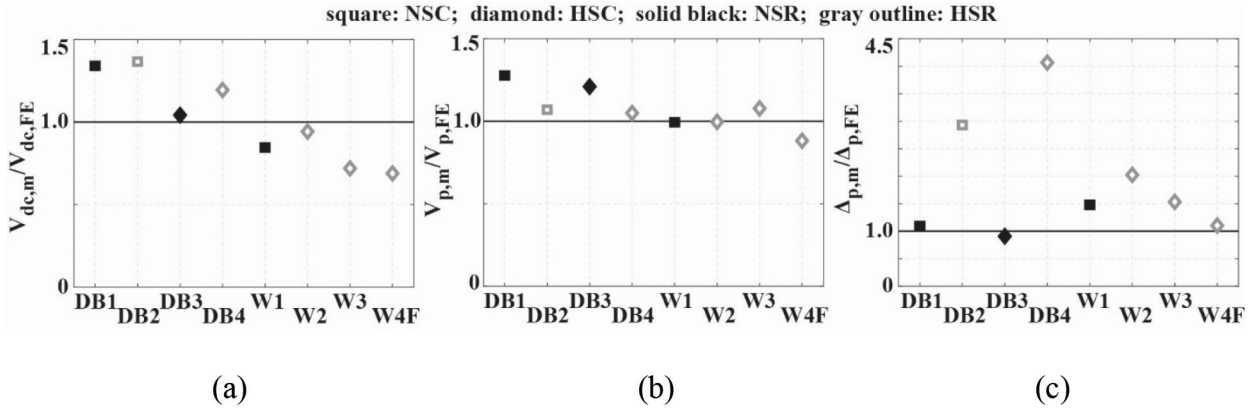


Fig. 7—Measured-to-predicted ratios for monotonic models: (a) $V_{dc,m}/V_{dc,FE}$; (b) $V_{p,m}/V_{p,FE}$; and (c) $\Delta_{p,m}/\Delta_{p,FE}$.

Table 4—Measured-to-predicted ratios for reversed-cyclic wall models

Specimen	$V_{dc,m}/V_{dc,FE}$		$V_{p,m}/V_{p,FE}$		$\Delta_{p,m}/\Delta_{p,FE}$	
	(+) Load	(–) Load	(+) Load	(–) Load	(+) Load	(–) Load
W1	0.88	0.83	1.07	1.06	1.00	1.00
W2	0.98	0.96	0.98	0.99	1.00	0.67
W3	0.80	0.86	1.09	1.03	1.00	1.00
W4F	0.85	0.98	0.94	1.01	1.01	1.06

Note: + is positive loading direction; – is negative loading direction.

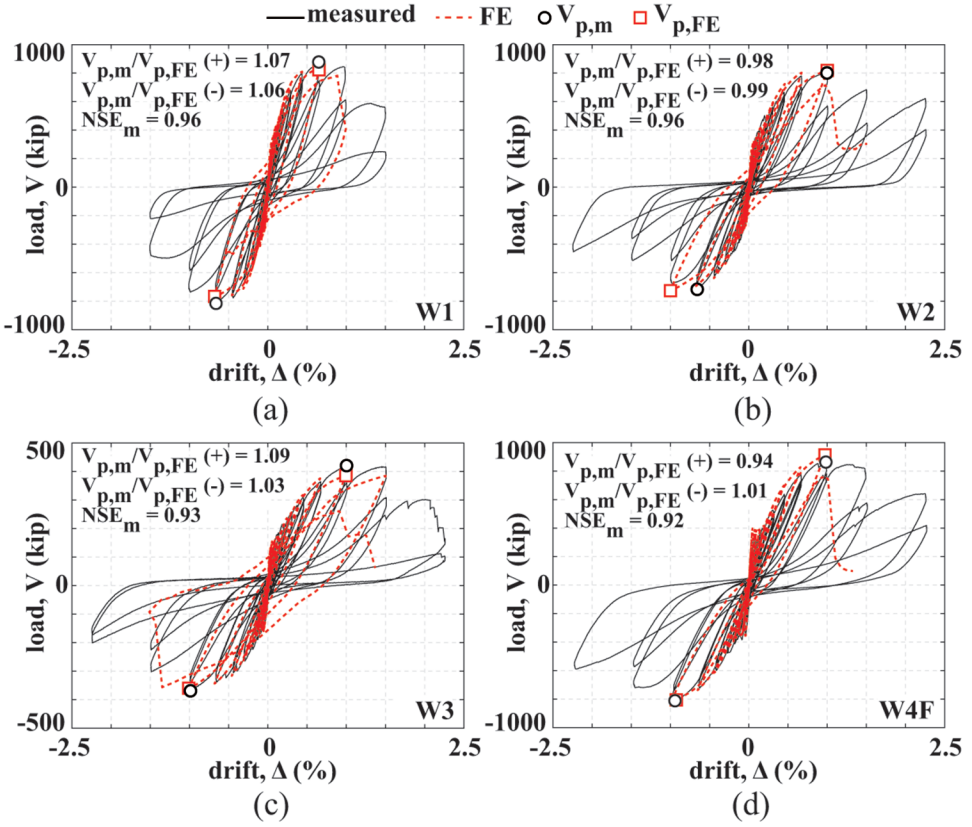


Fig. 8—Reversed-cyclic lateral load-drift behaviors: (a) W1; (b) W2; (c) W3; and (d) W4F. (Note: 1 kip = 4.45 kN.)

walls was evaluated because the simpler and computationally less-expensive monotonic analysis approach would be more useful in practice. The measured-to-predicted (subscripts *m* and *FE*, respectively) ratios for the diagonal-cracking strength V_{dc}, peak lateral strength V_p, and drift at peak lateral strength Δ_p, are shown in Fig. 7 and discussed as follows. A ratio greater than 1.0 indicates that the model underpredicted the measurement, while a ratio less than 1.0 indicates an overprediction.

Diagonal-cracking load

The numerical models provided reasonable simulations of the measured lateral load-drift behavior of the specimens up to diagonal cracking, with increasing deviations beyond this point. Diagonal cracking from each FE analysis was identified as when either: 1) a significant load drop occurred associated with concrete cracking away from the foundation interface; or 2) when the cracking pattern in the model qualitatively matched the measured 3-D digital image correlation (DIC) cracking pattern at initial diagonal cracking. The models generally showed more gradual cracking behavior rather than the sudden development of diagonal cracks in the experiments. As such, the selection of a specific diagonal-cracking load from the model results was subjective.

The predictions of diagonal-cracking load, V_{dc}, were: 1) conservative (that is, lower) for all the deep-beam specimens; and 2) unconservative by 5 to 30% ($V_{dc,m}/V_{dc,FE} = 0.69$ to 0.94) for all the shear-wall specimens, among which the best predictions were obtained for the rectangular Specimens W1 and W2 with $M_b/(V_b l_w) = 0.5$. The overprediction of the diagonal-cracking load for the wall specimens was likely related to the use of monotonic analyses to predict the results from reversed-cyclic tests, as demonstrated later by the cyclic analysis results of these specimens. In terms of the effect of HSC and HSR on the prediction of diagonal-cracking load, the results were as good or better when using HSM for specimens with the same base moment-to-shear ratio of $M_b/(V_b l_w) = 0.5$ (that is, all deep-beam specimens and rectangular wall Specimens W1 and W2). The incorporation of foundation interface elements with weakened tensile strength compared

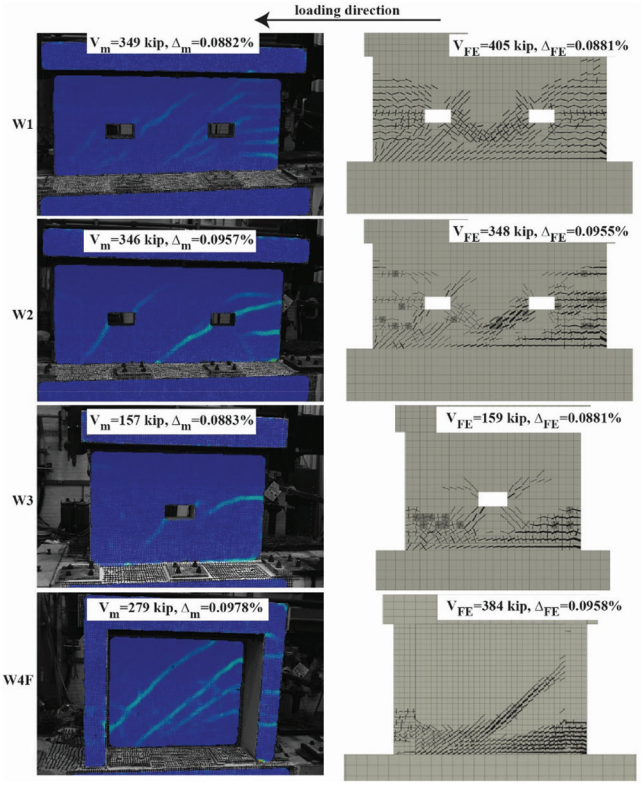


Fig. 9—Cracking comparisons for shear-wall specimens at target applied drift of Δ ≅ +0.09%: (a) 3-D DIC maximum principal strain measurements; and (b) reversed-cyclic FE model cracking patterns. (Note: 1 kip = 4.45 kN.)

to the surrounding concrete may improve the predictions of cracking behavior.

Peak lateral strength and corresponding drift

The predictions of peak lateral strength, V_p, were: 1) conservative (lower) for all the deep-beam specimens; 2) accurate for the rectangular wall specimens ($V_{p,m}/V_{p,FE}$ of 0.99, 1.00, and 1.08 for Specimens W1, W2, and W3, respectively); and 3) slightly unconservative for the flanged wall specimen ($V_{p,m}/V_{p,FE}$ = 0.88 for Specimen W4F). For the deep beam models, the peak lateral strength, V_p, prediction was more accurate and still conservative for Specimens DB2 and DB4 with HSR ($V_{p,m}/V_{p,FE}$ = 1.07 and 1.05, respectively) than Specimens DB1 and DB3 with NSR ($V_{p,m}/V_{p,FE}$ of 1.16 and 1.28, respectively). Overall, the monotonic FE analyses were able to provide reasonable predictions of peak lateral strength of all specimens with normal- or high-strength materials. These results support the use of monotonic FE analyses to determine the peak lateral strength for squat walls with varied normalized base moment-to-shear ratios, material strengths, and section footprints (that is, rectangular and flanged).

The drift at peak lateral strength, Δ_p, was mostly underpredicted, with the largest discrepancies for Specimens DB2 and DB4. Both of these specimens experienced significant slip displacements at the cold-joint interface and some slip across diagonal cracks prior to achieving V_p, which were not modeled. The underprediction of Δ_p for the shear walls was also likely because the monotonic models did not simulate the cyclic stiffness degradation that occurred during testing.

CYCLIC ANALYSIS RESULTS

Figure 8 compares the reversed-cyclic FE analysis results to the measured lateral load versus drift behaviors of the wall specimens. The measured-to-predicted ratios for the diagonal-cracking strength V_{dc}, peak lateral strength V_p, and drift at peak strength Δ_p, are provided in Table 4.

Diagonal-cracking load

Overall, the predictions from the reversed-cyclic models overestimated the measured diagonal-cracking load, V_{dc}, of all the shear-wall specimens but were much improved (with no $V_{dc,m}/V_{dc,FE}$ less than 0.80) compared to the monotonic pushover analysis results presented previously. In terms of the effect of HSC and HSR on the prediction of diagonal-cracking load, the results were much better for W2 with HSM than W1 with NSM and the same base moment-to-shear ratio of $M_b/(V_b l_w)$ = 0.5. Similar to the monotonic analyses, the incorporation of foundation interface elements with weakened tensile strength compared to the surrounding concrete may improve the predictions of cracking behavior.

Cracking prior to peak lateral strength

In Fig. 9, the cracking patterns of the numerical models are compared to the measured cracking patterns at a target applied drift level of Δ ≅ +0.09%, which was chosen as a consistent drift level after diagonal cracking in the test specimens. The lines within the FE model results indicate cracking, with thicker lines indicating wider cracks (the scale of line thickness in each model was kept the same). The measured cracking patterns were determined using 3-D DIC, as described in Barbachyn et al. (2020) and Devine et al. (2020), where warmer colors indicate larger principal tension strains and cracking.

Overall, the models were able to predict the cracking locations and directions of the specimens reasonably well. For example, the models were able to capture the larger crack widths in Specimen W2 as compared with narrower but more closely spaced cracks in Specimen W1. As described in Barbachyn et al. (2020), this important difference in cracking was because of the use of reduced volumes of HSR (ρ_s = 0.83%) in Specimen W2 compared to higher volumes of NSR (ρ_s = 1.8%) in Specimen W1, which were designed to achieve similar lateral strengths. Furthermore, the cracking patterns of Specimens W3 and W4F were generally captured, with isolated diagonal cracks in the web. For the flanged wall WF4, significant releases of energy from the cracking of the tension flange resulted in fluctuations in the lateral load versus drift curve in Fig. 8(d); similar erratic behavior can be seen in the monotonic curve in Fig. 6(d) as well. This was consistent with the greater fluctuation of measured load associated with flange cracking in Specimen WF4 as compared with the other walls. Due to the lack of a weak interface modeled at the wall-to-foundation cold joint, increased horizontal cracking was generally observed in the

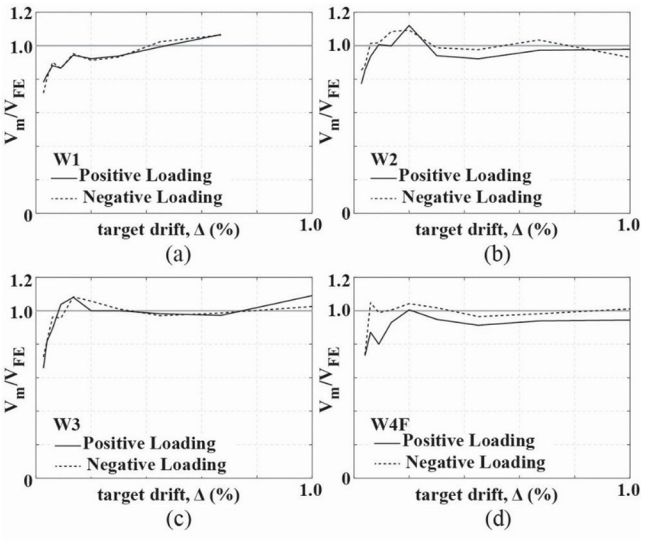


Fig. 10—Measured-to-predicted lateral load ratios at first cycle peaks for each displacement-controlled loading series up to $V_{p,m}$*: (a) W1; (b) W2; (c) W3; and (d) W4F.*

models above the wall-to-foundation interface compared to the experiments.

Loads prior to peak lateral strength

Figure 10 provides the measured-to-predicted lateral load ratio (V_m/V_{FE}) at the peak of the first cycle of each displacement-controlled series up to the peak lateral load, $V_{p,m}$, for all four wall specimens. The differences in V_m/V_{FE} between the positive (solid lines) and negative (dashed lines) loading directions were generally small. The results demonstrate that the models accurately captured the stiffness degradation and lateral loads at drift levels up to the peak lateral load. The largest variations were during the first applied drift (target drift $\Delta \cong 0.027\%$), where the models consistently overpredicted the lateral loads indicating generally larger simulated stiffnesses. As discussed previously, this was likely related to the lack of modeling of a weakened interface at the foundation cold-joint interface. With increasing drift, the model elements above the wall-to-foundation joint experienced cracking at increasing amounts, thus starting to better represent the stiffness degradation due to gap opening at the wall-to-foundation interface. This is evident by the improved V_m/V_{FE} with increased drift. In terms of the effect of HSC and HSR, the model predictions were, on average, better for W2 with HSM than W1 with NSM and the same base moment-to-shear ratio of $M_b/(V_b l_w) = 0.5$.

Peak lateral strength and corresponding drift

Critical for force-based designs, the peak lateral strength, V_p, of all four shear-wall specimens was accurately predicted (within 7%) in both loading directions. In terms of the effect of HSC and HSR on the prediction of peak lateral strength, the results were more accurate for W2 with HSM than W1 with NSM and the same base moment-to-shear ratio of $M_b/(V_b l_w) = 0.5$.

Additionally, the reversed-cyclic models accurately predicted the drift at peak load—that is, Δ_p—for all four specimens, which is an important improvement of the reversed-cyclic analyses as compared to the monotonic analyses. The only inaccurate prediction of Δ_p was for Specimen W2 (with HSM) in the negative loading direction, where the model predicted the peak load to be achieved in the subsequent cycle (that is, $\Delta_{p,FE} = -1.0\%$) than was observed in the experiment (that is, $\Delta_{p,m} = -0.67\%$). Because the measured lateral load at $\Delta = -1.0\%$ for Specimen W2 was very close to (within 6% of) the peak lateral strength, $V_{p,m}$, the one-cycle inaccuracy in Δ_p was deemed to be within reasonable variability of experimental testing of shear-critical RC structures. Overall, qualitative evaluation of all the cyclic lateral load versus drift behaviors presented in Fig. 8 demonstrates more accurate representations of the shear-wall specimen behaviors than the monotonic analysis results in Fig. 6.

Diagonal compression strut behavior

Figure 11 compares the measured minimum principal 3-D DIC strains (that is, maximum compression strains) at $\Delta_{p,m}$ in the positive loading direction with the minimum principal (that is, maximum compression) stresses at the same drift level of the FE models. The color scale for the maximum compression stresses is given in terms of the measured f_c' of each specimen to display the relative magnitude of the stresses within the diagonal compression struts. It is important to note that because significant concrete crushing had not occurred at this point during the analyses, the concrete minimum principal (maximum compression) strain patterns from the models were similar to the minimum principal stress patterns.

Overall, the FE models provided accurate estimates of the diagonal-compression struts, which demonstrates the ability of the models to capture the primary shear-dominant load-resistance mechanism of the specimens. The compression stresses in Specimen W1 were larger in proportion to f_c' than in W2, which matched the observed increased concrete damage in W1 at the point of V_p. Additionally, the models captured the larger compression strut width surrounding the left penetration in W1 than in W2.

For Specimen W3, the model captured the shape of the compression strut and compression region at the left toe of the wall. Furthermore, the models accurately depicted that the largest concrete compression stresses occurred in Specimen W4F compared to the other specimens with HSC and were located at the web-to-flange intersection, where damage typical of diagonal-compression failure manifested. These increased stresses were in the same location as the largest measured compression strains from 3-D DIC.

Compression flange behavior of Specimen W4F

Figure 12 compares the measured out-of-plane displacements of the compression flange (that is, displacements normal to the flange face and in line with the web) using 3-D DIC to those from the 3-D FE model of Specimen W4F at $+\Delta_{p,m}$. The FE model results have been mirrored on the web centerline to provide a full flange view. Two reference heights are also shown at $h_{LA}/6$ (9.00 in. [228.6 mm]) and $h_{LA}/2$ above the wall-to-foundation interface.

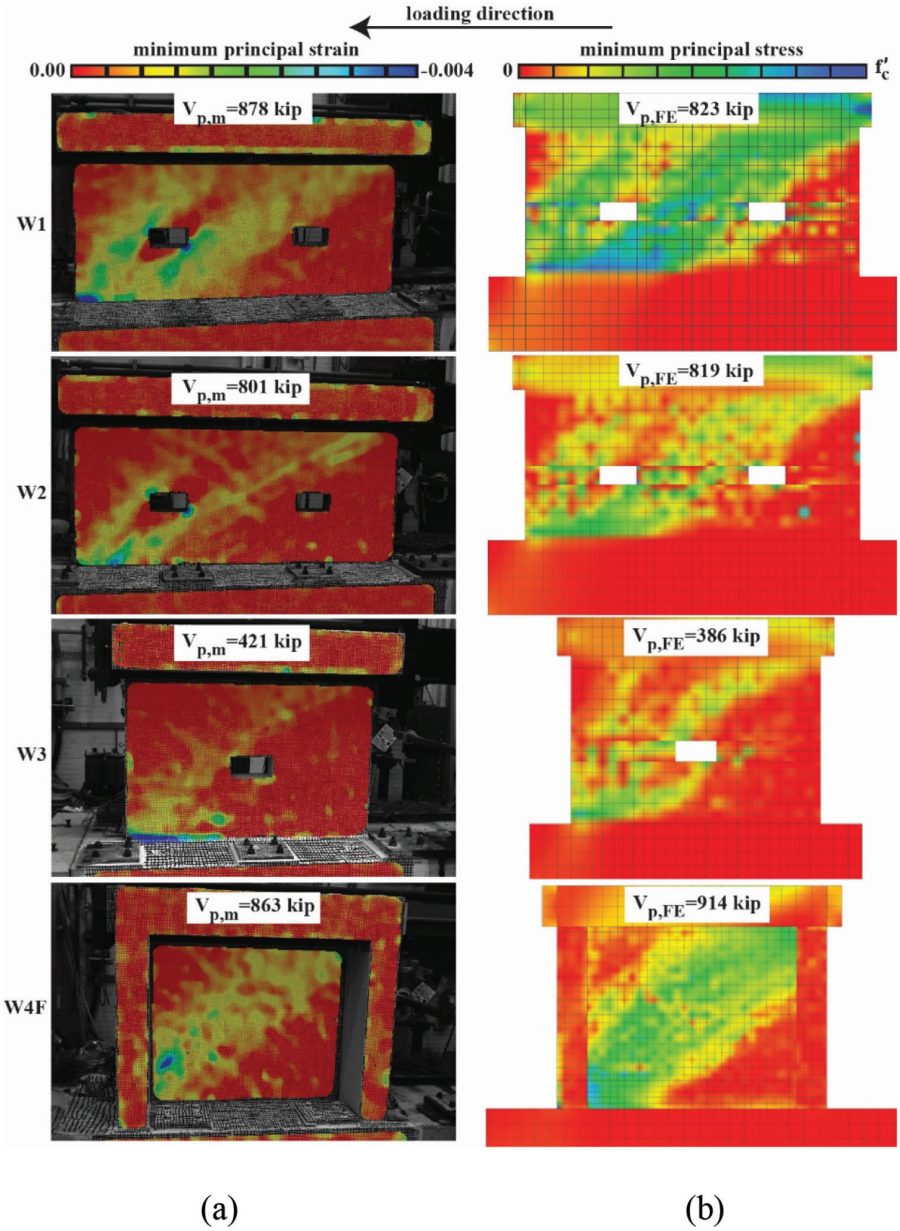


Fig. 11—Compression strut comparisons at peak lateral load: (a) 3-D DIC minimum principal strain measurements; and (b) FE model minimum principal stresses. (Note: Cooler colors indicate larger compression strains in (a) and stresses in (b) [full-color PDF can be accessed at www.concrete.org]; 1 kip = 4.45 kN.)

The model underestimated the out-of-plane displacements of the flange near the wall base. This was due to the assumed fixed-base condition in the model, compared to the experiment where base slip and uplift at the cold joint increased the out-of-plane displacements of the flange. Again, the use of interface elements at the wall-to-foundation cold joint may improve these predictions. While the magnitude of the displacements was underpredicted, the model captured the general out-of-plane bulging of the flange, as shown by the gradient of displacements increasing from the flange ends to the web centerline. This is evident at $h_{LA}/6$ above the wall-to-foundation interface, where the color scheme in Fig. 12 transitions from dark blue at the flange end (that is, smaller displacements) to light blue at the web centerline (that is, larger displacements).

Cyclic behavior and energy dissipation

Table 5 evaluates the cyclic behavior and energy dissipation of the FE models up to the peak lateral load, V_p (that is, up to and including the Δ_p drift cycle) of each wall specimen using the following three accuracy metrics: 1) Nash-Sutcliffe efficiency, *NSE* (Nash and Sutcliffe 1970); 2) energy error, ED_e; and 3) a modified Nash-Sutcliffe efficiency, *NSE'* (Pozo et al. 2020).

The *NSE* is a statistical measure that determines the relative magnitude of the residual variance as compared to the variance of the measured data. This metric was computed using the lateral load versus drift data from the first cycle of all displacement-controlled load series up to and including Δ_p per Eq. (1)

Table 5—Reversed-cyclic model accuracy metrics

Metric	W1	W2	W3	W4F	Mean
NSE	0.96	0.96	0.94	0.94	0.95
ED_e	0.14	0.08	0.19	0.20	0.15
NSE′	0.96	0.96	0.93	0.92	0.94

$$NSE = 1 - \frac{\sum_{i=1}^{n}(V_{i,m} - V_{i,FE})^2}{\sum_{i=1}^{n}(V_{i,m} - \overline{V_{i,m}})^2} \quad (1)$$

where $V_{i,m}$ is the measured lateral load at ith value of the drift data; n is the total number of data points; $V_{i,FE}$ is the predicted load at the same drift level; and $\overline{V_{i,m}}$ is the average measured load for the whole data set. The *NSE* metric can range from $-\infty$ to 1.00, with 1.00 indicating perfect agreement of the predictions with the measured behavior.

The energy error, ED_e, was calculated per Eq. (2)

$$ED_e = \left|\frac{ED_{t,m} - ED_{t,FE}}{ED_{t,m}}\right| \quad (2)$$

where $ED_{t,m}$ is the measured total energy dissipated (calculated as the sum of the areas enclosed by the lateral load versus displacement hysteresis loops) considering the first cycles of the displacement-controlled loading series in the experiments; and $ED_{t,FE}$ is the total energy dissipated considering the corresponding hysteresis loops in the numerical model, up to and including the Δ_p drift cycle. ED_e represents the percent error difference between the measured total energy dissipation and the numerical model prediction. An ED_e value of 0 indicates perfect agreement of the predicted total energy dissipation with the measured behavior.

Finally, the *NSE′* metric, developed by Pozo et al. (2020) to overcome the limitations of using *NSE* and ED_e alone, was evaluated per Eq. (3) and (4)

$$NSE' = NSE - ED_{ef} \quad (3)$$

$$ED_{ef} = \min\left(0.15, 65e^{-10(1-ED_e)} - 0.00295\right) \quad (4)$$

where ED_{ef} is an energy error factor. According to Pozo et al. (2020), $NSE' > 0.95$ is indicative of good agreement between numerical and experimental hysteretic load-drift behaviors, while the match is satisfactory for $0.95 > NSE' > 0.85$, unsatisfactory for $0.85 > NSE' > 0.75$, and poor for $NSE' < 0.75$. Based on this classification, the *NSE′* values for Specimens W1 and W2 were greater than 0.95, indicating a good match of the model behaviors with the corresponding experimental measurements, regardless of material strengths. The *NSE′* metrics for Specimens W3 and W4F were classified as satisfactory, indicating that the models did not predict the behaviors of these specimens with $M_b/(V_b l_w) = 0.75$ as well as Specimens W1 and W2 with $M_b/(V_b l_w) = 0.5$.

To further investigate the modeling accuracy of energy dissipation, the cumulative energy dissipation ratio, $ED_c/ED_{t,m}$, was determined at each target applied drift up to and including Δ_p for both the experiments and the models, where ED_c is the cumulative energy dissipated up to and including the specified target drift cycle. The solid lines in Fig. 13

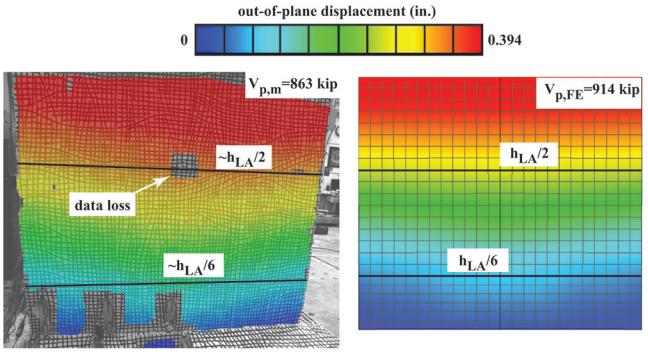


Fig. 12—Out-of-plane displacements (that is, perpendicular to flange face) of compression flange at $+\Delta_{p,m}$: (a) 3D DIC; and (b) FE model. (Note: Warmer colors indicate larger displacements [full-color PDF can be accessed at www.concrete.org]. 1 kip = 4.45 kN; 1 in.= 25.4 mm.)

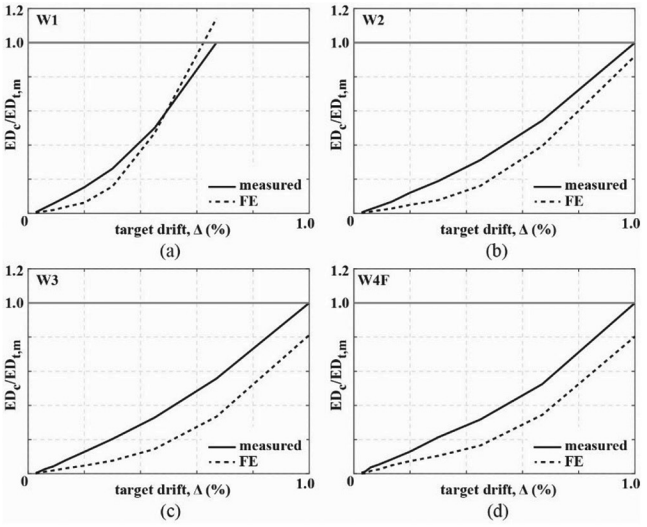


Fig. 13—Cumulative energy dissipation comparisons: (a) W1; (b) W2; (c) W3; and (d) W4F.

represent the cumulative measured energy dissipation ratio $ED_{c,m}/ED_{t,m}$, whereas the dashed lines represent the cumulative FE model energy dissipation ratio, $ED_{c,FE}/ED_{t,m}$. All the solid lines end with a value of 1.0 because the cumulative measured energy dissipation, $ED_{c,m}$, at $\Delta_{p,m}$ is equal to the total dissipation, $ED_{t,m}$. Drifts where the solid line is above the dashed line indicate that at that drift level, the experimental specimen had dissipated more cumulative energy than that predicted by the numerical model.

The results in Fig. 13 show that for Specimen W1 with NSC and NSR, the total energy dissipation at Δ_p was overpredicted, whereas the energy dissipation was underpredicted for Specimens W2, W3, and W4F. For all four wall specimens, the models typically underestimated the energy dissipation in the early cycles, but the relative discrepancies were reduced during the larger drift cycles. The models overpredicted the energy dissipation of Specimens W1 and W2 during the final cycle to Δ_p, which compensated for the underpredictions during the earlier drift cycles, leading to more accurate predictions of the total energy dissipation (that

is, smaller ED_e) for these specimens. For Specimens W3 and W4F, the energy dissipation was more accurately predicted during the larger drift cycles compared to Specimens W1 and W2, which led to larger underpredictions of the total energy dissipation (that is, larger ED_e), as the underpredictions during the smaller drift cycles were not compensated.

SUMMARY AND CONCLUSIONS

The following conclusions and recommendations are made from the nonlinear finite element (FE) modeling study of the behavior of four deep beam and four squat shear-wall test specimens described in this paper. Note that these conclusions may be limited to the tested specimens and their property ranges (for example, material strengths and base moment-to-shear ratios) used in the comparisons, as well as the FE model features in the ATENA-GiD software.

1. Monotonic lateral load analyses can be used to determine reasonably accurate predictions of the peak lateral strength for squat walls with varied base moment-to-shear ratios, material strengths, and section footprints (that is, rectangular and flanged).

2. As a limitation, monotonic analyses overpredicted the diagonal-cracking strength and underpredicted the drift at peak lateral load. These behaviors are generally difficult to model in squat reinforced concrete (RC) walls due to their shear-dominant load-resistance mechanism.

3. Reversed-cyclic models are recommended for improved analyses of squat RC shear walls, as these models provided more accurate predictions of the cyclic lateral load versus drift behavior, including cracking, stiffness degradation, lateral load-resistance mechanism, peak strength and corresponding drift, and energy dissipation of the test specimens.

4. The model results were as good or better when using high-strength materials (HSM) for specimens with the same base moment-to-shear ratio. Thus, the use of higher-strength materials did not negatively impact the ability of the models to predict wall behavior. This is important because most prior work on the numerical modeling of squat shear walls was conducted for normal-strength materials (NSM).

5. Qualitatively, the reversed-cyclic models accurately captured the differences in cracking behavior and diagonal-compression strut behavior between the wall specimens with different material strengths and section shapes.

6. The out-of-plane flange displacements measured in Specimen W4F were captured by the three-dimensional (3-D) model of the specimen. This may have implications for practicing engineers who need to predict the behavior of intersecting walls in 3-D.

It is hypothesized that many of the identified model limitations related to cracking behavior may be improved by incorporating discrete contact interface elements at the foundation cold joint where gap and slip displacements developed in the test specimens. Interface elements were not included in the current models and they are not expected to be preferred by practicing engineers, because not incorporating interface elements resulted in considerably simpler models.

AUTHOR BIOS

ACI member **Robert D. Devine** *is an Associate III at Wiss, Janney, Elstner Associates, Inc. When this research was performed, he was a PhD Student at the University of Notre Dame, Notre Dame, IN, where he received his BS in civil engineering in 2015. He is a member of ACI Committees 349, Concrete Nuclear Structures; 363, High-Strength Concrete; and 564, 3-D Printing with Cementitious Materials; Joint ACI-ASCE Committee 445, Shear and Torsion; and Joint ACI-ASCE Subcommittee 445-B, Shear & Torsion-Seismic Shear. His research interests include novel reinforced concrete design and sustainable concrete construction practices.*

ACI member **Steven M. Barbachyn** *is a Research Scientist and the Manager of the Theodore V. Galambos Structural Engineering Laboratory and Multi-Axial Subassemblage Testing (MAST) Laboratory at the University of Minnesota, Minneapolis, MN. When this research was performed, he was a Postdoctoral Research Associate at the University of Notre Dame, where he received his MS and PhD in civil engineering in 2011 and 2019, respectively. His research interests include the seismic behavior, analysis, and design of reinforced concrete structures.*

ACI member **Yahya C. Kurama** *is a Professor of civil engineering at the University of Notre Dame. He is a member of ACI Committees 374, Performance-Based Seismic Design of Concrete Buildings, and 555, Concrete with Recycled Materials; and Joint ACI-ASCE Committee 550, Precast Concrete Structures. His research interests include the behavior and design of reinforced concrete structures under extreme loading from earthquakes and fire, sustainable construction, and precast/prestressed concrete.*

ACI member **Ashley P. Thrall** *is the Myron and Rosemary Noble Associate Professor of Structural Engineering at the University of Notre Dame. She received her MSE and PhD in civil and environmental engineering from Princeton University, Princeton, NJ, in 2008 and 2011. She is a member of ACI Committee 564, 3-D Printing with Cementitious Materials, and Joint ACI-ASCE Committee 550, Precast Concrete Structures. Her research interests include modular, deployable, and rapidly erectable structures.*

ACKNOWLEDGMENTS

This work was supported by the Advanced Methods for Manufacturing (NEET-1) Program of the U.S. Department of Energy (DOE) under Award No. DE-NE0008432. The authors gratefully acknowledge the support of Federal Points of Contact, T. Selekler and A. Hahn, and Technical Points of Contact, B. Landrey and J. Lance, of the NEET-1 Program. This material is based upon work supported under a DOE Integrated University Program Graduate Fellowship, Award No. NE0008363. Collaborators S. Sanborn and J. Hogancamp of Sandia National Laboratories and M. Van Liew of AECOM are gratefully acknowledged. Any opinions, findings, conclusions, or recommendations expressed in the paper are those of the authors and do not necessarily reflect the views of the DOE Office of Nuclear Energy, DOE staff, or individuals or other organizations acknowledged.

NOTATION

A_1	=	hysteretic model parameter for reinforcing steel
A_2	=	hysteretic model parameter for reinforcing steel
cs_{min}	=	concrete crack spacing minimum
d_{agg}	=	maximum concrete aggregate size
E_c	=	concrete elastic modulus
ED_c	=	cumulative energy dissipated up to and including specified drift cycle
ED_e	=	energy error
ED_{ef}	=	energy error factor
ED_t	=	total energy dissipated considering all drift cycles up to and including Δ_p
E_s	=	steel elastic modulus
FR	=	fixed/rotating crack coefficient
f_c'	=	concrete compressive strength
f_{co}	=	concrete compression stress at onset of nonlinear behavior
f_{sy}	=	specified reinforcement yield strength
f_t	=	concrete tensile strength
f_y	=	measured reinforcement yield strength
G_f	=	concrete fracture energy
h_b	=	beam depth
h_{LA}	=	wall height from foundation to lateral load application point
h_w	=	wall height
l_{LA}	=	beam length from foundation to lateral load application point
l_w	=	wall length
M_b	=	base moment
NSE	=	Nash-Sutcliffe efficiency

NSE' = modified Nash-Sutcliffe efficiency
R_o = hysteretic model parameter for reinforcing steel
r_c = compressive strength reduction limit factor due to cracking of concrete
S_F = shear factor for concrete in tension
TS = concrete tension-stiffening factor
V_b = base shear
V_{dc} = diagonal-cracking strength
Vi = ith value of lateral load data
V_p = peak lateral strength
w_d = concrete critical compression softening displacement
β = return direction of plastic-flow multiplier for concrete in compression
Δ_p = drift at peak lateral strength
ε_{cp} = concrete strain at compressive strength
ε_c^p = concrete plastic strain at compressive strength

REFERENCES

ACI Committee 318, 2019, "Building Code Requirements for Structural Concrete (ACI 318-19) and Commentary (ACI 318R-19) (Reapproved 2022)," American Concrete Institute, Farmington Hills, MI, 624 pp.

ASCE, 1994, "Stiffness of Low Rise Reinforced Concrete Shear Walls," American Society of Civil Engineers, Reston, VA, 196 pp.

ASTM A706/A706M-16, 2016, "Standard Specification for Deformed and Plain Low-Alloy Steel Bars for Concrete Reinforcement," ASTM International, West Conshohocken, PA, 7 pp.

ASTM A1035/A1035M-20, 2020, "Standard Specification for Deformed and Plain, Low-Carbon, Chromium, Steel Bars for Concrete Reinforcement," ASTM International, West Conshohocken, PA, 7 pp.

Barbachyn, S. M.; Devine, R. D.; Thrall, A. P.; and Kurama, Y. C., 2017a, "Effect of High-Strength Materials on Lateral Strength of Stocky Reinforced Concrete Walls," *ACI Structural Journal*, V. 114, No. 4, July-Aug., pp. 923-936. doi: 10.14359/51689722

Barbachyn, S. M.; Devine, R. D.; Thrall, A. P.; and Kurama, Y. C., 2017b, "Economic Evaluation of High-Strength Materials in Stocky Reinforced Concrete Shear Walls," *Journal of Construction Engineering and Management*, ASCE, V. 143, No. 10, Oct., p. 04017074. doi: 10.1061/(ASCE)CO.1943-7862.0001377

Barbachyn, S. M.; Devine, R. D.; Thrall, A. P.; and Kurama, Y. C., 2020, "Behavior of Nuclear RC Shear Walls Designed for Similar Lateral Strengths Using Normal-Strength versus High-Strength Materials," *Journal of Structural Engineering*, ASCE, V. 146, No. 11, Nov., p. 04020252. doi: 10.1061/(ASCE)ST.1943-541X.0002818

Červenka, V., 1985, "Constitutive Model for Cracked Reinforced Concrete," *ACI Journal Proceedings*, V. 82, No. 6, Nov.-Dec., pp. 877-882.

Červenka, V.; Jendele, L.; and Červenka, J., 2018, "ATENA Program Documentation: Part 1: Theory," Červenka Consulting s.r.o., Prague, Czech Republic.

Chandra, J., and Teng, S., 2022, "Simplified Strut-and-Tie Model for Shear Strength Prediction of Reinforced Concrete Low-Rise Walls," *ACI Structural Journal*, V. 119, No. 2, Mar., pp. 61-74. doi: 10.14359/51734330

Devine, R. D., 2020, "Prefabricated High-Strength Headed Steel Reinforcement with High-Strength Concrete for Accelerated Construction of Shear Walls in Nuclear Structures," PhD dissertation, Department of Civil and Environmental Engineering and Earth Sciences, University of Notre Dame, Notre Dame, IN, 645 pp.

Devine, R. D; Barbachyn, S. M.; Thrall, A. P.; and Kurama, Y. C., 2018, "Experimental Evaluation of Deep Beams with High-Strength Concrete and High-Strength Reinforcing Bar," *ACI Structural Journal*, V. 115, No. 4, July, pp. 1023-1036. doi: 10.14359/51702229

Devine, R. D.; Barbachyn, S. M.; Thrall, A. P.; and Kurama, Y. C., 2020, "Effect of Aspect Ratio, Flanges, and Material Strength on Squat Reinforced Concrete Shear Walls," *ACI Structural Journal*, V. 117, No. 5, Sept., pp. 283-300. doi: 10.14359/51725845

Epackachi, S., and Whittaker, A. S., 2018, "A Validated Numerical Model for Predicting the In-Plane Seismic Response of Lightly Reinforced, Low-Aspect Ratio Reinforced Concrete Shear Walls," *Engineering Structures*, V. 168, Aug., pp. 589-611. doi: 10.1016/j.engstruct.2018.04.025

Farrar, C. R.; Reed, J. W.; and Salmon, M. W., 1993, "Failure Modes of Low-Rise Shear Walls," *Journal of Energy Engineering*, ASCE, V. 119, No. 2, Aug., pp. 119-138. doi: 10.1061/(ASCE)0733-9402(1993)119:2(119)

Farvashany, F. E., 2017, "Parametric Studies on Reinforced Concrete Shear Walls: An Engineering Response to Einstein's Riddle?" *ACI Structural Journal*, V. 114, No. 5, Sept.-Oct., pp. 1099-1108. doi: 10.14359/51700777

Farvashany, F. E.; Foster, S. J.; and Rangan, B. V., 2008, "Strength and Deformation of High-Strength Concrete Shearwalls," *ACI Structural Journal*, V. 105, No. 1, Jan.-Feb., pp. 21-29.

Filippou, F. C.; Popov, E. P.; and Bertero, V. V., 1983, "Effects of Bond Deterioration on Hysteretic Behavior of Reinforced Concrete Joints," Report No. UCB/EERC-83/19, Earthquake Engineering Research Center, University of California, Berkeley, Berkeley, CA, 212 pp.

Gulec, C. K., 2009, "Performance-Based Assessment and Design of Squat Reinforced Concrete Shear Walls," PhD dissertation, State University of New York at Buffalo, Buffalo, NY, 719 pp.

Gulec, C. K., and Whittaker, A. S., 2011, "Empirical Equations for Peak Shear Strength of Low Aspect Ratio Reinforced Concrete Walls," *ACI Structural Journal*, V. 108, No. 1, Jan.-Feb., pp. 80-89.

Gulec, C. K.; Whittaker, A. S.; and Stojadinovic, B., 2008, "Shear Strength of Squat Rectangular Reinforced Concrete Walls," *ACI Structural Journal*, V. 105, No. 4, July-Aug., pp. 488-497.

Gulec, C. K.; Whittaker, A. S.; and Stojadinovic, B., 2009, "Peak Shear Strength of Squat Reinforced Concrete Walls with Boundary Barbells or Flanges," *ACI Structural Journal*, V. 106, No. 3, May-June, pp. 368-377.

Hordijk, D. A., 1991, "Local Approach to Fatigue of Concrete," doctoral dissertation, Delft University of Technology, Delft, the Netherlands, 216 pp.

Iwashita, K.; Ishimura, K.; Kurihara, K.; and Imai, M., 1991, "Study on Reactor Building Structure Using Ultrahigh Strength Materials: Part 5: Nonlinear Analysis of RC Shear Wall," *Transactions of the 11th International Conference on Structural Mechanics in Reactor Technology (SMiRT 11)*, Tokyo, Japan, pp. 383-388.

Kabele, P.; Červenka, V.; and Červenka, J., 2010, "ATENA Program Documentation: Part 8: User's Manual for ATENA-GiD Interface," Červenka Consulting s.r.o., Prague, Czech Republic.

Luna, B. N.; Rivera, J. P.; and Whittaker, A. S., 2015, "Seismic Behavior of Low-Aspect-Ratio Reinforced Concrete Shear Walls," *ACI Structural Journal*, V. 112, No. 5, Sept.-Oct., pp. 593-604. doi: 10.14359/51687709

Menegotto, M., and Pinto, P. E., 1973, "Method of Analysis for Cyclically Loaded R.C. Plane Frames Including Changes in Geometry and Non-Elastic Behavior of Elements under Combined Normal Force and Bending," *Proceedings of IASBE Symposium on Resistance and Ultimate Deformability of Structures Acted on by Well Defined Repeated Loads*, Lisbon, Portugal, pp. 15-22.

Menétrey, P., and Willam, K. J., 1995, "Triaxial Failure Criterion for Concrete and Its Generalization," *ACI Structural Journal*, V. 92, No. 3, May-June, pp. 311-318.

Nagender, T.; Parulekar, Y. M.; and Appa Rao, G., 2019, "Performance Evaluation and Hysteretic Modeling of Low Rise Reinforced Concrete Shear Walls," *Earthquakes and Structures*, V. 16, No. 1, Jan., pp. 41-54.

Nash, J. E., and Sutcliffe, J. V., 1970, "River Flow Forecasting through Conceptual Models Part I – A Discussion of Principles," *Journal of Hydrology*, V. 10, No. 3, Apr., pp. 282-290. doi: 10.1016/0022-1694(70)90255-6

Palermo, D., and Vecchio, F. J., 2003, "Compression Field Modeling of Reinforced Concrete Subjected to Reversed Loading: Formulation," *ACI Structural Journal*, V. 100, No. 5, Sept.-Oct., pp. 616-625.

Palermo, D., and Vecchio, F. J., 2004, "Compression Field Modeling of Reinforced Concrete Subjected to Reversed Loading: Verification," *ACI Structural Journal*, V. 101, No. 2, Mar.-Apr., pp. 155-164.

Petrone, F.; McKenna, F.; Do, T.; and McCallen, D., 2021, "A Versatile Numerical Model for the Nonlinear Analysis of Squat-to-Tall Reinforced-Concrete Shear Walls," *Engineering Structures*, V. 242, Sept., Article No. 112406. doi: 10.1016/j.engstruct.2021.112406

Pozo, J. D.; Hube, M. A.; and Kurama, Y. C., 2020, "Quantitative Assessment of Nonlinear Macro-Models for Global Behavior and Design of Planar RC Walls," *Engineering Structures*, V. 224, Dec., Article No. 111190. doi: 10.1016/j.engstruct.2020.111190

Sozen, M. A., and Moehle, J. P., 1993, "Stiffness of Reinforced Concrete Walls Resisting In-Plane Shear," Report No. EPRI TR-102731, Electrical Power Research Institute, Palo Alto, CA, 201 pp.

Syed, S., and Gupta, A., 2015, "Seismic Fragility of RC Shear Walls in Nuclear Power Plant Part 2: Influence of Uncertainty in Material Parameters on Fragility of Concrete Shear Walls," *Nuclear Engineering and Design*, V. 295, Dec., pp. 587-596. doi: 10.1016/j.nucengdes.2015.09.038

van Mier, J. G. M., 1986, "Multiaxial Strain-Softening of Concrete: Part I: Fracture," *Materials and Structures*, V. 19, No. 3, May, pp. 179-190. doi: 10.1007/BF02472034

Vecchio, F. J., and Collins, M. P., 1986, "The Modified Compression-Field Theory for Reinforced Concrete Elements Subject to Shear," *ACI Journal Proceedings*, V. 83, No. 2, Mar.-Apr., pp. 219-231.

Wang, J.-J.; Liu, C.; Nie, X.; Ding, R.; and Zhu, Y.-J., 2022, "Biaxial Constitutive Models for Simulation of Low-Aspect-Ratio Reinforced Concrete Shear Walls," *Journal of Engineering Mechanics*, ASCE, V. 148, No. 2, Feb., p. 04021157. doi: 10.1061/(ASCE)EM.1943-7889.0002030

Wong, P. S.; Vecchio, F. J.; and Trommels, H., 2013, "VecTor2 & FormWorks User's Manual: Second Edition," VecTor Analysis Group, 347 pp.

ACI STRUCTURAL JOURNAL TECHNICAL PAPER

Title No. 121-S78

Thermomechanical Hysteresis of Reinforced Concrete Beams Retrofitted with Carbon Fiber-Reinforced Polymer and Ultra-High-Performance Concrete

by Yail J. Kim and Ibrahim Bumadian

This paper presents the behavior of reinforced concrete beams retrofitted with carbon fiber-reinforced polymer (CFRP) sheets and ultra-high-performance concrete (UHPC) jackets in a multi-hazard environment. Following the procedural protocol of a published standard, the beams are cyclically loaded under thermomechanical distress at elevated temperatures, varying from 25 to 175°C (77 to 347°F), to examine their hysteretic responses alongside ancillary testing. The thermal conductivity of UHPC is higher than that of ordinary concrete by more than 62% and, according to a theoretical inference, premature delamination would not occur within the foregoing temperature range. The difference in load-carrying capacities between the strengthened and unstrengthened beams declines with temperature. While the UHPC+CFRP retrofit scheme is beneficial, CFRP plays a major role in upgrading the flexural resistance. The thermomechanical loading deteriorates the hysteretic loops of the beams, thereby lowering the stiffness and capacity. Elevated temperatures are concerned with the pinching, plasticity, characteristic rigidity, stress redistributions, and energy-release patterns of the beams. Due to the retrofit, the configuration of plastic hinges alters, and the localized sectional deformations form a narrow damage zone. The adverse effects of the temperatures on rotational stiffness are pronounced during the early loading stage of the beams.

Keywords: carbon fiber-reinforced polymer (CFRP); hysteresis; retrofit; strengthening; thermomechanical loading.

INTRODUCTION

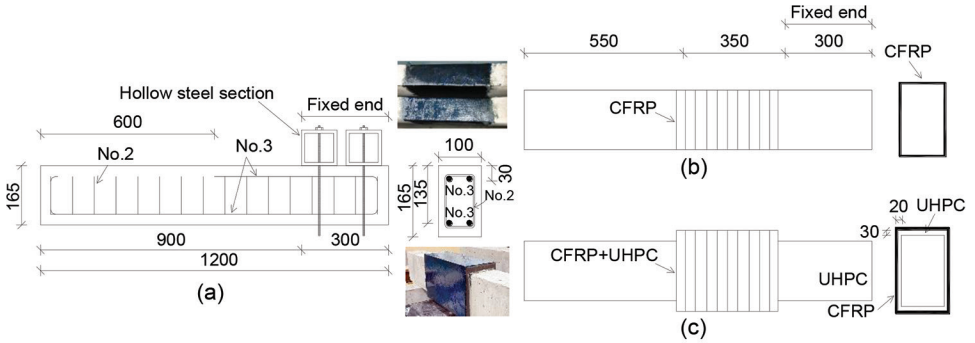
Multihazards are not part of most seismic design specifications. For instance, ASCE/SEI 43-05[1] offers four limit-state criteria solely based on structural deformations in line with response spectrum parameters. Precedent research claims that seismic vulnerability increases significantly when incorporating secondary loadings such as tsunami,[2] flood,[3] wind,[4] scour,[5] and fire.[6] Traditional approaches separately treat structural loads without integrating individual actions[7]; as a result, disastrous incidents that were unexpected during the design procedure may arise.[8] A case study on the 2004 Indian Ocean catastrophe, where earthquake-wave-combined loadings brought about massive destruction of buildings, recommends that multi-hazards be explicitly allowed for in designing critical structures.[9]

Seismic deficiency is a ubiquitous challenge facing the built-environment community and an annual budget of $6.1 billion is estimated to cope with earthquake risks for the U.S. building stock.[10] Inappropriately detailed structures undergo flawed energy dissipation appertaining to capacity reductions and pinched hysteresis loops.[11] Instead of replacement that necessitates unaffordable resources and societal costs, owners prefer conducting repairs and renovations.[12] Whereas state-of-the-art papers promote the positive impact of various techniques,[13,14] practical issues are often acknowledged in established methods: magnified self-weight, escalated sectional geometries, modified stiffness, intensive labor, and prolonged downtime.[14,15] Furthermore, upgrading substandard structures is correlated with large uncertainties and incurs financial expenditure.[16,17] Rehabilitation methodologies should, thus, be selected rigorously.

Composite materials are receiving special attention for retrofitting deficient concrete members, such as ultra-high-performance concrete (UHPC) and carbon fiber-reinforced polymer (CFRP).[18,19] The high compressive strength of UHPC, over $f_c' = 120$ MPa (17 ksi), provides the means to reduce architectural dimensions required for ordinary concrete with remarkable durability.[20,21] Experimental investigations report that UHPC jacketing improved the axial/flexural capacities of building elements and relieved brittle failure under cyclic loading.[22,23] Likewise, CFRP confinement furnishes several advantages—namely, enhanced rotational resistance, mitigated concrete-splitting, restricted reinforcing bar buckling, morphological adaptability, compliance with published standards, and broad coverage from component to system levels.[24] Members retrofitted with CFRP are, however, intrinsically vulnerable to temperature-induced distress because the performance of the strengthening system is reliant upon polymeric adhesives.[25] Such a situation is instantiated by an earthquake that prompts fires alongside the continued displacement reversals of strengthened members resulting from main- and after-shocks.[26-28] Despite the significance of thermomechanical loadings, specific information is not stipulated in existing design guidelines with regard to externally bonded CFRP sheets,[24,29] which warrants sophisticated research for the advancement of current knowledge. In addition, a new opportunity may be created by coupling these proven materials for multihazard applications.

This paper explores the behavior of reinforced concrete beams retrofitted with CFRP and UHPC subjected to

ACI Structural Journal, V. 121, No. 5, September 2024.
MS No. S-2023-271.R1, doi: 10.14359/51740864, received February 3, 2024, and reviewed under Institute publication policies. Copyright © 2024, American Concrete Institute. All rights reserved, including the making of copies unless permission is obtained from the copyright proprietors. Pertinent discussion including author's closure, if any, will be published ten months from this journal's date if the discussion is received within four months of the paper's print publication.



[1 mm = 0.0394 in.]

Fig. 1—Beam details: (a) dimension; (b) strengthening with CFRP; and (c) strengthening with UHPC plus CFRP.

simulated earthquake drifts at elevated temperatures. The objective of the present experimental study is twofold: 1) to explicate the undiscovered failure mechanism of CFRP-strengthened beams under concurrent thermomechanical loadings; and 2) to ascertain the potential of a rehabilitation method comprising UHPC jackets layered with CFRP sheets. Hysteretic responses, performance degradation, and inelastic deformations are expounded for the sake of understanding the retrofit systems' functionality in the aggressive loading environments.

RESEARCH SIGNIFICANCE

Multihazard design is an emerging concept that can address complex interactions and cumulative demands concerning the operational safety of structures.[7] The outcomes of multihazard loadings are dissimilar to those of respective ones; accordingly, arithmetic sums in each load deviate from actual effects.[30] Notwithstanding the broad adoption of nonconventional materials for strengthening concrete structures, the behavior of members with these materials under thermal and cyclic loadings is not well elucidated yet. In light of this, there are practical needs to evaluate the response of retrofitted members simultaneously exposed to earthquakes and elevated temperatures, which is not an uncommon scenario during a seismic event.[31] Attempts are made to document the ramifications of thermomechanical loadings for the seismic performance of cantilevered beams retrofitted with CFRP and UHPC+CFRP systems.

EXPERIMENTAL PROCEDURE

Commensurate with the aim of the aforementioned research program, laboratory testing is performed to examine the synergistic implications of thermal and cyclic loadings for the behavior of cantilever beams strengthened with CFRP and UHPC. Outlined as follows are descriptions on materials, specimens, strengthening details, and a loading protocol.

Materials

Concrete was mixed to accomplish a specified strength of 25 MPa (3630 psi) in compression (mixture ratio of water:cement:sand:gravel = 1:1.9:5.1:7.3 by weight). After 28 days of curing in a moisture-controlled chamber (99% humidity at 23°C [73°F]), cylinders were tested in accordance with ASTM C39,[32] and an average strength of f_c' = 24.9 MPa (3610 psi) was obtained. Steel bars with a yield strength of f_y = 414 and 250 MPa (60 and 36 ksi) were used for flexural and shear reinforcement (No. 3, 9.53 mm [0.375 in.] in diameter, and No. 2, 6.35 mm [0.25 in.] in diameter, respectively) to accommodate practical aspects in the field. Unidirectional CFRP composite sheets, consisting of dry carbon fabrics impregnated in a two-part epoxy resin, required a curing time of 7 days at room temperature for the succeeding properties based on an equivalent fiber thickness t_f = 0.165 mm (0.0065 in.): tensile strength (f_{fu}) = 3800 MPa (550 ksi), elastic modulus (E_f) = 227 GPa (33,000 ksi), ultimate strain (ε_{fu}) = 0.0167, and glass transition temperature (T_g) = 71°C (163°F). The epoxy that was mixed with a resin and a hardener at a mass ratio of 3:1 possessed a tensile strength of f_{epu} = 55 MPa (8000 psi) with an elastic modulus of E_{ep} = 3 GPa (440 ksi). The coefficient of thermal expansion of the CFRP and epoxy was $\alpha_f = -0.38\times10^{-6}$/°C ($-0.21\times10^{-6}$/°F), and $\alpha_{ep} = 35\times10^{-6}$/°C ($20\times10^{-6}$/°F), respectively. A commercial UHPC product was employed and its guaranteed properties are: compressive strength ($f_{c\text{-}UHPC}$) = 120 MPa (17.4 ksi); flexural strength ($f_{r\text{-}UHPC}$) = 14 MPa (2030 psi); elastic modulus (E_{UHPC}) = 30 GPa (4350 ksi); shrinkage < 0.01%; and ASTM C230 flow = 280 mm (11 in.).

Specimens

As depicted in Fig. 1(a), concrete beams were cast with dimensions of 100 mm (4 in.) x 165 mm (6.5 in.) x 1200 mm (3.9 ft). Two No. 3 bars were longitudinally placed at an effective depth of 135 mm (5.3 in.) and multiple No. 2 bars were arranged at spacings of 75 mm (3 in.). To resist negative bending, compression reinforcing bars were extended to the midlength of the beams.

Retrofit

Strengthening work was undertaken to upgrade the seismic performance of the beams, which would be tested under a cantilever condition. To determine the zone of retrofit, a plastic hinge length was calculated as per ACI 440.2R-17[24] and rounded to be 350 mm (13.8 in.) for practical convenience. Two retrofit strategies were implemented with CFRP and UHPC+CFRP. The first scheme involved the complete wrapping of the critical region using the CFRP sheets (Fig. 1(b)). After roughening the target concrete surface with an electric steel-wire brush, the blended epoxy was applied, and single-layer carbon fabrics were impregnated as part of a

Table 1—Test matrix

Beam	Strengthening	Loading	Temperature	Ultimate load, kN		
				Positive (P_u^+)	Negative (P_u^-)	Absolute ($\lvert P_u \rvert$)
M25NO	None	Monotonic	25°C	15.8	N/A	15.8
M25CF	CFRP	Monotonic	25°C	32.8	N/A	32.8
C25CF	CFRP	Cyclic	25°C	30.5	–30.7	30.7
C75CF	CFRP	Cyclic	75°C	21.7	–21.0	21.7
C125CF	CFRP	Cyclic	125°C	17.8	–19.9	19.9
C175CF	CFRP	Cyclic	175°C	14.9	–10.8	14.9
C25UC	UHPC+CFRP	Cyclic	25°C	32.4	–33.4	33.4
C75UC	UHPC+CFRP	Cyclic	75°C	25.4	–24.1	25.4
C125UC	UHPC+CFRP	Cyclic	125°C	21.7	–17.4	21.7
C175UC	UHPC+CFRP	Cyclic	175°C	15.6	–11.0	15.6

Note: Positive is downward loading; negative is upward loading; absolute is maximum load in either directional loading; °F = °C(9/5) + 32; 1 kN = 0.225 kip.

wet-layup process. The orientation of the fibers was perpendicular to the longitudinal reinforcing bars. The composite system was then cured for 7 days at room temperature. For the second scheme, a UHPC jacket was added (Fig. 1(c)) and the CFRP sheets fully enclosed the 28-day cured jacket. Table 1 summarizes the identification of these retrofitted beams together with loading schemes; namely, the first letter denotes a loading type (M is monotonic and C is cyclic), the second component pertains to elevated temperatures in degrees Celsius, and the last part manifests the type of strengthening (NO is unstrengthened, CF is CFRP, and UC is UHPC+CFRP).

Testing

Ancillary tests—To attain the thermal conductivity (K) of the ordinary concrete and UHPC mixtures, a non-contacting thermometer was used (Fig. 2(a): a concrete disk was placed on the electric apparatus and the progression of heat was measured by a non-contacting thermometer)

$$K = \frac{Qd}{A\Delta T} \tag{1}$$

where Q is the supplied heat energy (Q = 3 W [10.2 BTU/hr]); d and A are, respectively, the depth and cross-sectional area of the specimen (d = 0.08 m [3.15 in.] and A = 0.002 m^2 [3 in.^{2}]); and ΔT is the difference in temperature. The physical significance of measuring the thermal conductivity is that it dominates the formation of temperature gradients, thereby affecting the thermal strains of the ordinary concrete and UHPC (the conductivity of thin CFRP composites is negligible relative to that of concrete[33]). A thermal camera monitored the temperature variation of the concrete specimens for infrared thermography. The camera, built upon the multi-spectral dynamic imaging technology, generated images at a resolution of 19,200 pixels with a sensitivity of less than 0.06°C (0.11°F) and a frame rate of 9 Hz.[34] The frequency of temperature sampling was every 5 minutes for a period of 3 hours, which was sufficient to cover structural examinations (to be described), and the test was replicated three times.

Thermomechanical loading—All beams were cantilevered with a custom-made fixture and the distance from the fixed end to the center of the loading bracket was 700 mm (27.5 in.), as shown in Fig. 2(b) and (c). The fixture was composed of two hollow steel sections (100 x 100 x 16 mm [4 x 4 x 0.625 in.] thick), ASTM A325 threaded steel rods (16 mm [0.63 in.] in diameter), and a rigid support that was anchored to the strong floor. The portion of each beam embedded in the fixture with a length of 300 mm (11.8 in.) was confined by the CFRP sheets to preclude premature failure. For the application of heat, the retrofitted part of the beams was wrapped with a glass-reinforced silicon rubber pad and steel wires (Fig. 2(c)). The pad was electrically powered and perfluoroalkoxy lead wires generated thermal energy: this system is frequently used to simulate heat transfer in laboratory research.[35,36] Given that the temperatures of insulated CFRP-strengthened members subjected to fire are below 150°C (302°F) over an exposure period of 2 to 3 hours on many occasions,[37,38] the investigation range of the present study was set from 25 to 175°C (77 to 347°F) with an assumption that the members were adequately insulated. The preset temperature of the heating pad was automatically adjusted by a digital controller (Fig. 2(c), inset). Subsequently, the prepared beams were loaded mechanically and thermomechanically (Fig. 2(b) and (c), respectively) in conformity with the loading protocol of FEMA 461[39] (Fig. 2(d)). It should be noted that the beams cyclically loaded without thermal distress (C25CF and C25UC) can represent situations where an earthquake-induced fire does not break out; on the contrary, other beams (C75CF to C175CF and C75UC to C175UC) encompass instances with combined load scenarios.

Instrumentation—A load cell and a displacement sensor, which were built in the servo-actuator unit, recorded the behavior of the test beams. Temperatures on the surface of CFRP (inside the heating pad) were logged by thermocouple wires. A preheating period of 10 minutes was required for all thermomechanically loaded beams, and the target temperatures were maintained until the beams failed (Fig. 2(e)).

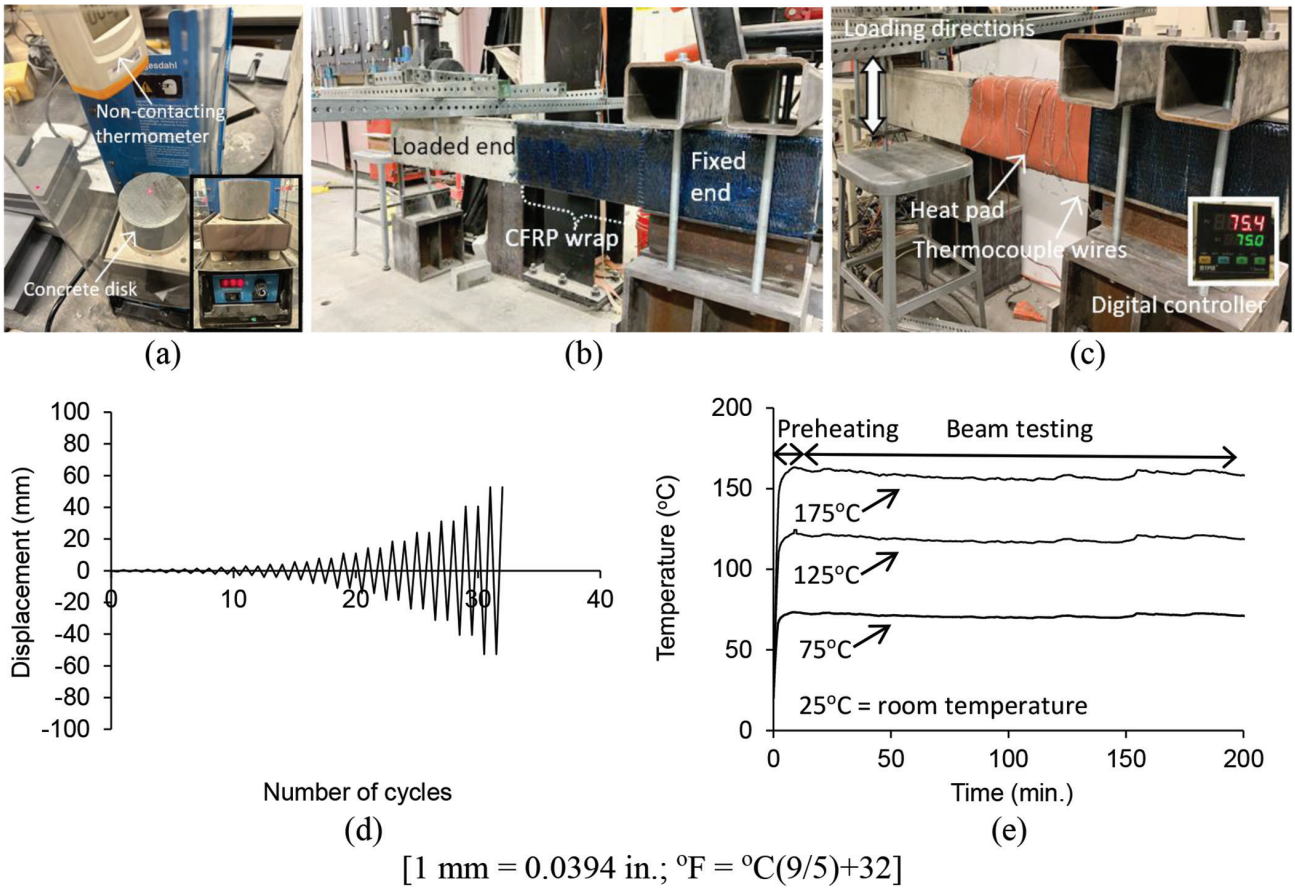


Fig. 2—Laboratory testing: (a) thermal conductivity; (b) setup of CFRP-strengthened cantilever beam; (c) thermomechanical loading and instrumentation; (d) displacement-controlled loading scheme based on FEMA 461[39]; and (e) thermocouple readings.

RESULTS AND DISCUSSION

Diverse technical aspects are expatiated from material and structural points of view to comprehend the performance of retrofitted cantilever beams subjected to thermomechanical loadings. Emphasis is placed on the thermal properties of ordinary concrete and UHPC, as well as their conceptual performance reliability, and on the hysteretic responses and flexural characteristics of the beams.

Thermal conduction

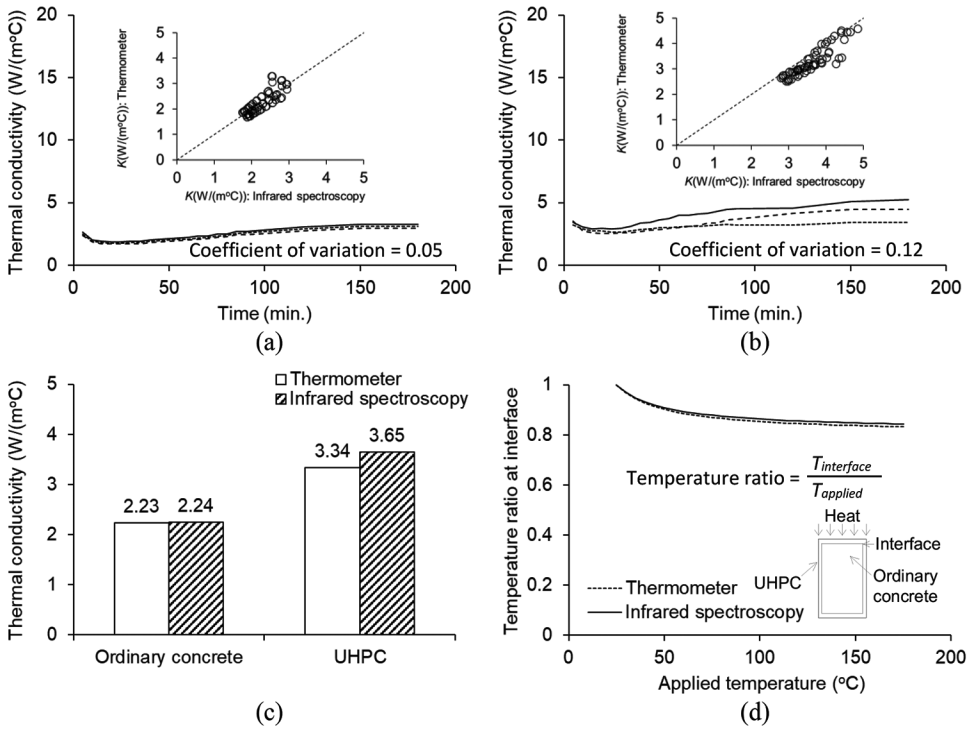
The thermometer-measured conductivities of the concrete specimens are shown in Fig. 3(a) and (b). Also shown are comparative plots against the conductivities quantified by the infrared spectroscopy. While the thermal response of the ordinary concrete was consistent (coefficient of variation = 0.05, Fig. 3(a)), that of UHPC was somewhat irregular (coefficient of variation = 0.12, Fig. 3(b)). This observation is explained by their different mineralogical compositions: the crystallinity of densely packed quartz sands in the UHPC mixture enabled a rapid flux of heat in multiple directions.[40] The average conductivity of UHPC was higher by up to 62.9% relative to the case of the ordinary concrete (Fig. 3(c)), which aligns with the fact that the vulnerability of high-strength concrete to a fire (thermal spalling) is higher than its low-strength counterpart.[41]

With a consideration that heat currents in materials sharing contact surfaces are equal,[42] the conductivity test results were used to estimate temperatures at the interface between the beam concrete and UHPC (Fig. 1(c))

$$T_{interface} = \frac{\alpha T_{applied} + T_0}{1 + \alpha} \tag{2}$$

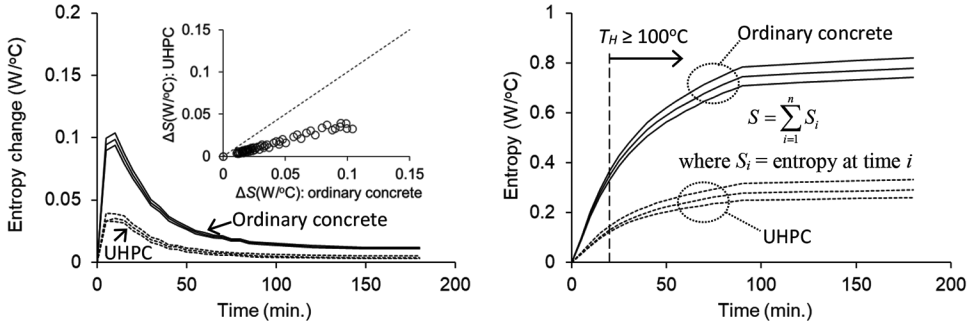
$$\alpha = \frac{K_{UHPC} t_{concrete}}{K_{concrete} t_{UHPC}} \tag{3}$$

where $T_{interface}$ is the interface temperature; $T_{applied}$ and T_0 are the applied and initial temperatures of the beam system, respectively (T_0 in the beam concrete was assumed 25°C [77°F]); $t_{concrete}$ and t_{UHPC} are the thickness of the ordinary concrete and UHPC, respectively (for demonstration purposes, $t_{concrete}$ = 82.5 mm [3.25 in.] and t_{UHPC} = 30 mm [1.2 in.] were used, Fig. 1(c)). When the applied temperature was increased, the ratio of $T_{interface}$ to $T_{applied}$ dwindled and stabilized (Fig. 3(d)). Therefore, practically speaking, the proposed UHPC-retrofit system would not experience premature delamination as long as the beam is properly insulated: previous research[43] reports that interfacial deterioration can take place between ordinary concrete and UHPC at a temperature above 300°C (572°F).



[1 W = 3.41 BTU/hr; 1 m = 3.28 ft; °F = °C(9/5)+32]

Fig. 3—Thermal conductivity: (a) ordinary concrete with non-contacting thermometer; (b) UHPC with non-contacting thermometer; (c) average conductivity of ordinary concrete and UHPC; and (d) predicted temperature ratio at interface between UHPC and ordinary concrete.



[1 W = 3.41 BTU/hr; °F = °C(9/5)+32]

Fig. 4—Entropy: (a) change with time; and (b) development.

Suitability of UHPC as retrofit material

The amount of disorder in the concrete composition was appraised by the change of entropy (ΔS)

$$\Delta S = \frac{Q}{(1/T_L - 1/T_H)} \tag{4}$$

where T_L and T_H are the temperatures at the top and bottom of the specimen (Fig. 2(a)), respectively. In statistical physics,[44] entropy is regarded as a representative metric to figure out the degree of randomness in a system (tantamount to disorder). The entropy change of the concrete mixtures precipitously rose when the heat energy was applied and ebbed with time (Fig. 4(a)). The positive values of entropy ($\Delta S > 0$) impart that the elevated temperatures incurred an irreversible process in the mixtures,[45] including chemical and physical alterations in the microstructures.[46] The ordinary concrete reacted more quickly than UHPC, meaning that the composition of the ordinary concrete possessed a higher likelihood for variability in terms of material stability. Examples can be found in literature[47]: compared with UHPC, the compressive strength and bond of ordinary concrete degrade swiftly in aggressive environments. The development of entropy is portrayed in Fig. 4(b). Even if the tangent of the ordinary concrete's curve was remarkably stiff within a time period between 0 and 25 minutes the difference against the tangent of UHPC disappeared after 100 minutes. Part of the water in the mixtures commenced to release and evaporate when the applied temperature exceeded 100°C (212°F), as marked in Fig. 4(b), which is believed to be a driving force for making the internal composition of the mixtures stable through a phase transformation.[48,49] Contemplating the equivalence of entropy and uncertainty,[50] the low-entropy UHPC was

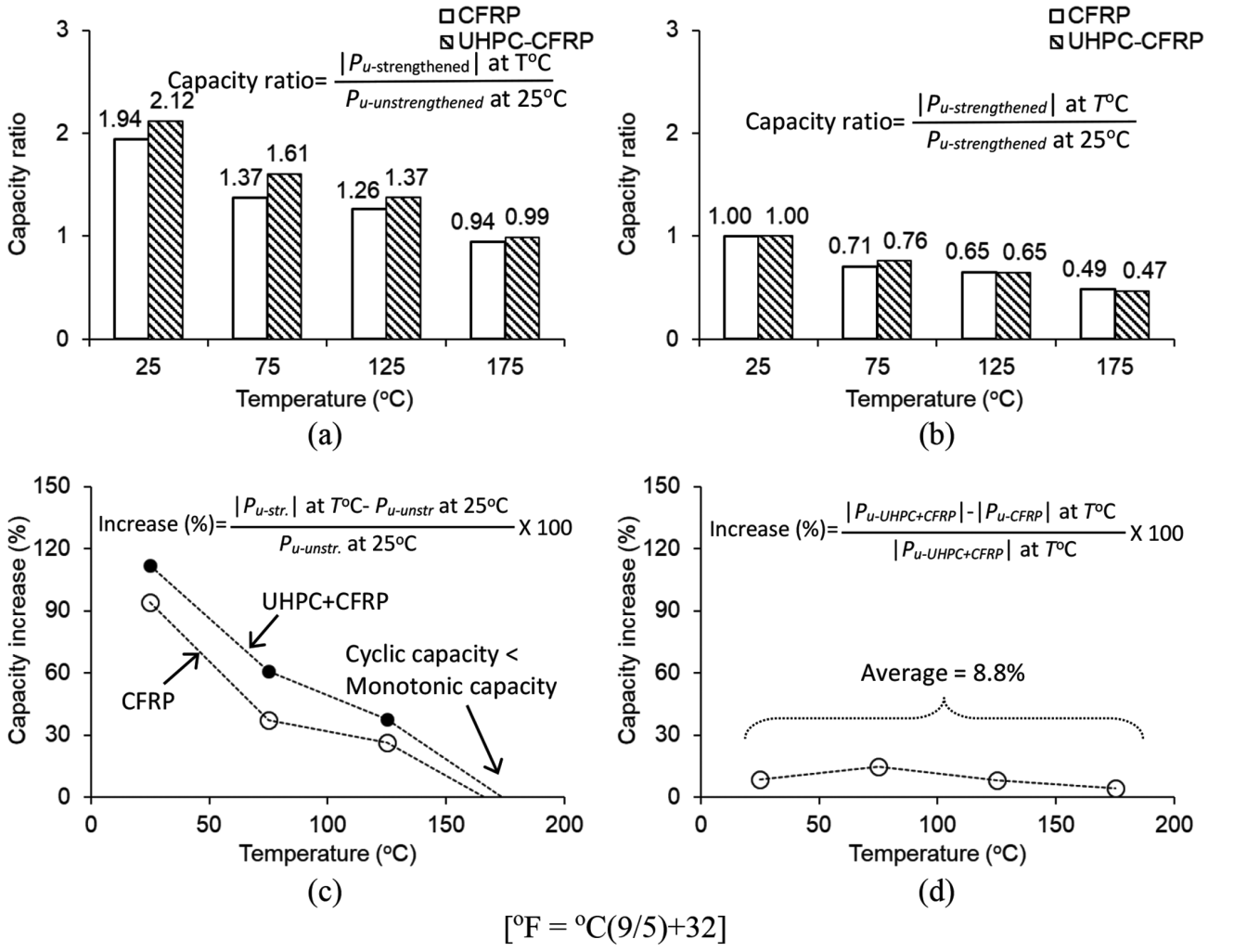


Fig. 5—Capacity ratio: (a) cyclic strengthened versus monotonic control beams; (b) cyclically loaded beams; (c) contribution of retrofit elements; and (d) contribution of UHPC.

notionally confirmed as a suitable material for upgrading existing structural members with high reliability.

Load-bearing capacity

Figure 5 exhibits the flexural capacity of the test beams. The capacities of the CF and UC series under the cyclic loading without thermal exposure (the absolute maximum values at 25°C [77°F] in Table 1) were 1.94 and 2.12 times higher than the capacity of the monotonically loaded unstrengthened control beam (Fig. 5(a)). With the increased temperature, the efficacy of the retrofit systems decreased by degrees and the capacity of the strengthened beams fell below the level of the unstrengthened beam at 175°C (347°F). Shown in Fig. 5(b) are the repercussions of the thermal distress for the capacity of the periodically loaded CF and UC beams. The heat-induced capacity reduction of the beams was prominent when the applied temperature went over the glass transition temperature of the epoxy resin ($T_{applied} > T_g$ = 71°C [163°F]). The almost identical reduction rates of the CF and UC beams imply that the CFRP sheets were the major constituent from a load-carrying standpoint; scilicet, the role of CFRP was greater than that of UHPC in resisting the sinusoidal mechanical load.

To further investigate the individual contribution of CFRP and UHPC under the cyclic load environment, the relative capacity of the strengthened beams at elevated temperatures ($\Delta P_{rc}(T)$) was extracted from the capacity of the unstrengthened beam tested at 25°C (77°F)

$$\Delta P_{rc}(T) = \frac{|P_{u-str.}(T)| - P_{u-unstr.}(25°C)}{P_{u-unstr.}(25°C)} \quad (5)$$

where $P_{u-str.}(T)$ and $P_{u-unstr.}(25°C)$ are the capacities of the strengthened and unstrengthened beams at a temperature T and 25°C (77°F), respectively. As graphed in Fig. 5(c), the effects of the retrofit elements were clearly distinguishable. The synergistic combination of UHPC and CFRP better raised the beams' capacity in comparison with the case involving CFRP alone; nonetheless, the average fraction of UHPC was 8.8% in the increased capacity (Fig. 5(d)). This fact reaffirms that the CFRP confinement accounting for the rest (91.2%) was the primary component of the strength gain.

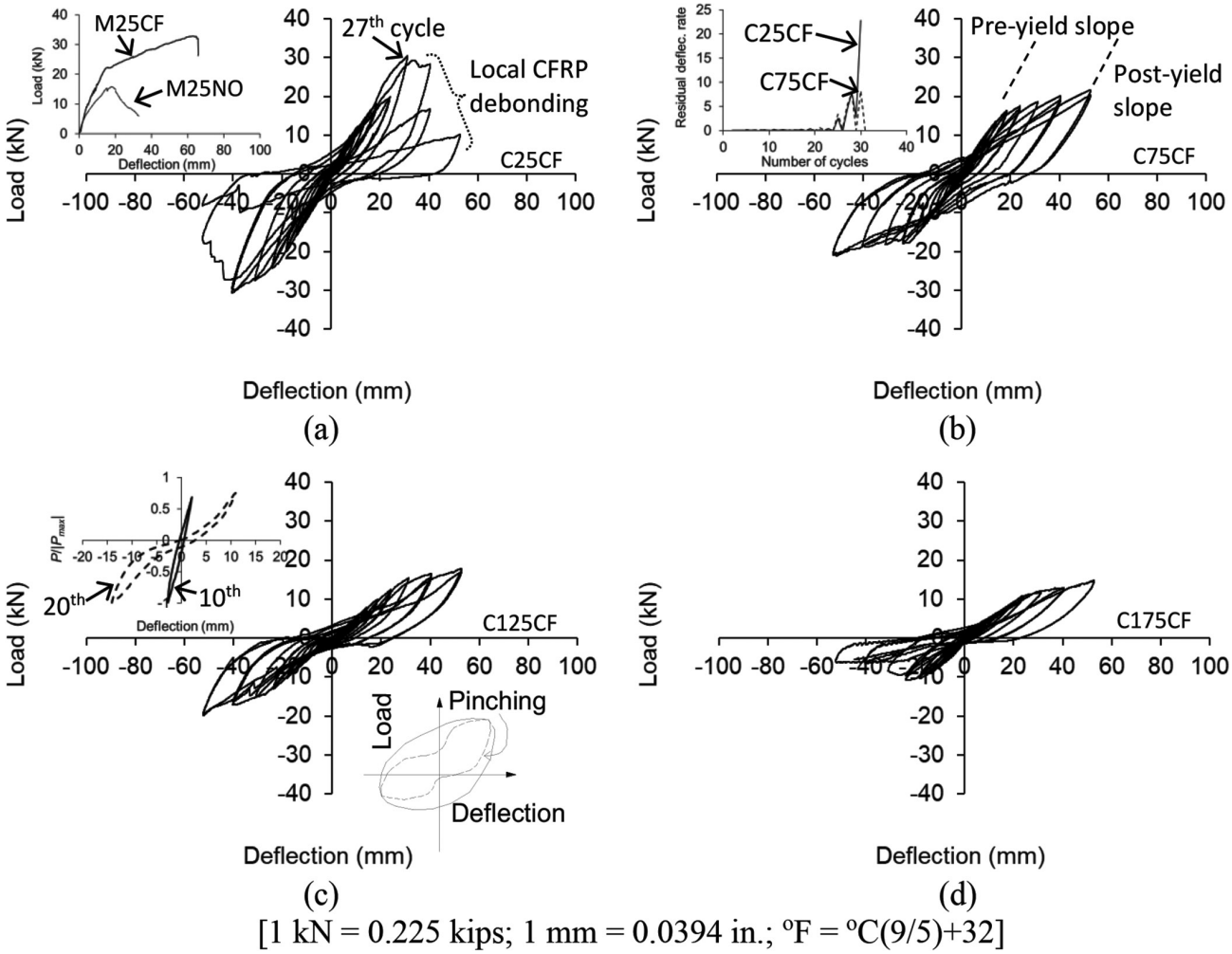


Fig. 6—Load-deflection behavior of beams strengthened with CFRP under cyclic loading: (a) 25°C; (b) 75°C; (c) 125°C; and (d) 175°C.

Flexural behavior

Hysteresis of beams with CFRP—The load-deflection diagram of the CF series beams is described in Fig. 6. For reference purposes, the behavior of the monotonically loaded beams (M25NO and M25CF) is also visible in the inset of Fig. 6(a). The strengthened beam subjected to mechanical loading at 25°C (77°F) revealed steady responses until the 26th cycle (Fig. 6(a)), after which a sudden increase in deflection was noted with successively decrementing post-peak loads. This was ascribed to the occurrence of local CFRP debonding in C25CF, which was related to the wet-layup process that could entail nonuniform bond quality.[51] Besides, during the course of increasing deflection amplitude in compliance with the FEMA's test protocol (Fig. 2(d)), the repeated slippage between the concrete substrate and CFRP caused internal friction that exacerbated the amicable dissipation of excitation energy.[52]

As shown in Fig. 6(b), the transmitted heat above the glass transition temperature of the epoxy accelerated the synergistic degradation of the CFRP-strengthened beam; consequently, the loading slope of the hysteretic loops gradually descended with the increased cycle. The unloading curves of C75CF in the first and third quadrants were deemed elastic because the reversal of the mechanical loading released the accumulated stresses of the beam; hence, the post-peak slopes were nearly parallel to the pre-yield slopes. Unlike the occasion of C25CF, the residual deflection of C75CF regularly developed with respect to the number of cycles (Fig. 6(b), inset), indicating that the partly flawed wet-layup of the C25CF beam was merely an unintended experimental fault.

When the applied temperature was increased to 125 and 175°C (257 and 347°F), the influence of the thermomechanical distress became obvious (Fig. 6(c) and (d)). The thermally weakened CFRP sheets combined with enlarged concrete cracks after yielding abated the load-carrying ability of the beams. In addition, the pinching of the reciprocating curves, accompanied by the softened slopes while the beams were loaded and unloaded (a schematic illustration is available in Fig. 6(c)), was noticed. Specifically, the pinching effect was negligible prior to the yielding of the reinforcing bars, whereas it was prominent in the post-yield domain of the hysteretic loop: the response of the beams is given in the inset of Fig. 6(c) with normalized loads ($P/|P_{max}|$) at the 10th and 20th cycles. Given that the extent of pinching is governed by the progression of a hysteretic slip,[53] the thermomechanical loading was certainly responsible for

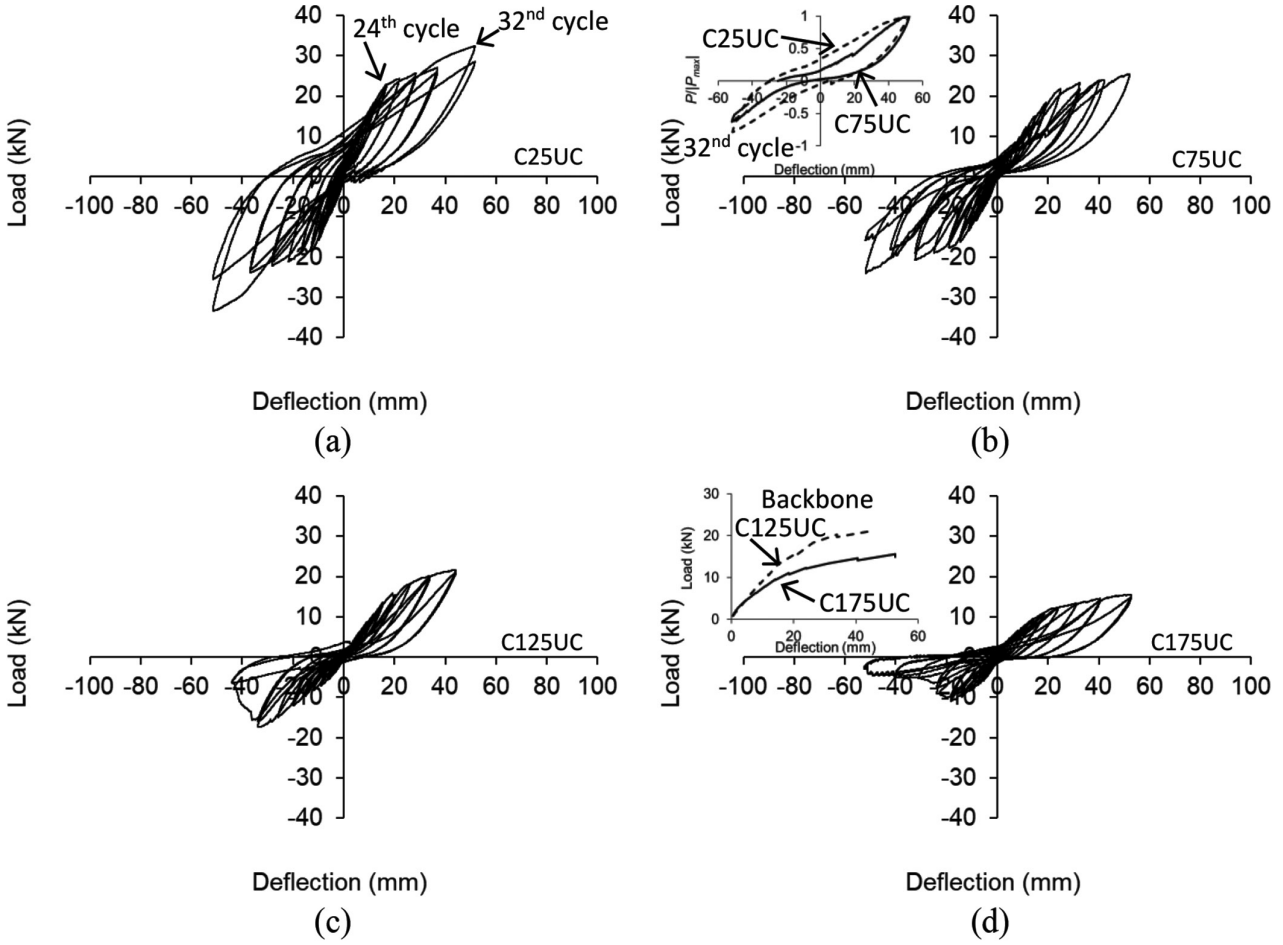


Fig. 7—Load-deflection behavior of beams strengthened with UHPC+CFRP under cyclic loading: (a) 25°C; (b) 75°C; (c) 125°C; and (d) 175°C.

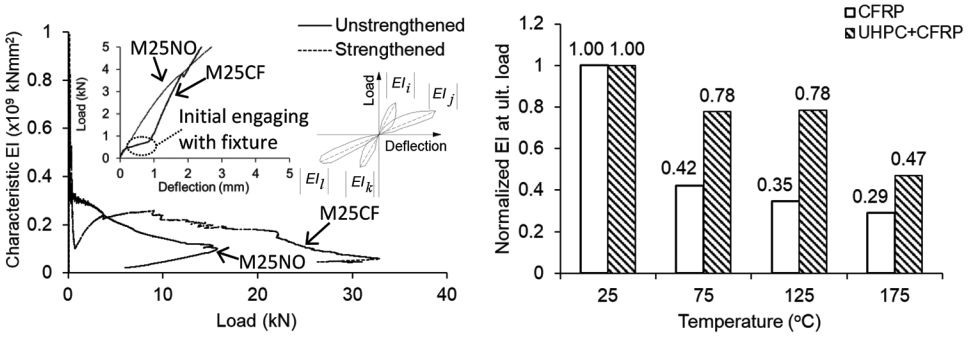
expanding the interfacial dislocation of the CFRP retrofit system.

Hysteresis of beams with UHPC and CFRP—Figure 7 displays the hysteretic behavior of the UC-series beams. The stresses stemming from positive bending should be completely lost when a load reversal commenced for negative bending. However, such an ideal circumstance was not seen due to the growth of internal damage in the load-bearing system. The stiffness of C25UC was retained until the 24th cycle; then, a reduction in the slope was observed with a considerable increase in the deflection (Fig. 7(a)). Passing through the surged deflection at the 32nd cycle, the beam failed with localized damage outside the retrofitted zone (to be elaborated). When the thermal loading was applied, the pinched hysteresis loop of the UC beam became conspicuous (Fig. 7(b)): the loops of C25UC and C75UC are compared at the 32nd cycle in the inset of Fig. 7(b). This fact substantiates that significant plasticity arose in the retrofit system owing to the elevated temperature. Comprehensive discussions on the relationship between pinching and plasticity are found elsewhere.[54]

As the temperature was raised over 125°C (257°F), the configuration of the hysteretic loops altered in the positive and negative loading directions (Fig. 7(c) and (d)). The so-called Bauschinger effect can account for this shifting of the loops from the third to the first quadrants in C125UC and C175UC. According to the Bauschinger mechanism,[55] the cyclic thermomechanical loading redistributed the internal stresses of the beams and cumulatively dislocated their constituents in conjunction with strain hardening at every load reversal. The degree of damage accrual during the loading process was a function of the thermal exposure as well. The backbone curve of C175UC began to bifurcate from the curve of C125UC at 5 kN (1.1 kip) and the former's response slope was consistently lower than the slope of the latter (Fig. 7(d), inset). The softening of the backbone curve is a clear indication for the unfavorable evolution of plastic damage in the microstructures of the beam concrete and the retrofit elements, which provoked non-homogeneous deformations.[56]

Bending characteristics

The characteristic flexural rigidity of the unstrengthened and strengthened beams under monotonic loading (M25NO and M25CF, respectively) is provided in Fig. 8(a). The characteristic rigidity (EI_{ch}) of the cantilever beams derived from their secant stiffness (Fig. 8(a), inset) was calculated semi-empirically by



[1 kN = 0.225 kips; 1 kNmm^2 = 0.00035 kip-in.^{2}; °F = °C(9/5)+32]

Fig. 8—Flexural rigidity: (a) characteristic rigidity (EI) under monotonic loading; and (b) normalized comparison of characteristic EI under thermomechanical loading.

$$EI_{ch} = \frac{|P_{imax} L^3|}{3\,\delta_i} \quad (6)$$

where P_{imax} is the maximum load of the i-th cycle in either the positive or negative loading direction; δ_i is the deflection corresponding to P_{imax}; and L is the loading span. It is worth noting that the characteristic rigidity is intended to comparatively examine the performance of the test beams at elevated temperatures. The rigidity of M25CF was higher than that of M25NO, as shown in Fig. 8(a), except for the early loading stage where an abrupt increase in the deflection of M25CF took place at a load of 0.75 kN (0.17 kip) owing to the initial engaging of the beam with the fixture (Fig. 8(a), inset). The effectiveness of the retrofit systems subjected to the thermomechanical loading is studied in Fig. 8(b), where the characteristic rigidity of the CF and UC series beams at high temperatures was normalized by the rigidity at 25°C (77°F). The rigidity of both categories at their ultimate loads descended with temperature, corroborating the adverse thermal exposure in the matter of lowering the ability to resist bending. The slow reaction rate of the UC series against the CF series in Fig. 8(b) supports the efficaciousness of the UHPC jacket as a supplementary retrofit element.

Energy dissipation

Figures 9(a) and (b) demonstrate the hysteretic energy of the CF and UC beams, respectively, that was dissipated with an increase in the loading cycle. The energy dissipation in this context corresponds to the release of strain energy stored in the beams when the mechanical loading was reversed: the area under the alternating loops in Fig. 6 and 7 was numerically integrated to obtain energy values. Aligning with repeated crack-opening-and-closing actions, the periodic iterations of the beams in the positive and negative directions led to the up-and-down trend of the energy curves. The amplification of the energy was marginal until the 23rd cycle; afterward, soaring spikes were recorded because of the enlarged inelastic deformation of the impaired concrete.[57] Moreover, the exponentially growing energy is attributed to the coalescence of microcracks that accrued during the preceding cycles and their unstable propagation.[58] Figure 9(c) plots the energy fraction of the test beams (the i-th cycle energy (E_i) divided by the maximum energy (E_{max}) of the respective beams). Contrary to the CF series (Fig. 9(c), inset), the development of the energy fraction in the UC series was dependent upon the thermomechanical cycles. It accords with previous research in that thermally deteriorated micro-pores can lower the fracture resistance of UHPC by partially decomposing calcium-silicate-hydrate (C-S-H) gels[59]; as a consequence, the amount of the dissipated energy increased at elevated temperatures. The energy release rate of selected beams (Fig. 9(a) and (b)) with respect to the mechanical cycle is graphically assessed in Fig. 9(d). The presence of heat changed the pattern of energy release in the CF beams (similar observations made for the UC beams were omitted due to the page limit). The abrupt release rate of the CF beam at 25°C (77°F) subsided as the temperature went up to 175°C (347°F); however, this temperature-sensitive rate was not contingent upon the retrofit scheme (Fig. 9(d), inset) for the reason that the softened CFRP sheets redistributed the applied mechanical stresses, as discussed earlier, and the waned interface between the retrofit systems and the beams did not transfer the entire stresses owing to the loss of bond.[60]

INELASTIC PERSPECTIVES

Three major facets associated with the post-yield behavior of the thermomechanically loaded beams are of interest: plastic hinges, deformation localization, and potential energy. These inelastic responses are a prerequisite for construing the near-failure state of the beams.

Formation of plastic hinges

Figure 10 pictures the typical failure mode of the unstrengthened and strengthened beams. Although the elastic moment of the cantilever was maximum at the fixed end, the flexural and flexure-shear cracks of the unstrengthened beam were 80 to 420 mm (3.1 to 16.5 in.) away from the support (Fig. 10(a)), where substantial rotations ensued to form a plastic hinge. Regarding the strengthened beams (Fig. 10(b) and (c)), concentrated cracking occurred immediately outside the retrofitted region and the longitudinal reinforcing bars did not buckle because of the closed stirrups (Fig. 10(b), inset). With the onset of steel-yielding, the plastic deformation of the cracked beams was aggravated, the width of the cracks widened, and finally the concrete spalled (Fig. 10(b) and (c)). The heated retrofit system

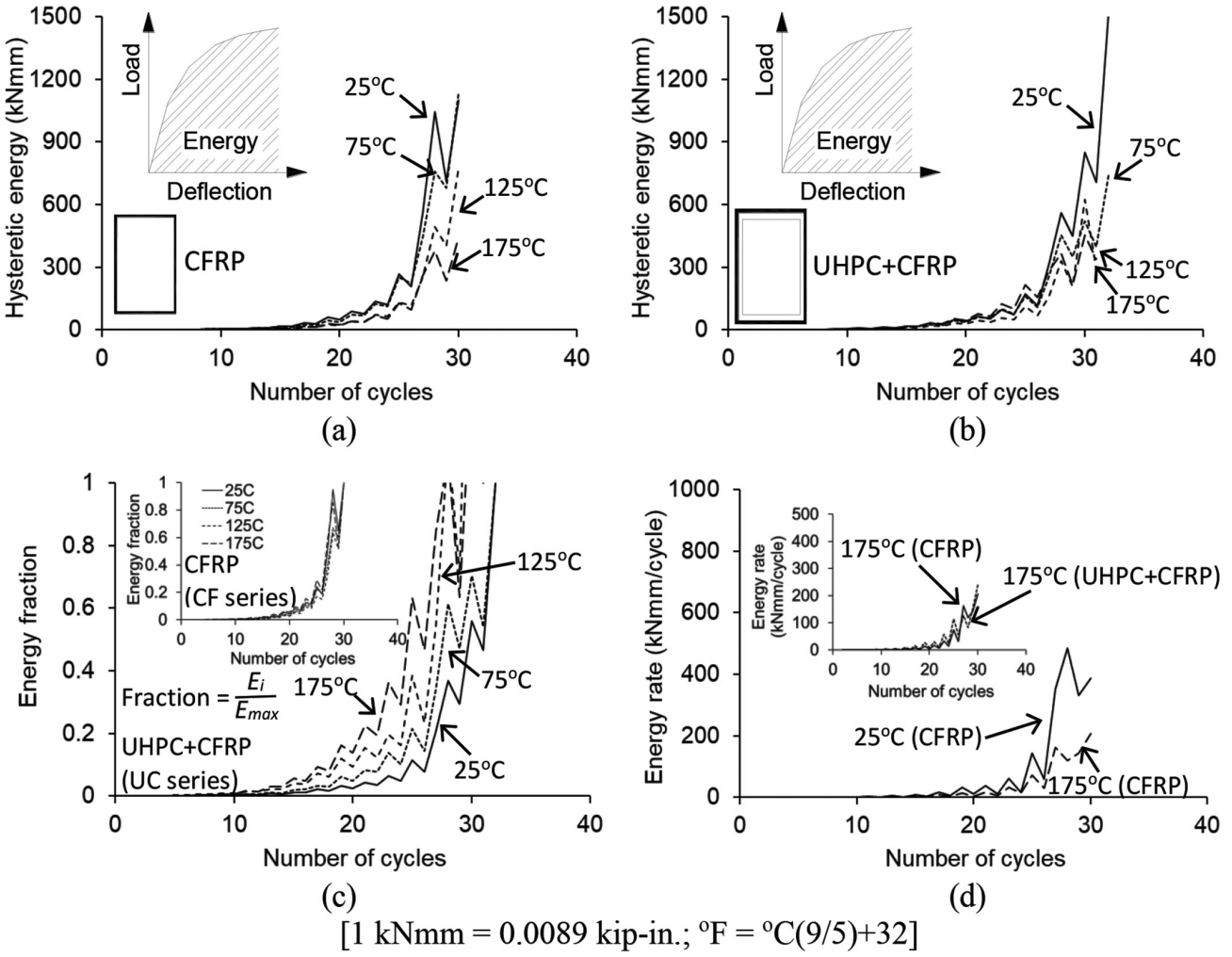


Fig. 9—Hysteretic energy: (a) beams with CFRP; (b) beams with UHPC+CFRP; (c) energy fraction; and (d) rate per cycle.

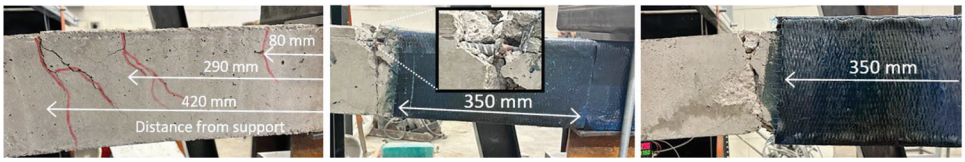


Fig. 10—Failure mode: (a) M25NO; (b) C175CF; and (c) C175UC.

preserved its conformational integrity under the incremental load reversals; as such, no visual damage was noticeable at the surface level.

Localized deformation

A relationship between the thermal loading and the maximum deflection range (δ_{max}) of the strengthened beams is shown in Fig. 11(a). The declining propensity of the deflection range with temperature points out that the progressive breakdown of the interfacial bond in the retrofit system was influential on the translational response of the cantilevers under the displacement-controlled loading condition. In other words, the heat energy degraded the structural adequacy of CFRP; accordingly, the ability to withstand the external excitation diminished alongside the reduced quantity of elastic recovery.[61] As charted in Fig. 11(b), where the drift ratio of the beams ($\lambda = \delta_{max}/L$) at 75 to 175°C (167 to 347°F) was normalized by that of the beams at 25°C (77°F), the drift ratio of the UC series was positioned below the ratio of the CF series because the UHPC jacket played a role as a stress-transfer medium between the concrete substrate and CFRP with retained adhesion at the elevated temperatures.[62]

Figure 11(c) illustrates the effective curvature of the test beams (ψ) at failure

$$\psi = \frac{(\delta_{up}/L_{un} + \delta_{down}/L_{un})}{L_{pe}} \quad (7)$$

where δ_{up} and δ_{down} are the upward and downward deflections of the beam, respectively ($\delta_{max} = \delta_{up} + \delta_{down}$); L_{un} is the length

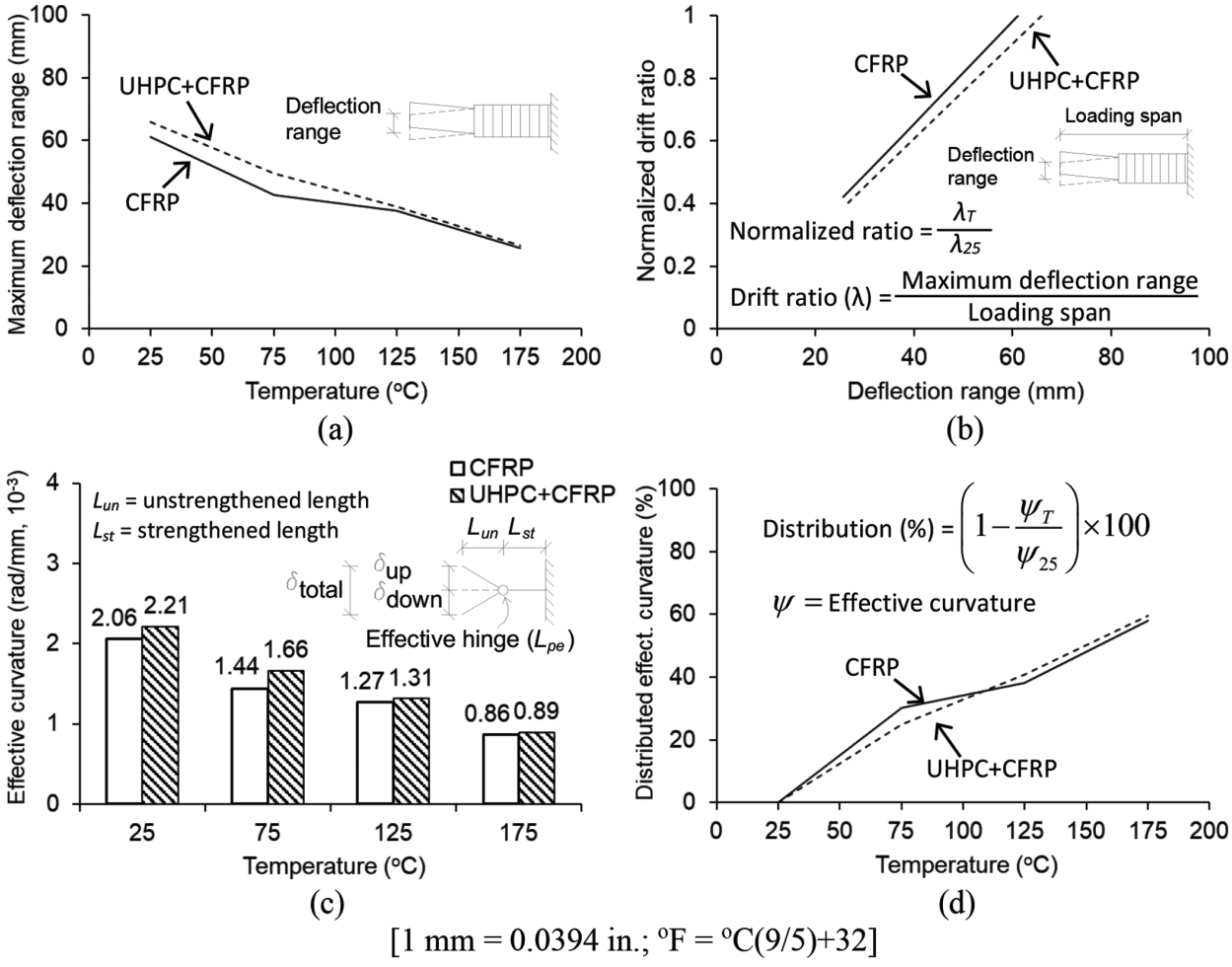


Fig. 11—Localized deformation of strengthened beams: (a) deflection range; (b) drift ratio; (c) effective curvature; and (d) distributed effective curvature.

of the unstrengthened zone; and L_{pe} is the length of the effective plastic hinge (L_{pe} = 85 mm [3.35 in.] was measured, on average). In contrast with the conventional assumption on the rotation of a beam at the center of a plastic hinge ($L_p/2$),[63] the pivot of rotation in L_{pe} was right next to the CFRP termination where stresses were concentrated (Fig. 11(c), inset). The magnitude of the effective curvature was inversely proportional to the temperature (Fig. 11(c)): the deteriorated retrofit system alleviated the degree of bending so that the cantilever beams had a tendency to straighten with the lessened flexural rigidity. Additionally, the effective curvature of the beams was distributed under the thermomechanical loading (Fig. 11(d)). The importance of these curvature distributions is that the hinged region underwent appreciable deterioration, arising from the large inelastic deformations, and considerable strain energy was dissipated over the strengthened portion of the beams (L_{st}) subjected to the heat.

Potential energy

The conformation of the cantilever may be idealized as a single-degree-of-freedom (SDOF) system with a rotational spring (Fig. 12(a)). This simplification cannot accurately reflect localized deformations in the vicinity of the CFRP termination; however, the SDOF representation is appropriate to holistically analyze the detrimental features of the thermomechanical loadings: the spring characterizes the total strain energy absorbed by the beam. The potential energy of the cantilever (Π) is expressed by

$$\Pi = \frac{1}{2}k\theta^2 - PL\sin\theta \tag{8}$$

where θ is the angle of rotation in radians; and k is the rotational stiffness, which is attained from the equilibrium condition of Eq. (8) ($d\Pi/d\theta = 0$)

$$k = \frac{PL\cos\theta}{\theta} \tag{9}$$

When the angle of rotation ascended, the stiffness k went down asymptotically and the gap between the thermally conditioned and unconditioned cases decreased as well (Fig. 12(a) and (b)). These responses clarify that the influence of the heat-generated distress was more pronounced during the early stage of the mechanical loading ($\theta \le 0.02$ rad). As far as the retrofit method is concerned, the UHPC jacket intensified the rotational stiffness regardless of temperature (Fig. 12(b), inset). Figure 12(c) shows the experimentally quantified potential energy of the beams. With the exception of C25CF suffering the wet-layup debonding, the potential energy of all other specimens rose in a linear manner up to

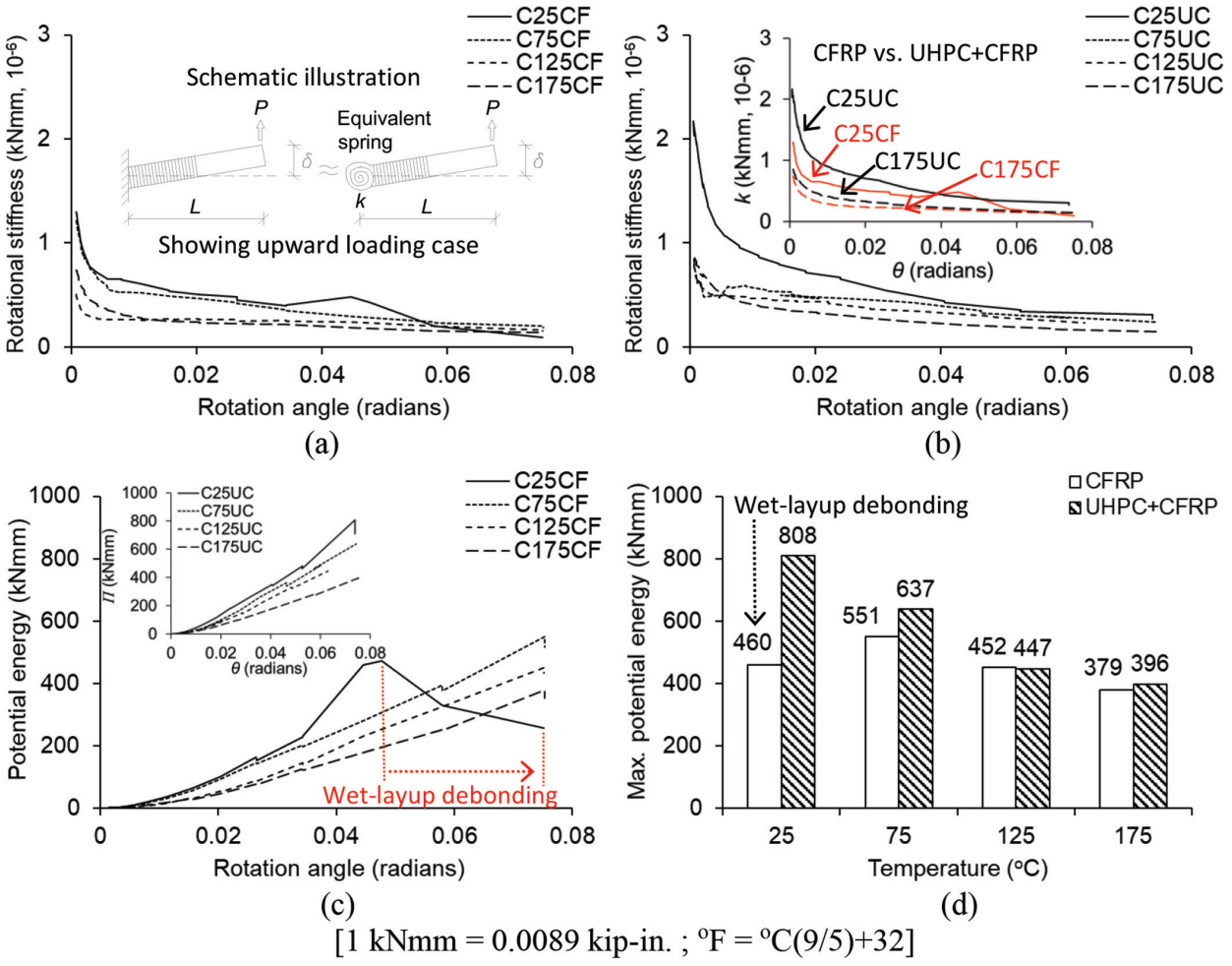


Fig. 12—Single-degree-of-freedom system: (a) rotational stiffness of CF series; (b) rotational stiffness of UC series; (c) potential energy of CF series; and (d) maximum potential energy.

failure. The temperature-dependent variation of the potential energy signifies that the thermal loading controlled the buildup of the internal strain energy linked with the work done by the mechanical load. Besides, the uncertain distinction of the maximum potential energy in the CF and UC series above 125°C (257°F) accentuates the reliance of the retrofit system on the performance of CFRP that was vulnerable to the high temperatures (Fig. 12(d)).

SUMMARY AND CONCLUSIONS

This paper has dealt with the thermomechanical behavior of reinforced concrete beams strengthened with carbon fiber-reinforced polymer (CFRP) sheets and ultra-high-performance concrete (UHPC) jackets. The beams were cyclically tested in a cantilever condition as per the protocol of FEMA 461[39] at elevated temperatures varying from 25 to 175°C (77 to 347°F). After performing ancillary experiments, the hysteretic responses of the retrofitted beams were investigated with a focus on load-deflection relationships, flexural rigidity, energy dissipation, and inelastic failure states. The following are concluded.

- The thermal conductivity of UHPC was over 62% higher than the conductivity of the ordinary concrete. The predicted temperature variation at the interface between the ordinary concrete and UHPC indicated that premature delamination would not occur. The entropy-based inference of UHPC corroborated its adequacy as a retrofit material with low uncertainty.
- The superior load-carrying capacity of the retrofitted beams to that of the unstrengthened beam decreased when applied temperatures exceeded the glass transition temperature of the CFRP sheets. While the synergy of UHPC integrated with CFRP was apparent in flexural resistance, the contributive portion of UHPC and CFRP was 8.8% and 91.2%, respectively, on average.
- On the hysteretic behavior of the retrofitted beams, the thermomechanical loading degraded the stiffness and capacity. An obvious difference was noticed between the loading and unloading curves under cyclic load reversals, including damage propagation and stress release. Elevated temperatures raised the extent of pinching, especially in the post-yield domain of the response loops, which signifies the developed plasticity and redistributed stresses of the load-bearing system.
- Although the characteristic rigidity of all strengthened beams declined owing to the thermal exposure, those with UHPC+CFRP outperformed their CFRP-only counterparts. The amount of energy dissipation leaped

when the inelastic deformation of the beams went beyond a threshold limit. The applied heat altered the beams' energy release patterns from abrupt to gradual.

- The plastic hinge length of 350 mm (13.8 in.) calculated by ACI 440.2R-17[24] was reasonable for the unstrengthened cantilever, showing a cracked region of 80 to 420 mm (3.1 to 16.5 in.) from the support. For the strengthened beams, the plastic hinge formed right outside the retrofit zone with an average pivot length of 85 mm (3.35 in.).
- As defined by simplified single-degree-of-freedom cantilevers, the effects of the thermal distress on rotational stiffness were more detrimental during the beams' early loading stage, and the efficaciousness of UHPC intensified the stiffness.

AUTHOR BIOS

Yail J. Kim, *FACI, is President of the Bridge Engineering Institute, An International Technical Society, and a Professor in the Department of Civil Engineering at the University of Colorado Denver, Denver, CO. He is Chair of ACI Subcommittee 440-I, FRP-Prestressed Concrete; past Chair of ACI Committee 345, Bridge Construction and Preservation; and a member of ACI Committees 342, Evaluation of Concrete Bridges and Bridge Elements; 377, Performance-Based Structural Integrity & Resilience of Concrete Structures; 440, Fiber-Reinforced Polymer Reinforcement; and Joint ACI-ASCE Committee 343, Concrete Bridge Design. He received the ACI Chester Paul Siess Award for Excellence in Structural Research in 2019. His research interests include advanced composite materials for rehabilitation, structural informatics, complex systems, and science-based structural engineering including statistical, interfacial, and quantum physics.*

Ibrahim Bumadian *is a PhD Student in the Department of Civil Engineering at the University of Colorado Denver, where he received his MS in civil engineering in 2014. His research interests include the behavior of constructed structures in corrosive service conditions and the implications of multi-hazard.*

ACKNOWLEDGMENTS

The authors would like to acknowledge financial support from the U.S. Department of Transportation through the Mountain Plains Consortium. Technical contents presented in this paper are based on the opinion of the authors and do not necessarily represent that of others. P.W. Weber at ceEntek donated UHPC mixtures. Proprietary information is not provided to avoid commercialism.

REFERENCES

1. ASCE/SEI 43-05, "Seismic Design Criteria for Structures, Systems, and Components in Nuclear Facilities," American Society of Civil Engineers, Reston, VA, 2005, 81 pp.

2. Huang, S., and Liu, C., "A Computational Framework for Fluid-Structure Interaction with Applications on Stability Evaluation of Breakwater under Combined Tsunami-Earthquake Activity," *Computer-Aided Civil and Infrastructure Engineering*, V. 38, No. 3, 2023, pp. 325-352. doi: 10.1111/mice.12880

3. Argyroudis, S. A., and Mitoulis, S. A., "Vulnerability of Bridges to Individual and Multiple Hazards- Floods and Earthquakes," *Reliability Engineering & System Safety*, V. 210, 2021, p. 107564. doi: 10.1016/j.ress.2021.107564

4. Li, C.; Liu, Y.; and Li, H.-N., "Fragility Assessment and Optimum Design of a Steel-Concrete Frame Structure with Hybrid Energy-Dissipated Devices under Multi-Hazards of Earthquake and Wind," *Engineering Structures*, V. 245, 2021, p. 112878. doi: 10.1016/j.engstruct.2021.112878

5. Badroddin, M., and Chen, Z., "Probabilistic Understanding of Seismic Performance of River-Crossing Bridges with Scour Effects: A Critical Review and Investigation of Seismic-Scour Damage Effects," *International Journal of Civil Engineering*, V. 21, No. 6, 2023, pp. 915-931. doi: 10.1007/s40999-022-00794-1

6. Kamalvand, M.; Massumi, A.; and Homami, P., "Prediction of Post-Fire Seismic Performance of Reinforced Concrete Frames," *Structures*, V. 56, 2023, p. 104874. doi: 10.1016/j.istruc.2023.104874

7. Bruneau, M.; Barbato, M.; Padgett, J. E.; Zaghi, A. E.; Mitrani-Reiser, J.; and Li, Y., "State of the Art of Multihazard Design," *Journal of Structural Engineering*, ASCE, V. 143, No. 10, 2017, p. 03117002. doi: 10.1061/(ASCE)ST.1943-541X.0001893

8. Hain, A.; Zaghi, A.; Padgett, J. E.; and Tafur, A., "Case Studies of Multihazard Damage: Investigation of the Interaction of Hurricane Maria and the January 2020 Earthquake Sequence in Puerto Rico," *Frontiers in Built Environment*, V. 9, 2023, p. 1128573. doi: 10.3389/fbuil.2023.1128573

9. Ghobarah, A.; Saatcioglu, M.; and Nistor, I., "The Impact of the 26 December 2004 Earthquake and Tsunami on Structures and Infrastructure," *Engineering Structures*, V. 28, No. 2, 2006, pp. 312-326. doi: 10.1016/j.engstruct.2005.09.028

10. FEMA P-366, "Hazus® Estimated Annualized Earthquake Losses for the United States," Federal Emergency Management Agency, Washington, DC, 2017.

11. Sengupta, P., and Li, B., "Hysteresis Behavior of Reinforced Concrete Walls," *Journal of Structural Engineering*, ASCE, V. 140, No. 7, 2014, p. 04014030. doi: 10.1061/(ASCE)ST.1943-541X.0000927

12. Pohoryles, D. A.; Bournas, D. A.; Da Porto, F.; Caprino, A.; Santarsiero, G.; and Triantafillou, T., "Integrated Seismic and Energy Retrofitting of Existing Buildings: A State-of-the-Art Review," *Journal of Building Engineering*, V. 61, 2022, p. 105274. doi: 10.1016/j.jobe.2022.105274

13. Cao, X.-Y.; Shen, D.; Feng, D.-C.; Wang, C.-L.; Qu, Z.; and Wu, G., "Seismic Retrofitting of Existing Frame Buildings Through Externally Attached Sub-Structures: State of the Art Review and Future Perspectives," *Journal of Building Engineering*, V. 57, 2022, p. 104904. doi: 10.1016/j.jobe.2022.104904

14. Echeverria, M. J.; Mohammadgholibeyki, N.; Liel, A. B.; and Koliou, M., "Achieving Functional Recovery Through Seismic Retrofit of Existing Buildings: Barriers and Opportunities," *Journal of Performance of Constructed Facilities*, V. 37, No. 4, 2023, p. 04023027. doi: 10.1061/JPCFEV.CFENG-4395

15. Engindeniz, M.; Kahn, L. F.; and Zureick, A.-H., "Repair and Strengthening of Reinforced Concrete Beam-Column Joints: State of the Art," *ACI Structural Journal*, V. 102, No. 2, Mar-Apr. 2005, pp. 187-197.

16. Williams, M. S., and Sexsmith, R. G., "Seismic Damage Indices for Concrete Structures: A State-of-the-Art Review," *Earthquake Spectra*, V. 11, No. 2, 1995, pp. 319-349. doi: 10.1193/1.1585817

17. Ying, F. J.; Wilkinson, S.; and Corner, J., "Challenges to Seismic Rehabilitation Decision Process in New Zealand: A Focus of Decision Environment," *International Journal of Strategic Property Management*, V. 20, No. 3, 2016, pp. 305-315. doi: 10.3846/1648715X.2016.1190419

18. Siddika, A.; Mamun, M. A. A.; Ferdous, W.; and Alyousef, R.,"Performances, Challenges and Opportunities in Strengthening Reinforced Concrete Structures by Using FRPs- A State-of-the-Art Review," *Engineering Failure Analysis*, V. 111, 2020, p. 104480. doi: 10.1016/j.engfailanal.2020.104480

19. Mirdan, D., and Saleh, A. R., "Flexural Performance of Reinforced Concrete (RC) Beam Strengthened by UHPC Layer," *Case Studies in Construction Materials*, V. 17, 2022, p. e01655. doi: 10.1016/j.cscm.2022.e01655

20. Fehling, E.; Schmidt, M.; Walraven, J.; Leutbecher, T.; and Frohlich, S., *Ultra-High Performance Concrete UHPC: Fundamentals, Design, Examples*, Ernst & Sohn, Wiley, Berlin, Germany, 2014.

21. Amran, M.; Huang, S.-S.; Onaizi, A. M.; Makul, N.; Abdelgader, H. S.; and Ozbakkaloglu, T., "Recent Trends in Ultra-High-Performance Concrete (UHPC): Current Status, Challenges, and Future Prospects," *Construction and Building Materials*, V. 352, 2022, p. 129029. doi: 10.1016/j.conbuildmat.2022.129029

22. Shao, Y., Kuo, C.-W., Hung, C.-C., "Seismic Performance of Full-Scale UHPC-Jacket-Strengthened RC Columns Under High Axial Loads," *Engineering Structures*, V. 243, 2021, p. 112657. doi: 10.1016/j.engstruct.2021.112657

23. Zhang, Y.; Yang, J.; Li, T.; and Deng, M., "Mechanical Behavior of RC Columns Strengthened with Thin UHPC Jacket under Cyclic Loads," *Journal of Building Engineering*, V. 49, 2022, p. 104065. doi: 10.1016/j.jobe.2022.104065

24. ACI Committee 440, "Guide for the Design and Construction of Externally Bonded FRP Systems for Strengthening Concrete Structures (ACI 440.2R-17)," American Concrete Institute, Farmington Hills, MI, 2017, 112 pp.

25. Jarrah, M.; Najafabadi, E. P.; Khaneghahi, M. H.; and Oskouei, A. V., "The Effect of Elevated Temperatures on the Tensile Performance of GFRP and CFRP Sheets," *Construction and Building Materials*, V. 190, 2018, pp. 38-52. doi: 10.1016/j.conbuildmat.2018.09.086

26. Beavan, J.; Motagh, M.; Fielding, E. J.; Donnelly, N.; and Collett, D., "Fault Slip Models of the 2010-2011 Canterbury, New Zealand, Earthquakes from Geodetic Data and Observations of Postseismic Ground

Deformation," *New Zealand Journal of Geology and Geophysics*, V. 55, No. 3, 2012, pp. 207-221. doi: 10.1080/00288306.2012.697472

27. Shafaei, H., and Naderpour, H., "Seismic Fragility Evaluation of FRP-Retrofitted RC Frames Subjected to Mainshock-Aftershock Records," *Structures*, V. 27, 2020, pp. 950-961. doi: 10.1016/j.istruc.2020.07.018

28. Dahal, P., and Mullen, C., "Incorporation of Post-Earthquake Fire (PEF) and Subsequent Aftershock for Performance Analysis of Steel Buildings," *Structures*, V. 33, 2021, pp. 3810-3821. doi: 10.1016/j.istruc.2021.06.104

29. *fib*, "Design and use of Externally Bonded Fibre Reinforced Polymer Reinforcement (FRP EBR) for Reinforced Concrete Structures (*fib* Bulletin 14)," federation internationale du beton, Lausanne, Switzerland, 2001.

30. Padgett, J.; DesRoches, R.; Nielson, B.; Yashinsky, M.; Kwon, O.-S.; Burdette, N.; and Tavera, E., "Bridge Damage and Repair Costs from Hurricane Katrina," *Journal of Bridge Engineering*, ASCE, V. 13, No. 1, 2008, pp. 6-14. doi: 10.1061/(ASCE)1084-0702(2008)13:1(6)

31. Bénichou, N.; Mostafaei, H.; Green, M. F.; and Hollingshead, K., "The Impact of Fire on Seismic Resistance of Fibre Reinforced Polymer Strengthened Concrete Structural systems," *Canadian Journal of Civil Engineering*, V. 40, No. 11, 2013, pp. 1044-1049. doi: 10.1139/cjce-2012-0521

32. ASTM C39/C39M-16, "Standard Test Method for Compressive Strength of Cylindrical Concrete Specimens," ASTM International, West Conshohocken, PA, 2016, 3 pp.

33. Adamczyk, W. P.; Pawlak, S.; and Ostrowski, Z., "Determination of Thermal Conductivity of CFRP Composite Materials Using Unconventional Laser Flash Technique," *Measurement*, V. 124, 2018, pp. 147-155. doi: 10.1016/j.measurement.2018.04.022

34. FLIR, "User's Manual FLIR Ex Series," FLIR Systems, Inc., Nashua, NH, 2019.

35. Zhou, H.; Fernando, D.; Torero, J. L.; Torres, J. P.; Maluk, C.; and Emberley, R., "Bond Behavior of CFRP-to-Steel Bonded Joints at Mild Temperatures: Experimental Study," *Journal of Composites for Construction*, ASCE, V. 24, No. 6, 2020, p. 04020070. doi: 10.1061/(ASCE)CC.1943-5614.0001073

36. Jahani, Y.; Baena, M.; Gomez, J.; Barris, C.; and Torres, L., "Experimental Study of the Effect of High Service Temperature on the Flexural Performance of Near-Surface Mounted (NSM) Carbon Fiber-Reinforced Polymer (CFRP)-Strengthened Concrete Beams," *Polymers*, V. 13, No. 6, 2021, p. 920. doi: 10.3390/polym13060920

37. Altunişik, A. C.; Akbulut, Y. E.; Adanur, S.; Kaya, A.; Gunaydin, M.; Mostofi, S.; and Mosallam, A., "Evaluating the High-Temperature Endurance of FRP-Strengthened Concrete Using an Innovative Insulation System: Experimental Investigation," *Journal of Building Engineering*, V. 73, 2023, p. 106444. doi: 10.1016/j.jobe.2023.106444

38. Turkowski, P., "Fire Resistance of Fire-Protected Reinforced Concrete Beams Strengthened with Externally Bonded Reinforcement Carbon Fibre-Reinforced Polymers at the Full Utilisation Degree," *Materials (Basel)*, V. 16, No. 15, 2023, p. 5234. doi: 10.3390/ma16155234

39. FEMA 461, "Interim Testing Protocols for Determining the Seismic Performance Characteristics of Structural and Nonstructural Components," Federal Emergency Management Agency, Washington, DC, 2007.

40. Khan, M., "Factors Affecting the Thermal Properties of Concrete and Applicability of its Prediction Models," *Building and Environment*, V. 37, No. 6, 2002, pp. 607-614. doi: 10.1016/S0360-1323(01)00061-0

41. Neville, A. M., *Properties of Concrete*, Pearson, Essex, UK, 1996.

42. Young, H. D., and Freedman, R. A., *University Physics*, Pearson, London, UK, 2019.

43. Chen, Q.; Zhu, Z.; Ma, R.; Jiang, Z.; Zhang, Y.; and Zhu, H., "Insight Into the Mechanical Performance of the UHPC Repaired Cementitious Composite System After Exposure to High Temperatures," *Materials (Basel)*, V. 14, No. 15, 2021, p. 4095. doi: 10.3390/ma14154095

44. Gould, H., and Tobochnik, J., *Statistical and Thermal Physics with Computer Applications*, Princeton University Press, Princeton, NJ, 2021.

45. Chabay, R. W., and Sherwood, B. A., *Matter and Interactions*, Wiley, Hoboken, NJ, 2015.

46. Kim, K. Y.; Yun, T. S.; and Park, K. P., "Evaluation of Pore Structures and Cracking in Cement Paste Exposed to Elevated Temperatures by X-Ray Computed Tomography," *Cement and Concrete Research*, V. 50, 2013, pp. 34-40. doi: 10.1016/j.cemconres.2013.03.020

47. Wang, D.; Shi, C.; Wu, Z.; Xiao, J.; Huang, Z.; and Fang, Z., "A Review on Ultra-High-Performance Concrete: Part II. Hydration, Microstructure and Properties," *Construction and Building Materials*, V. 96, 2015, pp. 368-377. doi: 10.1016/j.conbuildmat.2015.08.095

48. Lee, J.; Xi, Y.; and Willam, K., "Properties of Concrete After High-Temperature Heating and Cooling," *ACI Materials Journal*, V. 105, No. 4, July-Aug. 2008, pp. 334-341.

49. Zhang, B., "Effects of Moisture Evaporation (Weight Loss) on Fracture Properties of High-Performance Concrete Subjected to High Temperatures," *Fire Safety Journal*, V. 46, No. 8, 2011, pp. 543-549. doi: 10.1016/j.firesaf.2011.07.010

50. Mishra, S., and Ayyub, B. M., "Shannon Entropy for Quantifying Uncertainty and Risk in Economic Disparity," *Risk Analysis*, V. 39, No. 10, 2019, pp. 2160-2181. doi: 10.1111/risa.13313

51. Ghosh, K. K., and Karbhari, V. M., "Use of Infrared Thermography for Quantitative Non-Destructive Evaluation in FRP Strengthened Bridge Systems," *Materials and Structures*, V. 44, No. 1, 2011, pp. 169-185. doi: 10.1617/s11527-010-9617-5

52. Zhang, W.; Tang, Z.; Yang, Y.; Wei, J.; and Stanislav, P., "Mixed-Mode Debonding Behavior Between CFRP Plates and Concrete Under Fatigue Loading," *Journal of Structural Engineering*, ASCE, V. 147, No. 5, 2021, p. 04021055. doi: 10.1061/(ASCE)ST.1943-541X.0003032

53. Baber, T. T., and Noori, M. N., "Random Vibration of Degrading, Pinching Systems," *Journal of Engineering Mechanics*, ASCE, V. 111, No. 8, 1985, pp. 1010-1026. doi: 10.1061/(ASCE)0733-9399(1985)111:8(1010)

54. Yu, J.; Yu, K.; Shang, X.; and Lu, Z., "New Extended Finite Element Method for Pinching Effect in Reinforced Concrete Columns," *ACI Structural Journal*, V. 113, No. 4, July-Aug. 2016, pp. 689-699. doi: 10.14359/51688747

55. Zhuang, Z.; Liu, Z.; and Cui, Y., *Dislocation Mechanisms-Based Crystal Plasticity*, Academic Press, Elsevier, London, UK, 2019.

56. Placidi, L.; Barchiesi, E.; Misra, A.; and Timofeev, D., "Micromechanics-Based Elasto-Plastic–Damage Energy Formulation for Strain Gradient Solids with Granular Microstructure," *Continuum Mechanics and Thermodynamics*, V. 33, No. 5, 2021, pp. 2213-2241. doi: 10.1007/s00161-021-01023-1

57. Wang, B.; Huo, G.; Sun, Y.; and Zheng, S., "Hysteretic Behavior of Steel Reinforced Concrete Columns Based on Damage Analysis," *Applied Sciences (Basel, Switzerland)*, V. 9, No. 4, 2019, p. 687. doi: 10.3390/app9040687

58. Keerthana, K., and Kishen, J. M. C., "Micromechanics of Fracture and Failure in Concrete Under Monotonic and Fatigue Loadings," *Mechanics of Materials*, V. 148, 2020, p. 103490. doi: 10.1016/j.mechmat.2020.103490

59. Zhu, Y.; Hussein, H.; Kumar, A.; and Chen, G., "A Review: Material and Structural Properties of UHPC at Elevated Temperatures or Fire Conditions," *Cement and Concrete Composites*, V. 123, 2021, p. 104212. doi: 10.1016/j.cemconcomp.2021.104212

60. Ahmed, A., and Kodur, V. K. R., "Effect of Bond Degradation on Fire Resistance of FRP-Strengthened Reinforced Concrete Beams," *Composites. Part B, Engineering*, V. 42, No. 2, 2011, pp. 226-237. doi: 10.1016/j.compositesb.2010.11.004

61. Hamad, R. J. A., and Haddad, R. H., and MegatJohari, M. A., "New Anchorage System of Bars to Improve the Mechanical Performance of Post-Heated FRP-Reinforced Concrete Beams," *Construction and Building Materials*, V. 229, 2019, p. 117090. doi: 10.1016/j.conbuildmat.2019.117090

62. Baloch, W. L.; Siad, H.; Lachemi, M.; and Sahmaran, M., "Effect of High Temperatures on Hot-Bonded SCC/ECC and SCC/UHPC Composite Systems," *Construction and Building Materials*, V. 369, 2023, p. 130507. doi: 10.1016/j.conbuildmat.2023.130507

63. Priestly, M. J. N., and Park, R., "Strength and Ductility of Concrete Bridge Columns Under Seismic Loading," *ACI Structural Journal*, V. 84, No. 1, Jan.-Feb. 1987, pp. 61-76.

ACI STRUCTURAL JOURNAL TECHNICAL PAPER

Title No. 121-S79

Effectiveness of Carbon Fiber-Reinforced Polymer Sheets for Torsional Strengthening of Reinforced Concrete Beams

by Yail J. Kim and Abdulaziz Alqurashi

This paper presents the torsional behavior of reinforced concrete beams strengthened with carbon fiber-reinforced polymer (CFRP) sheets. Assorted retrofit schemes are implemented with variable widths and number of single- and double-layer CFRP U-wraps. After loading 27 beams (three unstrengthened and 24 strengthened), test data were collected to investigate the efficacy of those U-wrap configurations. The width and layer of the bonded sheets dominate the capacity of the beams, whereas the number of the U-wraps in the longitudinal direction is an insignificant attribute. Although the CFRP retrofit decreases structural ductility, the placement of the U-wraps impedes stiffness-reduction rates, reduces twist angles, and redistributes torque-induced stresses. The identified characteristic effective shear modulus of the strengthened beams demarcates the pattern of energy drops, which are related to the degree of brittleness in failure. As far as effective strains are concerned, the applicability of existing equations is appraised, and a new expression is proposed through reliability theory and stochastic simulations.

Keywords: carbon fiber-reinforced polymer (CFRP); rehabilitation; strengthening; torsion.

INTRODUCTION

Torsion is deemed a major consideration on many occasions, such as for spandrel beams, canopies, balconies, and curved girders. Depending upon load paths, the transmission of torsional stresses changes appreciably, and, in view of it, equilibrium torsion and compatibility torsion are stipulated in building codes.[1,2] Representative theories accounting for the behavior of reinforced concrete members subjected to a twisting moment are the space truss and the thin-walled tube models.[3] Conforming to a traditional assumption that constituent elements do not interact,[1] the torsional capacity of a beam is computed, and longitudinal reinforcing bars are arrayed with closed stirrups to resist the curvilinear formation of spiral cracks. Torsional deficiency is, however, often problematic as a consequence of excessive live load, accumulated damage, or a combination thereof.[4,5]

Rehabilitation is commonplace to address issues arising from a lack of load-bearing capacities in constructed structures,[6] and practitioners are actively seeking sustainable solutions that can extend the longevity of deficient buildings and bridges. Externally bonded carbon fiber-reinforced polymer (CFRP) composites have gained popularity since the 1990s.[7] Among many benefits, the tailorability of noncorrosive high-strength CFRP sheets suitable to a variety of morphological and physical conditions enables their widespread adoption for upgrading deteriorated members around the globe.[8] In spite of this proven track record, the majority of applications were concerned with flexural, shear, and axial strengthening,[9] while limited endeavors were expended on the topic of torsion. Ameli et al.[10] reported the torsional behavior of reinforced concrete beams strengthened with CFRP sheets. Test parameters involved continuous and discrete fully and U-wrapped CFRP. The beams' capacity was ameliorated by CFRP bonding, whereas theoretical rationales were not well articulated. Hii and Al-Mahaidi[11] prepared solid and hollow beams enclosed by CFRP sheets, and twisting moments were applied. Interactions between the externally bonded sheets and concrete cracking prompted a large scatter in strain readings. Design approaches were reviewed and compared against experimental data, which yielded substantial discrepancies. Deifalla and Ghobarah[12] tested inverted tee beams retrofitted with CFRP sheets under shear-torsion-combined loadings. The stem of the beams was fully covered by CFRP, which was then fastened using threaded steel rods. The mechanical anchorage delayed the premature failure of CFRP and improved the ductility of the beams. Additional research was suggested to better recognize the adequacy of CFRP for torsional retrofit. Supplementary information on the torsion of CFRP-strengthened beams is available in a state-of-the-art article.[13]

As acknowledged previously, little is known about the functionality of CFRP U-wraps for the retrofit of reinforced concrete beams under torsional distress, which demands comprehensive examinations with diverse configurations. This paper deals with an experimental campaign that takes a detailed look at the performance of a strengthening system comprising a series of different U-wrap features: width, number, and thickness. Analytical models are explored to construe laboratory findings and recommend technical guidance.

RESEARCH SIGNIFICANCE

The distortion of a concrete section caused by torque creates rotations and shearing stresses that crack the beam around its longitudinal axis, necessitating the placement of a proper amount of reinforcement. Inadequate torsional stiffness and strength may lead to catastrophic collapses,[4,14,15] which justifies the need for restoring structural conditions from unacceptable to acceptable states. The paucity

ACI Structural Journal, V. 121, No. 5, September 2024.

MS No. S-2023-303.R1, doi: 10.14359/51740867, received March 21, 2024, and reviewed under Institute publication policies. Copyright © 2024, American Concrete Institute. All rights reserved, including the making of copies unless permission is obtained from the copyright proprietors. Pertinent discussion including author's closure, if any, will be published ten months from this journal's date if the discussion is received within four months of the paper's print publication.

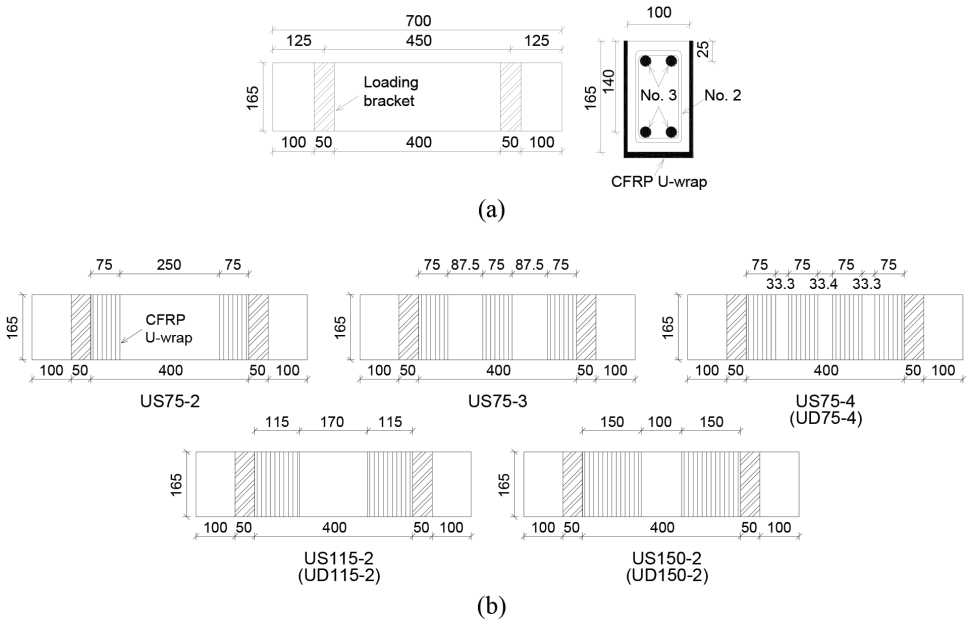


Fig. 1—Beam details: (a) dimensions; and (b) strengthening scheme. (Note: Units in mm; 1 mm = 0.0394 in.)

of research on the torsional retrofit of reinforced concrete members employing CFRP is the source of ambiguous acquaintance in the rehabilitation community; as a result, most specifications do not contain provisions relating to this subject.[9,16] The current work aims to shed light on contemporary engineering practices by definitizing the usability of CFRP U-wraps to accomplish safe, durable, and cost-efficient strengthening strategies.

EXPERIMENTAL PROGRAM

A total of 27 reinforced concrete beams were loaded to torsional failure. Following are descriptions of materials, specimens, strengthening schemes, a test protocol, and instrumentation details.

Materials

The specified compressive strength of concrete was f_c' = 27 MPa (4000 psi), and cylinders tested per ASTM C39/C39M-15[17] showed an average strength of 26 MPa (3800 psi). Two types of reinforcing bars were used: No. 3 reinforcing bars for flexure (d_b = 9.5 mm [0.38 in.], A_s = 71 mm^2 [0.11 in.^{2}], and f_y = 414 MPa [60 ksi], where d_b and A_s are the diameter and cross-sectional area of each bar, respectively, and f_y is the yield strength of the steel) and No. 2 reinforcing bars for shear (d_b = 6.4 mm [0.25 in.], A_s = 32 mm^2 [0.05 in.^{2}], and f_y = 250 MPa [36 ksi]). Both bars possessed an elastic modulus of E_s = 200 GPa (29,000 ksi). Unidirectional CFRP sheets were produced by a wet layup process, in which a continuous carbon fabric layer was impregnated in a two-part epoxy that was mixed with a resin and a hardener at a mass ratio of 3:1. The tensile strength of fully cured CFRP (7 days) was f_{fu} = 3800 MPa (550 ksi), with an elastic modulus of E_f = 227 GPa (33,000 ksi) and an ultimate strain of ε_{fu} = 0.0167, based on an equivalent fiber thickness of t_f = 0.165 mm (0.006 in.). The nominal tensile strength and modulus of the epoxy were f_p = 55 MPa (8000 psi) and E_p = 3 GPa (435 ksi).

Specimens

Twenty-seven rectangular reinforced concrete beams were cast with dimensions of 100 mm (4 in.) wide by 165 mm (6.5 in.) deep by 700 mm (27.5 in.) long (Fig. 1(a)). To resist torsional distress, four No. 3 reinforcing bars were placed at each corner of the beam in the longitudinal direction, closed stirrups with No. 2 reinforcing bars were arranged at spacings of 50 mm (2 in.), and CFRP U-wraps were bonded using the epoxy adhesive (Fig. 1(b)). It is worth noting that the internal reinforcement scheme satisfies the requirements of ACI 318-19,[1] and U-wraps are an archetypal element for torsional strengthening.[13] In compliance with the aforementioned research objectives, test groups were categorized (Table 1 and Fig. 1(b)): CON (unstrengthened control), US (single-layer U-wraps), and UD (double-layer U-wraps). The number of U-wraps varied from two to four, and each category was replicated three times. Accordingly, the identification of the test specimens was designated as follows: the first part indicates the type of strengthening (CON, US, and UD), the second part points out the width of the U-wraps (w_f = 75, 115, and 150 mm [3, 4.5, and 6 in.]), the third part denotes the number of the bonded U-wraps, and the last part marks the number of repetitions. For example, US75-4-1 means a beam was strengthened with a single layer of U-wraps with a width of 75 mm (3 in.) that was bonded at four locations and tested first.

Test setup

A custom-made bracket was fabricated to apply torsional loading (Fig. 2(a)). The bracket was composed of two hollow steel sections (HSS) connected by threaded rods and nuts (Fig. 2(b)). The prepared beams were simply supported on steel supports (Grade = ASTM A36/A36M and yield strength = 250 MPa [36 ksi]), which would allow rotations (Fig. 2(c)), and torque was generated using HSS spreader beams placed in the diagonal direction (Fig. 2(d)). A load cell was situated underneath the actuator, and linear

Table 1—Test specimens

Identification	CFRP strengthening				Ultimate		
	No. of layers	Width, mm	Spacing, mm	Cross-sectional area, mm^2	Load P_u, kN	Torque T_u, kN·m	Rotation angle* q, rad
CON-1	0	—	—	—	30.8	10.2	0.091
CON-2	0	—	—	—	25.9	8.5	0.083
CON-3	0	—	—	—	30.2	10.0	0.070
US75-2-1	1	75	325	25	31.2	10.3	0.058
US75-2-2	1	75	325	25	27.7	9.2	0.070
US75-2-3	1	75	325	25	28.7	9.5	0.062
US75-3-1	1	75	163	25	30.9	10.2	0.058
US75-3-2	1	75	163	25	30.8	10.2	0.063
US75-3-3	1	75	163	25	28.1	9.3	0.077
US75-4-1	1	75	108	25	33.9	11.2	0.068
US75-4-2	1	75	108	25	32.0	10.6	0.071
US75-4-3	1	75	108	25	28.1	9.3	0.064
UD75-4-1	2	75	108	50	28.3	9.3	0.066
UD75-4-2	2	75	108	50	32.0	10.6	0.090
UD75-4-3	2	75	108	50	35.8	11.8	0.045
US115-2-1	1	115	285	38	33.0	10.9	0.037
US115-2-2	1	115	285	38	40.6	13.4	0.065
US115-2-3	1	115	285	38	31.2	10.3	0.032
UD115-2-1	2	115	285	38	32.6	10.8	0.072
UD115-2-2	2	115	285	38	37.8	12.5	0.074
UD115-2-3	2	115	285	38	36.3	12.0	0.074
US150-2-1	1	150	250	50	37.3	12.3	0.033
US150-2-2	1	150	250	50	31.1	10.3	0.082
US150-2-3	1	150	250	50	38.2	12.6	0.033
UD150-2-1	2	150	250	100	41.1	13.6	0.081
UD150-2-2	2	150	250	100	41.3	13.6	0.065
UD150-2-3	2	150	250	100	44.1	14.5	0.078

*Average of rotation angles at both ends of beam.

Note: 1 mm = 0.0394 in.; 1 kN = 0.225 kip; 1 kN·m = 0.738 kip·ft.

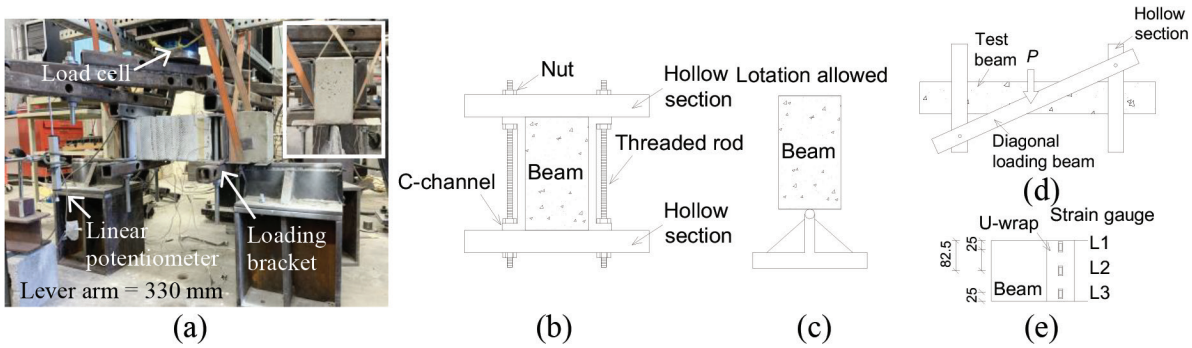


Fig. 2—Test setup: (a) beam; (b) custom-made bracket; (c) beam positioned on top of support; (d) torsional loading; and (e) strain gauges. (Note: Units in mm; 1 mm = 0.0394 in.)

potentiometers were positioned next to the loading brackets to measure torsional angles (angle = displacement/lever arm, Fig. 2(a)). Strain gauges were bonded to the top, middle, and bottom of the U-wraps to monitor the occurrence of local debonding (Fig. 2(e)).

RESULTS AND DISCUSSION

The test results are discussed to study the effectiveness of U-wraps, with an emphasis on the load-carrying capacities, rotational responses, and failure modes of strengthened beams subjected to torsional loading. Subsidiary aspects

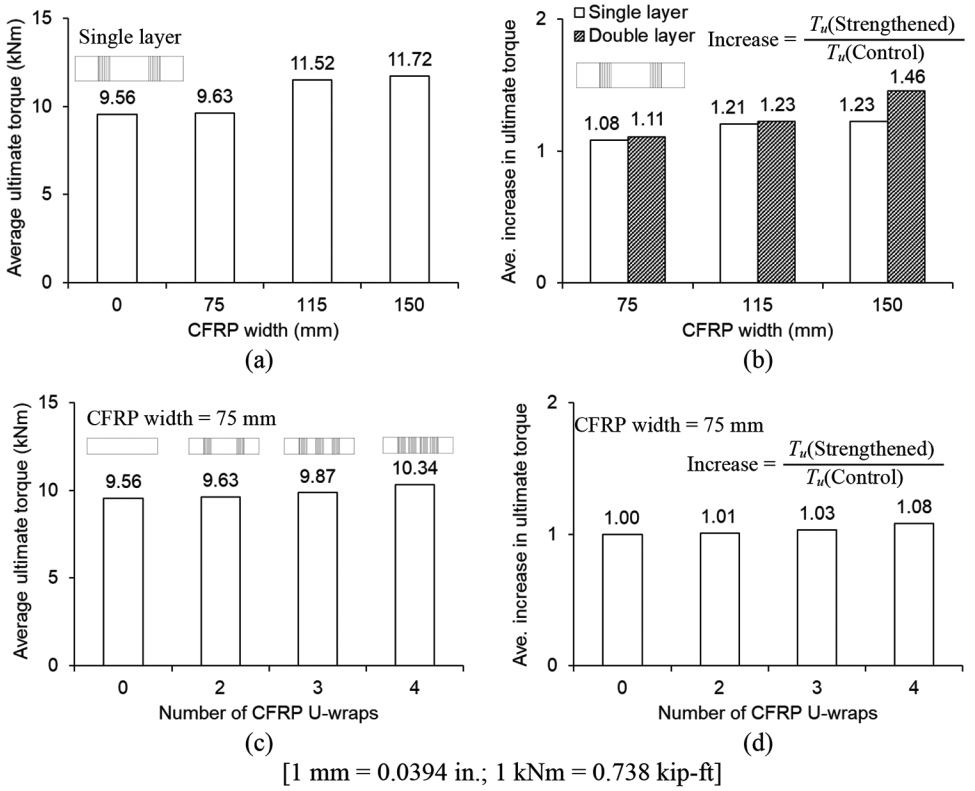


Fig. 3—Average torsional capacity: (a) CFRP width; (b) increase with number of layers; (c) number of U-wraps; and (d) increase with number of U-wraps.

involve resistance against angular twisting, strain energy in connection with applied torques, stress control across concrete sections, and the progression of CFRP strains.

Torsional capacity

Contingent upon the width of the CFRP U-wraps, the ultimate torque (T_u) of the single-layer beams is compared in Fig. 3(a). A negligible difference was noticed between the control and US75-2 beams (0 and 75 mm [0 and 3 in.] widths with T_u = 9.56 and 9.63 kN·m [7.06 and 7.11 kip·ft], respectively). By contrast, there was an obvious increase from a width of 75 to 115 mm (3 to 4.5 in.). These observations adduce that the width of the U-wraps was a crucial attribute affecting the torsional resistance of the strengthened beams. Figure 3(b) displays the implications of the CFRP layers using the ultimate torque of the US and UD categories. From a mechanics standpoint,[18] the double-layer U-wraps increased the shear flow of the strengthened beams along the near-surface perimeter; consequently, the ultimate torque of the UD beams was higher than that of the US beams. This propensity was also a function of the CFRP-covered area: the marginal improvement associated with the widths of 75 and 115 mm (3 and 4.5 in.) drastically changed when the width was enlarged to 150 mm (6 in.). The thickness of the composite sheets should, thus, be taken into account in tandem with the U-wrap width. Unlike the cases of the CFRP width and layers (Fig. 3(a) and (b)), the influence of the U-wrap numbers was minimal (Fig. 3(c)). The average capacity difference of less than 8% between the CON and US75-4 beams (Fig. 3(d)) substantiates that augmenting the number of the U-wraps caused redundancy in torsional strength.

Torsional behavior

Rotation—Figure 4 exhibits the torque-rotation relationship of the test beams. The response of the individual beams was reasonably consistent (Fig. 4(a)), and the change in the initial slopes pointed out the occurrence of torsional cracking. As the applied torque ascended over a typical service level of the control beam (approximately 40 to 50% of the ultimate torques in Fig. 4(a)), a gradual decrease in the stiffness was noted owing to the propagation of the concrete cracks (to be elaborated). Figure 4(b) shows the representative behavior of the strengthened beams, with a focus on the width of the CFRP U-wraps. The progressive stiffness reduction of the CON beam tended to disappear with the broadened U-wrap width, signifying that wide CFRP coverage was beneficial in terms of crack control. The escalated coverage, however, downgraded the overall ductility of the beams: the area under the torque-rotation curves of the CON and US150-2 beams up to the ultimate torques in Fig. 4(b), which characterized the ability of energy dissipation, was 0.6 kN·m·rad (5.3 kip·in.·rad) and 0.2 kN·m·rad (1.8 kip·in.·rad), respectively. The effect of the CFRP layers is given in Fig. 4(c). While the capacity of the double-layer beams was consistently higher than their single-layer counterparts, the rotation angles of the UD series were greater than the angles of the US series. This can be explained by the fact that the interfacial stress between the concrete substrate and the U-wraps, raised by the thickened composite sheets,[19] promoted the shear deformation of the bonding agent and

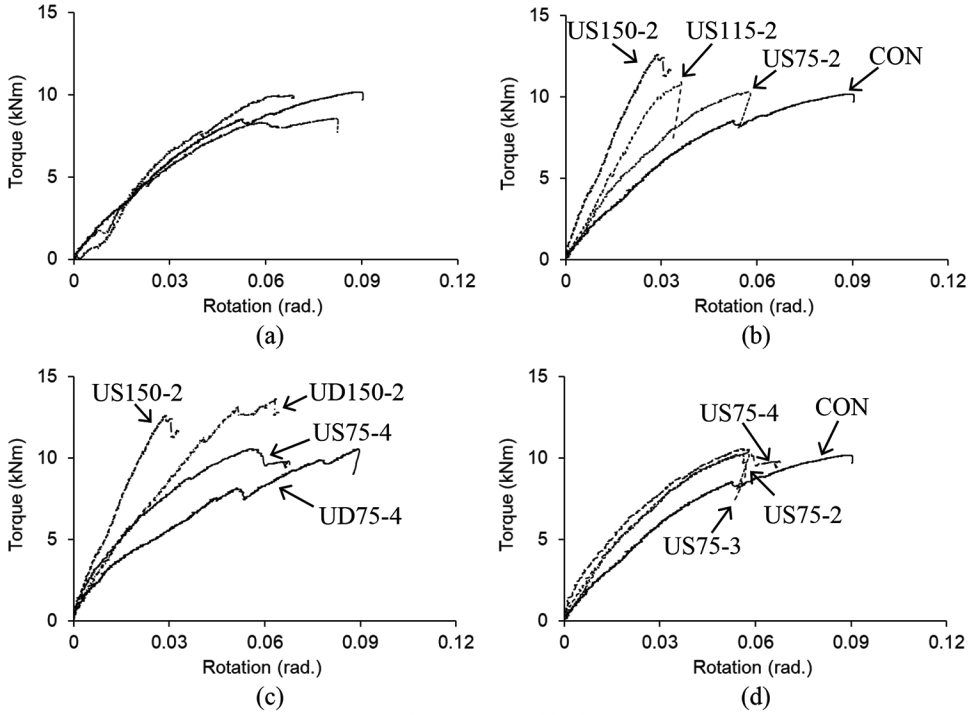


Fig. 4—Torque-rotation relationship: (a) unstrengthened control; (b) CFRP width; (c) number of layers; and (d) number of U-wraps.

facilitated rotations in the strengthened sections. The previously discussed retrofit redundancy was reaffirmed in Fig. 4(d), where the torsional responses of the US75 beams were not reliant upon the number of the U-wraps.

Rigidity—The angular twist of the beams per unit length was calculated using Eq. (1) and is plotted in Fig. 5

$$K = \frac{T}{\theta L} \tag{1}$$

where K is the torsional rigidity required for a unit twist in the loading span L (center-to-center distance between the loading brackets); T is the applied torque; and θ is the twist angle. The torsional rigidity of the control beams was initially erratic due to the sensitivity of the measuring devices, whereas the responses stabilized after the loading brackets were appropriately engaged with the test beams (Fig. 5(a)). Despite some inconsistency within a torque range of $T = 0.5$ to 3 kN·m (4.43 to 26.6 kip·in.) stemming from the early cracking of the concrete, the rigidity of the beams declined by degrees with a torque until failure, which was related to the preceding crack propagation. Figure 5(b) depicts the rigidity of the US75-series beams. Because the increased number of U-wraps constrained the twisting of the strengthened beams, the magnitude and descending trend of the rigidity differed from those of the control (Fig. 5(b), inset). It is worthwhile to note that the variation of the torsional rigidity is concerned with the serviceability of the beams rather than the load-carrying capacities stated previously. Figures 5(c) and (d) demonstrate the average rigidity of the beams in each category. The insignificant disparity between the CON and US75-2 beams at variable torque levels altered with the use of wider U-wraps (Fig. 5(c)). The CFRP sheets of US115-2 and US150-2 sufficiently enveloped torsional cracks that initiated from the loading position; hence, such an appreciable enhancement was recorded. As visible in Fig. 5(d), the U-wrap width was more influential on the torsional rigidity of the strengthened beams than the layers. Because of the elevated shear stresses and interfacial deformations in the double-layer U-wraps, UD75-4 and UD150-2 revealed lower rigidities than US75-4 and US150-2.

Strain energy—The strain energy of the test beams (U) is calculated by

$$U = \frac{T^2 L}{2JG_{eff}} \text{ for } T < T_{cr} \tag{2}$$

$$T_{cr} = k_{cr}\sqrt{f_c'}ab^2 \tag{3}$$

where J and G_{eff} are the polar moment of inertia and the effective shear modulus of the beam, respectively; T_{cr} is the nominal cracking torque of the section[20]; k_{cr} is the torsional constant (k_{cr} = 2 and 0.17 for U.S. customary and metric units, respectively[20]); and a and b are the long and short dimensions of the rectangular beam, respectively. Because the progression of torsional cracks is complex in the out-of-plane direction, the energy of the beams was comparatively examined at a torque just before the cracking of the control beam. The polar moment of inertia may be expressed as[21]

$$J = I_x + I_y \tag{4}$$

where I_x and I_y are the moment of inertia of the beam section about the strong and weak axes, respectively, which are derived from the parallel axis theorem and transformed

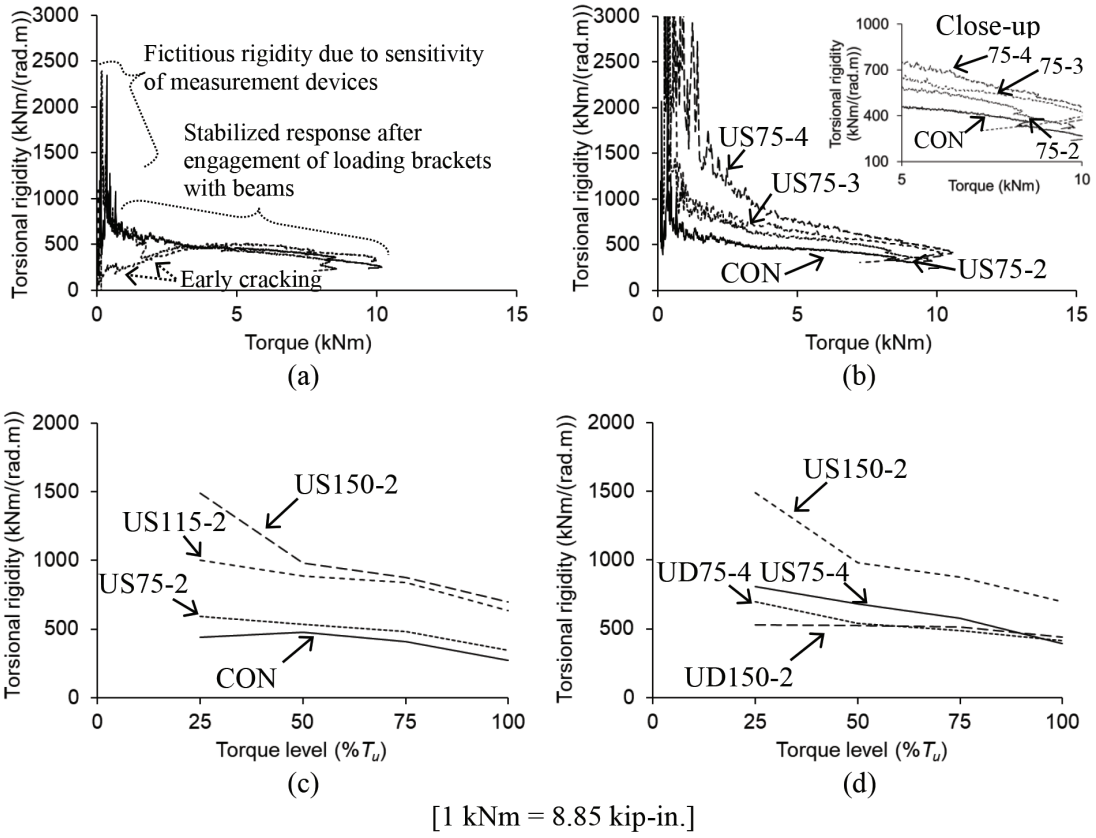


Fig. 5—Torsional rigidity required for unit twist in loading span: (a) control; (b) number of U-wraps; (c) average rigidity with CFRP width; and (d) average rigidity with number of layers.

section theory. The effective shear modulus of the strengthened section (G_{eff}) can be obtained from the theory of elasticity[22]

$$G_{eff} = \frac{T}{\beta a b^3 \theta} \tag{5}$$

where β is a geometric constant (β = 0.219 for the current beam section of a = 165 mm [6.5 in.] and b = 100 mm [4 in.]). Although the geometric constant represents the cross section of a rectangular beam without considering CFRP, strengthening effects are implicitly reflected in Eq. (5) by the twist angle of the strengthened beams (θ).

Figure 6(a) describes the full-range behavior of the effective shear modulus in the UD115-2 category (a similar propensity was found for other categories). As the torsional rotation increased, the effective modulus decreased asymptotically, and the ordinate values corresponding to T_{cr} were located in the transition between the plunging and steady zones. The average effective shear moduli of all beams just before T_{cr} are charted in Fig. 6(b). The moduli of all strengthened beams were higher than that of the control beam, corroborating the efficacy of the retrofit with regard to intensifying torsional resistance against rotation. The increased number of the U-wraps incremented the effective modulus by up to 117.5%: G_{eff} = 5.7 GPa (827 ksi) and 12.4 GPa (1798 ksi) for the CON and US75-4 beams, respectively. Contrarily, the augmented CFRP layers brought down the moduli as low as 35.5%: G_{eff} = 13.8 GPa (2001 ksi) and 8.9 GPa (1290 ksi) for the US150-2 and UD150-2 beams, respectively. As shown in Fig. 6(c), the average strain energy of the beams is dependent upon the configuration of the U-wraps. The retrofit apparently diminished the energy, which is in line with the fact that externally bonded CFRP sheets lessen the energy absorption of a strengthened beam.[9] The relationship between the effective modulus and strain energy of the beams was established by an exponential curve at a coefficient of determination of R^2 = 0.954 (Fig. 6(d)). The characteristic modulus of the beams was then figured out through the application of tangent lines (Fig. 6(d), inset), which divides the pattern of the energy drop into rapid and moderate domains. Practically speaking, when the effective shear modulus of a strengthened beam with U-wraps exceeds G_{eff} = 10 GPa (1450 ksi), its strain energy is expected to be limited; for this reason, the likelihood of brittle failure rises under torsional loading.

Internal stress distribution—The profile of torsional shear stress across the concrete section is rendered in Fig. 7, which was predicted by Timoshenko and Goodier[23]

$$\tau_{yz} = \frac{16 G_c \theta_{cr} a}{\pi^2} \sum_{n=1,3,5..}^{\infty} \frac{1}{n^2} (-1)^{\frac{n-1}{2}} \left[1 - \frac{\cosh(n\pi y/2a)}{\cosh(n\pi b/2a)}\right] \sin\left(\frac{n\pi x}{2a}\right) \tag{6}$$

where τ_{yz} is the shear stress in the y-z plane (Fig. 7(a), inset); G_c is the shear modulus of the concrete ($G_c = E_c/[2(1 + \nu)]$, in which E_c and ν are, respectively, the elastic modulus and Poisson's ratio of the concrete ($E_c = 57{,}000\sqrt{f_c'}$ and 4730

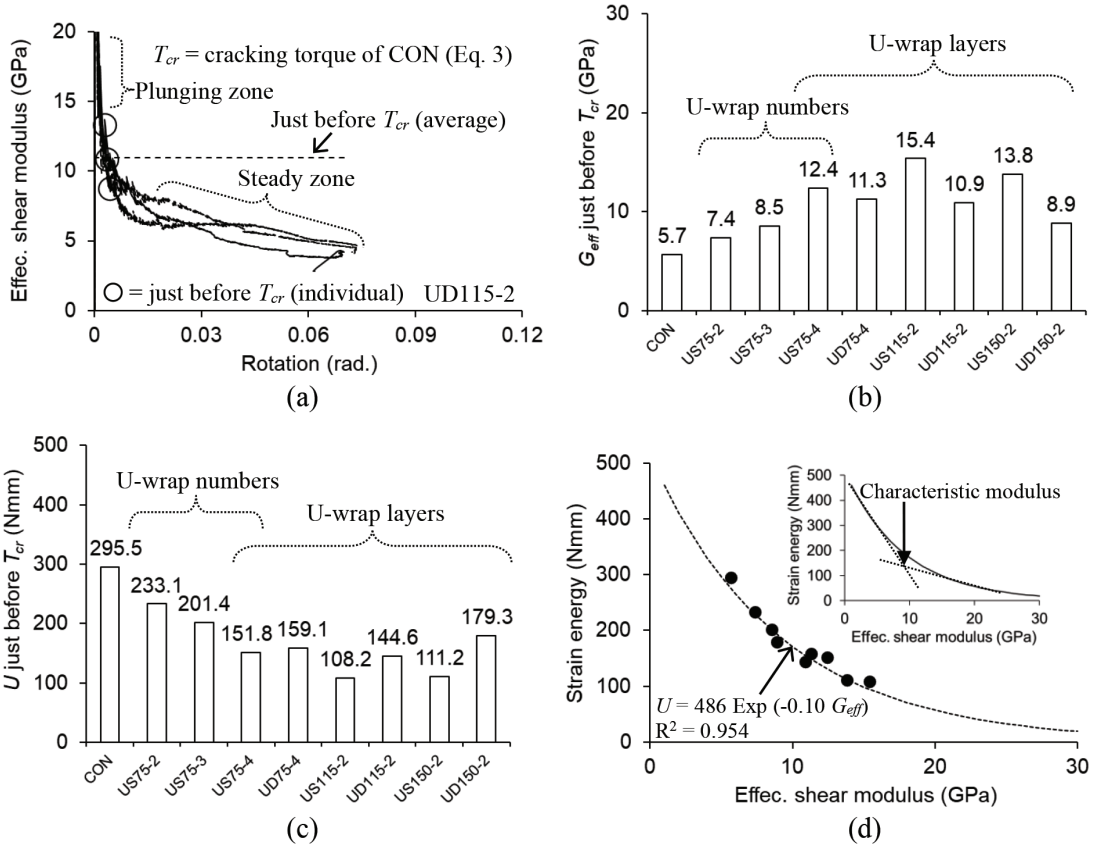


Fig. 6—Strain energy: (a) full-range response of effective shear modulus in UD115-2 beams; (b) average effective shear moduli just before cracking of control beam (T_{ct}); (c) average strain energy just before cracking of control beam (T_{ct}); and (d) relationship between average effective shear moduli and average strain energy.

$\sqrt{f_c'}$ in U.S. customary and metric units, respectively,[1] and v = 0.2)); θ_{cr} is the rotation angle at τ_{cr}; and n is a constant for the series expansion (n = 1 was used for convenience). Because the normalized internal shear stresses across the section in the abscissa and ordinate (τ_{xz} and τ_{yz}, respectively) exhibited the same feature with their maximum values at the edges of the beams (Fig. 7(a)), the normalized ordinate of the test categories was presented to simplify technical investigations. The widened U-wraps scaled down the internal stress, particularly noticeable for US115-2 and US150-2 (Fig. 7(b)). As regards inhibiting the evolution of the stress, the single-layer U-wraps outperformed the double-layer ones (Fig. 7(c)); furthermore, the efficaciousness of confinement was up by increasing the number of the U-wraps along the span (Fig. 7(d)).

Failure mode

The failure modes of the beams are pictured in Fig. 8. The cracks of the control beam formed near the loading bracket and progressed in the direction perpendicular to the principal tensile stresses at an approximate angle of 45 degrees (Fig. 8(a)). The nonplanar development of these cracks resulted in compression struts through which the applied torque was transferred. The uncracked concrete segments resisted part of the twisting stress, and the reinforcement carried the remaining: the dowel action of the longitudinal bars and the axial tension of the stirrups. The reduced number of diagonal cracks in the US75-series beams (Fig. 8(b) to (d)) implies that the U-wraps properly confined the concrete and redistributed the stress outside the retrofitted regions. The plane of the compressive concrete was not normal to the longitudinal reinforcing bars in conformity with the skewed failure surface of the beams (Fig. 8(c) and (d)); as such, internal stresses across the beams were irregularly transmitted to the CFRP-bonded sections. There was a correlation between the U-wrap spacing and crack angle in the US75 series: as the spacing became narrow, the angle was inclined steeply because of spatial constraints. Generally, the torsion-induced cracks emerged in the vicinity of the U-wrap edges owing to stress concentrations at the CFRP termination points (Fig. 8(e) to (i)). Premature concrete crushing did not take place in all strengthened beams.

Development of CFRP strain

Figure 9(a) graphs CFRP strains measured at the three locations on the U-wrap of US75-2. The strain values were similar up to a torque of 4 kN·m (35 kip·in.), beyond which a bifurcation was seen at the middle gauge (L2). This deviation tendency illustrates that diagonal cracks grew with the torque and penetrated the U-wrap through the midheight of the beam; afterward, the cracks were widened by the increased torque and gave rise to the L2 strain. The abruptly varying strain of the bottom gauge (L3) on the verge of the torsional failure at 10.3 kN·m (91.2 kip·in.) was attributable

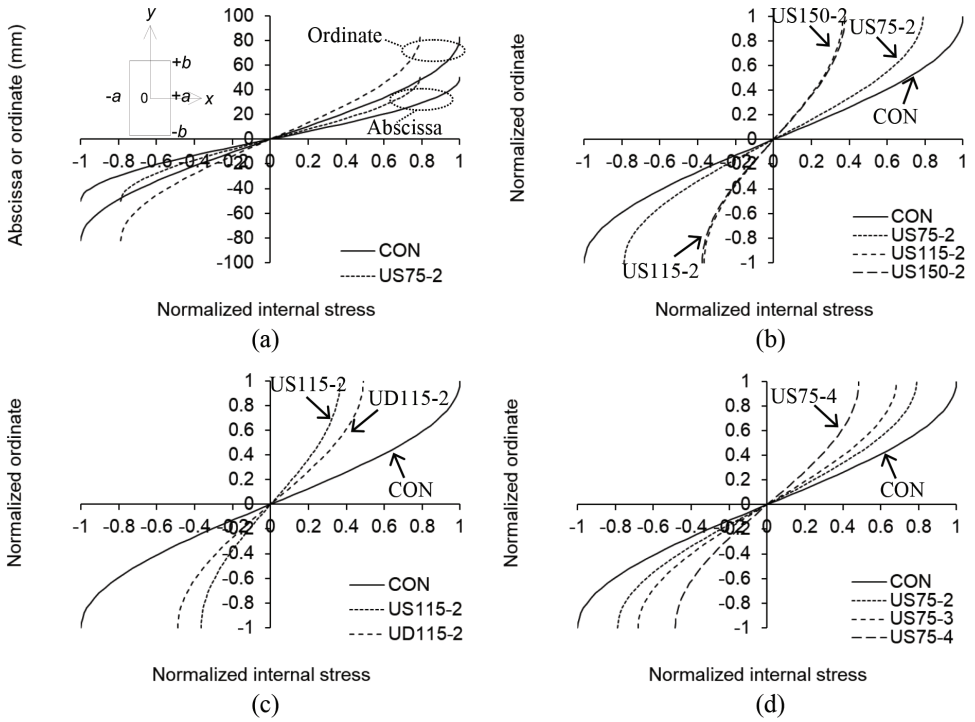


Fig. 7—Torsional stress distribution across concrete section: (a) ordinate versus abscissa; (b) CFRP width; (c) number of layers; and (d) number of U-wraps.

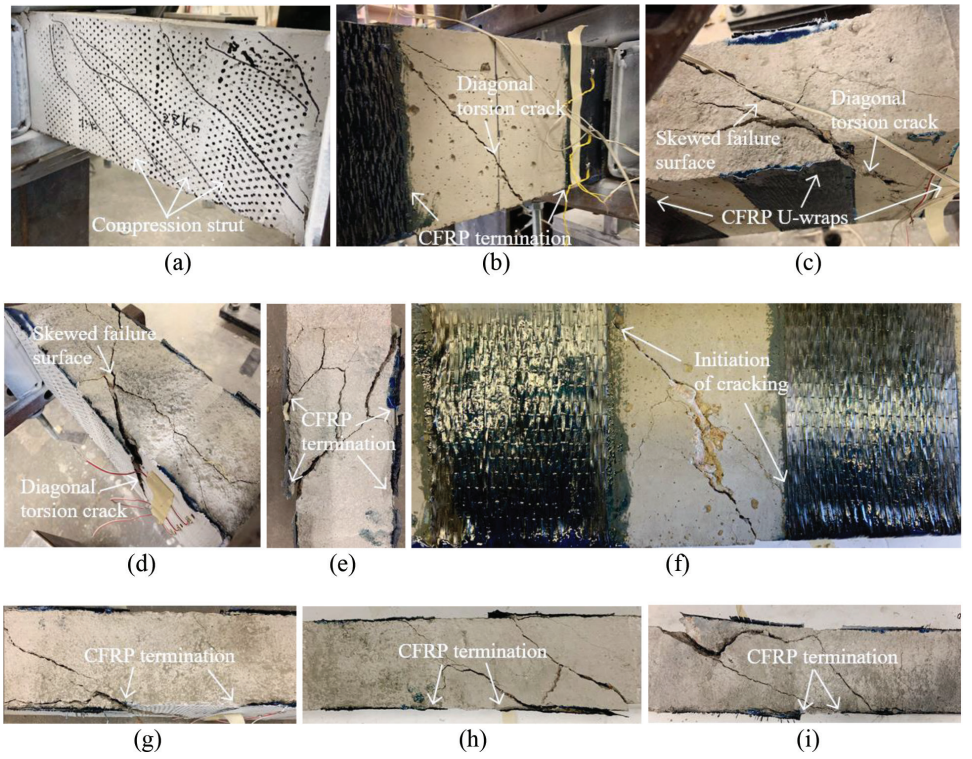


Fig. 8—Failure mode: (a) CON; (b) US75-2; (c) US75-3; (d) US75-4; (e) UD75-4; (f) US115-2; (g) UD115-2; (h) US150-2; and (i) UD150-2.

to the unstable warping of the beam. Knowing the vulnerable location of the U-wrap where local debonding was associated with the enlarged cracks, the strain readings of other beams at the L2 gauge were collated and are compared in Fig. 9(b) to (d). The extended width of CFRP better resisted crack propagation inside the U-wraps, leading to a reduction in the strains (Fig. 9(b)). As mentioned earlier, the double-layer U-wraps allowed more deformations; on that account, the UD beams were prone to showing greater strains than the US beams (Fig. 9(c)). Nonetheless, the former's response

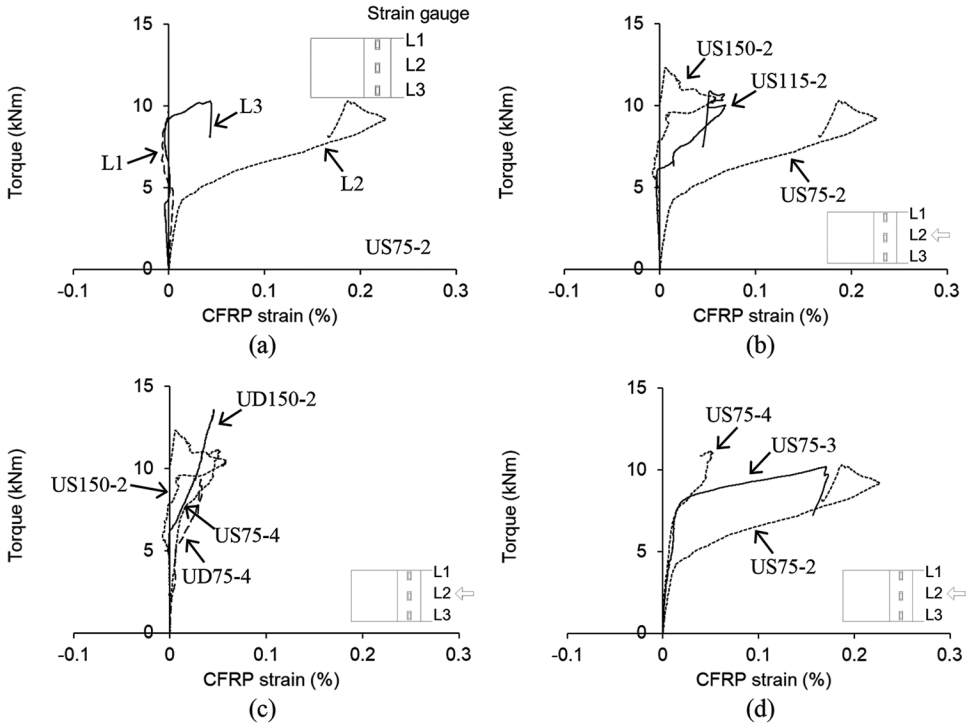


Fig. 9—Development of CFRP strains: (a) vertical direction; (b) CFRP width; (c) number of layers; and (d) number of U-wraps.

appeared steadier due to the dimensional stability resulting from the overlapped CFRP sheets. Regarding the number of the U-wraps (Fig. 9(d)), small discrepancies were logged among the US75-series beams until 4 and 8 kN·m (35 and 70 kip·in.), at which the strains of US75-2 and US75-3 began to diverge from that of US75-4, respectively. The advantage of wrapping concrete along the span was thus apparent in the context of confining the sections with the restrained U-wrap deformations, even if doing so truncated the strain energy of the beams (Fig. 6(c)).

EFFECTIVE CFRP STRAIN

From a design point of view, the maximum usable strains of CFRP should be informed to estimate the torsional resistance of U-wrapped beams. A procedure is explicated in accordance with specification articles, including the evaluation of previously documented methods. By means of functional reliability and stochastic simulations, a new formula is calibrated, and its applicability is delineated.

Formulation

The torsional capacity of the retrofitted beams (T_n) can be written as Eq. (7) in conjunction with constituent terms[1,18,24]

$$T_n = T_c + T_s + T_l + T_f \tag{7}$$

$$T_c = k_1\sqrt{f_c'}\Sigma ab^2 \tag{8}$$

$$T_s = \frac{2A_0A_tf_{yt}}{s}\cot\theta \tag{9}$$

$$T_l = \frac{2A_0A_lf_y}{p_h\cot\theta} \tag{10}$$

where T_c, T_s, T_l, and T_f are the resistance provided by the concrete, stirrups, longitudinal reinforcement, and CFRP sheets, respectively; k_1 is a factor (k_1 = 0.8 and 0.066 for U.S. customary and metric units, respectively); A_0 is the area surrounded by the shear-flow path of the section; A_t and A_l are the cross-sectional area of the single-leg shear and longitudinal reinforcing bars, respectively; and f_{yt}, s, and p_h are the yield strength, spacing, and perimeter of the stirrups, respectively. The resistance of the CFRP-bonded portion may be attained by

$$T_f = \frac{2A_{of}A_fE_f\varepsilon_{fe}}{s_f}\cot\theta \tag{11}$$

where A_{of} is the area enclosed by the shear-flow path in the strengthened section; and A_f, ε_{fe}, and s_f are the cross-sectional area, effective strain, and spacing of the U-wraps, respectively. Given that the A_{of} term of the U-wrapped section is positioned in between the shear-flow-enclosed areas of the unstrengthened and fully wrapped sections, Eq. (12) is proposed, as in the case of a bearing-force transfer through a column-footing assembly where nonuniform stresses are conjoined[1]

$$A_{of} = \psi A_{core} \tag{12}$$

$$\psi = \sqrt{A_g/A_{core}} \tag{13}$$

where A_g and A_{core} are the gross and core areas of the beam section, respectively. The effective strain of CFRP is derived

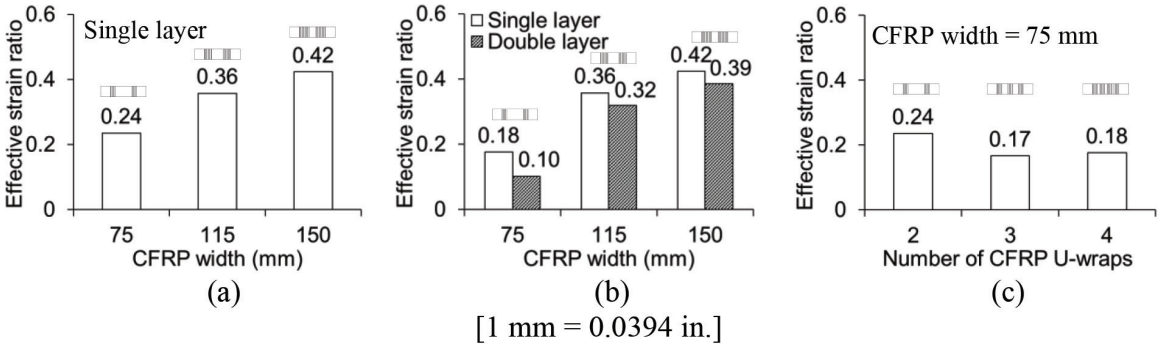


Fig. 10—Effective CFRP strain: (a) CFRP width; (b) number of layers; and (c) number of U-wraps.

by rearranging Eq. (11) with the post-cracking adjustment parameter ($A_{of}' = 0.85A_{of}$)[1]

$$\varepsilon_{fe} = \frac{T_f s_f}{2A_{of}' A_f E_f \cot\theta} \leq \varepsilon_{fu} \tag{14}$$

Implementation

Manipulating the capacities of the experimental beams (T_n, Eq. (7)) and the analytical expressions (Eq. (8) to (14)), the average effective strains of the individual categories were calculated and are shown in Fig. 10. The strain ratio ($\varepsilon_{fe}/\varepsilon_{fu}$) of the US series supports that the normalized usable U-wrap strains at the failure of the strengthened beams were proportionate to the CFRP width (Fig. 10(a)), which was linked with the curbed diagonal cracks. The effectiveness of the retrofit decreased when the U-wraps were double-layered (Fig. 10(b)), and the amount of decrement pertained to the CFRP width: 44.4%, 11.1%, and 7.1% for the 75, 115, and 150 mm (3, 4.5, and 6 in.) U-wraps, respectively. Likewise, the increased number of the U-wraps lowered the usable strain ratios (Fig. 10(c)). These indicate the necessity for refined investigations to clarify the dependency of U-wrap configurations on the torsional upgrade of reinforced concrete beams.

Appraisal

Figure 11 assesses the effective strain expressions proposed by others against the test-based strains employing Eq. (15)

$$Err = \frac{\sum(R_{measured} - R_{predicted})^2}{\sum(R_{measured})^2} \tag{15}$$

where *Err* is the relative error between the measured ($R_{measured}$) and predicted ($R_{predicted}$) values (*Err* = 0: perfect agreement). The *fib* method[25] offered substantially low $\varepsilon_{fe}/\varepsilon_{fu}$, with a relative error of *Err* = 0.7 (Fig. 11(a)). The empirical constants of the *fib* equation, originating from CFRP fracture, were inappropriate for torsional retrofit. The constant effective strain of $\varepsilon_{fe} = 0.003$ in Ghobarah et al.[26] led to a relative error of *Err* = 0.238, which seems to be acceptable for situations with an $\varepsilon_{fe}/\varepsilon_{fu} \leq 0.25$. The Deifalla and Ghobarah[27] equation underestimated the strain ratios in an unsteady manner (Fig. 11(c)), possibly owing to the intricate combination of the property terms in the denominator. The simple Zureick et al.[28] approach given in Fig. 11(d), however, overestimated the ratios on most occasions. Overall, none of the existing expressions furnished satisfactory outcomes concerning the effective strain of CFRP; therefore, an alternative appears to be necessary.

Design recommendation

Sensitivity analysis—The relevance of the constituents in Eq. (14) was studied through reliability theory. To stipulate the workable boundary of the effective strain (ε_{fe}), a performance function (G) was defined as

$$G = \varepsilon_{fe\text{-limit}} - \frac{T_f s_f}{2A_{of}' A_f E_f \cot\theta} \tag{16}$$

where $\varepsilon_{fe\text{-limit}}$ is the limit of the effective strain ($\varepsilon_{fe\text{-limit}} = 0.75\varepsilon_{fu}$, ACI 440.2R-17[9]). The gradients of the performance function (∇G) were obtained with respect to the variables in Eq. (16) for the calculation of a reliability index (β)[29]

$$\beta = \frac{\mu_G}{|(\nabla G)\sigma|} \tag{17}$$

where μ_G is the mean of the performance function; and σ is the standard deviation of the variable. The sensitivity of the performance function with variable i is then computed by[29]

$$\frac{\partial\beta}{\partial\mu_i} = \frac{\partial G / \partial i}{\left|\left(\partial G / \partial i\right)\sigma_i\right|} \tag{18}$$

The quantified sensitivity of the respective parameters is provided in Fig. 12(a). Compared with others, except for the crack angle term ($\cot\theta$) that is generally assumed to be unity (θ = 45 degrees), the geometric properties of the retrofit system were more impactful to the reliability of the performance function: the spacing (s_f) and cross-sectional area (A_f) of the U-wraps were instrumental in configuring a condition that the effective strain of CFRP (ε_{fe}) would exceed the preset threshold of $0.75\varepsilon_{fu}$ under the feasible operating boundaries enumerated in Table 2. It is important to acknowledge that the sensitivity plot does not necessarily impart a sequential order to establish a one-to-one relationship between the parameters and the effective strain, whereas it mathematically identifies those contributory factors to suggest a design

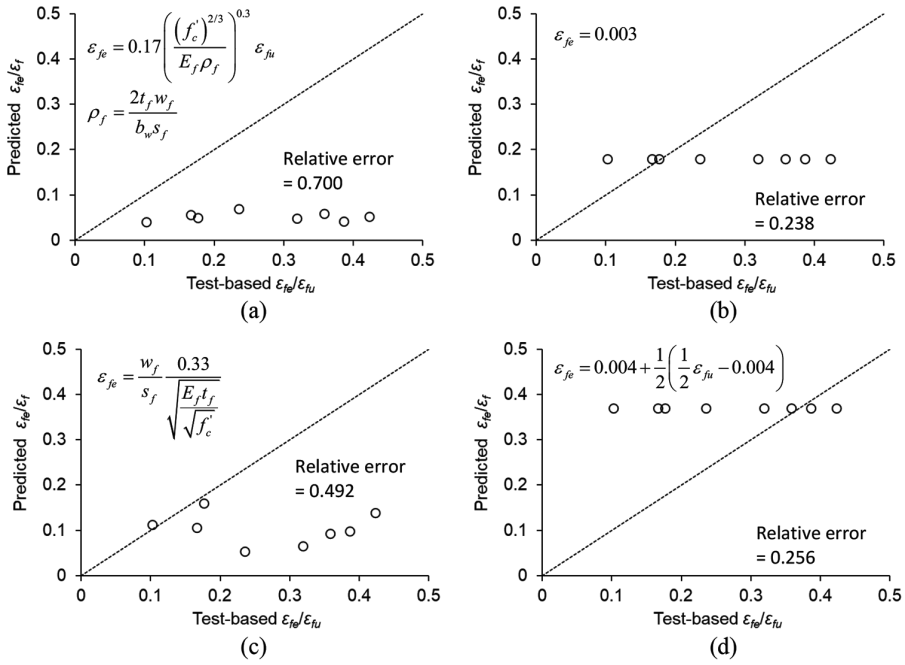


Fig. 11—Appraisal of existing expressions for effective CFRP strain: (a) fib *Bulletin No. 14[25]; (b) Ghobarah et al.[26]; (c) Deifalla and Ghobarah[27]; and (d) Zureick et al.[28]*

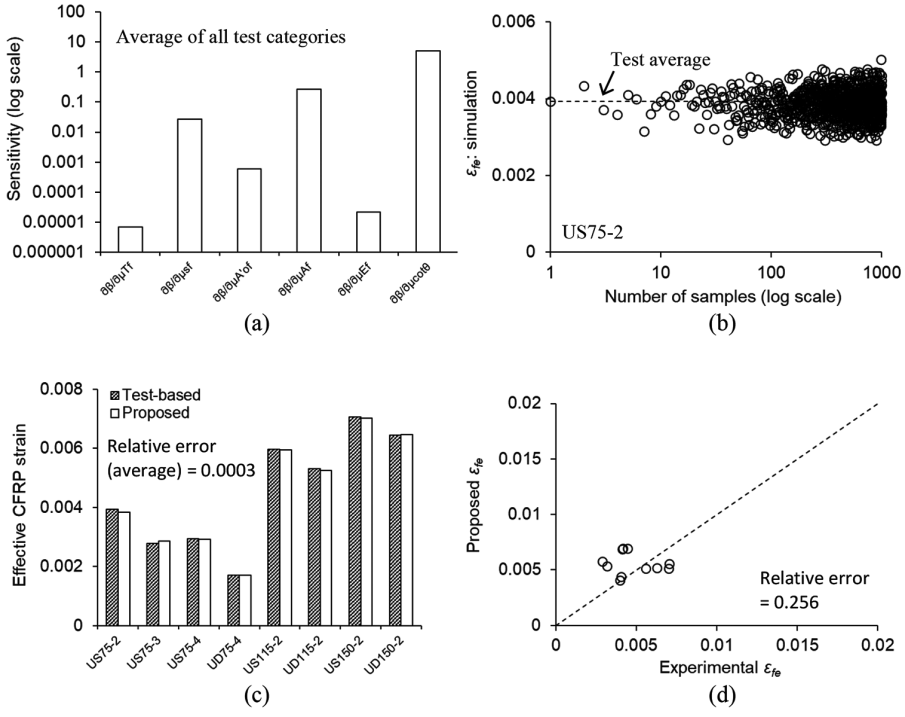


Fig. 12—Design proposal: (a) sensitivity analysis; (b) simulated effective strains of US75-2; (c) comparison between simulated and test-based average effective strains; and (d) assessment against published data.[26,30-32]

proposal. Considering that the torsional resistance of CFRP (T_f) is the consequence of predicting the effective strain and that the adjusted shear-flow area (A_{of}') and the crack angle (cotθ) tied with the conformation of the beams before undertaking torsional strengthening, the remaining parameters in Eq. (14) were confirmed to be crucial for the analytical expression of the effective strain.

Proposal—Notwithstanding the absence of torsional retrofit, ACI 440.2R-17[9] contains a provision on the effective strain of U-wraps for shear, comprising $f_c'^{2/3}$, ε_{fu}, E_f, and t_f. In light of a formational analogy, which also aligns with the findings of the sensitivity analysis, it was decided to revise the *fib* equation instead of devising another formula. To overcome the limitations of the insufficient test data, Monte Carlo simulations were conducted using Eq. (14) alongside the nominal properties and the statistical information listed in Table 2. Subsequently, an optimization technique (generalized reduced gradient[38]) was undertaken based on

Table 2—Statistical properties used for Monte Carlo simulations

Variable	COV	Distribution	Reference
Torsional resistance of CFRP	0.753	Lognormal	Authors
Geometry of beams	0.05	Normal	Okeil et al.[33]
Crack angle	0.179	Lognormal	Zakaria et al.[34]
Geometry of CFRP	0.05	Lognormal	Atadero and Karbhari[35]
Elastic modulus of CFRP	0.05	Normal	Sánchez-Heres et al.[36]
Rupture strain of CFRP	0.09	Normal	Biscaia et al.[37]

Note: COV is coefficient of variation.

numerically generated strains (Fig. 12(b)) to calibrate the empirical constants at the minimum relative errors belonging to all strengthened beams. Figure 12(c) portrays the test-based and proposed effective strains calculated by

$$\varepsilon_{fe} = 0.98\left(\frac{(f_c')^{2/3}}{E_f\rho_f}\right)^{0.34}\varepsilon_{fu} \quad (19)$$

$$\rho_f = \frac{2t_f w_f}{b_w s_f} \quad (20)$$

where b_w is the width of the beam. For an independent evaluation of Eq. (19), effective strains were collected from published experimental programs[26,30-32] and are presented in Fig. 12(d). The degree of prediction was significantly improved at a relative error of $Err = 0.256$ without biased responses (Fig. 11(b) and (d)).

SUMMARY AND CONCLUSIONS

This paper has sought to elucidate the effectiveness of carbon fiber-reinforced polymer (CFRP) sheets for strengthening reinforced concrete beams under torsional loading. A total of 27 beams (three unstrengthened and 24 strengthened) were monotonically loaded to study the ramifications of various retrofit schemes comprising the variable widths and number of U-wraps with single- and double-layer configurations. Of interest were the capacities, angular rotations, and failure modes of the beams, as well as their rigidity, strain energy, and stress distributions. With the aim of updating practice guidelines, attention was paid to the effective strain of CFRP. The following conclusions are drawn:

- The width of the U-wraps played a central role in increasing the torsional capacity of the strengthened beams. The use of double-layer CFRP was beneficial for raising the shear flow of the beams, thereby elevating the capacity; however, the number of the U-wraps along the loading span was not a dominant factor.
- The stiffness of the strengthened beams dwindled with the gradual propagation of diagonal cracks. While the widened U-wraps retarded stiffness-reduction rates, these configurations lessened the ductility of the beams. The presence of the U-wraps upgraded resistance against the angular twist of the beams per unit length, which was especially advantageous when the width was enlarged.
- The increased effective shear modulus of the beams by the retrofit intensified torsional resistance, and a characteristic modulus of 10 GPa (1450 ksi) was found to be a demarcation dividing the pattern of energy drops between rapid and moderate regions, which are related to the brittleness of failure. The internal stress of concrete sections in the U-wrapped beams was lower than the stress in the unstrengthened beams.
- Contrary to the control beams demonstrating multiple diagonal tension cracks, those incorporating U-wraps failed with a reduced number of cracks owing to the redistributed stress of the beam sections. The midheight of the retrofit zone was vulnerable to local debonding, and the level of strain localization was governed by the conformation of the U-wraps.
- The usable strain ratios of CFRP rose as the width of the U-wraps was expanded, whereas an opposite trend was noticed for the case with the increased number of U-wraps. Existing expressions for the effective strain of the bonded sheets showed unacceptable estimations at a relative error of up to 0.70; contrarily, the newly calibrated equation enhanced the degree of predictability at a relative error of 0.26 without skewed responses.

AUTHOR BIOS

Yail J. Kim, *FACI, is President of the Bridge Engineering Institute, An International Technical Society, and a Professor in the Department of Civil Engineering at the University of Colorado Denver, Denver, CO. He is Chair of ACI Subcommittee 440-I, FRP-Prestressed Concrete; past Chair of ACI Committee 345, Bridge Construction and Preservation; and a member of ACI Committees 342, Evaluation of Concrete Bridges and Bridge Elements; 377, Performance-Based Structural Integrity & Resilience of Concrete Structures; and 440, Fiber-Reinforced Polymer Reinforcement; and Joint ACI-ASCE Committee 343, Concrete Bridge Design. He received the ACI Chester Paul Siess Award for Excellence in Structural Research in 2019. His research interests include advanced composite materials for rehabilitation; structural informatics; complex systems; and science-based structural engineering, including statistical, interfacial, and quantum physics.*

Abdulaziz Alqurashi *is a Lecturer in the Department of Civil Engineering at the Islamic University of Madinah, Medina, Saudi Arabia, and a PhD Student in the Department of Civil Engineering at the University of Colorado Denver, where he received his MS in civil engineering in 2015. His research interests include the behavior of concrete structures subjected to unconventional loadings and the application of advanced materials.*

ACKNOWLEDGMENTS

The authors would like to acknowledge financial support from the Saudi Arabian Cultural Mission and the U.S. Department of Transportation through the Mountain-Plains Consortium. Technical contents presented in this paper are based on the opinions of the writers and do not necessarily represent those of others. Proprietary information such as product names and manufacturers was not provided to avoid commercialism.

REFERENCES

1. ACI Committee 318, "Building Code Requirements for Structural Concrete (ACI 318-19) and Commentary (ACI 318R-19) (Reapproved 2022)," American Concrete Institute, Farmington Hills, MI, 2019, 624 pp.

2. *fib*, "*fib* Model Code for Concrete Structures (2020)," International Federation for Structural Concrete, Lausanne, Switzerland, 2023, 780 pp.

3. Lee, J.-Y.; Kim, K.-H.; Lee, S. H.; Kim, C.; and Kim, M.-H., "Maximum Torsional Reinforcement of Reinforced Concrete Beams Subjected to Pure Torsion," *ACI Structural Journal*, V. 115, No. 3, May 2018, pp. 749-760. doi: 10.14359/51701108

4. Etemadi, A., and Balkaya, C., "Collapsed-RC Building Failure Mechanisms with a Forensic Engineering Approach," *Journal of Performance of Constructed Facilities*, ASCE, V. 34, No. 5, Oct. 2020, p. 04020086. doi: 10.1061/(ASCE)CF.1943-5509.0001462

5. Alzabidi, S. M.; Diaa, G.; Abadel, A. A.; Sennah, K.; and Abdalla, H., "Rehabilitation of Reinforced Concrete Beams Subjected to Torsional Load Using Ferrocement," *Case Studies in Construction Materials*, V. 19, Dec. 2023, Article No. e02433. doi: 10.1016/j.cscm.2023.e02433

6. Delgado, J. M. P. Q., ed., *Building Rehabilitation and Sustainable Construction*, Springer, Cham, Switzerland, 2022, 156 pp.

7. Askar, M. K.; Hassan, A. F.; and Al-Kamaki, Y. S. S., "Flexural and Shear Strengthening of Reinforced Concrete Beams Using FRP Composites: A State of the Art," *Case Studies in Construction Materials*, V. 17, Dec. 2022, Article No. e01189. doi: 10.1016/j.cscm.2022.e01189

8. Naser, M. Z.; Hawileh, R. A.; and Abdalla, J. A., "Fiber-Reinforced Polymer Composites in Strengthening Reinforced Concrete Structures: A Critical Review," *Engineering Structures*, V. 198, Nov. 2019, Article No. 109542. doi: 10.1016/j.engstruct.2019.109542

9. ACI Committee 440, "Guide for the Design and Construction of Externally Bonded FRP Systems for Strengthening Concrete Structures (ACI 440.2R-17)," American Concrete Institute, Farmington Hills, MI, 2017, 112 pp.

10. Ameli, M.; Ronagh, H. R.; and Dux, P. F., "Behavior of FRP Strengthened Reinforced Concrete Beams under Torsion," *Journal of Composites for Construction*, ASCE, V. 11, No. 2, Apr. 2007, pp. 192-200. doi: 10.1061/(ASCE)1090-0268(2007)11:2(192)

11. Hii, A. K. Y., and Al-Mahaidi, R., "Torsional Capacity of CFRP Strengthened Reinforced Concrete Beams," *Journal of Composites for Construction*, ASCE, V. 11, No. 1, Feb. 2007, pp. 71-80. doi: 10.1061/(ASCE)1090-0268(2007)11:1(71)

12. Deifalla, A., and Ghobarah, A., "Strengthening RC T-Beams Subjected to Combined Torsion and Shear Using FRP Fabrics: Experimental Study," *Journal of Composites for Construction*, ASCE, V. 14, No. 3, June 2010, pp. 301-311. doi: 10.1061/(ASCE)CC.1943-5614.0000091

13. Alabdulhady, M. Y., and Sneed, L. H., "Torsional Strengthening of Reinforced Concrete Beams with Externally Bonded Composites: A State of the Art Review," *Construction and Building Materials*, V. 205, Apr. 2019, pp. 148-163. doi: 10.1016/j.conbuildmat.2019.01.163

14. Moncarz, P. D.; Hooley, R.; Osteraas, J. D.; and Lahnert, B. J., "Analysis of Stability of L'Ambiance Plaza List-Slab Towers," *Journal of Performance of Constructed Facilities*, ASCE, V. 6, No. 4, Nov. 1992, pp. 232-245. doi: 10.1061/(ASCE)0887-3828(1992)6:4(232)

15. Malomo, D.; Scattarreggia, N.; Orgnoni, A.; Pinho, R.; Moratti, M.; and Calvi, G. M., "Numerical Study on the Collapse of the Morandi Bridge," *Journal of Performance of Constructed Facilities*, ASCE, V. 34, No. 4, Aug. 2020, p. 04020044. doi: 10.1061/(ASCE)CF.1943-5509.0001428

16. AS 5100.8:2017, "Bridge Design, Part 8: Rehabilitation and Strengthening of Existing Bridges," Standards Australia, Sydney, NSW, Australia, 2017, 130 pp.

17. ASTM C39/C39M-15, "Standard Test Method for Compressive Strength of Cylindrical Concrete Specimens," ASTM International, West Conshohocken, PA, 2015, 7 pp.

18. Nawy, E. G., *Reinforced Concrete: A Fundamental Approach*, sixth edition, Pearson, Upper Saddle River, NJ, 2009, 944 pp.

19. Täljsten, B., "Defining Anchor Lengths of Steel and CFRP Plates Bonded to Concrete," *International Journal of Adhesion and Adhesives*, V. 17, No. 4, Nov. 1997, pp. 319-327. doi: 10.1016/S0143-7496(97)00018-3

20. Hsu, T. T. C., "Torsion of Structural Concrete–Plain Concrete Rectangular Sections," *Torsion of Structural Concrete*, ACI SP-18, G. P. Fisher, ed., American Concrete Institute, Farmington Hills, MI, 1968, pp. 203-238.

21. Meriam, J. L.; Kraige, L. G.; and Bolton, J. N., *Engineering Mechanics: Statics*, John Wiley & Sons, Inc., Hoboken, NJ, 2018.

22. Ugural, A. C., and Fenster, S. K., *Advanced Strength and Applied Elasticity*, third edition, Prentice Hall, Upper Saddle River, NJ, 1995, 570 pp.

23. Timoshenko, S. P., and Goodier, J. N., *Theory of Elasticity*, McGraw Hill, New York, NY, 1969, 567 pp.

24. Wight, J. K., and MacGregor, J. G., *Reinforced Concrete: Mechanics and Design*, fifth edition, Prentice Hall, Upper Saddle River, NJ, 2009, 1112 pp.

25. *fib* Task Group 9.3, "Externally Bonded FRP Reinforcement for RC Structures," *fib* Bulletin No. 14, International Federation for Structural Concrete, Lausanne, Switzerland, 2001, 138 pp.

26. Ghobarah, A.; Ghorbel, M. N.; and Chidiac, S. E., "Upgrading Torsional Resistance of Reinforced Concrete Beams Using Fiber-Reinforced Polymer," *Journal of Composites for Construction*, ASCE, V. 6, No. 4, Nov. 2002, pp. 257-263. doi: 10.1061/(ASCE)1090-0268(2002)6:4(257)

27. Deifalla, A., and Ghobarah, A., "Full Torsional Behavior of RC Beams Wrapped with FRP: Analytical Model," *Journal of Composites for Construction*, ASCE, V. 14, No. 3, June 2010, pp. 289-300. doi: 10.1061/(ASCE)CC.1943-5614.0000085

28. Zureick, A.-H.; Ellingwood, B. R.; Nowak, A. S.; Mertz, D. R.; and Triantafillou, T. C., "Recommended Guide Specification for the Design of Externally Bonded FRP Systems for Repair and Strengthening of Concrete Bridge Elements," NCHRP Report 655, National Cooperative Highway Research Program, Transportation Research Board, Washington, DC, 2010, 118 pp.

29. Choi, S.-K.; Grandhi, R. V.; and Canfield, R. A., *Reliability-based Structural Design*, Springer, London, UK, 2007, 306 pp.

30. Higazy, E. M., and El-Kateb, M., "Strengthening of Reinforced Concrete Beams under Torsion Using CFRP Sheets," *Proceedings of the 36th Conference on Our World in Concrete & Structures*, C. T. Tam, K. C. G. Ong, S. Teng, and M. H. Zhang, eds., Singapore, Aug. 2011, pp. 241-248.

31. Ma, S.; Bunnori, N. M.; and Choong, K. K., "Torsional Behaviour of RC Box Beams Strengthened by CFRP under Combined Shear and Torsion," *Proceedings of the Institution of Civil Engineers – Structures and Buildings*, V. 175, No. 12, Dec. 2022, pp. 950-964.

32. Chen, X.; Wang, Z.; Li, X.; Leng, Y.; Harries, K. A.; and Xu, Q., "Torsional Strengthening Using Carbon Fiber Reinforced Polymer of Reinforced Concrete Beams Subject to Combined Bending, Shear and Torsion," *Advances in Structural Engineering*, V. 26, No. 2, Jan. 2023, pp. 272-286. doi: 10.1177/13694332221124624

33. Okeil, A. M.; El-Tawil, S.; and Shahawy, M., "Flexural Reliability of Reinforced Concrete Bridge Girders Strengthened with Carbon Fiber-Reinforced Polymer Laminates," *Journal of Bridge Engineering*, ASCE, V. 7, No. 5, Sept. 2002, pp. 290-299. doi: 10.1061/(ASCE)1084-0702(2002)7:5(290)

34. Zakaria, M.; Ueda, T.; Wu, Z.; and Meng, L., "Experimental Investigation on Shear Cracking Behavior in Reinforced Concrete Beams with Shear Reinforcement," *Journal of Advanced Concrete Technology*, V. 7, No. 1, 2009, pp. 79-96. doi: 10.3151/jact.7.79

35. Atadero, R. A., and Karbhari, V. M., "Calibration of Resistance Factors for Reliability Based Design of Externally-Bonded FRP Composites," *Composites Part B: Engineering*, V. 39, No. 4, June 2008, pp. 665-679. doi: 10.1016/j.compositesb.2007.06.004

36. Sánchez-Heres, L. F.; Ringsberg, J. W.; and Johnson, E., "Influence of Mechanical and Probabilistic Models on the Reliability Estimates of Fibre-Reinforced Cross-Ply Laminates," *Structural Safety*, V. 51, Nov. 2014, pp. 35-46. doi: 10.1016/j.strusafe.2014.06.001

37. Biscaia, H. C.; Chastre, C.; Cruz, D.; and Viegas, A., "Prediction of the Interfacial Performance of CFRP Laminates and Old Timber Bonded Joints with Different Strengthening Techniques," *Composites Part B: Engineering*, V. 108, Jan. 2017, pp. 1-17. doi: 10.1016/j.compositesb.2016.09.097

38. Lasdon, L. S.; Fox, R. L.; and Ratner, M. W., "Nonlinear Optimization Using the Generalized Reduced Gradient Method," National Technical Information Service, Springfield, VA, 1973, 63 pp.

CALL FOR ACTION

ACI Invites You To...

Share your expertise

Do you have EXPERTISE in any of these areas?

- BIM
- Chimneys
- Circular Concrete Structures Prestressed by Wrapping with Wire and Strand
- Circular Concrete Structures Prestressed with Circumferential Tendons
- Concrete Properties
- Demolition
- Deterioration of Concrete in Hydraulic Structures
- Electronic Data Exchange
- Insulating Concrete Forms, Design, and Construction
- Nuclear Reactors, Concrete Components
- Pedestal Water Towers
- Pipe, Cast-in-Place
- Strengthening of Concrete Members
- Sustainability

Then become a REVIEWER for the *ACI Structural Journal* or the *ACI Materials Journal*.

Become a Reviewer for the ACI Journals

How to become a Reviewer:

1. Go to: **http://mc.manuscriptcentral.com/aci**;
2. Click on "Create Account" in the upper right-hand corner; and
3. Enter your E-mail/Name, Address, User ID and Password, and Area(s) of Expertise.

Update your Manuscript Central user account information

Did you know that the database for MANUSCRIPT CENTRAL, our manuscript submission program, is separate from the ACI membership database?

How to update your user account:

1. Go to **http://mc.manuscriptcentral.com/aci**;
2. Log in with your current User ID & Password; and
3. Update your E-mail/Name, Address, User ID and Password, and Area(s) of Expertise.

QUESTIONS?

E-mail any questions to Journals.Manuscripts@concrete.org.

American Concrete Institute

Always advancing

ACI STRUCTURAL JOURNAL

The American Concrete Institute (ACI) is a leading authority and resource worldwide for the development and distribution of consensus-based standards and technical resources, educational programs, and certifications for individuals and organizations involved in concrete design, construction, and materials, who share a commitment to pursuing the best use of concrete.

Individuals interested in the activities of ACI are encouraged to explore the ACI website for membership opportunities, committee activities, and a wide variety of concrete resources. As a volunteer member-driven organization, ACI invites partnerships and welcomes all concrete professionals who wish to be part of a respected, connected, social group that provides an opportunity for professional growth, networking, and enjoyment.



American Concrete Institute